Politecnico di Torino

ScuDo
Scuola di Dottorato ~ Doctoral School
WHAT YOU ARE, TAKES YOU FAR

Department of Mechanical and Aerospace Engineering
Doctoral Program in Mechanical Engineering (38^{th} cycle)

Doctoral Dissertation in
Aerospace Structures and Design (IIND-01/D)

Nonlinear analysis of hyperelastic materials and structures using higher-order finite elements

by:
Piero Chiaia

* * * * *

Supervisors
Prof. Alfonso Pagani, Supervisor
Prof. Matteo Filippi, Co-supervisor

Doctoral Examination Committee:
Prof. Alexander Humer, Referee, Johannes Kepler University Linz
Prof. Vincenzo Gulizzi, Referee, Università degli Studi di Palermo

---

Politecnico di Torino
February 6^{th}, 2026

I hereby declare that, the contents and organisation of this dissertation constitute my own original work and does not compromise in any way the rights of third parties, including those relating to the security of personal data.

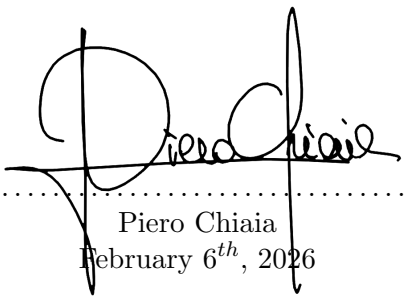

Piero Chiaia
February 6^{th}, 2026

"Mi hai chiesto se una persona comune, studiando tanto, può arrivare a immaginare le cose come le immagino io. Certo! Io ero una persona normale che studiava tanto. Non esistono persone miracolose. Succede solo che si sono interessati a questa cosa e le hanno imparate.

Sono solo persone.

Non esiste un talento speciale, una capacità miracolosa di comprendere la meccanica quantistica o una capacità miracolosa di immaginare il campo elettromagnetico che si ottiene senza la pratica, la lettura, l'apprendimento e lo studio.

Quindi se si prende una persona comune che è disposta a dedicare una grande quantità di tempo allo studio, al lavoro, al pensare e alla matematica, allora diventa uno scienziato."

- Richard Feynman

Summary

In continuum mechanics, hyperelastic materials are used to describe solids that can undergo large elastic and recoverable deformations. These materials are increasingly adopted across multiple engineering fields for their unique mechanical properties, including enhanced flexibility and resilience. In aerospace and mechanical engineering, these materials are adopted in the design of deployable and adaptive structures, such as inflatable components, seals, and damping elements, which must maintain reliability under extreme thermomechanical conditions. In civil engineering, elastomeric bearings and vibration isolators for seismic applications exploit the nonlinear properties of soft materials in dynamic contexts to mitigate seismic and dynamic effects on structures. In particular, hyperelastic materials are widely used in biomedical engineering for modeling soft biological tissues, such as arterial walls, tendons, and ligaments, enabling mechanical characterization for the design and testing of medical implants, prosthetics, and tissue-engineered devices.

The present research is devoted to the development and implementation of refined high-order finite element models for the static, linearized modal, and three-dimensional stress analysis of isotropic and fiber-reinforced hyperelastic structures. The proposed formulation is capable of handling both compressible and nearly incompressible material behaviors, analyzing either the behavior of classical isotropic and multilayered structures, and extending the proposed methodology to the numerical simulations of anisotropic biological tissues. The adopted nonlinear constitutive law is derived within the classical continuum mechanics framework, providing a thermodynamically consistent description of stress–strain relationships under finite deformation. The governing equations of the elasto-dynamic problems at finite strain are derived from variational principles under a Total Lagrangian approach, including classical linearization arguments, and solved using incremental-iterative schemes based on the Newton-Raphson method.

The proposed finite element approach based on higher-order structural modeling is implemented within the well-established Carrera Unified Formulation (CUF), which provides a compact, hierarchical, and efficient framework for structural analysis. The CUF provides a unified formalism for beam, plate, and shell theories of structures, allowing the definitions of the governing equations in matrix form in terms of a few elementary building blocks known as Fundamental Nuclei (FN). This recursive notation allows the straightforward implementation of any refined finite element model, independent of the structural approximation theory adopted, thereby improving flexibility, consistency, and generality. The proposed nonlinear formulation incorporates the full three-dimensional kinematics required for large-strain analysis while maintaining accuracy and computational efficiency. The versatility and robustness of the developed computational framework are demonstrated by performing extensive comparisons with analytical solutions, available numerical results, and experimental data from the literature. Several benchmark problems and case studies are presented, including isotropic and anisotropic beam and plate multilayered structures subjected to finite strain. The results demonstrate the capabilities of the proposed higher-order approach to simulate complex three-dimensional problems in both compressible and

nearly-incompressible incompressible regimes. Overall, the proposed high-order finite element approach provides a novel, efficient computational tool for the nonlinear analysis of hyperelastic materials and structures. This research advances the numerical simulation of soft material structures by relying on physically consistent analyses in engineering design, material characterization, and biomechanics.

Keywords: Hyperelasticity, Beam models, Plate models, Higher-order Finite Element, Biological Tissue, Nonlinear Analysis, Linearized Vibration.

Acknowledgements

First, I would like to extend my deepest gratitude Professor Alfonso Pagani, who, from the very beginning — since meeting me during my Master's thesis — has always shown sincere and immense trust in my abilities, inspiring me with novel and profound research challenges. I am deeply grateful for all the time he has dedicated to me over these years, filled with constructive discussions and invaluable guidance. My warmest thanks go to Professor Maria Cinefra, without whom what I have the pleasure of presenting today would never have existed. I am sincerely grateful for her immense availability and kindness, for accompanying me throughout this PhD journey from afar, yet always by my side with her presence and guidance. I would also like to express my heartfelt appreciation to Professor Matteo Filippi, who has always supported and listened to me throughout this long research path, always showing me with pleasure how much he appreciates my willingness and desire to work together. To Professor Erasmo Carrera, for his invaluable guidance and for the genuine pleasure he has always shown in seeing me at work. His exceptional scientific contribution and the numerous inspirational discussions we shared on research topics have been a constant source of motivation and intellectual growth, encouraging me to explore new perspectives and to pursue excellence in my work.

This research was carried out within the project PRE-ECO: A new paradigm to re-engineering printed composites, funded by the European Research Council under the European Union's Horizon 2020 research and innovation programme (Grant Agreement No. 850437).

Quando ho accettato di intraprendere il mio percorso di dottorato lontano da casa, sapevo che Torino sarebbe stata crudele con me. Un sentito, doveroso, ringraziamento, a tutti coloro che hanno reso Torino una vera seconda casa.

Ai ragazzi dell'Ufficio 29: Marianna, Elisa, Francesca, Martina, Daniele e Shabnam. Ai ragazzi dell'Ufficio 30: Alberto, Dario e Chiara. Al duo di "Miseria e Nobilità"- "Don Giovanni", Karim e Giuseppe, ai nostri posti al tavolo disposti necessariamente nello stesso ordine, al nostro Krinbab e "diavola, provola e cipolla rossa". A Salvatore e Dario, i primi compagni di vita con cui ho avuto il piacere di poter condividere alcuni dei ricordi indimenticabili di questa avventura, tra pranzi, cene e condivisione in ufficio. A Giulio, a colui arrivato come collega di scrivania ma che ben presto è diventato il più importante riferimento di questi anni, alla immensa fortuna di aver potuto condividere gli indelebili momenti tra le nostre affiancate scrivanie e fuori dall'ufficio.

Al “boss” Alessandro Caligola, per il suo aiuto durante la ripresa dal mio infortunio con grande professionalità, creando tanti momenti di spensieratezza durante le sedute di fisioterapia.
A “Burrachino e Gelatino”, Alessandro e Claudio, le mie due colonne portanti torinesi. Alla fortuna immensa di potervi reincontrare e trascorrere questi anni sempre assieme.
Ad Andrea, per avermi accolto qui a Torino con la sua travolgente gioia ed essere ancora qui al mio fianco.
Agli amici più cari, che non hanno mai mancato di farmi sentire il loro calore e la loro vicinanza, alla parte migliore di me: Fabiana, Giada, Alessandro Z., Nicola, Luca, Samuel, Riccardo ed Ignazio.

A mia madre e mio padre. Per tutto quello che, anche loro, hanno affrontato in questi anni col proprio figlio lontano da casa. A quel tentativo di colmare la distanza e farmi sentire costantemente al loro fianco, col loro interesse rivolto a tutti gli aspetti della mia vita, professionale e personale. All’orgoglio che hanno sempre provato nel vedermi crescere e realizzarmi. Alla mia famiglia, per il loro costante interessamento e supporto.

Spero, nel mio piccolo, di avervi anche in minima parte ricambiato di tutto l’affetto che mi avete incondizionatamente donato, e di cui vi sarò per sempre grato.

De remi facemmo ali.

Contents

List of Tables

List of Figures

Chapter 1

Introduction

1.1 Motivation

Hyperelastic materials are a broad class of soft solids characterized by their ability to undergo large elastic deformations without permanent damage [1]. Differently from the classical linear elastic constitutive stress-strain relation, valid only within the hypothesis of small strain [2], the constitutive hyperelastic law is characterized within the framework of extreme, fully recoverable strains, often up to several hundred percent, while fully recovering their original shape and structural configuration during unloading [3]. One of the key features explored by hyperelastic soft materials is incompressibility, thus the capability to change their shape while keeping constant the overall material volume constant. This peculiar behavior arises from their microstructural constitution, typically composed of cross-linked polymer chains or fibrous networks [4], which deform primarily through configurational rearrangements rather than bond rupture [5, 6]. Generally, the material modeling for the mechanical characterization of soft materials, like rubber, requires a multi-scale approach [7]. The internal microstructure of such material plays a crucial role when developing a mathematical theory of large deformations [8]. The interactions between different phases at the meso-scale may determine the macroscopic behavior of the material, including the widely analyzed stiffening and hardening behavior of anisotropic soft materials. Therefore, accurate multi-scale, global-local models for describing the macroscopic behavior of such materials, which involve passing through meso- and micro-scale modeling, remain a challenging mathematical aspect to this day [9].
At the macroscopic level, soft materials are modeled within the general framework of continuum mechanics , following the theory of continuum thermomechanics to directly include mesoscopic information into the constitutive model [5]. This extensive modeling approach enabled researchers and industries to describe and characterize the mechanical properties of these materials, allowing them to exploit their unique features in various engineering fields. In civil and structural engineering, hyperelastic materials are utilized in elastomeric bearings and seismic isolation systems [10], where their ability to sustain large shear strains is leveraged to mitigate the effects of earthquakes on buildings and bridges [11]. Similarly, in mechanical and automotive engineering, components such as tires [12], seals, and gaskets [13] rely on soft matter to combine durability, resilience, and high deformation capacity under complex loading scenarios [14]. The aerospace sector also exploits hyperelastic seals and dampers in environments where reliability under cyclic and large deformations is critical. Beyond these sectors, hyperelastic polymers and foams are widely employed for their nonlinear dynamic properties [15]. In soft robotics, silicone-based elastomers enable the fabrication of compliant actuators [16], artificial muscles,

and bioinspired grippers [17], which exploit hyperelasticity to achieve large shape transformations, adaptability, and safe human–robot interaction [18].

At the same time, one of the scientific fields in which hyperelasticity has been extensively investigated for its most extensive application is the modeling of biological tissues [19]. The capabilities of a constitutive model to correctly capture and describe the full nonlinear and anisotropic deformation behavior of soft materials and structures are essential [20]. The theory of large deformation in a hyperelastic scenario has been extensively investigated in many clinical and anatomic contexts [21]. The strongly nonlinear, anisotropic response closely reproduces the experimentally observed behavior of biological tissues such as arteries [22], myocardium [23], or skin [24], making them indispensable for patient-specific implants or surgical simulations [25]. A representative case of biological tissue constitutive modeling, that has been attracting the attention of researchers over the last few decades, is arterial wall modeling. In the case of cardiac tissues, including arteries and veins, both anisotropy and multi-scale effects must be taken into account in an efficient and accurate constitutive model [26]. A graphical representation of a healthy carotid artery is provided in Fig. 1.1.

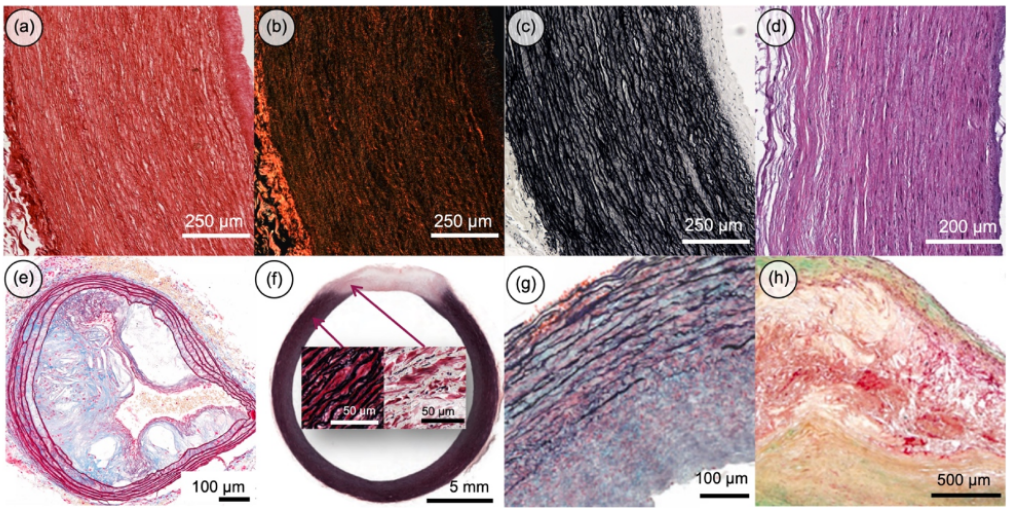

Figure 1.1: Graphical representation of healthy arterial tissue cross-sections. Adapted from [27].

An artery wall can be schematized as a multilayered structure made of three principal layers: intima, media, and adventitia, where different microconstituents of elastic and collagen fibers are embedded and oriented in distinct ways [28]. The intima is the inner layer of the artery, where collagen fibers are not uniformly distributed. The media is the middle layer of the artery, characterized by muscle cells embedding elastic and collagen fibrils. The adventitia, the outer layer, is characterized by a matrix of fibroblasts and fibrocytes embedded with collagen fibers, which contributes to the stability of the arterial wall. In general, from experimental evidences of arterial walls, the arrangement of fiber distributions within the layers makes the adventitia less stiff than the media in stress-free conditions [26]. A graphical representation of an artery and its microstructural configuration is provided in Fig. 1.2. The different mechanical properties of such micro-structural components, as well as the different microstructural arrangements of different sub-components, make the arterial structure a global complex structure where the inclusion of nearly-incompressible material behavior effects and anisotropy becomes fundamental when a constitutive model of an artery has to be proposed [29].

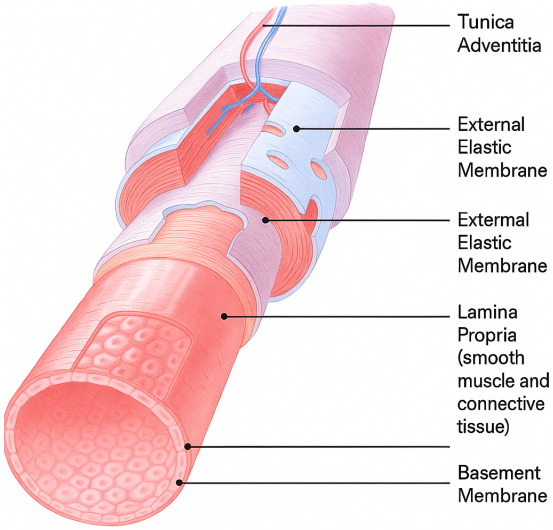

Figure 1.2: Graphical representation of the multilayered constitution of arterial tissue. AI generated, adapted from [29].

From a computational mechanics standpoint, hyperelastic material models have been acquiring increasing interest by researchers and scientists. In particular, due to the complex mathematical framework involved in the derivation of constitutive models, the analysis of such materials and structures typically relies on numerical simulations [30, 31]. More generally, analytical formulations that account for different features, varying from geometry, load conditions, and material features, are available only in a few special cases, due to the complexity of the final, resulting model [32]. For this reason, numerical models have been developed, proposing accurate and efficient tools, required by renewed interest in fluid-structure interaction problems [33], bio-engineering [34], advanced manufacturing processes allowed by the more recent 3D printing approach [35, 36], and innovative material configurations that allowed for the investigations of novel solutions to engineering problems [37], across various fields. These new possibilities, allowed many advances in the modeling framework of hyperelastic soft materials, have permitted to analyze complex, three-dimensional problems in structural health monitoring, novel structural design, and real-time simulations for medical processes and clinical applications [38].
Numerical simulations of biological tissues and hyperelastic soft materials have been extensively conducted within the framework of Finite Element Method (FEM) [39]. Over the years, the formulation of a hyperelastic finite element (FE) has proven a challenging task due to the combined nonlinear effects arising from the capability to undergo large elastic deformations (geometrical nonlinearities) and fully nonlinear stress-strain relationships (material nonlinearities) [40, 41]. Researchers have found many limitations of already available FE procedures when applied to a large strain context, thus innovative and more involved mathematical formulations, based on rigorous treatment of involved physical quantities [42, 43], have been proposed to and alleviate numerical limitations that arise in such nonlinear problems, as particularly observed in nearly-incompressible hyperelastic materials [44, 45]. The main aspect in FE modeling is the locking treatment at large strain. Locking is a numerical phenomenon typically manifesting as artificial stiffening due to spurious stresses or strains not present in the exact analytical problem [46]. These artificial effects arise when physical constraints of material conditions are not accurately represented by the FE formulation adopted. One key example, in hyperelastic FE modeling, is the volumetric locking [47], namely when the FE approach adopted cannot represent the zero

volumetric strain constraint, in a resulting overestimated material stiffness, producing poor convergence and spurious and nonphysical pressure/volumetric stresses [48]. Refined mathematical theories or computationally expensive models are required to accurately describe the complex, three-dimensional displacement, strain, and stress fields [49]. The present work is devoted to the rigorous analysis of the mathematical aspects of hyperelastic soft materials FE formulations, incorporating the constitutive nonlinear behavior for the development of refined, fully nonlinear, higher-order models for the numerical simulation of hyperelastic structures and biological tissues, including anisotropy effects.

1.1.1 Constitutive modeling of anisotropic biological tissues

Soft biological tissues, including arterial walls, ligaments and tendons, or the tympanic membrane (eardrum), exhibit *anisotropic hyperelastic* behavior due to embedded collagen fibers, in a resulting direction-dependent material stiffness. Classical isotropic rubberlike models fail to capture this behavior; thus, specialized constitutive models are needed to relate the internal complex micro-structural to the macroscopic mechanical response [50]. In arteries, for example, collagen fibers in the medial layer are arranged in two symmetric helical families with minimal dispersion, making the tissue stiffer circumferentially. In contrast, the collagen orientations in the adventitia and intima are more widely dispersed [26]. Similar anisotropy is found in other tissues: ligaments and tendons have collagen fibrils predominantly aligned along the primary load direction [51], and the eardrum fibers arrangement is both radial and circumferential across layers [52].
Early pioneering work on soft tissue mechanics is given by Fung [53], which introduced a phenomenological model that fit experimental data with exponential-type strain-energy functions. The pseudoelastic model proposed in an exponential form has been validated using experimental data on different rabbit arteries, enabling a globally accurate description of the material nonlinear behavior when cylindrical coordinates are considered. Other models, based on the Fung-type exponential approach, have been proposed to simulate the classical "J-shaped" stress–strain response of different biological tissues [54]. However, these models often treat anisotropy by adopting global, simplified approaches without explicitly accounting for fiber architecture [55]. In the following, the constitutive models proposed in different biological tissue mathematical modeling are briefly discussed.
Ligaments are specialized bands, made of collagen fibers [56], of dense regular connective tissue that connect bones, whose primary function is to stabilize connecting joints, allowing physiologic motion [57]. Tendons are fibrous connective tissues between skeletal muscles and bones, for mechanical load transmission generated by muscle contraction, to allow motions [58]. They are primarily made of axially-loaded aligned collagen fibers [59] surrounded by an extracellular matrix, in a resulting high tensile strength and effective force transfer, allowing for efficient in energy storage and release during dynamic activities, as during the motion. Available material models for these biological functional tissues are typically limited by the microstructural assumption considered to influence the macroscopic level, or simplified fiber arrangements [60]. Typically, the mechanical behavior of these functional components is described by independently modeling of both the extracellular matrix and the fascicles. A graphical representation of the complex microstructural arrangements of a tendon is provided in Fig. 1.3.
Similar considerations can also be reported in the case of a detailed arterial wall mechanics modeling. From a modeling standpoint, modern constitutive models for anisotropic hyperelasticity arterial wall mechanics decompose the stored strain-energy density into an isotropic part, related to a soft ground-matrix, and one or more anisotropic fiber contributions [61]. The matrix

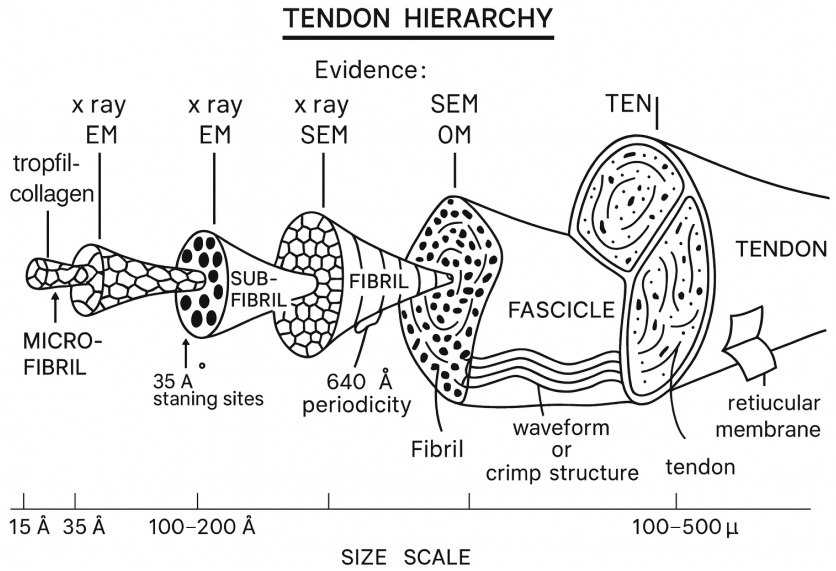

Figure 1.3: Multi-scale hierarchical tendon structure. AI generated, adapted from [59].

(ground substance) is often represented by isotropic models (as the Neo-Hookean model), while the fiber networks are modeled with nonlinear terms that provide stiffening effects when fiber straightening is considered, typically in an exponential form as historically provided by Fung [62]. One of the most commonly adopted models for arteries and veins is the Holzapfel-Gasser-Ogden (HGO) model, introduced in [63], where two families of collagen fibers embedded in an incompressible matrix are assumed. Each fiber family is characterized by a preferred orientation, initially assumed constant and unique. The main limitation of the original proposed model was found in the assumption of perfectly aligned fiber families [63]. From experimental evidences, this assumption has been considered valid only for specific arterial wall, such as the media (the load-carrying component of the arterial wall), in contrast to the case of the adventitia, where collagen fiber orientations are dispersed. A comparison between available preliminary models is discussed in [64]. Moreover, a more detailed analysis of the three-dimensional response of the arterial wall adopting multilayered models has been provided by Holzapfel *et al.* [65]. The proposed results, obtaned considering preliminary models, suggest the need to refine the constitutive model to account for the microstructural features of each arterial wall layer separately. To generalize the HGO model, later work proposed by Gasser *et al.* [26] introduced the concept of statistically dispersed fiber and the *fiber dispersion* parameter, for measuring the statistical distribution of fiber orientations about a mean preferential direction [66]. This evolution of the constitutive law enabled more accurate predictions of arterial mechanical behavior in layers with distributed collagen orientations. A comprehensive review of biomechanics of coronary arteries has been recently provided in [67].

The need for more accurate constitutive models also led to novel research topics in bioengineering, involving, in particular, the incorporation of microstructural modeling within the macroscopic constitutive law. These features have been widely analyzed through theoretical and numerical investigations within the framework of nonlinear anisotropy. Many researchers have devoted numerous studies to the incorporation of fiber reinforcement in a nonlinear constitutive framework. A pioneering work in nonlinear elasticity and the analysis of general fiber networks and arrangements in a hyperelastic scenario is provided by Merodio and Ogden [68], where

the authors proposed a physical interpretation and analysis of the role of anisotropic invariants. Peng *et al.* [69] introduced an anisotropic constitutive model for the detailed analysis of the fiber-matrix interactions for the human annulus, adopting a single quadratic and quartic fiber reinforcement model with a switch contribution, imposing a reinforcement behavior when the fibers are under traction. Pandolfi and Vasta [70] instead proposed the simplified HGO model imposing a Generalized Structural Tensor approach to fiber reinforcement, implementing a statistical distribution approach to define the anisotropic strain energy density. Freed *et al.* proposed an invariant approach for the anisotropic modeling of cardiac tissue for aortic valve applications [71]. Holzapfel *et al.* analyzed the mechanical behavior of the rat arterial wall in a numerical and experimental scenario considering the Fung potential for the material model description [22]. The studies proposed by Mansouri *et al.* [72] analyzed the effects of fiber-matrix interactions, proposing a standard quadratic reinforcement model where an additional pseudoinvariant has been introduced to incorporate the effects of fiber rearrangements due to the applied stretch into the anisotropic part of the strain energy functions. Nolan *et al.* analyzed the effects of the rescaled or total Cauchy-Green strain measure on the hyperelastic anisotropic HGO model, to provide more consistent physical models for anisotropic hyperelastic materials [73].

1.1.2 Constitutive modeling of tension/compression fiber behavior

Constitutive modeling of biological tissues has evolved significantly to capture the key features of such materials under physiological loading conditions [74]. Most soft tissues are composed of a ground matrix reinforced by embedded collagen fibers arranged in specific orientations [75]. A major challenge in modeling is accounting for fiber dispersion, namely the statistical distribution of fiber orientations rather than assuming perfectly aligned fiber families [63]. Recently, Holzapfel *et al.* [19] proposed a comprehensive review regarding the advances in constitutive modeling of such fibrous structures, and discussed the most commonly adopted models in the collagen fiber dispersion modeling.
Many proposed approaches leverage on the experimentally observed asymmetric response of the collagen fibers when loaded in tension and compression. From the practical standpoint, it is considered that collagen fibers are unable to carry any compression load; thus, they do not contribute to the global strain energy when subjected to compression. The exclusion of compressed fiber in the constitutive modeling of such materials remains a challenging research topic to this day. Federico and Gasser [76] proposed the concept of mean average direction for dispersed fiber, including a Heaviside-kind switch function to activate or exclude the compressed fibers but, as stated by the authors, discontinuities in the stress tensor and tangent elasticity tensor are then introduced. Melnik *et al.* [77] adopted the Generalized Structural Tensor (GST) approach for the compressed fiber exclusion, applying the statistical approach to axisymmetric dispersed fibers. Li *et al.* [78] analyzed instead the Angular Integration (AI) approach for excluding fibers under compression in the constitutive modeling of biological tissues. However, it has been shown that the AI approach leads to computationally burdensome models that are not applicable even if realistic [78, 79, 70], thus the GST approach emerges as a more valuable practical approach to simulate biological tissue. Benitez and Montans proposed an extensive review of the proposed model in the literature for the hyperelastic modeling of skin, including anisotropic effects, again adopting the GST and AI approach [80]. More recently, Li *et al.* [81] proposed a novel computational approach, based on the AI excluding method, to develop a numerical approach for achieving accurate 3D fiber dispersion models. In available commercial

software, other simplified procedures have been proposed to exclude compressed fibers, as implemented in the built-in HGO model in ABAQUS commercial software, where the Macauley brackets are exploited. However, it has been demonstrated by Holzapfel *et al.* [82] that the switch function adopted in the ABAQUS model leads to inappropriate results since it is based on the use of the rescaled stretch in the fiber direction and does not penalize the specific stretch contribution of the generalized structural tensor, including also unwanted isotropic effects. Similar considerations have been addressed by Vergori *et al.* [83], where the authors showed that the built-in HGO model does not predict the real physical response of anisotropic hyperelastic spheres in the small strain regime when subjected to hydrostatic pressure. An energetic approach for the analysis of anisotropic hyperelastic media has also been developed by Federico *et al.* [84].

1.1.3 Finite element modeling of hyperelastic structures

The Finite Element Method (FEM) allows the analysis of complex structural problem, by discretizing a continuum into elementary elements defined according to specific kinematic and constitutive assumptions. In this sense, different investigations regarding complex geometries, boundary conditions or material configurations can be carried out without relying on expensive physical tests. Within the framework of classical continuum mechanics, these elements can be one-dimensional (1D) beams, two-dimensional (2D) plates or shells, or three-dimensional (3D) solids. The kinematic formulations of such elements are typically derived from well-established structural theories, such as those proposed by Euler [85] and Timoshenko [86] for beams, and by Love [87], Reissner [88], and Mindlin [89] for plates and shells. While FE models based on these classical theories are computationally efficient, they often yield inaccurate or inconsistent results when applied to nonlinear problems [90]. The most precise approach to solving the governing equilibrium equations generally involves using 3D elements, which directly discretize the unknown field variables without relying on any structural kinematic assumptions. However, the use of 3D elements can be computationally expensive, particularly in the analysis of thin-walled structures or ultra-thin composite laminates. The foundations for a general finite element formulations for large strain analysis of nonlinear elastic materials deal with two main aspects: (i) the complexity of the final, resulting, nonlinear governing equations in the boundary-value problem when finite deformations are considered; (ii) the lack of uniqueness of the constitutive relation when real materials are subjected to large strain, thus many models can be used to represent the same phenomenon [91]. Historically, the development of numerical, finite element models for nonlinear elastic bodies has been analyzed particularly in incompressible elasticity, motivated by the physically observed response of rubber-like materials, the most common example of nonlinear elastic materials [92]. Mathematically, incompressibility manifests itself as a constraint on the space of admissible solutions to the boundary value problem [93].
In the last decades, many numerical approaches for hyperelasticity have been proposed. Ahmadi *et al.* [94] presented a two-dimensional formulation for plain strain problems of compressible structures adopting one- and three-field variational formulations, including the numerical simulations of composites. Alvarez *et al.* [95] proposed a mixed-order interpolation and a 3D hexahedral model to analyze arterial walls. Ansari *et al.* [96] proposed a variational differential quadrature technique for the 3D analysis of compressible materials in a large deformation context. The same mathematical formalism has been adopted by Hassani *et al.* [97], who conducted plain strain analyses of isotropic compressible and nearly incompressible bodies. Velayati *et al.* [98] proposed a three-dimensional model for the free-edge stress analysis of plate hyperelastic structures under bending loads. Balzani *et al.* [99] proposed a quadrilateral shell element for

the numerical simulation of anisotropic fiber reinforced shell using an enhanced strain approach. Firouzi *et al.* [100] analyzed the pure mechanical analysis of thin shells in an anisotropic context using quadrilateral plane stress elements. Hong [101] proposed an inverse Lagrangian approach for the large strain analysis of hyperelastic isotropic bodies. The more recent Virtual Element Method (VEM), introduced by [102], has been adopted by Van Huyssteen *et al.* [103, 45] to investigate locking phenomena and novel procedures in isotropic and transversely isotropic hyperelasticity. Karabelas *et al.* [104] proposed a tetrahedral and hexahedral pure 3D formulation for the finite torsion and bending of hyperelastic beams. Lejeunes *et al.* [105] proposed a 3D FE formulation based on reduction methods for the analysis of a multilayered bearing under compressive and shear loads. [106]. The IsoGeometric Analysis (IGA) framework, adopted in improved shell elements formulations, has also been extended to the hyperelastic material framework. Leonetti *et al.* [106] proposed a hierarchical formulation of shell elements for the finite bending and torsion of compressible and nearly-incompressible curved membranes. Kiendl *et al.* [107] proposed an isogeometric Kirchhoff-Love formulation for the analysis of cardiac valves. The same framework has been exploited by Nitti *et al.* [108] to analyze multi-physics problems involving soft muscular tissues. Additionally, the same framework based on Kirchhoff-Love shell assumption has been exploited by Schulte *et al.* [109]. The multi-physics analysis of soft materials structures has been also conducted by many authors, analyzing the effects of thermal variations or electro-mechanical coupling within dielectric elastomers, as proposed by Hansy-Staudigl *et al.* [110] and Humer *et al.* [111]. Furthermore, Liu *et al.* [112] proposed a curvilinear shell framework for the analysis of inflated curved thin membranes. Pascon *et al.* [113] proposed a plane stress formulation for the large strain analysis of a functionally graded hyperelastic beam. Additionally, the same authors analyzed the same framework to model 2D structures with triangular elements [114]. Nayyar *et al.* [115] analyzed wrinkles in stretched membranes adopting plane-stress formulations. Dadgar-Rad and Sahraee [116] developed a nonlinear formulation for curved hyperelastic beams adopting again plane stress assumptions. Similarly, Hu *et al.* [117] proposed enriched triangular elements for the plane-stress analysis of elastomers. Dadgar-Rad and Firouzi [118] extended the same two-dimensional approach to the analysis of visco-hyperelastic beams. Salamatova *et al.* [119] analyzed instead new strain measures in a two-dimensional plane-stress formulation under finite element formulations. Firouzi and Amabili [120] analyzed the mechanics of growth in soft tissues adopting plane-stress models. Reese *et al.* [121] analyzed the capabilities of 3D brick elements in pneumatic applications for the implementation of through-the-thickness shell integration methods. Suchocki [122] presents an extensive general invariant-based framework for formulating user-defined subroutines in ABAQUS commercial software, analyzing both the implementation of 2D and 3D material models and finite elements. From a computational standpoint, the numerical simulation of materials and structures within the nonlinear domain requires a detailed stress analysis for further investigations. However, particularly within the hyperelastic context, stress components are strongly influenced by the type of load applied (conservative and non-conservative) and the boundary conditions considered; thus, a detailed and rigorous mathematical treatment of the stress tensor involved in the FE approach must be taken into account [123, 124]. The need for accurate models that comprehend all these features is nowadays an active research area, due to the already known limitations of classical FE approaches and involved mathematical derivation procedures.

1.1.4 Refined fully nonlinear unified models

The simulation of nonlinear materials at large strains is a challenging task that requires refined, fully nonlinear models. In this sense, three-dimensional formulations based on classical

3D approaches have been extensively proposed in the literature, as well as 2D plane-strain ones. A complete three-dimensional strain and stress analysis has been proposed adopting simplified models based on cylindrical or polar coordinates, approach the incompressibility modeling exploiting convenient reference frames involved in typical geometries of biological tissues [125].

In the nonlinear finite element scenario, over the last few decades, novel numerical procedures have been proposed within the well-established Carrera Unified Formulation (CUF) framework [126]. The CUF provides a versatile tool for formulating any theory of structure in a hierarchical manner, exploiting a recursive index formalism to rewrite the governing equations in a compact form [127]. The key feature of CUF is given by the implementation of any possible theory of structure, either for beam/plate/shell structures, following the same mathematical formalism. In this sense, therefore, the formalism imposed allows to consider the structural theory as a formal input of the model considered, establishing a direct relation between the axiomatic order of the structural theory and the desired level of accuracy [128]. Leveraging on this modeling strategy, the CUF has been utilized to develop refined, fully nonlinear finite elements for 1D beam and 2D plate/shell structures with three-dimensional capabilities. From a governing equations point of view, the recursive and hierarchical form of the physical quantities defined in the CUF formalism permits the definition of elementary building blocks of the model, the so-called Fundamental Nuclei (FN), by which pure displacement-based FE models are straightforwardly established [129]. Following this approach, FE procedures independent of the mathematical theory adopted in the element definition are directly implemented without any loss of generality [129]. The capabilities of the proposed approach have also been demonstrated in the last decade, also in the field of nonlinear analysis of structures. The pioneering work of Pagani and Carrera [130] for the geometrically nonlinear analysis of beam structures, Carrera *et al.* [131] for the large displacement and post-buckling analysis of plate structures, and Wu *et al.* [132] for the large displacement analysis of 2D shell structures has demonstrated the capabilities of the CUF framework within the context of geometrically nonlinear analysis of thin-walled or compact isotropic and multilayered structures. Additionally, the same approach has been exploited within various engineering fields, demonstrating the consistency of the CUF approach in the definition of higher-order, fully nonlinear models. In the context of higher-order theory of structures for geometrically nonlinear problems, the present formulation has been applied to the accurate modeling of thin walled structures [133, 134, 135, 136], nonlinear rotordynamic analysis [137, 138, 139], progressive failure analysis [140, 141], as well as application to multiphysics problems [142, 143, 144, 145]. The extensive literature available on higher-order CUF models makes the proposed approach a versatile and appealing numerical tool to analyze soft material structures, at large strain, exploiting the three-dimensional capabilities of the proposed higher-order modeling of structures.

1.2 Objectives and outline

The accurate prediction of the nonlinear response of advanced biological systems requires the development of robust theoretical and computational frameworks. Traditional finite element are often limited, in terms of accuracy and efficiency, when nonlinear anisotropic constitutive laws are included. Additionally, the inclusion of the incompressibility constraint, which is essential, leads to computationally expensive models or involved mathematical formulations when large deformations are accounted for.

In this perspective, the present thesis proposes the implementation of a novel finite element formulation for hyperelasticity, within the well-established Carrera Unified Formulation (CUF).

The adoption of the CUF formalism allows for the straightforward implementation of invariant-based hyperelastic approaches within a FE procedure, exploring the higher-order modeling of the theory of structure approximation, in an resulting enrichment of the structural kinematics within the element definition accounting for three-dimensional capabilities. On this foundation, the existing modeling framework is now extended to the nonlinear analysis of isotropic and anisotropic hyperelastic materials at large strains, with a particular focus on biological-like structure systems.
This thesis proposes the extension of the unified formalism for beam and plate theories and their finite element implementation, within the framework of hyperelasticity. The nonlinear governing equations are formulated independently of the discretization model and the adopted hyperelastic strain energy function constitutive assumptions. The exploited formulation allows for the definition of numerical models with enhanced robustness and efficiency, as demonstrated also within the field of strongly nonlinear problems. Consistent physical quantities within the numerical framework are derived following classical continuum mechanics arguments, thus closed-form analytical expressions of stress tensors, kinematic measures, and linearized physical quantities are derived independently of the chosen constitutive law. In this way, consistency and straightforward implementation across different hyperelastic models are guaranteed.

The objective of this research is twofold: (i) to advance the theoretical foundations of hyperelastic modeling through CUF-based finite element formulations and unified approaches, exploiting the unified approach to formulate hyperelastic finite elements based on higher-order beam and plate theories of structures; (ii) to provide practical numerical tools that enable accurate nonlinear analyses of isotropic and anisotropic structures, proposing a numerical framework for the simulation of the pure mechanical behavior of biological tissues.
The present thesis is divided into several chapters, each devoted to a specific aspect of the mathematical framework of continuum mechanics for hyperelasticity, the unified formulation of beam and plate theories, and the formulation of the present higher-order finite element methodology for anisotropic nonlinear materials and structures. The numerical simulations carried out in the fields of isotropic, transversely isotropic, and orthotropic hyperelasticity are extensively analyzed, listing the key findings and main conclusions.

1. Chapter 2 introduces the kinematics concepts, focusing on the kinematics descriptors adopted in the definition of a continuum body motion. The strain and rotation measures adopted in the following work. Moreover, the stress measures and balance principles in the material and spatial reference frames are introduced;

2. Chapter 3 introduces the hyperelastic continuum mechanics framework. The strain energy function approach to hyperelasticity and the nonlinear constitutive relations are presented in an invariant formulation. The constitutive modeling of compressible and nearly-incompressible isotropic and anisotropic materials is presented, deriving the expression of stress tensors and consistent linearized tangent elasticity tensor under different formulations.

3. Chapter 4 introduces the adopted framework for higher-order one-dimensional (1D) and two-dimensional (2D) formulation of beam and plate theories. The proposed approach is formulated under the CUF formalism, introducing the structural kinematics as a generic polynomial expansion of the generalized displacement components along the beam cross-section or plate thickness. In the work, both Taylor expansion models (TE models) and Lagrange expansion models (LE models) will be employed to describe the kinematics of beam cross-sections or plate thickness. In this sense, Equivalent-Single-Layer (ESL) models

and Layer-Wise (LW) or Component-Wise (CW) modeling approaches are introduced. The description of the two proposed approaches is provided in this chapter, along with a detailed list of literature references.

4. Chapter 5 introduces the proposed finite element implementation developed in this thesis. Starting from the definition of higher-order beam and plate models, the nonlinear governing equations defined by variational principles are rewritten in matrix form, introducing all the physical quantities in the CUF domain. In this way, the Fundamental Nuclei (FN) are introduced, rewriting the governing equations under the hierarchical and recursive notation, independent of the kinematic models adopted along the reference directions and theory of structure approximations imposed.

5. Chapter 6 provides the numerical schemes adopted for the iterative solution of a nonlinear algebraic system of equations. In this chapter, both the classical load control procedure and the modified path-following method based on the Crisfield line-search methods are fully described.

6. Chapter 7 discusses the numerical results obtained in the numerical simulation of isotropic hyperelastic materials. The refined, fully nonlinear 1D and 2D CUF models are validated against reference solutions, such as analytical or numerical solutions obtained via commercial software. Specifically, the uniaxial and simple shear tension tests are performed to validate the proposed approach. Then, the static and linearized vibration analysis of slender, thin-walled, or compact thick beams is then performed to assess the capabilities of the CUF models in cases involving large strain problems. Finally, the capabilities of the present modeling approaches are also investigated considering the static and linearized analysis of a multilayered nearly-incompressible plate. The results demonstrate the robustness and the accuracy of the present higher-order modeling approach in isotropic hyperelasticity.

7. Chapter 8 discusses the numerical results obtained in the numerical simulation of transversely hyperelastic materials. The refined, fully nonlinear 1D and 2D CUF models are validated against available analytical solutions in the case of a simple shear tension test. Subsequently, the proposed methodology has been applied to the static and linearized vibration analysis of circular fiber reinforced plates, multilayered compressible and nearly incompressible beams, analyzing the effects of kinematics models and theory of structure approximation on the mechanical performance of different compressible and nearly-incompressible soft structures under large strain and displacement conditions. Thanks to the adoption of a higher-order theory of structures, local effects and complex modal phenomena are analyzed with enhanced accuracy compared to classical 3D FE formulations.

8. Chapter 9 discusses the numerical results obtained in the numerical simulation of biological tissues. The validated nonlinear 1D and 2D CUF models are adopted here for the numerical simulation of biological systems, such as veins and arteries, incorporating anisotropic effects in the constitutive modeling. The proposed approach is validated considering reference solutions obtained by analytical models or available literature results. The effects of fiber reinforcement and fiber dispersion, as well as other anisotropic effects, are investigated using higher-order FE models in the context of large-strain problems or linearized modal behavior along non-trivial equilibrium states.

9. Chapter 10 presents the discussion of the general conclusions of the work, highlighting

the most important outcomes of the present work, proposing also the future applications arising from the present model.

10. Appendix A provides the detailed list of published journal articles and conference proceedings, resulting from the present work.

11. Appendix B provides the analytic, closed form expression found for the orthotropic elasticity tensor, derived for further manipulations and investigations during the present work, whose expression is extensively used in the numerical modeling of hyperelastic materials.

12. Appendix C provides the implementation of variable-kinematics finite element models for the geometrically nonlinear analysis of complex structures, preliminary framework developed within the context of the present work for future developments in large strain analysis of complex hyperelastic structures.

Chapter 2

Kinematics

2.1 Continuum body

2.1.1 Motion

In the classical continuum mechanics framework, a macroscopic system is identified with the concept of a *continuum body*, namely a closed volume in Euclidean space with a continuous distribution of matter in space and time. The body is then imagined as a collection of *continuum particles*, in such a way that physical quantities, such as mass and volume, can be measured with continuous functions. To introduce the concept of a continuum body, the concept of a *simple* body is generally used as a starting point.

A *simple* body is defined as an open subset of the Euclidean space $\mathcal{B} \subset \mathbb{R}^3$. A *configuration* of the body, instead, is defined as the mapping $\phi : \mathcal{B} \to \mathbb{R}^3$. The concept of configuration is related to the actual state of the body at a generic time frame. In general, during the evolution of the body, one can describe each evolved state, in space and time, of the deformed body by considering the collection of all possible configurations described by the mapping ϕ [146].

The material particles $\mathbf{P} \in \mathcal{B}$ of the simple body are the basic elements to describe each possible configuration of the body at each time instant, thus $\phi = \phi(\mathbf{P}, t)$. At the *initial* time, typically considered $t = 0$, the *reference* or *material* configuration $\boldsymbol{\Omega}_0$ of the body is obtained considering $\phi_0 : \mathcal{B} \to \boldsymbol{\Omega}_0 \subset \mathbb{R}^3$ [146]. Introducing the Cartesian reference frame $(\mathbf{E}_1, \mathbf{E}_2, \mathbf{E}_3)$, called *material* reference frame, for each point of $\boldsymbol{\Omega}_0$ the material particles are uniquely identified with the position vector $\boldsymbol{X} = X_I \mathbf{E}_I$, where X_I are the Cartesian components [63]. Considering, instead, the generic configuration at the time t, denoted as the *actual* or *spatial* configuration of the body $\boldsymbol{\Omega}$, the mapping $\phi_t : \mathcal{B} \to \boldsymbol{\Omega} \subset \mathbb{R}^3$, describes the closed volume of actual material particles, denoted by $\boldsymbol{x} = x_i \mathbf{e}_i$, where $(\mathbf{e}_1, \mathbf{e}_2, \mathbf{e}_3)$ is the Cartesian *spatial* reference frame [63].

A *motion* of the body is the mapping $\boldsymbol{\chi} : \boldsymbol{\Omega}_0 \to \boldsymbol{\Omega}$, where $\boldsymbol{\Omega}$ is the configuration of the body at the generic time t described as the evolved configuration from the material one. The motion can also be defined as the map $\boldsymbol{\chi}(\boldsymbol{X}, t) : \boldsymbol{X} \to \boldsymbol{x}(t)$, thus considering the evolution of the material particles of the body. In general, some mathematical conditions are imposed on $\boldsymbol{\chi}$ to satisfy the physical admissibility of the motion [146]. The evolution of the continuum body described with respect to the material coordinates is referred to as *Lagrangian* description; instead, referring to the spatial coordinates, the motion description is referred to as *Eulerian* description [147]. The material configuration is described in the $\{\mathbf{E}_i\}$ reference frame, instead

the spatial configuration in the $\{\mathbf{e}_i\}$ reference frame, that can be generally different [146]. In this context, the *Lagrangian* displacement field as the map $\boldsymbol{u} : \boldsymbol{\Omega}_0 \to \mathbb{R}^3$ given by:

$$\boldsymbol{u}(\boldsymbol{X}, t) = \boldsymbol{x} - \boldsymbol{X} = \boldsymbol{\chi}(\boldsymbol{X}, t) - \boldsymbol{X} \tag{2.1}$$

Additionally, the *Eulerian* displacement field is defined as the map $\boldsymbol{u}^* : \boldsymbol{\Omega} \to \mathbb{R}^3$ given by:

$$\boldsymbol{u}^*(\boldsymbol{X}, t) = \boldsymbol{x} - \boldsymbol{X} = \boldsymbol{x} - \boldsymbol{\chi}^{-1}(\boldsymbol{x}, t) \tag{2.2}$$

A graphical representation of the introduced mathematical quantities, as well as the concept of simple body and material and spatial configurations, is provided in Fig. 2.1.

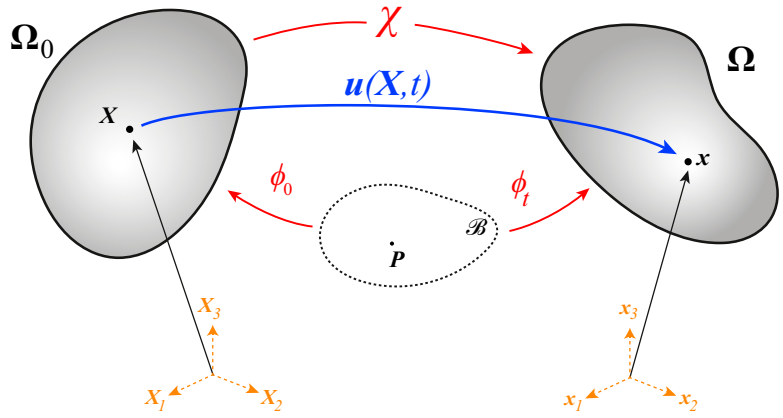

Figure 2.1: Continuum body: definition of simple, continuum body, material, and spatial reference frame.

The behavior in the neighborhood of the material particle $\boldsymbol{X}$ is described by the *deformation gradient* $\mathbf{F}$ [148]:

$$\mathbf{F}(\boldsymbol{X}, t) = \frac{\partial \boldsymbol{\chi}(\boldsymbol{X}, t)}{\partial \boldsymbol{X}} = \nabla_{\boldsymbol{X}} \boldsymbol{\chi} \qquad F_{iJ} = \frac{\partial \chi_i}{\partial X_J} \tag{2.3}$$

where the symbol $\nabla_{\boldsymbol{X}}$ denotes the gradient with respect to the $\boldsymbol{X}$ coordinates. The definition of $\mathbf{F}$ in Eq. (2.3) corresponds to a *two-point tensor*, involving points in different body configurations [146]. Generally, physical admissibility conditions of motion are expressed in terms of mathematical conditions imposed on $\mathbf{F}$. Under the hypothesis of smooth motion, considering thus $\boldsymbol{\chi}$ invertible, one can define its inverse function, namely the map $\boldsymbol{\chi}^{-1} : \boldsymbol{\Omega} \to \boldsymbol{\Omega}_0$ and the inverse of the deformation gradient [63]:

$$\mathbf{F}^{-1}(\boldsymbol{x}, t) = \frac{\partial \boldsymbol{\chi}^{-1}(\boldsymbol{x}, t)}{\partial \boldsymbol{x}} = \nabla_{\boldsymbol{x}} \boldsymbol{\chi}^{-1} \qquad (F^{-1})_{Ij} = \frac{\partial \chi^{-1}{}_I}{\partial x_j} \tag{2.4}$$

Starting from these definitions,the *fundamental kinematics relation* is automatically derived:

$$\mathbf{H} = \nabla \mathbf{u} = \nabla_{\boldsymbol{X}} \boldsymbol{\chi}(\boldsymbol{X}, t) - \nabla_{\boldsymbol{X}} \boldsymbol{X} = \mathbf{F} - \mathbf{I} \tag{2.5}$$

Within the context of nonlinear solid mechanics, the *volume change* has a crucial role, especially in the case of compressible and nearly-incompressible materials. The *volume ratio*

$J(\boldsymbol{X}, t)$ is defined as the determinant of $\mathbf{F}$, and relates the infinitesimal volume change from the material and spatial configurations:

$$dv = J(\boldsymbol{X}, t)dV \tag{2.6}$$

where dv and dV are the infinitesimal volumes in the neighborhood of the actual particle $\boldsymbol{x}$ and reference particle $\boldsymbol{X}$, respectively. Consider now a unit versor $\mathbf{N}$, mounted in the point $\mathbf{P}$ of the material configuration, and the associated infinitesimal vector $d\boldsymbol{X} = dS\mathbf{N}$. By means of the motion $\boldsymbol{\chi}$, the material point is now located at $\mathbf{p}$, denoting also with $d\boldsymbol{x} = ds\mathbf{n}$ the infinitesimal vector after the deformation. A graphical representation of the described scenario is proposed in Fig. 2.2.

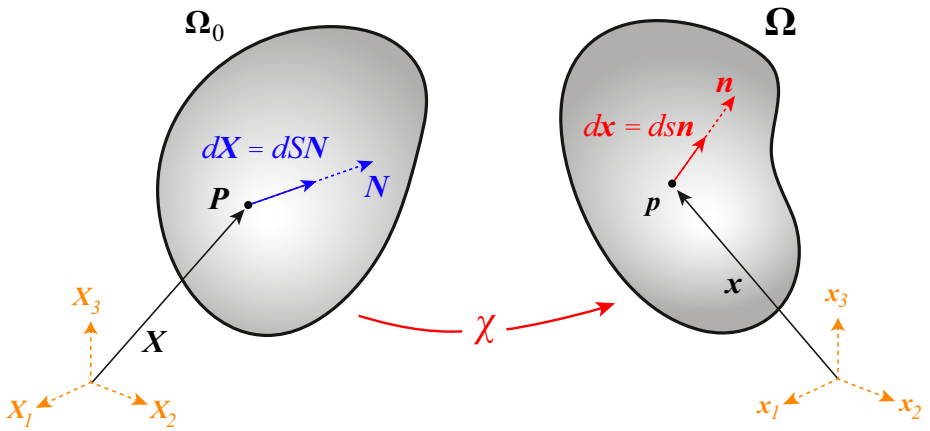

Figure 2.2: Continuum body: definition of motion in the neighborhood of a continuum particle.

Through these definitions, the tensor operations of push-forward and pull-back on vector quantities can be introduced. The deformation gradients map the material elementary vector $d\boldsymbol{X}$ to the spatial vector $d\boldsymbol{x}$, and they can be described either in terms of material and spatial reference frames [147]. When the elementary vector $d\boldsymbol{x}$ is written in terms of $d\boldsymbol{X}$ and material coordinates, it can be considered as the *push-forward* of the material vector $d\boldsymbol{X}$ to the actual spatial reference frame [147]:

$$d\boldsymbol{x} = \Phi_*[d\boldsymbol{X}] = \mathbf{F}d\boldsymbol{X} \tag{2.7}$$

Vice versa, if the elementary vector $d\boldsymbol{X}$ is written in terms of $d\boldsymbol{x}$ and spacial coordinates, it can be considered as the *pull-back* of the spatial vector $d\boldsymbol{x}$ to the material reference frame [147]:

$$d\boldsymbol{X} = \Phi_*^{-1}[d\boldsymbol{x}] = \mathbf{F}^{-1}d\boldsymbol{x} \tag{2.8}$$

The power of these two operations is related to the possibility of expressing any quantity in the preferred reference frame [146], interchanging variable dependence by means of the deformation gradient. The pull-back and push-forward operations give the possibility to change the material or spatial description of physical quantities by the deformation gradient, the fundamental kinematic descriptor in continuum mechanics [146]. These two operations are extensively employed in the derivation of material or spatial description of governing equations, stress and strain measures, and balance laws.

2.1.2 Strain measures

The deformation gradient is the fundamental kinematic descriptor used in continuum mechanics to analyze the behavior of the continuum body. In continuum mechanics, and particularly in numerical methods for finite deformation analysis, alternative strain measures are typically adopted, which are strictly related to the material or actual frames. In general, during the evolution of the body, the strain measures are defined by analyzing the behavior of the continuum body in the neighborhood of a continuum particle. Let $\mathbf{P}$ be a material particle described by the material position vector $\boldsymbol{X}$, and $\mathbf{Q}_1$ and $\mathbf{Q}_2$ two related material particles in the neighborhood of $\mathbf{P}$ identified by the elementary vectors $d\boldsymbol{X}_1$ and $d\boldsymbol{X}_2$. The deformation $\boldsymbol{\chi}$ maps these entities in the positions $\mathbf{p}$, identified by the spatial position vector $\boldsymbol{x}$, $\mathbf{q}_1$ and $\mathbf{q}_2$, respectively, identifying thus the elementary vectors $d\boldsymbol{x}_1$ and $d\boldsymbol{x}_2$. A graphical representation of the described scenario is provided in Fig. 2.3.

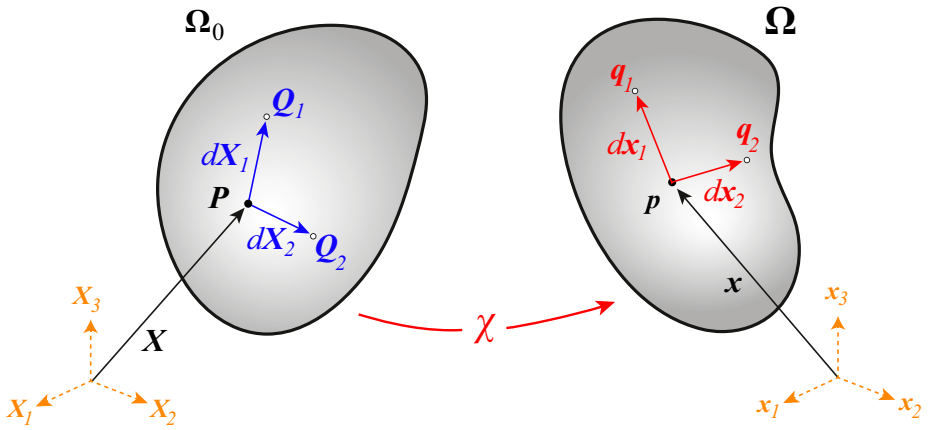

Figure 2.3: Continuum body: motion in the neighborhood of a continuum particle.

A generic strain measure is introduced by means of the scalar product between the elementary vectors. Analyzing the variation of these two elementary vectors and their scalar products, both stretching effects and changes in angles are then investigated. Introducing then the quantities $d\boldsymbol{x}_1 \cdot d\boldsymbol{x}_2$ and $d\boldsymbol{X}_1 \cdot d\boldsymbol{X}_2$, recalling the introduced definition of push-forward operation Eq. (2.7):

$$d\boldsymbol{x}_1 \cdot d\boldsymbol{x}_2 = (\mathbf{F} d\boldsymbol{X}_1) \cdot (\mathbf{F} d\boldsymbol{X}_2) = d\boldsymbol{X}_1^T (\mathbf{F}^T \mathbf{F}) d\boldsymbol{X}_2 = d\boldsymbol{X}_1 \cdot \mathbf{C} d\boldsymbol{X}_2 \tag{2.9}$$

where the tensor $\mathbf{C} = \mathbf{F}^T\mathbf{F}$ is the right Cauchy-Green strain tensor, given in terms of the deformation gradient. A key aspect of this tensor, as can be observed by Eq. (2.9), is that it acts directly on elementary vectors defined in the material reference frame. For this reason, the right Cauchy-Green strain tensor is a material tensor quantity, whose components can be written as $C_{IJ} = F_{kI}F_{kJ}$. Alternatively, the proposed scalar product can be equivalently expressed in terms of spatial vectors, exploiting the pull-back operation Eq. (2.8):

$$d\boldsymbol{X}_1 \cdot d\boldsymbol{X}_2 = (\mathbf{F}^{-1} d\boldsymbol{x}_1) \cdot (\mathbf{F}^{-1} d\boldsymbol{x}_2) = d\boldsymbol{x}_1^T (\mathbf{F}^{-T} \mathbf{F}^{-1}) d\boldsymbol{x}_2 = d\boldsymbol{x}_1 \cdot \mathbf{b}^{-1} d\boldsymbol{x}_2 \tag{2.10}$$

where the tensor $\mathbf{b} = \mathbf{F}\mathbf{F}^T$ is the left Cauchy-Green strain tensor, given in terms of the deformation gradient. A key aspect of this tensor, as can be observed by Eq. (2.10), is that it acts directly on the elementary vectors defined in the spatial reference frame. For this reason, the left Cauchy-Green strain tensor is a spatial tensor quantity, whose components can be written as $b_{ij} = F_{iK}F_{jK}$.

The right Cauchy-Green strain tensor represents a useful physical quantity and strain measure, since it is related to the material reference frame. One can prove that this tensor is strictly related to the geometrical description of the assigned body and metric arguments [146].

Given these physical quantities, one can also explore the variation in the scalar product between the two elementary vectors. Expressing this variation in terms of material reference quantities, applying then the push-forward operations on the vector $d\boldsymbol{x}$:

$$\frac{1}{2}(d\boldsymbol{x}_1 \cdot d\boldsymbol{x}_2 - d\boldsymbol{X}_1 \cdot d\boldsymbol{X}_2) = \frac{1}{2}(d\boldsymbol{X}_1 \cdot \mathbf{C} d\boldsymbol{X}_2 - d\boldsymbol{X}_1 \cdot d\boldsymbol{X}_2) = d\boldsymbol{X}_1 \cdot \mathbf{E} d\boldsymbol{X}_2 \tag{2.11}$$

where the tensor $\mathbf{E} = 1/2(\mathbf{C} - \mathbf{I})$ has been introduced in Eq. (2.11). The tensor $\mathbf{E}$ is the Green-Lagrange strain tensor, related again to the material reference frame. Alternatively, expressing again the same variation in terms of spatial quantities:

$$\frac{1}{2}(d\boldsymbol{x}_1 \cdot d\boldsymbol{x}_2 - d\boldsymbol{X}_1 \cdot d\boldsymbol{X}_2) = \frac{1}{2}(d\boldsymbol{x}_1 \cdot d\boldsymbol{x}_2 - d\boldsymbol{x}_1 \cdot \mathbf{b}^{-1} d\boldsymbol{x}_2) = d\boldsymbol{x}_1 \cdot \mathbf{e} d\boldsymbol{x}_2 \tag{2.12}$$

where the tensor $\mathbf{e} = 1/2(\mathbf{I} - \mathbf{b}^{-1})$ has been introduced. The tensor $\mathbf{e}$ is the Almansi strain tensor, related to the spatial reference frame. These two tensors are the classical strain measure adopted either in a Total Lagrangian or Eulerian scenario, since they are defined within the same reference frame. Unlike the deformation gradient, which is a two-point tensor, these tensors provide information about the local strain behavior in the infinitesimal neighborhood of particles in the material and spatial frames, respectively [146]. Due to their physical behavior, since the deformation must be objective, namely independent of the reference frame adopted for its description, one can write the following equality:

$$d\boldsymbol{x}_1 \cdot \mathbf{e} d\boldsymbol{x}_2 = d\boldsymbol{X}_1 \cdot \mathbf{E} d\boldsymbol{X}_2 \tag{2.13}$$

From Eq. (2.13), one can apply again the already introduced concepts of pull-back and push-forward for vectors and define the same algebraic operation for tensorial quantities. In this sense, the following operators are here defined [147]:

$$\text{Push-forward:} \quad \mathbf{e} = \Phi_*[\mathbf{E}] = \mathbf{F}^{-T}\mathbf{E}\mathbf{F}^{-1} \tag{2.14}$$

$$\text{Pull-back:} \quad \mathbf{E} = \Phi_*^{-1}[\mathbf{e}] = \mathbf{F}^{T}\mathbf{e}\mathbf{F} \tag{2.15}$$

The right Cauchy-Green and Green-Lagrange strain tensors can be expressed in terms of the displacement gradient $\mathbf{H}$, exploiting the fundamental kinematic relation Eq. (2.5):

$$\begin{aligned} \mathbf{C} = \mathbf{F}^T\mathbf{F} &= (\mathbf{H}+\mathbf{I})^T(\mathbf{H}+\mathbf{I}) = \mathbf{H}^T\mathbf{H} + \mathbf{H}^T\mathbf{I} + \mathbf{I}^T\mathbf{H} + \mathbf{I}^T\mathbf{I} = \\ &= \mathbf{H}^T\mathbf{H} + \mathbf{H}^T + \mathbf{H} + \mathbf{I} \end{aligned} \tag{2.16}$$

$$\begin{aligned} \mathbf{E} &= \frac{1}{2}\Big(\mathbf{F}^T\mathbf{F} - \mathbf{I}\Big) = \frac{1}{2}\Big(\mathbf{H}^T\mathbf{H} + \mathbf{H}^T + \mathbf{H} + \mathbf{I} - \mathbf{I}\Big) = \\ &= \frac{1}{2}\Big(\mathbf{H}^T\mathbf{H} + \mathbf{H}^T + \mathbf{H}\Big) \end{aligned} \tag{2.17}$$

2.2 Polar Decomposition Theorem

The characterization of the body motion and the behavior in the neighborhood of a material particle is characterized in a local sense by means of the deformation gradient. Adopting this

reference kinematic measure, also, infinitesimal local vectors $d\mathbf{X}$ are associated with the corresponding $d\boldsymbol{x}$. This fundamental kinematic measure is further investigated by introducing the concepts of rotation and pure stretch, which can be conveniently used to characterize local body motion. Exploiting from the Polar Decomposition Theorem [63], the deformation $\mathbf{F}$ is split and expressed by means of a pure *stretch* tensor $\mathbf{U}$ and a pure *rotation* tensor $\mathbf{R}$:

$$\mathbf{F} = \mathbf{R}\mathbf{U} \tag{2.18}$$

In Eq. (2.18), the quantity $\mathbf{U}$ is the symmetric, unique, and positive-definite *stretch tensor* that measures local variations (stretch or contractions) of infinitesimal material lines in the neighborhood of a material particle, thus local shape changes are measured. As it will be now shows, this tensor can be characterized by means of the Cauchy-Green strain tensor:

$$\mathbf{U}^2 = \mathbf{U}\mathbf{U} = \mathbf{C} \tag{2.19}$$

Additionally, the stretch tensor can be seen as a measure of local stretching/contraction along the local eigenvectors, namely the principal directions, in the neighborhood of the continuum body [148]. Instead, $\mathbf{R}$ is the unique rotation matrix defined in such a way $\mathbf{R}^T\mathbf{R} = \mathbf{I}$. The physical interpretation of the tensor $\mathbf{U}$ can be found in the definition of the stretch vector and its variation during the deformation.
Considering a continuum body in its material and spatial configuration. Denote again with $\boldsymbol{X} \in \boldsymbol{\Omega}_0$ the material particle in the material reference frame, and with $\boldsymbol{x} \in \boldsymbol{\Omega}$ the correlated position in the spatial reference frame. Additionally, at the point $\boldsymbol{X}$, consider the unit vector $\mathbf{a}_0$, on which an infinitesimal volume neighborhood is identified, considering a sphere of radius $d\varepsilon_0$ centered in $\boldsymbol{X}$. After the deformation, the change in the infinitesimal volume such defined is given by the deformation gradient, which maps also the versor $\boldsymbol{a}_0$ in the actual $\boldsymbol{a}$, identifying the vector $d\varepsilon\boldsymbol{a}$ in the spatial reference frame. The *stretch vector* $\boldsymbol{\lambda}_{\boldsymbol{a}_0}$, measured in the material reference frame, is defined as follows:

$$\boldsymbol{\lambda}_{\boldsymbol{a}_0}(\boldsymbol{X}, t) = \mathbf{F}(\boldsymbol{X}, t)\boldsymbol{a}_0 \tag{2.20}$$

If now $\boldsymbol{P}$, $\boldsymbol{Q} \in \boldsymbol{\Omega}_0$ and $\boldsymbol{p}$, $\boldsymbol{q} \in \boldsymbol{\Omega}$ are the corresponding points in the material and spatial reference frame, the infinitesimal neighborhood of the points in the material reference frame are described by the quantity $\boldsymbol{Q} - \boldsymbol{P} = d\varepsilon_0\mathbf{a}_0$, as shown in Fig. 2.4. The evolution of the stretch vector can again be expressed adopting the previously introduced linearization procedure:

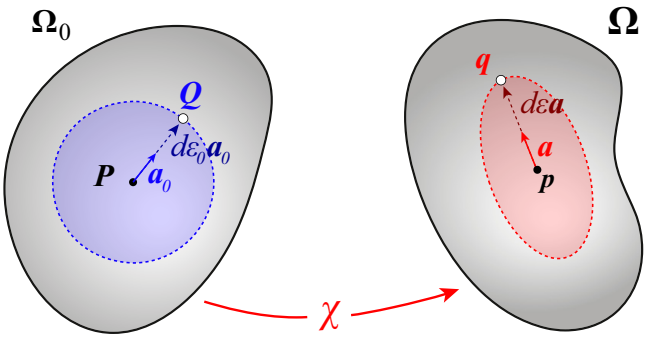

Figure 2.4: Continuum body: stretch during a deformation.

$$\boldsymbol{q}-\boldsymbol{p}=\mathbf{F}(\boldsymbol{Q}-\boldsymbol{P})=\mathbf{F}d\varepsilon_0\boldsymbol{a}_0=\boldsymbol{\lambda}_{\boldsymbol{a}_0}d\varepsilon_0 \tag{2.21}$$

The squared modulus of this last vector gives the physical interpretation of the stretch ratio and its definition in terms of deformation gradient and right Cauchy-Green strain tensor:

$$|\boldsymbol{q}-\boldsymbol{p}|=\sqrt{(\boldsymbol{q}-\boldsymbol{p})\cdot(\boldsymbol{q}-\boldsymbol{p})}=\sqrt{\boldsymbol{\lambda}_{\mathbf{a}_0}\cdot\boldsymbol{\lambda}_{\mathbf{a}_0}}d\varepsilon_0=\lambda_{\boldsymbol{a}}d\epsilon \tag{2.22}$$

$$\lambda^2=|\boldsymbol{\lambda}_{\boldsymbol{a}}|^2=\boldsymbol{\lambda}_{\boldsymbol{a}_0}\cdot\boldsymbol{\lambda}_{\boldsymbol{a}_0}=\mathbf{F}\boldsymbol{a}_0\cdot\mathbf{F}\boldsymbol{a}_0=\boldsymbol{a}_0^T\mathbf{F}^T\mathbf{F}\boldsymbol{a}_0=\boldsymbol{a}_0^T\mathbf{C}\boldsymbol{a}_0 \tag{2.23}$$

Equation (2.23) provides additional information on the physical meaning of the tensor $\mathbf{C}$. The components of the right Cauchy-Green strain tensor measure the *pure stretches* between two neighborhood points during the evolution process. Additionally, using the Polar Decomposition Theorem:

$$\lambda^2=(\mathbf{R}\mathbf{U}\boldsymbol{a}_0)\cdot(\mathbf{R}\mathbf{U}\boldsymbol{a}_0)=\boldsymbol{a}_0\mathbf{U}^T\mathbf{R}^T\mathbf{R}\mathbf{U}\boldsymbol{a}_0=\boldsymbol{a}_0\mathbf{U}^T\mathbf{U}\boldsymbol{a}_0=(\mathbf{U}\boldsymbol{a}_0)\cdot(\mathbf{U}\boldsymbol{a}_0)=|\mathbf{U}\boldsymbol{a}_0|^2 \tag{2.24}$$

Since the stretch ratio is uniquely related to the stretch tensor $\mathbf{U}$, the tensor $\mathbf{C}$ does not provide any information about the local change in orientation of two neighborhood points in the material configuration after the deformation [147].

From its definition, similar considerations can be addressed for the Green-Lagrange strain tensor, whose components are here reported for further manipulations. If $\mathbf{u}=u_x\mathbf{E}_1+u_y\mathbf{E}_2+u_z\mathbf{E}_3$ is the Lagrangian displacement field, applying the definition given by Eq. (2.18):

$$\varepsilon_{xx}=\frac{\partial u_x}{\partial x}+\frac{1}{2}\left[\left(\frac{\partial u_x}{\partial x}\right)^2+\left(\frac{\partial u_y}{\partial x}\right)^2+\left(\frac{\partial u_z}{\partial x}\right)^2\right] \tag{2.25}$$

$$\varepsilon_{yy}=\frac{\partial u_y}{\partial x}+\frac{1}{2}\left[\left(\frac{\partial u_x}{\partial y}\right)^2+\left(\frac{\partial u_y}{\partial y}\right)^2+\left(\frac{\partial u_z}{\partial y}\right)^2\right] \tag{2.26}$$

$$\varepsilon_{zz}=\frac{\partial u_x}{\partial z}+\frac{1}{2}\left[\left(\frac{\partial u_x}{\partial z}\right)^2+\left(\frac{\partial u_y}{\partial z}\right)^2+\left(\frac{\partial u_z}{\partial z}\right)^2\right] \tag{2.27}$$

$$\gamma_{xy}=\frac{1}{2}\left(\frac{\partial u_x}{\partial y}+\frac{\partial u_y}{\partial x}\right)+\frac{1}{2}\left[\frac{\partial u_x}{\partial x}\frac{\partial u_x}{\partial y}+\frac{\partial u_y}{\partial x}\frac{\partial u_y}{\partial y}+\frac{\partial u_z}{\partial x}\frac{\partial u_z}{\partial y}\right] \tag{2.28}$$

$$\gamma_{xz}=\frac{1}{2}\left(\frac{\partial u_x}{\partial z}+\frac{\partial u_z}{\partial x}\right)+\frac{1}{2}\left[\frac{\partial u_x}{\partial x}\frac{\partial u_x}{\partial z}+\frac{\partial u_y}{\partial x}\frac{\partial u_y}{\partial z}+\frac{\partial u_z}{\partial x}\frac{\partial u_z}{\partial z}\right] \tag{2.29}$$

$$\gamma_{xz}=\frac{1}{2}\left(\frac{\partial u_y}{\partial z}+\frac{\partial u_z}{\partial y}\right)+\frac{1}{2}\left[\frac{\partial u_x}{\partial y}\frac{\partial u_x}{\partial z}+\frac{\partial u_y}{\partial y}\frac{\partial u_y}{\partial z}+\frac{\partial u_z}{\partial y}\frac{\partial u_z}{\partial z}\right] \tag{2.30}$$

2.3 Linearized kinematics

In the development of linearized consistent models, typically required in the context of non-linear elasticity, linearized kinematic quantities are therefore needed. It is then required to derive linearized physical quantities when small perturbations to the motion are considered. This can be performed both in the material and spatial reference frames.

Let $\bar{\mathbf{u}}(\boldsymbol{x})$ be a small perturbation of the displacement field, defined in the spatial frame $\boldsymbol{\Omega}$. The linearization of the deformation gradient is performed considering the directional derivative of $\mathbf{F}$ with respect to the direction $\bar{\mathbf{u}}$ [146]:

$$D\mathbf{F}[\bar{\mathbf{u}}] = \frac{d}{d\varepsilon}\mathbf{F}(\boldsymbol{x}+\varepsilon\bar{\mathbf{u}})\bigg|_{\varepsilon=0} = \frac{\partial\bar{\mathbf{u}}}{\partial\boldsymbol{X}} = \nabla_{\boldsymbol{X}}\bar{\mathbf{u}} = (\nabla_{\boldsymbol{x}}\bar{\mathbf{u}})\mathbf{F} \tag{2.31}$$

where the symbol $D\mathbf{F}[\bar{\mathbf{u}}]$ is employed to denote the directional derivative. If the perturbation $\bar{\mathbf{u}}$ is given in terms of material coordinates, thus $\bar{\mathbf{u}} = \bar{\mathbf{u}}(\boldsymbol{X})$, then $D\mathbf{F}[\bar{\mathbf{u}}] = \nabla_{\boldsymbol{X}}\bar{\mathbf{u}}$.

The linearization of the deformation gradient automatically allow for the definition of the linearized Green-Lagrange strain tensor, obtained by applying the directional derivative at Eq. (2.18) and its properties:

$$\begin{aligned} D\mathbf{E}[\bar{\mathbf{u}}] &= \frac{1}{2}\Big(\mathbf{F}^T D\mathbf{F}[\bar{\mathbf{u}}] + (D\mathbf{F}[\bar{\mathbf{u}}])^T\mathbf{F}\Big) = \frac{1}{2}(\mathbf{F}^T(\nabla_{\boldsymbol{X}}\bar{\mathbf{u}})\mathbf{F} + \mathbf{F}^T(\nabla_{\boldsymbol{X}}\bar{\mathbf{u}})^T\mathbf{F}) = \\ &= \mathbf{F}^T\left(\frac{(\nabla_{\boldsymbol{X}}\bar{\mathbf{u}})^T + \nabla_{\boldsymbol{X}}\bar{\mathbf{u}}}{2}\right)\mathbf{F} = \mathbf{F}^T\boldsymbol{\varepsilon}\mathbf{F} = \Phi_*^{-1}[\boldsymbol{\varepsilon}] \end{aligned} \tag{2.32}$$

The last relation in Eq. (2.32) means that the linearized Green-Lagrange strain tensor is given by the pull-back of the linear strain tensor, in the spatial reference frame, arising from the assigned perturbation displacements.

2.4 Stress measure

Consider the material configuration of a continuum body $\boldsymbol{\Omega}_0$ subjected to surface and volume forces, and geometrical constraints. Considering a generic material point inside the body $\boldsymbol{X} \in \boldsymbol{\Omega}_0$, let Π be a plane, passing through this point, and let $\mathbf{N}$ be its normal vector; this plane identifies two distinct portions of the body, identified as $\boldsymbol{\Omega}_0^+$ and $\boldsymbol{\Omega}_0^+$. During the evolution of the continuum body, also the normal vector $\mathbf{N}$ is transformed into the normal vector $\mathbf{n}$ in the actual reference frame, identifying then in the material point $\boldsymbol{x} \in \boldsymbol{\Omega}$ the cutting plane, by which the two half-bodies $\boldsymbol{\Omega}^+$ and $\boldsymbol{\Omega}^-$ are defined, as depicted in Fig. 2.5.

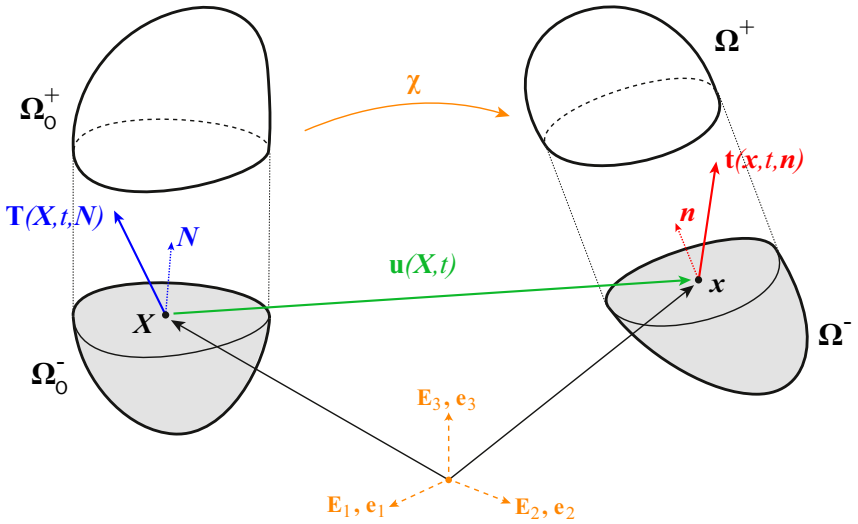

Figure 2.5: Continuum body: stress analysis, concept of traction vector.

In the actual reference frame, the *Euler-Cauchy deformable body assumptions*, also known as *Cauchy's section principle*, are considered. In an infinitesimal neighborhood dA of $\boldsymbol{x}$, lying on a cutting plane, the action of a sub-body on the other one is a surface traction force field defined over dA. If $d\mathbf{R}$ is the resultant vector of this field, Cauchy's section principle states that $d\mathbf{R}$ admits a finite limit when the infinitesimal neighborhood dA approaches zero:

$$\mathbf{t}^{(\boldsymbol{n})}(\boldsymbol{x}) = \lim_{dA \to 0} \frac{\mathbf{R}^{(\boldsymbol{n})}}{dA} \tag{2.33}$$

This finite limit is called *Cauchy traction vector*, evaluated in the point $\boldsymbol{x}$ and related to the plane of normal vector $\boldsymbol{n}$. The traction vector is then depending of both the spatial point and the cutting plane; however, fixing the particle, the traction vector changes only if the normal vector of the cutting plane changes.
Global equilibrium conditions for a deformable body are given by *Cauchy's Theorem* for a continuum body. Let $\boldsymbol{\Omega}$ be the spatial configuration of a continuum body, supposing to known the internal forces and external forces fields, the equilibrium under the Cauchy assumptions relates the traction vector to the *Cauchy stress tensor* $\boldsymbol{\sigma}$, in such a way $\mathbf{t}^{(\boldsymbol{n})}(\boldsymbol{x}) = \boldsymbol{\sigma}(\boldsymbol{x}, t)\boldsymbol{n}$. In addition, the equilibrium of the continuum body is governed by:

1. *Static* translational equilibrium of the body: if the only load considered is the volume force field $\mathbf{b}$, the translational equilibrium is

$$\mathrm{div}_{\boldsymbol{x}}\boldsymbol{\sigma} + \mathbf{b} = 0 \tag{2.34}$$

   where $\mathrm{div}_{\boldsymbol{x}}$ denotes the divergence operator with respect to the $\boldsymbol{x}$ coordinates:

$$\mathrm{div}_{\boldsymbol{x}}(\cdot) = \frac{\partial(\cdot)}{\partial x_1} + \frac{\partial(\cdot)}{\partial x_2} + \frac{\partial(\cdot)}{\partial x_3} \tag{2.35}$$

2. Rotational equilibium: the stress tensor is symmetric

$$\boldsymbol{\sigma}(\boldsymbol{x}, t) = \boldsymbol{\sigma}^T(\boldsymbol{x}, t) \tag{2.36}$$

Let $\{\mathbf{e}_1, \mathbf{e}_2, \mathbf{e}_3\}$ be the orthonormal Cartesian reference frame in the actual configuration. The generic nine Cartesian components of the stress tensor can be characterized by considering the three planes passing through the material point $\boldsymbol{x}$ and parallel to the coordinate planes. By fixing as a normal vector of the cutting plane the three normal vectors of the Cartesian basis, *normal stress components* and *tangential stress components* can be identified:

$$\begin{aligned}
\sigma_{xx} &= \mathbf{t}_1^{(\boldsymbol{n})} \cdot \mathbf{e}_1 = (\boldsymbol{\sigma}\ \mathbf{e}_1) \cdot \mathbf{e}_1 & \tau_{xy} &= \mathbf{t}_1^{(\boldsymbol{n})} \cdot \mathbf{e}_2 = (\boldsymbol{\sigma}\ \mathbf{e}_1) \cdot \mathbf{e}_2 & \tau_{xz} &= \mathbf{t}_1^{(\boldsymbol{n})} \cdot \mathbf{e}_3 = (\boldsymbol{\sigma}\ \mathbf{e}_1) \cdot \mathbf{e}_3 \\
\tau_{yx} &= \mathbf{t}_2^{(\boldsymbol{n})} \cdot \mathbf{e}_1 = (\boldsymbol{\sigma}\ \mathbf{e}_2) \cdot \mathbf{e}_1 & \sigma_{yy} &= \mathbf{t}_2^{(\boldsymbol{n})} \cdot \mathbf{e}_2 = (\boldsymbol{\sigma}\ \mathbf{e}_2) \cdot \mathbf{e}_2 & \tau_{yz} &= \mathbf{t}_2^{(\boldsymbol{n})} \cdot \mathbf{e}_3 = (\boldsymbol{\sigma}\ \mathbf{e}_2) \cdot \mathbf{e}_3 \\
\tau_{zx} &= \mathbf{t}_3^{(\boldsymbol{n})} \cdot \mathbf{e}_1 = (\boldsymbol{\sigma}\ \mathbf{e}_3) \cdot \mathbf{e}_1 & \tau_{zy} &= \mathbf{t}_3^{(\boldsymbol{n})} \cdot \mathbf{e}_2 = (\boldsymbol{\sigma}\ \mathbf{e}_3) \cdot \mathbf{e}_2 & \sigma_{zz} &= \mathbf{t}_3^{(\boldsymbol{n})} \cdot \mathbf{e}_3 = (\boldsymbol{\sigma}\ \mathbf{e}_3) \cdot \mathbf{e}_3
\end{aligned}$$

2.5 Balance principles

2.5.1 Reynolds' Transport Theorem

The equilibrium equations describing the evolution of a deformable continuum body are typically expressed in both strong and weak forms, namely in differential and integral forms, respectively [146]. In this section, the governing equations for the elastodynamic problem of a deformable body are briefly presented, with a focus on their material and spatial definitions.
The starting point for a generic balance equation in a continuum mechanics framework is the Reynolds Transport Theorem. If $\varphi(\boldsymbol{x}, t)$ is a general scalar quantity of a particle per unit volume, namely the intensive physical quantity, the related extensive (volume-dependent) quantity is defined as:

$$\Phi(\boldsymbol{x}, t) = \int_{\Omega} \varphi(\boldsymbol{x}, t) dv \tag{2.37}$$

where $\Omega = \text{vol}(\boldsymbol{\Omega})$ is the actual volume after the deformation. From this definition, the material time derivative that gives the rate of Φ is expressed as:

$$\frac{d\Phi}{dt} = \int_{\Omega} \left(\text{div}_{\boldsymbol{x}}(\varphi \boldsymbol{v}) + \frac{\partial \varphi}{\partial t} \right) dv = \int_{\Omega} \frac{D\varphi}{Dt} dv = \int_{\Omega} \frac{\partial \varphi}{\partial t} dv + \int_{\partial\Omega} \varphi \boldsymbol{v} \cdot \boldsymbol{n} ds \tag{2.38}$$

where $\boldsymbol{v}$ is the spatial velocity vector, $\boldsymbol{n}$ is the unitary outward vector from the boundary surface $\partial\Omega$. In Eq. (2.38), the rate of change in time of a generic quantity has been compactly introduced by means of the total time derivative, denoted with the symbol $\dfrac{D(\cdot)}{Dt}$, defined as:

$$\frac{D(\cdot)}{Dt} = \frac{\partial(\cdot)}{\partial t} + \text{div}_{\boldsymbol{x}}(\ (\cdot)\ \boldsymbol{v}) \tag{2.39}$$

Equation (2.38) is the most general form of the Reynolds' Transport Theorem. In continuum mechanics, balance principles are typically written applying the transport theorem to fundamental mechanical quantities such as mass or linear momentum. In this way, a straightforward derivation of the governing equation can be easily proposed.

2.5.2 Conservation of mass

In the case of the mass continuity equation, the balance equation is given by considering $\varphi(\boldsymbol{x}, t) = \rho(\boldsymbol{x}, t)$, where ρ is the mass density in the spatial reference frame, thus $m(t) = \displaystyle\int_{\Omega} \rho(\boldsymbol{x}, t) dv$. Applying Eq. (2.38) to the mass definition given, in the case of a closed domain that does not exchange mass with the external ambient considered, one can derive the integral mass conservation equation:

$$\frac{dm}{dt} = \int_{\Omega} \left(\frac{\partial \rho(\boldsymbol{x}, t)}{\partial t} + \text{div}_{\boldsymbol{x}}(\rho(\boldsymbol{x}, t) \boldsymbol{v}) \right) dv = 0 \tag{2.40}$$

Equation (2.40) is the most general form of the mass continuity equation for a closed system. For the sake of completeness, applying the Localization Theorem [146], one can write the same equation in strong form as:

$$\frac{\partial \rho(\boldsymbol{x}, t)}{\partial t} + \text{div}_{\boldsymbol{x}}(\rho(\boldsymbol{x}, t) \boldsymbol{v}) = 0 \tag{2.41}$$

Equation (2.41) is helpful in defining the transport equation and balance law for a vector-valued function weighted by the material density, as can be seen, for example, in the definition of linear momentum. Starting from the definition of intensive and extensive quantities, let $\mathbf{u}$ be a generic vector field defined over the actual reference frame and configuration. Introducing now:

$$\varphi(\boldsymbol{x},t) = \rho(\boldsymbol{x},t)\mathbf{u}(\boldsymbol{x},t); \qquad \Phi(t) = \int_\Omega \rho(\boldsymbol{x},t)\mathbf{u}(\boldsymbol{x},t)dv \tag{2.42}$$

The general transport equation for the extensive quantity $\Phi(t)$ will be written following the Reynolds Transport Theorem:

$$\begin{aligned}
\frac{d\Phi}{dt} &= \int_\Omega \left[\frac{\partial(\rho\mathbf{u})}{\partial t} + \mathrm{div}_{\boldsymbol{x}}(\rho\mathbf{u}\otimes\boldsymbol{v})\right]dv = \\
&= \int_\Omega \left(\frac{\partial\rho}{\partial t}\mathbf{u} + \rho\frac{\partial\mathbf{u}}{\partial t} + \mathbf{u}\mathrm{div}_{\boldsymbol{x}}(\rho\boldsymbol{v}) + \rho\boldsymbol{v}\cdot\nabla_{\boldsymbol{x}}\boldsymbol{u}\right)dv = \\
&= \underbrace{\int_\Omega \mathbf{u}\left(\frac{\partial\rho}{\partial t} + \mathrm{div}_{\boldsymbol{x}}(\rho\boldsymbol{v})\right)dv}_{\text{Mass conservation, }=0} + \int_\Omega \left(\rho\frac{\partial\mathbf{u}}{\partial t} + \rho\boldsymbol{v}\cdot\nabla_{\boldsymbol{x}}\boldsymbol{u}\right)dv = \int_\Omega \rho\frac{D\mathbf{u}}{Dt}dv
\end{aligned} \tag{2.43}$$

where the total time derivative for a generic vector field, considering that the mass balance equation holds, has been introduced as:

$$\frac{D\mathbf{u}}{Dt} = \frac{\partial\mathbf{u}}{\partial t} + \boldsymbol{v}\cdot\nabla_{\boldsymbol{x}}\boldsymbol{u} \tag{2.44}$$

In this way, any balance law for density-weighted fields can be easily proposed.

2.5.3 Conservation of linear momentum

Consider a continuum body $\mathcal{B}$ occupying the actual configuration $\boldsymbol{\Omega}$ at the generic time instant t. In this configuration, the position vector $\boldsymbol{x} = \boldsymbol{\chi}(\boldsymbol{X},t)$, the spatial mass density $\rho(\boldsymbol{x},t)$ and the spatial velocity $\boldsymbol{v}(\boldsymbol{x},t)$. Conversely, from the undeformed reference configuration $\boldsymbol{\Omega}_0$ the material mass density $\rho_0(\boldsymbol{X},t)$ and material velocity $\boldsymbol{V}(\boldsymbol{X},t)$ are respectively defined. The linear momentum $\mathbf{Q}(t)$ is defined as the vector integral function:

$$\mathbf{Q}(t) = \int_\Omega \rho(\boldsymbol{x},t)\boldsymbol{v}(\boldsymbol{x},t)dv = \int_{\Omega_0} \rho(\boldsymbol{x},t)\boldsymbol{V}(\boldsymbol{X},t)J(\boldsymbol{X},t)dV = \int_{\Omega_0} \rho_0(\boldsymbol{X},t)\boldsymbol{V}(\boldsymbol{X},t)dV \tag{2.45}$$

The balance of linear momentum is postulated as the governing equation for the material time derivative given by the Reynolds Transport Theorem and Newton's laws of motion [149]:

$$\frac{d\mathbf{Q}(t)}{dt} = \int_\Omega \rho(\boldsymbol{x},t)\frac{D\boldsymbol{v}(\boldsymbol{x},t)}{Dt}dv = \int_{\Omega_0} \rho_0(\boldsymbol{X},t)\dot{\boldsymbol{V}}(\boldsymbol{X},t)dV = \boldsymbol{F}(t) \tag{2.46}$$

where D/Dt denotes again the total time derivative operator, and $\boldsymbol{F}(t)$ denotes the global external force vector applied to the continuum body. Different acting forces are considered in the definition of the global external force vector. On a portion of the boundary surface $\partial\Omega$ of the actual domain, it is supposed the application of a traction vector $\mathbf{t}^{(\boldsymbol{n})}(\boldsymbol{x},t)$ where $\boldsymbol{n}$ is the

outward normal of the actual configuration boundary. Instead, the global volume force $\mathbf{b}(\boldsymbol{x}, t)$ is the vector field of the force per unit volume applied to the body (e.g., gravitational forces). In this way, the external force vector is written as:

$$\boldsymbol{F}(t) = \int_{\partial\Omega} \mathbf{t}^{(\boldsymbol{n})}(\boldsymbol{x}, t)dv + \int_{\Omega} \mathbf{b}(\boldsymbol{x}, t)dv \tag{2.47}$$

Equations (2.46)-(2.47) are the starting elements for the definition of linear momentum balance equilibrium, both in terms of material and spatial description.

Considering the traction vector force load applied to the structure, one can apply classical calculus arguments to derive:

$$\int_{\partial\Omega} \mathbf{t}^{(\boldsymbol{n})}(\boldsymbol{x}, t)dv = \int_{\partial\Omega} \boldsymbol{\sigma}(\boldsymbol{x}, t)\boldsymbol{n}dv = \int_{\Omega} \mathrm{div}_{\boldsymbol{x}}\boldsymbol{\sigma}(\boldsymbol{x}, t)dv \tag{2.48}$$

where $\boldsymbol{\sigma}(\boldsymbol{x}, t)$ is the Cauchy stress tensor introduced in Sec. 2.4. Applying now Eq. (2.46) referring to the spatial description of the balance law, imposing the integral term related to the traction vector field in the spatial description into the definition of external force vector Eq. (2.47), one can obtain:

$$\int_{\Omega} \rho(\boldsymbol{x}, t)\frac{D\boldsymbol{v}(\boldsymbol{x}, t)}{Dt}dv = \int_{\Omega} \mathrm{div}_{\boldsymbol{x}}\boldsymbol{\sigma}(\boldsymbol{x}, t)dv + \int_{\Omega} \mathbf{b}(\boldsymbol{x}, t)dv \tag{2.49}$$

Applying now the Localization Theorem [146], one can retrieve the global translational equilibrium equation in strong form, also known as Cauchy's first equation of motion, written with respect to the spatial reference frame:

$$\rho(\boldsymbol{x}, t)\frac{D\boldsymbol{v}(\boldsymbol{x}, t)}{Dt} = \mathrm{div}_{\boldsymbol{x}}\boldsymbol{\sigma}(\boldsymbol{x}, t) + \mathbf{b}(\boldsymbol{x}, t) \tag{2.50}$$

Equation (2.50) is the starting point for the analysis of the elasto-dynamic problem in nonlinear solid mechanics when pure mechanical loads are considered. Typically, equilibrium equations are written in the material reference frame, adopting alternative strain and stress measures, based on energetic arguments and duality. These considerations will be addressed from a variational perspective in the following section.

2.6 Variational formulation

The mathematical foundations of finite element formulation frequently involves the introduction of linearized virtual quantities, which allow for the consistent representation of small variations in kinematic fields [149]. The adoption of the configuration concepts is helpful when *variations* have to be considered. Considering a continuum body, the set of all possible configurations that satisfy the geometric constraints is the set of *admissible* configurations [150]. Within this set, only one configuration satisfies the equilibrium conditions. From this true configuration, the set of admissible ones is then restricted to those in its neighborhood, and they are obtained considering *infinitesimal variations* from this equilibrated state. A *virtual* variation is a small perturbation, experienced by a mechanical system in its equilibrium configuration, to define another compatible and admissible configuration [150]. As stated by Reddy [150]: "*[...] the displacements are called virtual because they are imagined to take place (i.e, hypothetical), with the actual loads acting at their fixed values*". The application of the calculus of variations [149, 151] and appropriate variational principle provides a rigorous framework for deriving the governing equations in a weak and global form.

2.6.1 Virtual variation and linearized quantities

Let $\delta\mathbf{u}(\boldsymbol{x})$ be a small perturbation of the displacement field defined in the spatial configuration $\boldsymbol{x}$, considered to define the *variation* of the displacement field, supposed arbitrary and *virtual*. In this sense, the concept of variation is not referred to an actual change but to a possible realization of the displacements [149]. The linearized kinematics approach described in Sec. 2.3 is now employed, adopting the same formalism, to define the virtual variation of the kinematic measures introduced before.
Given the virtual displacement $\delta\mathbf{u}(\boldsymbol{x})$, one can derive:

$$\nabla_{\boldsymbol{x}}(\delta\boldsymbol{u}) = \frac{\partial(\delta\boldsymbol{u})}{\partial\boldsymbol{x}} = \frac{\partial(\delta\boldsymbol{u})}{\partial\boldsymbol{X}}\frac{\partial\boldsymbol{X}}{\partial\boldsymbol{x}} = \nabla_{\boldsymbol{X}}(\delta\boldsymbol{u})\mathbf{F}^{-1} \tag{2.51}$$

Starting from the above definitions and following Eq. (2.31), one can derive the virtual variation of the deformation gradient $\delta\mathbf{F}$ by means of the directional derivative [147]:

$$\delta\mathbf{F} = D\mathbf{F}[\delta\boldsymbol{u}] = \frac{d}{d\varepsilon}\mathbf{F}(\boldsymbol{x}+\varepsilon\delta\boldsymbol{u})\bigg|_{\varepsilon=0} = \frac{\partial(\delta\boldsymbol{u})}{\partial\boldsymbol{X}} = \nabla_{\boldsymbol{X}}(\delta\boldsymbol{u}) \tag{2.52}$$

Applying the properties of the directional derivative, and exploited the obtained relation in Eq. (2.52), the virtual variation of the Green-Lagrange strain tensor is rapidly obtained [147]:

$$\begin{aligned}
\delta\mathbf{E} &= \frac{1}{2}\delta(\mathbf{F}^T\mathbf{F}-\mathbf{I}) = \frac{1}{2}\delta(\mathbf{F}^T\mathbf{F}) = \frac{1}{2}((\delta\mathbf{F})^T\mathbf{F}+\mathbf{F}^T\delta\mathbf{F}) = \\
&= \frac{1}{2}((\nabla_{\boldsymbol{X}}(\delta\boldsymbol{u}))^T\mathbf{F}+\mathbf{F}^T(\nabla_{\boldsymbol{X}}(\delta\boldsymbol{u}))) = \frac{1}{2}((\mathbf{F}^T(\nabla_{\boldsymbol{X}}(\delta\boldsymbol{u}))^T+\mathbf{F}^T(\nabla_{\boldsymbol{X}}(\delta\boldsymbol{u}))) = \\
&= \mathrm{sym}(\mathbf{F}^T(\nabla_{\boldsymbol{X}}(\delta\boldsymbol{u})))
\end{aligned} \tag{2.53}$$

The property of symmetry expressed in Eq. (2.53) is useful when integral energetic contributions will be derived. From this derivation, the virtual variation of the strain tensor in the spatial reference frame $\delta\mathbf{e}$ is carried out starting from the push-forward of the tensor $\delta\mathbf{E}$:

$$\begin{aligned}
\delta\mathbf{e} = \Phi_*[\delta\mathbf{E}] &= \mathbf{F}^{-T}\delta\mathbf{E}\mathbf{F}^{-1} = \mathbf{F}^{-T}\left[\frac{1}{2}\left(\mathbf{F}^T(\nabla_{\boldsymbol{X}}(\delta\boldsymbol{u}))+\mathbf{F}^T(\nabla_{\boldsymbol{X}}(\delta\boldsymbol{u}))\right)\right]\mathbf{F}^{-1} = \\
&= \frac{1}{2}\left[\mathbf{F}^{-T}(\nabla_{\boldsymbol{X}}(\delta\boldsymbol{u}))^T\mathbf{F}\mathbf{F}^{-1}+\mathbf{F}^{-T}\mathbf{F}^T(\nabla_{\boldsymbol{X}}(\delta\boldsymbol{u}))\mathbf{F}^{-1}\right] = \\
&= \frac{1}{2}\left((\nabla_{\boldsymbol{x}}(\delta\boldsymbol{u}))^T+\nabla_{\boldsymbol{x}}(\delta\boldsymbol{u})\right)
\end{aligned} \tag{2.54}$$

2.6.2 Governing equation in weak form in spatial description

Let $\boldsymbol{\Omega}$ be the spatial actual configuration of the continuum body. Let $\boldsymbol{u}$ be the displacement field and let the body be in equilibrium under Cauchy's conditions. Assume the equilibrium conditions Eq. (2.50), assuming $\mathbf{b}$ is the vector of volume forces. Geometrical and load constraints have to be defined, characterizing the initial and boundary value problem. On the surface subdomain $\partial\Omega_\sigma$ of the whole external surface $\partial\Omega$, a generic load application is supposed. Instead, in the subdomain $\partial\Omega_u$ geometrical constraints are considered, in such a way $\partial\Omega = \partial\Omega_\sigma \cup \partial\Omega_u$. Considering this problem statement, the governing equation in strong form is then coupled with

initial and boundary conditions to define the boundary-value problem of the elastodynamic problem, written in the spatial reference frame:

$$\begin{cases} \rho(\boldsymbol{x},t)\dfrac{D\boldsymbol{v}(\boldsymbol{x},t)}{Dt} = \mathrm{div}_{\boldsymbol{x}}\boldsymbol{\sigma}(\boldsymbol{x},t) + \mathbf{b}(\boldsymbol{x},t) \\ \boldsymbol{u}(\boldsymbol{x},t) = \bar{\boldsymbol{u}}(\boldsymbol{x},t) \quad \text{on } \partial\Omega_u \\ \boldsymbol{t}(\boldsymbol{x},t) = \bar{\boldsymbol{t}}(\boldsymbol{x},t) \quad \text{on } \partial\Omega_\sigma \end{cases} \tag{2.55}$$

The set of governing equations Eq. (2.55) is not generally solvable analytically in the most general case, for any boundary conditions or load configurations. Exact reference solutions are available only in special and idealized cases [150]. The most common approach to finding a general solution is the implementation of numerical procedures based on the variational principles. In this sense, the governing equations are rewritten in a global, integral form, where a discretization technique is applied for the approximation of the solution numerically. Most variational principles are based on the *fundamental lemma of calculus of variations* [152], which is briefly presented here for the application of the present thesis.
Starting from the equilibrium equation Eq. (2.55), considering a generic $\boldsymbol{\eta}(\boldsymbol{x}) : \boldsymbol{\Omega} \to \mathbb{R}^3$ vector-valued function, defined over the spatial configuration of the continuum body at equilibrium, the following functional is introduced [63]:

$$f(\boldsymbol{u}(\boldsymbol{x}), \boldsymbol{\eta}(\boldsymbol{x})) = \int_\Omega \left(\mathrm{div}_{\boldsymbol{x}}\boldsymbol{\sigma}(\boldsymbol{x},t) + \mathbf{b}(\boldsymbol{x},t) - \rho(\boldsymbol{x},t)\frac{D\boldsymbol{v}(\boldsymbol{x},t)}{Dt} \right) \cdot \boldsymbol{\eta}(\boldsymbol{x}) dv = 0 \tag{2.56}$$

In the context of the calculus of variation, the generic $\boldsymbol{\eta}(\boldsymbol{x})$ is called *test function*. By the definition of the test function, one can automatically retrieve the equilibrium condition in strong form by the previous statement through the fundamental lemma of calculus of variations. Since the test function is arbitrary, the argument of the functional (that is, multiplied by $\boldsymbol{\eta}(\boldsymbol{x})$) must be zero in the whole domain of integration to satisfy the above condition. In other words, the solution of the strong form equilibrium equations is equivalent to the solution of the weak form equation. Within the context of finite element procedures for nonlinear elasticity, the arbitrary test-function $\boldsymbol{\eta}(\boldsymbol{x})$ considered is typically the virtual variation of the displacement field, namely $\delta\boldsymbol{u}$. Given by the physical interpretation of the virtual displacements introduced before, the *Principle of Virtual Work* is then introduced:

$$\int_\Omega \left(\mathrm{div}_{\boldsymbol{x}}\boldsymbol{\sigma}(\boldsymbol{x},t) + \mathbf{b}(\boldsymbol{x},t) - \rho(\boldsymbol{x},t)\frac{D\boldsymbol{v}(\boldsymbol{x},t)}{Dt} \right) \cdot \delta\boldsymbol{u} \; dv = 0 \tag{2.57}$$

Exploiting tensor algebra and related properties [153], remembering that Cauchy's stress tensor $\boldsymbol{\sigma}(\boldsymbol{x},t)$ is a symmetric tensor and the virtual variation of the strain tensor in the spatial description is given by Eq. (2.54), the first integral contribution in Eq. (2.57) can be rewritten as:

$$\begin{aligned} \mathrm{div}_{\boldsymbol{x}}\boldsymbol{\sigma}(\boldsymbol{x},t)\cdot\delta\boldsymbol{u} &= \mathrm{div}_{\boldsymbol{x}}(\boldsymbol{\sigma}^T(\boldsymbol{x},t)\delta\boldsymbol{u}) - \boldsymbol{\sigma}(\boldsymbol{x},t) : \nabla_{\boldsymbol{x}}(\delta\boldsymbol{u}) \\ &= \mathrm{div}_{\boldsymbol{x}}(\boldsymbol{\sigma}^T(\boldsymbol{x},t)\delta\boldsymbol{u}) - \boldsymbol{\sigma}(\boldsymbol{x},t) : \frac{1}{2}\big((\nabla_{\boldsymbol{x}}(\delta\boldsymbol{u}))^T + \nabla_{\boldsymbol{x}}(\delta\boldsymbol{u})\big) \\ &= \mathrm{div}_{\boldsymbol{x}}(\boldsymbol{\sigma}^T(\boldsymbol{x},t)\delta\boldsymbol{u}) - \boldsymbol{\sigma}(\boldsymbol{x},t) : \delta\mathbf{e} \end{aligned} \tag{2.58}$$

Substituting the obtained expression into Eq. (2.57), applying the Divergence Theorem and analyzing separately each term, one obtains finally the classical expression of weak-form governing

equation for the elasto-dynamic nonlinear problem:

$$\int_{\Omega} \boldsymbol{\sigma}(\boldsymbol{x},t) : \delta\mathbf{e} dv = \int_{\partial\Omega} \boldsymbol{\sigma}(\boldsymbol{x},t)^T \boldsymbol{n} \cdot \delta\boldsymbol{u} dv + \int_{\Omega} \mathbf{b}(\boldsymbol{x},t) \cdot \delta\boldsymbol{u} dv - \int_{\Omega} \rho(\boldsymbol{x},t) \frac{D\boldsymbol{v}(\boldsymbol{x},t)}{Dt} \cdot \delta\boldsymbol{u} dv \quad (2.59)$$

This final statement is one of the most straightforward variational principles used for constructing finite element procedures in nonlinear continuum mechanics. Denoting with $\boldsymbol{a}(\boldsymbol{x},t)$ the spatial acceleration, from Eq. (2.59), the internal, external, and inertial virtual work contributions are defined:

$$\delta\mathcal{L}_{int} = \int_{\Omega} \boldsymbol{\sigma} : \delta\mathbf{e} \; dv \quad (2.60)$$

$$\delta\mathcal{L}_{ext} = \int_{\Omega} \boldsymbol{\sigma}(\boldsymbol{x},t)^T \boldsymbol{n} \cdot \delta\boldsymbol{u} dv + \int_{\Omega} \mathbf{b}(\boldsymbol{x},t) \cdot \delta\boldsymbol{u} dv \quad (2.61)$$

$$\delta\mathcal{L}_{ine} = \int_{\Omega} \rho(\boldsymbol{x},t) \frac{D\boldsymbol{v}(\boldsymbol{x},t)}{Dt} \cdot \delta\boldsymbol{u} dv = \int_{\Omega} \rho(\boldsymbol{x},t) \boldsymbol{a}(\boldsymbol{x},t) \cdot \delta\boldsymbol{u} dv \quad (2.62)$$

2.6.3 First Piola-Kirchhoff stress tensor

The final weak-form equation Eq. (2.59), is written in the spatial reference frame, as can be observed from the volume integral computation, referred to the actual configuration $\boldsymbol{\Omega}$. Alternative forms of the equilibrium conditions are adopted in finite element scenarios, when referred to the material undeformed state. From tensor algebra [153] and mathematical manipulations, the weak-form balance law referring to the material reference frame can be introduced.
Staring from the definition of internal work Eq. (2.60):

$$\delta\mathcal{L}_{int} = \int_{\Omega} \boldsymbol{\sigma} : \delta\mathbf{e} \; dv = \int_{\Omega_0} \boldsymbol{\sigma} : \nabla_{\boldsymbol{x}}(\delta\boldsymbol{u}) \; JdV =$$

$$= \int_{\Omega_0} \boldsymbol{\sigma} : \nabla_{\boldsymbol{X}}(\delta\boldsymbol{u}) \; \mathbf{F}^{-1} \; JdV = \int_{\Omega_0} (J\boldsymbol{\sigma}\mathbf{F}^{-T}) : \nabla_{\boldsymbol{X}}(\delta\boldsymbol{u}) \; dV = \int_{\Omega_0} \mathbf{P} : \delta\mathbf{F} \; dV \quad (2.63)$$

where the tensor $\mathbf{P} = J\boldsymbol{\sigma}\mathbf{F}^{-T}$ is the first Piola-Kirchhoff stress tensor (PK1), defined as a two-point unsymmetric stress tensor whose components are given by:

$$\mathbf{P} = P_{iJ}\mathbf{e}_i \otimes \mathbf{E}_J; \qquad P_{iJ} = J\sigma_{ik}(\mathbf{F})^{-1}_{Jk} \quad (2.64)$$

The physical meaning of the PK1 stress tensor, provided in Eq. (2.64), is given by Nanson's formula [63] and the analysis of the force per unit area, as done in the definition of Cauchy's stress tensor. For an infinitesimal area described by the vector $d\boldsymbol{a} = da\boldsymbol{n}$, the elemental force $d\boldsymbol{p}$ acting on da is given by the traction vector:

$$d\boldsymbol{p}(\boldsymbol{x},t) = \boldsymbol{t}^{(\boldsymbol{n})}(\boldsymbol{x},t)da = \boldsymbol{\sigma}(\boldsymbol{x},t)d\boldsymbol{a} = J\boldsymbol{\sigma}(\boldsymbol{x},t)\mathbf{F}^{-T}d\boldsymbol{A} = \mathbf{P}(\boldsymbol{X},t)d\boldsymbol{A} \quad (2.65)$$

where $d\boldsymbol{A}$ is the infinitesimal area vector around the $\boldsymbol{X}$ material particle in the material configuration. In this sense, by Eq. (2.65) gives the physical meaning of the PK1 stress tensor, that relates the *spatial* force per unit *undeformed* area, introduced as the concept of *material traction vector* $\mathbf{T}^{(\boldsymbol{N})}(\boldsymbol{X},t) = \mathbf{P}(\boldsymbol{X},t)\boldsymbol{N}$. Therefore, the $\mathbf{P}$ tensor is not strictly related to the material condition [147].

2.6.4 Governing equation in weak form in material description

The material description of the balance equation can be obtained exploiting the definition of the first Piola-Kirchhoff stress tensor. Starting from Eq. (2.57), applying again the fundamental lemma of calculus of variation, the material description of the governing equation can be retrieved:

$$\begin{aligned}
0 &= \int_{\Omega}\left(\mathrm{div}_{\boldsymbol{x}}\boldsymbol{\sigma}(\boldsymbol{x},t)+\mathbf{b}(\boldsymbol{x},t)-\rho(\boldsymbol{x},t)\frac{D\boldsymbol{v}(\boldsymbol{x},t)}{Dt}\right)\cdot\delta\boldsymbol{u}dv = \\
&= \int_{\Omega_0}\left(\mathrm{div}_{\boldsymbol{x}}\boldsymbol{\sigma}(\boldsymbol{x},t)+\mathbf{b}(\boldsymbol{x},t)-\rho(\boldsymbol{x},t)\frac{D\boldsymbol{v}(\boldsymbol{x},t)}{Dt}\right)\cdot\delta\boldsymbol{u}\ J(\boldsymbol{X},t)dV = \\
&= \int_{\Omega}J(\boldsymbol{X},t)\mathrm{div}_{\boldsymbol{x}}\boldsymbol{\sigma}(\boldsymbol{x},t)\cdot\delta\boldsymbol{u}dV+\int_{\Omega_0}J(\boldsymbol{X},t)\mathbf{b}(\boldsymbol{x},t)\cdot\delta\boldsymbol{u}dV-\int_{\Omega_0}J(\boldsymbol{X},t)\rho(\boldsymbol{x},t)\frac{D\boldsymbol{v}(\boldsymbol{x},t)}{Dt}\cdot\delta\boldsymbol{u} = \\
&= \int_{\Omega_0}J(\boldsymbol{X},t)\mathrm{div}_{\boldsymbol{x}}\boldsymbol{\sigma}(\boldsymbol{x},t)\cdot\delta\boldsymbol{u}dV+\int_{\Omega_0}\mathbf{B}(\boldsymbol{X},t)\cdot\delta\boldsymbol{u}dV-\int_{\Omega_0}\rho_0(\boldsymbol{X},t)\dot{\boldsymbol{V}}(\boldsymbol{X},t)dV \qquad (2.66)
\end{aligned}$$

where, in the last equality of Eq. (2.66), the vector $\mathbf{B}(\boldsymbol{X},t)$ denotes the reference body forces, $\rho_0(\boldsymbol{X},t)$ is the density function evaluated in the material reference frame and $\dot{\boldsymbol{V}}(\boldsymbol{X},t)$ represent the material velocity, exploiting a derivation in time since no convective terms of the total time derivative are involved. The first term of Eq. (2.66) is analyzed separately starting from the definition of PK1 tensor Eq. (2.64) and the properties of the divergence operator [153]:

$$\mathrm{div}_{\boldsymbol{X}}\mathbf{P}=\mathrm{div}_{\boldsymbol{X}}(J\boldsymbol{\sigma}\mathbf{F}^{-T})=\nabla_{\boldsymbol{X}}(\boldsymbol{\sigma}):J\mathbf{F}^{-T}+\boldsymbol{\sigma}\mathrm{div}_{\boldsymbol{X}}(J\mathbf{F}^{-T})=J\mathrm{div}_{\boldsymbol{x}}(\boldsymbol{\sigma}) \qquad (2.67)$$

where the Piola Identity $\mathrm{div}_{\boldsymbol{X}}(J\mathbf{F}^{-T})=0$ has been applied [63]. In this way, the weak-form equation is rewritten as:

$$\begin{aligned}
&\int_{\Omega_0}\mathrm{div}_{\boldsymbol{X}}\mathbf{P}\cdot\delta\boldsymbol{u}dV+\int_{\Omega_0}\mathbf{B}(\boldsymbol{X},t)\cdot\delta\boldsymbol{u}dV-\int_{\Omega_0}\rho_0(\boldsymbol{X},t)\dot{\boldsymbol{V}}(\boldsymbol{X},t)\cdot\delta\boldsymbol{u}dV \quad = \\
&\qquad = \int_{\Omega_0}\left(\mathrm{div}_{\boldsymbol{X}}\mathbf{P}+\mathbf{B}(\boldsymbol{X},t)-\rho_0(\boldsymbol{X},t)\dot{\boldsymbol{V}}(\boldsymbol{X},t)\right)\cdot\delta\boldsymbol{u}dV \quad = \quad 0 \qquad (2.68)
\end{aligned}$$

Considering the Fundamental Lemma of Calculus of Variation, the strong-form equilibrium equation written in the material reference frame is obtained from Eq. (2.68):

$$\rho_0(\boldsymbol{X},t)\dot{\boldsymbol{V}}(\boldsymbol{X},t)=\mathrm{div}_{\boldsymbol{X}}\mathbf{P}(\boldsymbol{X},t)+\mathbf{B}(\boldsymbol{X},t) \qquad (2.69)$$

This final statement provides the material expression of the variational principle for constructing a finite element procedure in nonlinear continuum mechanics. Denoting with $\boldsymbol{A}(\boldsymbol{x},t)$ the material acceleration, from Eq. (2.69), the internal, external, and inertial virtual work contributions are defined in the material reference frame as:

$$\delta\mathcal{L}_{int} = \int_{\Omega_0}\mathbf{P}:\delta\mathbf{F}dv \qquad (2.70)$$

$$\delta\mathcal{L}_{ext} = \int_{\Omega_0}\mathbf{P}(\boldsymbol{X},t)^T\boldsymbol{N}\cdot\delta\boldsymbol{u}dv+\int_{\Omega_0}\mathbf{B}(\boldsymbol{X},t)\cdot\delta\boldsymbol{u}dv \qquad (2.71)$$

$$\delta\mathcal{L}_{ine} = \int_{\Omega_0}\rho_0(\boldsymbol{X},t)\dot{\boldsymbol{V}}(\boldsymbol{X},t)\cdot\delta\boldsymbol{u}dv=\int_{\Omega_0}\rho_0(\boldsymbol{x},t)\boldsymbol{A}(\boldsymbol{X},t)\cdot\delta\boldsymbol{u}dv \qquad (2.72)$$

2.6.5 Second Piola-Kirchhoff stress tensor

In the material description of the continuum body, the PK1 stress tensor is not commonly adopted because it refers to physical quantities related to the actual spatial reference frame. From Eq. (2.65), one can consider the pull-back of the spatial elemental force vector $d\boldsymbol{p}$ to define the related force vector $d\boldsymbol{\mathcal{P}}$ in the material configuration:

$$d\boldsymbol{\mathcal{P}} = \Phi_*^{-1}[d\boldsymbol{p}] = \Phi_*^{-1}[J\boldsymbol{\sigma}\mathbf{F}^{-T}d\boldsymbol{A}] = J\mathbf{F}^{-1}\boldsymbol{\sigma}\mathbf{F}^{-T}d\boldsymbol{A} = \mathbf{S}d\boldsymbol{A} \tag{2.73}$$

where the tensor $\mathbf{S} = J\mathbf{F}^{-1}\boldsymbol{\sigma}\mathbf{F}^{-T}$ is the *second Piola-Kirchhoff stress tensor*. In the practical application, the PK2 stress tensor has no physical meaning; it relates the *material* force per unit *material* area. In addition, by its definition, the PK2 stress tensor $\mathbf{S}$ is the pull-back on the material configuration of the Cauchy's stress tensor $\boldsymbol{\sigma}$ in the spatial configuration, scaled by a factor of J. This tensor transformation is called *Piola transform* on contravariant tensors [146]:

$$\text{(a)} \quad \mathbf{S} = J\Phi_*^{-1}[\boldsymbol{\sigma}] \qquad \text{(b)} \quad \boldsymbol{\sigma} = J\Phi_*[\mathbf{S}] \tag{2.74}$$

As seen in the previous derivation, the PK2 stress tensor can be derived from energetic arguments. Starting from the definition of internal energy and using the push-forward operation on the Almansi strain Eq. (2.54), and remembering the properties of the trace and contraction operators [153], one can write:

$$\begin{aligned}
\delta\mathcal{L}_{int} &= \int_\Omega \boldsymbol{\sigma} : \delta\mathbf{e}\ dv = \int_{\Omega_0} \boldsymbol{\sigma} : (\mathbf{F}^{-T}\delta\mathbf{E}\mathbf{F}^{-1})JdV = \int_{\Omega_0} \mathrm{tr}((\mathbf{F}^{-T}\delta\mathbf{E}\mathbf{F}^{-1})(J\boldsymbol{\sigma}))dV = \\
&= \int_{\Omega_0} \mathrm{tr}(J(\mathbf{F}^{-1}\boldsymbol{\sigma}\mathbf{F}^{-T})\delta\mathbf{E})dV = \int_{\Omega_0} (J\mathbf{F}^{-1}\boldsymbol{\sigma}\mathbf{F}^{-T}) : \delta\mathbf{E}dV = \\
&= \int_{\Omega_0} \mathbf{S} : \delta\mathbf{E}dV
\end{aligned} \tag{2.75}$$

From these introduced quantities, then, the internal strain energy, namely the energy stored during the deformation process, can be equivalently written in the material or spatial configuration as:

$$\delta\mathcal{L}_{int} = \int_{\Omega_0} \mathbf{P} : \delta\mathbf{F}\ dV = \int_{\Omega_0} \mathbf{S} : \delta\mathbf{E}dV = \int_\Omega \boldsymbol{\sigma} : \delta\mathbf{e}\ dv \tag{2.76}$$

In other words, the deformation gradient $\mathbf{F}$ is the *work-conjugate* of the first Piola-Kirchhoff $\mathbf{P}$ stress tensor, the Green-Lagrange strain tensor $\mathbf{E}$ is the *work-conjugate* of the second Piola-Kirchhoff $\mathbf{S}$ stress tensor, and the Almansi strain tensor $\mathbf{r}$ is the *work-conjugate* of the Cauchy $\boldsymbol{\sigma}$ stress tensor.

Chapter 3

Hyperelasticity

"*The task of the theorist is to bring order into the chaos of the phenomena of nature, to invent a language by which a class of these phenomena can be described efficiently and simply.*"

- "The Non-Linear Field Theories of Mechanics", Truesdell and Noll, 1992.

3.1 Basics of isotropic hyperelastic constitutive modeling

3.1.1 Helmholtz free energy

The constitutive theory for hyperelastic materials is based on the existence of a Helmholtz free-energy function Ψ, denoted as the strain energy density function per unit volume. The material model is characterized by the definition of Ψ. In general, a hyperelastic material is classified as *homogeneous* or *non-homogeneous*. In the case of homogeneous hyperelasticity, the distribution of internal structure is considered uniform across the scales (from macro- to micro-scale), and the material model is fully characterized by the deformation gradient, thus $\Psi = \Psi(\mathbf{F})$. Instead, in the case of non-homogeneous materials, the strain energy function per unit volume will depend on both the deformation gradient and the position vector of the particle considered in the continuum body.

In the present thesis, perfectly elastic homogeneous materials will be considered. From the definition of "perfectly" elastic, a general hypothesis on the *dissipative* behavior is considered, expressed in mathematical terms by means of the Coleman-Noll procedure [146]:

$$\mathcal{D}_{int} = \mathbf{P} : \dot{\mathbf{F}} - \dot{\Psi} = \left(\mathbf{P} - \frac{\partial \Psi(\mathbf{F})}{\partial \mathbf{F}} \right) : \dot{\mathbf{F}} = 0, \qquad \forall \mathbf{X} \in \mathbf{\Omega}_0 \tag{3.1}$$

where $\mathcal{D}_{int}$ is the internal dissipation energy, $\mathbf{P}$ is the first Piola-Kirchhoff stress tensor, and $\dot{\mathbf{F}}$ is the rate of change of the deformation gradient during the evolution of the continuum body. For perfectly elastic structures, since the internal dissipation is required to be null *for each arbitrarily chosen* $\dot{\mathbf{F}}$, the constitutive law for hyperelastic material is obtained:

$$\mathbf{P} = \frac{\partial \Psi(\mathbf{F})}{\partial \mathbf{F}} \tag{3.2}$$

In the constitutive theory of hyperelasticity, typically physical admissibility conditions are imposed directly on the admissible values of the strain energy function model Ψ:

- *Normalization condition*: in the *ground* state, the undeformed configuration characterized by $\mathbf{F} = \mathbf{I}$, a stress free condition is imposed, thus

$$\Psi(\mathbf{I}) = 0 \tag{3.3}$$

- *Non-negativeness condition*: in every possible deformed configuration, the strain energy function satisfies the condition $\Psi(\mathbf{F}) \geq 0$.

In the present approach, under these hypotheses, the strain energy function Ψ admits only a global minimum in $\mathbf{F} = \mathbf{I}$. This can also be addressed as *pure convexity* of Ψ. Additionally, in the literature, numerous models for hyperelastic materials have been analyzed under the *poly-convexity* assumptions, considering more complex models for the analysis of large strains, damage, progressive failure, and constitutive theories of biological tissue [154].

3.1.2 Equivalent and reduced forms of constitutive law

The basic assumption of the constitutive modeling of materials is *objectivity*. This aspect has to be incorporated in the constitutive law in order to be physically admissible [155]. It is generally assumed that the strain energy function $\Psi(\mathbf{F})$ is objective when the motion $\boldsymbol{\chi}$ is considered, condition that is expressed as:

$$\tilde{\Psi}(\mathbf{F}) = \tilde{\Psi}(\mathbf{R}^T\mathbf{F}) = \tilde{\Psi}(\mathbf{R}^T\mathbf{R}\mathbf{U}) = \bar{\Psi}(\mathbf{U}) \tag{3.4}$$

where $\mathbf{R}$ is the proper orthogonal rotation tensor introduced in the Polar representation theorem, and $\mathbf{U}$ is the stretch tensor. From Eq. (3.4), one can note that the strain energy function depends only on the pure stretch tensor, and the rotational part of the deformation gradient does not affect the total energy stored during the deformation process. This condition is necessary and sufficient to incorporate, in the constitutive modeling of materials, objectivity for superimposed rigid body motion and physical consistency of the material model.

Moreover, one can rewrite the dependence of the material model given by Ψ in terms of the right Cauchy-Green strain tensor $\mathbf{C}$ and the Green-Lagrange strain tensor $\mathbf{E}$. Since these strain measures, as discussed in Sec. 2.1.2, do not depend on the rotational part of the deformation gradient, they can be both assumed to completely characterize the strain energy density function:

$$\tilde{\Psi}(\mathbf{F}) = \hat{\Psi}(\mathbf{E}) = \Psi(\mathbf{C}) \tag{3.5}$$

Starting from this point, it is possible to rewrite the material model in an alternative form, depending on the specific application. In the framework of numerical models for simulations of materials and structures, typically the right Cauchy-Green strain tensor and Green-Lagrange strain tensor are adopted, since they are related to the material reference [156].

Considering the time derivative of the strain energy function, by means of the chain rule and classical continuum mechanics arguments, one can write:

$$\dot{\Psi} = \mathrm{tr}\left[\left(\frac{\partial\tilde{\Psi}(\mathbf{F})}{\partial\mathbf{F}}\right)^T\dot{\mathbf{F}}\right] = \mathrm{tr}\left[\left(2\frac{\partial\Psi(\mathbf{C})}{\partial\mathbf{C}}\right)\mathbf{F}^T\dot{\mathbf{F}}\right] \tag{3.6}$$

$$\left(\frac{\partial\tilde{\Psi}(\mathbf{F})}{\partial\mathbf{F}}\right)^T = 2\left(\frac{\partial\Psi(\mathbf{C})}{\partial\mathbf{C}}\right)\mathbf{F}^T \tag{3.7}$$

Alternative expression for the first and second Piola-Kirchhoff stress tensor can be automatically retrieved from Eq. (3.7):

$$\boldsymbol{\sigma} = 2J^{-1}\mathbf{F}\frac{\partial\Psi(\mathbf{C})}{\partial\mathbf{C}}\mathbf{F}^T \tag{3.8}$$

$$\mathbf{P} = 2\mathbf{F}\frac{\partial\Psi(\mathbf{C})}{\partial\mathbf{C}} \tag{3.9}$$

$$\mathbf{S} = 2\frac{\partial\Psi(\mathbf{C})}{\partial\mathbf{C}} = \frac{\partial\hat{\Psi}(\mathbf{E})}{\partial\mathbf{E}} \tag{3.10}$$

These definitions of the stress tensors Eqs. (3.8)-(3.10) are the starting point for the implementation of structural mechanics numerical models, and represent the fundamental relations adopted in the hyperelastic material framework for the stress analysis and balance principle definitions.

3.1.3 Representation theorem

One of the most important results in continuum mechanics is the *representation theorem*. If a scalar-valued function is invariant under rotations, such as the strain energy density function discussed in Sec. 3.1.1, this can be expressed in terms of principal invariants of the argument. Considering the definition of $\Psi = \Psi(\mathbf{C})$ in terms of the right Cauchy-Green strain tensor, the principal invariants of the argument $\mathbf{C}$ are defined as:

$$I_1(\mathbf{C}) = \mathrm{tr}(\mathbf{C}) = \mathbf{I} : \mathbf{C} \tag{3.11}$$

$$I_2(\mathbf{C}) = \frac{1}{2}\Big((\mathrm{tr}(\mathbf{C}))^2 - \mathrm{tr}(\mathbf{C}^2)\Big) \tag{3.12}$$

$$I_3(\mathbf{C}) = \det(\mathbf{C}) = J^2 \tag{3.13}$$

where $\mathbf{I}$ is the identity tensor and the symbol ":" denotes the double contraction operator. Therefore, the strain energy function can be written as $\Psi = \Psi(I_1(\mathbf{C}), I_2(\mathbf{C}), I_3(\mathbf{C}))$. These fundamental results have been extensively adopted in the constitutive modeling of hyperelastic materials, utilizing constitutive models that depend only on the relations between the invariants of the tensor $\mathbf{C}$, while analyzing the physical interpretation of each component.

To derive a general, closed-form expression of the constitutive law in terms of invariants, starting from the differentiation rule:

$$\frac{\partial\Psi(\mathbf{C})}{\partial\mathbf{C}} = \frac{\partial\Psi(\mathbf{C})}{\partial I_1}\frac{\partial I_1}{\partial\mathbf{C}} + \frac{\partial\Psi(\mathbf{C})}{\partial I_2}\frac{\partial I_2}{\partial\mathbf{C}} + \frac{\partial\Psi(\mathbf{C})}{\partial I_3}\frac{\partial I_3}{\partial\mathbf{C}} \tag{3.14}$$

The derivatives of the principal invariants Eqs. (3.11)-(3.13) can be retrieved from simple tensor calculus [153]:

$$\frac{\partial I_1}{\partial\mathbf{C}} = \frac{\partial(\mathbf{I} : \mathbf{C})}{\partial\mathbf{C}} = \mathbf{I} \tag{3.15}$$

$$\frac{\partial I_2}{\partial\mathbf{C}} = I_1\mathbf{I} - \mathbf{C} \tag{3.16}$$

$$\frac{\partial I_3}{\partial\mathbf{C}} = I_3\mathbf{C}^{-1} \tag{3.17}$$

The constitutive law in terms of the second Piola-Kirchhoff stress tensor Eq. (3.10) can be rewritten as:

$$\mathbf{S} = 2\frac{\partial\Psi(\mathbf{C})}{\partial\mathbf{C}} = 2\left[\left(\frac{\partial\Psi}{\partial I_1} + I_1\frac{\partial\Psi}{\partial I_2}\right)\mathbf{I} - \frac{\partial\Psi}{\partial I_2}\mathbf{C} + I_3\frac{\partial\Psi}{\partial I_3}\mathbf{C}^{-1}\right] \tag{3.18}$$

The adoption of the strain energy function in terms of the right Cauchy-Green strain tensor Eq. (3.5) and the constitutive law written, consequently, as done in Eq. (3.18) is referred to as the coupled hyperelastic formulation. This approach is typically useful is incompressible material modeling, for which $J = 1$, or internally constrained materials.

3.2 Compressible isotropic hyperelasticity

The mechanical response of some soft materials and structures is characterized by different deformation mechanisms. In particular, volumetric and isochoric deformations are typical mechanical responses observed under general boundary conditions. For this reason, it is convenient to split the definition of the strain energy density function in the so-called *volume-preserving* part and *volume-changing* part, under the Flory decomposition of the deformation gradient [157].

The *dilatational* and *distorsional* components of the strain energy functions are defined imposing the multiplicative decomposition into volumetric and isochoric components of the deformation gradient $\mathbf{F}$ and the right Cauchy-Green strain tensor $\mathbf{C}$.

$$\mathbf{F} = (J^{1/3}\mathbf{I})\bar{\mathbf{F}}, \qquad \bar{\mathbf{F}} = J^{-1/3}\mathbf{F} \tag{3.19}$$

$$\mathbf{C} = (J^{2/3}\mathbf{I})\bar{\mathbf{C}}, \qquad \bar{\mathbf{C}} = J^{-2/3}\mathbf{C} \tag{3.20}$$

These definitions provided in Eqs. (3.19)-(3.20) are useful in the constitutive modeling of nearly incompressible soft materials, for which dilatation changes (volume changes) require significantly more energy compared to distortional deformation [1]. In the following, the strain energy density function is the sum of a purely volumetric component and a purely distortional part:

$$\Psi(\mathbf{C}) = \Psi_{vol}(J) + \Psi_{iso}(\bar{\mathbf{C}}) = \Psi_{vol}(J) + \Psi_{iso}(\bar{I}_1, \bar{I}_2) \tag{3.21}$$

In the expression Eq. (3.21), the volumetric and dilatation parts are analyzed separately using the multiplicative decomposition of the kinematic measures. This approach has been extensively adopted in the numerical procedure to avoid numerical limitations of finite element approaches when incompressible materials are analyzed. The rescaled invariants of the modified right Cauchy-Green strain tensor are then straightforwardly introduced:

$$\bar{I}_1 = J^{-2/3}I_1; \qquad \bar{I}_2 = J^{-4/3}I_2 \tag{3.22}$$

The assumptions considered on the kinematic splitting of the deformation gradient are then imposed for the definition of the same constitutive law in terms of modified rescaled tensors $\bar{\mathbf{F}}$ and $\bar{\mathbf{C}}$. Starting from the chain rule, one can automatically derive the following differential relations:

$$\text{(a):} \quad \frac{\partial J}{\partial \mathbf{C}} = \frac{1}{2}J\mathbf{C}^{-1}; \qquad \text{(b):} \quad \frac{\partial J^{-2/3}}{\partial \mathbf{C}} = -\frac{1}{3}J^{-2/3}\mathbf{C}^{-1} \tag{3.23}$$

The definition of the constitutive law in terms of modified tensors requires the definition of the so-called *projection tensor*. The modified tensors are strictly a function of the deformation gradient through the volume ratio J dependence. In this sense, it is useful to consider the variation of the rescaled kinematic measure with respect to the reference Lagrangian strain measure adopted in the definition of a hyperelastic constitutive law [63]. Considering then:

$$\frac{\partial \bar{\mathbf{C}}}{\partial \mathbf{C}} = \frac{\partial (J^{-2/3}\mathbf{C})}{\partial \mathbf{C}} = \frac{\partial (J^{-2/3})}{\partial \mathbf{C}} \otimes \mathbf{C} + (J^{-2/3})\frac{\partial \mathbf{C}}{\partial \mathbf{C}} = J^{-2/3}\left(\mathbb{I} - \frac{1}{3}\mathbf{C}^{-1} \otimes \mathbf{C}\right) = J^{-2/3}\mathbb{P} \quad (3.24)$$

where the definition of $\mathbb{P}$, the projection tensor in the material reference frame, is exploited in Eq. (3.24). This tensor is required to correctly rewrite the balance equation in the material reference frame when considering the strain energy function splitting presented in Eq. (3.21). The second Piola-Kirchhoff stress tensor is defined imposing the decomposition of the strain energy density function Eq. (3.21):

$$\mathbf{S} = 2\frac{\partial \Psi}{\partial \mathbf{C}} = 2\frac{\partial \Psi_{vol}}{\partial \mathbf{C}} + 2\frac{\partial \Psi_{iso}}{\partial \mathbf{C}} = \mathbf{S}_{vol} + \mathbf{S}_{iso} \quad (3.25)$$

where the volumetric $\mathbf{S}_{vol}$ and dilatation $\mathbf{S}_{iso}$ terms are respectively defined as:

$$\mathbf{S}_{vol} = 2\frac{\partial \Psi_{vol}(J)}{\partial \mathbf{C}} = 2\frac{\partial \Psi_{vol}(J)}{\partial J}\frac{\partial J}{\partial \mathbf{C}} = Jp\mathbf{C}^{-1} \quad (3.26)$$

$$\begin{aligned} \mathbf{S}_{iso} &= 2\frac{\partial \Psi_{iso}(\bar{I}_1, \bar{I}_2)}{\partial \mathbf{C}} = 2\frac{\partial \Psi_{iso}(\bar{I}_1, \bar{I}_2)}{\partial \bar{\mathbf{C}}}\frac{\partial \bar{\mathbf{C}}}{\partial \mathbf{C}} = \\ &= J^{-2/3}\left(\mathbb{I} - \frac{1}{3}\mathbf{C}^{-1} \otimes \mathbf{C}\right) : \bar{\mathbf{S}} = J^{-2/3}\mathbb{P} : \bar{\mathbf{S}} = J^{-2/3}Dev(\bar{\mathbf{S}}) \end{aligned} \quad (3.27)$$

From the defintions provided in Eqs. (3.26)-(3.27), $p = \dfrac{\partial \Psi_{vol}(J)}{\partial J}$ is the hydrostatic pressure, $\bar{\mathbf{S}} = \dfrac{\partial \Psi_{iso}}{\partial \bar{\mathbf{C}}}$ is the rescaled second Piola-Kirchhoff stress tensors (RPK2), $\mathbb{P}$ is the projection tensor and $Dev(\cdot)$ is the *physically-consistent* deviatoric operator in the Lagrangian reference frame, defined as:

$$Dev(\mathbf{A}) = \mathbf{A} - \frac{1}{3}\big[\mathbf{A} : \mathbf{C}\big]\mathbf{C}^{-1} \quad (3.28)$$

The final expression of the second Piola-Kirchhoff stress tensors under the decoupled approach is retrieved:

$$\mathbf{S} = Jp\mathbf{C}^{-1} + J^{-2/3}\mathbb{P} : \bar{\mathbf{S}} \quad (3.29)$$

Under this formalism, the specific hyperelastic material model is implemented in the definition of the hydrostatic pressure and the RPK2 stress tensor, which are the only physical quantities depending on the strain energy density function model assigned. From the definition of rescaled invariants Eq. (3.22) and the derivative rules Eqs. (3.15)-(3.16):

$$\begin{aligned} \bar{\mathbf{S}} = 2\frac{\partial \Psi_{iso}(\bar{I}_1, \bar{I}_2)}{\partial \bar{\mathbf{C}}} &= 2\frac{\partial \Psi_{iso}(\bar{I}_1, \bar{I}_2)}{\partial \bar{I}_1} \cdot \frac{\partial \bar{I}_1}{\partial \bar{\mathbf{C}}} + 2\frac{\partial \Psi_{iso}(\bar{I}_1, \bar{I}_2)}{\partial \bar{I}_2} \cdot \frac{\partial \bar{I}_2}{\partial \bar{\mathbf{C}}} = \\ &= 2\left(\frac{\partial \Psi_{iso}(\bar{I}_1, \bar{I}_2)}{\partial \bar{I}_1} + \bar{I}_1\frac{\partial \Psi_{iso}(\bar{I}_1, \bar{I}_2)}{\partial \bar{I}_2}\right)\mathbf{I} - 2\frac{\partial \Psi_{iso}(\bar{I}_1, \bar{I}_2)}{\partial \bar{I}_2}\mathbf{C}^{-1} \end{aligned} \quad (3.30)$$

Once the constitutive model for the isochoric component is assigned, the RPK2 stress tensor is automatically assigned, computed by means of Eq. (3.30), thus the final isochoric component. Equations (3.18)-(3.30) are the most general expressions of the constitutive laws expressed in

terms of invariants of the deformations and hyperelastic material model Ψ. These expressions of the non-physical stress tensor represent the starting point for implementing Total Lagrangian numerical models, where all the involved quantities are referred to the undeformed structural configuration.

3.3 Tangent elasticity tensor

In the framework of numerical procedures for nonlinear problems, incremental procedures are adopted to solve the final nonlinear governing equations. In the context of hyperelasticity, a general representation of the incremental constitutive law is further required. Supposing that the stress tensor is only a function of the deformation state, the finite Δ (virtual δ) variation of the PK2 stress tensor during the evolution process is computed by the directional derivative of $\mathbf{S}$, introducing the linear relation [147]:

$$\Delta\mathbf{S} = \frac{1}{2}\mathbb{C}\Delta\mathbf{C} = \mathbb{C}\Delta\mathbf{E}; \qquad \delta\mathbf{S} = \frac{1}{2}\mathbb{C}\delta\mathbf{C} = \mathbb{C}\delta\mathbf{E}; \tag{3.31}$$

where $\mathbb{C}$ is the *tangent elasticity tensor*, also denoted as *tangent elastic moduli* or *material Jacobian tensor*. Following the fundamental kinematics relations and the constitutive law Eq. (3.10), the elasticity tensor introduced in Eq. (3.31) can be defined as:

$$\mathbb{C} = 2\frac{\partial\mathbf{S}(\mathbf{C})}{\partial\mathbf{C}} = \frac{\partial\mathbf{S}(\mathbf{E})}{\partial\mathbf{E}} = 4\frac{\partial^2\Psi}{\partial\mathbf{C}\partial\mathbf{C}} \tag{3.32}$$

The elasticity tensor $\mathbb{C}$ satisfies the *minor* symmetries, due to the symmetries of the right Cauchy-Green strain tensor $\mathbf{C}$ and the second Piola-Kirchhoff stress tensor $\mathbf{S}$; additionally, $\mathbb{C}$ satisfies the *major* symmetries by the Schwarz Theorem [63]. Hence, a hyperelastic material always possesses the major symmetries. Typically, the major symmetries of the tensor $\mathbb{C}$ are considered a necessary and sufficient condition for the existence of a strain energy function [63]. Therefore, only 21 independent components are required to fully characterize this fourth-order tensor [146]. The decoupled representation of the fourth-order tensor $\mathbb{C}$ is briefly provided, due to the relevance of involved terms, but the full analytic derivation of the following quantity can be found in [63, 147]. Following the split into volumetric and dilatation part introduced before, the tangent elastic moduli are also rewritten as:

$$\mathbb{C} = 2\frac{\partial\mathbf{S}}{\partial\mathbf{C}} = 2\frac{\partial\mathbf{S}_{iso}}{\partial\mathbf{C}} + 2\frac{\partial\mathbf{S}_{vol}}{\partial\mathbf{C}} = \mathbb{C}_{vol} + \mathbb{C}_{iso} \tag{3.33}$$

The volumetric contribution is defined as:

$$\mathbb{C}_{vol} = 2\frac{\partial\mathbf{S}_{vol}}{\partial\mathbf{C}} = 2\frac{\partial}{\partial\mathbf{C}}(Jp\mathbf{C}^{-1}) = J\left(p + J\frac{dp}{dJ}\right)\mathbf{C}^{-1}\otimes\mathbf{C}^{-1} - 2Jp\mathbf{C}^{-1}\odot\mathbf{C}^{-1} \tag{3.34}$$

$$\mathbb{C}_{iso} = 2\frac{\partial\mathbf{S}_{iso}}{\partial\mathbf{C}} = \mathbb{P} : \bar{\mathbb{C}} : \mathbb{P}^T + \frac{2}{3}J^{-2/3}(\bar{\mathbf{S}} : \mathbf{C})\tilde{\mathbb{P}} - \frac{2}{3}(\mathbf{C}^{-1}\otimes\mathbf{S}_{iso} + \mathbf{S}_{iso}\otimes\mathbf{C}^{-1}) \tag{3.35}$$

where the symbol $(\cdot)\odot(\cdot)$ denotes the Hadamard product, $\bar{\mathbb{C}}$ is the fictitious rescaled tangent elasticity tensor $\bar{\mathbb{C}} = \partial\Psi_{iso}/\partial\bar{\mathbf{C}}\partial\bar{\mathbf{C}}$ and $\tilde{\mathbb{P}}$ is the modified projection tensor:

$$\tilde{\mathbb{P}} = \mathbf{C}^{-1}\odot\mathbf{C}^{-1} - \frac{1}{3}\mathbf{C}^{-1}\otimes\mathbf{C}^{-1} \tag{3.36}$$

In some applications, the analytic closed-form expression of the tangent stiffness moduli under the coupled approach can be useful for the sake of convenience in implementing a numerical procedure. Supposing then the most general form of the strain energy function $\Psi = \Psi(I_1, I_2, I_3)$, applying the definition of the tangent elasticity tensor Eq. (3.32), one can derive the following expression:

$$\begin{aligned}
\mathbb{C} &= 4\left(\frac{\partial^2\Psi}{\partial I_1^2} + 2I_1\frac{\partial^2\Psi}{\partial I_1\partial I_2} + \frac{\partial\Psi}{\partial I_2} + I_1^2\frac{\partial^2\Psi}{\partial I_2^2}\right)\mathbf{I}\otimes\mathbf{I} + 4\left(\frac{\partial^2\Psi}{\partial I_1\partial I_2} + I_1\frac{\partial^2\Psi}{\partial I_2^2}\right)(\mathbf{I}\otimes\mathbf{C} + \mathbf{C}\otimes\mathbf{I}) + \\
&+ 4\left(I_3\frac{\partial^2\Psi}{\partial I_1\partial I_3} + I_1I_3\frac{\partial^2\Psi}{\partial I_2\partial I_3}\right)(\mathbf{I}\otimes\mathbf{C}^{-1} + \mathbf{C}^{-1}\otimes\mathbf{I}) + 4\frac{\partial^2\Psi}{\partial I_2^2}\mathbf{C}\otimes\mathbf{C} + \\
&- 4I_3\frac{\partial^2\Psi}{\partial I_2\partial I_3}(\mathbf{C}\otimes\mathbf{C}^{-1} + \mathbf{C}^{-1}\otimes\mathbf{C}) + 4\left(I_3\frac{\partial\Psi}{\partial I_3} + I_3^2\frac{\partial^2\Psi}{\partial I_3^2}\right)\mathbf{C}^{-1}\otimes\mathbf{C}^{-1} + \\
&- 4I_3\frac{\partial\Psi}{\partial I_3}\mathbf{C}^{-1}\odot\mathbf{C}^{-1} - 4\frac{\partial\Psi}{\partial I_2}\left(\frac{\mathbb{I}+\mathbb{I}^T}{2}\right)
\end{aligned} \tag{3.37}$$

with $\bar{\mathbb{I}} = \delta_{IL}\delta_{JK}\mathbf{E}_I\otimes\mathbf{E}_J\otimes\mathbf{E}_K\otimes\mathbf{E}_L$ denoting the fourth-order identity tensor, and δ_{ij} be the Kronecker delta.

3.4 Anisotropic hyperelastic constitutive modeling

Anisotropic hyperelastic materials exhibit directional stiffness and strength, as well as direction-dependent mechanical properties. Accurate constitutive models of such materials must take into account this directional dependence. These models extend the classical theory of isotropic hyperelasticity by incorporating structural tensors or fiber families that reflect the material's preferred orientations. The constitutive behavior of fiber-reinforced soft materials is modeled again following the classical hyperelastic arguments based on strain energy functions and the invariants approach.

3.4.1 Transversely isotropic hyperelasticity

In the case of a transversely isotropic hyperelastic material, at least two different phases can be identified within the material microstructural configuration, and the constitutive model is again established by assigning the strain energy function Ψ. Within this framework, a simple decomposition of the strain energy function is adopted, where two distinct terms, referred to as the isotropic *ground matrix* and the *fiber family*, are introduced [63]. The definition of strain energy function is given in terms of the isotropic invariants of the deformation (I_1, I_2, I_3), embedding instead the dependence of the fiber direction $\boldsymbol{a}_0 = (a_x, a_y, a_z)^T$ (expressed in Cartesian components) by means of a structural tensor $\boldsymbol{a}_0\otimes\boldsymbol{a}_0$, to fulfill objectivity arguments:

$$\Psi = \Psi(\mathbf{C}, \boldsymbol{a}_0\otimes\boldsymbol{a}_0) \tag{3.38}$$

The constitutive model, including fiber phases, is done, at a mathematical level, by including the dependence of the $\boldsymbol{a}_0\otimes\boldsymbol{a}_0$ tensor that modifies the constitutive equation. From objectivity arguments, the constitutive law is then expressed by two additional *pseudo-invariants* that depend on the fiber direction and the local deformation, given again by the tensor $\mathbf{C}$

$$\Psi = \Psi(I_1(\mathbf{C}), I_2(\mathbf{C}), I_3(\mathbf{C}), I_4(\mathbf{C}, \boldsymbol{a}_0), I_5(\mathbf{C}, \boldsymbol{a}_0)) \tag{3.39}$$

where the additional terms considered in Eq. (3.39) are defined by:

$$I_4 = \boldsymbol{a}_0 \cdot \mathbf{C}\boldsymbol{a}_0; \qquad I_5 = \boldsymbol{a}_0 \cdot \mathbf{C}^2\boldsymbol{a}_0 \tag{3.40}$$

The nonlinear constitutive law for transversely isotropic hyperelastic materials is carried out following the previously introduced procedure, as shown in Eq. (3.18):

$$\mathbf{S} = 2\frac{\partial \Psi(\mathbf{C})}{\partial \mathbf{C}} \tag{3.41}$$

where $\mathbf{S}$ is again the PK2 tensor. In the case of transversely isotropic hyperelastic materials, the chain rule and the derivative with respect to $\mathbf{C}$ are naturally extended as follows:

$$\frac{\partial \Psi(\mathbf{C})}{\partial \mathbf{C}} = \frac{\partial \Psi(\mathbf{C})}{\partial I_1}\frac{\partial I_1}{\partial \mathbf{C}} + \frac{\partial \Psi(\mathbf{C})}{\partial I_2}\frac{\partial I_2}{\partial \mathbf{C}} + \frac{\partial \Psi(\mathbf{C})}{\partial I_3}\frac{\partial I_3}{\partial \mathbf{C}} + \frac{\partial \Psi(\mathbf{C})}{\partial I_4}\frac{\partial I_4}{\partial \mathbf{C}} + \frac{\partial \Psi(\mathbf{C})}{\partial I_5}\frac{\partial I_5}{\partial \mathbf{C}} \tag{3.42}$$

Again, the closed-form expression of PK2 stress tensor is characterized completely by means of the derivatives of Ψ with respect to invariants of the deformation process. To characterize instead the transversely isotropic mechanical behavior, the derivatives of the additional pseudo-invariants have to be introduced [153]:

$$\frac{\partial I_4}{\partial \mathbf{C}} = \boldsymbol{a}_0 \otimes \boldsymbol{a}_0 \tag{3.43}$$

$$\frac{\partial I_5}{\partial \mathbf{C}} = \boldsymbol{a}_0 \otimes \mathbf{C}\boldsymbol{a}_0 + \boldsymbol{a}_0\mathbf{C} \otimes \boldsymbol{a}_0 \tag{3.44}$$

Substituting the above expressions into Eq.(3.42), the most general expression of the PK2 tensor under the coupled formulation is given by:

$$\mathbf{S} = 2\left[\left(\frac{\partial \Psi}{\partial I_1} + I_1\frac{\partial \Psi}{\partial I_2}\right)\mathbf{I} - \frac{\partial \Psi}{\partial I_2}\mathbf{C} + I_3\frac{\partial \Psi}{\partial I_3}\mathbf{C}^{-1} + \frac{\partial \Psi}{\partial I_4}\boldsymbol{a}_0 \otimes \boldsymbol{a}_0 + \frac{\partial \Psi}{\partial I_5}\left(\boldsymbol{a}_0 \otimes \mathbf{C}\boldsymbol{a}_0 + \boldsymbol{a}_0\mathbf{C} \otimes \boldsymbol{a}_0\right)\right] \tag{3.45}$$

In Eq.(3.45), the inclusion of anisotropic effects and direction-dependent mechanical response is obtained, including the additional terms referred to the strain energy function derivatives with respect to I_4 and to I_5, thus including in a straightforward manner the dependence with respect to the preferential direction within the constitutive law.

For nearly incompressible transversely isotropic materials, the same decomposition into isochoric and volumetric components of the strain energy function can be adopted, introducing a decoupled approach for fiber-reinforced hyperelastic materials. Within this framework, the strain energy function is written as the sum of the volumetric, isochoric, and anisotropic components, depending on the rescaled invariant and pseudo-invariants:

$$\Psi = \Psi_{vol}(J) + \bar{\Psi}(\bar{I}_1, \bar{I}_2, \bar{I}_4, \bar{I}_5) = \Psi_{vol}(J) + \bar{\Psi}_{iso}(\bar{I}_1, \bar{I}_2) + \bar{\Psi}_{aniso}(\bar{I}_1, \bar{I}_2, \bar{I}_4, \bar{I}_5) \tag{3.46}$$

where $\bar{\Psi}_{iso}$ depend on the already introduced rescaled isotropic invariants $(\bar{I}_1, \bar{I}_2)$ of $\bar{\mathbf{C}} = J^{-2/3}\mathbf{C}$, instead the additional anisotropic term $\bar{\Psi}_{aniso}$ depend on the rescaled invariants $\bar{I}_4 = J^{-2/3}I_4$ and $\bar{I}_5 = J^{-4/3}I_5$. Due to the generality of the proposed decoupled approach, the constitutive law is again characterized by the introduction of the projection tensor and RPK2 tensor, by which the final constitutive law is introduced:

$$\bar{\mathbf{S}} = 2\left[\left(\frac{\partial \bar{\Psi}}{\partial \bar{I}_1} + \bar{I}_1\frac{\partial \bar{\Psi}}{\partial \bar{I}_2}\right)\mathbf{I} - \frac{\partial \bar{\Psi}}{\partial \bar{I}_2}\bar{\mathbf{C}} + \frac{\partial \bar{\Psi}}{\partial \bar{I}_4}\boldsymbol{a}_0 \otimes \boldsymbol{a}_0 + \frac{\partial \bar{\Psi}}{\partial \bar{I}_5}\left(\boldsymbol{a}_0 \otimes \bar{\mathbf{C}}\boldsymbol{a}_0 + \boldsymbol{a}_0\bar{\mathbf{C}} \otimes \boldsymbol{a}_0\right)\right] \tag{3.47}$$

Incremental formulation and tangent elasticity tensor

The full explicit derivation of the tangent elasticity tensor for isotropic hyperelastic materials has been proposed in Eq. (3.37). Supposing now then the most general form of the strain energy function $\Psi = \Psi(I_1, I_2, I_3, I_4, I_5)$, applying the definition of tangent elasticity tensor Eq. (3.32) one can derive, in the case of transversly isotropic hyperelastic material, the following extension to the already introduced tangent elastic moduli, embedding now the effects of fiber direction:

$$
\begin{aligned}
\mathbb{C} &= 4\left(\frac{\partial^2\Psi}{\partial I_1^2} + 2I_1\frac{\partial^2\Psi}{\partial I_1\partial I_2} + \frac{\partial\Psi}{\partial I_2} + I_1^2\frac{\partial^2\Psi}{\partial I_2^2}\right)\mathbf{I}\otimes\mathbf{I} + 4\left(\frac{\partial^2\Psi}{\partial I_1\partial I_2} + I_1\frac{\partial^2\Psi}{\partial I_2^2}\right)(\mathbf{I}\otimes\mathbf{C} + \mathbf{C}\otimes\mathbf{I}) + \\
&+ 4\left(I_3\frac{\partial^2\Psi}{\partial I_1\partial I_3} + I_1I_3\frac{\partial^2\Psi}{\partial I_2\partial I_3}\right)(\mathbf{I}\otimes\mathbf{C}^{-1} + \mathbf{C}^{-1}\otimes\mathbf{I}) + 4\frac{\partial^2\Psi}{\partial I_2^2}\mathbf{C}\otimes\mathbf{C} + \\
&- 4I_3\frac{\partial^2\Psi}{\partial I_2\partial I_3}(\mathbf{C}\otimes\mathbf{C}^{-1} + \mathbf{C}^{-1}\otimes\mathbf{C}) + 4\left(I_3\frac{\partial\Psi}{\partial I_3} + I_3^2\frac{\partial^2\Psi}{\partial I_3^2}\right)\mathbf{C}^{-1}\otimes\mathbf{C}^{-1} + \\
&- 4I_3\frac{\partial\Psi}{\partial I_3}\mathbf{C}^{-1}\odot\mathbf{C}^{-1} - 4\frac{\partial\Psi}{\partial I_2}\mathcal{S} + 4\left(\frac{\partial^2\Psi}{\partial I_1\partial I_4} + I_1\frac{\partial^2\Psi}{\partial I_2\partial I_4}\right)(\mathbf{I}\otimes\boldsymbol{a}_0\otimes\boldsymbol{a}_0 + \boldsymbol{a}_0\otimes\boldsymbol{a}_0\otimes\mathbf{I}) + \\
&- 4\frac{\partial^2\Psi}{\partial I_2\partial I_4}(\mathbf{C}\otimes\boldsymbol{a}_0 + \boldsymbol{a}_0\otimes\boldsymbol{a}_0\otimes\mathbf{C}) + 4\frac{\partial^2\Psi}{\partial I_4^2}\boldsymbol{a}_0\otimes\boldsymbol{a}_0\otimes\boldsymbol{a}_0\otimes\boldsymbol{a}_0 + \\
&+ 4\left(\frac{\partial^2\Psi}{\partial I_1\partial I_5} + I_1\frac{\partial^2\Psi}{\partial I_2\partial I_5}\right)\left(\mathbf{I}\otimes\frac{\partial I_5}{\partial\mathbf{C}} + \frac{\partial I_5}{\partial\mathbf{C}}\otimes\mathbf{I}\right) - 4\frac{\partial^2\Psi}{\partial I_2\partial I_5}\left(\mathbf{C}\otimes\frac{\partial I_5}{\partial\mathbf{C}} + \frac{\partial I_5}{\partial\mathbf{C}}\otimes\mathbf{C}\right) + \\
&+ 4\frac{\partial^2\Psi}{\partial I_5^2}\left(\frac{\partial I_5}{\partial\mathbf{C}}\otimes\frac{\partial I_5}{\partial\mathbf{C}}\right) + 4\frac{\partial^2\Psi}{\partial I_4\partial I_5}\left(\boldsymbol{a}_0\otimes\boldsymbol{a}_0\otimes\frac{\partial I_5}{\partial\mathbf{C}} + \frac{\partial I_5}{\partial\mathbf{C}}\otimes\boldsymbol{a}_0\otimes\boldsymbol{a}_0\right) + \\
&+ 4\frac{\partial\Psi}{\partial I_5}\frac{\partial^2 I_5}{\partial\mathbf{C}\partial\mathbf{C}} + 4I_3\frac{\partial^2\Psi}{\partial I_3\partial I_4}(\boldsymbol{a}_0\otimes\boldsymbol{a}_0\otimes\mathbf{C}^{-1} + \mathbf{C}^{-1}\otimes\boldsymbol{a}_0\otimes\boldsymbol{a}_0) + \\
&+ 4I_3\frac{\partial^2\Psi}{\partial I_3\partial I_5}(\boldsymbol{a}_0\otimes\mathbf{C}\boldsymbol{a}_0\otimes\mathbf{C}^{-1} + \boldsymbol{a}_0\mathbf{C}\otimes\boldsymbol{a}_0\otimes\mathbf{C}^{-1} \\
&+ \mathbf{C}^{-1}\otimes\boldsymbol{a}_0\otimes\mathbf{C}\boldsymbol{a}_0 + \mathbf{C}^{-1}\otimes\boldsymbol{a}_0\mathbf{C}\otimes\boldsymbol{a}_0)
\end{aligned}
\tag{3.48}
$$

The full expressions of the terms $\mathbf{C}^{-1}\odot\mathbf{C}^{-1}$ and the fourth-order tensor $\mathcal{S} = (\mathbb{I} + \bar{\mathbb{I}})/2$ can be found in reference textbooks [153].

3.4.2 Anisotropic hyperelasticity with two fiber families

In the case of an hyperelastic composites, within the material microstructural configuration, two distinct and independent fiber families can be identified. The constitutive model, assigned by the strain energy function Ψ, is again extended following the same procedure proposed in the case of transversely isotropic materials. The definition of strain energy function proposed is now considered dependent of the isotropic invariants of the deformation (I_1, I_2, I_3), the first fiber direction $\boldsymbol{a}_0 = (a_x, a_y, a_z)^T$ (expressed in Cartesian components) by means of a structural tensor $\boldsymbol{a}_0 \otimes \boldsymbol{a}_0$, and the second fiber direction $\boldsymbol{g}_0 = (g_x, g_y, g_z)^T$ (expressed in Cartesian components) by means of a structural tensor $\boldsymbol{g}_0 \otimes \boldsymbol{g}_0$, to fulfill objectivity arguments:

$$\Psi = \Psi(\mathbf{C}, \boldsymbol{a}_0 \otimes \boldsymbol{a}_0, \boldsymbol{g}_0 \otimes \boldsymbol{g}_0) \tag{3.49}$$

The extension of the representation theorem, provided in Sec. 3.1.3, for an orthotropic material model is given by the inclusion of another two additional pseudo-invariants, depending now on the fiber direction $\boldsymbol{g}_0$:

$$\Psi = \Psi(I_1(\mathbf{C}), I_2(\mathbf{C}), I_3(\mathbf{C}), I_4(\mathbf{C}, \boldsymbol{a}_0), I_5(\mathbf{C}, \boldsymbol{a}_0), I_6(\mathbf{C}, \boldsymbol{g}_0), I_7(\mathbf{C}, \boldsymbol{g}_0)) \tag{3.50}$$

where the additional terms considered in Eq. (3.50) are defined by:

$$I_6 = \boldsymbol{g}_0 \cdot \mathbf{C}\boldsymbol{g}_0; \qquad I_7 = \boldsymbol{g}_0 \cdot \mathbf{C}^2\boldsymbol{g}_0; \tag{3.51}$$

Once assigned the strain energy function, the nonlinear constitutive law is carried out as shown in Eq. (3.18). In case of orthotropic models, the chain rule and the derivative with respect to $\mathbf{C}$ are naturally extended as follows:

$$\begin{aligned} \frac{\partial \Psi(\mathbf{C})}{\partial \mathbf{C}} &= \frac{\partial \Psi(\mathbf{C})}{\partial I_1}\frac{\partial I_1}{\partial \mathbf{C}} + \frac{\partial \Psi(\mathbf{C})}{\partial I_2}\frac{\partial I_2}{\partial \mathbf{C}} + \frac{\partial \Psi(\mathbf{C})}{\partial I_3}\frac{\partial I_3}{\partial \mathbf{C}} + \\ &+ \frac{\partial \Psi(\mathbf{C})}{\partial I_4}\frac{\partial I_4}{\partial \mathbf{C}} + \frac{\partial \Psi(\mathbf{C})}{\partial I_5}\frac{\partial I_5}{\partial \mathbf{C}} + \frac{\partial \Psi(\mathbf{C})}{\partial I_6}\frac{\partial I_6}{\partial \mathbf{C}} + \frac{\partial \Psi(\mathbf{C})}{\partial I_7}\frac{\partial I_7}{\partial \mathbf{C}} \end{aligned} \tag{3.52}$$

Again, the closed-form expression of PK2 stress tensor is characterized completely by means of the derivatives of Ψ with respect to invariants of the deformation process. To characterize instead the orthotropic mechanical behavior, the derivatives of the additional pseudo-invariants, exploited in Eq. (3.52), are introduced [153]:

$$\frac{\partial I_6}{\partial \mathbf{C}} = \boldsymbol{g}_0 \otimes \boldsymbol{g}_0 \tag{3.53}$$

$$\frac{\partial I_7}{\partial \mathbf{C}} = \boldsymbol{g}_0 \otimes \mathbf{C}\boldsymbol{g}_0 + \boldsymbol{g}_0\mathbf{C} \otimes \boldsymbol{g}_0 \tag{3.54}$$

Substituting the above expressions into Eq.(3.52) and subsequently in the definition of the constitutive law, the most general expression of the PK2 tensor under the coupled approach is given by:

$$\begin{aligned} \mathbf{S} &= 2\Bigg[\left(\frac{\partial \Psi}{\partial I_1} + I_1\frac{\partial \Psi}{\partial I_2}\right)\mathbf{I} - \frac{\partial \Psi}{\partial I_2}\mathbf{C} + I_3\frac{\partial \Psi}{\partial I_3}\mathbf{C}^{-1} + \frac{\partial \Psi}{\partial I_4}\boldsymbol{a}_0 \otimes \boldsymbol{a}_0 + \\ &+ \frac{\partial \Psi}{\partial I_5}\left(\boldsymbol{a}_0 \otimes \mathbf{C}\boldsymbol{a}_0 + \boldsymbol{a}_0\mathbf{C} \otimes \boldsymbol{a}_0\right) + \frac{\partial \Psi}{\partial I_6}\boldsymbol{g}_0 \otimes \boldsymbol{g}_0 + \frac{\partial \Psi}{\partial I_7}\left(\boldsymbol{g}_0 \otimes \mathbf{C}\boldsymbol{g}_0 + \boldsymbol{g}_0\mathbf{C} \otimes \boldsymbol{g}_0\right)\Bigg] \end{aligned} \tag{3.55}$$

In Eq.(3.55), the inclusion of anisotropic effects and direction-dependent mechanical response with respect to the second fiber family is obtained, including the additional terms referred to the strain energy function derivatives with respect to I_6 and to I_7, thus including in a straightforward manner the dependence with respect to the preferential direction within the constitutive law.

For nearly incompressible transversely isotropic materials, the same decomposition into isochoric and volumetric components of the strain energy function can be adopted, introducing a decoupled approach for orthotropic hyperelastic materials with two distinct fiber families. Within this framework, the strain energy function is written as the sum of the volumetric, isochoric, and anisotropic components, depending on the rescaled invariant and pseudo-invariants:

$$\Psi = \Psi_{vol}(J) + \bar{\Psi}(\bar{I}_1, \bar{I}_2, \bar{I}_4, \bar{I}_5, \bar{I}_6, \bar{I}_7) = \Psi_{vol}(J) + \bar{\Psi}_{iso}(\bar{I}_1, \bar{I}_2) + \bar{\Psi}_{aniso}(\bar{I}_1, \bar{I}_2, \bar{I}_4, \bar{I}_5, \bar{I}_6, \bar{I}_7) \quad (3.56)$$

where the isotropic and anisotropic terms related to the first fiber family have been already presented, instead the additional rescaled pseudo-invariant with respect to the second fiber direction are obtained similarly, given by $\bar{I}_6 = J^{-2/3} I_6$ and $\bar{I}_7 = J^{-4/3} I_7$. Due to the generality of the proposed decoupled approach, the constitutive law is again characterized by the introduction of the projection tensor and RPK2 tensor, by which the final constitutive law is introduced:

$$\begin{aligned} \bar{\mathbf{S}} &= 2\Bigg[\left(\frac{\partial \bar{\Psi}}{\partial \bar{I}_1} + \bar{I}_1 \frac{\partial \bar{\Psi}}{\partial \bar{I}_2}\right)\mathbf{I} - \frac{\partial \bar{\Psi}}{\partial \bar{I}_2}\bar{\mathbf{C}} + \frac{\partial \bar{\Psi}}{\partial \bar{I}_4}\boldsymbol{a}_0 \otimes \boldsymbol{a}_0 + \\ &+ \frac{\partial \bar{\Psi}}{\partial \bar{I}_5}\left(\boldsymbol{a}_0 \otimes \bar{\mathbf{C}}\boldsymbol{a}_0 + \boldsymbol{a}_0 \bar{\mathbf{C}} \otimes \boldsymbol{a}_0\right) + \frac{\partial \bar{\Psi}}{\partial \bar{I}_6}\boldsymbol{g}_0 \otimes \boldsymbol{g}_0 + \frac{\partial \bar{\Psi}}{\partial \bar{I}_7}\left(\boldsymbol{g}_0 \otimes \bar{\mathbf{C}}\boldsymbol{g}_0 + \boldsymbol{g}_0 \bar{\mathbf{C}} \otimes \boldsymbol{g}_0\right)\Bigg] \end{aligned} \quad (3.57)$$

The derivation of the tangent elastic moduli in the case of an orthotropic material model is reported in Appendix B, considering both fiber families' contribution up to the seventh invariants. These generalized rescaled tangent elastic moduli can be straightforwardly adopted also in the case of isotropic and transversely isotropic hyperelastic materials by neglecting the terms related to the fiber directions $\boldsymbol{a}_0$ and $\boldsymbol{g}_0$.

Chapter 4

Unified finite element formulation

4.1 Beam theories: Unified formulation

The unified formulation of beam theories is proposed here. Starting from classical approaches, such as the Euler-Bernoulli Beam Theory (EBBT) [158] or Timoshenko Beam Theory (TBT) [159], the three-dimensional displacement field is expressed through an expansion of the displacement variables following structural theories based on the geometric characteristics of the beam. In this way, simple and relatively cheap models have been defined. Due to certain superimposed kinematic assumptions, such as rigid cross-section behavior or constant transverse stresses across the cross-section, classical approaches are unable to capture the effective beam deformation [160] within many contexts. In hyperelasticity, where large strains are considered, several local phenomena, such as section warping or twisting, are observed; therefore, higher-order models are required. Many higher-order theories have been proposed in the literature, starting from the Third-Order Shear Deformation Theory (TSDT) by Reddy [161]. An extensive review of existing refined beam theories can be found in [162, 163]. The CUF offers the possibility of defining any beam theory of a structure in a unified manner. Under the CUF approach, the three-dimensional displacement field is defined through a polynomial expansion of the generalized nodal displacements, coupling directly the imposed theory of structure along the cross-section, of any order, with models describing the beam axis kinematics, under a recursive index notation [129]. In the classical orthonormal (x, y, z) Cartesian reference frame, the displacement field of a general beam theory is expressed as:

$$\boldsymbol{u}(x, y, z) = F_\tau(x, z)\boldsymbol{u}_\tau(y) \qquad \tau = 1, ..., M \tag{4.1}$$

where M is the dimension of the cross-section polynomial expansion basis, related to the order of the adopted theory of structure, and F_τ are the approximating expansion functions that characterize the CUF model adopted. The vector $\boldsymbol{u}_\tau(y)$ is the vector of generalized displacement components along the reference direction. In the following, the Einstein notation for repeated indices summation is exploited. This definition enables the implementation of any higher-order theory of structure by selecting the set of expansion functions $F_\tau(x, z)$, that characterizes the beam cross-section kinematics. The key advantage of the proposed methodology is in the recursive approach, which makes the structural theory and order of expansion parametric inputs of the problem under consideration [129].
From a theoretical standpoint, two distinct classes of expansion functions are discussed here for the cross-section kinematics: the Taylor expansion class (TE-class) and the Lagrange expansion class (LE-class). The adoption of these two different expansion classes leads to a distinct modeling approach.

4.1.1 Taylor Expansion models

In TE models for higher-order 1D beam formulation, 2D MacLaurin polynomials are exploited as F_τ basis functions for expanding the generalized displacement field [164]. Depending on the order of expansion, the behavior of the generalized displacements and beam cross-section kinematics can be axiomatically assumed [165]. Once the expansion order is chosen, higher-order beam theories are straightforwardly defined in a hierarchical manner. As examples, the TE-2 higher-order theory with constant, linear, and parabolic expansion terms is:

$$\begin{array}{rcccccccccccc} u_x &=& u_{x_1}(y) &+& x u_{x_2}(y) &+& z u_{x_3}(y) &+& x^2 u_{x_4}(y) &+& xz u_{x_5}(y) &+& z^2 u_{x_6}(y) \\ u_y &=& u_{y_1}(y) &+& x u_{y_2}(y) &+& z u_{y_3}(y) &+& x^2 u_{y_4}(y) &+& xz u_{y_5}(y) &+& z^2 u_{y_6}(y) \\ u_z &=& \underbrace{u_{z_1}(y)}_{\boldsymbol{u}_{\tau=1}} &+& x \underbrace{u_{z_2}(y)}_{\boldsymbol{u}_{\tau=2}} &+& z \underbrace{u_{z_3}(y)}_{\boldsymbol{u}_{\tau=3}} &+& x^2 \underbrace{u_{z_4}(y)}_{\boldsymbol{u}_{\tau=4}} &+& xz \underbrace{u_{z_5}(y)}_{\boldsymbol{u}_{\tau=5}} &+& z^2 \underbrace{u_{z_6}(y)}_{\boldsymbol{u}_{\tau=6}} \end{array} \tag{4.2}$$

where u_{x_τ}, u_{y_τ}, and u_{z_τ} are the generalized variables, related to the higher-order derivatives of the displacement field components, by which the final three-dimensional displacement field is reconstructed. More generally, the TE model for an M-*th* order expansion of the beam theory can be hierarchically derived as:

$$\begin{aligned} u_x &= \quad ... \quad + \sum_{N=0}^{M} x^{M-N}\, z^N\, u_{x_{1/2(N(N+1)+M+1)}} \\ u_y &= \quad ... \quad + \sum_{N=0}^{M} x^{M-N}\, z^N\, u_{y_{1/2(N(N+1)+M+1)}} \\ u_z &= \underbrace{...}_{1,...,M-1} + \underbrace{\sum_{N=0}^{M} x^{M-N}\, z^N\, u_{z_{1/2(N(N+1)+M+1)}}}_{M-\,order} \end{aligned} \tag{4.3}$$

From a multilayered structural modeling standpoint, TE models have been generally referred to as ESLm (Equivalent Single Layer Models). Within this modeling approach, the resulting structural features are assumed to be homogenized quantities that combines each cross-section sub-component or layer into an equivalent yet unique representative cross-sectional behavior, taking into account the features of the sub-components. A graphical representation of the present 1D beam TE class is provided in Fig. 4.1.

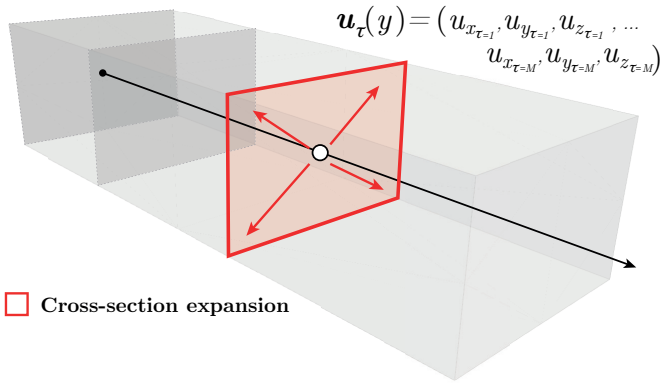

Figure 4.1: Unified formulation of beam theories, Taylor Expansion (TE) class.

4.1.2 Lagrange Expansion models

For LE-models, cross-section kinematics is defined starting from local sub-elements definitions, exploiting the set of 2D Lagrange polynomials [166]. The resulting, pure displacement-based, kinematic model is provided in terms of nodal Cartesian displacement components defined in correspondence of the Lagrange points adopted for the 2D interpolation. In LE-models, no rotation or higher-order terms are exploited. In the following, linear, parabolic, and cubic expansion models will be explored and denoted as linear four-node L4, parabolic nine-node L9, and sixteen-node cubic L16 cross-section expansion elements, referring to the total number of Lagrange Points adopted in the arbitrary sub-modeling of the cross-section. As a representative example, the displacement field of a 1D-L9 parabolic expansion model is here reported:

$$\begin{cases} u_x(x,y,z) = F_1(x,z)u_{x_{\tau=1}}(y) + F_2(x,z)u_{x_{\tau=2}}(y) + \ \ldots \ + F_9(x,z)u_{x_{\tau=9}}(y) \\ u_y(x,y,z) = F_1(x,z)u_{y_{\tau=1}}(y) + F_2(x,z)u_{y_{\tau=2}}(y) + \ \ldots \ + F_9(x,z)u_{y_{\tau=9}}(y) \\ u_z(x,y,z) = F_1(x,z)u_{z_{\tau=1}}(y) + F_2(x,z)u_{z_{\tau=2}}(y) + \ \ldots \ + F_9(x,z)u_{z_{\tau=9}}(y) \end{cases} \tag{4.4}$$

where u_{x_τ}, u_{y_τ} and u_{z_τ} are the Cartesian displacement components defined in the Lagrange Point. A complete list of adopted 2D elements in the cross-section expansion and the relative shape functions involved is detailed in Table 4.2, where these polynomials are exploited in natural coordinates [129]. The cross-section can be modeled with multiple LE sub-domains, thus refining the cross-sectional behavior without increasing the polynomial order but adopting refined discretization with more sub-models. The key feature of LE-class models is given by the capability to model independently different beam cross-section sub-components or layers, and for this reason they are generally referred to as Component-Wise models (CWm) or Layer-Wise models (LWm). A graphical representation of the 1D LE expansion class is provided in Fig. 4.2.

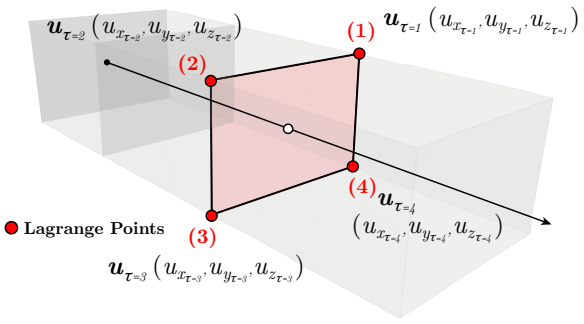

Figure 4.2: Unified formulation of beam theories, Lagrange Expansion (LE) class.

4.1.3 Finite element approximation of the beam axis kinematic

Once the refined theory of structure approximation and expansion class have been chosen, the generalized displacement field components along the beam axis are further discretized exploiting classical 1D FE approach:

$$\boldsymbol{u}_\tau(y) = N_i(y)\boldsymbol{u}_{\tau i} \qquad i = 1, ..., N_n \tag{4.5}$$

where the generalized displacement components are formulated as a general linear combination of $N_i(y)$ shape functions and the discrete generalized displacements $\boldsymbol{u}_{\tau i}$, final unknowns of the model. In Eq. (4.5), the index i is exploited for the summation, considering the total N_n finite nodes per element adopted in the beam axis discretization, along the y-direction. The final

expression of the 3D displacement field in the CUF domain is then written a coupled finite element approximation with expansion of structural theories, written then as:

$$\boldsymbol{u}(x,y,z) = F_\tau(x,z)\boldsymbol{u}_\tau(y) = F_\tau(x,z)N_i(y)\boldsymbol{u}_{\tau i} \tag{4.6}$$

The 1D FE discretization elements along the beam axis will be generally referred to as linear B2, parabolic B3, and cubic B4 elements, following the total number of nodes involved. Equation (4.6) is the most general expression, within the CUF framework, of the displacement field. Refined higher-order models for beam structures are defined in a hierarchical manner, as the given definition is independent of the polynomial basis adopted for either the beam axis or the structural theory considered. A graphical representation of a higher-order CUF model is provided in Fig. 4.3.

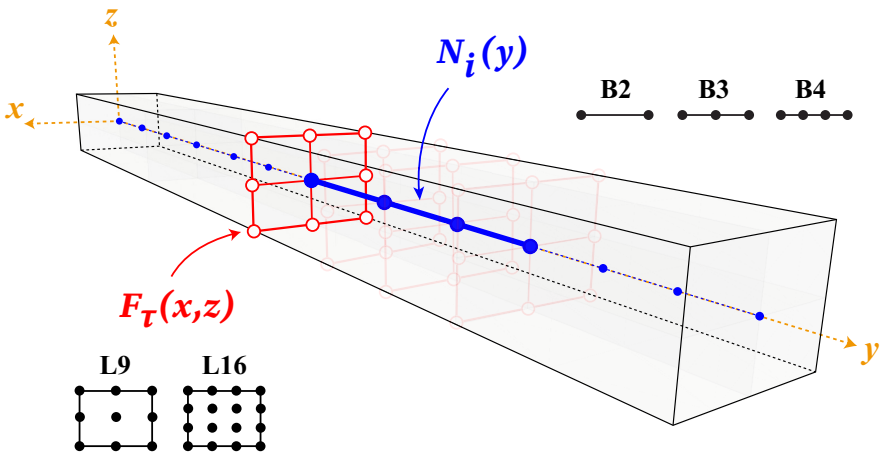

Figure 4.3: Unified formulation of beam theories: graphical representation of a 1D CUF model.

The finite element approximation of the beam axis is established by discretizing the continuous field of generalized displacement variables within the framework of a classical one-dimensional formulation. This key concept is introduced in the framework of CUF by considering the interpolation of the expanded displacement field by linear, quadratic, or cubic shape functions, thereby enabling the definition of any one-dimensional beam model with three-dimensional capabilities. In particular, in each finite node involved in the discretized beam axis, the selected structural theory is consistently superimposed. The final, nodal degrees of freedom of the models are thus defined following the present approach:

1. **TE models**: for each i-*th* node involved in the 1D beam axis discretization, the vectors of the τ-*th* generalized displacement components $(\boldsymbol{u}_{\tau_1},...,\boldsymbol{u}_{\tau_M})_i$ is considered. For each $\boldsymbol{u}_{\tau i}$ the respective terms related to the M-*th* order of expansion of the three-dimensional displacement field are considered, thus $\boldsymbol{u}_{\tau i} = (u_{x_{\tau i}}, u_{y_{\tau i}}, u_{z_{\tau i}})$. The final vector of the global unknowns is then:

$$\boldsymbol{u}_{DOF} = \left[\begin{array}{c} \left.\begin{array}{c} (u_{x_{i=1,\tau=1}}, u_{y_{i=1,\tau=1}}, u_{z_{i=1,\tau=1}})^T \\ \vdots \\ (u_{x_{i=1,\tau=M}}, u_{y_{i=1,\tau=M}}, u_{z_{i=1,\tau=M}})^T \end{array}\right\} \text{Node } i{=}1 \\ \hdashline \left.\begin{array}{c} (u_{x_{i=2,\tau=1}}, u_{y_{i=2,\tau=1}}, u_{z_{i=2,\tau=1}})^T \\ \vdots \\ (u_{x_{i=2,\tau=M}}, u_{y_{i=2,\tau=M}}, u_{z_{i=2,\tau=M}})^T \end{array}\right\} \text{Node } i{=}2 \\ \hdashline \vdots \\ \vdots \\ \vdots \\ \hdashline \left.\begin{array}{c} (u_{x_{i=N_n,\tau=1}}, u_{y_{i=N_n,\tau=1}}, u_{z_{i=N_n,\tau=1}})^T \\ \vdots \\ (u_{x_{i=N_n,\tau=M}}, u_{y_{i=N_n,\tau=M}}, u_{z_{i=N_n,\tau=M}})^T \end{array}\right\} \text{Node } i{=}N_n \end{array}\right] \tag{4.7}$$

2. **LE models**: the DOF definition follows the same introduced approach in TE models, obtaining the final vector as done in Eq. (4.7), however for each i-*th* node involved in the 1D beam axis discretization, the vectors of the τ-*th* generalized displacement components $(\boldsymbol{u}_{\tau_1}, ..., \boldsymbol{u}_{\tau_M})_i$ are now the physical Cartesian displacement components of the discretized $\boldsymbol{u}_{\tau i}$-*th* node:

$$\boldsymbol{u}_{DOF} = \left[\begin{array}{c} \left.\begin{array}{c} (u_{x_{i=1,\tau=1}}, u_{y_{i=1,\tau=1}}, u_{z_{i=1,\tau=1}})^T \text{ } \} \text{ Node } \tau{=}1 \\ \vdots \\ (u_{x_{i=1,\tau=(M+1)^2}}, u_{y_{i=1,\tau=(M+1)^2}}, u_{z_{i=1,\tau=(M+1)^2}})^T \text{ } \} \text{ Node } \tau{=}(M{+}1)^2 \end{array}\right\} \text{Node } i{=}1 \\ \hdashline \vdots \\ \vdots \\ \vdots \\ \hdashline \left.\begin{array}{c} (u_{x_{i=1,\tau=1}}, u_{y_{i=1,\tau=1}}, u_{z_{i=1,\tau=1}})^T \text{ } \} \text{ Node } \tau{=}1 \\ \vdots \\ (u_{x_{i=1,\tau=(M+1)^2}}, u_{y_{i=1,\tau=(M+1)^2}}, u_{z_{i=1,\tau=(M+1)^2}})^T \text{ } \} \text{ Node } \tau{=}(M{+}1)^2 \end{array}\right\} \text{Node } i{=}N_n \end{array}\right] \tag{4.8}$$

The extension to higher-order structural theories is achieved in a straightforward manner, resulting in a final one-dimensional beam model with three-dimensional capabilities, while preserving computational efficiency through higher-order interpolation. A graphical representation of the final, discretized, beam CUF model is provided in Fig. 4.4. The complete list of 1D finite element interpolation adopted and the respective shape functions involved are presented in Table 4.1.

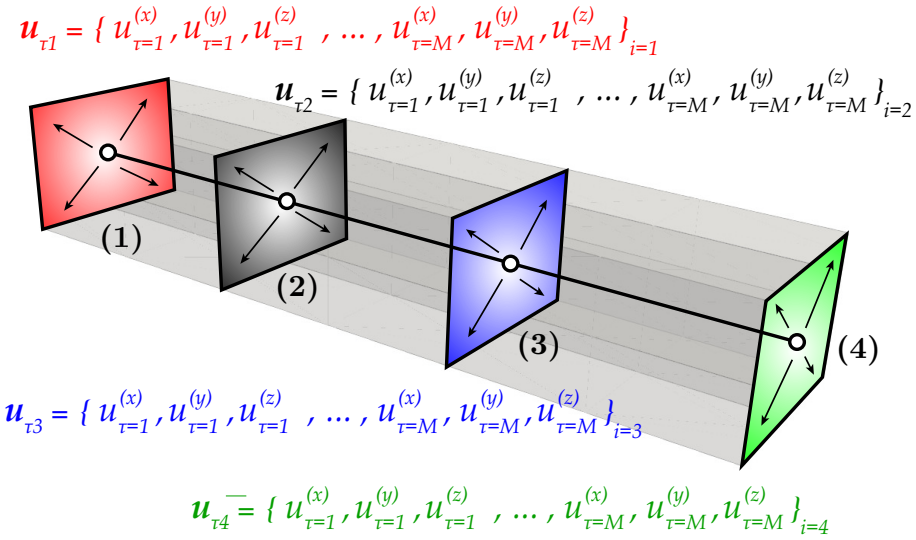

(a) TE models

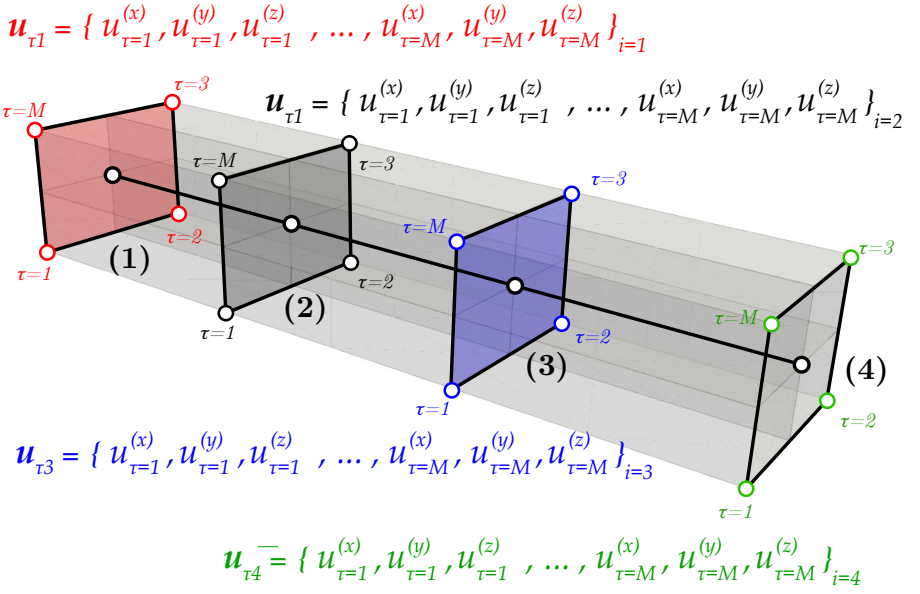

(b) LE models

Figure 4.4: Unified formulation of beam theories: graphical representation of the final 1D CUF model with explicit DOF representation

B2 element, linear 1D interpolation	$N_1(\xi) = \frac{1}{2}(1-\xi)$
	$N_2(\xi) = \frac{1}{2}(1+\xi)$
B3 element, quadratic 1D interpolation	$N_1(\xi) = \frac{1}{2}(\xi^2-\xi)$
	$N_2(\xi) = 1-\xi^2$
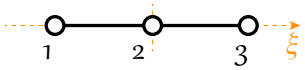	$N_3(\xi) = \frac{1}{2}(\xi^2+\xi)$
B4 element, cubic 1D interpolation	$N_1(\xi) = \frac{1}{16}(\xi-1)(1-9\xi^2)$
	$N_2(\xi) = \frac{9}{16}(1-\xi^2)(1-3\xi)$
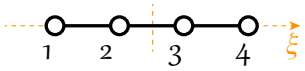	$N_3(\xi) = \frac{9}{16}(1-\xi^2)(1+3\xi)$
	$N_4(\xi) = \frac{1}{16}(\xi+1)(9\xi^2-1)$

Table 4.1: Finite element interpolation in one dimension: local internal numbering and shape functions expressions.

4.2 Plate theories: Unified formulation

The Unified formulation of plate theories is proposed here. Starting from classical approaches, such as the Kirchhoff-Love theory [167] or the Reissner-Mindlin plate theory (RM) [168], also known as the First-Order Shear Deformation Theory (FSDT), the three-dimensional displacement field is expressed through an expansion of the displacement field following structural theories based on the geometric characteristics of the plate. In this way, simple and relatively cheap models have been defined. Due to certain superimposed kinematic assumptions, such as constant rotation or through-the-thickness stretching, neglecting transverse shear effects, classical approaches are unable to capture the effective plate behavior within many contexts [127], thus higher-order structural theories are required [169]. In hyperelasticity, where large strains are considered, several local phenomena, such as localized stretching and out-of-plane stress arising from complex three-dimensional deformation states, typically require higher-order models [170]. Many higher-order theories have been proposed in the literature. An extensive review of existing plate theories can be found in [171]. The CUF offers the possibility to define any plate theory of structure in a unified manner. Under the CUF approach, the three-dimensional displacement field is defined through a polynomial expansion of the generalized nodal displacements,, coupling directly the imposed theory of structure along the thickness, of any order, with models describing the reference plate mid-surface kinematics, under a recursive index notation. In the classical orthonormal (x, y, z) Cartesian reference frame, the displacement field of a general plate theory is expressed as:

$$\boldsymbol{u}(x,y,z) = F_\tau(z)\boldsymbol{u}_\tau(x,y) \qquad \tau = 1, ..., M \tag{4.9}$$

where M is the dimension of the thickness polynomial expansion basis, related to the order of the theory of structure approximation, and F_τ are the approximating expansion polynomials. Finally, the vector $\boldsymbol{u}_\tau(x,y)$ is the vector of generalized displacement components along the reference direction. In the following, the Einstein notation for repeated indices summation is

exploited. This definition enables the implementation of any higher-order theory of structure by selecting the set of expansion functions $F_\tau(z)$, which characterizes the plate's thickness kinematics. The key advantage of the proposed methodology lies in its recursive definition of the displacement field, which makes the structural theory and order of expansion parametric inputs to the problem under consideration [129].
From a theoretical standpoint, two distinct classes of expansion functions are discussed here for the through-the-thickness kinematics: the Taylor expansion class (TE-class) and the Lagrange expansion class (LE-class). The adoption of these two different expansion classes leads to a distinct modeling approach.

4.2.1 Taylor Expansion models

In TE models for higher-order 2D plate formulation, 1D MacLaurin polynomials are exploited as F_τ basis functions for expanding the generalized displacement field [128]. As discussed in the case of 1D TE models, depending on the order of expansion, the behavior of the generalized displacements and through-the-thickness plate kinematics can be axiomatically assumed [128]. Once the expansion order is chosen, higher-order plate theories are straightforwardly defined in a hierarchical manner. As examples, we present the TE-3 cubic expansion model:

$$\begin{array}{rcccccccc} u_x &=& u_{x_1}(x,y) &+& z u_{x_2}(x,y) &+& z^2 u_{x_3}(x,y) &+& z^3 u_{x_4}(x,y) \\ u_y &=& u_{y_1}(x,y) &+& z u_{y_2}(x,y) &+& z^2 u_{y_3}(x,y) &+& z^3 u_{y_4}(x,y) \\ u_x &=& \underbrace{u_{z_1}(x,y)}_{\boldsymbol{u}_{\tau=1}} &+& z\,\underbrace{u_{z_2}(x,y)}_{\boldsymbol{u}_{\tau=2}} &+& z^2\,\underbrace{u_{z_3}(x,y)}_{\boldsymbol{u}_{\tau=3}} &+& z^3\,\underbrace{u_{z_4}(x,y)}_{\boldsymbol{u}_{\tau=4}} \end{array} \tag{4.10}$$

where u_{x_τ}, u_{y_τ}, and u_{z_τ} are the generalized variables, related to the higher-order derivatives of the displacement field components, by which the final three-dimensional displacement field is reconstructed. From a multilayered structural modeling standpoint, TE-class models are generally referred to as ESLMs (Equivalent-Single-Layer Models). In this structural modeling approach, the final mechanical features of plate structures are assumed as an homogenized structural behavior, where different thickness layers or sub-components are homogenized in an equivalent but unique representative through-the-thickness behavior, taking into account the features of each sub-component. As discussed in the case of 1D TE models, the generalized unknowns represent are again related to the higher-order derivatives of the displacement field components. A graphical representation of the present 1D beam TE class is provided in Fig. 4.5.

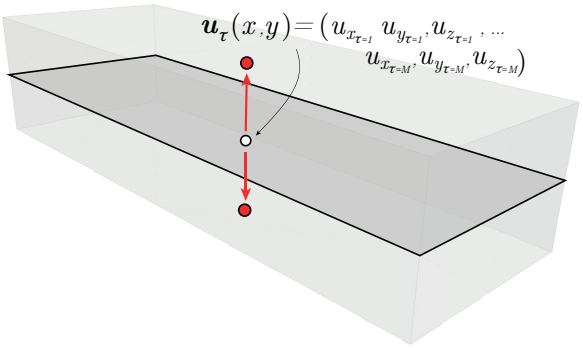

Figure 4.5: Unified formulation of plate theories, Taylor Expansion (TE) class.

4.2.2 Lagrange Expansion models

For LE-models, the through-the-thickness kinematics is defined starting from local sub-layer definitions, exploiting the set of 1D Lagrange polynomials [129]. The resulting, pure displacement-based, kinematic model is provided in terms of nodal Cartesian displacement components defined in correspondence of the Lagrange points adopted for the 2D interpolatio. In LE models, no rotation or higher-order terms are exploited. In the following, linear, parabolic, and cubic expansion models will be explored and referred to as two-node linear LE1, three-node quadratic LE2, and four-node cubic LE3 thickness expansion models, based on the total number of nodes used in the arbitrary sub-modeling of the thickness. As an example, the displacement field of a 2D-LE2 quadratic model is reported here:

$$\begin{cases} u_x(x,y,z) = F_1(z)u_{x_{\tau=1}}(x,y) + F_2(z)u_{x_{\tau=2}}(x,y) + F_3(z)u_{x_{\tau=3}}(x,y) \\ u_y(x,y,z) = F_1(z)u_{y_{\tau=1}}(x,y) + F_2(z)u_{y_{\tau=2}}(x,y) + F_3(z)u_{y_{\tau=3}}(x,y) \\ u_z(x,y,z) = F_1(z)u_{z_{\tau=1}}(x,y) + F_2(z)u_{z_{\tau=2}}(x,y) + F_3(z)u_{z_{\tau=3}}(x,y) \end{cases} \tag{4.11}$$

where u_{x_τ}, u_{y_τ} and u_{z_τ} are the Cartesian displacement components defined in the Lagrange Point. A complete list of adopted 1D elements in the cross-section expansion and the relative shape functions involved is detailed in Table 4.1 [129], where these polynomials are exploited in natural coordinates. The through-the-thickness kinematics can be modeled using multiple LE elements, thereby refining the behavior without increasing the polynomial order, while adopting a refined discretization with more sub-models. The key feature of LE-class models is given by the capability to model independently different plate thickness sub-components or layers, for this reason they are generally referred to as Layer-Wise (LWm) models. A graphical representation of the 2D LE expansion class is provided in Fig. 4.6.

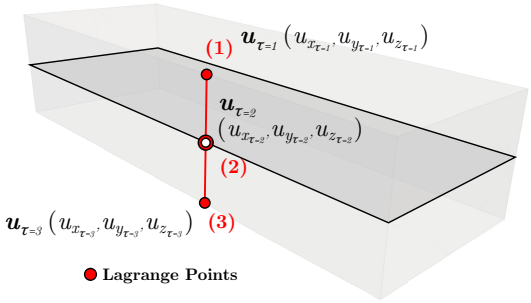

Figure 4.6: Unified formulation of plate theories, Lagrange Expansion (LE) class.

4.2.3 Finite element approximation of the plate reference mid-surface

Once the refined theory of structure approximation and expansion class have been chosen, the generalized displacement field components along the plate mid-surface axis are further discretized exploiting classical 2D FE approach:

$$\boldsymbol{u}_\tau(x,y) = N_i(x,y)\boldsymbol{u}_{\tau i} \quad i = 1, ..., N_n \tag{4.12}$$

where the displacement components of the plate mid-surface are written exploiting a general linear combination of the discrete generalized displacements $\boldsymbol{u}_{\tau i}$, final unknowns of the model, and $N_i(x,y)$ shape functions. In Eq. (4.12), the index i is exploited for the summation, considering the total N_n finite nodes per element adopted in the plate mid-surface discretization, along the

(x, y) directions. The final expression of the 3D displacement field in the CUF domain is then written a coupled finite element approximation with expansion of structural theories, written then as:

$$\boldsymbol{u}(x, y, z) = F_\tau(z)\boldsymbol{u}_\tau(x, y) = F_\tau(z)N_i(x, y)\boldsymbol{u}_{\tau i} \tag{4.13}$$

The 2D FE discretization models along the reference plate mid-surface will be generally referred to as four-node linear Q4, nine-node parabolic Q9, and sixteen-node cubic Q16 elements, following the total number of nodes involved. Equation (4.13) is the most general expression, within the CUF framework, of the displacement field. Refined higher-order models for plate structures are defined in a hierarchical manner, as the given definition is independent of the polynomial basis adopted, whether for the beam axis or the structural theory considered. A graphical representation of a higher-order CUF model is provided in Fig. 4.7.

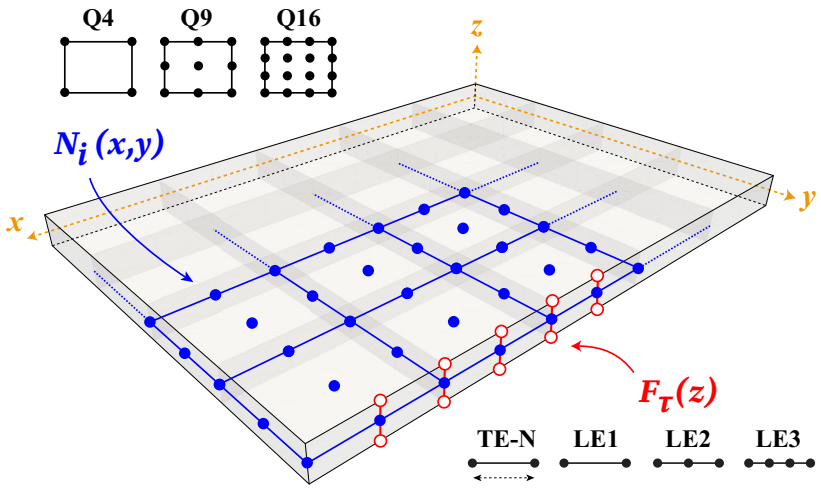

Figure 4.7: Unified formulation of plate theories: graphical representation of a 2D CUF model.

The finite element approximation of the reference plate mid-surface is established by discretizing the continuous field of generalized displacement variables within the framework of a classical two-dimensional formulation. This key concept is introduced in the framework of CUF by considering the interpolation of the expanded displacement field by linear, quadratic, or cubic shape functions, thereby enabling the definition of any two-dimensional plate model with three-dimensional capabilities. In particular, in each finite node involved in the discretized reference mid-surface, the selected structural theory is consistently superimposed. The final, nodal degrees of freedom of the models are thus defined following the present approach:

1. **TE models**: for each i-*th* node involved in the 2D plate mid-surface discretization, the vectors of the τ-*th* generalized displacement components $(\boldsymbol{u}_{\tau_1}, ..., \boldsymbol{u}_{\tau_M})_i$ is considered. For each $\boldsymbol{u}_{\tau i}$ the respective terms related to the M-*th* order of expansion of the three-dimensional displacement field are considered, thus $\boldsymbol{u}_{\tau i} = (u_{x_{\tau i}}, u_{y_{\tau i}}, u_{z_{\tau i}})$. The final vector of the global unknowns is then:

$$\boldsymbol{u}_{DOF} = \left[\begin{array}{c} \left.\begin{array}{c} (u_{x_{i=1,\tau=1}}, u_{y_{i=1,\tau=1}}, u_{z_{i=1,\tau=1}})^T \\ \vdots \\ (u_{x_{i=1,\tau=M}}, u_{y_{i=1,\tau=M}}, u_{z_{i=1,\tau=M}})^T \end{array}\right\} \text{Node } i\text{=}1 \\ \hdashline \left.\begin{array}{c} (u_{x_{i=2,\tau=1}}, u_{y_{i=2,\tau=1}}, u_{z_{i=2,\tau=1}})^T \\ \vdots \\ (u_{x_{i=2,\tau=M}}, u_{y_{i=2,\tau=M}}, u_{z_{i=2,\tau=M}})^T \end{array}\right\} \text{Node } i\text{=}2 \\ \hdashline \vdots \\ \vdots \\ \vdots \\ \hdashline \left.\begin{array}{c} (u_{x_{i=N_n,\tau=1}}, u_{y_{i=N_n,\tau=1}}, u_{z_{i=N_n,\tau=1}})^T \\ \vdots \\ (u_{x_{i=N_n,\tau=M}}, u_{y_{i=N_n,\tau=M}}, u_{z_{i=N_n,\tau=M}})^T \end{array}\right\} \text{Node } i\text{=}N_n \end{array}\right] \tag{4.14}$$

2. **LE models**: the DOF definition follows the same introduced approach in TE models, obtaining the final vector as done in Eq. (4.14), however for each i-*th* node involved in the 2D plate mid-surface discretization, the vectors of the τ-*th* generalized displacement components $(\boldsymbol{u}_{\tau_1}, ..., \boldsymbol{u}_{\tau_M})_i$ are now the physical Cartesian displacement components of the discretized $\boldsymbol{u}_{\tau i}$-*th* node:

$$\boldsymbol{u}_{DOF} = \left[\begin{array}{c} \left.\begin{array}{c} \left.(u_{x_{i=1,\tau=1}}, u_{y_{i=1,\tau=1}}, u_{z_{i=1,\tau=1}})^T\right\} \text{Node } \tau\text{=}1 \\ \vdots \\ \left.(u_{x_{i=1,\tau=M+1}}, u_{y_{i=1,\tau=M+1}}, u_{z_{i=1,\tau=M+1}})^T\right\} \text{Node } \tau\text{=}M\text{+}1 \end{array}\right\} \text{Node } i\text{=}1 \\ \hdashline \vdots \\ \vdots \\ \vdots \\ \hdashline \left.\begin{array}{c} \left.(u_{x_{i=1,\tau=1}}, u_{y_{i=1,\tau=1}}, u_{z_{i=1,\tau=1}})^T\right\} \text{Node } \tau\text{=}1 \\ \vdots \\ \left.(u_{x_{i=1,\tau=M+1}}, u_{y_{i=1,\tau=M+1}}, u_{z_{i=1,\tau=M+1}})^T\right\} \text{Node } \tau\text{=}M\text{+}1 \end{array}\right\} \text{Node } i\text{=}N_n \end{array}\right] \tag{4.15}$$

The extension to higher-order structural theories is achieved in a straightforward manner, resulting in a final one-dimensional plate model with three-dimensional capabilities, while preserving computational efficiency through higher-order interpolation. A graphical representation of the final, discretized, beam CUF model is provided in Fig. 4.8. The complete list of 2D finite element interpolation adopted and the respective shape functions involved are presented in Table 4.2.

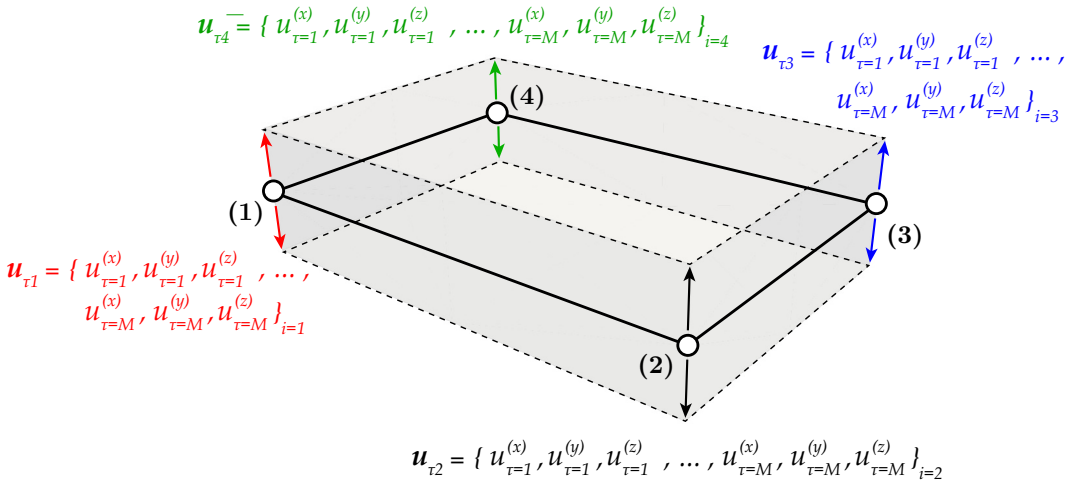

(a) TE models

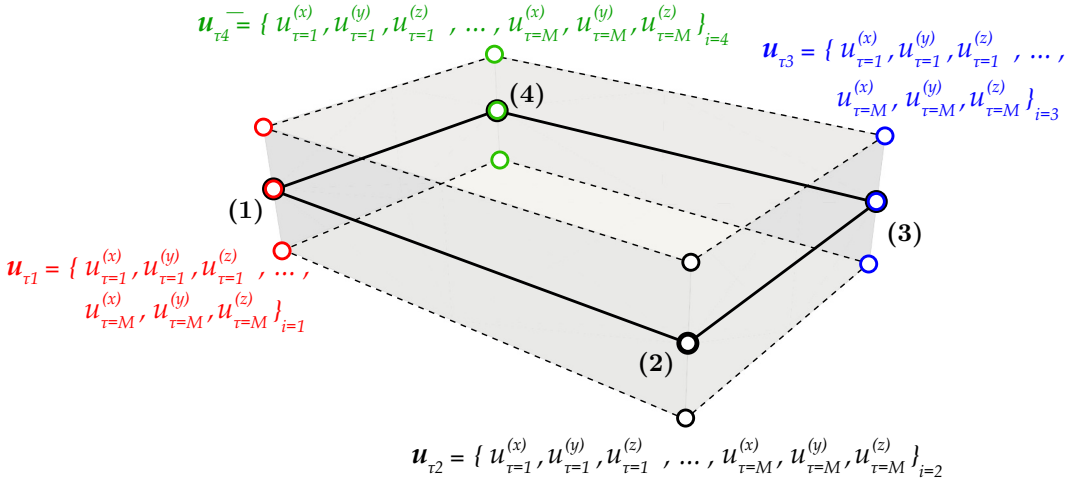

(b) LE models

Figure 4.8: Unified formulation of beam theories: graphical representation of the final 1D CUF model with explicit DOF representation

Q4 element, linear 2D interpolation

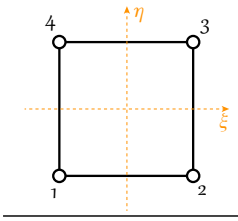

$$N_1(\xi,\eta) = \frac{1}{4}(1-\xi)(1-\eta) \qquad N_2(\xi,\eta) = \frac{1}{4}(1+\xi)(1-\eta)$$

$$N_3(\xi,\eta) = \frac{1}{2}(1+\xi)(1+\eta) \qquad N_4(\xi,\eta) = \frac{1}{4}(1-\xi)(1+\eta)$$

Q9 element, quadratic 2D interpolation

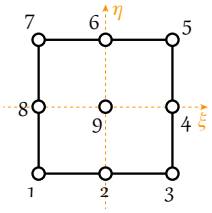

$$N_1(\xi,\eta) = \frac{1}{4}(\xi^2-\xi)(\eta^2-\eta) \qquad N_6(\xi,\eta) = \frac{1}{2}(1-\xi^2)(\eta^2+\eta)$$

$$N_2(\xi,\eta) = \frac{1}{2}(1-\xi^2)(\eta^2-\eta) \qquad N_7(\xi,\eta) = \frac{1}{4}(\xi^2-\xi)(\eta^2+\eta)$$

$$N_3(\xi,\eta) = \frac{1}{4}(\xi^2+\xi)(\eta^2-\eta) \qquad N_8(\xi,\eta) = \frac{1}{2}(\xi^2-\xi)(1-\eta^2)$$

$$N_4(\xi,\eta) = \frac{1}{2}(\xi^2+\xi)(1-\eta^2) \qquad N_9(\xi,\eta) = (1-\xi^2)(1-\eta^2)$$

$$N_5(\xi,\eta) = \frac{1}{4}(\xi^2+\xi)(\eta^2+\eta)$$

Q16 element, cubic 2D interpolation

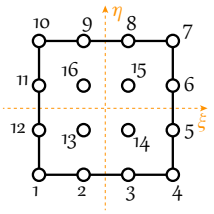

$$N_1(\xi,\eta) = \left[\frac{1}{16}(\xi-1)(1-9\xi^2)\right]\cdot\left[\frac{1}{16}(\eta-1)(1-9\eta^2)\right]$$

$$N_2(\xi,\eta) = \left[\frac{9}{16}(1-\xi^2)(1-3\xi)\right]\cdot\left[\frac{1}{16}(\eta-1)(1-9\eta^2)\right]$$

$$N_3(\xi,\eta) = \left[\frac{9}{16}(1-\xi^2)(1+3\xi)\right]\cdot\left[\frac{1}{16}(\eta-1)(1-9\eta^2)\right]$$

$$N_4(\xi,\eta) = \left[\frac{1}{16}(1+\xi)(9\xi^2-1)\right]\cdot\left[\frac{1}{16}(\eta-1)(1-9\eta^2)\right]$$

$$N_5(\xi,\eta) = \left[\frac{1}{16}(1+\xi)(9\xi^2-1)\right]\cdot\left[\frac{9}{16}(1-\eta^2)(1-3\eta)\right]$$

$$N_6(\xi,\eta) = \left[\frac{1}{16}(1+\xi)(9\xi^2-1)\right]\cdot\left[\frac{9}{16}(1-\eta^2)(1+3\eta)\right]$$

$$N_7(\xi,\eta) = \left[\frac{1}{16}(1+\xi)(9\xi^2-1)\right]\cdot\left[\frac{1}{16}(1+\eta)(9\eta^2-1)\right]$$

$$N_8(\xi,\eta) = \left[\frac{9}{16}(1-\xi^2)(1+3\xi)\right]\cdot\left[\frac{1}{16}(1+\eta)(9\eta^2-1)\right]$$

$$N_9(\xi,\eta) = \left[\frac{9}{16}(1-\xi^2)(1-3\xi)\right]\cdot\left[\frac{1}{16}(1+\eta)(9\eta^2-1)\right]$$

$$N_{10}(\xi,\eta) = \left[\frac{1}{16}(\xi-1)(1-9\xi^2)\right]\cdot\left[\frac{1}{16}(1+\eta)(9\eta^2-1)\right]$$

$$N_{11}(\xi,\eta) = \left[\frac{1}{16}(\xi-1)(1-9\xi^2)\right]\cdot\left[\frac{9}{16}(1-\eta^2)(1+3\eta)\right]$$

$$N_{12}(\xi,\eta) = \left[\frac{1}{16}(\xi-1)(1-9\xi^2)\right]\cdot\left[\frac{9}{16}(1-\eta^2)(1-3\eta)\right]$$

$$N_{13}(\xi,\eta) = \left[\frac{9}{16}(1-\xi^2)(1-3\xi)\right]\cdot\left[\frac{9}{16}(1-\eta^2)(1-3\eta)\right]$$

$$N_{14}(\xi,\eta) = \left[\frac{9}{16}(1-\xi^2)(1+3\xi)\right]\cdot\left[\frac{9}{16}(1-\eta^2)(1-3\eta)\right]$$

$$N_{15}(\xi,\eta) = \left[\frac{9}{16}(1-\xi^2)(1+3\xi)\right]\cdot\left[\frac{9}{16}(1-\eta^2)(1+3\eta)\right]$$

$$N_{16}(\xi,\eta) = \left[\frac{9}{16}(1-\xi^2)(1-3\xi)\right]\cdot\left[\frac{9}{16}(1-\eta^2)(1+3\eta)\right]$$

Table 4.2: Finite element interpolation in two dimension: local internal numbering and shape functions expressions.

4.3 Equivalent-Single-Layer and Layer-Wise models

Multilayered structures, widely adopted in many engineering fields, as composites, laminates, or complex biological materials, exhibit a complex mechanical behavior due to the mechanical interactions between layers or sub-components with differing material properties and orientations. The performance of these structural components depends on interlaminar stresses, delamination, and local effects that cannot be accurately described with lower-order models [172, 173]. Therefore, refined theories of structure approximations are essential to effectively capture the through-the-thickness behavior and the complex anisotropic structural response [170]. Within the framework of CUF, and more generally in a finite element scenario for multilayered structures, numerical models are dependent on the choice of through-the-thickness kinematics description. In this sense, two different approaches have been proposed: Equivalent-Single-Layer models (ESLm) or Layer-Wise (LW) / Component-Wise (CW) models. These models have already been introduced, but a comprehensive description of the two approaches is provided here. Multilayered structures exhibit an anisotropic behavior at least in the thickness direction, where different through-the-thickness material properties are encountered [174]. This anisotropy can lead to non-negligible displacement gradients, where discontinuities in the displacement slopes can be observed at interfaces [175], arising in the zig-zag form of the displacements [176]. Furthermore, from equilibrium equations, the interlaminar continuity of transverse normal and shear stress components at interfaces is also required when modeling multilayered structures [177], as well as displacement components. In a Total Lagrangian finite element scenario, where the governing equations for a hyperelastic material are written in the material reference frame, the first Piola-Kirchhoff stress components (P_{xz}, P_{yz}, P_{zz}) must be continuous at layer interfaces [178]. The interlaminar continuity conditions of stress and displacement components in the through-the-thickness direction, as well as the compatibility at structural interfaces and boundary conditions, are called C_z^0 requirements [179]. These conditions must be fulfilled in a finite element scenario to accurately compute and predict the structural response of materials and structures. These can be achieved by adopting appropriate theory of structure approximations in the numerical modeling of multilayered structures [175].

In the case of ESLm, as described in the definition of higher-order 1D and 2D models, Taylor polynomials are employed in the kinematic modeling of the displacement field along the thickness or cross-sectional direction. In this sense, the number of unknown variables is defined regardless of the beam cross-section sub-components or plate layers [126]. The final unknowns of the problem are the generalized displacement components, namely the higher-order derivatives of the 3D displacement field, which are obtained as a higher-order expansion of the displacement field in the cross-section direction of thickness, as for example introduced in Eqs. (4.2) and (4.10). Classical TE-based models, generalized up to any order, have been referred to as extensions of the Classical Laminated Theories (CLTs) [180], where refinements in the classical First-Order Shear-Deformation theory (FSDT) allowed for the fulfillment of some compatibility requirements [172]. In the CUF framework, the ESLm are exploited by adopting TE models, which define a unique expression of the displacement field expanded up to the M*-th* order hierarchically. In this way, it is possible to analyze the behavior of each possible theory of structure up to any order. The main limitation of this approach is the insensitivity to the specific layer properties, and the final kinematic description of the structural behavior is given by a homogenized resultant behavior, where the mechanical properties across layers or sub-components have been homogenized in a resulting, unique model [179].

Naturally, the simple idea of incorporating zig-zag effects into the theory of structural approximation led to the definition of LW or CW models. In this sense, the classical TE models are defined at the layer-component level; thus, each structural sub-component is modeled independently, imposing the compatibility conditions between interfaces as additional constraints of the model. As historically done [181, 160], in the CUF framework, LW/CW models have been introduced by adopting LE models. In this theory of structure approximation, the through-the-thickness or cross-section expansion of the displacement field is made through the adoption of 1D or 2D Lagrange's polynomials [182]. The expansion direction is discretized into several local beam sub-domains or plate layers, over which Lagrange's polynomials are defined to interpolate the displacement field [183]. In this way, the definition of local independent discretizations for each sub-component is naturally achieved, and different kinematics can be assigned independently from those of other components. A graphical representation of the two approaches is provided in Fig. 4.9.

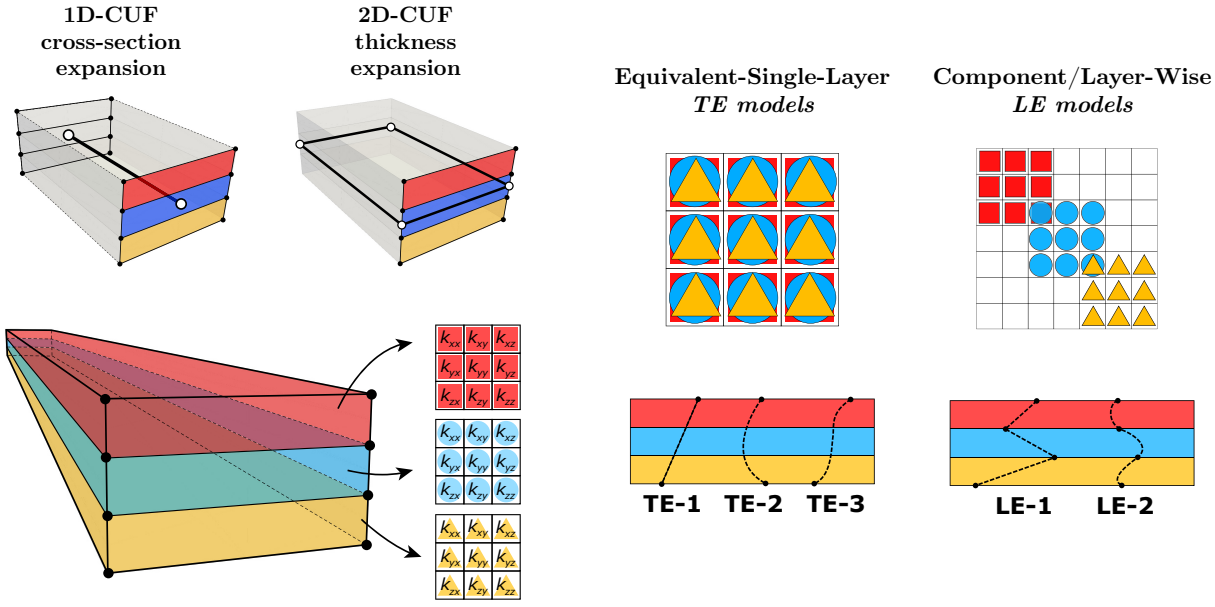

Figure 4.9: Multilayered structures: ESLm and CW-LWm.

Chapter 5

Governing equations in matrix form

In the present chapter, the proposed nonlinear finite element procedure based on higher-order CUF model is extensively described. All the physical quantities involved will be introduced. The Principle of Virtual Work (PVW) is the starting point in the definition of the nonlinear governing equation, implementing then the proposed formalism to rewrite the matrix-form of the governing equation. Therefore, the Fundamental Nuclei (FN) formalism is introduced, defining the basic elementary blocks of the present approach, in a resulting definition of the governing equation in a compact and hierarchical form. The nonlinear governing equations will be solved numerically by means of a linearized-incremental scheme based on the Newton-Raphson linearization, introducing the tangent stiffness matrix and the residual nodal force vector. In particular, the description of the present isoparametric approach, the numerical quadrature rule and the assembling procedure of FN are also proposed.

5.1 Preliminaries

Let (x, y, z) be the Cartesian reference frame and let $\boldsymbol{u}$ be the continuous displacement field of the body, described in the material configuration:

$$\boldsymbol{u} = \boldsymbol{u}(x, y, z) = \{ \ u_x(x, y, z), \ u_y(x, y, z), \ u_z(x, y, z) \ \}^{\mathrm{T}} \tag{5.1}$$

In the following, the Voigt notation is adopted for symmetric tensorial quantites. Thus, the Green-Lagrange strain tensor $\mathbf{E}$, the second Piola-Kirchhoff stress tensor $\mathbf{S}$ are referred to as:

$$\mathbf{E} = \{ \ \varepsilon_{xx}, \varepsilon_{yy}, \varepsilon_{zz}, 2\gamma_{xz}, 2\gamma_{yz}, 2\gamma_{xy} \ \}^{\mathrm{T}} \tag{5.2}$$

$$\mathbf{S} = \{ \ S_{xx}, S_{yy}, S_{zz}, S_{xz}, S_{yz}, S_{xy} \ \}^{\mathrm{T}} \tag{5.3}$$

The components of the Green-Lagrange strain tensor Eqs. (2.25)-(2.30) are then written in compact formal:

$$\boldsymbol{\varepsilon} = (\mathbf{b}_l + \mathbf{b}_{nl})\boldsymbol{u} \tag{5.4}$$

where the matrices $\mathbf{b}_l$ and $\mathbf{b}_{nl}$ are the formal matrices of the linear and non-linear derivative operators [148] defined as follow:

$$\mathbf{b}_l = \begin{bmatrix} \frac{\partial}{\partial x} & 0 & 0 \\ 0 & \frac{\partial}{\partial y} & 0 \\ 0 & 0 & \frac{\partial}{\partial z} \\ \frac{\partial}{\partial z} & 0 & \frac{\partial}{\partial x} \\ 0 & \frac{\partial}{\partial z} & \frac{\partial}{\partial y} \\ \frac{\partial}{\partial y} & \frac{\partial}{\partial x} & 0 \end{bmatrix} \qquad \mathbf{b}_{nl} = \begin{bmatrix} \frac{1}{2}\left(\frac{\partial}{\partial x}\right)^2 & \frac{1}{2}\left(\frac{\partial}{\partial x}\right)^2 & \frac{1}{2}\left(\frac{\partial}{\partial x}\right)^2 \\ \frac{1}{2}\left(\frac{\partial}{\partial y}\right)^2 & \frac{1}{2}\left(\frac{\partial}{\partial y}\right)^2 & \frac{1}{2}\left(\frac{\partial}{\partial y}\right)^2 \\ \frac{1}{2}\left(\frac{\partial}{\partial z}\right)^2 & \frac{1}{2}\left(\frac{\partial}{\partial z}\right)^2 & \frac{1}{2}\left(\frac{\partial}{\partial z}\right)^2 \\ \frac{\partial}{\partial x}\frac{\partial}{\partial z} & \frac{\partial}{\partial x}\frac{\partial}{\partial z} & \frac{\partial}{\partial x}\frac{\partial}{\partial z} \\ \frac{\partial}{\partial y}\frac{\partial}{\partial z} & \frac{\partial}{\partial y}\frac{\partial}{\partial z} & \frac{\partial}{\partial y}\frac{\partial}{\partial z} \\ \frac{\partial}{\partial x}\frac{\partial}{\partial y} & \frac{\partial}{\partial x}\frac{\partial}{\partial y} & \frac{\partial}{\partial x}\frac{\partial}{\partial y} \end{bmatrix} \tag{5.5}$$

For further manipulations, the Green-Lagrange strain tensor is here rewritten now under the CUF formalism, expressing it in terms of generalized nodal displacements and polynomial expansion. Suppressing the variable dependence to obtain a more general formulation of the strain tensor, independent of the 1D or 2D approach chosen, one can rewrite then:

$$\mathbf{E} = (\mathbf{b}_l + \mathbf{b}_{nl})\ \boldsymbol{u} = (\mathbf{b}_l + \mathbf{b}_{nl}) F_\tau N_i \boldsymbol{u}_{\tau i} = (\mathbf{B}_l^{\tau i} + \mathbf{B}_{nl}^{\tau i}) \boldsymbol{u}_{\tau i} \tag{5.6}$$

The formal matrices of derivatives operator $\mathbf{b}_l$ and $\mathbf{b}_{nl}$ Eq. (5.5) applied to the discretized displacement field provide the algebraic matrices $\mathbf{B}_l^{\tau i}$ and $\mathbf{B}_{nl}^{\tau i}$, adopted for the strain interpolation [130]. In the case of 1D and 2D beam and plate models, these algebraic matrices can be straightforwardly derived from the definition of the 3D displacement field, specialized in both cases:

1D CUF beam models [130]

$$\mathbf{B}_l^{\tau i} = \begin{bmatrix} F_{\tau,x} N_i & 0 & 0 \\ 0 & F_\tau N_{i,y} & 0 \\ 0 & 0 & F_{\tau,z} N_i \\ F_{\tau,z} N_i & 0 & F_{\tau,x} N_i \\ 0 & F_{\tau,z} N_i & F_\tau N_{i,y} \\ F_\tau N_{i,y} & F_{\tau,x} N_i & 0 \end{bmatrix} \tag{5.7}$$

$$\mathbf{B}_{nl}^{\tau i} = \frac{1}{2} \begin{bmatrix} u_{x,x} F_{\tau,x} N_i & u_{y,x} F_{\tau,x} N_i & u_{z,x} F_{\tau,x} N_i \\ u_{x,y} F_\tau N_{i,y} & u_{y,y} F_\tau N_{i,y} & u_{z,y} F_\tau N_{i,y} \\ u_{x,z} F_{\tau,z} N_i & u_{y,z} F_{\tau,z} N_i & u_{z,z} F_{\tau,z} N_i \\ u_{x,x} F_{\tau,z} N_i + u_{x,z} F_{\tau,x} N_i & u_{y,x} F_{\tau,z} N_i + u_{y,z} F_{\tau,x} N_i & u_{z,x} F_{\tau,z} N_i + u_{z,z} F_{\tau,x} N_i \\ u_{x,y} F_{\tau,z} N_i + u_{x,z} F_\tau N_{i,y} & u_{y,y} F_{\tau,z} N_i + u_{y,z} F_\tau N_{i,y} & u_{z,y} F_{\tau,z} N_i + u_{z,z} F_\tau N_{i,y} \\ u_{x,x} F_\tau N_{i,y} + u_{x,y} F_{\tau,x} N_i & u_{y,x} F_\tau N_{i,y} + u_{y,y} F_{\tau,x} N_i & u_{z,x} F_\tau N_{i,y} + u_{z,y} F_{\tau,x} N_i \end{bmatrix} \tag{5.8}$$

2D CUF plate models [184]

$$\mathbf{B}_l^{\tau i} = \begin{bmatrix} F_\tau N_{i,x} & 0 & 0 \\ 0 & F_\tau N_{i,y} & 0 \\ 0 & 0 & F_{\tau,z} N_i \\ F_{\tau,z} N_i & 0 & F_\tau N_{i,x} \\ 0 & F_{\tau,z} N_i & F_\tau N_{i,y} \\ F_\tau N_{i,y} & F_\tau N_{i,x} & 0 \end{bmatrix} \tag{5.9}$$

$$\mathbf{B}_{nl}^{\tau i} = \frac{1}{2} \begin{bmatrix} u_{x,x} F_\tau N_{i,x} & u_{y,x} F_\tau N_{i,x} & u_{z,x} F_\tau N_{i,x} \\ u_{x,y} F_\tau N_{i,y} & u_{y,y} F_\tau N_{i,y} & u_{z,y} F_\tau N_{i,y} \\ u_{x,z} F_{\tau,z} N_i & u_{y,z} F_{\tau,z} N_i & u_{z,z} F_{\tau,z} N_i \\ u_{x,x} F_{\tau,z} N_i + u_{x,z} F_\tau N_{i,x} & u_{y,x} F_{\tau,z} N_i + u_{y,z} F_\tau N_{i,x} & u_{z,x} F_{\tau,z} N_i + u_{z,z} F_\tau N_{i,x} \\ u_{x,y} F_{\tau,z} N_i + u_{x,z} F_\tau N_{i,y} & u_{y,y} F_{\tau,z} N_i + u_{y,z} F_\tau N_{i,y} & u_{z,y} F_{\tau,z} N_i + u_{z,z} F_\tau N_{i,y} \\ u_{x,x} F_\tau N_{i,y} + u_{x,y} F_\tau N_{i,x} & u_{y,x} F_\tau N_{i,y} + u_{y,y} F_\tau N_{i,x} & u_{z,x} F_\tau N_{i,y} + u_{z,y} F_\tau N_{i,x} \end{bmatrix} \tag{5.10}$$

where the symbol $(\cdot)_{,(\cdot)}$ stands for the partial derivative operator in compact form.
In the implementation of a FE procedure based on variational principles, the virtual variation of the displacement field and strain field are required, as described in Sec. 2.6. Adopting now the same index notation, the explicit expression of virtual displacements and virtual strains is exploited adopting independent indices, using the j index for kinematic models along the beam axis and plate mid-surface nodes, and the s index for the CUF theory of structure approximation expansion [129]:

$$\delta \boldsymbol{u}(x,y,z) = F_s \delta \boldsymbol{u}_s = F_s N_j \delta \boldsymbol{u}_{sj} \qquad j = 1,2,..,N_n, \quad s = 1,...,M \tag{5.11}$$

The virtual variation of the strain measure is written again in compact form following the previous procedure explicited in Eq. (5.6):

$$\delta \mathbf{E} = \delta((\mathbf{B}_l^{\tau i} + \mathbf{B}_{nl}^{\tau i})\boldsymbol{u}_{\tau i}) = (\mathbf{B}_l^{sj} + 2\mathbf{B}_{nl}^{sj})\delta \boldsymbol{u}_{sj} \tag{5.12}$$

where the algebraic matrices $\mathbf{B}_l^{sj}$ and $\mathbf{B}_{nl}^{sj}$ are defined as done in Eqs. (5.7)-(5.10) using the polynomial expansion basis $F_s N_j$ instead of $F_\tau N_i$.

5.2 Weak-form of the governing equation

In the present thesis, the large strain analysis of hyperelastic soft structure is considered. Therefore, it is necessary to analyze structures undergoing large displacements, rotations and deformation by considering the full Green-Lagrange strain tensor in the FE procedure [156]. In particular, to develop a Total Lagrangian approach, the work-conjugate of the Cauchy-Green strain tensor is used, thus the stress tensor considered is the second Piola-Kirchhoff stress tensor [148]. The nonlinear governing equation in weak form are derived by the PVW, carried out in Eq. (2.59):

$$\delta \mathcal{L}_{int} + \delta \mathcal{L}_{ine} = \delta \mathcal{L}_{ext} \tag{5.13}$$

where $\mathcal{L}_{int}$ is the internal strain energy, $\mathcal{L}_{ext}$ is the work done by external loads, $\mathcal{L}_{ine}$ is the work done by inertia loads and δ denotes the virtual variation. Introducing the Voigt notation in the definition of integral terms Eqs. (2.60)-(2.62), one can write

$$\text{(a) } \delta\mathcal{L}_{int} = \int_{\Omega_0} \delta\mathbf{E}^{\mathrm{T}}\mathbf{S}dV \qquad \text{(b) } \delta\mathcal{L}_{ext} = \int_{\Omega_0} \delta\boldsymbol{u}^{\mathrm{T}}\boldsymbol{f}dV \qquad \text{(c) } \delta\mathcal{L}_{ine} = \int_{\Omega_0} \delta\boldsymbol{u}^{\mathrm{T}}\rho\ddot{\boldsymbol{u}}dV \tag{5.14}$$

where $\mathbf{E}$ is the Green-Lagrange strain tensor, $\mathbf{S}$ is the PK2 stress tensor, $\ddot{\boldsymbol{u}}$ is the acceleration vector and $\boldsymbol{f}$ is the vector of external loads. In the present approach, a Total Lagrangian approach is exploited, thus all volume integrals are evaluated with respect to the material configuration.
Starting from the integral contributions defined in Eq. (5.14), the matrix-form of the governing equations is carried out imposing the CUF-FEM approximation of the general displacement field. As it will be proven, the matrix-form of the governing equation will be expressed in terms of few basic building block, denoted as Fundamental Nuclei (FN), defined regardless of the polynomial basis adopted in the finite element definition [129]. The final governing equation will be a unique set of nonlinear algebraic equations where the only, final, unknowns of the problem are the generalized nodal displacements [130]. All involved FE matrices are defined in the CUF formalism and presented in a hierarchical form. In the following derivation, all the variable dependence will be suppressed to derive a more general formulation of matrix-form equations independently of the CUF model adopted.

Internal energy contribution

The internal strain energy defined in Eq.(5.14)(a) is rewritten as:

$$\delta\mathcal{L}_{int} = \int_{\Omega_0} \delta\boldsymbol{u}_{sj}^{\mathrm{T}}(\mathbf{B}_l^{sj} + 2\mathbf{B}_{nl}^{sj})^{\mathrm{T}}\mathbf{S}dV = \delta\boldsymbol{u}_{sj}^{\mathrm{T}}\left[\int_{\Omega_0} (\mathbf{B}_l^{sj} + 2\mathbf{B}_{nl}^{sj})^{\mathrm{T}}\mathbf{S}\ dV\right] = \delta\boldsymbol{u}_{sj}^{\mathrm{T}}\mathbf{F}_{int}^{sj} \tag{5.15}$$

where the 3x1 FN $\mathbf{F}_{int}^{sj}$ of the internal forces vector is:

$$\mathbf{F}_{int}^{sj} = \int_{\Omega_0} (\mathbf{B}_l^{sj} + 2\mathbf{B}_{nl}^{sj})^{\mathrm{T}}\mathbf{S}dV \tag{5.16}$$

External load contribution

Following the previous derivation procedure for the internal strain contribution, the matrix-form of the external load term in the variational principle is expressed starting from the definition in Eq. (5.14)(b):

$$\delta\mathcal{L}_{ext} = \int_{\Omega_0} \delta\boldsymbol{u}^{\mathrm{T}}\boldsymbol{f}dV = \int_{\Omega_0} \delta\boldsymbol{u}_{sj}^{\mathrm{T}}F_sN_j\boldsymbol{f}\ dV = \delta\boldsymbol{u}_{sj}^{\mathrm{T}}\mathbf{F}_{ext}^{sj} \tag{5.17}$$

where the 3x1 FN $\mathbf{F}_{ext}^{sj}$ of the external forces vector is:

$$\mathbf{F}_{ext}^{sj} = \int_{\Omega_0} F_sN_j\boldsymbol{f}\ dV \tag{5.18}$$

Inertia load contribution

The inertial contribution given by Eq. (5.14)(c) is defined in matrix form starting from the definitions:

$$\delta\mathcal{L}_{ine} = \int_{\Omega_0} \delta\boldsymbol{u}^{\mathrm{T}}\rho\ \ddot{\boldsymbol{u}}dV = \int_{\Omega_0} \delta\boldsymbol{u}_{sj}^{\mathrm{T}}F_sN_j\rho F_\tau N_i\ddot{\boldsymbol{u}}_{\tau i}dV = \delta\boldsymbol{u}_{sj}^{T}\mathbf{M}^{\tau sij}\ddot{\boldsymbol{u}}_{\tau i} \tag{5.19}$$

where the 3x3 FN $\mathbf{M}^{\tau sij}$ of the constant mass matrix is:

$$\mathbf{M}^{\tau sij} = \int_{\Omega_0} F_s N_j \ \rho \ \mathbf{I} \ F_\tau N_i dV \tag{5.20}$$

Considering then Eq. (5.16), Eq. (5.18) and Eq. (5.20), the variational principle written in matrix form is:

$$\delta \boldsymbol{u}_{sj} : \qquad \mathbf{F}^{sj}_{int} + \mathbf{M}^{\tau sij} \ddot{\boldsymbol{u}}_{\tau i} = \mathbf{F}^{sj}_{ext} \tag{5.21}$$

In the CUF framework, the basic entries of finite element matrices defined in Eqs. (5.16)-(5.20) are carried out and defined regardless of the polynomial expansion basis used for the displacement fields, thus the final nonlinear matrix-form equation Eq. (5.21) is valid for any arbitrarily chosen FE definition of the displacement field. Once the specific 1D beam axis or 2D mid-surface kinematics are assigned, namely the set of N_i and N_j shape functions, and the theory of structure approximation F_τ and F_s along the beam cross-section or plate mid-surface are chosen, the final form of the nonlinear governing equation is exploited by means of the recursive summation over the indices considered (namely i, j, τ and s) [129], as will be described in the following.

The summation over the four introduced indices provides the final, matrix form, of the assembles internal and external forces vectors and the mass matrix, straightforwardly obtained by the CUF assembling procedure [129]. Once the final matrix form contributions are assembled, the PVW in matrix form states:

$$\mathbf{F}_{int}(\boldsymbol{u}) + \mathbf{M}\ddot{\boldsymbol{u}} = \mathbf{F}_{ext}(\boldsymbol{f}) \tag{5.22}$$

Due to the presence of both geometrical and material nonlinearities in the constitutive modeling, the final governing equation Eq. (5.22) is a strongly nonlinear set of differential equations, that is typically solved through the adoption of linearized incremental-iterative numerical schemes. Historically, the internal energy contribution has been defined, within the context of nonlinear analysis, through the adoption of the secant stiffness matrix [130]. Although this has been the classical modeling approach, in the context of hyperelasticity where a nonlinear constitutive law is encountered, the secant stiffness matrix can not be introduced and therefore the internal strain energy contribution is written directly in terms of the second Piola-Kirchhoff stress tensor. In linear elasticity, instead, it is possible to derive the expression of the internal strain energy in terms of secant stiffness matrix, as detailed in Appendix C.1.

5.3 Static problem, linearization of the governing equation

The resulting, strongly nonlinear, governing equations are commonly solved adopting solution algorithms based on linearized incremental procedures. In the case of a static, nonlinear analysis, the final governing equation Eq. (5.22) is written as an equivalent minimization problem of the residual function [185]. Neglecting the inertial contribution, one can define the *unbalanced nodal forces vector* as:

$$\boldsymbol{\varphi}_{res}(\boldsymbol{u}, \boldsymbol{f}) \equiv \mathbf{F}_{int} - \mathbf{F}_{ext} \tag{5.23}$$

From a mathematical standpoint, the non-trivial equilibrium state $\boldsymbol{u}$, given by the application of the load vector $\boldsymbol{f}$, is equivalently identified by root of Eq. (5.23) since, due to balance at equilibrium, the residual nodal force vector is null.

Considering a known equilibrium condition $(\boldsymbol{u}^k, \boldsymbol{f}^k)$, the residual nodal forces vector is expanded considering a first order Taylor's expansion of an increment $(\Delta\boldsymbol{u}, \Delta\boldsymbol{f})$:

$$\boldsymbol{\varphi}_{res}(\boldsymbol{u}^k + \Delta\boldsymbol{u}^k, \boldsymbol{f}^k + \Delta\boldsymbol{f}^k) = \boldsymbol{\varphi}_{res}(\boldsymbol{u}^k, \boldsymbol{f}^k) + \left.\frac{\partial\boldsymbol{\varphi}_{res}}{\partial\boldsymbol{u}}\right|_{(\boldsymbol{u}^k,\boldsymbol{f}^k)} \Delta\boldsymbol{u}^k + \left.\frac{\partial\boldsymbol{\varphi}_{res}}{\partial\boldsymbol{f}}\right|_{(\boldsymbol{u}^k,\boldsymbol{f}^k)} \Delta\boldsymbol{f}^k \tag{5.24}$$

In the present approach, $\boldsymbol{f}$ is the vector of *conservative* loads, thus independent of the deformed configuration. Therefore, the finite variation of the external load vector is rewritten in terms of the load factor:

$$\boldsymbol{f}^k = \lambda^k \boldsymbol{f}_{ref} \quad \rightarrow \quad \Delta\boldsymbol{f}^k = \Delta\lambda^k \boldsymbol{f}_{ref} \tag{5.25}$$

Following Eq. (5.24), the tangent stiffness matrix is defined as $\dfrac{\partial\boldsymbol{\varphi}_{res}}{\partial\boldsymbol{u}} = \mathbf{K}_T$ [148], and $\dfrac{\partial\boldsymbol{\varphi}_{res}}{\partial\boldsymbol{f}} = -\mathbf{I}$ under the hypothesis of dead loads. Afterwards, to impose an equilibrium condition in the state $(\boldsymbol{u}^k + \Delta\boldsymbol{u}^k, \boldsymbol{f}^k + \Delta\boldsymbol{f}^k)$, the residual nodal force vector is considered zero, obtaining the following incremental equation:

$$\mathbf{K}_T(\boldsymbol{u}^k)\Delta\mathbf{u}^k = \Delta\lambda^k \boldsymbol{f}_{ref} - \boldsymbol{\varphi}_{res}(\boldsymbol{u}^k, \boldsymbol{f}^k) \tag{5.26}$$

In Eq. (5.26), the unknowns are given by both $\Delta\boldsymbol{u}^k$ and $\Delta\lambda^k$. The load scale parameter λ is now an additional variable of the problem, thus an additional constraint equation is coupled with the incremental equation, to close algebraically the nonlinear system of equations [186]:

$$\begin{cases} \mathbf{K}_T(\boldsymbol{u}^k)\Delta\mathbf{u}^k = \Delta\lambda^k \boldsymbol{f}_{ref} - \boldsymbol{\varphi}_{res}(\boldsymbol{u}^k, \boldsymbol{f}^k) \\ c(\Delta\boldsymbol{u}^k, \Delta\lambda^k) = 0 \end{cases} \tag{5.27}$$

Eq. (5.27) is the final system of equation to be solved to obtain the new updated configuration $(\boldsymbol{u}^{k+1}, \boldsymbol{f}^{k+1}) = (\boldsymbol{u}^k + \Delta\boldsymbol{u}^k, \boldsymbol{f}^k + \Delta\boldsymbol{f}^k)$. This algorithm is iteratively repeated until a certain convergence tolerance on the unbalanced nodal forces vector, namely $|\boldsymbol{\varphi}_{res}| < \varepsilon$ is reached. In the proposed solver, additional convergence criteria are imposed on the variations $\Delta\boldsymbol{u}^k$ and $\Delta\lambda^k$, to correctly predict complex structural phenomena as snap-back or snap-through [187].

5.3.1 Derivation of the tangent stiffness matrix

The matrix form of the tangent stiffness matrix, introduced in Eq. (5.26) is here defined within the CUF formalism, by considering the linearization of the equilibrium equation Eq. (5.23) [148]. Under the hypothesis of dead loads, the only non-null linearized contribution to be considered is the related to the internal strain energy, thus:

$$\Delta(\delta\mathcal{L}_{int}) = \int_{\Omega_0} \Delta(\delta\mathbf{E}^{\mathrm{T}}\mathbf{S})dV = \int_{\Omega_0} \delta\mathbf{E}^{\mathrm{T}}\Delta\mathbf{S}dV + \int_{\Omega_0} \Delta(\delta\mathbf{E}^{\mathrm{T}})\mathbf{S}dV \tag{5.28}$$

Linearization of the constitutive law

The first term of Eq. Eq. (5.28) is related to the linearization of constitutive law. This variation has been already presented in Eq. (3.31), thus the variation of the second Piola-Kirchhoff stress tensor can be defined as:

$$\Delta\mathbf{S} = \mathbb{C}\frac{1}{2}\Delta\mathbf{C} = \mathbb{C}\Delta\mathbf{E} = \mathbb{C}(\mathbf{B}_l^{\tau i} + 2\mathbf{B}_{nl}^{\tau i})\Delta\boldsymbol{u}_{\tau i} \tag{5.29}$$

where $\mathbb{C}$ is the tangent elasticity tensor. Therefore, the linearized energetic term considered is written as [148]:

$$\begin{aligned}\int_{\Omega_0} \delta\mathbf{E}^{\mathrm{T}}\Delta\mathbf{S}dV &= \int_{\Omega_0} \delta\boldsymbol{u}_{sj}^{\mathrm{T}}(\mathbf{B}_l^{sj}+2\mathbf{B}_{nl}^{sj})^{\mathrm{T}}\mathbb{C}(\mathbf{B}_l^{\tau i}+2\mathbf{B}_{nl}^{\tau i})\Delta\boldsymbol{u}_{\tau i}\ dV = \\ &= \delta\boldsymbol{u}_{sj}^{\mathrm{T}}\mathbf{K}_{ll}^{\tau sij}\Delta\boldsymbol{u}_{\tau i}+\delta\boldsymbol{u}_{sj}^{\mathrm{T}}\mathbf{K}_{lnl}^{\tau sij}\Delta\boldsymbol{u}_{\tau i}+\delta\boldsymbol{u}_{sj}^{\mathrm{T}}\mathbf{K}_{nll}^{\tau sij}\Delta\boldsymbol{u}_{\tau i}+\delta\boldsymbol{u}_{sj}^{\mathrm{T}}\mathbf{K}_{nlnl}^{\tau sij}\Delta\boldsymbol{u}_{\tau i} \quad (5.30)\\ &= \delta\boldsymbol{u}_{sj}^{\mathrm{T}}\mathbf{K}_{ll}^{\tau sij}\Delta\boldsymbol{u}_{\tau i}+\delta\boldsymbol{u}_{sj}^{\mathrm{T}}\mathbf{K}_{T_1}^{\tau sij}\Delta\boldsymbol{u}_{\tau i} \quad (5.31)\end{aligned}$$

where $\mathbf{K}_{T_1}^{\tau sij}=\mathbf{K}_{lnl}^{\tau sij}+\mathbf{K}_{nll}^{\tau sij}+\mathbf{K}_{nlnl}^{\tau sij}$ is 3x3 FN nonlinear contribution to the tangent stiffness matrix given by the nonlinear strain components of the Green-Lagrange strain tensor, instead $\mathbf{K}_{ll}^{\tau sij}$ is the 3x3 FN of the "linear" contribution, coming from the linear strain components. The terms defined in Eq. (5.30) are here explicitly reported:

$$\begin{cases}\mathbf{K}_{ll}^{\tau sij}=\displaystyle\int_{\Omega_0}\mathbf{B}_l^{sjT}\mathbb{C}\mathbf{B}_l^{\tau i}dV\\ \mathbf{K}_{lnl}^{\tau sij}=\displaystyle\int_{\Omega_0}2\mathbf{B}_l^{sjT}\mathbb{C}\mathbf{B}_{nl}^{\tau i}dV\\ \mathbf{K}_{nll}^{\tau sij}=\displaystyle\int_{\Omega_0}2\mathbf{B}_{nl}^{sjT}\mathbb{C}\mathbf{B}_l^{\tau i}dV\\ \mathbf{K}_{nlnl}^{\tau sij}=\displaystyle\int_{\Omega_0}4\mathbf{B}_{nl}^{sjT}\mathbb{C}\mathbf{B}_{nl}^{\tau i}dV\end{cases} \quad (5.32)$$

At this level, the FN of the tangent stiffness matrix are defined regardless of the hyperelastic material model adopted, either independent of the adopted expression and formulation of the tangent elastic moduli. The present FN expression is defined for a generic 6×6 elasticity tensor. Once the material model is given, the FN expression is specialized by the evaluation of the tangent elasticity tensor $\mathbb{C}$ in the hyperelastic framework, depending of the model considered.

Linearization of the geometrical relations

The second term of Eq. (5.28) is related to the linearization of geometrical relations. The finite variation of the virtual strain involved in this term is carried out following the same rule of the previous derivation, introducing the formal matrix of derivative operators [148]. Analytically, this finite variation is expressed as [148]:

$$\Delta(\delta\mathbf{E})=\begin{bmatrix}(\delta u_{x,x})_v\ \delta u_{x,x}+(\delta u_{y,x})_v\ u_{x,y}+(\delta u_{z,x})_v\ \delta u_{z,x}\\ (\delta u_{x,y})_v\ \delta u_{x,y}+(\delta u_{y,y})_v\ u_{y,y}+(\delta u_{z,y})_v\ \delta u_{z,y}\\ (\delta u_{x,z})_v\ \delta u_{x,z}+(\delta u_{y,z})_v\ u_{y,z}+(\delta u_{z,z})_v\ \delta u_{z,z}\\ [(\delta u_{x,x})_v\ \delta u_{x,z}+u_{x,x}(\delta u_{x,z})_v\ ]+[(\delta u_{y,x})_v\ \delta u_{y,z}+u_{y,x}(\delta u_{y,z})_v\ ]+[(\delta u_{z,x})_v\ \delta u_{z,z}+u_{z,x}(\delta u_{z,z})_v\ ]\\ [(\delta u_{x,y})_v\ \delta u_{x,z}+u_{x,y}(\delta u_{x,z})_v\ ]+[(\delta u_{y,y})_v\ \delta u_{y,z}+u_{y,y}(\delta u_{y,z})_v\ ]+[(\delta u_{z,y})_v\ \delta u_{z,z}+u_{z,y}(\delta u_{z,z})_v\ ]\\ [(\delta u_{x,x})_v\ \delta u_{x,y}+u_{x,x}(\delta u_{x,y})_v\ ]+[(\delta u_{y,x})_v\ \delta u_{y,y}+u_{y,x}(\delta u_{y,y})_v\ ]+[(\delta u_{z,x})_v\ \delta u_{z,y}+u_{z,x}(\delta u_{z,y})_v\ ]\end{bmatrix} \quad (5.33)$$

where the notation $(\cdot)_v$ is used for the finite variation operator in compact form. Applying now the CUF approximation of the real and virtual displacement field, the term $\Delta(\delta\mathbf{E})$ can

be rewritten in compact form introducing the algebraic $\mathbf{B}^*_{nl}$, as similarly done for the Green-Lagrange strain tensor:

$$\Delta(\delta \boldsymbol{E}) = \mathbf{B}^*_{nl} \begin{Bmatrix} \Delta u_{x_{\tau i}} \delta u_{x_{sj}} \\ \Delta u_{y_{\tau i}} \delta u_{y_{sj}} \\ \Delta u_{z_{\tau i}} \delta u_{z_{sj}} \end{Bmatrix} \tag{5.34}$$

where the matrix $\mathbf{B}^*_{nl}$ is defined again both for 1D and 2D beam models following the definitions of each displacement field approximation:

1D CUF beam models [130]

$$\mathbf{B}^*_{nl} = \begin{bmatrix} F_{s,x} N_j F_{\tau,x} N_i & F_{s,x} N_j F_{\tau,x} N_i & F_{s,x} N_j F_{\tau,x} N_i \\ F_s N_{j,y} F_\tau N_{i,y} & F_s N_{j,y} F_\tau N_{i,y} & F_s N_{j,y} F_\tau N_{i,y} \\ F_{s,z} N_j F_{\tau,z} N_i & F_{s,z} N_j F_{\tau,z} N_i & F_{s,z} N_j F_{\tau,z} N_i \\ F_{s,x} N_j F_{\tau,z} N_i + F_{s,z} N_j F_{\tau,x} N_i & F_{s,x} N_j F_{\tau,z} N_i + F_{s,z} N_j F_{\tau,x} N_i & F_{s,x} N_j F_{\tau,z} N_i + F_{s,z} N_j F_{\tau,x} N_i \\ F_s N_{j,y} F_{\tau,z} N_i + F_{s,z} N_j F_\tau N_{i,y} & F_s N_{j,y} F_{\tau,z} N_i + F_{s,z} N_j F_\tau N_{i,y} & F_s N_{j,y} F_{\tau,z} N_i + F_{s,z} N_j F_\tau N_{i,y} \\ F_{s,x} N_j F_\tau N_{i,y} + F_s N_{j,y} F_{\tau,x} N_i & F_{s,x} N_j F_\tau N_{i,y} + F_s N_{j,y} F_{\tau,x} N_i & F_{s,x} N_j F_\tau N_{i,y} + F_s N_{j,y} F_{\tau,x} N_i \end{bmatrix} \tag{5.35}$$

2D CUF plate models [184]

$$\mathbf{B}^*_{nl} = \begin{bmatrix} F_s N_{j,x} F_\tau N_{i,x} & F_s N_{j,x} F_\tau N_{i,x} & F_s N_{j,x} F_\tau N_{i,x} \\ F_s N_{j,y} F_\tau N_{i,y} & F_s N_{j,y} F_\tau N_{i,y} & F_s N_{j,y} F_\tau N_{i,y} \\ F_{s,z} N_j F_{\tau,z} N_i & F_{s,z} N_j F_{\tau,z} N_i & F_{s,z} N_j F_{\tau,z} N_i \\ F_s N_{j,x} F_{\tau,z} N_i + F_{s,z} N_j F_\tau N_{i,x} & F_s N_{j,x} F_{\tau,z} N_i + F_{s,z} N_j F_\tau N_{i,x} & F_s N_{j,x} F_{\tau,z} N_i + F_{s,z} N_j F_\tau N_{i,x} \\ F_s N_{j,y} F_{\tau,z} N_i + F_{s,z} N_j F_\tau N_{i,y} & F_s N_{j,y} F_{\tau,z} N_i + F_{s,z} N_j F_\tau N_{i,y} & F_s N_{j,y} F_{\tau,z} N_i + F_{s,z} N_j F_\tau N_{i,y} \\ F_s N_{j,x} F_\tau N_{i,y} + F_s N_{j,y} F_\tau N_{i,x} & F_s N_{j,x} F_\tau N_{i,y} + F_s N_{j,y} F_\tau N_{i,x} & F_s N_{j,x} F_\tau N_{i,y} + F_s N_{j,y} F_\tau N_{i,x} \end{bmatrix} \tag{5.36}$$

Therefore, the term given by the linearized geometrical relations is:

$$\begin{aligned} \int_{\Omega_0} \delta(\Delta \mathbf{E})^{\mathrm{T}} \mathbf{S} dV &= \int_{\Omega_0} \begin{Bmatrix} \Delta u_{x_{\tau i}} \delta u_{x_{sj}} \\ \Delta u_{y_{\tau i}} \delta u_{y_{sj}} \\ \Delta u_{z_{\tau i}} \delta u_{z_{sj}} \end{Bmatrix}^{\mathrm{T}} \mathbf{B}^{*T}_{nl} \mathbf{S} dV = \int_{\Omega_0} \delta \boldsymbol{u}^{\mathrm{T}}_{sj} \, \mathrm{diag}(\mathbf{B}^{*T}_{nl} \mathbf{S}) \, \Delta \boldsymbol{u}_{\tau i} dV = \\ &= \delta \boldsymbol{u}^{\mathrm{T}}_{sj} \mathbf{K}^{\tau sij}_{\sigma} \Delta \boldsymbol{u}_{\tau i} \end{aligned} \tag{5.37}$$

where the term $\int_{\Omega_0} \mathrm{diag}(\mathbf{B}^{*T}_{nl} \mathbf{S}) dV$ in Eq. (5.37) is a 3×3 diagonal matrix with the components of the vector $\mathbf{B}^{*T}_{nl} \mathbf{S}$. This contribution defines the FN of geometric stiffness matrix $\mathbf{K}^{\tau sij}_{\sigma}$. For the sake of completeness, the FN of the geometric stiffness matrix is here reported, for both 1D beam and 2D plate models:

1D CUF beam models [130]

$$\begin{aligned}\mathbf{K}_{\sigma}^{\tau sij} &= \int_{\Omega_0}\Big(S_{xx}F_{s,x}N_jF_{\tau,x}N_i + S_{yy}F_sN_{j,y}F_{\tau}N_{i,y} + S_{zz}F_{s,z}N_jF_{\tau,z}N_i + \\ &+ S_{xy}F_{s,x}N_jF_{\tau}N_{i,y} + S_{xy}F_sN_{j,y}F_{\tau,x}N_i + S_{xz}F_{s,x}N_jF_{\tau,z}N_i + \\ &+ S_{xz}F_{s,z}N_jF_{\tau,x}N_i + S_{yz}F_sN_{j,y}F_{\tau,z}N_i + S_{yz}F_{s,z}N_jF_{\tau}N_{i,y}\Big)dV\mathbf{I} \end{aligned} \tag{5.38}$$

2D CUF plate models [184]

$$\begin{aligned}\mathbf{K}_{\sigma}^{\tau sij} &= \int_{\Omega_0}\Big(S_{xx}F_sN_{j,x}F_{\tau}N_{i,x} + S_{yy}F_sN_{j,y}F_{\tau}N_{i,y} + S_{zz}F_{s,z}N_jF_{\tau,z}N_i + \\ &+ S_{xy}F_sN_{j,x}F_{\tau}N_{i,y} + S_{xy}F_sN_{j,y}F_{\tau}N_{i,x} + S_{xz}F_sN_{j,x}F_{\tau,z}N_i + \\ &+ S_{xz}F_{s,z}N_jF_{\tau}N_{i,x} + S_{yz}F_sN_{j,y}F_{\tau,z}N_i + S_{yz}F_{s,z}N_jF_{\tau}N_{i,y}\Big)dV\mathbf{I} \end{aligned} \tag{5.39}$$

Afterwards, once the two terms have been defined separately, the final 3×3 FN of the tangent stiffness matrix is obtained:

$$\begin{aligned}\Delta(\delta\mathcal{L}_{int}) &= \int_{\Omega_0}\delta\mathbf{E}^{\mathrm{T}}\Delta\mathbf{S}dV + \int_{\Omega_0}\Delta(\delta\mathbf{E})^{\mathrm{T}}\mathbf{S}dV = \\ &= \delta\mathbf{u}_{sj}^{\mathrm{T}}\mathbf{K}_{ll}^{\tau sij}\Delta\boldsymbol{u}_{\tau i} + \delta\mathbf{u}_{sj}^{\mathrm{T}}\mathbf{K}_{T_1}^{ij}\Delta\mathbf{u}_{\tau i} + \delta\boldsymbol{u}_{sj}^{\mathrm{T}}\mathbf{K}_{\sigma}^{\tau sij}\Delta\boldsymbol{u}_{\tau i} = \\ &= \delta\mathbf{u}_{sj}^{\mathrm{T}}\mathbf{K}_{T}^{\tau sij}\Delta\boldsymbol{u}_{\tau i} \end{aligned} \tag{5.40}$$

As discussed in the derivation procedures of the FN of internal and external force vectors and mass matrix, again all the 3×3 sub-matrices of the tangent stiffness matrix FN, exploited in Eq. (5.40), are again defined regardless of the discretization model adopted. The CUF formalism exploited in the finite element definition allow to derive the final incremental equation in matrix form regardless of the kinematic and theory of structure approximation considered [130].

5.4 Linearized free vibration in non-trivial equilibrium states

The problem of linearized vibrations around non-trivial equilibrium states becomes fundamental when investigating the modal and dynamic properties of hyperelastic materials [188, 189]. In a large strain context, the effect of pre-stress on the structure can significantly modify the modal and dynamic structural response. The problem of linearized vibrations is here defined, including pre-stress effects in the linearized vibration analysis of these materials and structures, examining how natural frequencies and modal shapes are affected by highly deformed states. The governing equations for the undamped vibration problem in non-trivial equilibrium states are carried out again adopting the PVW. Starting from Eq. (5.22), the residual nodal forces vector is defined now including the non-negligible inertial loads:

$$\boldsymbol{\varphi}_{res}(\boldsymbol{u}, \ddot{\boldsymbol{u}}, \boldsymbol{f}) = \mathbf{F}_{int} + \mathbf{M}\ddot{\boldsymbol{u}} - \mathbf{F}_{ext} \tag{5.41}$$

The generic equilibrium condition is equivalently expressed by the formal condition $\boldsymbol{\varphi}_{res}(\boldsymbol{u}, \ddot{\boldsymbol{u}}, \boldsymbol{f}) = 0$. If $(\boldsymbol{u}_0, \ddot{\boldsymbol{u}}_0, \boldsymbol{f}_0)$ is a known equilibrium state, the residual nodal force vector is expanded by a

Taylor series, truncated at first order, considering an increment $(\Delta\boldsymbol{u}, \Delta\ddot{\boldsymbol{u}}, \Delta\boldsymbol{f})$:

$$\begin{aligned}\boldsymbol{\varphi}_{res}(\boldsymbol{u}_0+\Delta\boldsymbol{u}, \ddot{\boldsymbol{u}}_0+\Delta\ddot{\boldsymbol{u}}, \boldsymbol{f}_0+\Delta\boldsymbol{f}) &= \boldsymbol{\varphi}_{res}(\boldsymbol{u}_0, \ddot{\boldsymbol{u}}_0, \boldsymbol{f}_0) + \frac{\partial\boldsymbol{\varphi}_{res}}{\partial\boldsymbol{u}}\Delta\boldsymbol{u} + \frac{\partial\boldsymbol{\varphi}_{res}}{\partial\ddot{\boldsymbol{u}}}\Delta\ddot{\boldsymbol{u}} + \frac{\partial\boldsymbol{\varphi}_{res}}{\partial\boldsymbol{f}}\Delta\boldsymbol{f} = \\ &= \boldsymbol{\varphi}_{res}(\boldsymbol{u}_0, \ddot{\boldsymbol{u}}_0, \boldsymbol{f}_0) + \frac{\partial\mathbf{F}_{int}}{\partial\boldsymbol{u}}\Delta\boldsymbol{u} + \frac{\partial}{\partial\ddot{\boldsymbol{u}}}\left(\mathbf{M}\ddot{\boldsymbol{u}}\right)\Delta\ddot{\boldsymbol{u}} - \frac{\partial\mathbf{F}_{ext}}{\partial\boldsymbol{f}}\Delta\boldsymbol{f} = \\ &= \boldsymbol{\varphi}_{res}(\boldsymbol{u}_0, \ddot{\boldsymbol{u}}_0, \boldsymbol{f}_0) + \mathbf{K}_T\Delta\boldsymbol{u} + \mathbf{M}\Delta\ddot{\boldsymbol{u}} - \mathbf{I}\Delta\lambda\boldsymbol{f}_{ref} \qquad (5.42)\end{aligned}$$

where again the tangent stiffness matrix is introduced as done in the case of static analysis, and exploiting again the assumption of conservative loads for the variation of the applied loads. The three terms in this final equation are related to the finite variation of internal work, external work, and inertial work, respectively. Under the assumption of linear inertial loads with respect to the constant mass matrix, one can write in the Taylor expansion around the known condition:

$$\Delta(\delta\mathcal{L}_{ine}) = \Delta(\delta\boldsymbol{u}_{sj}^T\mathbf{M}^{\tau sij}\ddot{\boldsymbol{u}}_{\tau i}) = \delta\boldsymbol{u}_{sj}^{\mathrm{T}}\Delta\mathbf{M}^{\tau sij}\ddot{\boldsymbol{u}}_{\tau i} + \delta\boldsymbol{u}_{sj}^{\mathrm{T}}\mathbf{M}^{\tau sij}\Delta\ddot{\boldsymbol{u}}_{\tau i} = \delta\boldsymbol{u}_{sj}^{\mathrm{T}}\mathbf{M}^{\tau sij}\Delta\ddot{\boldsymbol{u}}_{\tau i} \qquad (5.43)$$

In the successive, generic, non-trivial equilibrium state of the structures, the equilibrium is imposed by considering the null unbalanced nodal force vector, thus $\boldsymbol{\varphi}_{res}(\boldsymbol{u}+\Delta\boldsymbol{u}, \ddot{\boldsymbol{u}}_0+\Delta\ddot{\boldsymbol{u}}, \boldsymbol{f}_0+\Delta\boldsymbol{f}) = 0$. The incremental equation is then rewritten now as:

$$\mathbf{K}_T(\boldsymbol{u})\Delta\boldsymbol{u} + \mathbf{M}\Delta\ddot{\boldsymbol{u}} = -\boldsymbol{\varphi}_{res}(\boldsymbol{u}_0, \ddot{\boldsymbol{u}}_0, \boldsymbol{f}_0) + \mathbf{I}\Delta\lambda\boldsymbol{f}_{ref} \qquad (5.44)$$

In the case of linearized, undamped vibration analysis, once the structure is considered in a known non-trivial equilibrium state, all the residual nodal vectors of Eq. (5.42) are null, as well as load variations, thus $\Delta\lambda = 0$ is considered. Under these considerations, the governing equation for the linearized free-vibration problem around the k-th non-trivial condition $\boldsymbol{u}^k$ is:

$$\mathbf{K}_T(\boldsymbol{u}^k)\Delta\boldsymbol{u}^k + \mathbf{M}\Delta\ddot{\boldsymbol{u}}^k = 0 \qquad (5.45)$$

The classical linear eigenvalue problem, around the non-trivial equilibrium state is introduced by imposing a generic harmonic increment $\Delta\boldsymbol{u}^k = \boldsymbol{\Phi}^k e^{i\omega_k t}$:

$$\mathbf{K}_T(\boldsymbol{u}^k)\boldsymbol{\Phi}^k e^{i\omega t} - \omega_k^2\mathbf{M}\boldsymbol{\Phi}^k e^{i\omega_k t} = 0 \qquad (5.46)$$

$$(\mathbf{K}_T(\boldsymbol{u}^k) - \omega_k^2\mathbf{M})\boldsymbol{\Phi}^k e^{i\omega_k t} = 0 \qquad (5.47)$$

$$(\mathbf{K}_T(\boldsymbol{u}^k) - \omega_k^2\mathbf{M})\boldsymbol{\Phi}^k = 0 \qquad (5.48)$$

where $\boldsymbol{\Phi}^k$ is the set of eigenvectors, representing the normal modes of vibration around the deformed k-th pre-stressed structural configuration, and ω_k is the natural frequency of oscillation around the k-th deformed configuration. Equation (5.48) is the classical linear eigenvalue problem, defining thus the small-amplitude free vibration problem, solved numerically employing already available libraries and packages of linear mechanical analysis. The linear eigenvalues problem is then uniquely defined in each equilibrium state by means of the related tangent stiffness matrix $\mathbf{K}_T(\boldsymbol{u}^k)$. From the classical eigenvalue problem Eq. (5.48), the natural frequencies and normal modes of vibration around the deformed equilibrium state (different from the trivial one) are obtained. Figure 5.1 provide a graphical representation of the adopted algorithm in the proposed linearized vibration analysis.

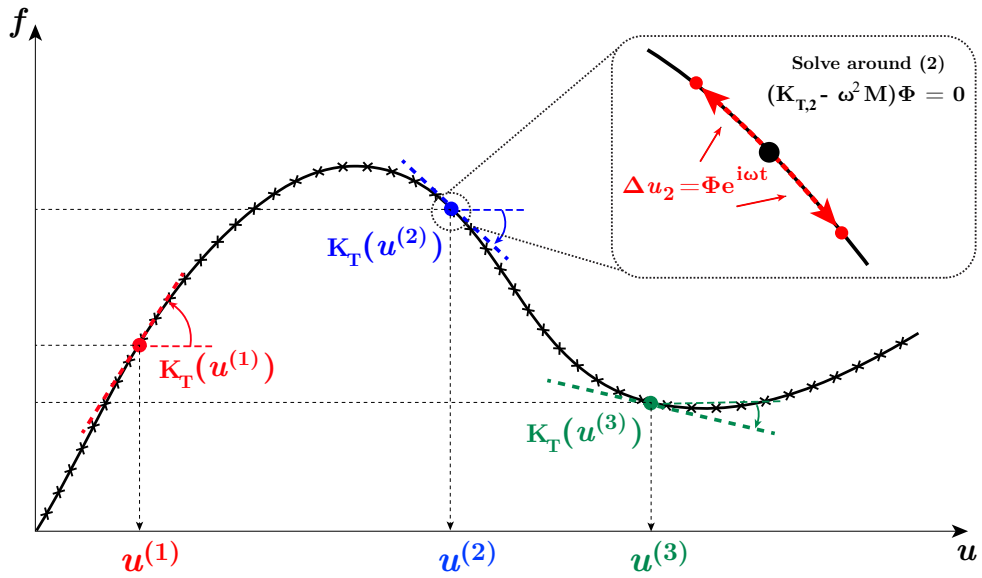

Figure 5.1: Linearized vibration problem around non-trivial equilibrium states: representation scheme.

5.5 Assembling procedure of FN

In the present work, the CUF approach allow the definition of the governing equation in a hierarchical form, whose expression is independent of the finite element model adopted. The previous definitions of the FN of the internal force vector Eq. (5.16), the external force vector Eq. (5.18), the mass matrix Eq. (5.20) and the tangent stiffness matrix Eq. (5.40) allow for a compact redefinition of the equilibrium and incremental equations depending only on elementary blocks defined in terms of the generic polynomial expansion bases chosen for the theory of structure approximation F_τ and F_s and kinematic model along the beam axis or plate mid-surface N_i and N_j [129]. This approach can be seen as a recursive definition of the elementary entries of the FE matrices, starting from the basic unity of the present higher-order finite element modeling approach [129]. In the present section, a detailed description of the CUF assembling procedure is provided. For the sake of clarity, vector indices will be proposed following the order $\mathbf{F}^{sj}$, matrices indices instead with the order $\mathbf{K}^{sj\tau i}$, to better clarify the summations involved.
For each FE node of the beam axis or plate mid-surface the structural theory DOF are mounted. In this sense, for each i-th node of the finite element, the total M generalized displacements DOF are mounted. This can be equivalently considered for the virtual displacement field, overlapped to the real displacement field, in the same definition. The global FE matrices for the discretization model adopted are obtained considering the summation over the recursive index notation of the FN. In the present approach, in total four loops have to be performed to define the overall FE matrices, instead two loops are required for defining the overall force vector [129]. The proposed methodology is now detailed and explained with a representative example on the equilibrium equation in matrix form Eq. (5.21). Consider a representative linear B2 1D beam CUF model and a single L4 expansion model. In this case, for each node involved in the beam axis discretization (2), the theory of structure approximation DOF are mounted (3 DOF $\times$ 4 Lagrange Points), in a resulting model of 24 DOF. The expanded equation of motion, following the summation over the repeated indices is then:

$$\underbrace{\delta\boldsymbol{u}_{1,1}^{\mathrm{T}}\mathbf{F}_{ext}^{1,1}+\ldots+\delta\boldsymbol{u}_{4,1}^{\mathrm{T}}\mathbf{F}_{ext}^{4,1}}_{\text{Sum over s, } j=1}+\underbrace{\delta\boldsymbol{u}_{1,2}^{\mathrm{T}}\mathbf{F}_{ext}^{1,2}+\ldots+\delta\boldsymbol{u}_{4,2}^{\mathrm{T}}\mathbf{F}_{ext}^{4,2}}_{\text{Sum over s, } j=2}=$$

$$\text{Sum over s, } j\text{=1:}\begin{cases}\delta\boldsymbol{u}_{1,1}^{\mathrm{T}}\big[\underbrace{\mathbf{M}^{1,1,1,1}\ddot{\boldsymbol{u}}_{1,1}+\ldots+\mathbf{M}^{1,1,4,1}\ddot{\boldsymbol{u}}_{4,1}}_{\text{Sum over }\tau,\ i=1}+\underbrace{\mathbf{M}^{1,1,1,2}\ddot{\boldsymbol{u}}_{1,2}+\ldots+\mathbf{M}^{1,1,4,2}\ddot{\boldsymbol{u}}_{4,2}}_{\text{Sum over }\tau,\ i=2}\big]+\\ \qquad\qquad\qquad\qquad\qquad\qquad\qquad\qquad\qquad\qquad+\cdots+\\ \delta\boldsymbol{u}_{4,1}^{\mathrm{T}}\big[\underbrace{\mathbf{M}^{4,1,1,1}\ddot{\boldsymbol{u}}_{1,1}+\ldots+\mathbf{M}^{4,1,4,1}\ddot{\boldsymbol{u}}_{4,1}}_{\text{Sum over }\tau,\ i=1}+\underbrace{\mathbf{M}^{4,1,1,2}\ddot{\boldsymbol{u}}_{1,2}+\ldots+\mathbf{M}^{4,1,4,2}\ddot{\boldsymbol{u}}_{4,2}}_{\text{Sum over }\tau,\ i=2}\big]+\end{cases}$$

$$\text{Sum over s, } j\text{=2:}\begin{cases}\delta\boldsymbol{u}_{1,2}^{\mathrm{T}}\big[\underbrace{\mathbf{M}^{1,2,1,1}\ddot{\boldsymbol{u}}_{1,1}+\ldots+\mathbf{M}^{1,2,4,1}\ddot{\boldsymbol{u}}_{4,1}}_{\text{Sum over }\tau,\ i=1}+\underbrace{\mathbf{M}^{1,2,1,2}\ddot{\boldsymbol{u}}_{1,2}+\ldots+\mathbf{M}^{1,2,4,2}\ddot{\boldsymbol{u}}_{4,2}}_{\text{Sum over }\tau,\ i=2}\big]+\\ \qquad\qquad\qquad\qquad\qquad\qquad\qquad\qquad\qquad\qquad+\cdots+\\ \delta\boldsymbol{u}_{4,2}^{\mathrm{T}}\big[\underbrace{\mathbf{M}^{4,2,1,1}\ddot{\boldsymbol{u}}_{1,1}+\ldots+\mathbf{M}^{4,2,4,1}\ddot{\boldsymbol{u}}_{4,1}}_{\text{Sum over }\tau,\ i=1}+\underbrace{\mathbf{M}^{4,2,1,2}\ddot{\boldsymbol{u}}_{1,2}+\ldots+\mathbf{M}^{4,2,4,2}\ddot{\boldsymbol{u}}_{4,2}}_{\text{Sum over }\tau,\ i=2}\big]+\end{cases}$$

$$+\underbrace{\delta\boldsymbol{u}_{1,1}^{\mathrm{T}}\mathbf{F}_{int}^{1,1}+\ldots+\delta\boldsymbol{u}_{4,1}^{\mathrm{T}}\mathbf{F}_{int}^{4,1}}_{\text{Sum over s, } j=1}+\underbrace{\delta\boldsymbol{u}_{1,2}^{\mathrm{T}}\mathbf{F}_{int}^{1,2}+\ldots+\delta\boldsymbol{u}_{4,2}^{\mathrm{T}}\mathbf{F}_{int}^{4,2}}_{\text{Sum over s, } j=2} \tag{5.49}$$

Starting from the general equilibrium equation Eq. (5.21), one can observe that for the specific DOF, given by the s-th term of the theory of structure summation expansion over the j-th finite node, the specific equilibrium equation is found. Therefore, the indices (s, j) give the entry rows of FE matrices, corresponding also to the specific functions to be further integrated. From the Polynomials Identity Theorem, since this equation is valid for all possible values of $\delta \boldsymbol{u}_{sj}$, one can rearrange the full expression obtained in Eq. (5.49) in a set of algebraic equation as follows:

$$
\begin{aligned}
\delta \boldsymbol{u}_{1,1}: \quad \mathbf{F}_{ext}^{1,1} &= \underbrace{\mathbf{M}^{1,1,1,1}\ddot{\boldsymbol{u}}_{1,1} + \cdots + \mathbf{M}^{1,1,4,1}\ddot{\boldsymbol{u}}_{4,1}}_{\text{Sum over } \tau,\ i=1} + \underbrace{\mathbf{M}^{1,1,1,2}\ddot{\boldsymbol{u}}_{1,2} + \ldots + \mathbf{M}^{1,1,4,2}\ddot{\boldsymbol{u}}_{4,2}}_{\text{Sum over } \tau,\ i=2} + \mathbf{F}_{int}^{1,1} \\
&\vdots \\
\delta \boldsymbol{u}_{4,1}: \quad \mathbf{F}_{ext}^{4,1} &= \underbrace{\mathbf{M}^{4,1,1,1}\ddot{\boldsymbol{u}}_{1,1} + \ldots + \mathbf{M}^{4,1,4,1}\ddot{\boldsymbol{u}}_{4,1}}_{\text{Sum over } \tau,\ i=1} + \underbrace{\mathbf{M}^{4,1,1,2}\ddot{\boldsymbol{u}}_{1,2} + \cdots + \mathbf{M}^{4,1,4,2}\ddot{\boldsymbol{u}}_{4,2}}_{\text{Sum over } \tau,\ i=2} + \mathbf{F}_{int}^{4,1} \\
\delta \boldsymbol{u}_{1,2}: \quad \mathbf{F}_{ext}^{1,2} &= \underbrace{\mathbf{M}^{1,2,1,1}\ddot{\boldsymbol{u}}_{1,1} + \cdots + \mathbf{M}^{1,2,4,1}\ddot{\boldsymbol{u}}_{4,1}}_{\text{Sum over } \tau,\ i=1} + \underbrace{\mathbf{M}^{1,2,1,2}\ddot{\boldsymbol{u}}_{1,2} + \cdots + \mathbf{M}^{1,2,4,2}\ddot{\boldsymbol{u}}_{4,2}}_{\text{Sum over } \tau,\ i=2} + \mathbf{F}_{int}^{1,2} \\
&\vdots \\
\delta \boldsymbol{u}_{4,2}: \quad \mathbf{F}_{ext}^{4,2} &= \underbrace{\mathbf{M}^{4,2,1,1}\ddot{\boldsymbol{u}}_{1,1} + \cdots + \mathbf{M}^{4,2,4,1}\ddot{\boldsymbol{u}}_{4,1}}_{\text{Sum over } \tau,\ i=1} + \underbrace{\mathbf{M}^{4,2,1,2}\ddot{\boldsymbol{u}}_{1,2} + \cdots + \mathbf{M}^{4,2,4,2}\ddot{\boldsymbol{u}}_{4,2}}_{\text{Sum over } \tau,\ i=2} + \mathbf{F}_{int}^{4,2}
\end{aligned}
\tag{5.50}
$$

A graphical scheme of the CUF assembling procedure of FN, following the procedure derived from the Polynomial Identity Theorem, is provided in Fig. 5.2.

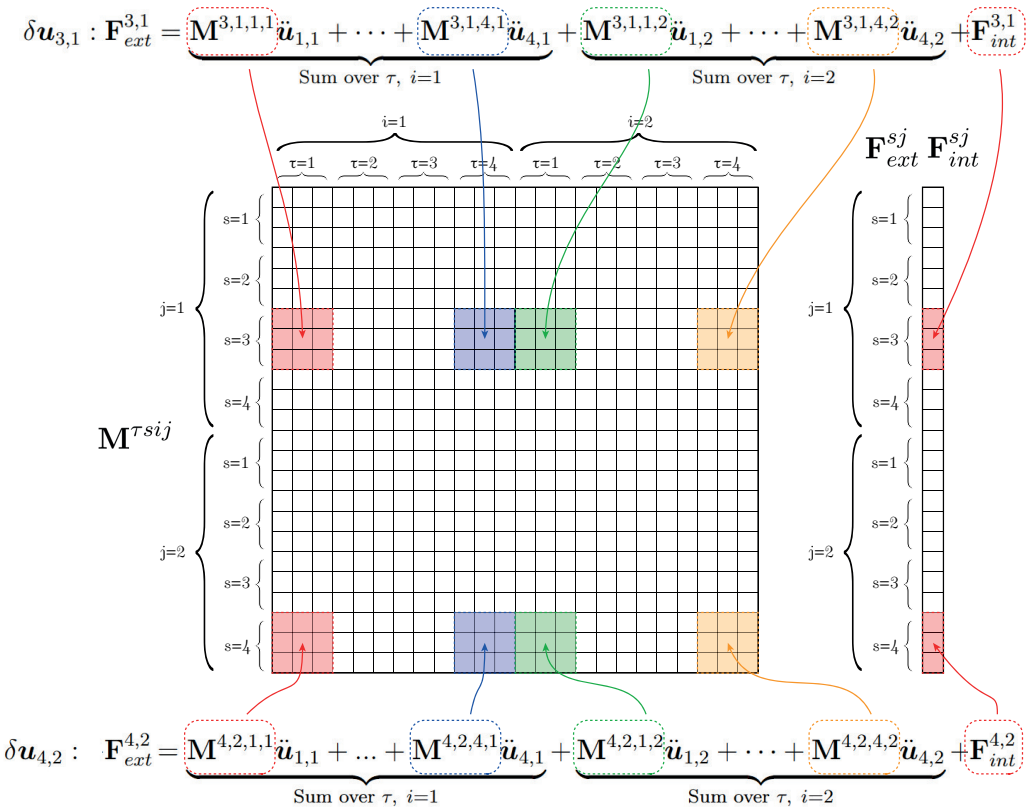

Figure 5.2: Assembling procedure of Fundamental Nuclei: graphical representation.

As observed in the derivation procedure, one can conclude that the summation over the indices $(i-\tau)$ provide the final $(j-s)$ algebraic equation, and each term will be now referred to the contribution related to the τ-th term of the theory of structure expansion around the finite node i. In this sense, from an algebraic point of view, the recursive index notation adopted for the polynomial expansion of the displacement field is also explicitly addressing the contribution of the FE matrices. The four looping indices are both indicating the function to be integrated in the FN definition and the relative contribution to the global FE matrices by the index meaning. A graphical representation of the CUF assembling procedure from nodal DOF theory to the whole element is provided in Fig. 5.3, but more details can be found in the reference [129].

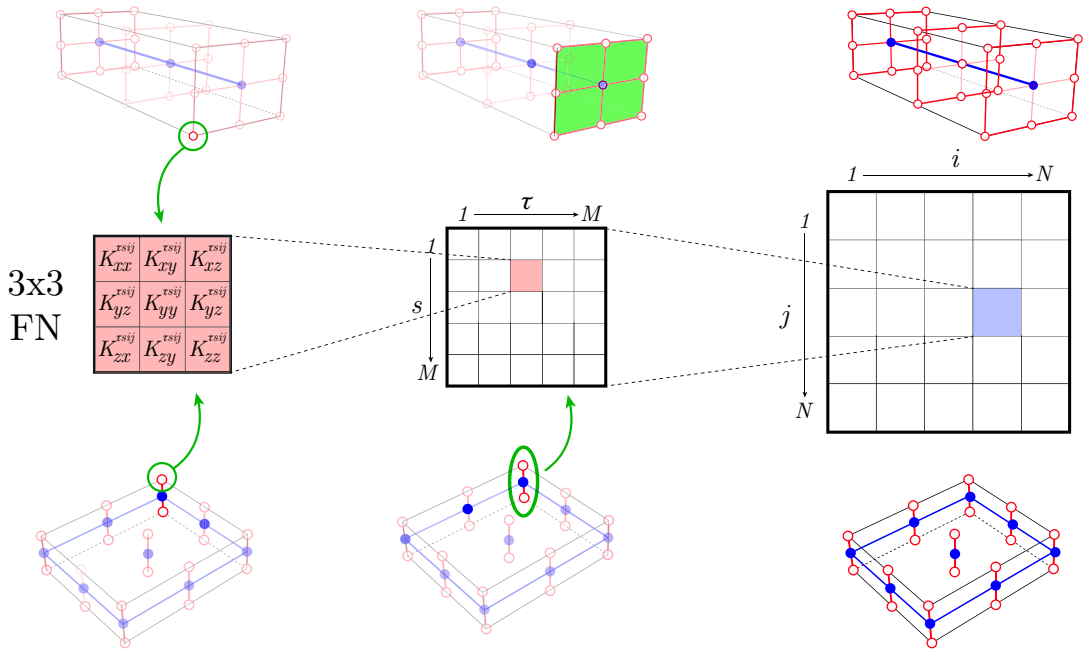

Figure 5.3: Assembling procedure of Fundamental Nuclei: global assembling from nodal quantities to general FE matrix.

5.6 Isoparametric approach

The FN definition of FE matrices, such as the tangent stiffness matrix or mass matrix, involves the computation of interpolating shape functions, their derivatives with respect to the global Cartesian reference frame, and displacement gradients. In an hyperelastic finite element framework, the volume integral related to the material configuration has to be computed considering also the dependence from the three dimensions of the tangent elasticity tensor within the element domain, differently with respect to classical linear elastic materials where the elasticity tensor is constant. From Eqs. (5.7)-(5.10), the basic algebraic matrices to build the FN, one can observe that the integration over the domain involves both shape functions derivative and displacement gradients. Classical FE approaches, as in the case of the preset thesis, rely on the isoparametric approach. The element geometry and related field variables are approximated adoping the same set of interpolation functions, defined in a natural coordinate system. This approach ensures consistency, allows the automation of quadrature procedures, and it is adopt to map each possible distorted element of the computational domain into a simple unitary domain. The physical reconstruction of field variables is then performed by means of the Jacobian of the transformation.

In a 2D sense, both for 2D FE approximation of the reference plate mid-surface and 1D expansion with LE models, geometrical recontruction and partial derivatives are performed in the so-called natural reference frame, that maps the physical domain by means of a simple squared domain $[-1;1] \times [-1,1]$. Figure 5.4 illustrates the definition of a general quadrilateral plane element and its mapping in the natural reference frame.

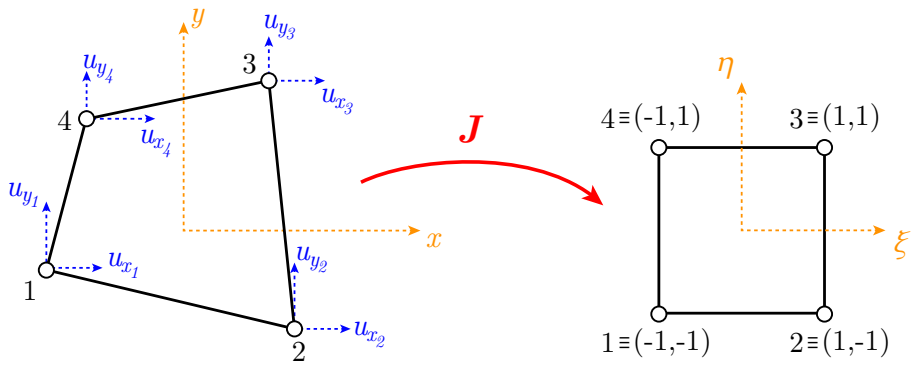

Figure 5.4: Jacobian and element mapping from the global to natural reference frame.

Typically, the set of interpolating functions is given in terms of natural coordinates, defined in (ξ, η) domain. The derivatives of the interpolating functions with respect to the natural coordinates are obtained by means of the chain rule, starting from the natural derivatives:

$$\text{2D FEM:} \begin{cases} \dfrac{\partial N_i}{\partial \xi} = \dfrac{\partial N_i}{\partial x}\dfrac{\partial x}{\partial \xi} + \dfrac{\partial N_i}{\partial y}\dfrac{\partial y}{\partial \xi} \\ \dfrac{\partial N_i}{\partial \eta} = \dfrac{\partial N_i}{\partial x}\dfrac{\partial x}{\partial \eta} + \dfrac{\partial N_i}{\partial y}\dfrac{\partial y}{\partial \eta} \end{cases} \qquad \text{1D CUF:} \begin{cases} \dfrac{\partial F_\tau}{\partial \xi} = \dfrac{\partial F_\tau}{\partial x}\dfrac{\partial x}{\partial \xi} + \dfrac{\partial F_\tau}{\partial z}\dfrac{\partial z}{\partial \xi} \\ \dfrac{\partial F_\tau}{\partial \eta} = \dfrac{\partial F_\tau}{\partial x}\dfrac{\partial x}{\partial \eta} + \dfrac{\partial F_\tau}{\partial z}\dfrac{\partial z}{\partial \eta} \end{cases} \tag{5.51}$$

Considering the N_n total nodes of the element definition, either in the case of 2D FEM element definition or Lagrange domains for cross-section expansions, the geometry is reconstructed using

the physical coordinates of the Lagrange points of the imposed interpolation:

$$\text{2D FEM:} \begin{cases} x = \sum_{i=1}^{N_n} N_i(\xi,\eta)\cdot x_i \\ y = \sum_{i=1}^{N_n} N_i(\xi,\eta)\cdot y_i \end{cases} \qquad \text{1D CUF:} \begin{cases} x = \sum_{\tau=1}^{M} F_\tau(\xi,\eta)\cdot x_\tau \\ z = \sum_{\tau=1}^{M} F_\tau(\xi,\eta)\cdot z_\tau \end{cases} \tag{5.52}$$

Using this definition, one can compute by means of the Lagrange points coordinates the derivatives of the physical coordinates with respect to natural variables:

$$\text{2D FEM:} \begin{cases} \dfrac{\partial x}{\partial \xi} = \sum_{i=1}^{N_n} \dfrac{\partial N_i(\xi,\eta)}{\partial \xi}\cdot x_i & \dfrac{\partial x}{\partial \eta} = \sum_{i=1}^{N_n} \dfrac{\partial N_i(\xi,\eta)}{\partial \eta}\cdot x_i \\ \dfrac{\partial y}{\partial \xi} = \sum_{i=1}^{N_n} \dfrac{\partial N_i(\xi,\eta)}{\partial \xi}\cdot y_i & \dfrac{\partial y}{\partial \eta} = \sum_{i=1}^{N_n} \dfrac{\partial N_i(\xi,\eta)}{\partial \eta}\cdot y_i \end{cases}$$

$$\text{1D CUF:} \begin{cases} \dfrac{\partial x}{\partial \xi} = \sum_{\tau=1}^{M} \dfrac{\partial F_\tau(\xi,\eta)}{\partial \xi}\cdot x_\tau & \dfrac{\partial x}{\partial \eta} = \sum_{\tau=1}^{M} \dfrac{\partial F_\tau(\xi,\eta)}{\partial \eta}\cdot x_\tau \\ \dfrac{\partial z}{\partial \xi} = \sum_{\tau=1}^{M} \dfrac{\partial F_\tau(\xi,\eta)}{\partial \xi}\cdot z_\tau & \dfrac{\partial z}{\partial \eta} = \sum_{\tau=1}^{M} \dfrac{\partial F_\tau(\xi,\eta)}{\partial \eta}\cdot z_\tau \end{cases}$$

By means of chain rule then, and the introduction of the Jacobian matrix, the derivatives with respect to the natural reference frame are:

$$\text{2D FEM:} \begin{Bmatrix} \dfrac{\partial}{\partial \xi} \\ \dfrac{\partial}{\partial \eta} \end{Bmatrix} = \underbrace{\begin{bmatrix} \dfrac{\partial x}{\partial \xi} & \dfrac{\partial y}{\partial \xi} \\ \dfrac{\partial x}{\partial \eta} & \dfrac{\partial y}{\partial \eta} \end{bmatrix}}_{\mathbf{J}^{(2D)}} \begin{Bmatrix} \dfrac{\partial}{\partial x} \\ \dfrac{\partial}{\partial y} \end{Bmatrix} \qquad \text{1D CUF:} \begin{Bmatrix} \dfrac{\partial}{\partial \xi} \\ \dfrac{\partial}{\partial \eta} \end{Bmatrix} = \underbrace{\begin{bmatrix} \dfrac{\partial x}{\partial \xi} & \dfrac{\partial z}{\partial \xi} \\ \dfrac{\partial x}{\partial \eta} & \dfrac{\partial z}{\partial \eta} \end{bmatrix}}_{\mathbf{J}^{(2D)}} \begin{Bmatrix} \dfrac{\partial}{\partial x} \\ \dfrac{\partial}{\partial z} \end{Bmatrix} \tag{5.53}$$

Inverting the $\mathbf{J}^{(2D)}$ Jacobian matrix, the derivatives with respect to the physical reference frame are straightforwardly obtained, obtaining then a computational and simple approach for the derivative computation, depending only on the geometrical features of the elements.

The same procedure can be also considered in the case of 1D shape function, involved typically in 1D beam axis discretization models and 2D through-the-thickness LE models. In this sense, the numerical evaluation of physical derivatives is straightforward since the change of variables is performed in a single direction. Again, the set of interpolating functions is given in terms of natural coordinates, defined thus in $(\nu) \in [-1;+1]$ natural domain. Considering the nn total nodes of the 1D element definition, the geometry is reconstructed using the nodal coordinates and the imposed interpolation:

$$\text{1D FEM:} \quad y = \sum_{i=1}^{nn} N_i(\nu)\cdot y_i \tag{5.54}$$

$$\text{2D CUF expansion:} \quad z = \sum_{i=1}^{nn} F_\tau(\nu)\cdot z_i \tag{5.55}$$

By means of the chain rule:

$$\text{1D FEM:} \quad \frac{\partial N_i}{\partial y} = \frac{\partial N_i}{\partial \nu}\frac{\partial \nu}{\partial y} = \frac{1}{|\mathbf{J}^{(1D)}|}\frac{\partial N_i}{\partial \nu} \tag{5.56}$$

$$\text{2D CUF expansion:} \quad \frac{\partial F_\tau}{\partial z} = \frac{\partial F_\tau}{\partial \nu}\frac{\partial \nu}{\partial z} = \frac{1}{|\mathbf{J}^{(1D)}|}\frac{\partial F_\tau}{\partial \nu} \tag{5.57}$$

This approach is extensively used in cross-sectional mapping, geometry reconstruction and implementation of numerical quadrature techniques that allows recursive implementation into finite element program.

5.7 Numerical integration

The FN of finite element matrices is a scalar function of three variables, to be integrated over the closed volume domain of the element definition. A function can be integrated using different techniques. Compared to analytical integration, the numerical quadrature technique is preferred for its versatility and generality, as it can be applied to any domain. The Gauss-Legendre quadrature here proposed involves computing the integrals in the so-called natural reference frame, with coordinates (ξ, η, ν), each defined in the domain $[-1,1]$. The numerical approximation of the integral is carried out through a sum of a fixed number of contributions depending on the value of the integrand and on a quadrature weights. In the natural reference system, the generic quantity $f(\xi, \eta, \nu)$ integrated over the natural domain is:

$$\int_{-1}^{1}\int_{-1}^{1}\int_{-1}^{1} f(\xi,\eta,\nu)d\xi d\eta d\nu = \sum_{i=1}^{N_{GP}}\sum_{j=1}^{N_{GP}}\sum_{k=1}^{N_{GP}} f(\xi_i,\eta_j,\nu_k)w_i w_j w_k \tag{5.58}$$

From this general definition, both 2D and 1D numerical evaluations of integrals can be directly defined with this approximation, the calculation of integrals requires only the evaluation of the integrand at specific points of the natural domain, called *Gauss Points* (GP), multiplied by real constants called *quadrature weights*, which depend on the number of quadrature points used and are tabulated; their value is known a priori. In the case of polynomial functions, depending on the order of the integrating functions, there exists also a specific number of Gauss Points with related coordinates which guarantees the exactness of the numerically evaluated integral.
As an example, here the quadrature technique applied to a generic component of the tangent stiffness matrix is provided. Considering the component $\mathbf{K}^{xx}_{T,ll}$, namely the (1,1) component of the linear stiffness matrix of a 2D plate model, one can write applying the definition:

$$\begin{aligned}
\mathbf{K}^{xx}_{T,ll} = &\int_{\Omega_0} \mathbb{C}_{44}F_{s,z}F_{\tau,z}N_iN_jdV \quad + \underbrace{\int_{\Omega_0} \mathbb{C}_{14}F_{s,z}F_\tau N_{i,x}N_jdV}_{(*)} + \int_{\Omega_0} \mathbb{C}_{46}F_{s,z}F_\tau N_{i,y}N_jdV + \\
&+ \int_{\Omega_0} \mathbb{C}_{14}F_sF_{\tau,z}N_iN_{j,x}dV \quad + \int_{\Omega_0} \mathbb{C}_{11}F_sF_\tau N_{i,x}N_{j,x}dV + \int_{\Omega_0} \mathbb{C}_{46}F_sF_{\tau,z}N_iN_{j,y}dV + \\
&+ \int_{\Omega_0} \mathbb{C}_{66}F_sF_\tau N_{i,y}N_{j,y}dV \quad + \int_{\Omega_0} \mathbb{C}_{16}F_sF_\tau N_{i,y}N_{j,x}dV + \int_{\Omega_0} \mathbb{C}_{16}F_sF_\tau N_{i,x}N_{j,y}
\end{aligned} \tag{5.59}$$

In general, as shown in Eq. (5.59), the generic integration considers as integrand the product of the derivatives of shape functions, for example $N_{i,x}$ and $N_{j,x}$, as i and j vary, coupled with the

derivatives and nominal values of through-the-thickness expansion polynomials. To generalize the numerical quadrature procedure, the generic integrand is written in terms of natural coordinates, performing a change of variables. Applying this transformation to the $(*)$ term of the stiffness matrix component, one can write:

$$\int_{\Omega_0} \mathbb{C}_{14} F_{s,z} F_\tau N_{i,x} N_j dV = \int_{-1}^{1}\int_{-1}^{1}\int_{-1}^{1} \mathbb{C}_{14}(\xi,\eta,\nu) F_{s,z}(\xi,\eta) F_\tau(\xi,\eta) N_{i,x}(\nu) N_j(\nu) |\mathbf{J}^{(2D)}||\mathbf{J}^{(1D)}| d\xi d\eta d\nu \tag{5.60}$$

Applying now the numerical quadrature, the integral over the natural (mapped) domain can be rewritten as:

$$\begin{aligned} &\int_{-1}^{1}\int_{-1}^{1}\int_{-1}^{1} \mathbb{C}_{14}(\xi,\eta,\nu) F_{s,z}(\xi,\eta) F_\tau(\xi,\eta) N_{i,x}(\nu) N_j(\nu) |\mathbf{J}^{(2D)}||\mathbf{J}^{(1D)}| d\xi d\eta d\nu = \\ &= \sum_{l=1}^{N_{GP}^l}\sum_{n=1}^{N_{GP}^n}\sum_{m=1}^{N_{GP}^m} \mathbb{C}_{14}(\xi_l,\eta_n,\nu_m) F_{s,z}(\xi_l,\eta_n) F_\tau(\xi_l,\eta_n) N_{i,x}(\nu_m) N_j(\nu_m) \times \\ &\times \quad |\mathbf{J}^{(2D)}(\xi_l,\eta_n)||\mathbf{J}^{(1D)}(\nu_m)| w_l w_n w_m \end{aligned} \tag{5.61}$$

In the case of hyperelastic isotropic and anisotropic soft materials and structures one can observe that, differently to the classical quadrature procedure proposed in linear elasticity, the integral has to be computed in a *pseudo-3D* sense, since the approximation of polynomial expansion could be possible separating the variables, thus performing two different integrations for the FEM approximation and the CUF expansion, however the presence of the generic term of the tangent elastic moduli within the element domain do not allow for the automatic splitting of the integrals in different directions. In this sense, since material coefficients vary point-wise in the whole volume domain, they need to be included into the 3D formulation.
Looking at Eq. (5.61), to compute the approximate value of the integral for the stiffness matrix element, it is therefore necessary to know the derivatives of the shape functions evaluated at the Gauss Point (through the natural coordinates), and the value of the Jacobian, the term that measures the change in volume between the physical and natural reference systems, by adopting the isoparametric formulation. The pseudo-3D integration is performed considering a global 3D Jacobian obtained as the product of the Jacobians along the FEM approximation and the CUF expansion. The global 3D location of the Gauss point is used for the numerical computation of the tangent elasticity tensor, to be consistent with the quadrature rules in the two different directions. In this sense, the considered models behave as beam- or plate-like models, exploiting 3D interpolation with different orders of approximation in different directions. The accuracy and exactness of the integral thus calculated are directly dependent on the number of Gauss Points used. In some cases, it is even preferable to reduce the number of Gauss Points to deliberately underestimate the stiffness matrix and mitigate numerical issues arising from the method. More details about the quadrature rule applied in a CUF-based finite element scenario can be found in Carrera *et al.* [129].

Chapter 6

Numerical schemes

Generally, the presence of both material and geometrical nonlinearities lead to strongly nonlinear governing equations that can not be solved directly. For this reason, iterative and incremental solvers are mainly adopted for such problems, thus linearized procedures are adopted to find, iteratively, the equilibrium conditions. In this chapter, the two algorithms adopted in the present thesis are presented.

6.1 Load-control procedure

Newton *load-control* method is an iterative method adopted to find the equilibrium equations at a given assigned load condition, namely the maximum load applied, postulating a sequence of intermediate steps between the undeformed and final configurations by a fixed variation of the load at each step. In this sense, the final solution of the problem for λ_{max} is obtained considering different N load steps where, for each step, a fixed load variation $\Delta\lambda = \lambda_{max}/N$ is considered. For each i-th step, the structural configuration is analyzed at $\lambda_i = (i/N)\lambda_{max}$, considering iterative solvers to find the new equilibrium condition that satisfies the governing equations. In this sense, this algorithm is intended as an iterative-incremental solver where only displacement variables are considered as final unknowns, since load variations are assigned.
Each i-th *incremental* step is obtained *iteratively*, up to a certain convergence tolerance, with m-th internal iterations steps. Following this procedure, one can compute the equilibrium state for increasing values of the load applied, until the final requested load condition is obtained. Suppose to start from a known equilibrium condition identified by $(\boldsymbol{u}^{(k)}, \lambda^k)$, where the internal forces vector is known and the external load vector is $\mathbf{F}_{ext}^{(k)} = \lambda^k \boldsymbol{f}_{ref}$. From this condition, a load variation of $\Delta\lambda$ is considered, to analyze the structure at the load condition $\mathbf{F}_{ext}^{(k+1)} = \lambda^{(k+1)} \boldsymbol{f}_{ref}$. This is analyzed by means of the incremental equation for the static nonlinear problem Eq. (5.26):

$$\mathbf{K}_T(\boldsymbol{u}^{(k)}, \lambda^k)\delta\boldsymbol{u}_{j=1}^{(k+1)} = \Delta\lambda \boldsymbol{f}_{ref} - \underbrace{\varphi_{res}(\boldsymbol{u}^{(k)}, \lambda^k)}_{=0,\ \mathbf{F}_{ext}^{(k)}=\mathbf{F}_{int}^{(k)}} = \Delta\lambda \boldsymbol{f}_{ref} \tag{6.1}$$

The first internal increment $\delta\boldsymbol{u}_{j=1}^{(k+1)}$ is then found by solving Eq. (6.1). In this way, the provisional step $\boldsymbol{u}_{j=1}^{(k+1)}$ is obtained considering the initial displacement variation $\Delta\boldsymbol{u}_{j=1}^{(k)}$. Due to numerical approximation, the configuration given by the displacement vector $\boldsymbol{u}_{j=1}^{(k+1)}$ do not satisfy immediately the equilibrium equation Eq. (5.23), since the computation of internal force vector in the updated provisional step are still not balancing the applied external load.

For this reason, another linearization around the updated provisional step is performed to enforce the equilibrium equation in terms of unbalanced nodal vector:

$$\boldsymbol{\varphi}_{res}(\boldsymbol{u}_j^{(k+1)} + \delta\boldsymbol{u}_{j+1}^{(k+1)}, \lambda^{(k+1)}) = 0 \tag{6.2}$$

By expanding Eq. (6.2) truncating at the first order:

$$\boldsymbol{\varphi}_{res}(\boldsymbol{u}_j^{(k+1)}) + \mathbf{K}_T(\boldsymbol{u}_j^{(k+1)})\delta\boldsymbol{u}_{j+1}^{(k+1)} = 0 \tag{6.3}$$

The solution of Eq. (6.3) provide the internal increment $\delta\boldsymbol{u}_{j+1}^{(k+1)}$ by which the corrected variation of the displacement vector is found, thus $\Delta\boldsymbol{u}_{j+1}^{(k)} = \Delta\boldsymbol{u}_j^{(k)} + \delta\boldsymbol{u}_{j+1}^{(k+1)}$. Therefore, the updated provisional step of the $j+1$ iteration is obtained considering $\boldsymbol{u}_{j+1}^{(k+1)} = \boldsymbol{u}_j^{(k+1)} + \delta\boldsymbol{u}_{j+1}^{(k+1)} = \boldsymbol{u}^{(k)} + \Delta\boldsymbol{u}_{j+1}^{(k)}$, equivalently. In the updated provisional step, again, the equilibrium conditions are verified by the computation of the unbalanced residual nodal force vector in the updated condition, evaluating thus $\boldsymbol{\varphi}(\boldsymbol{u}_{j+1}^{(k+1)}, \lambda^{k+1})$. If the equilibrium condition is still not satified, Eq. (6.3) is again defined in the updated temporal configuration state, updated iteratively the deformed configuration until the unbalanced residual nodal force vector is null, or up to a certain convergece tolerance, thus $|\boldsymbol{\varphi}| < \varepsilon$. A graphical representation of the proposed algorithm, with the representation of unbalanced nodal force vectors and provisional steps, as well as correcting increment, is depicted in Fig. 6.1.

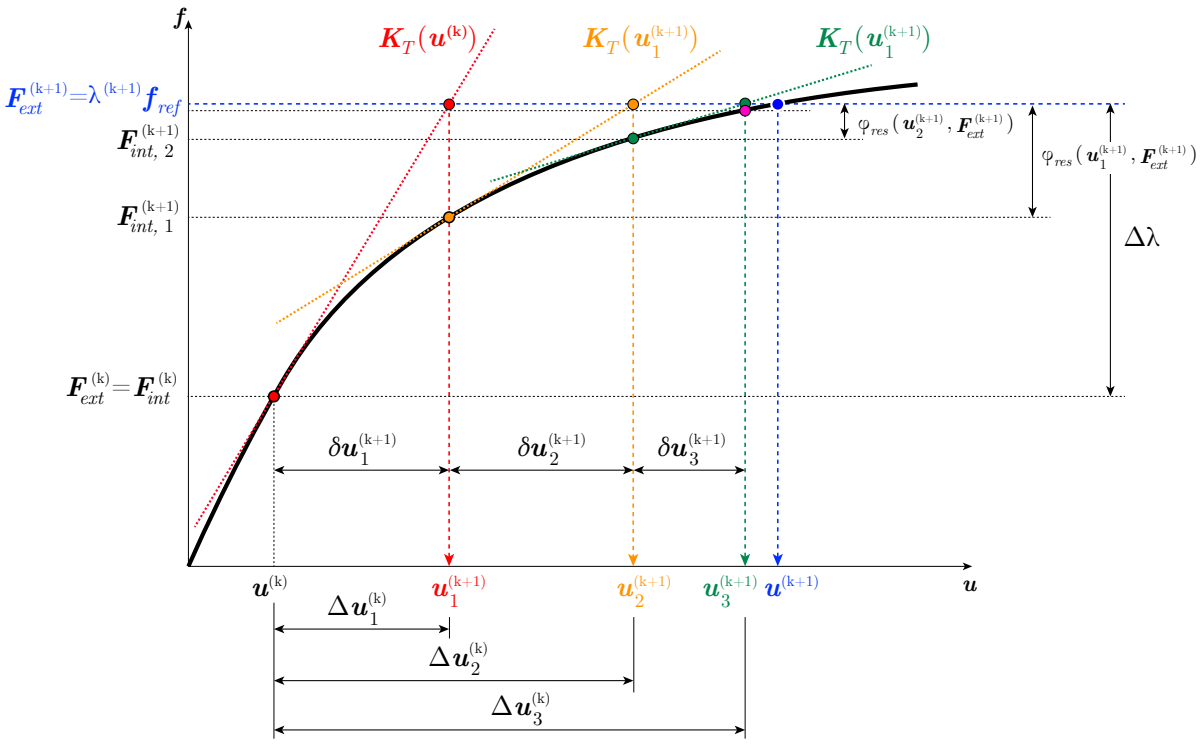

Figure 6.1: Iterative solvers for nonlinear algebraic system of equations: load-control procedure, graphical representation of the proposed algorithm.

6.2 Arc-length procedure

Arc-length method is an efficient incremental-iterative approach for nonlinear solvers, extensively adopted in the case of one or more critical points within the structural equilibrium path, handling negative slope in load–displacement curves and particularly effective within the context of geometric and material nonlinear problems (e.g., plasticity, large deformations). Differently with respect to the case of load-control procedures, this algorithm postulates a simultaneous variation of both displacements and load factor to achieve the new equilibrium conditions by considering simultaneous convergence criteria.
Each i-th *incremental* step is obtained *iteratively*, up to a certain convergence tolerance, with j-th internal iterations steps, on both displacements and load variations. To begin with the algorithm description, the following quantities will be introduced:

- $\delta_j^{(k)}(\cdot)$ indicates the internal finite variation, where k is the load step considered and j the internal iteration index within the $k-th$ load step. In this sense, this variation can be seen as $\delta_j^{(k)}(\cdot) = (\cdot)_j^{(k)} - (\cdot)_{(j-1)}^{(k)}$, as well as the global final convergent quantity $(\cdot)^{(k+1)} = (\cdot)^{(k)} + \sum_{j=1}^{m} \delta_j^{(k)}(\cdot)$;
- $k = 0$ is identically adopted for the initial condition, thus $\delta_j^0 \boldsymbol{u}$ is the initial known conditions and $\delta_j^0 \lambda$ is adopted to denote the initial load parameter increment;
- $\delta \boldsymbol{t}_j^{(k)} = \left(\delta \boldsymbol{u}_j^{(k)}, \delta \lambda_j^{(k)}\right)$ is the formal vector of configuration updating, used to map the updating provisional step during the internal convergence iterations;
- $\boldsymbol{t}^{(k)} = \boldsymbol{t}^{(k-1)} + \sum_{j=1}^{m} \delta \boldsymbol{t}_j^{(k)}$ relates the current solution to the previous one.

As performed in the case of load control procedures, suppose to start from a known equilibrium condition identified by $(\boldsymbol{u}^{(k)}, \lambda^k)$, where the internal forces vector is known and the external load vector is $\mathbf{F}_{ext}^{(k)} = \lambda^k \boldsymbol{f}_{ref}$. From this condition, simultaneous variations of both displacements and load scale factor are considered, to analyze the structure at a load condition $\mathbf{F}_{ext}^{(k+1)} = \lambda^{(k+1)} \boldsymbol{f}_{ref}$, where now $\lambda^{(k+1)}$ is unknown, differently with respect to the previous presented algorithm. This is analyzed by means of the incremental equation for the static nonlinear problem Eq. (5.26):

$$\mathbf{K}_T(\boldsymbol{u}^{(k)}) \delta \boldsymbol{u}_{j=1}^{(k+1)} = \underbrace{(\lambda_{j=1}^{k+1} - \lambda^k)}_{\delta \lambda_{j=1}^k} \boldsymbol{f}_{ref} - \varphi_{res}(\boldsymbol{u}^{(k)}, \lambda^k) \tag{6.4}$$

where the $\delta \lambda_{j=1}^k$ initial load variation is assigned and can be considered a tuning parameter of the algorithm. As already discussed within the load control algorithm, solving Eq. (6.4) for $\delta \boldsymbol{u}_{j=1}^{(k+1)}$ does not provide automatically the successive convergent equilibrium step, thus:

$$\boldsymbol{\varphi}_{res}(\boldsymbol{u}^k + \delta \boldsymbol{u}_{j=1}^{(k+1)}, \lambda^k + \delta \lambda_{j=1}^{(k+1)}) = \boldsymbol{F}_{int}(\boldsymbol{u}^k + \delta \boldsymbol{u}_{j=1}^{(k+1)}, \lambda^k + \delta \lambda_{j=1}^{(k+1)}) - (\lambda^k + \delta \lambda_{j=1}^{(k+1)}) \boldsymbol{f}_{ref} \neq 0 \tag{6.5}$$

Starting from this last provisional condition Eq. (6.5), one can again consider a linearization of $\boldsymbol{\varphi}_{res}(\boldsymbol{u}^k + \delta \boldsymbol{u}_{j=1}^{(k+1)}, \lambda^k + \delta \lambda_{j=1}^{(k+1)})$ with respect, again, both variables (since they are again unknowns), imposing thus a variation $(\delta \boldsymbol{u}_{j=2}^{(k+1)}, \delta \lambda_{j=2}^{(k+1)})$ that provide the following condition:

$$\boldsymbol{\varphi}_{res}(\boldsymbol{u}^k + \delta \boldsymbol{u}_{j=1}^{(k+1)} + \delta \boldsymbol{u}_{j=2}^{(k+1)}, \lambda^k + \delta \lambda_{j=1}^{(k+1)} + \delta \lambda_{j=2}^{(k+1)}) \tag{6.6}$$

Obtaining then the additional incremental equation:

$$\mathbf{K}_T(\boldsymbol{u}^k + \delta\boldsymbol{u}_{j=1}^{(k+1)}, \lambda^k + \delta\lambda_{j=1}^{(k+1)})\delta\boldsymbol{u}_{j=2}^{(k+1)} = \delta\lambda_{j=2}^{(k+1)}\boldsymbol{f}_{ref} - \boldsymbol{\varphi}_{res}(\boldsymbol{u}^k + \delta\boldsymbol{u}_{j=1}^{(k+1)}, \lambda^k + \delta\lambda_{j=1}^{(k+1)}) \quad (6.7)$$

That can be written, at this point, for the generic m-*th* iteration step, denoting as introduced before:

$$\mathbf{K}_T\left(\boldsymbol{u}^k + \sum_{j=1}^{m-1}\delta\boldsymbol{u}_j^{(k+1)}, \lambda^k + \sum_{j=1}^{m-1}\delta\lambda_j^{(k+1)}\right)\delta\boldsymbol{u}_{j=m}^{(k+1)} =$$

$$= \delta\lambda_{j=m}^{(k+1)}\boldsymbol{f}_{ref} - \boldsymbol{\varphi}_{res}\left(\boldsymbol{u}^k + \sum_{j=1}^{m-1}\delta\boldsymbol{u}_j^{(k+1)}, \lambda^k + \sum_{j=1}^{m-1}\delta\lambda_j^{(k+1)}\right) \quad (6.8)$$

This final incremental-updating equation for the increments $\delta\boldsymbol{u}_{j=m}^{(k+1)}$ and $\delta\lambda_{j=m}^{(k+1)}$ is solved following the numerical strategy proposed by Batoz and Dhatt[190], introducing now the pseudo-incremental equations and finally the Crisfield spherical arc-length constraint. It is assumed that the solution of this final incremental equation in two unknowns is written as:

$$\delta\boldsymbol{u}_{j=m}^{(k+1)} = \delta\lambda_{j=m}^{(k+1)}\left[\delta\boldsymbol{u}_{j=m}^{(k+1)}\right]_1 + \left[\delta\boldsymbol{u}_{j=m}^{(k+1)}\right]_2 \quad (6.9)$$

where:

$$\begin{cases} \mathbf{K}_T\left(\boldsymbol{u}^k + \sum_{j=1}^{m-1}\delta\boldsymbol{u}_j^{(k+1)}, \lambda^k + \sum_{j=1}^{m-1}\delta\lambda_j^{(k+1)}\right)\left[\delta\boldsymbol{u}_{j=m}^{(k+1)}\right]_1 = \boldsymbol{f}_{ref} \\ \mathbf{K}_T\left(\boldsymbol{u}^k + \sum_{j=1}^{m-1}\delta\boldsymbol{u}_j^{(k+1)}, \lambda^k + \sum_{j=1}^{m-1}\delta\lambda_j^{(k+1)}\right)\left[\delta\boldsymbol{u}_{j=m}^{(k+1)}\right]_2 = -\boldsymbol{\varphi}_{res}\left(\boldsymbol{u}^k + \sum_{j=1}^{m-1}\delta\boldsymbol{u}_j^{(k+1)}, \lambda^k + \sum_{j=1}^{m-1}\delta\lambda_j^{(k+1)}\right) \end{cases} \quad (6.10)$$

Adopting this decomposition proposed in Eq. (6.9) and computing the solutions of the two equations for the pseudo-increments (6.10), one can preserve the adoption of symmetric matrix solver and to avoid inversion of the tangent matrix [187, 190]. The arc-length constraint is now imposed. Introducing the *total variation vector* and its *variation*, as the "formal" vectors of two dimensions:

$$\mathbf{t}_m^k = \left(\sum_{j=1}^{m}\delta\boldsymbol{u}_j^{(k)}, \sum_{j=1}^{m}\delta\lambda_j^{(k)}\right) \quad (6.11)$$

$$\delta\mathbf{t}_m^k = \mathbf{t}_m^k - \mathbf{t}_{m-1}^k = \left(\delta\boldsymbol{u}_{j=m}^{(k)}, \delta\lambda_{j=m}^{(k)}\right) \quad (6.12)$$

It is assumed that the additional constraint equation is an expression that relates the possible variation of displacements and load variables, as proposed by [186]:

$$(\mathbf{t}_m^k)^{\mathrm{T}}(\mathbf{t}_m^k) = (\Delta l^0)^2 \quad (6.13)$$

Imposing then automatically a condition on the possible variation $\delta\mathbf{t}_m^k$, that must lie on the "spherical" constraint. The linearization of this constraint, by means of the already introduced variable variations, lead to the additional constraint equation for the admissible $\delta\lambda_{j=m}^{(k+1)}$:

$$a(\ \delta\lambda_{j=m}^{(k+1)}\ )^2 + b(\ \delta\lambda_{j=m}^{(k+1)}\ ) + c = 0 \quad (6.14)$$

where the three real constants are defined as follows:

$$a = \left[\delta \boldsymbol{u}_{j=m}^{(k+1)}\right]_1^{\mathrm{T}} \left[\delta \boldsymbol{u}_{j=m}^{(k+1)}\right]_1 + \boldsymbol{f}_{ref}^{\mathrm{T}} \boldsymbol{f}_{ref} \tag{6.15}$$

$$b = (\boldsymbol{u}_{j=m}^{(k+1)} - \boldsymbol{u}^{(k)})^{\mathrm{T}} \left[\delta \boldsymbol{u}_{j=m}^{(k+1)}\right]_1 + \left[\delta \boldsymbol{u}_{j=m}^{(k+1)}\right]_1^{\mathbf{T}} \left[\delta \boldsymbol{u}_{j=m}^{(k+1)}\right]_2 + (\lambda_{j=m}^{k+1} - \lambda^k) \boldsymbol{f}_{ref}^{\mathrm{T}} \boldsymbol{f}_{ref} \tag{6.16}$$

$$c = \left((\boldsymbol{u}_{j=m}^{(k+1)} - \boldsymbol{u}^{(k)}) + \left[\delta \boldsymbol{u}_{j=m}^{(k+1)}\right]_2\right)^{\mathrm{T}} \left((\boldsymbol{u}_{j=m}^{(k+1)} - \boldsymbol{u}^{(k)}) + \left[\delta \boldsymbol{u}_{j=m}^{(k+1)}\right]_2\right) \tag{6.17}$$

$$+(\lambda_{j=m}^{k+1} - \lambda^k)^2 \boldsymbol{f}_{ref}^{\mathrm{T}} \boldsymbol{f}_{ref} - (\Delta l_m^0)^2 \tag{6.18}$$

where the notation introduced for the total updated provisional step has been adopted for the final updated displacement and load configurations. Equation (6.14) provides the two possible load increment parameters $\delta\lambda_{j=m}^{(k+1)}$. This proposed algorithm has been extended also to handle complex structural phenomena, such as snap-back or snap-through behaviors, including more involved predictor load factor mathematical formulations [130, 187]. In the updated provisional step, again, the equilibrium conditions are again evaluated by the computation of the unbalanced residual nodal force vector in the updated condition, evaluating thus $\boldsymbol{\varphi}(\boldsymbol{u}^{(k+1)}, \lambda^{k+1})$. If the equilibrium condition is still not satisfied, Eq. (6.8) is again defined in the updated temporal configuration state, updating iteratively the deformed configuration until the unbalanced residual nodal force vector is null, or up to a certain convergece tolerance, thus $|\boldsymbol{\varphi}| < \varepsilon$. A graphical representation of the proposed algorithm, with the representation of unbalanced nodal force vectors and provisional steps, as well as correcting increment, is depicted in Fig. 6.2.

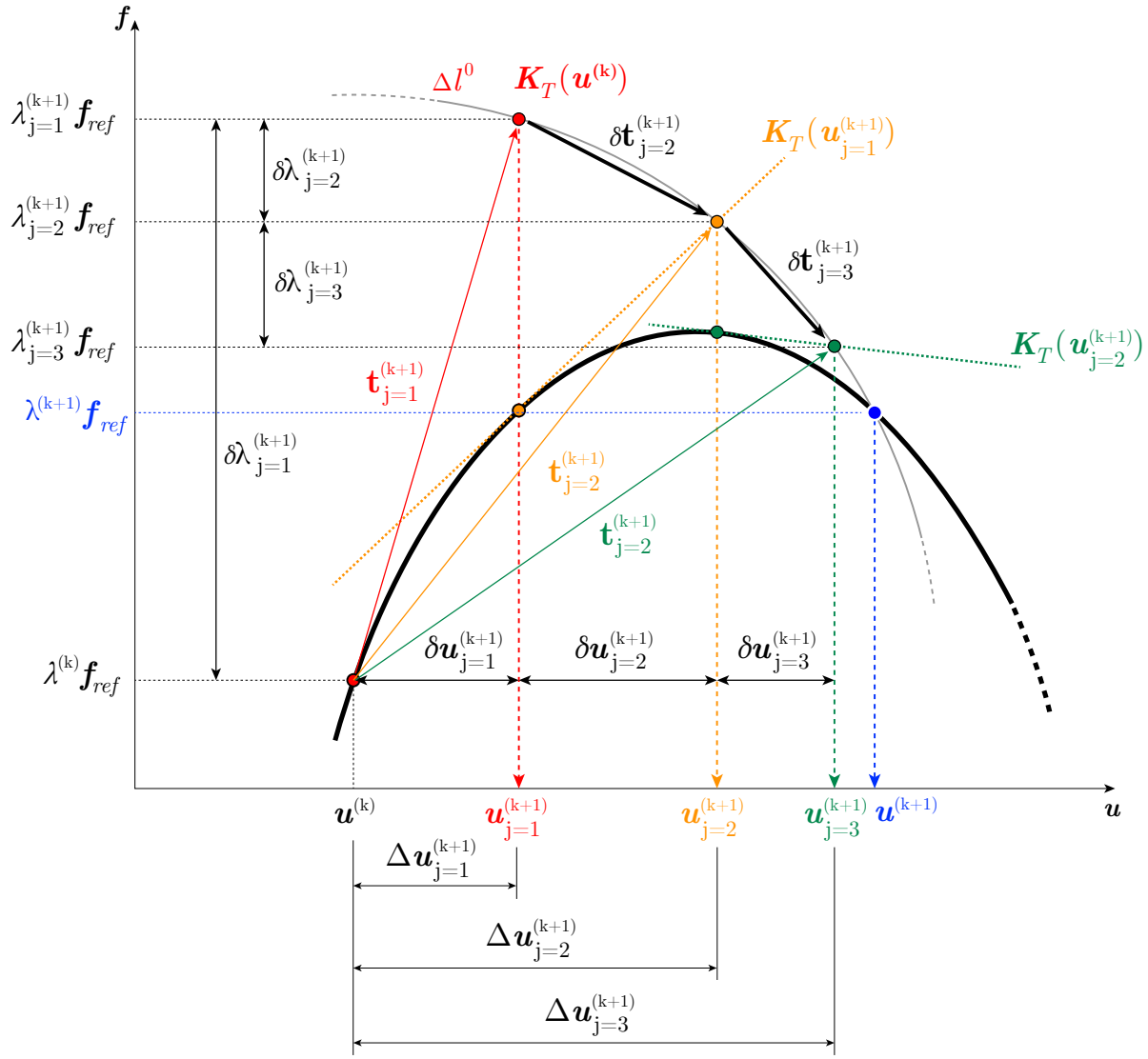

Figure 6.2: Iterative solvers for nonlinear algebraic system of equations: arc-length procedure, graphical representation of the proposed algorithm.

Chapter 7

Isotropic hyperelasticity

In the present chapter, the numerical results obtained for the static, modal and linearized vibration analysis of isotropic soft structures are proposed and discussed. The capabilities of the present model to analyze structures at large strains will be assessed, considering initially a validation of the present CUF-based FE approach comparing the results against exact analytical solutions, available only for few special cases. Moreover, the possibility to implement different hyperelastic material models in the following framework will be discussed, since the present approach is independent of the specific strain energy density function adopted when governing equations are carried out.

7.1 Validation procedure of the present methodology

The first case study analyzed is the large strain analysis of an incompressible cubic specimen. Two different cases will be analyzed: the uniaxial and the uniaxial and simple shear test. This classical test has been conducted by many authors, see [122, 191], since analytical solutions are available. These analysis are carried out to validate the proposed methodology, comparing the results with the reference exact solution. Typically, these patch-test problems are analyzed with single element discretization, to assess the consistency of the model implemented. In the following, then, both 1D beam and 2D plate model will be adopted and analyzed. The discretization exploited in this patch-test employ 1L4-1B2 linear models in the case of beam CUF element, and 1Q4-1LE2 linear models in the case of plate CUF element. A graphical representation of the two discretization model adopted is provided in Fig. 7.1.
In this proposed case study, a first-invariant hyperelastic strain energy framework is analyzed, through the classical quadratic volumetric model and a generic decoupled isochoric strain energy function:

$$\Psi(\mathbf{C}) = \Psi_{vol}(J) + \Psi_{iso}(\bar{\mathbf{C}}) = \frac{1}{D_1}(J-1)^2 + \bar{\Psi}(\bar{I}_1) \tag{7.1}$$

The strain energy densities adopted and the material constants are considered from Suchochi [122] and listed in Table 7.1.

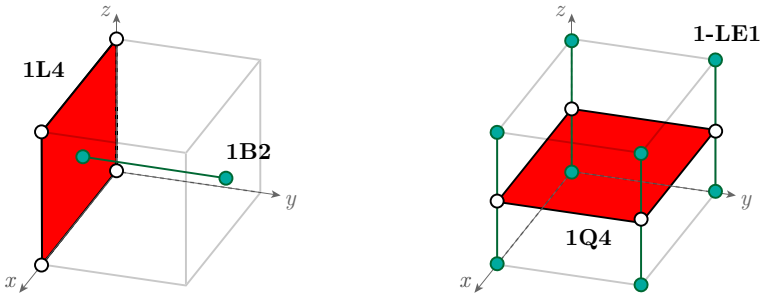

(a) 1D beam CUF model **(b)** 2D plate CUF model

Figure 7.1: Isotropic hyperelasticity, validation test: graphical representation of the single element path-test models adopted in the case study.

Model		**Parameters**
Gent	$\bar{\Psi}(\bar{I}_1) = -\frac{\mu J_m}{2}\log\left(1 - \frac{\bar{I}_1 - 3}{J_m}\right)$	$\mu = 0.27$ [MPa] $J_m = 85.91$
Exp-Ln	$\bar{\Psi}(\bar{I}_1) = A\left[\frac{1}{a}e^{(a(\bar{I}_1-3))} + b(\bar{I}_1 - 2)(1 - \log(\bar{I}_1 - 2)) - \frac{1}{a} - b\right]$	$A = 0.195$ [MPa] $a = 0.018$ $b = 0.22$
Fung-Demiray	$\bar{\Psi}(\bar{I}_1) = c[e^{(\beta(\bar{I}_1-3))} - 1]$	$c = 0.2$ [MPa] $\beta = 16$
Neo-Hookean	$\bar{\Psi}(\bar{I}_1) = \frac{\mu}{2}(\bar{I}_1 - 3)$	$\mu = 0.27$ [MPa]

Table 7.1: Isotropic hyperelasticity, validation test: hyperelastic isochoric first-invariant models, mathematical expressions and material constants adopted.

7.1.1 Uniaxial tension test of an incompressible cubic block

In the case of the uniaxial tension test, the geometry considered and boundary conditions applied are depicted in Fig. 7.2.

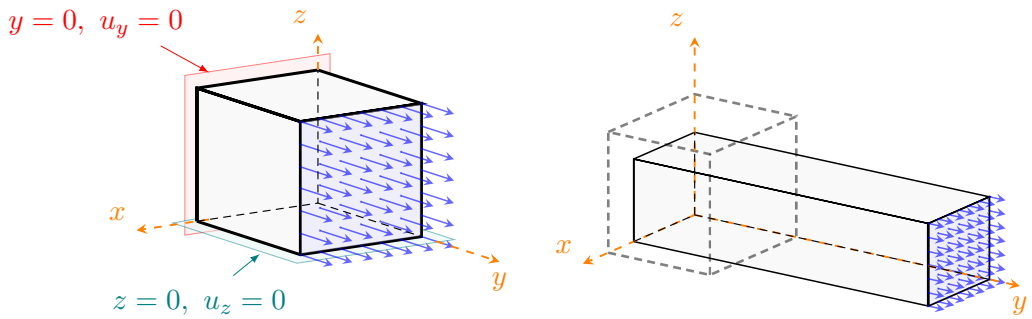

(a) Geometry and boundary conditions **(b)** Deformed configuration

Figure 7.2: Isotropic hyperelasticity, validation test: uniaxial test case, boundary conditions and load configuration.

Considering the first-invariant hyperelastic model described earlier, by assigning the explicit expression of deformation gradient, given the superimposed displacement field, the analytic expressions of first and second Piola-Kirchhoff, and Cauchy's stress tensors are known. If $\boldsymbol{X} = (x^0, y^0, z^0)$ are the coordinates of the point of the cube in the reference configuration, and $\boldsymbol{x} = (x, y, z)$ the coordinate in the actual deformed configuration, the deformation field components for the uniaxial tension problem are:

$$\boldsymbol{\chi}(x^0, y^0, z^0): \begin{cases} x = \lambda_1 x^0 \\ y = \lambda_2 y^0 \\ z = \lambda_3 z^0 \end{cases}$$

where λ_i are the (positive) stretches along the three normal axes. Imposing a single uniform stretch in the y direction, thus $\lambda_1 = \lambda_3$, and the incompressibility hypothesis, the deformation gradient $\mathbf{F}$ and the right Cauchy-Green tensor are expressed as follow:

$$\mathbf{F} = \begin{bmatrix} \lambda_1 & 0 & 0 \\ 0 & \lambda_2 & 0 \\ 0 & 0 & \lambda_1 \end{bmatrix} \qquad \det \mathbf{F} = \lambda_1^2 \lambda_2 = 1 \quad \rightarrow \quad \lambda_1 = \frac{1}{\sqrt{\lambda_2}} \tag{7.2}$$

$$\mathbf{C} = \mathbf{F}^T \mathbf{F} = \begin{bmatrix} \lambda_1^2 & 0 & 0 \\ 0 & \lambda_2^2 & 0 \\ 0 & 0 & \lambda_1^2 \end{bmatrix} = \begin{bmatrix} \dfrac{1}{\lambda_2} & 0 & 0 \\ 0 & \lambda_2^2 & 0 \\ 0 & 0 & \dfrac{1}{\lambda_2} \end{bmatrix} \qquad I_1 = \mathrm{tr}(\mathbf{C}) = \lambda_2^2 + \frac{2}{\lambda_2} \tag{7.3}$$

Since, for incompressibbility $J = \det \mathbf{F} = 1$, also the the volumetric component of $\mathbf{S}$ is identically null. Independently of the strain energyy function used, the components of the first and second Piola-Kirchhoff and Cauchy's stress tensors can be derived by analytical considerations, given the deformation gradient components in terms of the pure axial stretch:

$$P_{22} = \frac{\partial \Psi}{\partial \lambda_2} = \frac{\partial \Psi}{\partial I_1} \frac{\partial I_1}{\partial \lambda_2} = 2 \frac{\partial \Psi}{\partial I_1} \left(\lambda_2 - \frac{1}{\lambda_2^2} \right) \tag{7.4}$$

$$S_{22} = \frac{1}{\lambda_2} \frac{\partial \Psi}{\partial \lambda_2} = \frac{2}{\lambda_2} \frac{\partial \Psi}{\partial I_1} \left(\lambda_2 - \frac{1}{\lambda_2^2} \right) \tag{7.5}$$

In the case of uniaxial test, four different strain energy functions have been investigated and listed in Table 7.1. For each material model considered the uniaxial test case is performed. Figure 7.3 show the stress-strain curve obtained analytically and numerically, adopting the previously listed CUF models. The results proposed depict a perfect match across analytical and numerical solutions, in all the cases considered. In this sense, the present hyperelastic finite element formulation can be considered valid, the analytic solution has been used for validation purposes and the stress-strain constitutive law is verified by the described numerical model.

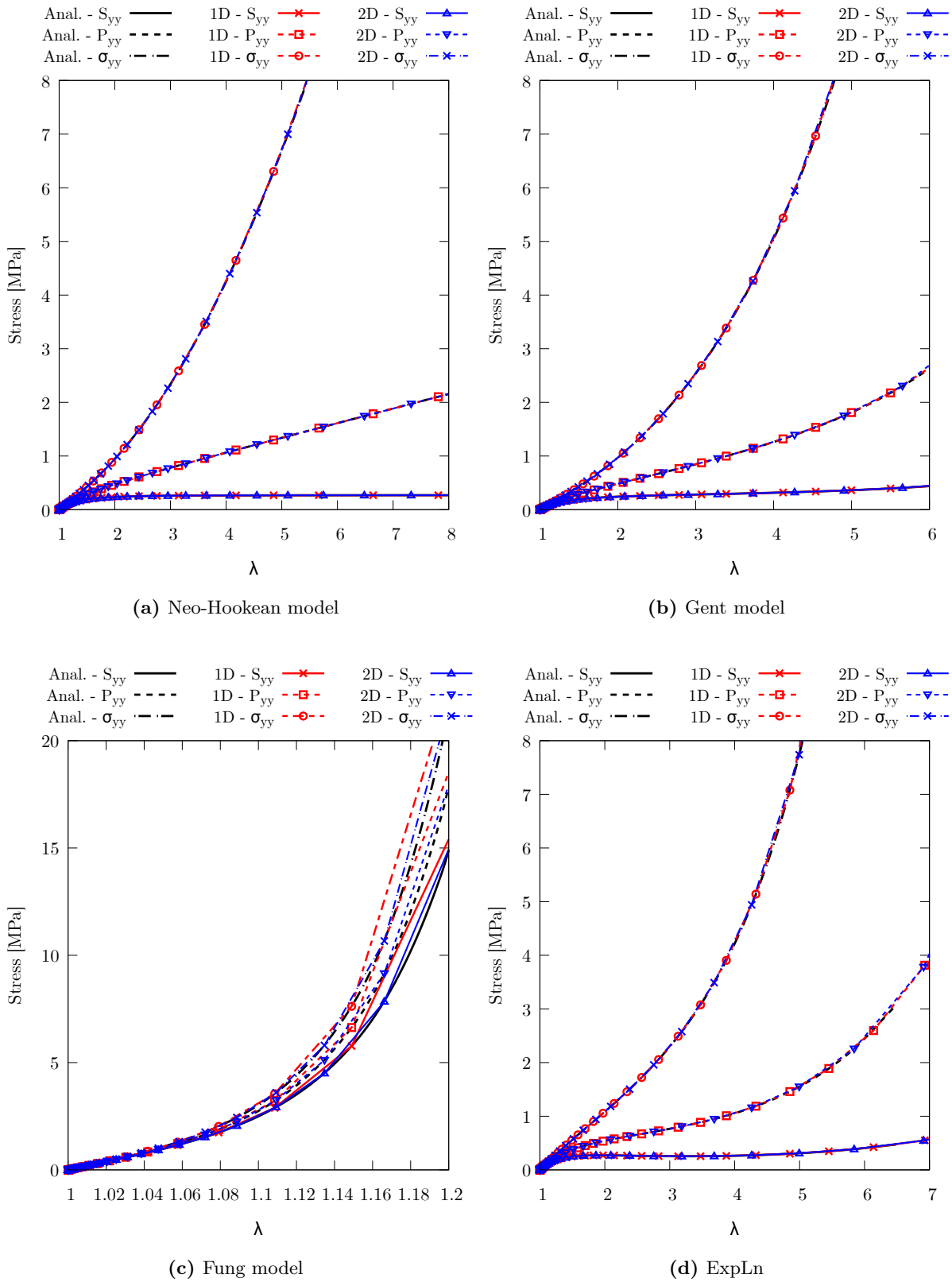

(a) Neo-Hookean model

(b) Gent model

(c) Fung model

(d) ExpLn

Figure 7.3: Isotropic hyperelasticity, uniaxial test case: stress-strain curve for the normal tension component. Comparison between analytical solution and CUF model results.

7.1.2 Shear test of an incompressible block

In the case of the simple shear tension test, the geometry considered and boundary conditions applied are depicted in Fig. 7.4.

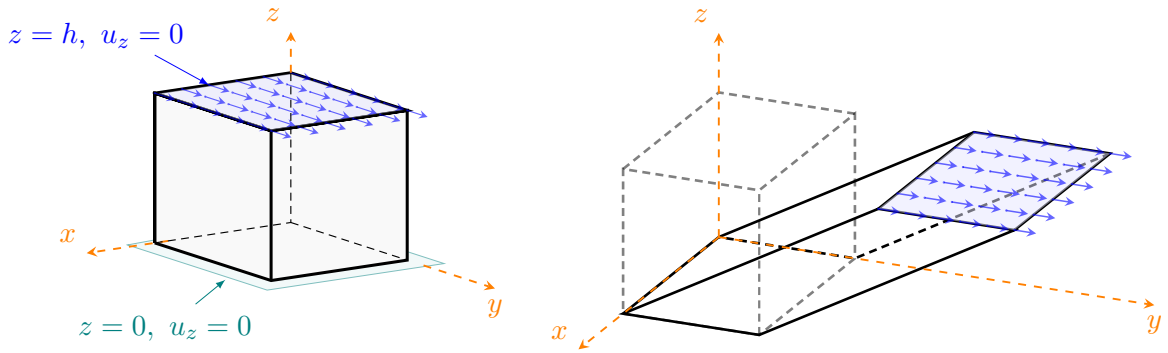

(a) Geometry and boundary conditions **(b)** Deformed configuration

Figure 7.4: Isotropic hyperelasticity, validation test: simple shear test case, boundary conditions and load configuration.

Starting again from the first-invariant constitutive model presented before, the analytic expression of the stress tensor components can be straightforwardly derived from the known deformation gradient components. Let again $\boldsymbol{X} = (x^0, y^0, z^0)$ be the reference coordinates of the specimen in the material configuration of the cube. After the deformation, the point is located in the $\boldsymbol{x} = (x, y, z)$ coordinates of the spatial configuration, measured again with respect to the same reference frame. In the case of simple shear condition applied in the $(y - z)$ plane:

$$\boldsymbol{\chi}(x^0, y^0, z^0) : \begin{cases} x = x^0 \\ y = y^0 + \gamma z^0 \\ z = z^0 \end{cases} \qquad \mathbf{F} = \frac{\partial \boldsymbol{\chi}}{\partial \boldsymbol{X}} = \begin{bmatrix} 1 & 0 & 0 \\ 0 & 1 & \gamma \\ 0 & 0 & 1 \end{bmatrix} \qquad \mathbf{C} = \mathbf{F}^T\mathbf{F} = \begin{bmatrix} 1 & 0 & 0 \\ 0 & 1 & \gamma \\ 0 & \gamma & 1+\gamma^2 \end{bmatrix}$$

where γ is a positive real number. Again, since incompressibility is imposed, $J = \det \mathbf{F} = 1$, hence the volumetric component of $\mathbf{S}$ is identically null. The analytic expression of the stress tensor $\mathbf{S}$ is obtained considering then:

$$\mathbf{S} = \mathbf{S}_{iso} = 2\frac{\partial \bar{\Psi}}{\partial \mathbf{C}} = 2J^{-\frac{2}{3}} \frac{\partial \bar{\Psi}}{\partial \bar{I}_1}\left(\mathbf{I} - \frac{1}{3}\bar{I}_1\mathbf{C}^{-1}\right) = \begin{bmatrix} -\gamma^2/3 & 0 & 0 \\ 0 & -\gamma^2/3(4+\gamma^2) & \gamma + \gamma^3/3 \\ 0 & \gamma + \gamma^3/3 & -\gamma^2/3 \end{bmatrix} \tag{7.6}$$

Furthermore, the analytic expression of PK1 stress tensor is obtained:

$$\mathbf{P} = \mathbf{F}\mathbf{S} = \frac{2}{3}\frac{\partial \bar{\Psi}}{\partial \bar{I}_1} \begin{bmatrix} -\gamma^2 & 0 & 0 \\ 0 & -\gamma^2 & 3\gamma \\ 0 & \gamma(\gamma^2+3) & -\gamma^2 \end{bmatrix} \tag{7.7}$$

In the case of simple shear test, three different strain energy functions have been investigated, analyzing the behavior of normal $(S_{yy}, P_{yy}, \sigma_{yy})$ and shear $(S_{yz}, P_{yz}, \sigma_{yz})$ components. Figure 7.5 shows the stress-strain curve obtained analytically and numerically, adopting the previously listed CUF models. The results proposed show again perfectly matching solution across analytical and numerical solutions, in all the cases considered.

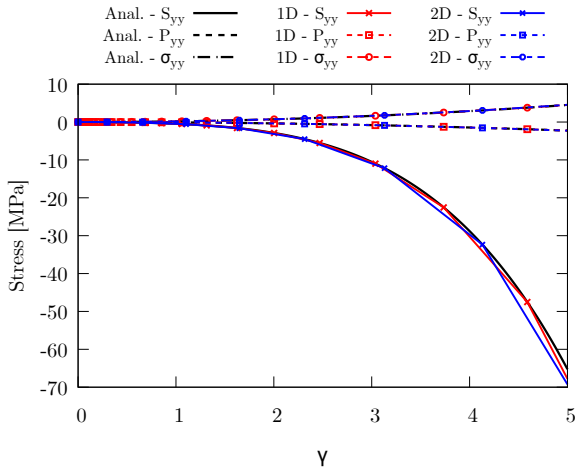

(a) Neo-Hookean model, normal component

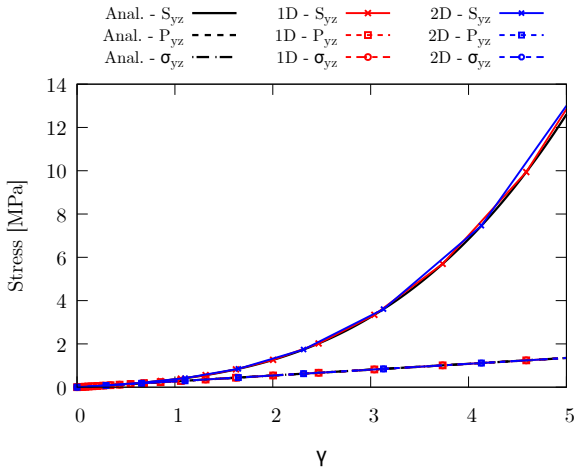

(b) Neo-Hookean model, transversal component

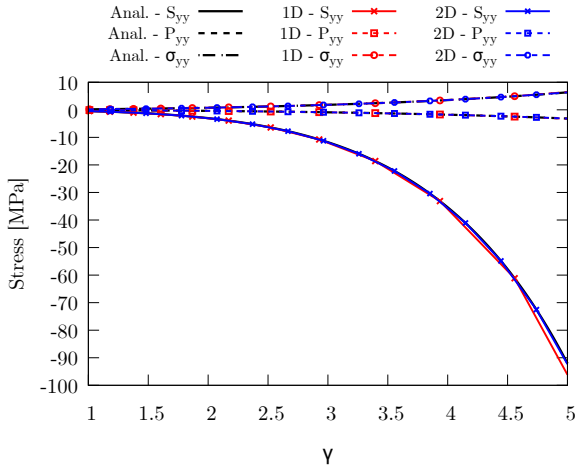

(c) Gent model, normal component

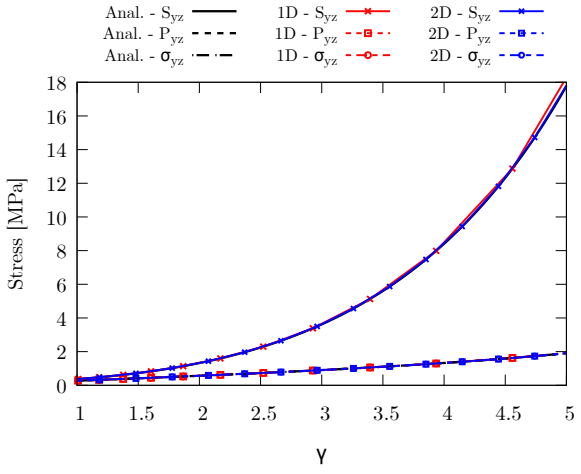

(d) Gent model, transversal component

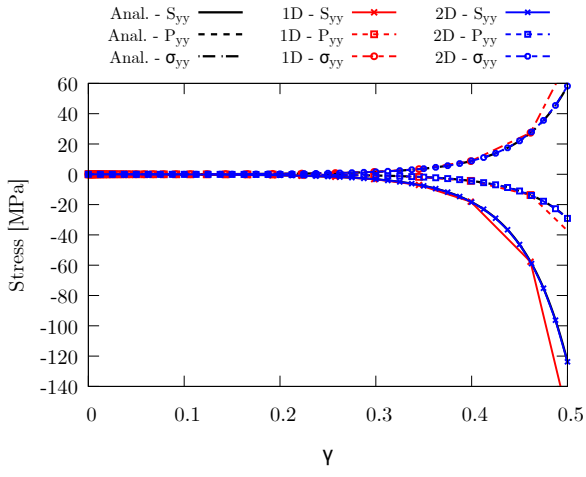

(e) Fung model, normal component

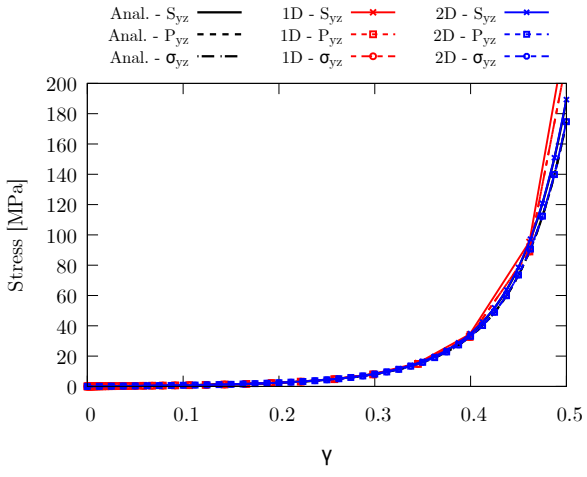

(f) Fung model, transversal component

Figure 7.5: Isotropic hyperelasticity, simple shear test case: stress-strain curve for the normal tension component. Comparison between analytical solution and CUF model results.

7.2 Free-vibration of a neo-Hookean thick and thin beam

This case study is proposed to investigate the accuracy of the proposed higher-order beam model for hyperelasticity by analyzing the undamped free vibration of a doubly clamped Neo-Hookean compressible soft beam. The free vibration analysis of a rectangular cross-section compressible beam is here considered, investigating the effect of kinematic models along the beam axis and theory of structure approximation on the modal response of the beam. The geometrical features are $h = 10$ mm and $w = 6$ mm. Two different slender ratio are here considered: a thick beam for which the slender ratio $L/h = 10$ and a thin beam for which instead $L/h = 100$. The geometry and boundary conditions are depicted in Fig. 7.6.

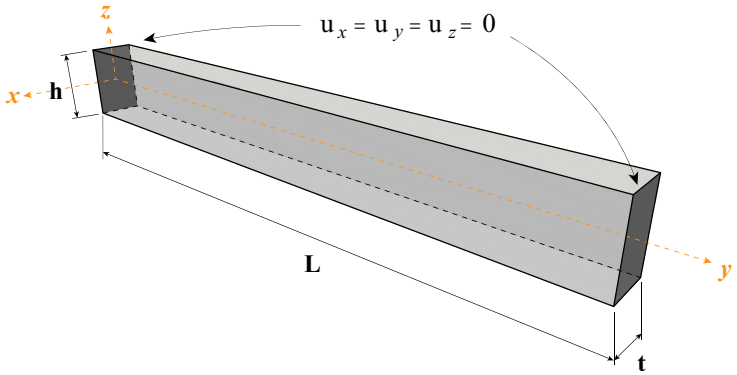

Figure 7.6: Free vibration of a Neo-Hookean clamped-clamped beam: geometrical features and boundary conditions.

The Neo-Hookean strain energy function is adopted to model the soft material structure:

$$\Psi = \Psi_{vol}(J) + \bar{\Psi}(\bar{I}_1) = \frac{k}{2}(J-1)^2 + \frac{\mu}{2}(\bar{I}_1 - 3) \tag{7.8}$$

where μ is the infinitesimal shear modulus, set equal to 50 MPa, k is the bulk modulus, set to $k = 2/3\mu$, in a resulting Poisson ratio $\nu = (3k - 2\mu)/(2(3k + 2\mu)) = 0$. In all further investigations of this case study, the material density of the hyperelastic beam is set to a typical value of silicone rubber, thus $\rho = 1340$ kg/m^3.
A convergence analysis is performed for various 1D CUF beam models in both thick and slender beam configurations. For each kinematic discretization along the beam axis, different cross-section expansion models are examined. In the following, cubic B4 (four-node) FE will be adopted in the discretizaion of beam axis, while cross-section approximations employ a single quadratic and cubic LE model, addressed as L9 (nine nodes) and L16 (sixteen nodes). The numerical solutions of the free-vibration problem obtained with 1D CUF elements are compared against reference solutions obtained by the commercial software ABAQUS. For the thick beam reference solution, 750 C3D20RH hexahedral elements (20-node quadratic brick, hybrid formulation, with reduced integration) are employed in the 3D discretization model, while 334 C3D20RH elements are employed for the slender beam. For comparison purposes, the total number of degrees of freedom (DOF) required by each model will be also discussed, as well as the relative percentage difference between CUF and 3D ABAQUS models, reported in brackets. Table 7.2 and Table 7.3 show the convergence analysis carried out in the case of a thick beam, analyzing the influence of total number of FE adopted along the beam axis and the polynomial order of expansion along the beam cross section, varying the theory of structure in a LE model

condition. The same investigations are carried out in the case of the thin beam with a slender ratio $L/h = 100$, and the proposed results are listed in Table 7.4 and Table 7.5. For coarser discretizations, notable discrepancies with respect to reference results are observed. In the case of L9 paravolic expansion model, discrepancies are found fo tigher order modes that are not affected by the beam axis discretization. At the same time, the adoption of cubic L16 expansion model instead let to an improvement in terms of accuracy, noticing also a slight influence of the beam axis discretization. From the proposed results, the effects of the discretization model are clearly assessed, concluding that the accuracy in computing the natural frequencies are strictly dependent of the theory of structure approximation adopted. In the following, 20 B4 elements along the axis of the beam will be employed in further analysis, for convergence reasons. In the case of TE models, higher-order theories are required in the case of thick beam, due to the limitation of classical models when thick structures are considered. Instead, in the case of very elongated structures, all Taylor models can capture correctly all the frequencies also adopting lower order models, results are in perfect agreement with the reference one. The same accuracy is guaranteed by higher order models (TE-3, TE-4, and L16) in the case of thick beam, or the adoption of LE model.

Since the free vibration problem is analyzed, these last results are compared with the natural frequencies obtained considering the equivalent linear elastic material. Adopting a 1D CUF model made of 20B4-L16 and 3D ABAQUS models described before, the natural frequencies of the equivalent material with Poisson ratio $\nu = 0$ and Young's modulus $E = 2\mu(1 + \nu) = 2\mu$ are investigated in both $L/h = 100$ and $L/h = 10$ configurations. Table 7.6 summarizes the results proposed in terms of natural frequencies obtained with convergent CUF models in the case of hyperelastic and equivalent linear elastic material. In the case of the Neo-Hookean models, the equivalent linear elastic material is able to provide reliable and consistent results in terms of natural frequencies spectrum, and perfectly matching results are observed.

	LE-2 (parabolic model)				LE-3 (cubic model)				ABQ 3D
Mode	**5B4**	**10B4**	**15B4**	**20B4**	**5B4**	**10B4**	**15B4**	**20B4**	**C8D20RH**
1	$165.776^{(0.297\%)}$	$165.748^{(0.003\%)}$	$165.747^{(0.280\%)}$	$165.747^{(0.280\%)}$	$165.327^{(0.025\%)}$	$165.290^{(0.003\%)}$	$165.287^{(0.001\%)}$	$165.285^{(0.000\%)}$	165.285
2	$268.728^{(0.731\%)}$	$268.707^{(0.723\%)}$	$268.707^{(0.723\%)}$	$268.707^{(0.723\%)}$	$266.849^{(0.026\%)}$	$266.796^{(0.007\%)}$	$266.789^{(0.004\%)}$	$266.785^{(0.003\%)}$	266.778
3	$447.768^{(0.713\%)}$	$447.199^{(0.585\%)}$	$447.188^{(0.583\%)}$	$447.187^{(0.582\%)}$	$445.269^{(0.151\%)}$	$444.642^{(0.010\%)}$	$444.612^{(0.003\%)}$	$444.601^{(0.001\%)}$	444.597
4	$702.324^{(1.457\%)}$	$701.908^{(1.397\%)}$	$701.900^{(1.396\%)}$	$701.900^{(1.395\%)}$	$693.016^{(0.112\%)}$	$692.372^{(0.019\%)}$	$692.323^{(0.012\%)}$	$692.287^{(0.007\%)}$	692.240
5	$856.881^{(7.635\%)}$	$860.799^{(8.128\%)}$	$860.704^{(8.116\%)}$	$852.887^{(7.134\%)}$	$799.437^{(0.420\%)}$	$797.447^{(0.170\%)}$	$797.092^{(0.125\%)}$	$797.612^{(0.190\%)}$	796.096
6	$861.709^{(1.974\%)}$	$852.980^{(0.941\%)}$	$852.894^{(0.931\%)}$	$860.686^{(1.853\%)}$	$849.345^{(0.511\%)}$	$845.238^{(0.025\%)}$	$845.089^{(0.008\%)}$	$845.043^{(0.002\%)}$	845.025
7	$1294.772^{(2.279\%)}$	$1291.848^{(2.048\%)}$	$1291.793^{(2.043\%)}$	$1291.788^{(2.043\%)}$	$1270.174^{(0.336\%)}$	$1266.414^{(0.039\%)}$	$1266.226^{(0.024\%)}$	$1266.079^{(0.012\%)}$	1265.924
8	$1365.896^{(1.404\%)}$	$1364.976^{(1.336\%)}$	$1365.896^{(1.404\%)}$	$1365.896^{(1.404\%)}$	$1360.741^{(1.022\%)}$	$1347.720^{(0.055\%)}$	$1347.175^{(0.014\%)}$	$1347.035^{(0.004\%)}$	1346.981
9	$1376.907^{(0.806\%)}$	$1365.896^{(0.000\%)}$	$1364.589^{(-0.096\%)}$	$1364.555^{(-0.098\%)}$	$1365.896^{(0.000\%)}$	$1365.896^{(0.000\%)}$	$1365.896^{(0.000\%)}$	$1365.896^{(0.000\%)}$	1365.896
10	$1724.067^{(8.242\%)}$	$1722.166^{(8.123\%)}$	$1721.977^{(8.111\%)}$	$1721.941^{(8.109\%)}$	$1599.650^{(0.431\%)}$	$1595.535^{(0.173\%)}$	$1594.822^{(0.128\%)}$	$1595.871^{(0.194\%)}$	1592.787
DOFs	432	837	1242	1647	768	1488	2208	2928	13086

Table 7.2: Free vibration of a Neo-Hookean clamped-clamped beam, case $L/h = 10$: convergence analysis on natural frequencies [Hz]. In brackets, the percentage difference between the proposed models and the 3D elasticity solution is given.

	1D CUF, Expansion theory						ABQ 3D
Mode	**TE-1**	**TE-2**	**TE-3**	**TE-4**	**LE-2**	**LE-3**	**C8D20RH**
1	$165.747^{(0.280\%)}$	$165.747^{(0.280\%)}$	$165.286^{(0.000\%)}$	$165.285^{(0.000\%)}$	$165.747^{(0.280\%)}$	$165.285^{(0.000\%)}$	165.285
2	$268.707^{(0.723\%)}$	$268.707^{(0.723\%)}$	$266.788^{(0.003\%)}$	$266.785^{(0.003\%)}$	$268.707^{(0.723\%)}$	$266.785^{(0.003\%)}$	266.778
3	$447.187^{(0.582\%)}$	$447.187^{(0.582\%)}$	$444.605^{(0.002\%)}$	$444.601^{(0.001\%)}$	$447.187^{(0.582\%)}$	$444.601^{(0.001\%)}$	444.597
4	$701.900^{(1.395\%)}$	$701.900^{(1.395\%)}$	$692.311^{(0.010\%)}$	$692.287^{(0.007\%)}$	$701.900^{(1.395\%)}$	$692.287^{(0.007\%)}$	692.240
5	$852.887^{(7.134\%)}$	$852.887^{(7.134\%)}$	$860.435^{(8.082\%)}$	$797.612^{(0.190\%)}$	$852.887^{(7.134\%)}$	$797.612^{(0.190\%)}$	796.096
6	$965.834^{(14.297\%)}$	$860.686^{(1.853\%)}$	$845.058^{(0.004\%)}$	$845.043^{(0.002\%)}$	$860.686^{(1.853\%)}$	$845.043^{(0.002\%)}$	845.025
7	$1291.788^{(2.043\%)}$	$1291.788^{(2.043\%)}$	$1266.185^{(0.021\%)}$	$1266.079^{(0.012\%)}$	$1291.788^{(2.043\%)}$	$1266.079^{(0.012\%)}$	1265.924
8	$1365.896^{(1.404\%)}$	$1364.555^{(1.305\%)}$	$1347.083^{(0.008\%)}$	$1347.035^{(0.004\%)}$	$1365.896^{(1.404\%)}$	$1347.035^{(0.004\%)}$	1346.981
9	$1364.555^{(-0.098\%)}$	$1365.896^{(0.000\%)}$	$1365.896^{(0.000\%)}$	$1365.896^{(0.000\%)}$	$1364.555^{(-0.098\%)}$	$1365.896^{(0.000\%)}$	1365.896
10	$1931.669^{(21.276\%)}$	$1721.941^{(8.109\%)}$	$1720.951^{(8.046\%)}$	$1595.871^{(0.194\%)}$	$1721.941^{(8.109\%)}$	$1595.871^{(0.194\%)}$	1592.787
DOFs	549	1098	1830	2745	1242	1647	13086

Table 7.3: Neo-Hookean doubly-clamped beam, free vibration analysis, case $L/h = 10$: effect of the expansion theory on natural frequencies [Hz]. The percentage difference between proposed results and the 3D elasticity solution is reported in brackets.

	LE-2 (parabolic model)				LE-3 (cubic model)				ABQ 3D
Mode	**5B4**	**10B4**	**15B4**	**20B4**	**5B4**	**10B4**	**15B4**	**20B4**	**C8D20RH**
1	$1.685^{(0.057\%)}$	$1.685^{(0.000\%)}$	$1.685^{(0.004\%)}$	$1.685^{(0.003\%)}$	$1.685^{(0.054\%)}$	$1.685^{(0.003\%)}$	$1.685^{(0.001\%)}$	$1.685^{(0.000\%)}$	1.685
2	$2.808^{(0.060\%)}$	$2.807^{(0.011\%)}$	$2.807^{(0.009\%)}$	$2.807^{(0.008\%)}$	$2.808^{(0.052\%)}$	$2.807^{(0.003\%)}$	$2.807^{(0.001\%)}$	$2.807^{(0.000\%)}$	2.807
3	$4.661^{(0.397\%)}$	$4.644^{(0.031\%)}$	$4.643^{(0.011\%)}$	$4.643^{(0.008\%)}$	$4.660^{(0.391\%)}$	$4.643^{(0.024\%)}$	$4.642^{(0.004\%)}$	$4.642^{(0.001\%)}$	4.642
4	$7.761^{(0.395\%)}$	$7.734^{(0.039\%)}$	$7.732^{(0.021\%)}$	$7.732^{(0.019\%)}$	$7.760^{(0.377\%)}$	$7.732^{(0.021\%)}$	$7.731^{(0.004\%)}$	$7.731^{(0.001\%)}$	7.731
5	$9.222^{(1.367\%)}$	$9.107^{(0.102\%)}$	$9.100^{(0.028\%)}$	$9.099^{(0.016\%)}$	$9.220^{(1.354\%)}$	$9.106^{(0.091\%)}$	$9.099^{(0.017\%)}$	$9.098^{(0.005\%)}$	9.097
6	$15.343^{(2.074\%)}$	$15.071^{(0.261\%)}$	$15.041^{(0.062\%)}$	$15.145^{(0.758\%)}$	$15.354^{(2.146\%)}$	$15.068^{(0.243\%)}$	$15.038^{(0.045\%)}$	$15.141^{(0.727\%)}$	15.031
7	$15.356^{(1.429\%)}$	$15.157^{(0.111\%)}$	$15.147^{(0.044\%)}$	$15.036^{(0.689\%)}$	$15.338^{(1.305\%)}$	$15.152^{(0.080\%)}$	$15.142^{(0.013\%)}$	$15.033^{(0.706\%)}$	15.140
8	$25.528^{(13.754\%)}$	$22.566^{(0.553\%)}$	$22.469^{(0.124\%)}$	$22.453^{(0.052\%)}$	$25.517^{(13.703\%)}$	$22.560^{(0.526\%)}$	$22.464^{(0.099\%)}$	$22.448^{(0.028\%)}$	22.442
9	$25.703^{(2.829\%)}$	$25.061^{(0.262\%)}$	$25.016^{(0.082\%)}$	$25.009^{(0.056\%)}$	$25.687^{(2.765\%)}$	$25.049^{(0.213\%)}$	$25.004^{(0.035\%)}$	$24.998^{(0.009\%)}$	24.996
10	$38.179^{(21.887\%)}$	$31.644^{(1.023\%)}$	$31.394^{(0.224\%)}$	$31.351^{(0.087\%)}$	$38.152^{(21.801\%)}$	$31.632^{(0.984\%)}$	$31.383^{(0.190\%)}$	$31.341^{(0.055\%)}$	31.324
DOFs	432	837	1242	1647	768	1488	2208	2928	9558

Table 7.4: Neo-Hookean doubly-clamped beam, free vibration analysis, case $L/h = 100$: convergence analysis on natural frequencies [Hz]. In brackets, the percentage difference between the proposed models and the 3D elasticity solution is given.

	1D CUF, Expansion theory						ABQ 3D
Mode	**TE-1**	**TE-2**	**TE-3**	**TE-4**	**LE-2**	**LE-3**	**C8D20RH**
1	$1.685^{(0.003\%)}$	$1.685^{(0.003\%)}$	$1.685^{(0.000\%)}$	$1.685^{(0.000\%)}$	$1.685^{(0.000\%)}$	$1.685^{(0.000\%)}$	1.685
2	$2.807^{(0.008\%)}$	$2.807^{(0.008\%)}$	$2.807^{(0.000\%)}$	$2.807^{(0.000\%)}$	$2.807^{(0.000\%)}$	$2.807^{(0.000\%)}$	2.807
3	$4.643^{(0.008\%)}$	$4.643^{(0.008\%)}$	$4.642^{(0.001\%)}$	$4.642^{(0.001\%)}$	$4.643^{(0.008\%)}$	$4.642^{(0.001\%)}$	4.642
4	$7.732^{(0.019\%)}$	$7.732^{(0.019\%)}$	$7.731^{(0.001\%)}$	$7.731^{(0.001\%)}$	$7.732^{(0.019\%)}$	$7.731^{(0.001\%)}$	7.731
5	$9.099^{(0.016\%)}$	$9.099^{(0.016\%)}$	$9.098^{(0.005\%)}$	$9.098^{(0.005\%)}$	$9.099^{(0.016\%)}$	$9.098^{(0.005\%)}$	9.097
6	$15.036^{(0.030\%)}$	$15.036^{(0.030\%)}$	$15.141^{(0.727\%)}$	$15.033^{(0.013\%)}$	$15.145^{(0.758\%)}$	$15.141^{(0.727\%)}$	15.031
7	$15.145^{(0.034\%)}$	$15.145^{(0.034\%)}$	$15.033^{(-0.706\%)}$	$15.141^{(0.004\%)}$	$15.036^{(-0.689\%)}$	$15.033^{(-0.706\%)}$	15.140
8	$22.453^{(0.052\%)}$	$22.453^{(0.052\%)}$	$22.448^{(0.028\%)}$	$22.448^{(0.028\%)}$	$22.453^{(0.052\%)}$	$22.448^{(0.028\%)}$	22.442
9	$25.009^{(0.056\%)}$	$25.009^{(0.056\%)}$	$24.998^{(0.009\%)}$	$24.998^{(0.009\%)}$	$25.009^{(0.056\%)}$	$24.998^{(0.009\%)}$	24.996
10	$31.351^{(0.087\%)}$	$31.351^{(0.087\%)}$	$31.341^{(0.055\%)}$	$31.341^{(0.055\%)}$	$31.351^{(0.087\%)}$	$31.341^{(0.055\%)}$	31.324
DOFs	549	1098	1830	2745	1242	1647	9558

Table 7.5: Neo-Hookean doubly-clamped beam, free vibration analysis, case $L/h = 100$: effect of the expansion theory on natural frequencies [Hz]. The percentage difference between proposed results and the 3D elasticity solution is reported in brackets.

	L/h = 100			L/h = 10		
Mode	**1D CUF Linear Elastic**	**3D ABQ Linear Elastic**	**1D CUF Hyperelastic**	**1D CUF Linear Elastic**	**3D ABQ Linear Elastic**	**1D CUF Hyperelastic**
1	1.685	1.685	1.685	165.285	165.285	165.285
2	2.807	2.807	2.807	266.785	266.778	266.785
3	4.642	4.642	4.642	444.601	444.597	444.601
4	7.731	7.731	7.731	692.287	692.240	692.287
5	9.098	9.097	9.098	797.612	796.096	797.612
6	15.141	15.031	15.141	845.043	845.025	845.043
7	15.033	15.140	15.033	1266.078	1265.924	1266.079
8	22.448	22.442	22.448	1347.035	1346.981	1347.035
9	24.998	24.996	24.998	1365.896	1365.896	1365.896
10	31.341	31.324	31.341	1595.871	1592.787	1595.871

Table 7.6: Neo-Hookean doubly-clamped beam, free vibration analysis, compressible cases for $L/h = 100$ and $L/h = 10$: comparison between natural frequencies obtained adopting the linear elastic constitutive law and hyperelastic constitutive law, frequencies in [Hz].

7.3 Effects of large displacements on the modal behavior of cantilever beams

The following case study is devoted to the linearized vibration analysis of a cantilever square cross-section beam in non-trivial equilibrium conditions. A square cross-section thick beam with $L = 100$ mm and $h = 10$ mm is loaded with two vertical concentrated forces applied at the free upper vertex and clamped at the opposite side. The equilibrium path is first evaluated through a static nonlinear analysis, investigating also the influence of different material compressibility modulus. Subsequently, the linearized vibration analysis is performed along the computed non-trivial equilibrium configurations. The effects of compressibility on the natural frequencies and mode shapes is again assessed through modal analysis at the selected points of interest. The geometrical features, the boundary conditions, and the discretization model are illustrated in Fig. 7.7(a). A convergent CUF model, adopted in the following investigations, is introduced employing 20 B4 cubic element along the beam axis and 2 cubic L16 expansion model, selected for convergence reasons and locking mitigation, represented in 7.7(b).

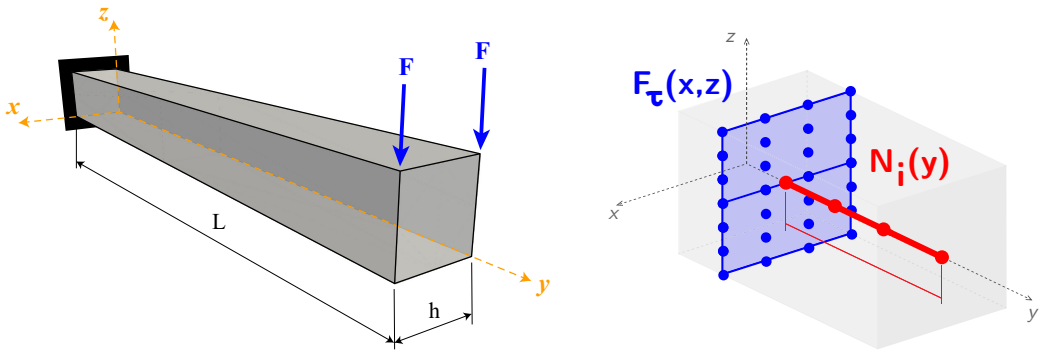

(a) Geometrical features and boundary conditions **(b)** 1B4-2L16 elem.

Figure 7.7: Neo-Hookean cantilever beam subjected to point loads: geometrical features, boundary conditions and discretization model adopted.

The material is again modeled using the Neo-Hookean strain energy density function defined in Eq. (7.8), as in the previous case. The parameters k and μ are chosen to analyze different Poisson's ratio, from a compressible condition ($\nu = 0.125$) toward the nearly incompressible limit ($\nu \to 0.5$). The specific values adopted in each case are listed in Table 7.7. The material density is identical to that used in the previous study, $\rho = 1340$ kg/m^3.

The numerical results obtained adopting a convergent 1D CUF models are compared against reference numerical solutions computed using the commercial finite element software ABAQUS, employing the same discretization described in Sec. 7.2.

	E [MPa]	$D_1 = 2/k$ [MPa^{-1}]	ν	μ [MPa]
Compressible	100	$4.5{\cdot}10^{-2}$	0.125	44.444
Nearly-incompressible, case 1	100	$1.2{\cdot}10^{-3}$	0.49	33.557
Nearly-incompressible, case 2	100	$1.2{\cdot}10^{-4}$	0.499	33.355
Nearly-incompressible, case 3	100	$1.2{\cdot}10^{-5}$	0.4999	33.355

Table 7.7: Neo-Hookean cantilever beam subjected to point loads: material properties adopted.

The first analysis is the nonlinear static analysis of the considered beam. Figure 7.8 illustrates the equilibrium paths of the cantilever beam analyzed in each material condition, analyzing the vertical tip displacement (measured at the point load application) versus the the modulus of single load value applied, comparing the nonlinear paths obtained with 3D elasticity reference solutions.

To further compare the accuracy of the present model, the values of the vertical displacement of the tip-free end for different load values applied in different configurations are reported Table 7.8, where both 1D CUF results and 3D ABAQUS solutions are reported. Minor differences are observed at extremely deformed configurations due to local compressibility effects.
Furthermore, the modal analysis in the computed non-trivial states is conducted for all different compressibility conditions considered. The dependence of deformed configuration is then investigated, solving the linearized vibration problem around different non-trivial equilibrium states, obtaining the associated natural frequencies and mode shapes.

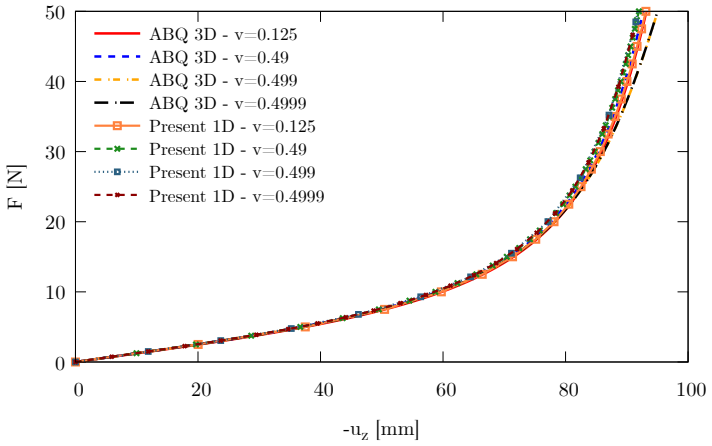

Figure 7.8: Neo-Hookean cantilever beam subjected to point loads: representation of the equilibrium paths for all material compressibility conditions considered.

	$F = 5$ N		$F = 10$ N		$F = 20$ N	
	1D CUF	3D ABQ	1D CUF	3D ABQ	1D CUF	3D ABQ
$\nu = 0.125$	-37.5140	-37.8263	-59.7240	-60.2539	-78.1179	-78.9955
$\nu = 0.49$	-36.6995	-37.3115	-58.7537	-59.6533	-77.1931	-78.4105
$\nu = 0.499$	-36.6035	-37.1045	-58.6403	-59.4295	-77.1168	-78.2279
$\nu = 0.4999$	-36.6480	-37.0770	-58.8465	-59.3996	-77.1154	-78.2030

Table 7.8: Neo-Hookean cantilever beam subjected to point loads: vertical displacement for different loads and material conditions [mm]. Comparison between 1D CUF and 3D ABAQUS results.

Table 7.9 lists the first five natural frequencies, computed for each material condition considered, evaluated in reported load conditions. Significant effects of the pre-stress applied are observed for higher frequency modes; instead, the material conditions do not affect the first five natural frequencies. The behavior of a wider spectrum of frequencies is now detailed analyzed. Figure 7.9 shows the load-frequency plots of the first twelve natural frequencies, comparing the behavior of each natural frequencies in each deformed configuration computed in the static nonlinear analysis. The results are proposed comparing the load-frequency curves obtained for

different values of the compressibility modulus. At low frequencies, even for large deformations, the effects of the material compressibility on the modal response is negligible, the natural frequencies vary with the load applied following comparable behavior, in both compressible and nearly-incompressible regimes. For higher frequencies, instead, deviations in the natural frequency behavior become more evident when compared to the compressible reference; however, in the nearly-incompressible regime, these analyzed modes still show an overall comparable evolution in terms of frequency-load behavior. In some cases, as for example mode 5-7-10, the natural frequencies appear to be insensitive to material compressibility condition. One can conclude then that, for some specific normal modes of vibration, the modal characteristics are governed by geometric and inertial effects rather than volumetric deformation constraints.

	F = 10 N				
	Mode 1	**Mode 2**	**Mode 3**	**Mode 4**	**Mode 5**
$\nu = 0.125$	51.983	55.394	248.576	272.316	403.699
$\nu = 0.49$	52.886	56.114	250.416	273.799	348.649
$\nu = 0.499$	53.459	56.876	250.209	274.392	345.918
$\nu = 0.4999$	52.787	55.998	250.693	273.831	344.717
	F = 30 N				
	Mode 1	**Mode 2**	**Mode 3**	**Mode 4**	**Mode 5**
$\nu = 0.125$	71.724	79.072	253.693	292.286	416.499
$\nu = 0.49$	72.943	79.975	254.757	287.430	367.265
$\nu = 0.499$	74.124	81.209	256.079	289.079	369.714
$\nu = 0.4999$	73.107	80.108	255.150	287.964	367.316

Table 7.9: Neo-Hookean cantilever beam subjected to point loads: natural frequencies in non-trivial equilibrium states for different material conditions [Hz].

Further investigations are now carried out analyzing the possible correlation between normal modes of vibration in different deformed states. Three distinct deformed configurations, obtained applying $F = 5$ N, $F = 15$ N, and $F = 25$ N, for both $\nu = 0.125$ and $\nu = 0.49$, are considered. Once the natural frequencies and full modal behavior of the structures in these non-trivial equilibrium states are determined, modal correlation is analyzed by means of the Modal Assurance Criterion (MAC) Eq. (7.9), to investigate the possible correlation between mode shapes, computed in different non-trivial equilibrium states, highlighting differences in the normal vibration modes of structures between the two analyzed set of eigenvectors. In general, for two sets A and B of eigenvectors, the MAC matrix is defined as:

$$MAC_{ij} = \frac{|\boldsymbol{\Phi}_{A_i}{}^T \boldsymbol{\Phi}_{B_j}|^2}{(\boldsymbol{\Phi}_{A_i}{}^T \boldsymbol{\Phi}_{A_i})(\boldsymbol{\Phi}_{B_j}{}^T \boldsymbol{\Phi}_{B_j})} \tag{7.9}$$

Figure 7.10 shows the MAC matrix, for the case $\nu = 0.49$, comparing mode shapes in different non-trivial equilibrium states with those of the undeformed configuration. The same correlation analysis is performed for the compressible material condition, with the resulting MAC matrices shown in Fig. 7.11. Along the equilibrium path, mode shapes are already interacting in the small strain regime. Increasing the load applied lead to a global different modal response in terms of mode shapes. Also, in the three different non-trivial equilibrium states listed before, the correlations between modal shapes for the compressible $\nu = 0.125$ and nearly-incompressible case of $\nu = 0.49$ are examined, and the resulting MAC matrices are presented in Fig. 7.12.

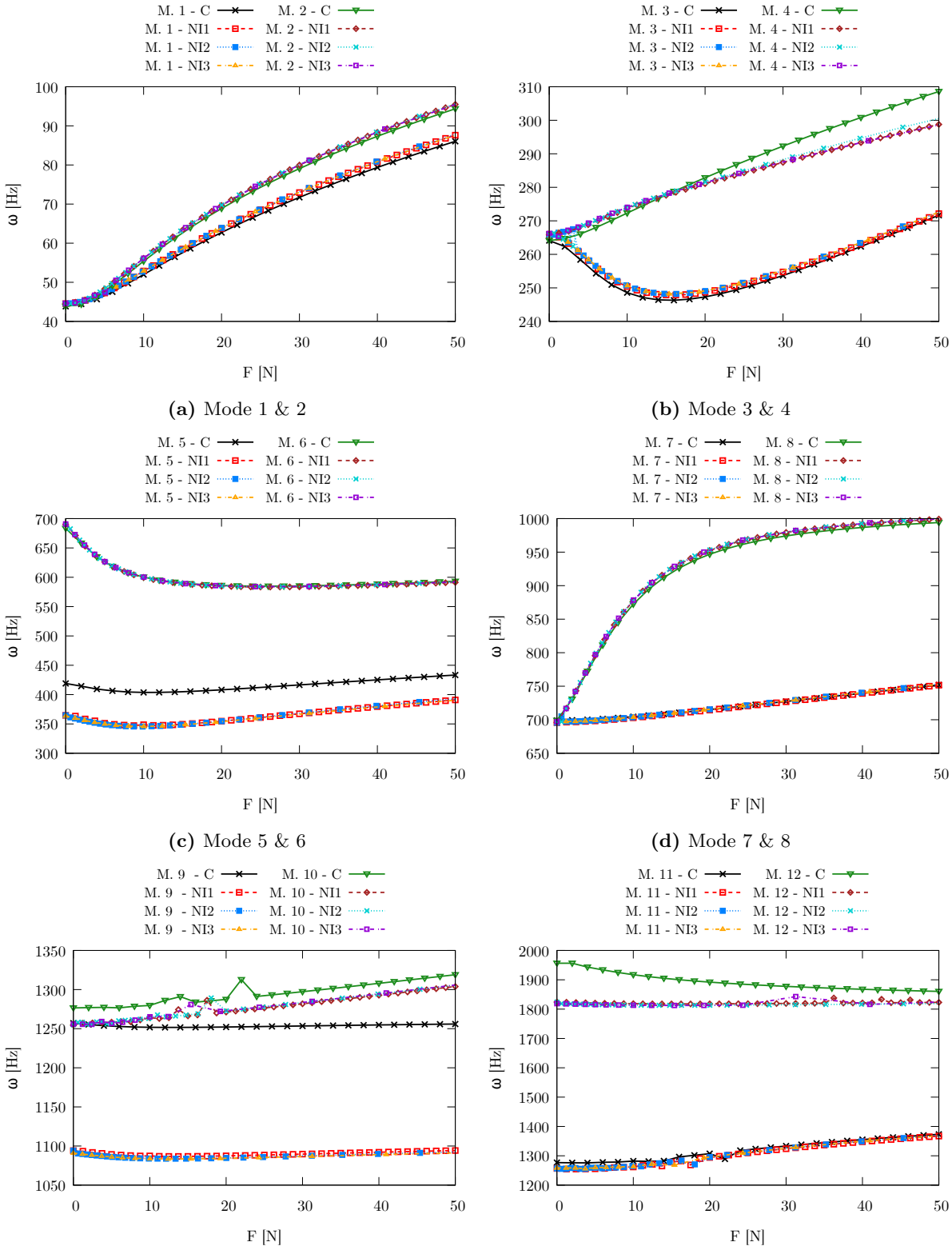

(a) Mode 1 & 2

(b) Mode 3 & 4

(c) Mode 5 & 6

(d) Mode 7 & 8

(e) Mode 9 & 10

(f) Mode 11 & 12

Figure 7.9: Neo-Hookean cantilever beam subjected to point loads: natural frequencies for increasing value of the free-end vertical load.

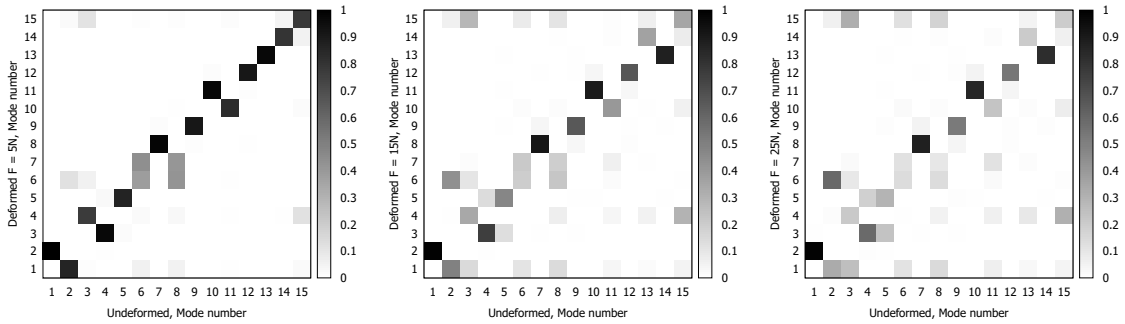

(a) Undef. vs $F = 5$ N **(b)** Undef. vs $F = 15$ N **(c)** Undef. vs $F = 25$ N

Figure 7.10: Neo-Hookean cantilever beam subjected to point loads: MAC matrix for the nearly-incompressible beam.

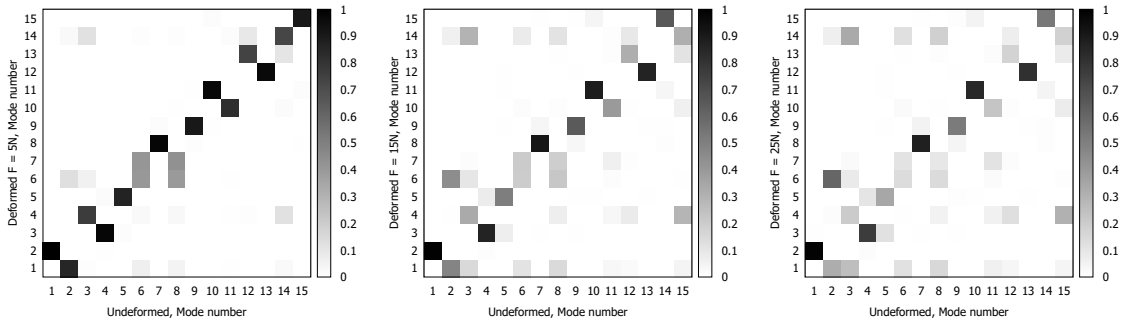

(a) Undef. vs $F = 5$ N **(b)** Undef. vs $F = 15$ N **(c)** Undef. vs $F = 25$ N

Figure 7.11: Neo-Hookean cantilever beam subjected to point loads: MAC analysis for the compressible beam.

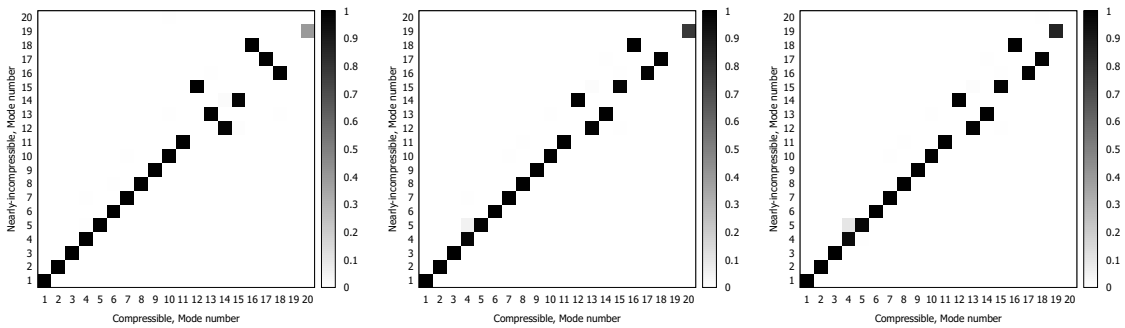

(a) $F = 5$ N **(b)** $F = 15$ N **(c)** $F = 25$ N

Figure 7.12: Neo-Hookean cantilever beam subjected to point loads: MAC between compressible and nearly-incompressible modal behavior in a specific nontrivial equilibrium state considered.

7.4 Effects of large strain on the modal behavior of thick beams

The case study here considered is the static and linearized vibration analysis of a square cross-section beam subjected to large strain. The focus of the present analysis is on the small-amplitude vibrations of a thick beam with a side length of $h = 10$ mm and a slender ratio of $L/h = 10$. The analysis is performed in two steps: first, a free vibration analysis around the trivial equilibrium state is performed to examine the influence of material compressibility on modal response of the structure; subsequently, the beam is analyzed under a uniform traction load applied to both the free ends, analyzing the effects of large strain on the natural frequencies and mode shapes of the square cross-section beam. The geometry, boundary conditions, and mesh discretization used are shown in Fig. 7.13.

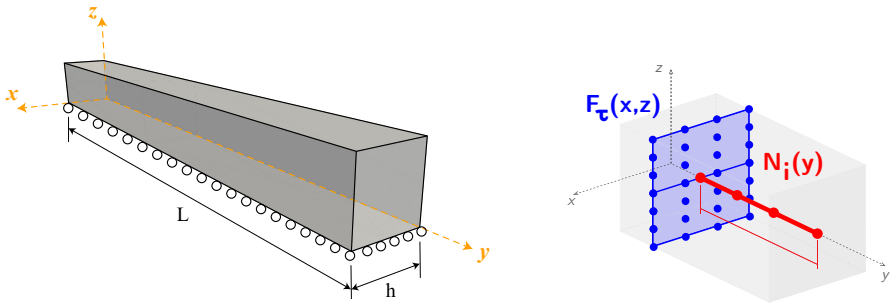

(a) Geometrical features and boundary conditions

(b) Single B4-L16 elem.

Figure 7.13: Neo-Hookean beam subjected to large axial strain: geometry, boundary conditions and discretization.

The material is once again modeled using the Neo-Hookean strain energy function, as defined in Eq. (7.8). Both compressible and nearly-incompressible material behaviors are considered. The related material properties employed in this case study are presented in Table 7.10. The density of the hyperelastic beam is set to $\rho = 1150$ kg/m^3.

	k [MPa]	**μ [MPa]**	**E [MPa]**	**ν**
Compressible	2.222222222	2.222222222	5	0.125
Nearly-incompressible	8333333.333	1.666666778	5	0.4999999

Table 7.10: Neo-Hookean beam subjected to large axial strain: material properties for different compressibility conditions.

Reference results are obtained by ABAQUS commercial software, with the same discretization adopted for the previous study case described in Sec. 7.3. The free vibration analysis is considered restricting only the possible translation in the z direction of the bottom plane, thus the beam is simulated as if it is resting on the bottom plane. For this reason, three possible rigid motions are possible (translation along x and y axis, rotation about z axis), therefore the first three natural frequencies are identically null. Figure 7.14(a) the first thirty natural frequencies comparing the trivial modal behavior of the compressible and nearly-incompressible beams. A comparison with a reference 3D ABAQUS solution is also proposed, and the computed natural frequencies are in a excellent agreement with the reference. Minor differences between structural responses in different material compressibility conditions are observed for

higher-frequency modes. This is also motivated by the MAC matrix shown in Fig. 7.14(b), where the normal modes of vibrations of the compressible beam have been compared with the nearly-incompressible beam ones. These particular boundary conditions have been investigated to address the behavior of the volumetric modes of vibrations. In the following, the effects of compressibility on the volumetric modes, induced by the possible unconstrained motions due to the boundary conditions, are analyzed. Figure 7.15 shows the computed volumetric modes, comparing the modal shapes of compressible and nearly incompressible beam.

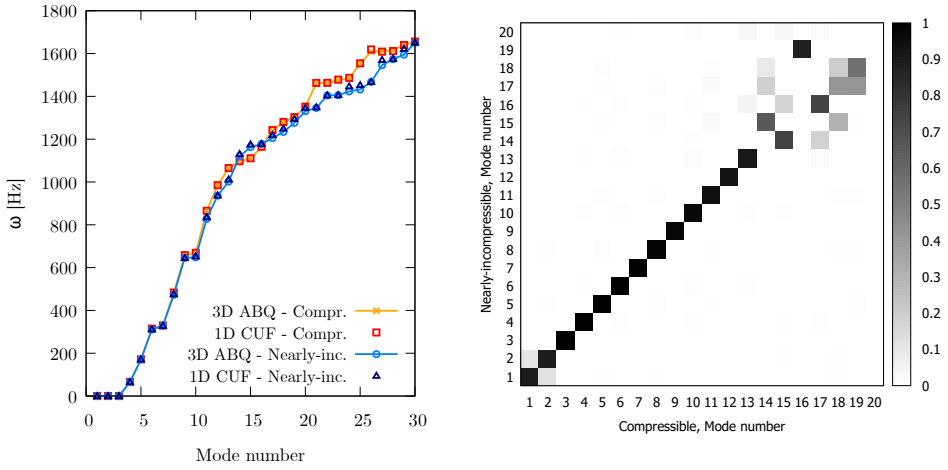

(a) Frequencies **(b)** MAC

Figure 7.14: Neo-Hookean beam subjected to large axial strain: natural frequencies in the compressible and nearly-incompressible material regime and MAC matrix comparing the two sets of solutions.

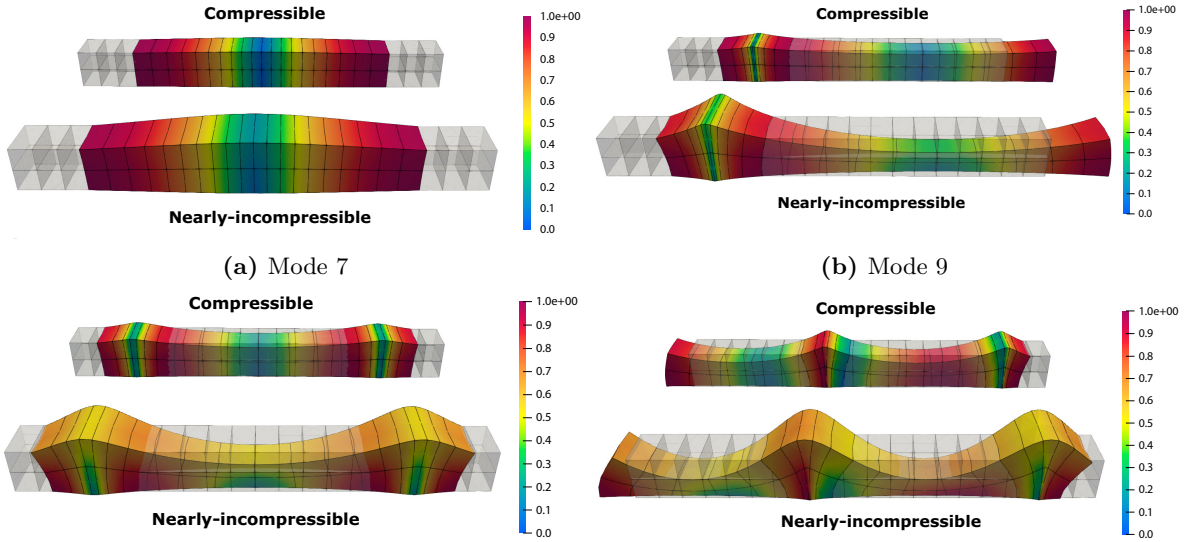

(a) Mode 7 **(b)** Mode 9

(c) Mode 12 **(d)** Mode 16-19

Figure 7.15: Neo-Hookean beam subjected to large axial strain: comparison between volumetric modes in different material regimes.

These modes have been associated with an axially moving waves. In nearly-incompressible material regime, differently to the case of compressible material, the deformation gradient satisfies the incompressibility condition given by $J = \det \mathbf{F} = 1$, therefore the components of the deformation gradient are dependent from each other. Due to incompressibility, shrinks and dilatations are observed periodically, differently with respect to the compressible case in which the components of the deformation gradient are free and independent from each other.
Furthermore, the nearly-incompressible beam is examined in the static case, to assess the impact of pre-stressed equilibrium states on its vibration behavior. A uniform axial traction is now applied to the beam free ends. The geometry, boundary conditions, and applied load are illustrated in Fig. 7.16(a). The beam discretization used employs a convergent 1D beam model, as discussed in the previous analysis, where 20 B4 - 2 L16 are adopted. Figure 7.16(b) depicts the equilibrium path, reported as a a stretch-load curve, where the axial stretch λ_y as a function of the tip axial pressure magnitude is investigated. Alongside, for further considerations, the total internal stress component S_{yy} is also reported. Analytically, it can be demonstrated that the axial component of the $\mathbf{S}$ second Piola-Kirchhoff stress tensor is a monotonically increasing function that approaches the asymptotic value of the infinitesimal shear modulus, as shown in the uniaxial tension test case in Sec. 7.1. This has also been observed also numerically.

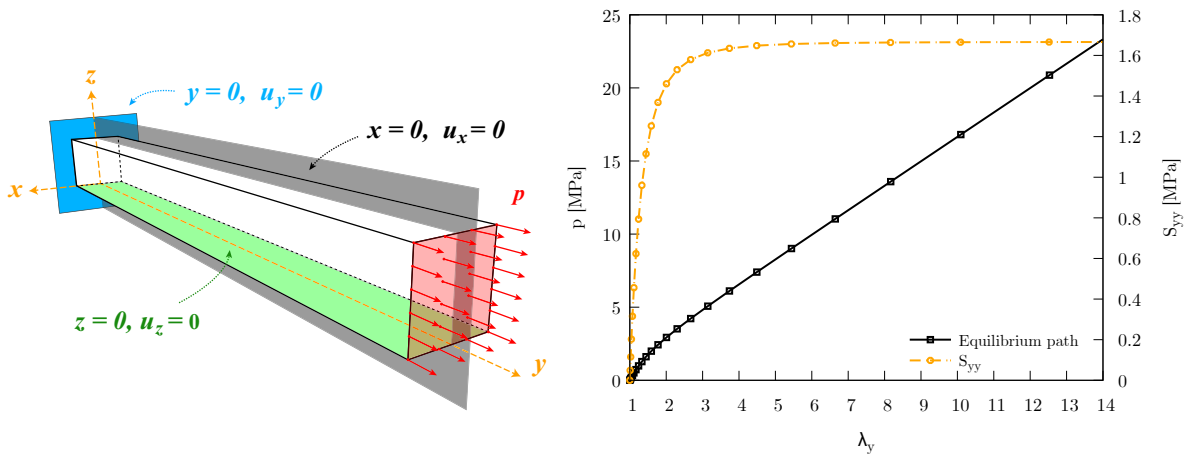

(a) Boundary conditions **(b)** Equilibrium path

Figure 7.16: Neo-Hookean beam subjected to large axial strain: load conditions and equilibrium paths.

In each computed non-trivial equilibrium state, the linearized vibration problem is solved to study the influence of the principal stretch λ_y on the dynamic beam response. Figure 7.17 shows the frequency-stretch curve for the first fifteen modes as functions of the stretch ratio, while Fig. 7.18 reports the same results in the small strain regime. Figure 7.19 displays the first six vibration modes for a pre-stretched condition of $\lambda_y = 2$. For low frequency modes, a general reduction in the natural frequency is observed. In contrast, higher modes initially increase due to the rise in axial internal stresses, followed by a monotonic decrease at high stretch. This behavior can be justified by the previously reported result, in terms of axial stress component, considering the mathematical nature of the tangent stiffness matrix. In general, an increase in stiffness can lead to an increase in natural frequency but, in the analyzed case, the internal stress is considered constant with the axial stretch up to a certain value. As S_{yy} reaches an asymptotic value, the only stiffening term is represented by the $\mathbf{K}_{T_1}$ matrix, and the geometric stiffness $\mathbf{K}_\sigma$ do not contribute with the increase of stretch.

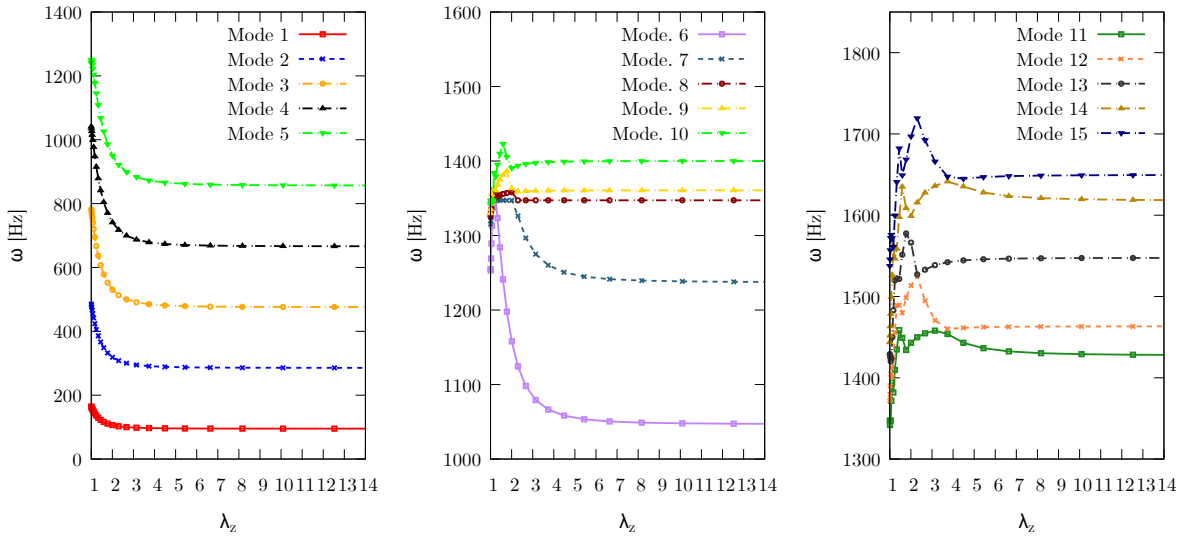

(a) Modes 1-5 **(b)** Modes 6-10 **(c)** Modes 11-15

Figure 7.17: Neo-Hookean beam subjected to large axial strain: natural frequencies versus traction pressure applied.

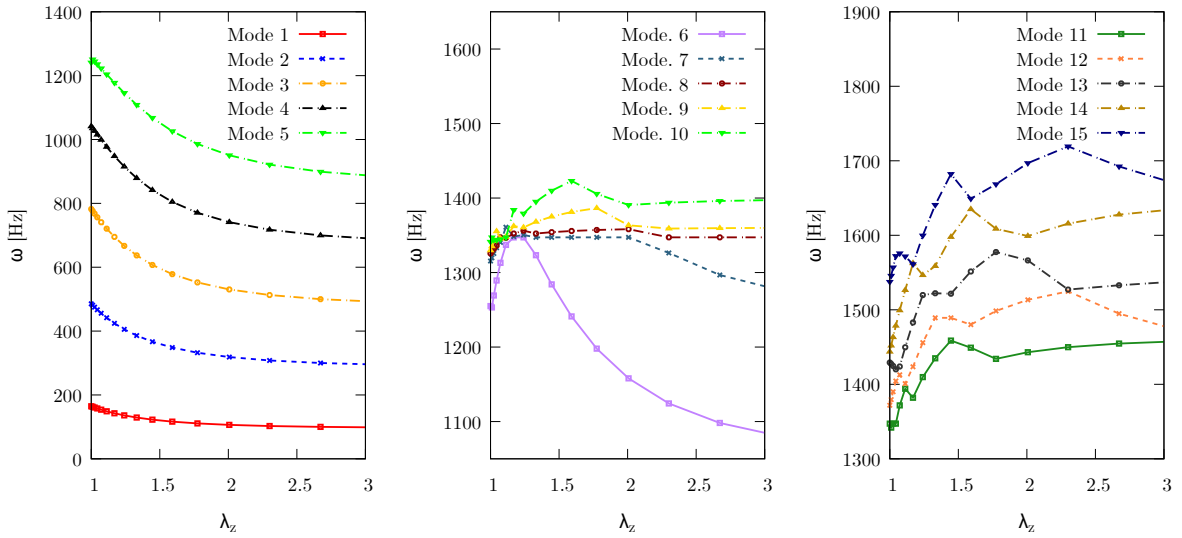

(a) Modes 1-5 **(b)** Modes 6-10 **(c)** Modes 11-15

Figure 7.18: Neo-Hookean beam subjected to large axial strain: natural frequencies versus traction pressure applied, nearly-incompressible case, small/moderate stretch regime.

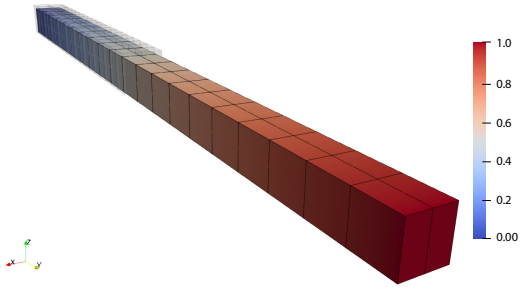

(a) Mode 1

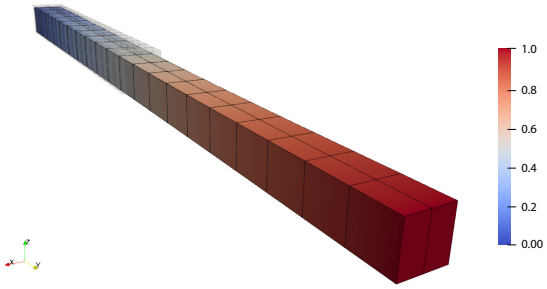

(b) Mode 2

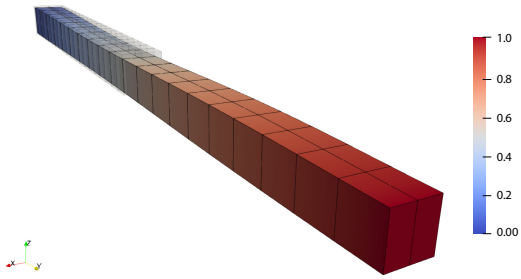

(c) Mode 3

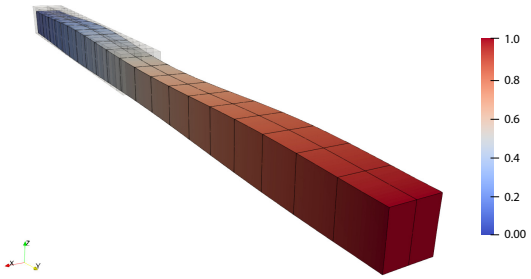

(d) Mode 4

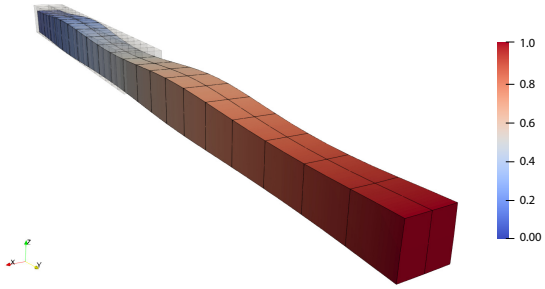

(e) Mode 5

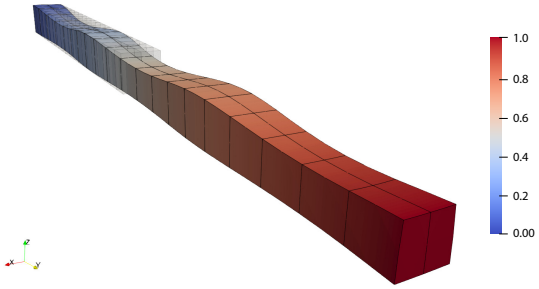

(f) Mode 6

Figure 7.19: Neo-Hookean beam subjected to large axial strain: normal modes of vibrations for $\lambda_y = 2$.

7.5 Effects of compressibility in thin-walled box beam

This case study is here addressed to show the capabilities of the proposed modeling approach when thin-walled structures are considered, for which computationally expensive 3D models are required. Again, both the static and linearized vibration analysis are performed considering a thin-walled box beam. The free vibration analysis of a beam with a total length of $L = 50$ mm, cross-section dimensions $a = 4$ mm and $b = 3$ mm, wall thickness $t = 0.2$ mm, considered clamped at both ends is initially analyzed. The geometry, boundary conditions, and discretization models adopted are shown in Fig. 7.20. The influence of material compressibility on the modal behavior is again examined, comparing a compressible and a nearly-incompressible material constitutive behavior. The material properties used in each condition are listed in Table 7.11.

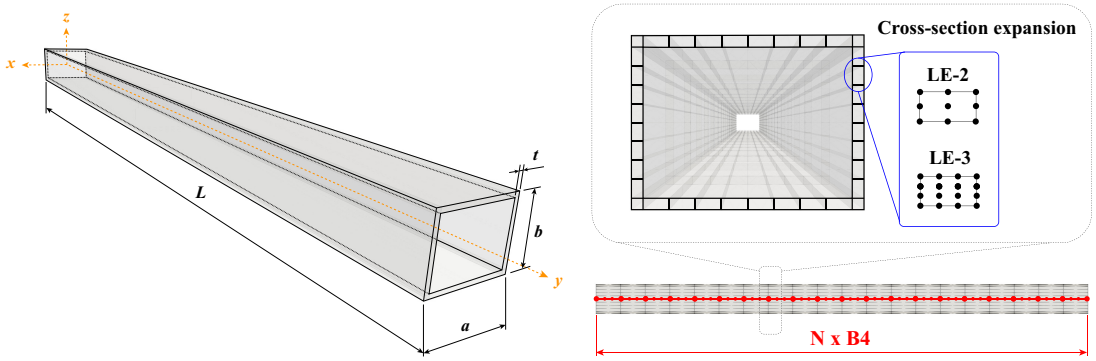

(a) Geometrical features **(b)** 1D CUF model

Figure 7.20: Thin-walled box beam, free vibration problem: geometrical features and discretization adopted.

The material is once again modeled using the Neo-Hookean model, as given in Eq. (7.8). The modal behavior of the thin-walled beam is analyzed under two different compressibility cases. In all simulations, the Young's modulus is set to $E = 0.5$ MPa, with the remaining parameters summarized in Table 7.11. The material density of the hyperelastic beam is taken as $\rho = 1150$ kg/m^3.

	k [MPa]	**μ [MPa]**	**E [MPa]**	**ν**
Compressible	0.416666	0.19230	0.5	0.3
Nearly-incompressible	16.66666	0.16722	0.5	0.495

Table 7.11: Thin-walled box beam, free vibration problem: material properties.

The numerical results obtained adopting 1D CUF beam models are compared with numerical reference solution obtained using the commercial software ABAQUS, adopting hexahedral models to compare with exact solution of equilibrium equation, without any superimposed kinematic theory. The 1D CUF model employs 36 cross-section expansion elements, as illustrated in Fig. 7.20(b), for convergence reasons. Two different expansion theories (parabolic L9 and cubic L16) are considered to analyze the influence of the polynomial order of expansion of cross-section kinematics. To further investigate the effects of the discretization, different beam axis kinematic models are proposed. The adopted model will be denoted, from now one, as $NB4 - 36LE\ T$,

where N indicates the number of finite elements along the beam axis and T refers to the polynomial order of the cross-section expansion. The total number of degrees of freedom (DOFs) for each configuration is also reported.

A convergence analysis is carried out for the free vibration problem about the trivial equilibrium state (undeformed configuration). The first five natural frequencies are examined for both compressible and nearly-incompressible materials under various discretization models. Table 7.12 and Table 7.13 show the first five natural frequencies for each compressibility condition, comparing the results with those of the numerical reference solution. For the compressible material case, each FE model proposed provide accurate results and predictions in terms of natural frequencies. However, in the nearly-incompressible case, the limitations of pure displacement-based FE formulations become apparent due to volumetric locking, necessitating the use of higher-order theories and refined kinematic models to achieve accuracy. Nevertheless, such numerical issues can be alleviated through refined theory of structures. In both material regimes, the use of 1D CUF models provides noticeable computational savings, due to the enhanced performance of the present model when thin-walled structures are analyzed, overcoming the limitation of classical models such as aspect-ratio constraints.

	36 L9 (parabolic model)			**36 L16 (cubic model)**			**ABQ 3D**
Mode	**10B4**	**15B4**	**20B4**	**10B4**	**15B4**	**20B4**	**C8D20RH**
1	$32.28^{(0.52\%)}$	$32.21^{(0.32\%)}$	$32.18^{(0.22\%)}$	$32.27^{(0.48\%)}$	$32.20^{(0.28\%)}$	$32.17^{(0.18\%)}$	32.11
2	$40.37^{(0.51\%)}$	$40.29^{(0.31\%)}$	$40.25^{(0.21\%)}$	$40.36^{(0.49\%)}$	$40.28^{(0.29\%)}$	$40.24^{(0.19\%)}$	40.16
3	$79.33^{(0.55\%)}$	$79.17^{(0.35\%)}$	$79.10^{(0.26\%)}$	$79.23^{(0.42\%)}$	$79.07^{(0.22\%)}$	$79.00^{(0.14\%)}$	78.90
4	$99.54^{(0.49\%)}$	$99.35^{(0.29\%)}$	$99.86^{(0.81\%)}$	$99.48^{(0.43\%)}$	$99.15^{(0.09\%)}$	$99.13^{(0.08\%)}$	99.06
5	$99.92^{(0.59\%)}$	$99.88^{(0.54\%)}$	$99.26^{(0.08\%)}$	$99.19^{(0.15\%)}$	$99.29^{(0.04\%)}$	$99.21^{(0.13\%)}$	99.34
DOFs	20088	29808	39528	40176	59616	79056	254118

Table 7.12: Thin-walled box beam, free vibration problem: first five natural frequencies in the compressible regime [Hz].

	36 L9 (parabolic model)			**36 L16 (cubic model)**			**ABQ 3D**
Mode	**10B4**	**15B4**	**20B4**	**10B4**	**15B4**	**20B4**	**C8D20RH**
1	$33.21^{(3.70\%)}$	$32.78^{(2.34\%)}$	$32.57^{(1.70\%)}$	$33.19^{(3.63\%)}$	$32.76^{(2.27\%)}$	$32.55^{(1.63\%)}$	32.03
2	$41.35^{(3.54\%)}$	$40.83^{(2.23\%)}$	$40.59^{(1.62\%)}$	$41.34^{(3.50\%)}$	$40.82^{(2.19\%)}$	$40.57^{(1.57\%)}$	39.94
3	$81.09^{(3.43\%)}$	$80.16^{(2.24\%)}$	$79.71^{(1.67\%)}$	$80.90^{(3.19\%)}$	$79.97^{(2.01\%)}$	$79.53^{(1.44\%)}$	78.40
4	$99.59^{(1.84\%)}$	$99.49^{(1.74\%)}$	$99.19^{(1.44\%)}$	$98.80^{(1.04\%)}$	$98.70^{(0.94\%)}$	$98.65^{(0.89\%)}$	97.79
5	$100.77^{(2.44\%)}$	$99.70^{(1.36\%)}$	$99.44^{(1.09\%)}$	$100.67^{(2.34\%)}$	$99.60^{(1.26\%)}$	$99.09^{(0.74\%)}$	98.36
DOFs	20088	29808	39528	40176	59616	79056	254118

Table 7.13: Thin-walled box beam, free vibration problem: first five natural frequencies in the nearly-incompressible regime [Hz].

The set of the first thirty natural frequencies is plotted in Fig. 7.21(a) for the compressible beam and Fig. 7.21(b) for the nearly-incompressible beam, comparing the results obtained for each discretization model and the numerical reference.

Finally, the normal modes of the compressible and nearly-incompressible cases are compared using the MAC matrix, based on eigenvectors from the 20B4-36L16 models. This comparison highlights potential correlations between vibration modes in different compressibility regimes, with results shown in Fig. 7.21(c).

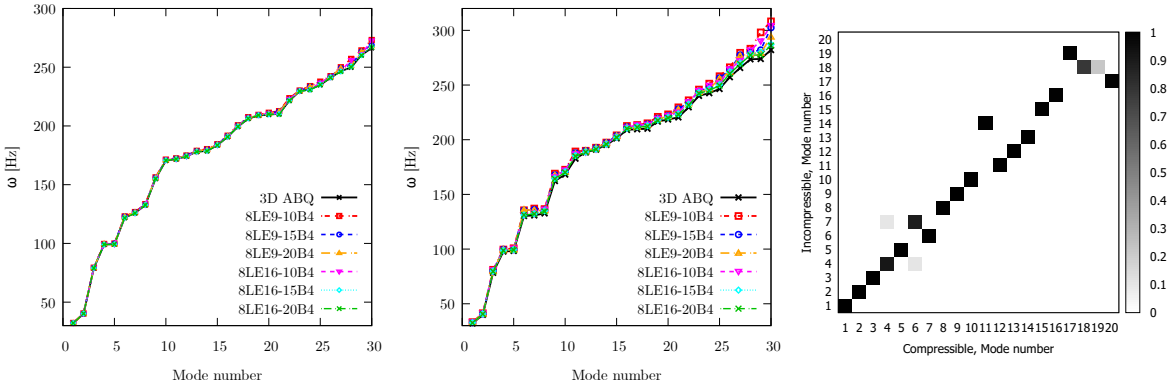

(a) Compressible **(b)** Incompressible **(c)** MAC

Figure 7.21: Thin-walled box beam: MAC comparison between modes, clamped configuration

In the second case, the modal behavior of the compressible beam is examined in non-trivial equilibrium conditions under a large strain context. First, a nonlinear static analysis of the same structure subjected to symmetry boundary conditions and uniaxial traction pressure applied at the free end section is considered. The boundary conditions and the load applied are depicted in Fig. 7.22(a). The same boundary conditions are then considered in the linearized vibration analysis. The results obtained are proposed in Fig. 7.22(b), where the stretch-pressure response and the stress-strain curve are proposed in the same graph. The model adopted for the computation of the non-trivial equilibrium states is the convergent model analyzed in the convergence analysis, thus 20 B4 finite element along the beam axis and 36 L9 element along the cross-section are adopted.

In each non-trivial equilibrium state computed, marked in the equilibrium path, the linearized vibration problem is solved, investigating then how natural frequencies are mode shapes are affected by the the axial stretch applied. Figure 7.23 presents the evolution of the first fifteen natural frequencies along the equilibrium curve. Due to the rapid increase in stress observed along the path, significant variations in natural frequencies occur in the small strain regime, as shown in Fig. 7.24.

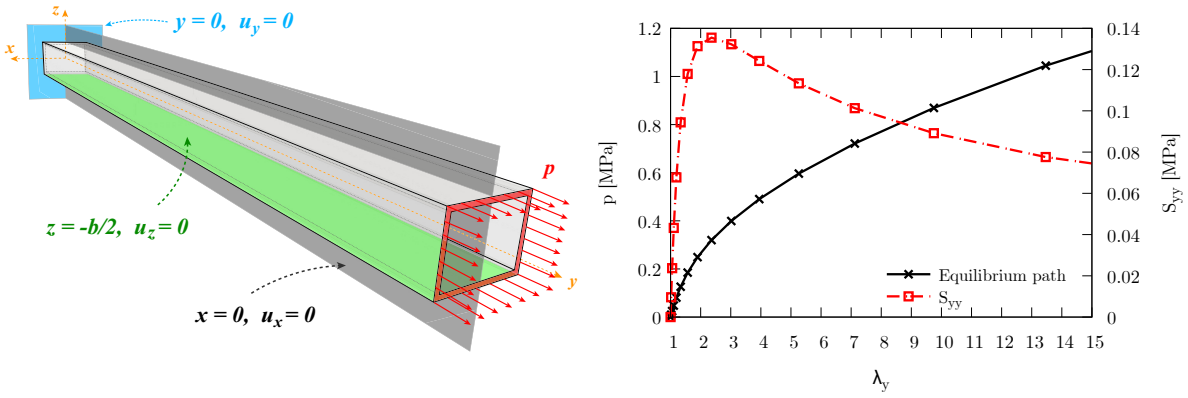

(a) Geometry and boundary conditions **(b)** Equilibrium path

Figure 7.22: Thin-walled box beam: equilibrium path for axial normal pressure.

Overall, an increasing behavior of the natural frequencies is observed at small strain. Instead, a monotonic decreasing behavior of each natural frequencies is observed thereafter, attributed again to the reduction of the principal stiffness component S_{yy} during the loading process. Again, also in this case, the effects of the geometrical stiffness is considered negligible since, for equilibrium, the internal stress component is not contributing to the material stiffening. The normal modes of vibration corresponding to a fixed stretch value of $\lambda_y = 3.94$ are finally displayed in Fig. 7.25.

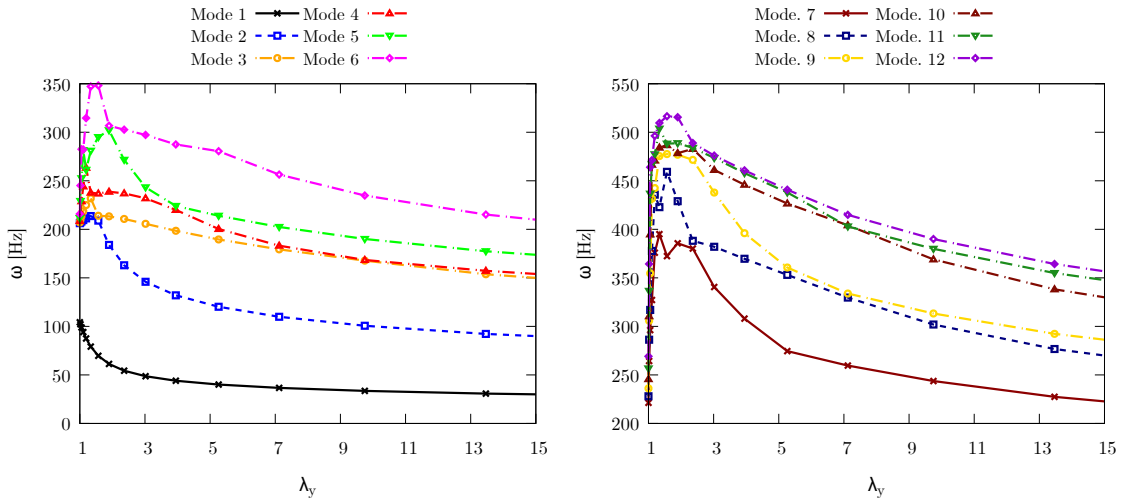

(a) Modes 1-6 **(b)** Modes 7-12

Figure 7.23: Thin-walled box beam, compressible case: variation of the first twelve natural frequencies along the equilibrium path. Global strain regime.

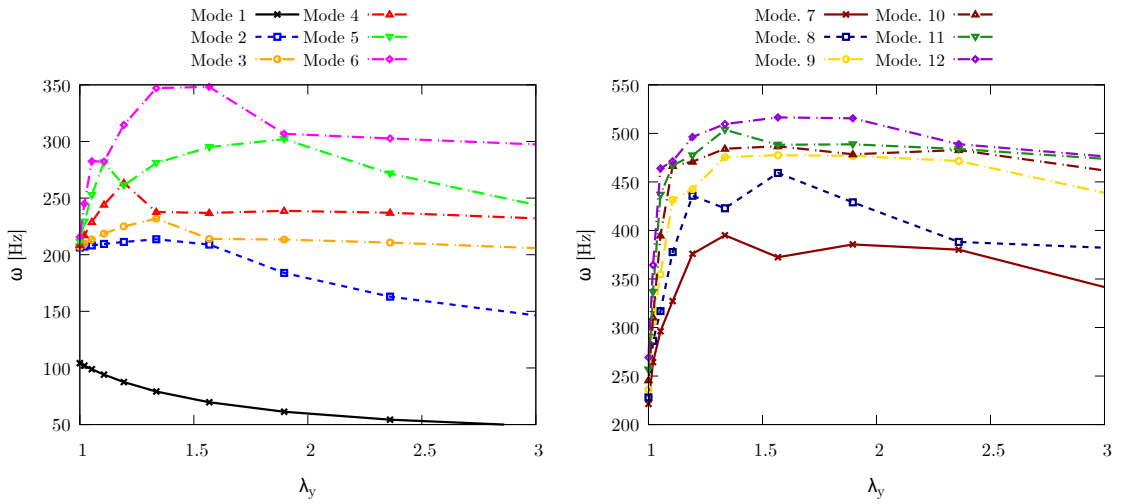

(a) Modes 1-6 **(b)** Modes 7-12

Figure 7.24: Thin-walled box beam, compressible case: variation of the first twelve natural frequencies along the equilibrium path. Small to moderate strain regime.

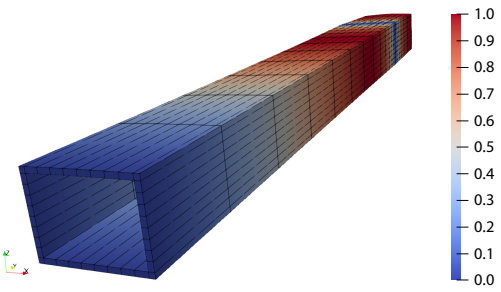

(a) Mode 2

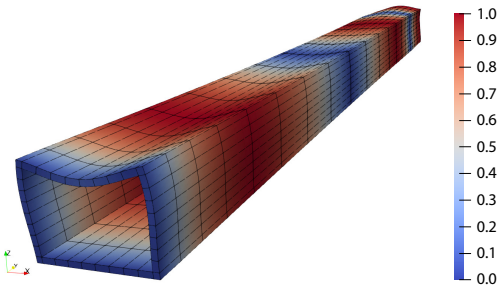

(b) Mode 4

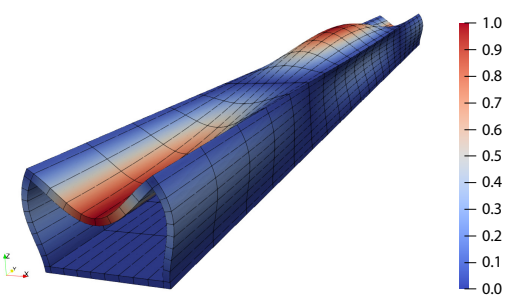

(c) Mode 6

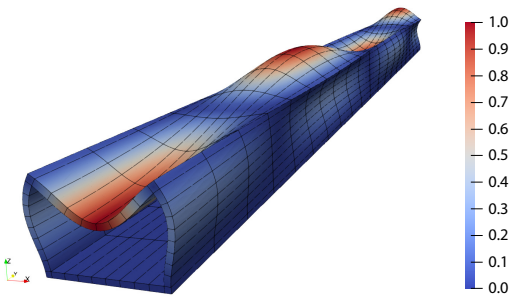

(d) Mode 8

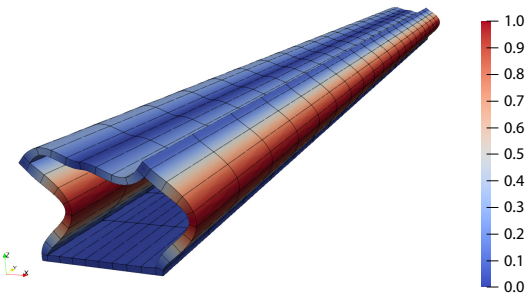

(e) Mode 10

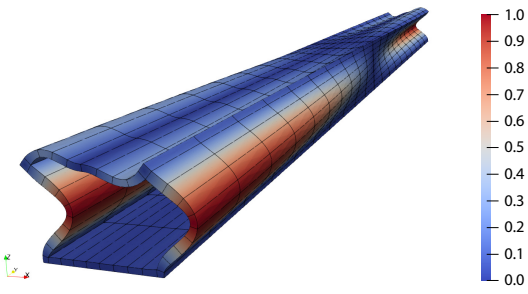

(f) Mode 12

Figure 7.25: Thin-walled box beam: normal modes of vibrations for $\lambda_y = 3.94$, eigenvector magnitude.

7.6 Multilayered compressible beam subjected to point load

The capabilities of the proposed higher-order approach are now investigated in terms of static (and) stress response of multilayered structures. The compatibility conditions and C_z^0 requirements will be here discussed , assessing the capabilities of the proposed modeling approach of multilayered structures. A multilayered square cross-section cantilever beam, of total length L and side a, is now considered. The three-layer beam is made of compressible Mooney-Rivlin material, adopting two distinct sets of material properties. The layer thickness is considered fixed to $h_A = h_B = a/3$, considering the square cross-section side as $a = 10$ mm. To investigate the influence of kinematic models and theory of structure approximation on the static and stress response of the present beam two configurations are considered: a thick beam with slenderness ratio $L/a = 10$ and a slender beam with $L/a = 100$. The beam is considered clamped at $y = 0$ mm and subjected to a concentrated transverse load at its free end. The geometrical features and boundary conditions describing the present scenario are illustrated in Fig. 7.26.

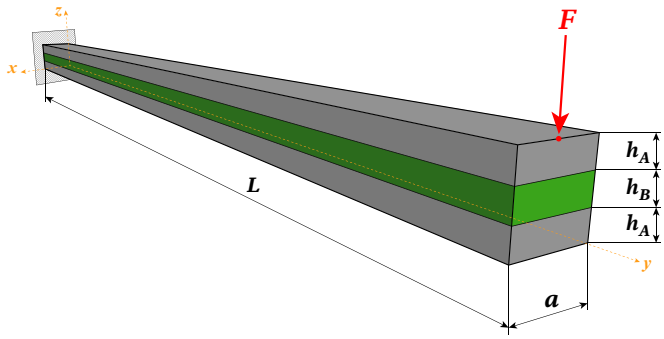

Figure 7.26: Cantilever multilayer beam: geometry and boundary conditions.

The material model adopted for each layer is the isotropic Mooney-Rivlin formulation and the standard volumetric strain energy function [192]:

$$\Psi = \Psi_{vol}(J) + \bar{\Psi}(\bar{I}_1, \bar{I}_2) = \frac{1}{D_1}(J-1)^2 + c_{10}(\bar{I}_1 - 3) + c_{01}(\bar{I}_2 - 3) \tag{7.10}$$

where c_{10} and c_{01} are material constants usually identified through experimental data fitting, and $D_1 = 2/k$ with k representing the bulk modulus. For this material model, the equivalent Young modulus E and bulk modulus k can be obtained from classical elasticity relations, considering the initial shear modulus given by $\mu = 2(c_{10} + c_{01})$. The material properties employed are listed in Table 7.14.

	c_{10} [MPa]	c_{01} [MPa]	μ [MPa]	ν [-]	E [MPa]	$D_1 = 2/k$ [MPa^{-1}]
Material A	30	-4	52	0.2	124.8	$2.8846{\cdot}10^{-2}$
Material B	10	1.5	23	0.3	59.8	$4.0133{\cdot}10^{-2}$

Table 7.14: Cantilever multilayered beam: material properties.

This case study is proposed to assess the capabilities and the accuracy of higher-order beam formulation. Specifically, both the effects of kinematics models along the beam axis discretization and, particularly, the influence of the theory of structure approximation adopted on the static mechanical response of the hyperelastic multilayered beam are investigated, analyzing

displacements and strss distribution, and discussing the results in terms of compatibility requirements. The aim of the present case study is to assess the accuracy and the capabilities of both ESLm and LWm are here investigated, analyzing the effects of both Taylor expansion models and Lagrange expansion models on the obtained numerical solution. The performances of the present implementation of higher-order beam models is extensively compared with a reference numerical solution provided by the 3D ABAQUS, both in terms of displacement and stress fields. The 3D FEM ABAQUS solution is adopted to compare the present model's capabilities with direct solution of the equilibrium equation given by standard 3D FE. In the following, for the thick beam, the discretization is performed with 8190 C3D20R hexahedral elements (20-node quadratic brick elements with reduced integration). For the slender beam, instead, 31320 C3D20R elements are adopted due to aspect ratio constraints inherent to classical 3D formulation. In the meanwhile, the 1D CUF models employed, for both thick and slender beams, adopt N cubic B4 finite elements along the beam axis discretization; instead both ESLm and LWm are comprehensively analyzed, adopting low- to higher-order models in both cases. In the case of LWm, N_E L9 parabolic (nine-node) or cubic L16 (sixteen-node) cross-sectional subdomains will be considered. The results will be discussed, where needed, in terms of non-dimensional quantities, defined as:

$$\bar{u}_z = \frac{u_z}{L} \qquad \%\text{diff}(\cdot) = \frac{(\cdot)_{\text{1D CUF}} - (\cdot)_{\text{3D}}}{(\cdot)_{\text{3D}}} \cdot 100\% \qquad \lambda = \frac{F}{F_{max}} \tag{7.11}$$

where u_z denotes the transverse displacement component and F_{max} the maximum applied load in the static analysis, when specified. The accuracy is quantified through the percentage difference between 1D CUF and 3D ABAQUS results, while the computational cost is measured by the total number of DOF required by the adopted discretization. The first analysis proposed is a convergence study, carried out to evaluate the accuracy and efficiency of the 1D beam formulations in predicting displacement distributions, considering both thick and slender beam configurations. Initially, LWm are adopted to further investigate the effects of beam axis discretization models. For the cross-section discretization, parabolic L9 (nine-node) and cubic L16 (sixteen-node) expansion models are considered. The adopted cross-section expansion subdomains are depicted in Fig. 7.27. In the simulations, the numerical solver is coupled with a load-control procedure, considering $F_{max} = 50$ N for the thick beam and $F_{max} = 1$ N for the slender beam.

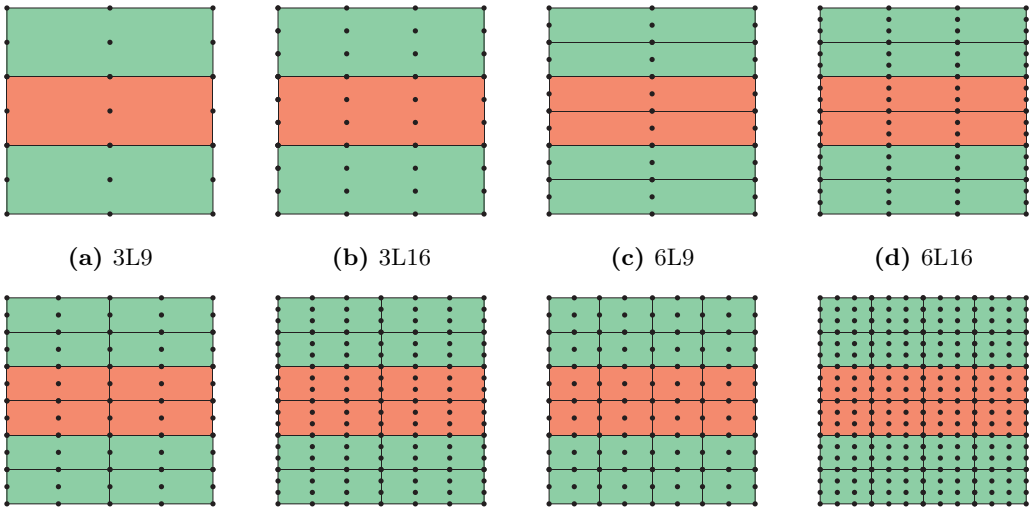

(a) 3L9 **(b)** 3L16 **(c)** 6L9 **(d)** 6L16

(e) 12L9 **(f)** 12L16 **(g)** 24L9 **(h)** 24L16

Figure 7.27: Cantilever multilayered beam: cross-section expansion adopted, LE models.

Table 7.15 lists the non-dimensional transverse displacement $\bar{u}_z$ for the thick beam case, measured at the load application, under various load condition applied. Both small to moderate/large displacement regimes are analyzed, allowing the assessment of both accuracy and efficiency of the model at small and large strain. Figure 7.28 depicts the equilibrium paths of the thick beam employing the convergent beam axis discretization model given by 20 B4 cubic FE, with different LWm, comparing the solution obtained with refined 1D beam models with the 3D ABAQUS reference path. Similarly, Table 7.16 reports the results obtained in the convergence analysis performed considering the slender beam case, analyzing again the non-dimensional transverse displacement $\bar{u}_z$ computed at the load application point. As proposed for the thick beam case, Fig. 7.29 shows the equilibrium paths computed again adopting the convergent model for the beam axis discretization, comparing different cross-section LW models. In both structural cases, the convergence study highlights accurate predictions. Regarding the slender beam case, all cross-sectional models provide perfectly matching results; in the thick beam case, instead, slight discrepancies are observed in the large displacement regime for strongly nonlinear equilibrium states. In the case of thick beam, more evidently with respect to the case of slender beam, a refined cross-section discretization allow for the computation of accurate results. In all load cases considered, a sensible reduction of the relative percentage difference is observed when refined cross-section expansion models are taken into account. Different with respect to the case of slender beam, a slight influence of the beam axis discretization is noted when the thick beam is considered. Vice versa, for slender beams, the computed percentage differences have been found below 1% across all proposed CUF models. In this case, for the computation of accurate displacement distributions, the choices of cross-section expansion or axial kinematic approximation have negligible influence on the displacement distributions. Accurate predictions are obtained with less refined discretization, for instance using only 10 B4 cubic elements along the axis, leading to a reduction of about 95% in DOF compared to the computational effort required by the convergent 3D model. Generally, convergent models have been reached employing 20 B4 cubic elements along the beam axis. Although minor deviations are observed among different discretizations, consistent solutions are achieved, especially with refined cross-section kinematics. Thereafter, the influence of structural theory approximation on the mechanical response of the beam is investigated, comparing different expansion classes. The most accurate cross-section expansion model, that exploits 24L16 subdomains, is now considered for comparison purposes, analyzing the influence of the theory of structure approximation in the case of ESLm. In the following, the pure LWm and 3D FE models are compared against the numerical solution obtained with TE models, considering the multilayered beam as an homogenized structure and the cross-section displacement field is approximated by means of higher-order Taylor polynomials. The proposed results will be compared, for both slender and thick beam, with respect to the reference ABAQUS solutions, comparing again the relative percentage difference and the total DOF required by the simulations. In the case of ESLm, the convergent beam axis model is adopted, i.e., 20 B4 cubic elements. Table 7.17 shows, for the slender beam case ($L/h = 100$), the non-dimensional transverse displacement $\bar{u}_z$ again computed at the load application point, comparing results obtained with different TE models against the corresponding LE models and 3D ABAQUS reference. The same comparison for the thick beam case ($L/h = 10$) is proposed in Table 7.18. Finally, Fig. 7.30 displays the full equilibrium paths obtained with higher-order TE models for both structural configuration considered. From the proposed results, accurate solutions are found even with lower-order ESLm in the slender beam case, whereas for the thick beam, the use of higher-order models is required to correctly compute the nonlinear equilibrium states.

		$u_z(P)/L$				
B4	**Expansion**	**F = 10 N**	**F = 20 N**	**F = 30 N**	**F = 40 N**	**DOFs**
10	3 L9	$0.31503^{(2.75\%)}$	$0.53003^{(2.34\%)}$	$0.65552^{(2.55\%)}$	$0.73188^{(2.41\%)}$	1953
	3 L16	$0.31488^{(2.79\%)}$	$0.52975^{(2.39\%)}$	$0.65514^{(2.61\%)}$	$0.73140^{(2.48\%)}$	3720
	6 L9	$0.31511^{(2.72\%)}$	$0.53021^{(2.31\%)}$	$0.65577^{(2.52\%)}$	$0.73217^{(2.37\%)}$	3627
	6 L16	$0.31489^{(2.79\%)}$	$0.52977^{(2.39\%)}$	$0.65517^{(2.61\%)}$	$0.73143^{(2.47\%)}$	7068
	12 L9	$0.31665^{(2.25\%)}$	$0.53335^{(1.73\%)}$	$0.66011^{(1.87\%)}$	$0.73758^{(1.65\%)}$	6045
	12 L16	$0.31731^{(2.04\%)}$	$0.53484^{(1.46\%)}$	$0.66242^{(1.53\%)}$	$0.74070^{(1.24\%)}$	12369
	24 L9	$0.31720^{(2.08\%)}$	$0.53457^{(1.51\%)}$	$0.66203^{(1.58\%)}$	$0.74022^{(1.30\%)}$	10881
	24 L16	$0.31784^{(1.88\%)}$	$0.53610^{(1.22\%)}$	$0.66464^{(1.20\%)}$	$0.74402^{(0.79\%)}$	22971
15	3 L9	$0.31528^{(2.67\%)}$	$0.53042^{(2.27\%)}$	$0.65594^{(2.49\%)}$	$0.73230^{(2.36\%)}$	2898
	3 L16	$0.31514^{(2.71\%)}$	$0.53016^{(2.32\%)}$	$0.65561^{(2.54\%)}$	$0.73189^{(2.41\%)}$	5520
	6 L9	$0.31543^{(2.63\%)}$	$0.53074^{(2.21\%)}$	$0.65637^{(2.43\%)}$	$0.73281^{(2.29\%)}$	5382
	6 L16	$0.31516^{(2.71\%)}$	$0.53023^{(2.31\%)}$	$0.65569^{(2.53\%)}$	$0.73200^{(2.40\%)}$	10488
	12 L9	$0.31750^{(1.99\%)}$	$0.53481^{(1.46\%)}$	$0.66183^{(1.61\%)}$	$0.73948^{(1.40\%)}$	8970
	12 L16	$0.31860^{(1.65\%)}$	$0.53723^{(1.02\%)}$	$0.66548^{(1.07\%)}$	$0.74438^{(0.75\%)}$	18354
	24 L9	$0.31836^{(1.72\%)}$	$0.53666^{(1.12\%)}$	$0.66467^{(1.19\%)}$	$0.74336^{(0.88\%)}$	16146
	24 L16	$0.31946^{(1.38\%)}$	$0.53944^{(0.61\%)}$	$0.66937^{(0.49\%)}$	$0.75020^{(0.03\%)}$	34086
20	3 L9	$0.31541^{(2.63\%)}$	$0.53060^{(2.24\%)}$	$0.65612^{(2.46\%)}$	$0.73247^{(2.33\%)}$	3843
	3 L16	$0.31528^{(2.67\%)}$	$0.53038^{(2.28\%)}$	$0.65584^{(2.51\%)}$	$0.73212^{(2.38\%)}$	7320
	6 L9	$0.31561^{(2.57\%)}$	$0.53103^{(2.16\%)}$	$0.65668^{(2.38\%)}$	$0.73312^{(2.25\%)}$	7137
	6 L16	$0.31533^{(2.66\%)}$	$0.53050^{(2.26\%)}$	$0.65600^{(2.48\%)}$	$0.73232^{(2.35\%)}$	13908
	12 L9	$0.31807^{(1.81\%)}$	$0.53571^{(1.30\%)}$	$0.66279^{(1.47\%)}$	$0.74050^{(1.26\%)}$	11895
	12 L16	$0.31963^{(1.33\%)}$	$0.53901^{(0.69\%)}$	$0.66764^{(0.75\%)}$	$0.74704^{(0.39\%)}$	24339
	24 L9	$0.31920^{(1.46\%)}$	$0.53806^{(0.86\%)}$	$0.66630^{(0.95\%)}$	$0.74533^{(0.62\%)}$	21411
	24 L16	$0.32088^{(0.94\%)}$	$0.54224^{(0.09\%)}$	$0.67323^{(0.08\%)}$	$0.75558^{(0.75\%)}$	45201
ABQ	8190 C3D20R	0.32393	0.54275	0.67269	0.74997	115314

Table 7.15: Cantilever Mooney-Rivlin multilayered beam: convergence analysis for the case $L/h = 10$. Comparison between 1D CUF and 3D ABAQUS solutions, for different load conditions. In brackets, the percentage difference between model results is proposed.

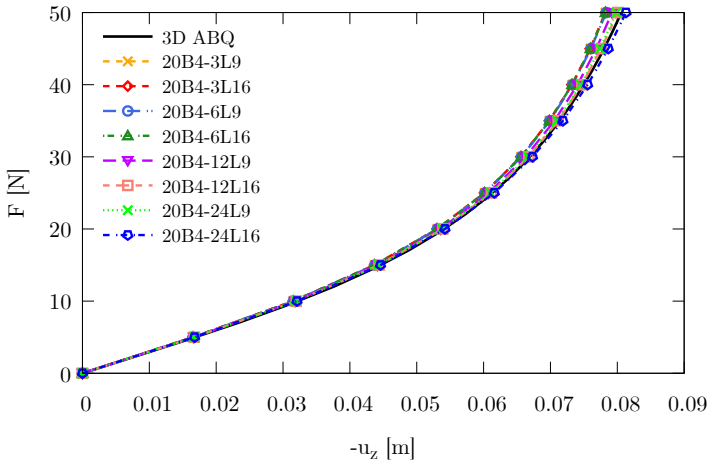

Figure 7.28: Cantilever Mooney-Rivlin multilayered beam, case $L/h = 10$: equilibrium paths for the thick beam computed, adopting 20 B4 along the beam axis.

		$\mathbf{u_z(P)/L}$				
B4	**Expansion**	**F = 0.2 N**	**F = 0.4 N**	**F = 0.6 N**	**F = 0.8 N**	**DOFs**
10	3 L9	$0.49028^{(0.15\%)}$	$0.66983^{(0.12\%)}$	$0.74601^{(0.11\%)}$	$0.78720^{(0.11\%)}$	1953
	3 L16	$0.48472^{(1.28\%)}$	$0.66559^{(0.75\%)}$	$0.74285^{(0.54\%)}$	$0.78466^{(0.43\%)}$	3720
	6 L9	$0.49028^{(0.15\%)}$	$0.66983^{(0.12\%)}$	$0.74601^{(0.11\%)}$	$0.78720^{(0.11\%)}$	3627
	6 L16	$0.49028^{(0.15\%)}$	$0.66983^{(0.12\%)}$	$0.74601^{(0.11\%)}$	$0.78720^{(0.11\%)}$	7068
	12 L9	$0.49028^{(0.15\%)}$	$0.66984^{(0.12\%)}$	$0.74602^{(0.11\%)}$	$0.78720^{(0.11\%)}$	6045
	12 L16	$0.49029^{(0.15\%)}$	$0.66984^{(0.12\%)}$	$0.74602^{(0.11\%)}$	$0.78720^{(0.11\%)}$	12369
	24 L9	$0.49029^{(0.15\%)}$	$0.66984^{(0.12\%)}$	$0.74602^{(0.11\%)}$	$0.78720^{(0.11\%)}$	10881
	24 L16	$0.49029^{(0.15\%)}$	$0.66984^{(0.12\%)}$	$0.74602^{(0.11\%)}$	$0.78720^{(0.11\%)}$	22971
15	3 L9	$0.49055^{(0.10\%)}$	$0.67015^{(0.07\%)}$	$0.74637^{(0.06\%)}$	$0.78760^{(0.06\%)}$	2898
	3 L16	$0.48499^{(1.23\%)}$	$0.66592^{(0.71\%)}$	$0.74321^{(0.49\%)}$	$0.78507^{(0.38\%)}$	5520
	6 L9	$0.49056^{(0.10\%)}$	$0.67016^{(0.07\%)}$	$0.74637^{(0.06\%)}$	$0.78760^{(0.06\%)}$	5382
	6 L16	$0.49056^{(0.09\%)}$	$0.67016^{(0.07\%)}$	$0.74637^{(0.06\%)}$	$0.78760^{(0.06\%)}$	10488
	12 L9	$0.49056^{(0.09\%)}$	$0.67016^{(0.07\%)}$	$0.74638^{(0.06\%)}$	$0.78760^{(0.06\%)}$	8970
	12 L16	$0.49056^{(0.09\%)}$	$0.67016^{(0.07\%)}$	$0.74638^{(0.06\%)}$	$0.78761^{(0.06\%)}$	18354
	24 L9	$0.49056^{(0.09\%)}$	$0.67016^{(0.07\%)}$	$0.74638^{(0.06\%)}$	$0.78761^{(0.06\%)}$	16146
	24 L16	$0.49056^{(0.09\%)}$	$0.67016^{(0.07\%)}$	$0.74638^{(0.06\%)}$	$0.78761^{(0.06\%)}$	34086
20	3 L9	$0.49068^{(0.07\%)}$	$0.67029^{(0.05\%)}$	$0.74651^{(0.05\%)}$	$0.78774^{(0.04\%)}$	3843
	3 L16	$0.49068^{(0.07\%)}$	$0.67029^{(0.05\%)}$	$0.74651^{(0.05\%)}$	$0.78774^{(0.04\%)}$	7320
	6 L9	$0.49068^{(0.07\%)}$	$0.67029^{(0.05\%)}$	$0.74651^{(0.05\%)}$	$0.78774^{(0.04\%)}$	7137
	6 L16	$0.49068^{(0.07\%)}$	$0.67029^{(0.05\%)}$	$0.74651^{(0.05\%)}$	$0.78774^{(0.04\%)}$	13908
	12 L9	$0.49069^{(0.07\%)}$	$0.67029^{(0.05\%)}$	$0.74651^{(0.05\%)}$	$0.78774^{(0.04\%)}$	11895
	12 L16	$0.49069^{(0.07\%)}$	$0.67030^{(0.05\%)}$	$0.74651^{(0.05\%)}$	$0.78775^{(0.04\%)}$	24339
	24 L9	$0.49069^{(0.07\%)}$	$0.67030^{(0.05\%)}$	$0.74651^{(0.05\%)}$	$0.78774^{(0.04\%)}$	21411
	24 L16	$0.49069^{(0.07\%)}$	$0.67030^{(0.05\%)}$	$0.74652^{(0.05\%)}$	$0.78775^{(0.04\%)}$	45201
ABQ	31320 C3D20R	0.49102	0.67065	0.74685	0.78806	445758

Table 7.16: Cantilever Mooney-Rivlin multilayered beam: convergence analysis for the case $L/h = 100$. Comparison between 1D CUF and 3D ABAQUS solutions, for different load conditions. In brackets, the percentage difference between model results is proposed.

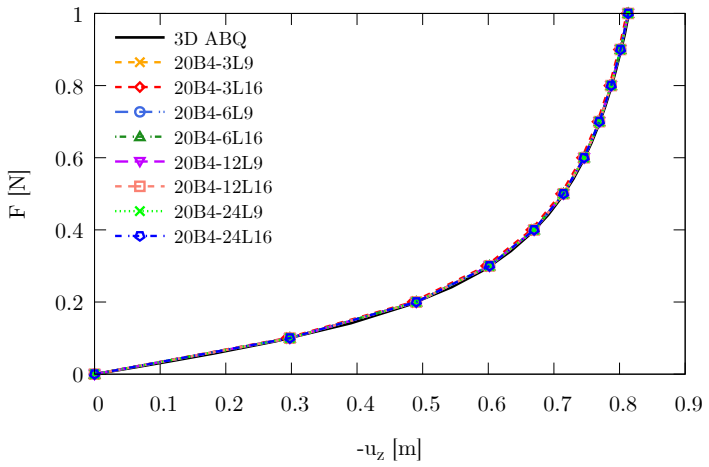

Figure 7.29: Cantilever Mooney-Rivlin multilayered beam, case $L/h = 100$: equilibrium paths for the slender beam, adopting 20 B4 along the beam axis.

B4	Expansion	F=0.2 N	F=0.4 N	F=0.6 N	F=0.8 N	DOFs
10	24 L16	$0.49029^{(0.15\%)}$	$0.66984^{(0.12\%)}$	$0.74602^{(0.11\%)}$	$0.78720^{(0.11\%)}$	22971
15	24 L16	$0.49056^{(0.09\%)}$	$0.67016^{(0.07\%)}$	$0.74638^{(0.06\%)}$	$0.78761^{(0.06\%)}$	34086
20	24 L16	$0.49069^{(0.07\%)}$	$0.67030^{(0.05\%)}$	$0.74652^{(0.05\%)}$	$0.78775^{(0.04\%)}$	45201
20	TE1	$0.45957^{(6.41\%)}$	$0.64623^{(3.64\%)}$	$0.72864^{(2.44\%)}$	$0.77361^{(1.83\%)}$	549
	TE2	$0.49051^{(0.10\%)}$	$0.67014^{(0.08\%)}$	$0.74638^{(0.06\%)}$	$0.78762^{(0.06\%)}$	1098
	TE3	$0.49053^{(0.10\%)}$	$0.67017^{(0.07\%)}$	$0.74641^{(0.06\%)}$	$0.78766^{(0.05\%)}$	1830
	TE4	$0.49055^{(0.10\%)}$	$0.67018^{(0.07\%)}$	$0.74642^{(0.06\%)}$	$0.78767^{(0.05\%)}$	2745
ABQ	31320 C3D20R	0.49102	0.67065	0.74685	0.78806	445758

Table 7.17: Cantilever Mooney-Rivlin multilayered beam, case $L/h = 100$: comparison between LW models and ESL models results, for different load conditions. Non-dimensional transversal displacement $\bar{u}_z$ measured at the point-load application.

B4	Expansion	F = 10 N	F = 20 N	F = 30 N	F = 40 N	DOFs
10	24 L16	$0.31784^{(1.88\%)}$	$0.53610^{(1.22\%)}$	$0.66464^{(1.20\%)}$	$0.74402^{(1.67\%)}$	22971
15	24 L16	$0.31946^{(1.38\%)}$	$0.53944^{(0.61\%)}$	$0.66937^{(0.49\%)}$	$0.75020^{(0.85\%)}$	34086
20	24 L16	$0.32088^{(0.94\%)}$	$0.54224^{(0.09\%)}$	$0.67323^{(0.08\%)}$	$0.75558^{(0.14\%)}$	45201
20	TE1	$0.28572^{(11.80\%)}$	$0.49389^{(9.00\%)}$	$0.62281^{(7.41\%)}$	$0.70373^{(6.99\%)}$	549
	TE2	$0.31289^{(3.41\%)}$	$0.52639^{(3.01\%)}$	$0.65099^{(3.23\%)}$	$0.72672^{(3.95\%)}$	1098
	TE3	$0.31387^{(3.11\%)}$	$0.52791^{(2.73\%)}$	$0.65270^{(2.97\%)}$	$0.72848^{(3.72\%)}$	1830
	TE4	$0.31376^{(3.14\%)}$	$0.52758^{(2.80\%)}$	$0.65215^{(3.05\%)}$	$0.72776^{(3.82\%)}$	2745
ABQ	8190 C3D20R	0.32393	0.54275	0.67269	0.75663	115314

Table 7.18: Cantilever Mooney-Rivlin multilayered beam, case $L/h = 10$: comparison between LE models results and TE models results, for different load conditions. Non-dimensional transversal displacement $\bar{u}_z$ measured at the point-load application.

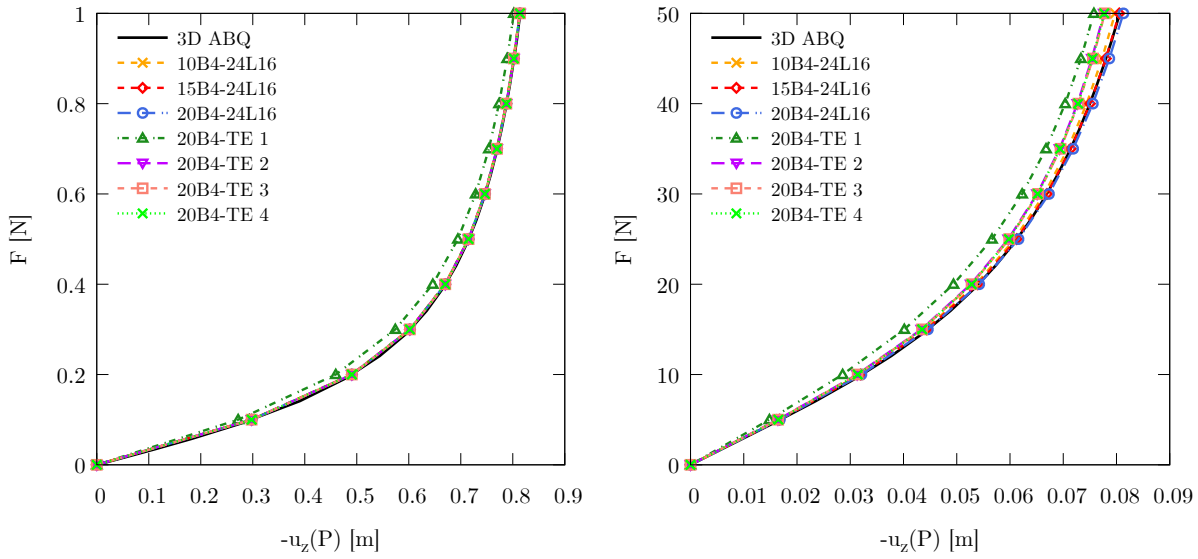

(a) Slender beam, $L/h = 100$

(b) Thick beam, $L/h = 10$

Figure 7.30: Cantilever Mooney-Rivlin multilayered beam: equilibrium paths for the slender and thick beam, comparison between LE expansion models and TE expansion models.

These results can be justified by the geometrical assumption made and the performances of low- to higher-order TE models, particularly effective when slender structures are considered, differently with respect to thick beams where higher-order models are required to describe the cross-sectional behavior and the computation of accurate solutions. Consequently, higher relative errors between TE and 3D reference solutions are observed for the thick beam due to the stronger influence of transverse shear effects, taken into account in the Mooney-Rivlin material models. From a computational standpoint, TE models also provide an evident efficiency advantage when displacement predictions are analyzed, observing for example the fourth-order TE formulation, that requires 2745 DOF. This corresponds to a reduction of approximately 99.4% in the total number of DOFs, while still providing accurate results. Such computational cost reduction while preserving accuracy is obtained by overcoming the aspect-ratio limitations inherent to 3D solid elements and by exploiting the enrichment of the cross-section displacement behavior independently of the beam axis discretization model.
For further considerations, a detailed three-dimensional stress analysis of the two considered beams is now performed. The accuracy of the present one-dimensional beam models with three-dimensional capabilities is now discussed both in terms of ESLm and fully LWm through a detailed stress analysis. Stress compatibility and equilibrium conditions are now discussed, particularly under moderate and large deformation regimes. In the following, all the proposed results are obtained considering 20 B4 cubic elements along the beam axis, and the previously defined cross-section expansion models, to investigate the influence of the theory of structure approximation on the prediction of three-dimensional stress states. Figure 7.31 shows the through-the-thickness distribution of the Cauchy stress components for the thick beam with slender ratio $L/a = 10$, evaluated at $x = a/2$ (symmetry section) and $y/L = 0.25$, comparing the results against the 3D ABAQUS reference solution, obtained without any superimposed kinematic assumption. For further investigations, Fig. 7.32 compares the results obtained in terms of Cauchy stress σ_{yz} and the corresponding first Piola–Kirchhoff stress component P_{yz} under different load conditions. The same comparison is proposed for the case of slender beam, where the three-dimensional Cauchy's stress components are depicted in Fig. 7.33. The analogous comparison between transverse shear Cauchy's σ_{yz} and first Piola-Kirchhoff stress component P_{yz} is reported for the slender beam in Fig. 7.34. Regarding the normal stress components, excellent agreement with the 3D reference is obtained for σ_{yy} and σ_{zz}, while minor deviations are observed in σ_{xx}, where a dependence of the cross-section kinematic model is found, since related to the out-of-plane bending behavior. Particularly, in the case of transverse shear stress σ_{yz}, non-zero values at the beam edges and non-symmetric distributions are detected, differently with respect to the case of first Piola-Kirchhoff stress component. The results clearly demonstrate that equilibrium and stress compatibility are rigorously satisfied by the first Piola–Kirchhoff tensor, defined in the material configuration and reference frame, where the balance laws are strictly defined. Due to balance, the compatibility and continuity equation on the transverse normal and shear stress component in the thickness direction, where the anisotropy is encountered, are enforced in the reference configuration. Additionally, in the case of the Cauchy stress tensor, compatibility is not strictly guaranteed under conservative loading, since equilibrium is expressed in the deformed configuration and the highly deformed structural states are then computed to balance external loads at deformed outer boundaries. As a result, non-symmetric distributions of σ_{yz} naturally arise to guarantee translational force equilibrium in highly deformed states. This outcome reflects, in the present work, the intrinsic link between the Cauchy stress tensor and the deformation gradient, which directly measures the moderate-to-large strain regime. The asymmetric shear stress distribution can therefore be interpreted as the internal mechanism by which the structure balances the applied external loads through shear force redistribution.

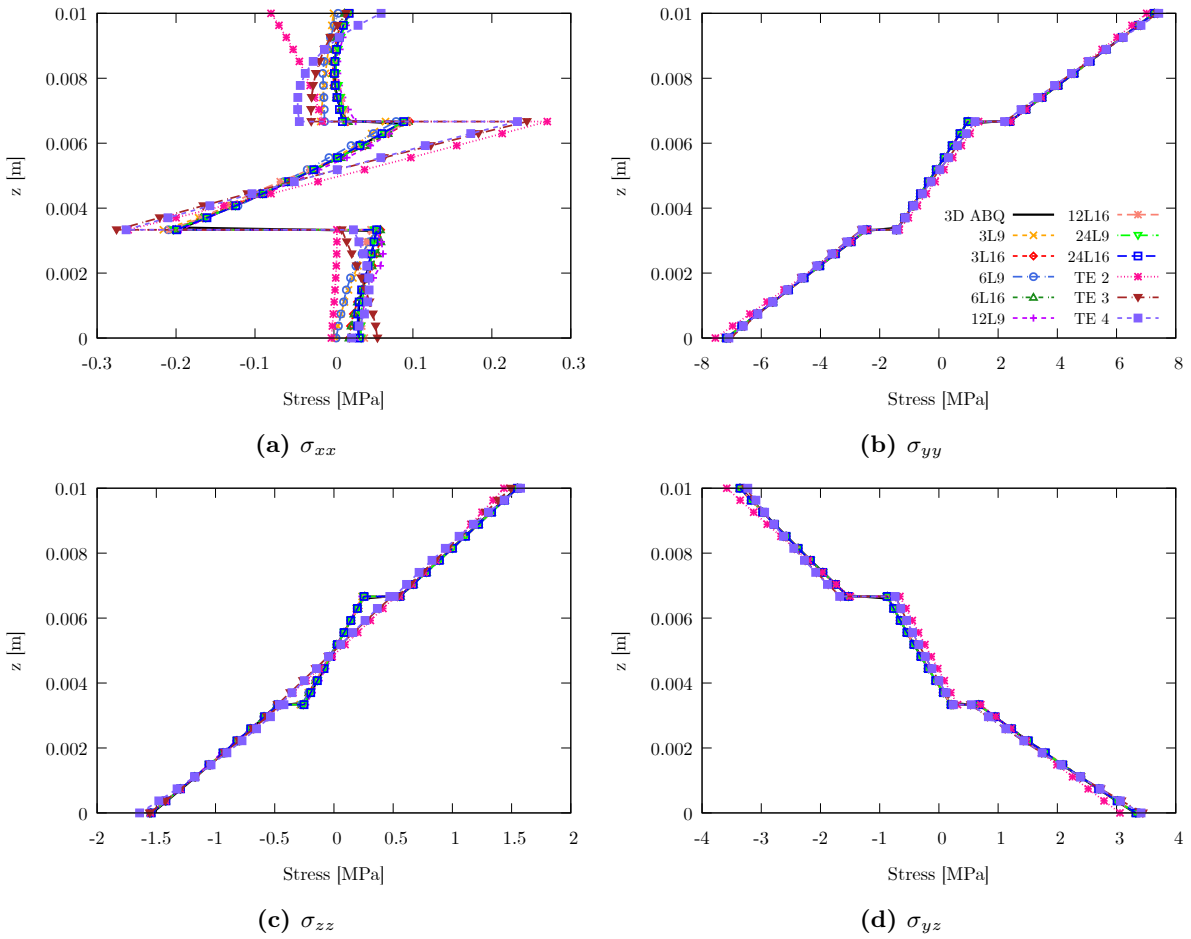

(a) σ_{xx} **(b)** σ_{yy}

(c) σ_{zz} **(d)** σ_{yz}

Figure 7.31: Cantilever Mooney-Rivlin multilayered beam, case $L/h = 10$: through-the-thickness stress distribution along for $y/L = 0.25$ and $x = a/2$. Comparison between 1D CUF solution and ABAQUS 3D reference.

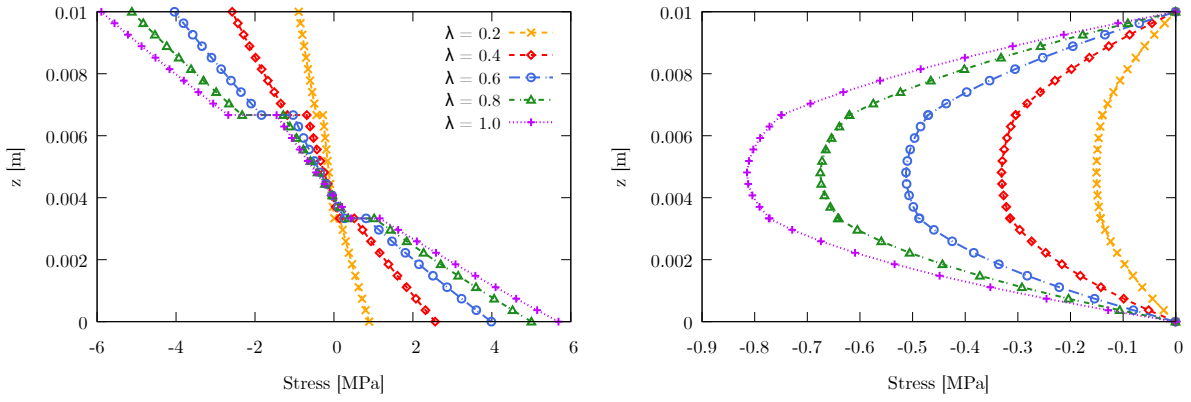

(a) σ_{yz} **(b)** P_{yz}

Figure 7.32: Cantilever Mooney-Rivlin multilayered beam, case $L/h = 10$: through-the-thickness distribution of the transverse stress components σ_{yz} and P_{yz} for $y/L = 0.25$ and $x = a/2$, for different load conditions.

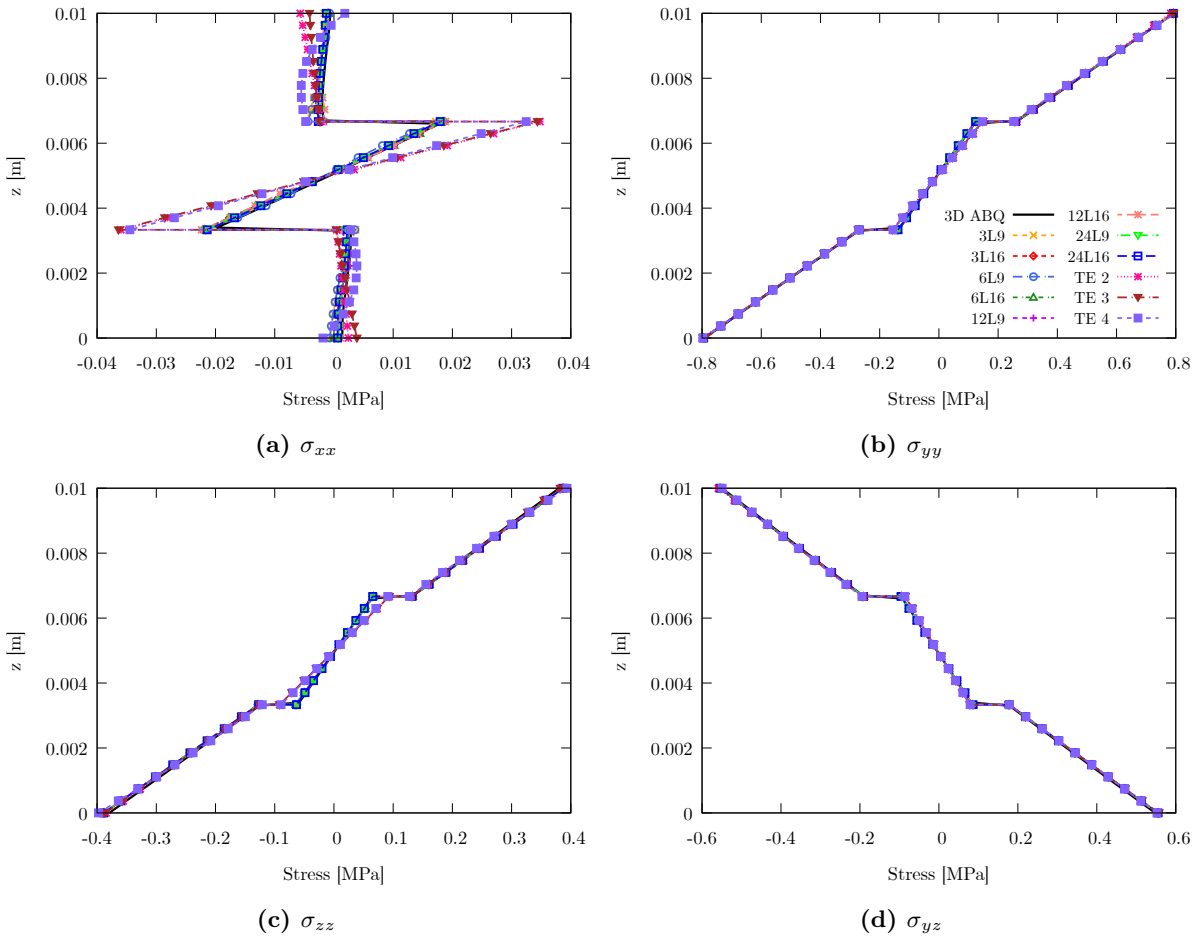

(a) σ_{xx} **(b)** σ_{yy}

(c) σ_{zz} **(d)** σ_{yz}

Figure 7.33: Cantilever Mooney-Rivlin multilayered beam, case $L/h = 100$: through-the-thickness stress distribution along for $y/L = 0.25$ and $x = a/2$. Comparison between 1D CUF solution and ABAQUS 3D reference.

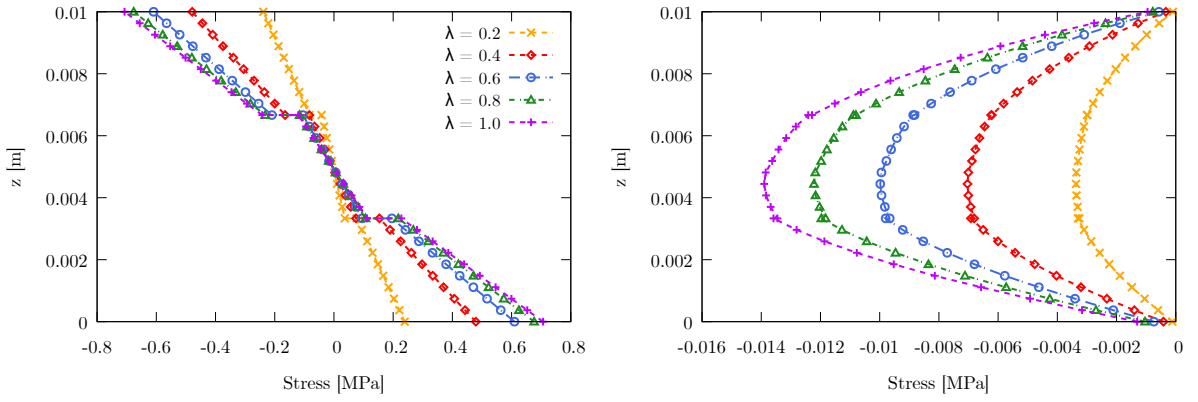

(a) σ_{yz} **(b)** P_{yz}

Figure 7.34: Cantilever Mooney-Rivlin multilayered beam, case $L/h = 100$: through-the-thickness distribution of the transverse stress components σ_{yz} and P_{yz} for $y/L = 0.25$ and $x = a/2$, for different load conditions.

7.7 Multilayered nearly-incompressible plate under pressure

The accuracy and the efficiency of the the proposed higher-order models for isotropic hyperelasticity is now established in the case of 2D plate models. A multilayered rectangular clamped plate, of total lateral sides $a = 20$ mm and $b = 10$ mm, is made of two soft layers of thickness $h = 1$ mm. In both cases, the structure is made by two different layers, with thickness $h_l = h/2$. The structure is considered made of two different Mooney-Rivlin material, whose hyperelastic strain energy function model is given in Eq. (7.12), adopting again two distinct sets of model's constants taken from available literature material properties [193] and listed in Table 7.19.

$$\Psi \quad = \quad \Psi_{vol}(J) + \bar{\Psi}(\bar{I}_1, \bar{I}_2) = \frac{1}{D_1}(J-1)^2 + c_{10}(\bar{I}_1 - 3) + c_{01}(\bar{I}_2 - 3) \tag{7.12}$$

To investigate the influence of kinematic models and theory of structure approximation on the static and linearized vibration response of the present plate structures higher-order theories along the plate thickness are considered, and increasing number of parabolic Q9 finite element along the reference mid-surface. The plate is considered clamped at $y = 0$ mm plane and subjected to a uniform transversal pressure applied at the top-surface. The geometrical features and boundary conditions describing the present scenario are illustrated in Fig. 7.35.

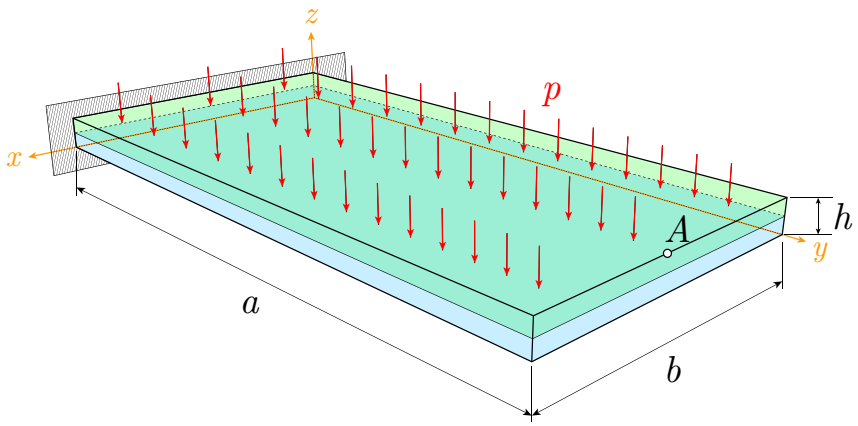

Figure 7.35: Multilayered cantilever plate: geometrical features and boundary conditions consiered.

This case study is proposed to assess the capabilities and the accuracy of higher-order plate formulation. Specifically, both the effects of kinematics models along the plate mid-surface discretization and, particularly, the influence of the theory of structure approximation adopted on the static mechanical response of the hyperelastic multilayered plate are investigated, analyzing displacements and natural frequencies, and discussing the results in terms of compatibility requirements. The aim of the present case study is to assess the accuracy and the capabilities of LW models, since the efficiency of TE-based models will been extensively analyzed in the following sections. The detailed analysis of TE models for plate structure will be directly proposed in the case of anisotropic hyperelastic structural analysis. The 3D FEM ABAQUS solution is adopted to compare the present model's capabilities with direct solution of the equilibrium equation given by standard FE approaches. In the following, for the thick plate, the discretization is performed with 12800 C3D20R hexahedral elements (20-node quadratic brick elements with reduced integration). For the thin plate, instead, 32160 C3D20R elements are adopted due to aspect ratio constraints inherent to classical 3D formulation.

	c_{10} [MPa]	c_{01} [MPa]	$D_1 = 2/k$ [MPa^{-1}]
Bottom layer	$1.1240 \cdot 10^{-2}$	$1.1240 \cdot 10^{-2}$	0.628
Top layer	$2.0780 \cdot 10^{-2}$	$1.9875 \cdot 10^{-2}$	0.445

Table 7.19: Multilayered cantilever plate: material properties considered.

In the meanwhile, the 2D CUF models employed, for both thick and slender beams, adopt $N \times N$ parabolic Q9 finite elements along the plate mid-surface; instead LWm are comprehensively analyzed, adopting N_E LE2 parabolic (three-node) or LE3 cubic (four-node) subdomains for each material layer. As proposed in the previous analyses, the accuracy is expressed through the percentage difference between 1D CUF and 3D ABAQUS results, while the computational cost is measured by the total number of DOF required by the adopted discretization. The first analysis considered is the convergence analysis with respect to the natural frequencies of the structure around the trivial equilibrium state, thus the undamped vibration problem is analyzed as first assessment case of multilayered plate elements. Tables 7.21 and 7.20 summarize the convergence analysis results for the two plates with different thickness, in which the influence of mid-surface discretization and theory of structure approximation on the first five natural frequencies is extensively analyzed. From the proposed convergence analysis, higher relative percentage differences are noted in the case of the thick plate, as expected, due to the classical arguments in modeling of thick structures. Small relative percentage difference, below 3% are noted within all the cases, demonstrating the consistency of the present approach. From the proposed results, a strong influence of the plate mid-surface discretization is noted, differently considering the theory of structure approximation that provide reliable and similar results for all expansion models considered.

	Mesh	**Expansion**	**Mode 1**	**Mode 2**	**Mode 3**	**Mode 4**	**Mode 5**	**DOF**
A	10x10	1 LE2 / layer	$6.330^{(-2.64\%)}$	$24.537^{(-0.23\%)}$	$38.744^{(-2.24\%)}$	$51.883^{(-1.54\%)}$	$79.917^{(-0.51\%)}$	6615
B		2 LE2 / layer	$6.329^{(-2.65\%)}$	$24.529^{(-0.26\%)}$	$38.735^{(-2.27\%)}$	$51.881^{(-1.54\%)}$	$79.883^{(-0.55\%)}$	11907
C		1 LE3 / layer	$6.329^{(-2.65\%)}$	$24.528^{(-0.26\%)}$	$38.735^{(-2.27\%)}$	$51.881^{(-1.54\%)}$	$79.882^{(-0.55\%)}$	9261
D		2 LE3 / layer	$6.329^{(-2.65\%)}$	$24.528^{(-0.26\%)}$	$38.734^{(-2.27\%)}$	$51.881^{(-1.54\%)}$	$79.880^{(-0.55\%)}$	17199
E	15x15	1 LE2 / layer	$6.353^{(-2.29\%)}$	$24.593^{(0.01\%)}$	$38.896^{(-1.86\%)}$	$52.011^{(-1.30\%)}$	$80.143^{(-0.22\%)}$	14415
F		2 LE2 / layer	$6.352^{(-2.30\%)}$	$24.586^{(-0.03\%)}$	$38.888^{(-1.88\%)}$	$52.010^{(-1.30\%)}$	$80.110^{(-0.27\%)}$	25947
G		1 LE3 / layer	$6.352^{(-2.30\%)}$	$24.585^{(-0.03\%)}$	$38.888^{(-1.88\%)}$	$52.010^{(-1.30\%)}$	$80.108^{(-0.27\%)}$	20181
H		2 LE3 / layer	$6.352^{(-2.30\%)}$	$24.585^{(-0.03\%)}$	$38.887^{(-1.88\%)}$	$52.010^{(-1.30\%)}$	$80.107^{(-0.27\%)}$	37479
I	20x20	1 LE2 / layer	$6.403^{(-1.51\%)}$	$24.722^{(0.53\%)}$	$39.264^{(-0.93\%)}$	$52.295^{(-0.76\%)}$	$80.685^{(0.45\%)}$	25215
J		2 LE2 / layer	$6.402^{(-1.52\%)}$	$24.714^{(0.50\%)}$	$39.256^{(-0.95\%)}$	$52.294^{(-0.76\%)}$	$80.652^{(0.41\%)}$	45837
K		1 LE3 / layer	$6.402^{(-1.52\%)}$	$24.714^{(0.49\%)}$	$39.255^{(-0.95\%)}$	$52.294^{(-0.76\%)}$	$80.650^{(0.41\%)}$	35301
L		2 LE3 / layer	$6.402^{(-1.52\%)}$	$24.714^{(0.49\%)}$	$39.255^{(-0.95\%)}$	$52.294^{(-0.76\%)}$	$80.649^{(0.41\%)}$	65559
	ABAQUS	12800 C3D20	6.501	24.592	39.633	52.694	80.323	187467

Table 7.20: Multilayered cantilever plate, thick case, modal analysis: convergence analysis for the first five natural frequencies [Hz]. Comparison between 2D CUF and 3D ABAQUS model results. In brackets, the percentage difference is given.

	Mesh	Expansion	Mode 1	Mode 2	Mode 3	Mode 4	Mode 5	DOF
A	10x10	1 LE2 / layer	$0.654^{(-0.09\%)}$	$2.589^{(1.05\%)}$	$4.096^{(1.53\%)}$	$8.604^{(1.54\%)}$	$11.795^{(4.14\%)}$	6615
B		2 LE2 / layer	$0.654^{(-0.09\%)}$	$2.589^{(1.05\%)}$	$4.095^{(1.52\%)}$	$8.604^{(1.54\%)}$	$11.795^{(4.14\%)}$	11907
C		1 LE3 / layer	$0.654^{(-0.10\%)}$	$2.589^{(1.05\%)}$	$4.095^{(1.52\%)}$	$8.604^{(1.54\%)}$	$11.795^{(4.14\%)}$	9261
D		2 LE3 / layer	$0.654^{(-0.10\%)}$	$2.589^{(1.05\%)}$	$4.095^{(1.52\%)}$	$8.604^{(1.54\%)}$	$11.795^{(4.14\%)}$	17199
E	15x15	1 LE2 / layer	$0.645^{(-1.38\%)}$	$2.573^{(0.46\%)}$	$4.014^{(-0.49\%)}$	$8.511^{(0.43\%)}$	$11.393^{(0.60\%)}$	14415
F		2 LE2 / layer	$0.645^{(-1.38\%)}$	$2.573^{(0.45\%)}$	$4.014^{(-0.49\%)}$	$8.510^{(0.43\%)}$	$11.393^{(0.59\%)}$	25947
G		1 LE3 / layer	$0.645^{(-1.38\%)}$	$2.573^{(0.45\%)}$	$4.014^{(-0.49\%)}$	$8.510^{(0.43\%)}$	$11.393^{(0.59\%)}$	20181
H		2 LE3 / layer	$0.645^{(-1.39\%)}$	$2.573^{(0.45\%)}$	$4.014^{(-0.49\%)}$	$8.510^{(0.43\%)}$	$11.393^{(0.59\%)}$	37479
I	20x20	1 LE2 / layer	$0.641^{(-2.01\%)}$	$2.565^{(0.14\%)}$	$3.979^{(-1.38\%)}$	$8.468^{(-0.07\%)}$	$11.231^{(-0.84\%)}$	25215
J		2 LE2 / layer	$0.641^{(-2.01\%)}$	$2.565^{(0.14\%)}$	$3.978^{(-1.38\%)}$	$8.468^{(-0.07\%)}$	$11.230^{(-0.84\%)}$	45837
K		1 LE3 / layer	$0.641^{(-2.01\%)}$	$2.565^{(0.14\%)}$	$3.978^{(-1.38\%)}$	$8.468^{(-0.07\%)}$	$11.230^{(-0.85\%)}$	35301
L		2 LE3 / layer	$0.641^{(-2.01\%)}$	$2.565^{(0.14\%)}$	$3.978^{(-1.38\%)}$	$8.468^{(-0.07\%)}$	$11.230^{(-0.85\%)}$	65559
	ABAQUS	12800 C3D20	0.654	2.562	4.034	8.474	11.326	298878

Table 7.21: Multilayered cantilever plate, thin case, modal analysis: convergence analysis for the first five natural frequencies [Hz]. Comparison between 2D CUF and 3D ABAQUS model results. In brackets, the percentage difference is given.

Furthermore, the proposed twelve models enumerated in the depicted Tables, the nonlinear static analysis of the cantilever plate under uniform transversal pressure is carried out. The results are proposed in terms of load-displacement equilibrium curves, denoting with p the applied value of the transversal pressure, measuring instead the transversal u_z displacement component at the point "A" indicated in Fig. 7.35. The results of the present static analysis are reported in Fig. 7.36, where the obtained equilibrium paths are depicted.

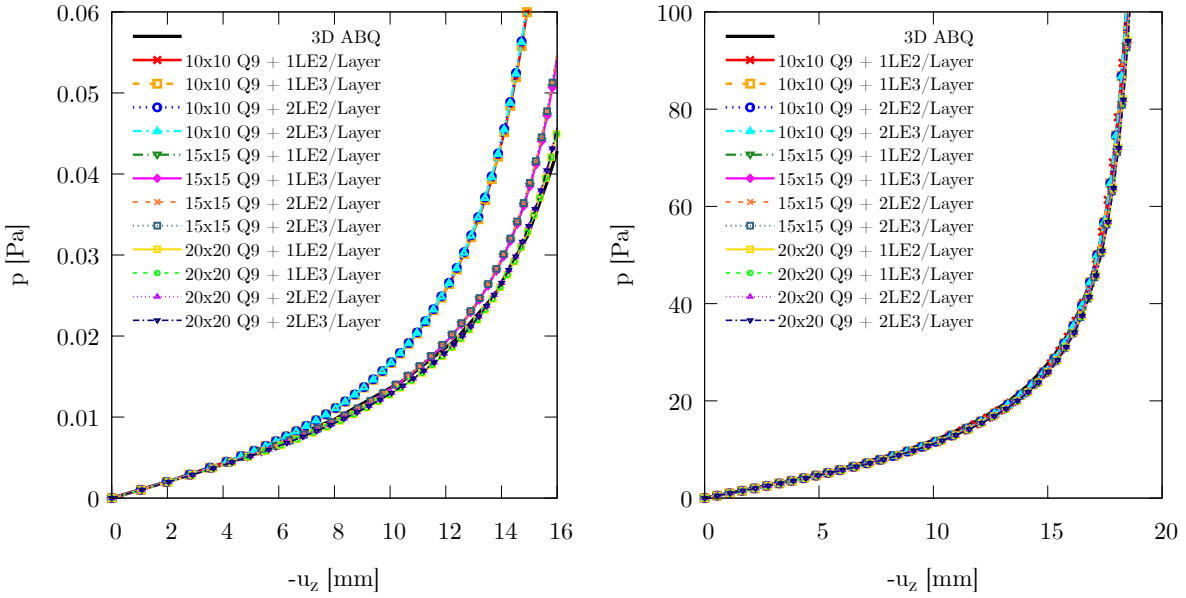

(a) Thin plate $h = 0.1$ mm

(b) Thick plate $h = 1$ mm

Figure 7.36: Multilayered cantilever plate: equilibrium path obtained both in the case of thin and thick plate. Comparison between higher-order 2D CUF models and 3D ABAQUS results.

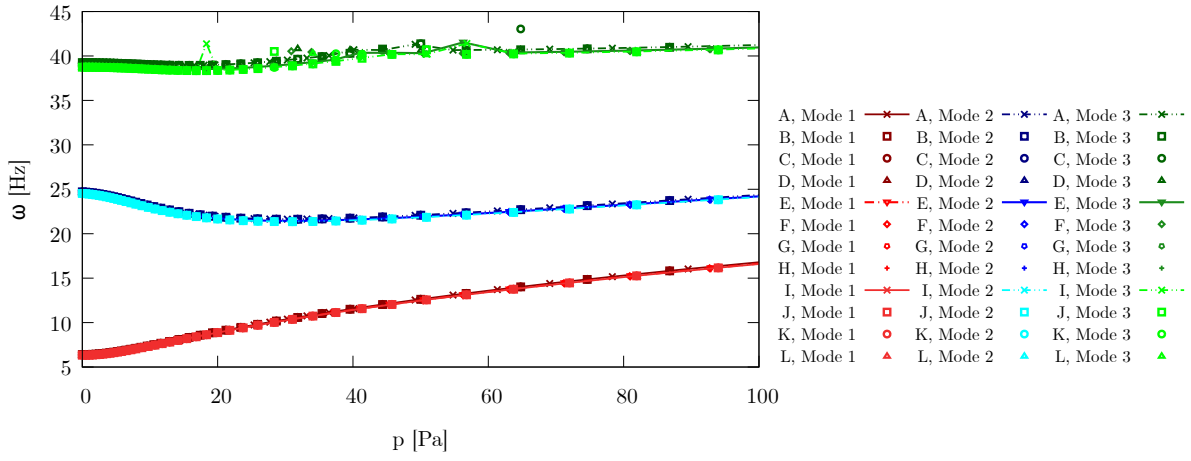

(a) Modes 1-3

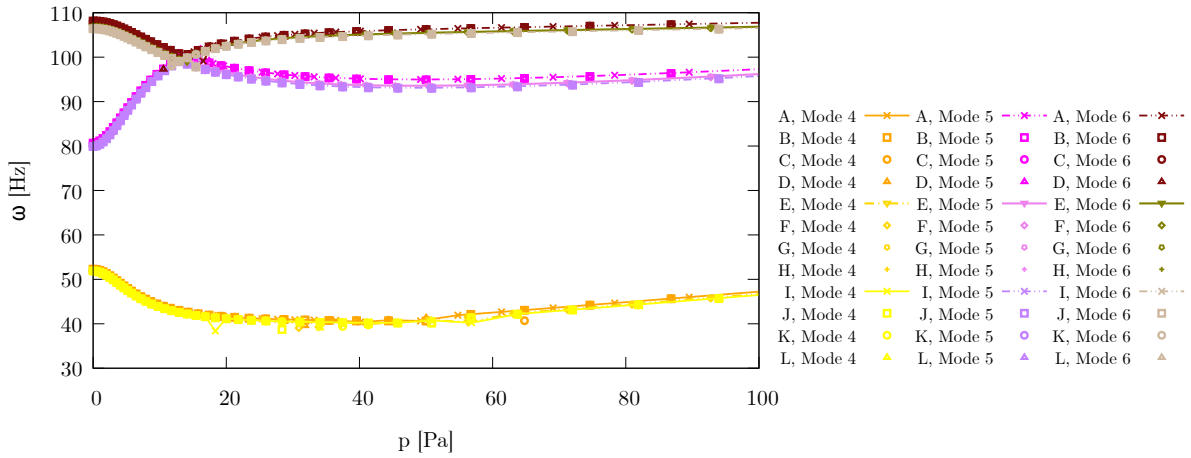

(b) Modes 4-6

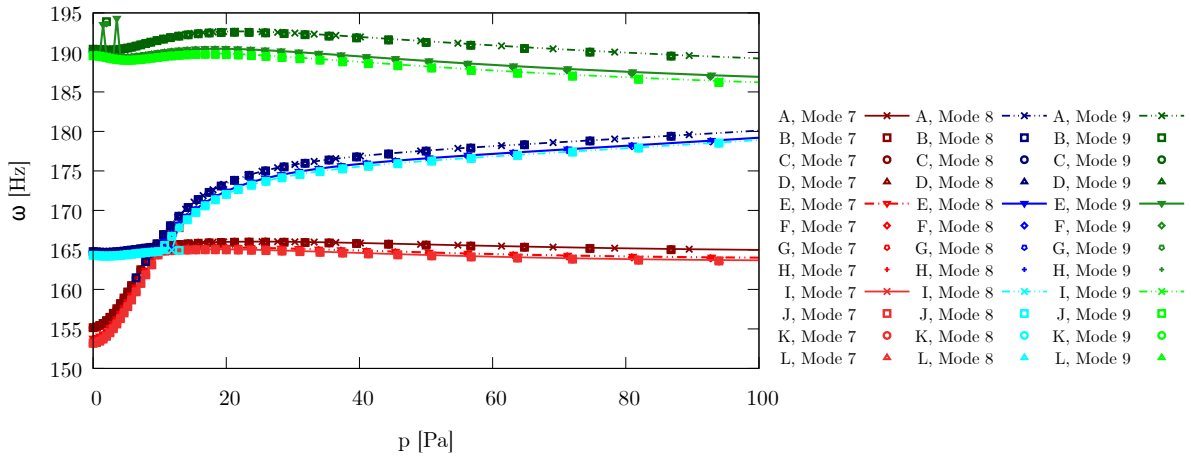

(c) Modes 7-9

Figure 7.37: Multilayered cantilever plate, thick case: variation of the first nine natural frequencies along the equilibrium path, large strain regime. Influence of structural theory and reference mid-surface discretization.

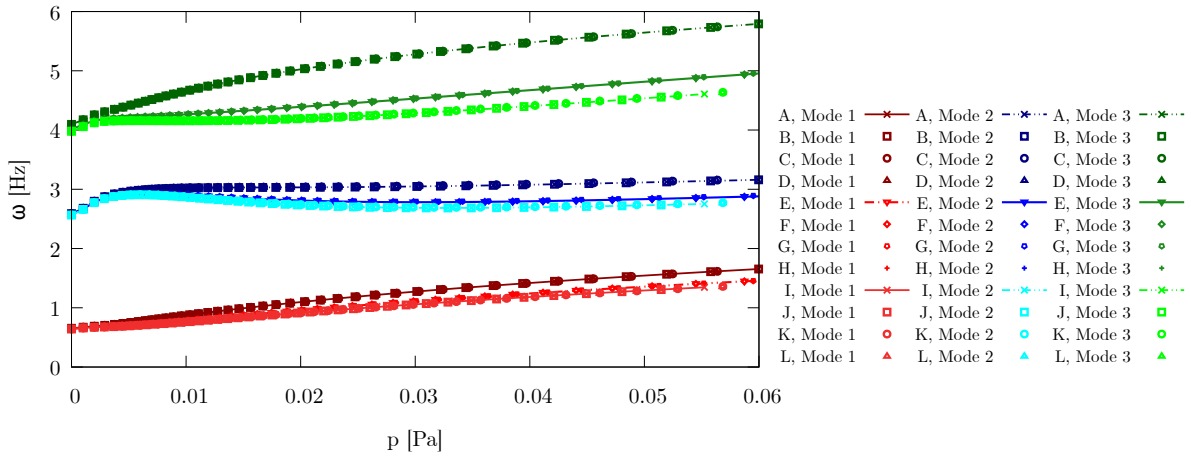

(a) Modes 1-3

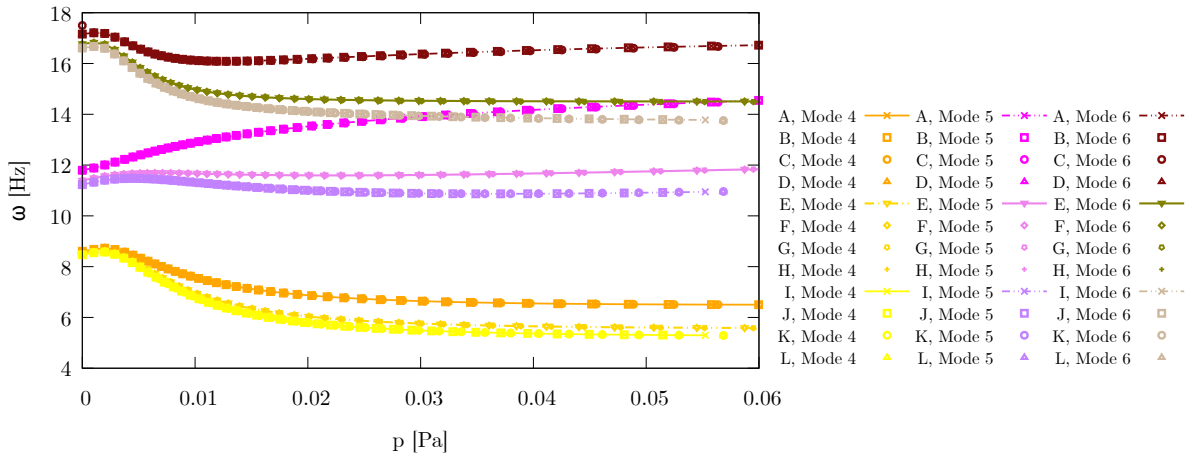

(b) Modes 4-6

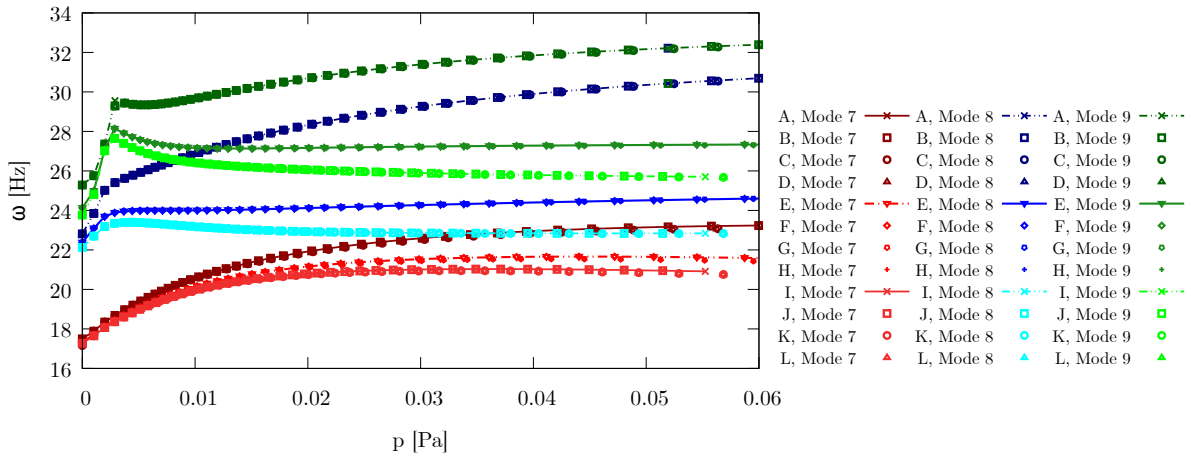

(c) Modes 7-9

Figure 7.38: Multilayered cantilever plate, thin case: variation of the first nine natural frequencies along the equilibrium path, large strain regime. Influence of structural theory and reference mid-surface discretization.

7.8 Discussion

The proposed results suggest that:

- The isotropic hyperelastic constitutive law has been successfully implemented in the proposed higher-order CUF modeling of soft materials and structures under an invariant approach, enabling the adoption of any hyperelastic model by providing the derivatives of the chosen strain energy function. The present implementation has been first validated through the uniaxial and simple shear tests, problems for which analytical reference solutions are available, demonstrating its accuracy and robustness.

- Some limitations of ESLm have been highlighted in the present study. While accurate displacement distributions and natural frequencies are provided, inconsistencies in the three-dimensional stress states have been observed due to the intrinsic restrictions of TE-based approaches. Fully layer-wise models, on the other hand, have provided accurate predictions of both displacement and stress fields, thereby guaranteeing a powerful tool for analyzing problems where stress resolution is critical.

- The present implementation of higher-order beam and plate models can handle the representation of complex constitutive behaviors in multilayered structures. Considering different cross-section or thickness polynomial expansion of the displacement field, the present higher-order models accurately capture the complex three-dimensional stress state while fulfilling the C_z^0 requirements. Moreover, the compatibility and equilibrium conditions have been correctly verified in terms of the first Piola–Kirchhoff stress tensor, the reference stress measure in a hyperelastic, total Lagrangian framework, where the equilibrium balance laws are written in the material reference frame.

- The computational efficiency and accuracy of the proposed approach have been demonstrated with several case studies involving the large strain analysis of isotropic soft structures. Convergence analyses have proven that the adoption of higher-order kinematic models along the beam axis or reference plate mid-surface allows for the definition of computationally advantageous FE models with fewer DOF, while maintaining high levels of accuracy, both in the static and modal analysis. In addition, the use of higher-order structural theories and LWm guarantees the computation of accurate predictions with less refined discretizations without affecting the solution quality;

- The convergence analysis carried out in terms of natural frequencies has shown that accurate predictions can be obtained with coarser discretizations, but with a sensible dependence on the material compressibility. For nearly incompressible materials, which typically enforce the adoption of refined discretization models where pure displacement-based formulations are adopted, higher-order models provide a consistent alternative to reduce computational effort while preserving accuracy;

- The linearized vibration analyses revealed that the dependence of natural frequencies on applied pre-stretch can exhibit ambiguous trends, which are strongly influenced by material compressibility. For compressible hyperelastic models, a decrease in natural frequencies was observed with increasing pre-stretch. This phenomenon can be explained by the reduction of internal stress levels at higher strains, which in turn lowers the geometric stiffness contributions to the tangent stiffness matrix.

Chapter 8

Transversely isotropic hyperelasticity

In the present chapter, the numerical results obtained for the static and linearized vibration analysis of transversely isotropic hyperelastic structures are proposed. The proposed higher-order finite element modeling approach is exploited to simulate continuously fibre-reinforced structures. The present model is validated comparing the results against reference solutions available in literature or numerical references obtained via classical FE hexahedral solutions. In particular, the numerical modeling of these structures is analyzed in terms of displacement and stress distributions to analyze the effects of the discretization model, the influence of the theory of structure approximation on the investigated physical quantities. Finally, the results are analyzed in terms of compatibility conditions and equilibrium equations, to discuss the C_z^0 requirements in laminated multilayered structures in terms of reference and actual stress measures.

8.1 Validation procedure of the present methodology

The first case study analyzed is the simple shear test of an incompressible, fiber-reinforced cubic specimen. As discussed in Sec. 7.1, an analytical solution is available for this simple configuration. These analysis are carried out to validate the proposed methodology, comparing the results with the reference exact solution. This patch-test problem is analyzed with a single element discretization, to assess the consistency of the model implemented. For this reason, in the following, both 1D beam and 2D plate model will be discussed. The mathematical models adopted in this patch-test employ 1L4-1B2 linear models in the case of beam CUF element, and 1Q4-1LE2 linear models in the case of plate CUF element, as already described in Sec. 7.1 . A graphical representation of the two discretization model adopted is provided in Fig. 7.1, instead the geometry and boundary conditions are depicted in Fig. 8.1.

The material model considered is a refined version of the classical Holzapfel-Gasser-Ogden (HGO) model for fiber-reinforced materials [26], analyzed in Mendez at al. [194]. This revisited model has been proposed to investigate the physical meaning of I_5 invariant, since the invariant I_4 is consistently defined in the kinematic framework. The strain energy function adopted is written as:

$$\Psi = \Psi_{vol}(J) + \Psi_{iso}(\bar{I}_1, \bar{I}_2) + \Psi_{ani}(\bar{I}_1, \bar{I}_2, \bar{I}_4, \bar{I}_5) \tag{8.1}$$

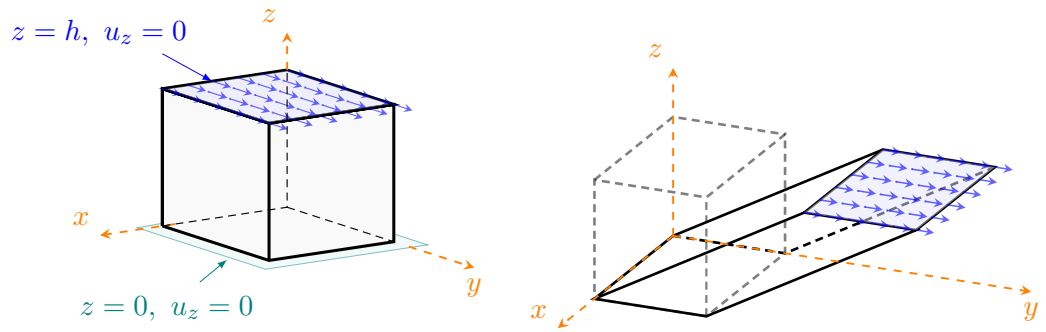

(a) Geometry and boundary conditions **(b)** Deformed configuration

Figure 8.1: Transversely isotropic hyperelasticity, validation test: simple shear test case, geometry considered and boundary conditions applied.

The three terms of the decoupled strain energy function Eq. (8.1) are then introduced:

$$\Psi_{vol}(I_3) = \frac{k}{2}(J-1)^2 \tag{8.2}$$

$$\Psi_{iso}(I_1, I_2, I_3) = \frac{c_1}{2}(\bar{I}_1 - 1) \tag{8.3}$$

$$\Psi_{aniso}(I_3, I_4, I_5) = \frac{c_2}{2c_3}\left[e^{c_3(\bar{I}_4-1)^2} - 1\right] + \frac{c_4}{2c_5}\left[e^{c_5(\bar{I}_5-\bar{I}_4{}^2)^2} - 1\right] \tag{8.4}$$

The material constants adopted in the following are taken from the reference work, and listed in Table 8.1.
The analytical solution of the approached problem is here carried out. Considering the known expression of the deformation gradient, one can straightforwardly derive the expression of the right Cauchy-Green strain tensor and, consequently the analytic expression of the additional pseudo-invariant of the deformation, function of the fiber reinforcement direction, it is possible then to derive analytically the second Piola-Kirchhoff stress tensor by the constitutive law written in the material reference frame, by the Piola transform of the first Piola-Kirchhoff and Cauchy's stress tensors. Let $\boldsymbol{X} = (x^0, y^0, z^0)$ the coordinates of the generic material point of the cube in the material configuration, denote also with $\boldsymbol{x} = (x, y, z)$ the coordinate of the deformed particle measured again the material configuration. For a simple shear test the deformation field components for the shear problem in the $y - z$ plane are:

$$\boldsymbol{\chi}(x^0, y^0, z^0) : \begin{cases} x = x^0 \\ y = y^0 + \gamma z^0 \\ z = z^0 \end{cases} \qquad \mathbf{F} = \frac{\partial \boldsymbol{\chi}}{\partial \boldsymbol{X}} = \begin{bmatrix} 1 & 0 & 0 \\ 0 & 1 & \gamma \\ 0 & 0 & 1 \end{bmatrix} \qquad \mathbf{C} = \mathbf{F}^T\mathbf{F} = \begin{bmatrix} 1 & 0 & 0 \\ 0 & 1 & \gamma \\ 0 & \gamma & 1+\gamma^2 \end{bmatrix}$$

where γ is a positive real number. Again, since incompressibility is imposed, thus $J = \det \mathbf{F} = 1$, the volumetric component of $\mathbf{S}$ is identically null. Supposing that $\boldsymbol{a}_0 = (a_x, a_y, a_z)^T$, the invariants and pseudo-invariants required for the computation of physical quantities are:

$$\begin{cases} I_1 = 3 + \gamma^2 \\ I_2 = -3 - 2\gamma^2 \\ I_3 = 1 \end{cases} \qquad \begin{cases} I_4 = a_x^2 + a_y(a_y + a_z\gamma) + a_z(a_y\gamma + a_z(1+\gamma^2)) \\ I_5 = a_x^2 + a_y(a_y + a_z\gamma^2) + a_z(a_y\gamma^2 + a_z(1+\gamma^2)^2) \end{cases}$$

Computing now the derivatives of strain energy function Eq. (8.1), characterized by the three terms imposed for isochoric, volumetric and anisotropic components, the analytic expression of the stress tensor **S** is obtained. In the proposed analysis, normal and transverse shear stress components are analyzed, whose analytical expression are given by:

$$\begin{aligned} S_{xx} &= \frac{1}{3}\Bigg[4a_x^2\left(\frac{\partial\bar{\Psi}}{\partial\bar{I}_4}+2\frac{\partial\bar{\Psi}}{\partial\bar{I}_5}\right)-2\left(\frac{\partial\bar{\Psi}}{\partial\bar{I}_1}\gamma^2+a_z^2\left(\frac{\partial\bar{\Psi}}{\partial\bar{I}_4}+2\frac{\partial\bar{\Psi}}{\partial\bar{I}_5}+\left(\frac{\partial\bar{\Psi}}{\partial\bar{I}_4}+6\frac{\partial\bar{\Psi}}{\partial\bar{I}_5}\right)\gamma^2+2\frac{\partial\bar{\Psi}}{\partial\bar{I}_5}\gamma^4\right)+\right. \\ &+ \left. a_y^2\left(\frac{\partial\bar{\Psi}}{\partial\bar{I}_4}+2\frac{\partial\bar{\Psi}}{\partial\bar{I}_5}(1+\gamma^2)\right)+2a_ya_z\gamma\left(\frac{\partial\bar{\Psi}}{\partial\bar{I}_4}+2\frac{\partial\bar{\Psi}}{\partial\bar{I}_5}(2+\gamma^2)\right)\right)\Bigg] \end{aligned} \tag{8.5}$$

$$\begin{aligned} S_{yy} &= \frac{1}{3}\Bigg[-2(a_x^2-2a_y^2+a_z^2)\left(\frac{\partial\bar{\Psi}}{\partial\bar{I}_4}+2\frac{\partial\bar{\Psi}}{\partial\bar{I}_5}\right)-4a_ya_z\left(\frac{\partial\bar{\Psi}}{\partial\bar{I}_4}+\frac{\partial\bar{\Psi}}{\partial\bar{I}_5}\right)\gamma+ \\ &- 2\left(4\frac{\partial\bar{\Psi}}{\partial\bar{I}_1}+a_x^2\left(\frac{\partial\bar{\Psi}}{\partial\bar{I}_4}+2\frac{\partial\bar{\Psi}}{\partial\bar{I}_5}\right)+(a_y^2+2a_z^2)\left(\frac{\partial\bar{\Psi}}{\partial\bar{I}_4}+4\frac{\partial\bar{\Psi}}{\partial\bar{I}_5}\right)\right)\gamma^2-4a_ya_z\left(\frac{\partial\bar{\Psi}}{\partial\bar{I}_4}+6\frac{\partial\bar{\Psi}}{\partial\bar{I}_5}\right)\gamma^3+ \\ &- 2\left(\frac{\partial\bar{\Psi}}{\partial\bar{I}_1}+2a_y^2\frac{\partial\bar{\Psi}}{\partial\bar{I}_5}+a_z^2\left(\frac{\partial\bar{\Psi}}{\partial\bar{I}_4}+8\frac{\partial\bar{\Psi}}{\partial\bar{I}_5}\right)\right)\gamma^4-8a_ya_z\frac{\partial\bar{\Psi}}{\partial\bar{I}_5}\gamma^5-4a_z^2\frac{\partial\bar{\Psi}}{\partial\bar{I}_5}\gamma^6\Bigg] \end{aligned} \tag{8.6}$$

$$\begin{aligned} S_{zz} &= \frac{1}{3}\Bigg[-2(a_x^2+a_y^2-2a_z^2)\left(\frac{\partial\bar{\Psi}}{\partial\bar{I}_4}+2\frac{\partial\bar{\Psi}}{\partial\bar{I}_5}\right)-4a_ya_z\left(\frac{\partial\bar{\Psi}}{\partial\bar{I}_4}+\frac{\partial\bar{\Psi}}{\partial\bar{I}_5}\right)\gamma+ \\ &- 2\left(\frac{\partial\bar{\Psi}}{\partial\bar{I}_1}+a_z^2\frac{\partial\bar{\Psi}}{\partial\bar{I}_4}+2a_y^2\frac{\partial\bar{\Psi}}{\partial\bar{I}_5}\right)\gamma^2-8a_ya_z\frac{\partial\bar{\Psi}}{\partial\bar{I}_5}\gamma^3-4a_z^2\frac{\partial\bar{\Psi}}{\partial\bar{I}_5}\gamma^4\Bigg] \end{aligned} \tag{8.7}$$

$$S_{xy} = 2a_x\left(a_y\left(\frac{\partial\bar{\Psi}}{\partial\bar{I}_4}+2\frac{\partial\bar{\Psi}}{\partial\bar{I}_5}\right)+a_z\frac{\partial\bar{\Psi}}{\partial\bar{I}_5}\gamma\right) \tag{8.8}$$

Due to the analytical complexity, the full expressions of the Cauchy's stress components are not reported here, as well as the expressions of the first Piola-Kirchhoff stress tensor, although they can be readily computed by the Piola transform:

$$\boldsymbol{\sigma} = \frac{1}{J}\mathbf{F}\mathbf{S}\mathbf{F}^T \tag{8.9}$$

The consistency and capabilities of the present CUF-based methodology are assessed by analyzing the simple shear test in six different fiber orientations, considering different generic fiber reinforcement vectors.

k [kPa]	c_1 [kPa]	c_2 [kPa]	c_3 [-]	c_4 [kPa]	c_5 [-]
$1 \cdot 10^8$	50	831.4	4.241	350.96	6.18

Table 8.1: Transversely isotropic hyperelasticity, validation test: material properties considered.

Figure 8.2 depicts, for each unitary versor $\boldsymbol{a}_0$ considered, the geometrical model of the fiber-reinforcement considered and the 1D CUF finite element adopted. The results, proposed in terms of strain-stress distributions in terms of the shear parameter γ, are here summarized. Figure 8.3(a)-(b) show the comparison between the analytical reference results and the CUF model results, in the case of simple shear test considering the unitary versor $\boldsymbol{a}_0$ along the y axis, respectively for 1D beam and 2D plate models. Figure 8.3(c)-(d) show the same comparison,

respectively for 1D beam and 2D plate models, considering the unitary versor $\boldsymbol{a}_0$ along the x axis. Figure 8.3(e)-(f) show the same comparison, respectively for 1D beam and 2D plate models, considering the unitary versor $\boldsymbol{a}_0$ along the z axis. In all the proposed cases, both 1D beam and 2D plate numerical results perfectly match with the analytical reference solution, in each fiber reinforcement configuration. In this sense, the present transversely isotropic hyperelastic finite element formulation can be considered valid, the analytic solution has been used for validation purposes and the stress-strain constitutive law is verified by the present numerical model. Following Mendez *et al.* [194], additional case studies are considered here. The mechanical response of the cubic specimen is now analyzed for an inclined preferential fiber direction, lying in the (y, z) plane, of an angle θ with respect to the y-axis. Three inclination angles are investigated: $\theta = 30°$, $\theta = 45°$, and $\theta = 60°$. Figure 8.4(a)-(b) show the comparison between the analytical reference results and the CUF model results, in the case of simple shear test considering the unitary versor $\boldsymbol{a}_0 = (0, \cos 30°, \sin 30°)$, respectively for 1D beam and 2D plate models. Figure 8.4(c)-(d) show the same comparison considering the unitary versor $\boldsymbol{a}_0 = (0, \cos 45°, \sin 45°)$. Figure 8.4(e)-(f) show the same comparison, considering the unitary versor $\boldsymbol{a}_0 = (0, \cos 60°, \sin 60°)$. Again, a perfect agreement is observed and both 1D beam and 2D plate numerical results perfectly predict the analytical reference solution, for each fiber reinforcement configuration.

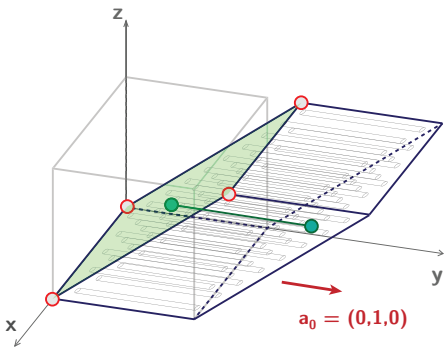

(a) Configuration $\boldsymbol{a}_0 = (0,1,0)$

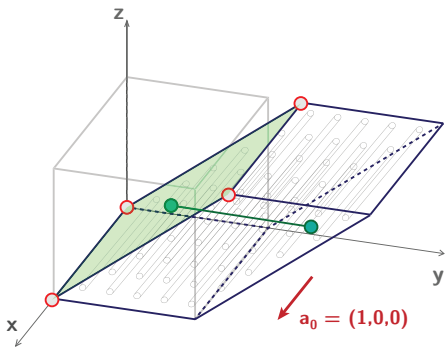

(b) Configuration $\boldsymbol{a}_0 = (1,0,0)$

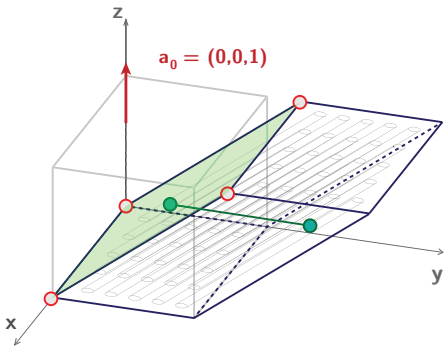

(c) Configuration $\boldsymbol{a}_0 = (0,0,1)$

Figure 8.2: Transversely isotropic hyperelasticity, validation test: fiber distributions considered

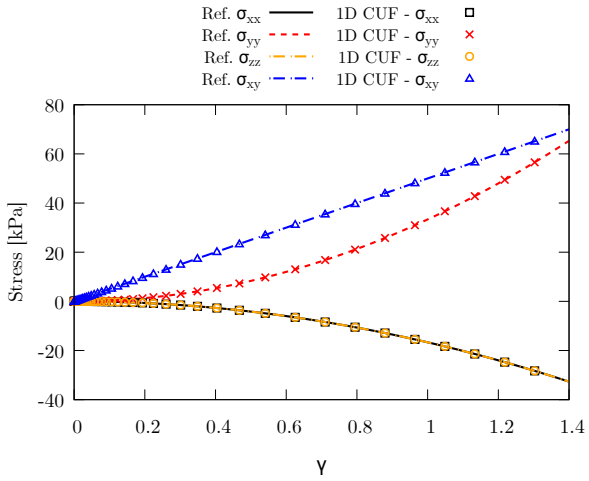

(a) $\boldsymbol{a}_0 = (0,1,0)$, 1D CUF model

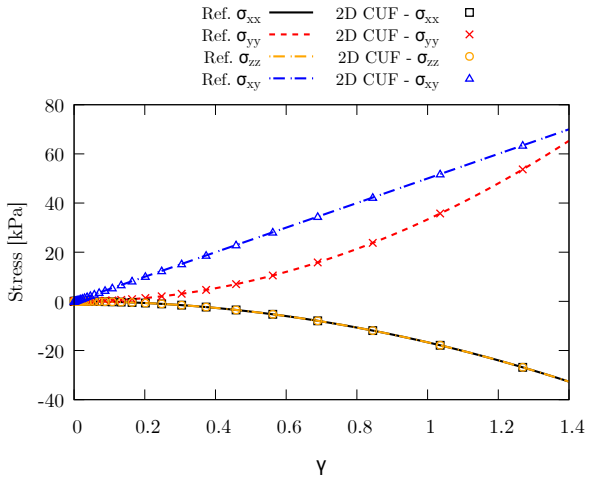

(b) $\boldsymbol{a}_0 = (0,1,0)$, 2D CUF model

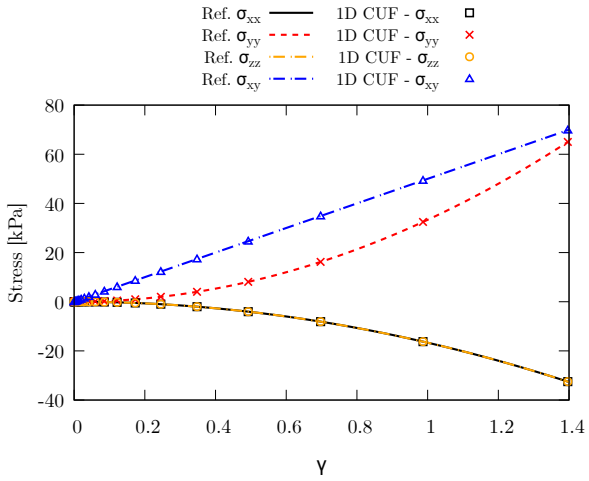

(c) $\boldsymbol{a}_0 = (1,0,0)$, 1D CUF model

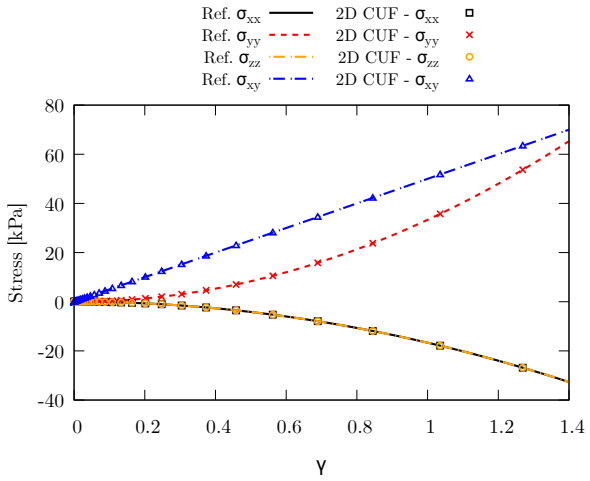

(d) $\boldsymbol{a}_0 = (1,0,0)$, 2D CUF model

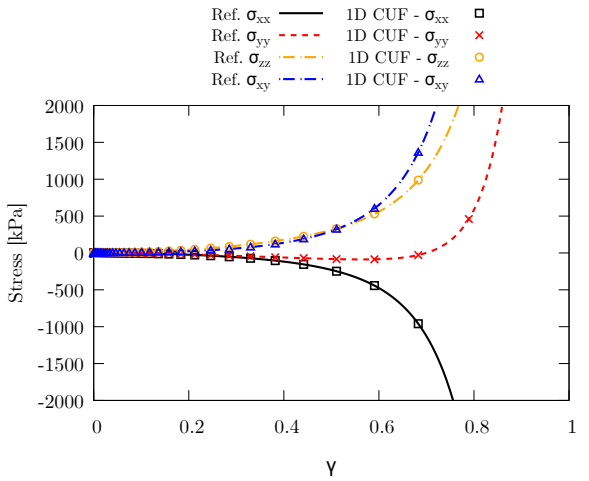

(e) $\boldsymbol{a}_0 = (0,0,1)$, 1D CUF model

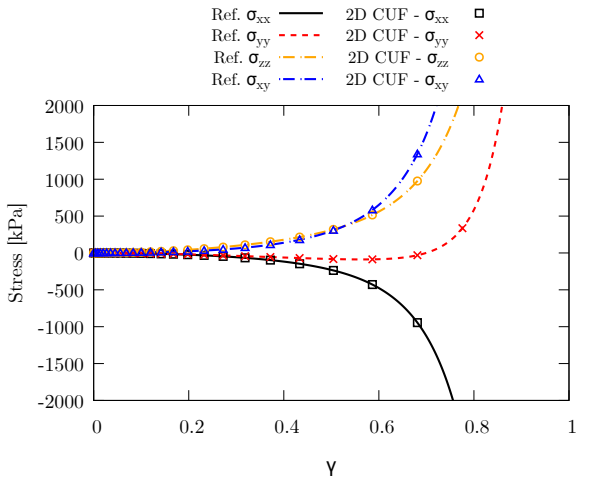

(f) $\boldsymbol{a}_0 = (0,0,1)$, 2D CUF model

Figure 8.3: Transversely isotropic hyperelasticity, validation test: comparison between analytical reference and 1D CUF numerical results. Comparison of different Cauchy's stress component, for different fiber orientations along the three Cartesian axes.

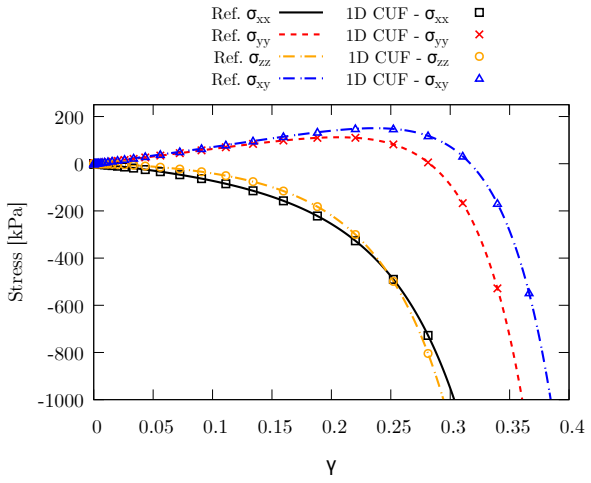

(a) $\boldsymbol{a}_0 = (0, \cos 30°, \sin 30°)$, 1D CUF model

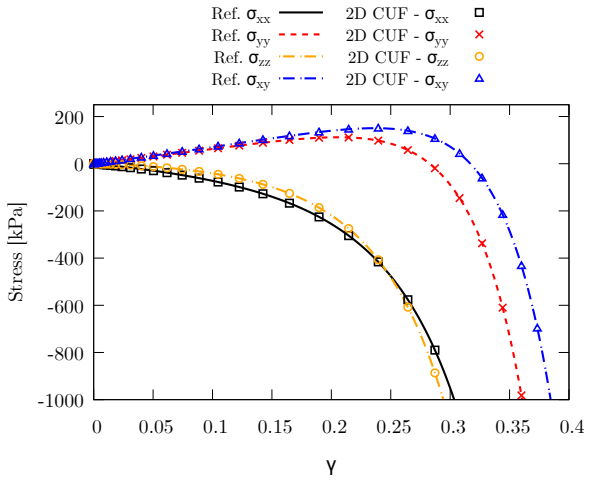

(b) $\boldsymbol{a}_0 = (0, \cos 30°, \sin 30°)$, 2D CUF model

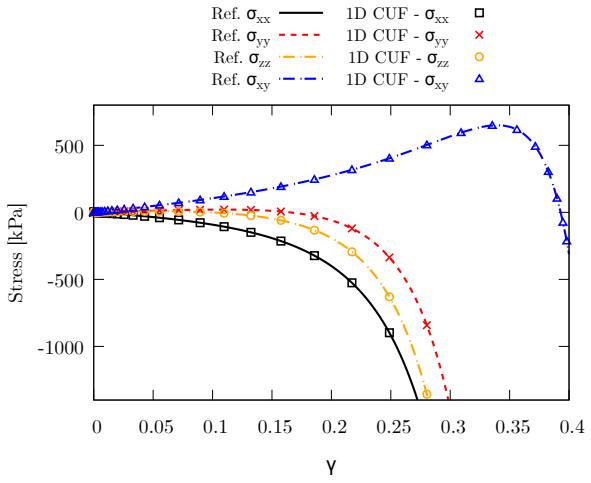

(c) $\boldsymbol{a}_0 = (0, \cos 45°, \sin 45°)$, 1D CUF model

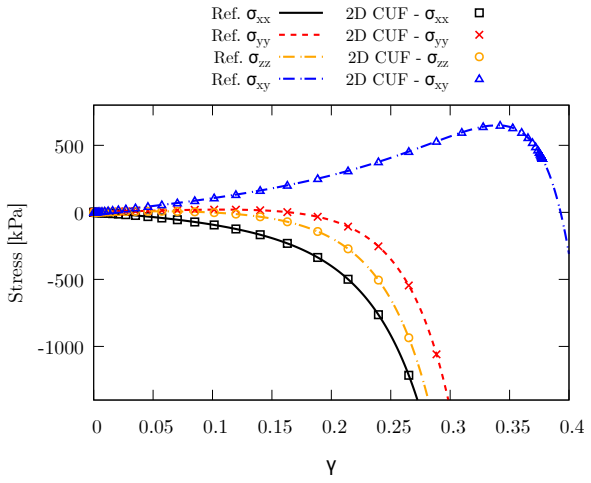

(d) $\boldsymbol{a}_0 = (0, \cos 45°, \sin 45°)$, 2D CUF model

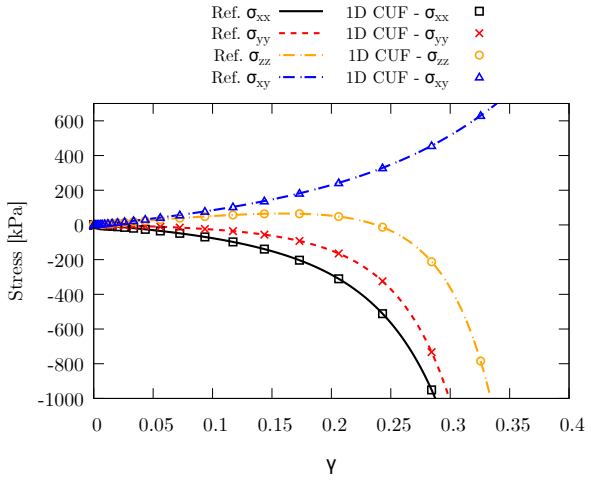

(e) $\boldsymbol{a}_0 = (0, \cos 60°, \sin 60°)$, 1D CUF model

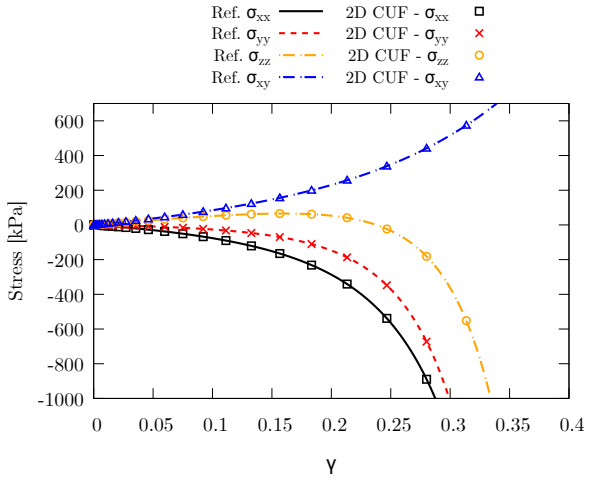

(f) $\boldsymbol{a}_0 = (0, \cos 60°, \sin 60°)$, 2D CUF model

Figure 8.4: Transversely isotropic hyperelasticity, validation test: comparison between analytical reference and 1D CUF numerical results. Comparison of different Cauchy's stress component, for different fiber orientations of type $\boldsymbol{a}_0 = (0, \cos\theta, \sin\theta)$.

8.2 Circular plate under uniform transversal pressure

As a second numerical example, the bending of a clamped circular plate, presented for the first time by Beheshti *et al.* [195] and lately analyzed by Chiaia *et al.* [196] is now discussed. The present implementation of higher-order plate models is employed to analyze 2D structures under large displacements conditions. The plate has a radius of $R = 50$ mm and a thickness of $h = 5$ mm, considered clamped along its lateral surface. The load condition considered is a transverse vertical pressure q_z applied to the top surface. The geometry and boundary conditions are depicted in Fig. 8.5.

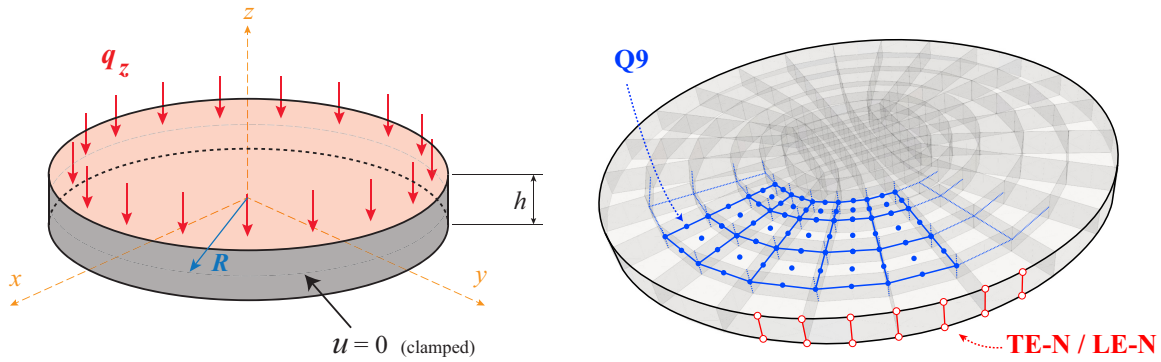

(a) Geometry and boundary conditions. **(b)** Mathematical model description.

Figure 8.5: Circular clamped plate under uniform pressure: geometrical features and discretization adopted

The mechanical response of the plate is investigated for different material conditions: (i) first, an isotropic soft plate is analyzed; (ii) an anisotropic hyperelastic plate with radial and tangential fiber reinforcement distributions is analyzed. The latter material condition is analyzed by means of a refined technique given by the numerical integration procedure. During the computation of integral quantities and FN of FE matrices, the unit vector $\boldsymbol{a}_0$ required for the evaluation of the physical quantities is locally defined at the Gauss integration points for the in-plane interpolation, for each element in the discretization, as illustrated in Fig. 8.6. The material model adopted, considered in [195], exploit the isotropic Neo-Hookean coupled model and a standard quadratic model for the fiber-reinforcement phase:

$$\Psi(\mathbf{C}) = \frac{\mu}{2}(I_1 - 3) + \frac{\lambda}{2}(J-1)^2 - \mu \log J + \gamma(I_4 - 1)^2 \tag{8.10}$$

The material constants consiered are $\mu = 1$ MPa, $\lambda = 4$ MPa $\gamma = 0.375$ MPa. To simulate the plate in the isotropic hyperelastic scenario, the constant γ is considered equal to zero.

8.2.1 Static nonlinear analysis

As a preliminary investigation, a convergence analysis is performed to assess the influence of finite element approximation of the reference mid-surface on the numerical results, as well as the effects of the adopted theory of structure approximation. Different FE discretization adopting Q9 parabolic elements along the reference mid-surface will be considered. Furthermore, the influence of TE models, together with LE models, is assessed. The former will be denoted as TEN (with N indicating the polynomial order), the latter instead as LE2 (parabolic Lagrange

expansion model), and LE3 (cubic Lagrange expansion model). The results obtained with 2D plate CUF elements are compared against available solutions taken from the literature.

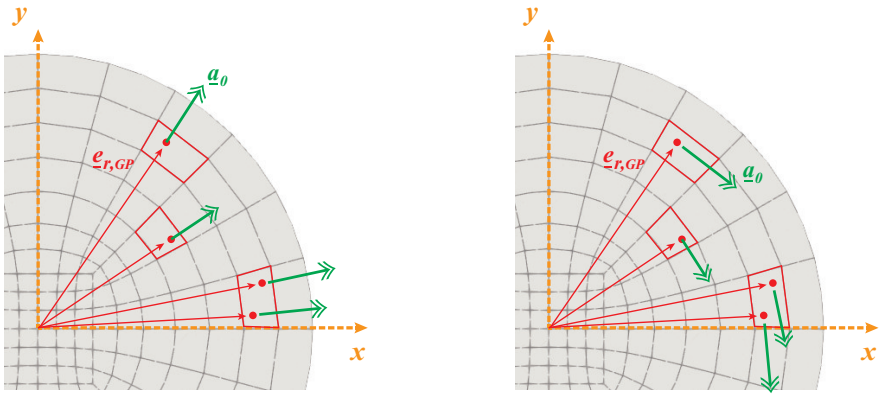

(a) Radial reinforcement. **(b)** Angular reinforcement.

Figure 8.6: Circular clamped plate under uniform pressure, anisotropic case: fiber distribution definition. By exploiting the numerical integration scheme used in the computation of the stiffness matrices, the vector $\boldsymbol{a}_0$ is defined from the physical coordinates of each Gauss integration point, thus allowing a globally accurate distribution of fibers to be obtained.

Figure 8.7(a) presents the equilibrium paths of the clamped plate with radial fiber distribution, measuring the transverse vertical displacement at the plate center (evaluated at the mid-surface), analyzing the influence of the mid-surface discretization. The proposed results are compared against reference solutions [195]. Each proposed model provide the equilibrium paths in good agreement with the reference solution. The same case study is analyzed by TR models, comparing the proposed solutions to LE models and reference literature solution in Fig. 8.7(b), reporting the same displacement component. Both ESLm and LWm provide reliable equilibrium paths and displacement distributions, confirming the accuracy of the predictions.

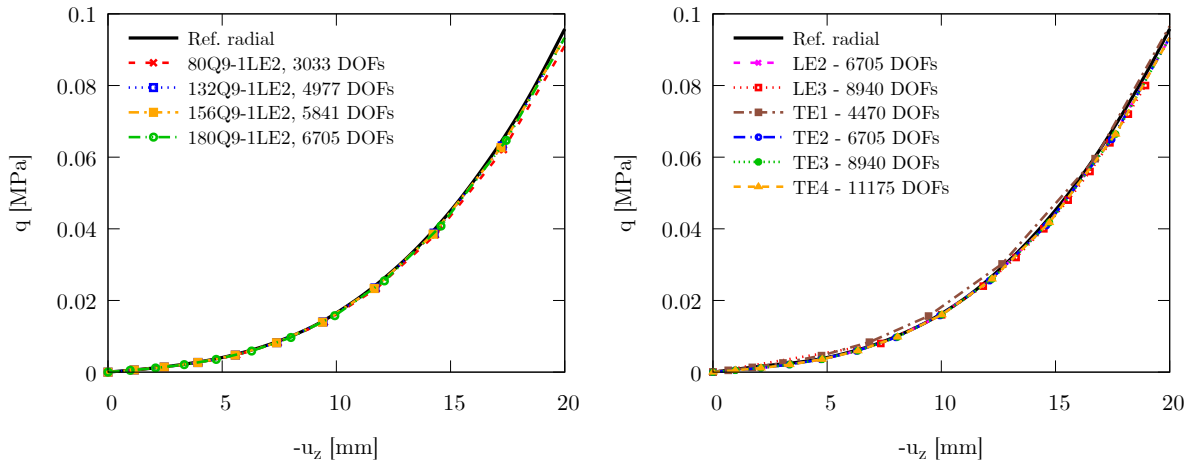

(a) Convergence analysis **(b)** Effect of theory expansion model

Figure 8.7: Circular clamped plate under uniform pressure, radial fiber case: effects of reference mid-surface discretization and structural theory on the equilibrium curves of the plate.

After assessing the capabilities of the proposed modeling approach, the nonlinear static analysis of the clamped plate is performed for each fiber reinforcement case considered. Both isotropic and fiber-reinforced cases are studied by adopting the convergent mathematical model previously identified, thus employing 180 Q9 parabolic elements for the mid-surface approximation and a single LE3 element for the through-the-thickness kinematic expansion. Figure 8.8 depict the equilibrium paths for all the considered material configurations, comparing the transverse displacement at the plate center (measured at the mid-surface) obtained with 2D CUF models against the available reference. The numerical predictions are in excellent agreement with the reference proposed solution in all analyzed material conditions. In general, a stiffer behavior is observed in the radial fiber distribution case, whereas the tangential (or circumferential) fiber distribution and isotropic condition show similar mechanical behavior. In the radial fiber case, Fig.8.9(a) shows the through-the-thickness distribution of transverse displacement, while Fig.8.9(b) illustrates the same displacement component in the longitudinal direction along the plate diameter at the mid-surface. Once again, the linear TE1 model fails to capture the correct transverse behavior due to the limitations of its theoretical assumptions. Figure 8.10 shows the contour plot of the displacement magnitude of the anisotropic radial reinforced plate for different loads, computed adopting the previous convergent model listed before.

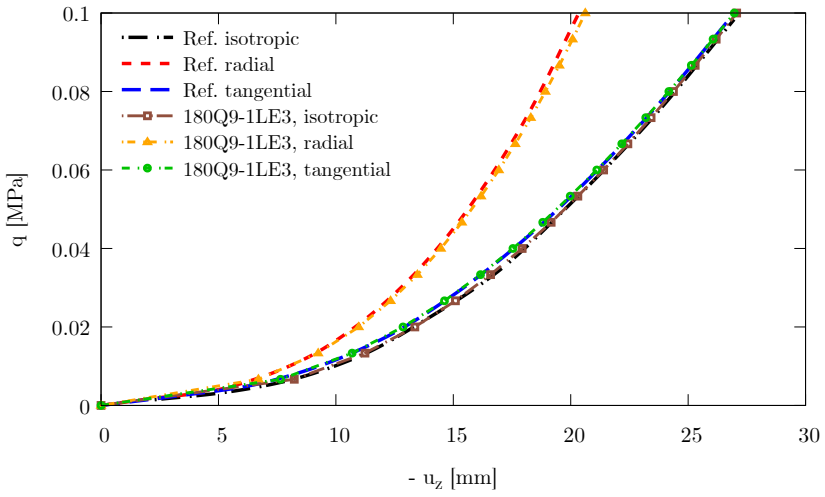

Figure 8.8: Circular clamped plate under uniform pressure: equilibrium paths computed for the convergent discretization model, in each material configuration considered.

The capabilities and the accuracy of the present higher-order implementation of plate theories is now discussed in terms of stress distributions. In an hyperelastic finite element scenario, both the Cauchy's stress component in the actual reference frame and second Piola-Kirchhoff stress components in the material reference frame are discussed, to analyze compatibility conditions and effects of theory of structure approximation on the obtained stress distributions. In the following, adopting the previously listed 180 Q9 FE discretization of the reference mid-surface, the stress analysis is performed at the point located at coordinates $(-3/4R, 0)$ mm on the plate mid-surface, for each material configuration considered. The first case considered is the isotropic material condition, when a pressure of $q_z = 0.1$ MPa is applied. Figure 8.11 shows the through-the-thickness distribution of each second Piola-Kirchhoff stress component S_{ij}, comparing the results obtained using lower- to higher-order TE and LE models.

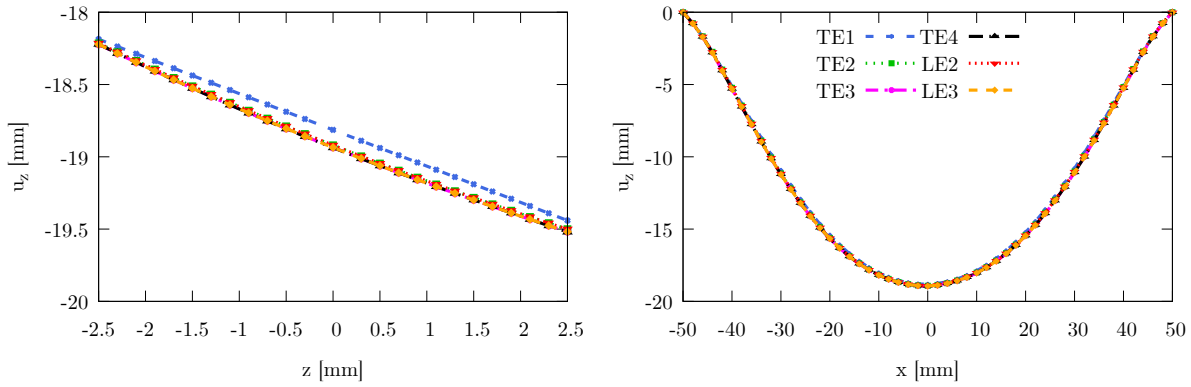

(a) Thickness distribution **(b)** Diametral distribution

Figure 8.9: Circular clamped plate under uniform pressure, radial fiber case: through-the-thickness and diametral displacement distributions, computed for each theory of structure considered.

The same comparison is proposed in terms of Cauchy's stress components σ_{ij} in Fig. 8.12, as well as first Piola-Kirchoff stress components for further considerations, depicted in Fig. 8.13. In all cases, minor differences are observed between higher-order models; notable differences are observed when lower-order TE models are compared against higher-order LE models. In particular, the TE1 model, which assumes a constant transverse strain throughout the thickness, cannot accurately capture the global stress state. This limitation is particularly evident in the prediction of the transverse stress components. From the proposed results, a direct incompatibility of transverse normal and shear stresses P_{xz} and P_{yz} is observed. Figure 8.13(c) shows the through-the-thickness distribution of the normal stress component P_{zz}, where the boundary condition fulfillment is correctly observed for different discretization models involving both ESLm and LWm. This has also been satisfied for the PK2 S_{zz} component: the boundary condition is satisfied at the top surface at $z = 0.25$. At the same time, the equilibrium condition at the plate edges is still not fulfilled for the P_{xz} stress component by higher-order LWm; the TE-4 model correctly predicts compatibility at the top and bottom surfaces. For the P_{yz} component, each discretization model considered yielded non-null transverse shear stress values, but these were relatively small (two orders of magnitude lower). These discrepancies are justified by the numerical approximation of the deformation gradient $\mathbf{F}$ in highly deformed states, which is required for post-processing the stress tensor components in a pure displacement-based method. In the present analysis, single-element LE2 and LE3 expansion models have been adopted to compare results with LWm and ESLm. However, adopting pure LWm is not sufficient to achieve equilibrium at large strains; refined discretization models with more through-the-thickness subdomains are needed. For these reasons, further analyses, including more subdomains in the through-the-thickness discretization, have been performed to assess the convergence of the present model's stresses, particularly with respect to the fulfillment of equilibrium and compatibility conditions. Furthermore, the same stress analysis is performed at the same point previously considered for the radial fiber reinforcement. The through-the-thickness stress distributions are compared now when a pressure of $q_z = 0.08$ MPa is applied, considering again the components of the first and second Piola-Kirchhoff stress tensors, as well as the Cauchy stress components. Figure 8.14 shows the through-the-thickness distribution of each second Piola-Kirchhoff stress component S_{ij}, comparing the results obtained using lower- to higher-order TE and LE models. The same comparison is proposed in terms of Cauchy's stress components σ_{ij} in Fig. 8.15, as well as first

Piola-Kirchoff stress components for further considerations, depicted in Fig. 8.16. Similar findings can be observed, comparing the proposed results to the isotropic case. In particular, for the transverse normal and shear PK1 stress components, compatibility and equilibrium are satisfied for the P_{xz} component by higher-order TE models or refined LWm. Similar considerations to the isotropic case can be applied to the P_{yz} component. However, higher-order models still yield inconsistent results regarding compatibility at $z = 0.25$.

The proposed results suggest that convergence has not been achieved with the adoption of these pure LWm; thus, a refined discretization, including more subdomains, is suggested to assess the capabilities of the present approach when LE models are analyzed. Figure 8.17 shows the through-the-thickness distribution of transverse shear components of each stress tensor, in the case of an isotropic plate under an applied pressure of $q_z = 0.1$ MPa, comparing the results obtained adopting different LE models. A similar comparison is provided in Fig. 8.18 for the radial fiber distribution case, for an applied pressure of $q_z = 0.08$ MPa. From the proposed results, looking at Fig. (8.17)(a), a parabolic behavior of the component P_{xz} is observed, and refined LWm satisfy the equilibrium conditions at plate edges correctly. Similar findings are observed in the case of transverse PK1 stress components for the fiber reinforced plate, as shown in Fig. 8.18(a) and 8.18(b), where the compatibility at plate edges is satisfied by the adoption of refined LWm with more subdomains. Still, minor discrepancies have been observed in some cases, where very small, yet non-zero, values of the stress components are observed, attributed again to numerical reasons or to FE convergence along the reference mid-surface. The adoption of higher-order expansion theories of the displacement field provides reliable distributions of the complex three-dimensional stress state, thereby improving the reliability of numerical predictions.

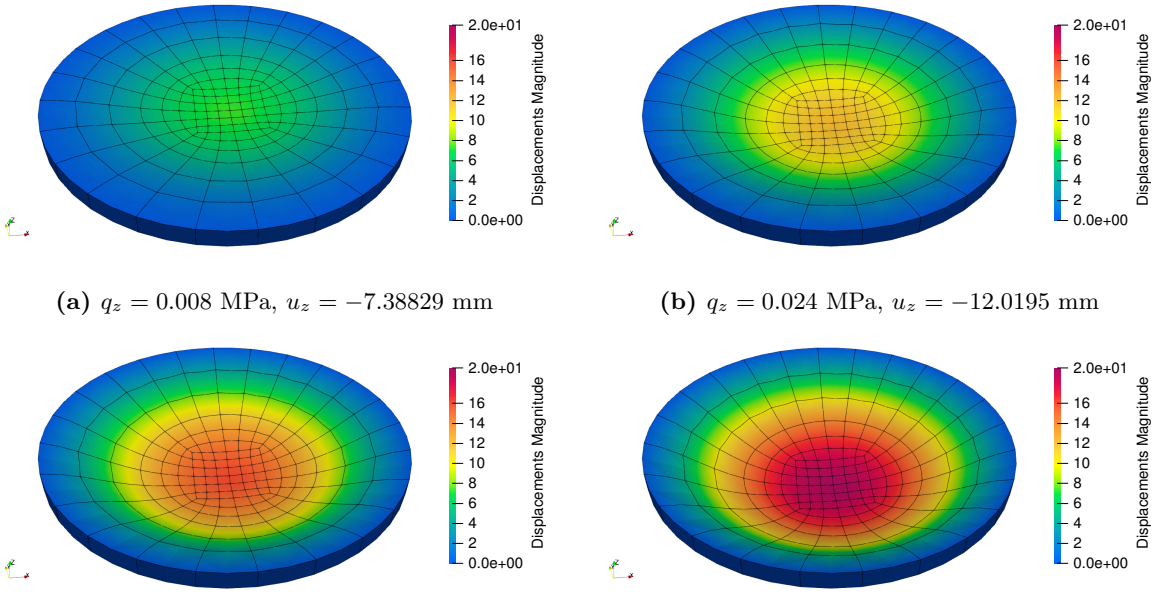

(a) $q_z = 0.008$ MPa, $u_z = -7.38829$ mm

(b) $q_z = 0.024$ MPa, $u_z = -12.0195$ mm

(c) $q_z = 0.048$ MPa, $u_z = -15.9218$ mm

(d) $q_z = 0.08$ MPa, $u_z = -19.5227$ mm

Figure 8.10: Circular clamped plate under uniform pressure: deformed configurations for different value of applied pressure, 180Q9-1LE3 model results.

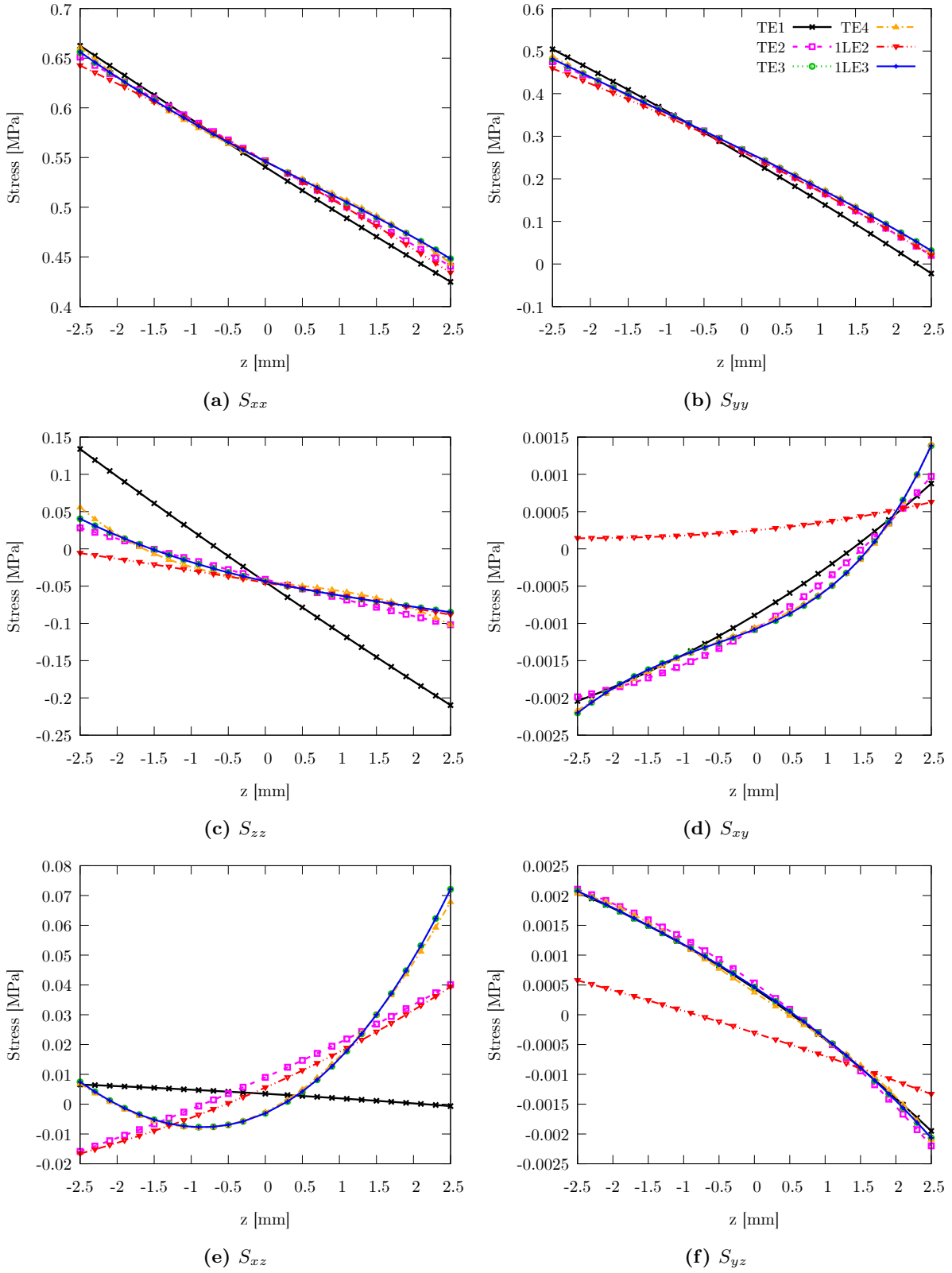

(a) S_{xx} **(b)** S_{yy}

(c) S_{zz} **(d)** S_{xy}

(e) S_{xz} **(f)** S_{yz}

Figure 8.11: Circular clamped plate under uniform pressure: effects of theory of structure approximation on the through-the-thickness stresses distribution, components of **S**, isotropic case and load condition $q_z = 0.1$ MPa.

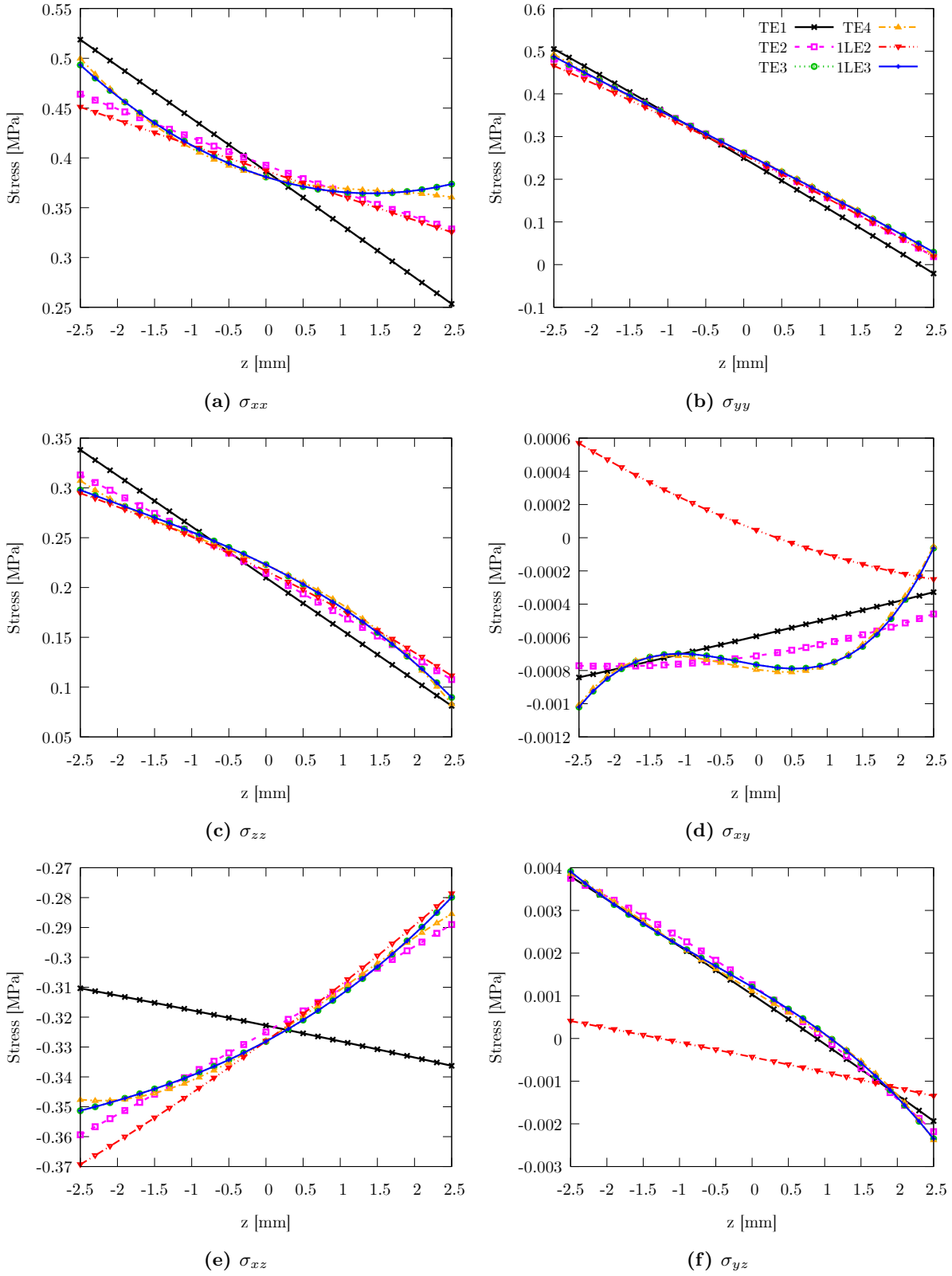

(a) σ_{xx} **(b)** σ_{yy}

(c) σ_{zz} **(d)** σ_{xy}

(e) σ_{xz} **(f)** σ_{yz}

Figure 8.12: Circular clamped plate under uniform pressure: effects of theory of structure approximation on the through-the-thickness stresses distribution, components of $\boldsymbol{\sigma}$, isotropic case and load condition $q_z = 0.1$ MPa.

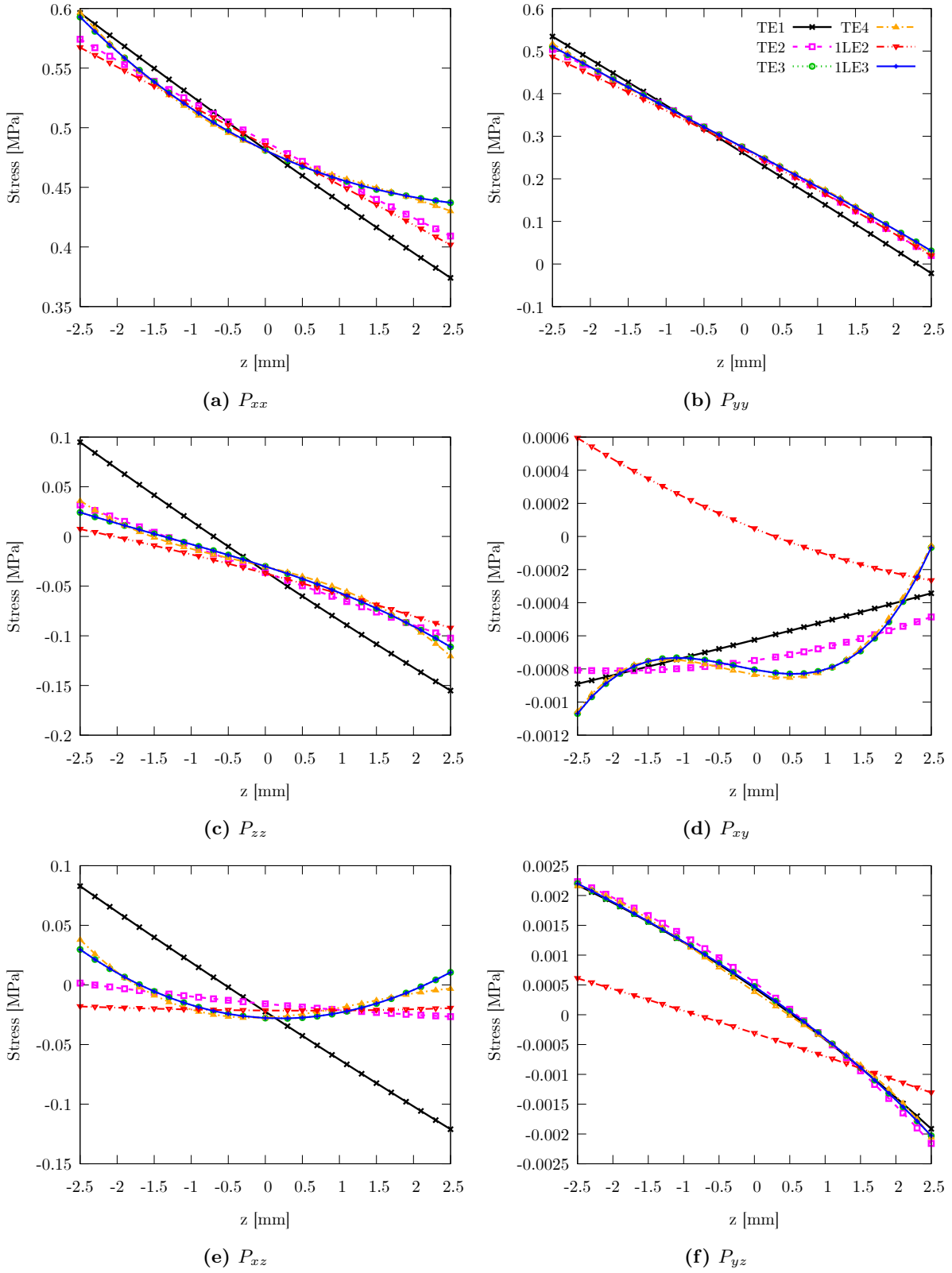

(a) P_{xx} **(b)** P_{yy}

(c) P_{zz} **(d)** P_{xy}

(e) P_{xz} **(f)** P_{yz}

Figure 8.13: Circular clamped plate under uniform pressure: effects of theory of structure approximation on the through-the-thickness stresses distribution, components of $\mathbf{P}$, isotropic case and load condition $q_z = 0.1$ MPa.

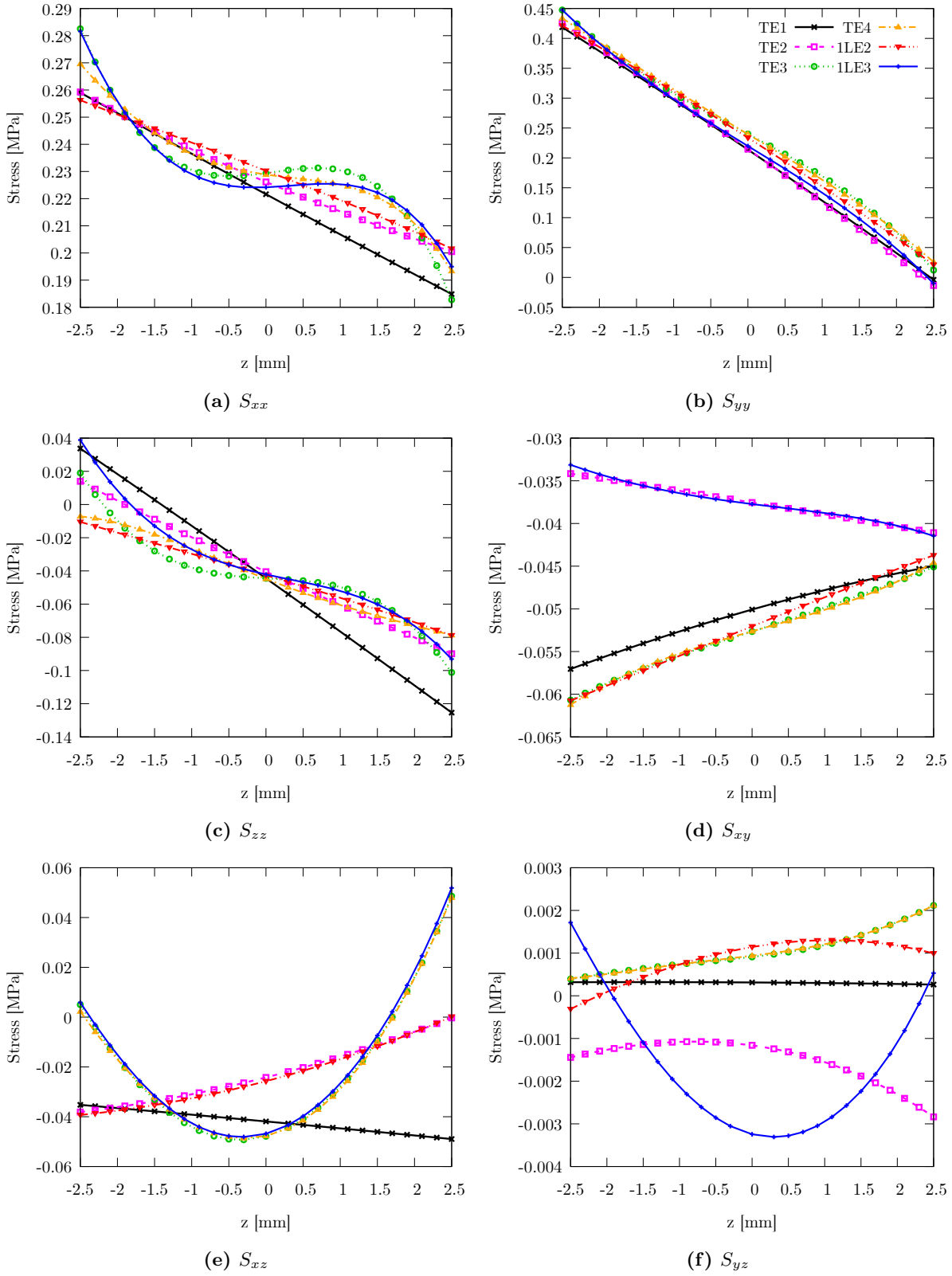

(a) S_{xx} **(b)** S_{yy}

(c) S_{zz} **(d)** S_{xy}

(e) S_{xz} **(f)** S_{yz}

Figure 8.14: Circular clamped plate under uniform pressure: effects of theory of structure approximation on the through-the-thickness stresses distribution, components of **S**, radial fiber case and load condition $q_z = 0.08$ MPa.

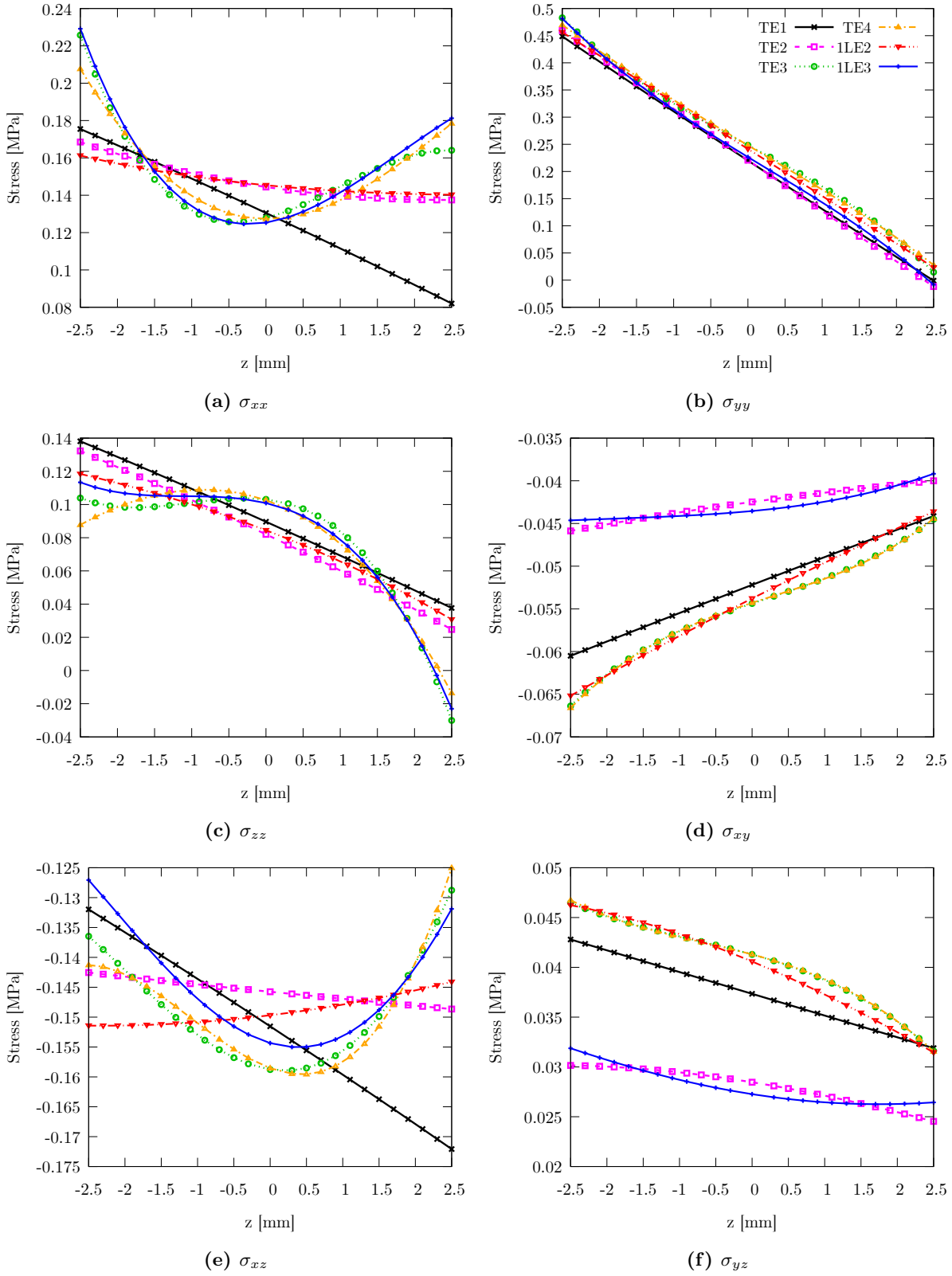

(a) σ_{xx} **(b)** σ_{yy}

(c) σ_{zz} **(d)** σ_{xy}

(e) σ_{xz} **(f)** σ_{yz}

Figure 8.15: Circular clamped plate under uniform pressure: effects of theory of structure approximation on the through-the-thickness stresses distribution, components of $\boldsymbol{\sigma}$, radial fiber case and load condition $q_z = 0.08$ MPa.

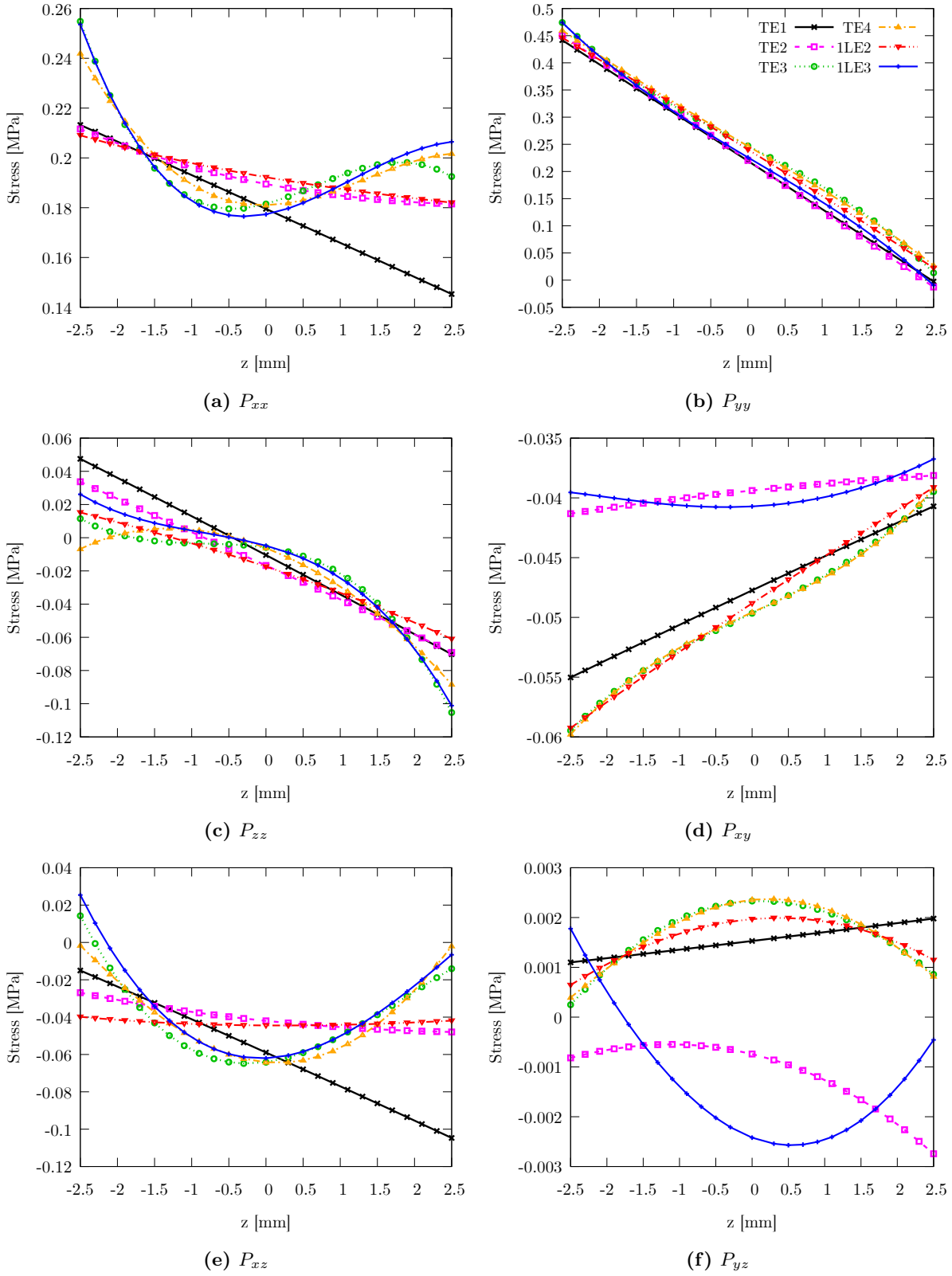

(a) P_{xx} **(b)** P_{yy}

(c) P_{zz} **(d)** P_{xy}

(e) P_{xz} **(f)** P_{yz}

Figure 8.16: Circular clamped plate under uniform pressure: effects of theory of structure approximation on the through-the-thickness stresses distribution, components of **P**, radial fiber case and load condition $q_z = 0.08$ MPa.

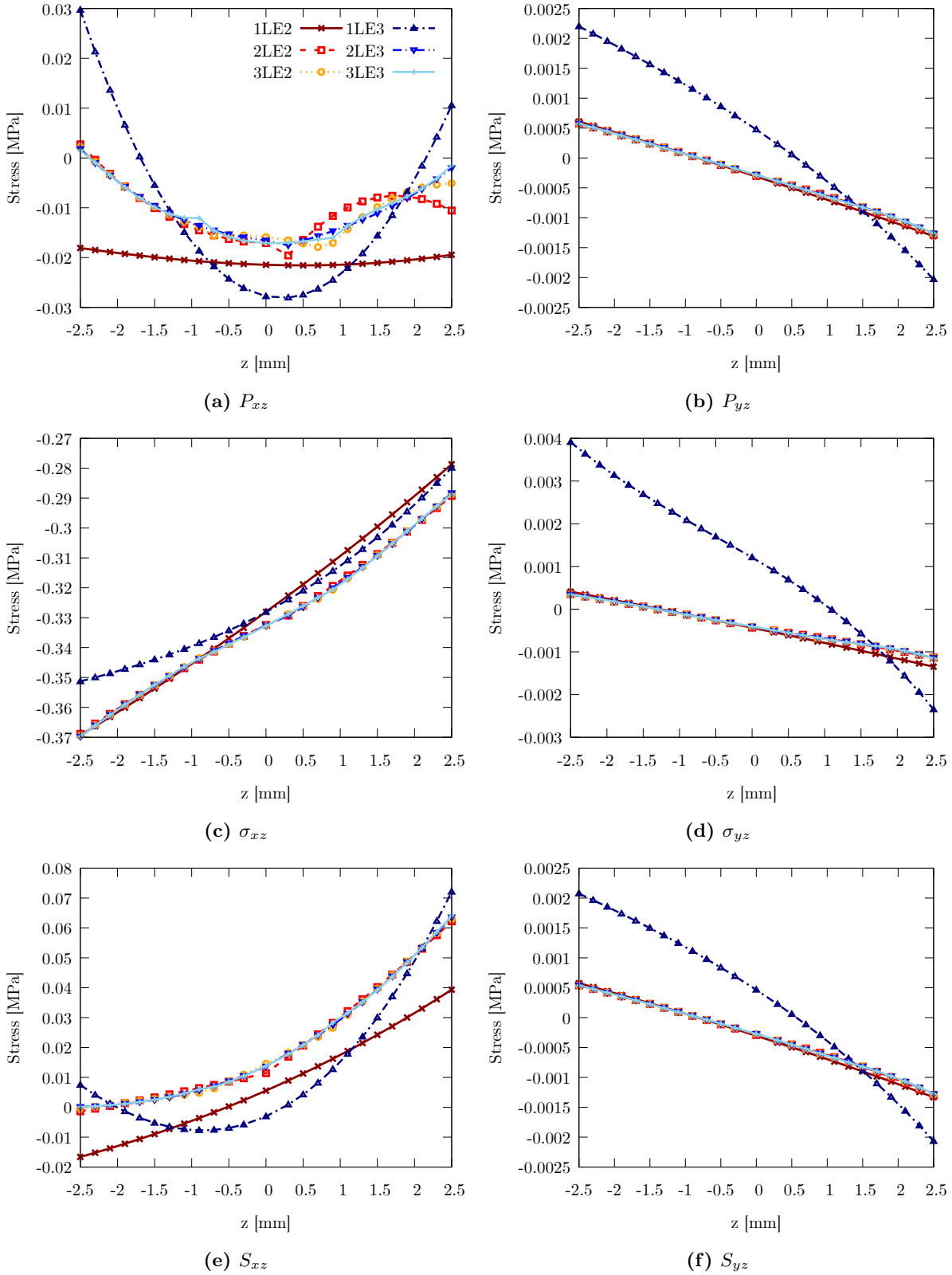

(a) P_{xz} **(b)** P_{yz}

(c) σ_{xz} **(d)** σ_{yz}

(e) S_{xz} **(f)** S_{yz}

Figure 8.17: Circular clamped plate under uniform pressure: influence of theory of structure approximation on the transverse normal and shear stresses components, isotropic case and load condition $q_z = 0.1$ MPa.

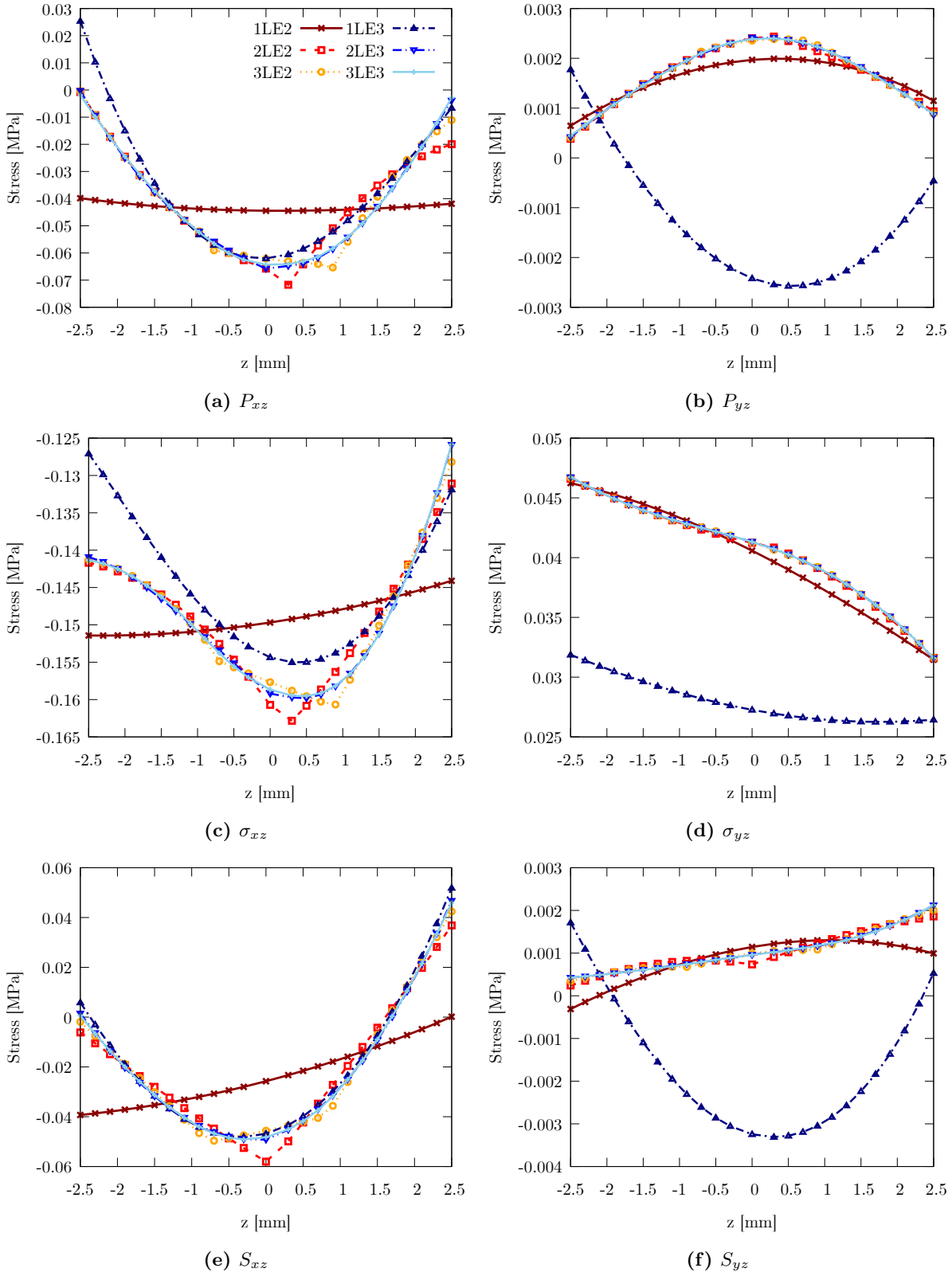

(a) P_{xz} **(b)** P_{yz}

(c) σ_{xz} **(d)** σ_{yz}

(e) S_{xz} **(f)** S_{yz}

Figure 8.18: Circular clamped plate under uniform pressure: influence of theory of structure approximation on the transverse normal and shear stresses components, radial fiber distribution case and load condition $q_z = 0.08$ MPa.

8.2.2 Linearized vibration analysis

Thereafter, in each computed (and marked in the equilibrium path) non-trivial equilibrium state, the linear eigenvalue problem is solved, evaluating then the natural frequencies and mode shapes around different deformed configurations. Figure 8.19 illustrates the pressure-frequency curve of the first ten natural frequencies along the equilibrium path for the radial fiber distribution, comparing the results obtained for different CUF expansion models. A similar comparison is conducted for the tangential fiber distribution case and presented in Fig. 8.20.
From the proposed results, one can observe different modal interactions both at small and large displacement regimes. In particular, both for radial and tangential fiber distribution cases, modal interactions are observed for high-frequency modes. To investigate the behavior of modal shapes in the interacting zone, different criteria can be adopted. For this proposed case study, the assessment of the proposed methodology, the mode shapes for the tangential distribution case are analyzed. Figure. 8.21 shows the eight modes of vibration, computed for different load conditions. The same comparison is proposed for the ninth mode of vibration in Fig. 8.22. From the pressure-frequency curve of the tangential distribution case, an evident modal interaction can be observed between modes 8 and 9, around the condition $q_z = 0.064$ MPa. By considering a single fiber reinforcement in two different configurations, different static and modal behaviors have been observed. The results suggest that, in the case of a radial fiber configuration, a stiffer behavior of the plate is observed, which is also confirmed in the linearized vibration analysis, where higher natural frequencies are observed across all cases. On the other hand, more evident modal interactions instead are observed in the case of tangential fiber distribution. These preliminary results are considered an assessment of the proposed procedure, further motivating investigations into the influence of pre-stressed conditions on the dynamic and modal analysis of structures.

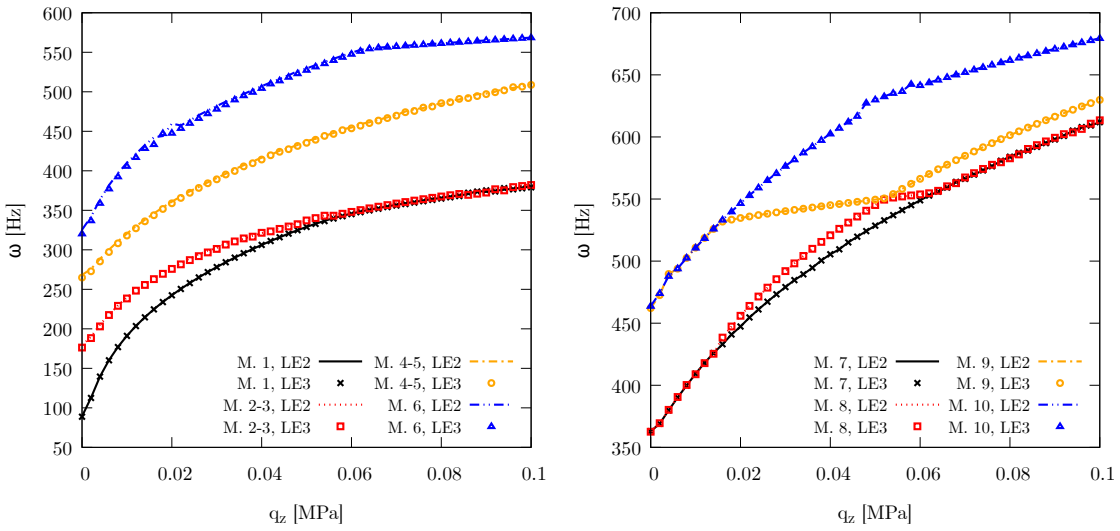

(a) Modes 1-6 **(b)** Modes 7-10

Figure 8.19: Compressible circular plate: radial fibre configuration, variation of the first ten natural frequencies along the equilibrium path.

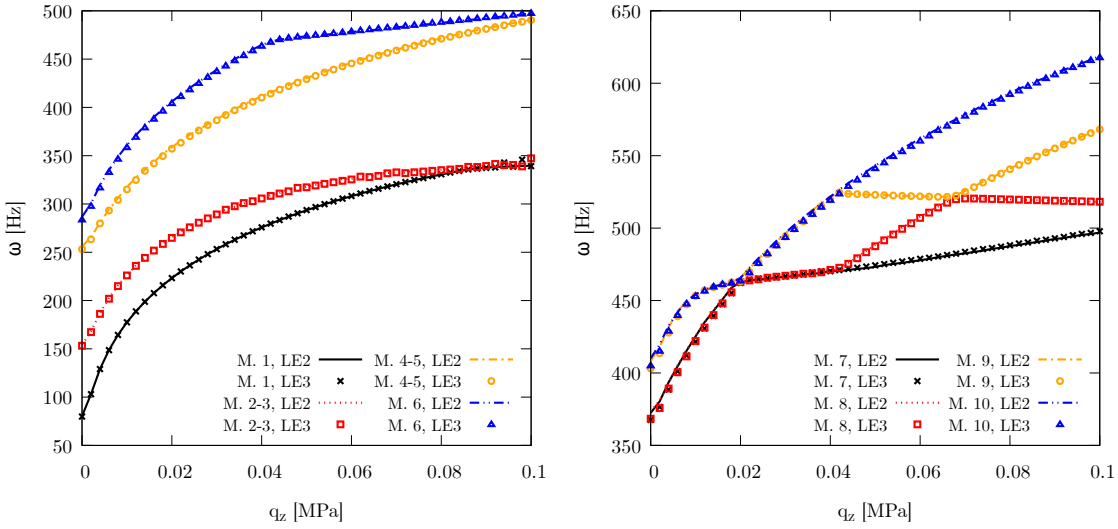

(a) Modes 1-6 **(b)** Modes 7-10

Figure 8.20: Compressible circular plate: tangential fibre configuration, variation of the first ten natural frequencies along the equilibrium path.

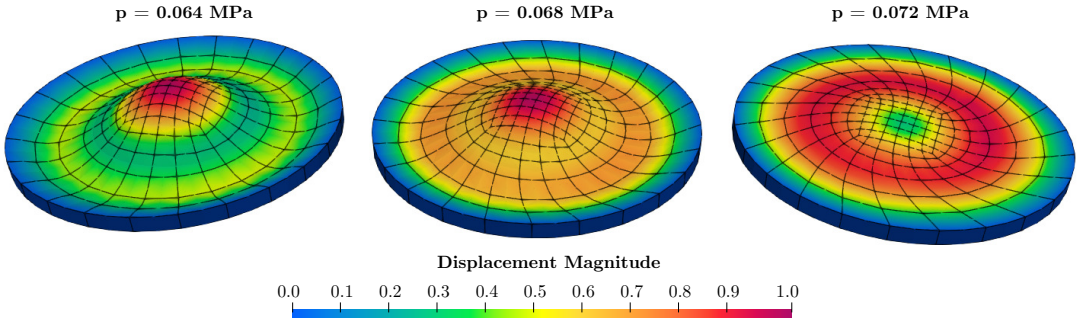

Figure 8.21: Compressible circular plate: tangential fiber configuration, eight mode of vibration for different deformed configurations. Eigenvalue represented on the undeformed configuration.

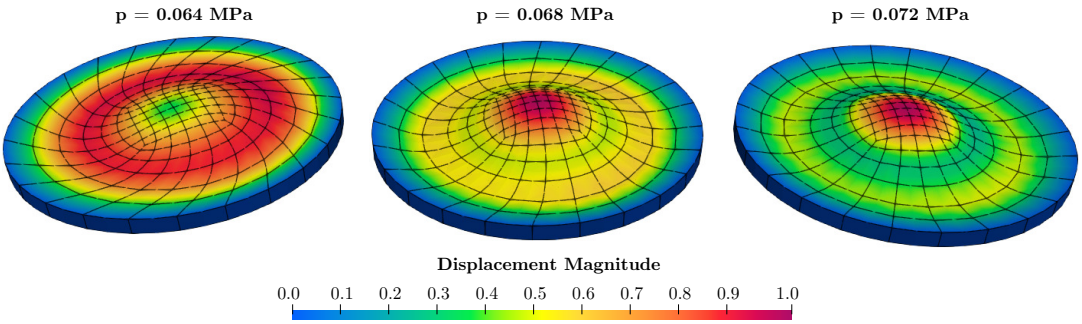

Figure 8.22: Compressible circular plate: tangential fiber configuration, nine mode of vibration for different deformed configurations. Eigenvalue represented on the undeformed configuration.

8.3 Finite strain analysis of a cantilever square plate

In this case study, the finite strain behavior of a fiber-reinforced cantilever square plate, as already investigated by Beheshti et al. [195], is discussed. The clamped square plate has a lateral dimension of $a = 20$ mm and a thickness of $t = 1$ mm, and it si considered subjected to a uniaxial tensile load applied at its free end. From previous discretization convergence analyses, the structure is discretized adopting higher-order 1D CUF models, exploiting 20 L9 parabolic elements along the clamped side of the plate and 15 cubic B4 elements along the beam axis in the y direction. The total number of DOF involved by the simulation is 16974. The geometrical features, boundary conditions and discretization exploited are illustrated in Fig. 8.23.

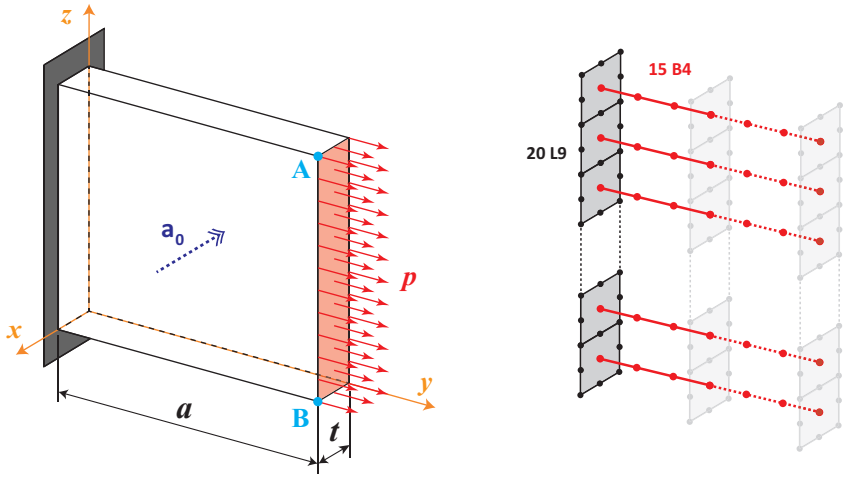

(a) Geometry and boundary conditions **(b)** Discretization

Figure 8.23: Finite strain analysis of a cantilever square plate: geometrical features, boundary conditions and discretization model adopted.

The square plate is modeled as a transversely isotropic hyperelastic material reinforced by a single fiber family. The variable fiber reinforcement considered is included by the unit vector $\boldsymbol{a}_0$ lying in the y–z plane, modeling thus a continuous planar fiber reinforcement, and inclined at an angle θ with respect to the y-axis, i.e., $\boldsymbol{a}_0 = (0, \cos\theta, \sin\theta)$. Different fiber orientations are considered, with θ varying from 0° to 90°. The material behavior is described using the same strain energy function introduced in Eq. (8.10), with material constants taken from [195]. The influence of anisotropy and fiber orientation is assessed by analyzing the horizontal displacement of points A and B, located at the free end of the plate, as the applied uniaxial load increases. The analysis performed is a static nonlinar analysis by which the equilibrium paths of the plate can be computed. The previously introduced discretization is analyzed for convergence reason and investigate the material response under different fiber orientation angles, guaranteeing accurate results compared with the literature reference. Figure 8.24(a) shows the equilibrium paths for fiber inclination angles $\theta = 0°$ and $\theta = 30°$. For $\theta = 0°$, the displacements of the two points coincide, since the fiber direction is aligned with the loading direction, and the plate exhibits a stiffer response. In contrast, for $\theta = 30°$ the fiber orientation introduces a transverse component, which affects the deformation process and results in an unsymmetric final configuration. Figure 8.24(b) depicts the equilibrium paths for $\theta = 60°$ and $\theta = 90°$. In these cases, the preferential direction is more inclined with respect to the loading axis, leading to a significantly softer structural response. For this reason, larger displacements and strains are observed at much

lower load conditions applied. For $\theta = 90°$, the fibers provide no resistance along the loading direction, and the resulting deformed configuration results again symmetric.

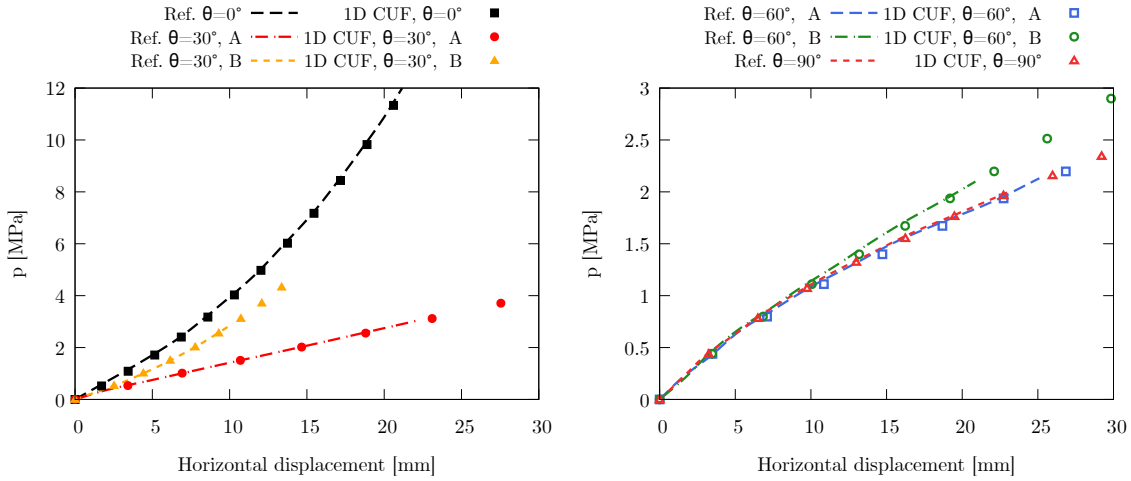

(a) Cases $\theta = 0°$ and $\theta = 30°$ **(b)** Cases $\theta = 60°$ and $\theta = 90°$

Figure 8.24: Finite strain analysis of a cantilever square plate: equilibrium curves for various fiber inclination. Comparison between 1D CUF model results and available literature reference.

Figure 8.25 illustrates the deformed configurations for different fiber orientations when the horizontal displacement of point B reaches approximately 19 mm. The results proposed highlight the strong influence on the mechanical response of the material from anisotropy effects and the preferential fiber direction orientation.

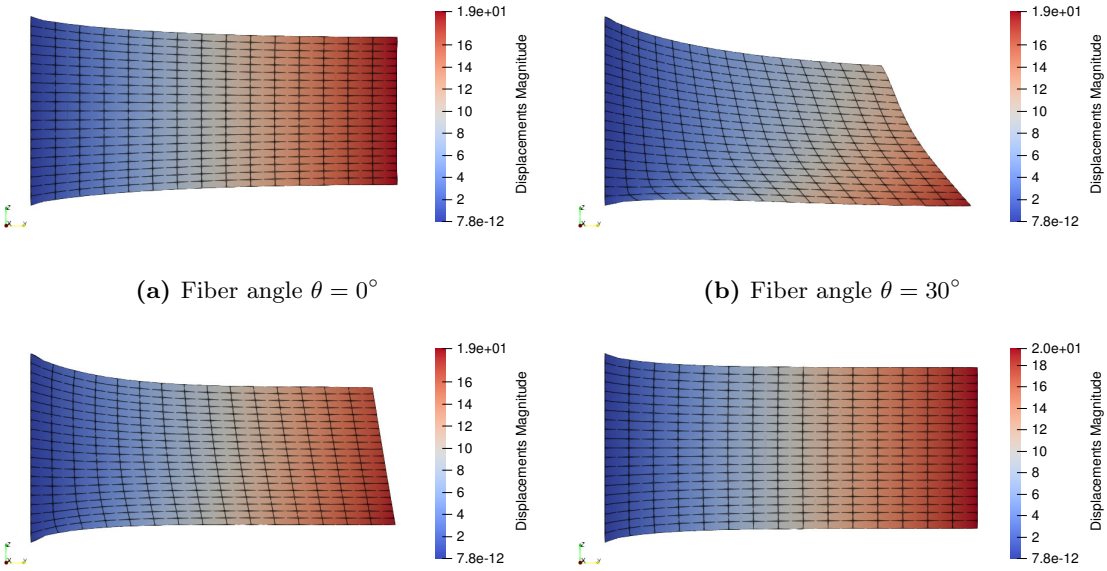

(a) Fiber angle $\theta = 0°$ **(b)** Fiber angle $\theta = 30°$

(c) Fiber angle $\theta = 60°$ **(d)** Fiber angle $\theta = 90°$

Figure 8.25: Finite strain analysis of a cantilever square plate: displacement magnitude contour, deformed configuration representation.

8.4 Multilayered laminated $0°/90°$ reinforced beam

The next case study focuses on the static analysis of a multilayered fiber-reinforced laminated beam. This case study is proposed to analyze the structure under large displacements and large strain. For this reason, two different geometrical configurations and loading conditions are considered to investigate the capabilities of the present implementation of higher-order FE model. In the first configuration, a doubly clamped cantilever beam of total length $L_b = 100$ mm with a square cross-section of lateral side $a = 5$ mm is analyzed under uniform transversal pressure applied to the top surface. In the second configuration, for a large strain analysis and a uniaxial tension test, a beam of length $L_s = 20$ mm and lateral side $a = 5$ mm is considered. Due to the symmetry of the structures and the applied load conditions, only one quarter of the model can be analyzed in the numerical simulations. The geometry and boundary conditions for the two problems, considering the applied symmetries and the considered quarter of the structures, are shown in Fig. 8.26(a) and Fig. 8.26(b), respectively.

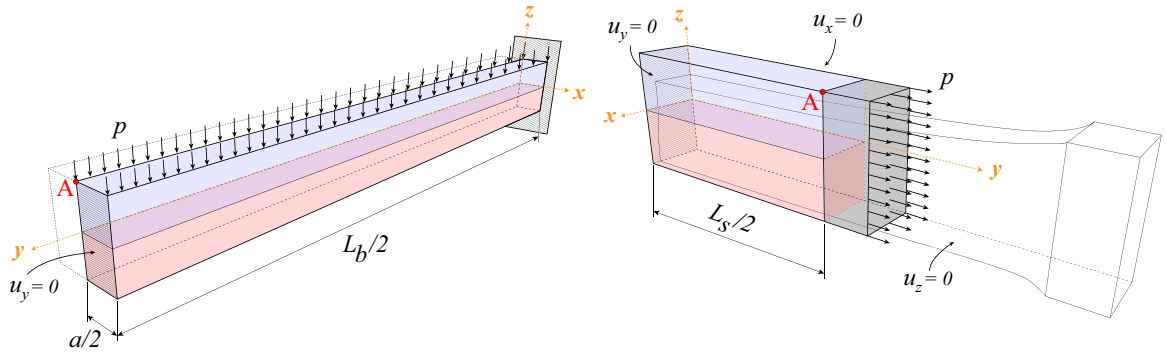

(a) Bending problem **(b)** Uniaxial test problem

Figure 8.26: Multilayered fiber-reinforced $0°/90°$ laminated beam: geometrical features and boundary conditions.

The material modeled adopt is given by the quadratic model for fiber reinforcement strain energy function given in [195], coupled with a Neo-Hookean model for the isotropic matrix and a stabilized volumetric strain energy function model:

$$\Psi = \Psi_{vol}(J) + \Psi_{iso}(I_1, I_2) + \Psi_{aniso}(I_4) = \frac{\mu}{2}(I_1 - 3) + \frac{\lambda}{2}(J-1)^2 - \mu \log J + \gamma(I_4 - 1)^2 \quad (8.11)$$

where $\mu = 1$ MPa is the infinitesimal shear modulus, $\lambda = 4$ MPa is the Lamé constant, and $\gamma = 0.375$ MPa. In both structural configuration the beam layers are arranged in a global stacking sequence given by $[0°/90°]$, with the fibers of the top layer oriented along the beam axis and those of the bottom layer oriented transversely, along the x axis. The influence of the adopted discretization models and the effects of the theory of structure approximation on the mechanical response of the structure are examined in both geometrical configuration, to assess the influence of the cross-section kinematics when large displacements or large strain conditions are analyzed. Based on the convergence studies discussed in the previous sections, 20 cubic B4 finite elements are adopted in the discretization along the beam axis. Different cross-section expansion models instead are then considered, employing either parabolic L9 (nine-node) or cubic L16 (sixteen-node) approximations. The computational cost is again measured in terms of the total DOFs associated with the chosen discretization. The two proposed configurations are analyzed separately in the following.

8.4.1 Uniform transverse pressure

Table 8.2 presents the numerical results for the transversal displacement u_z, evaluated at point "A" of the beam shown in Fig. 8.26(a), in correspondence of the symmetry section. The results are reported for different values of the applied transversal pressure and compared across the various cross-section expansion models. Figure 8.27 depicts the equilibrium path obtained using the cross-section expansion models listed in the previous table. The analyses are carried out through the static solver coupled with path-following type constraint. From the small-displacement regime to the moderate/large-displacement regime, the solutions obtained with the different cross-section kinematic models show an excellent agreement. Finally, Fig. 8.28 illustrates the through-the-thickness distribution of the transversal displacement u_z, measured at the x-symmetry section for $y = 40$ mm, near the y-symmetry section. From the proposed results, an almost linear variation of the transversal displacement component across the thickness is observed.

	$-u_z$ [mm]				
Model	$p = 2.52$ kPa	$p = 17.33$ kPa	$p = 81.94$ kPa	$p = 309.93$ kPa	**DOFs**
2L9	6.7890	15.2934	28.1352	48.2150	2745
2L16	6.7976	15.2973	28.1128	48.1427	5124
4L9	6.7954	15.3064	28.1584	48.2707	4941
4L16	6.7976	15.3109	28.1658	48.2870	9516
8L9	6.7966	15.3088	28.1620	48.2807	9333
8L16	6.7978	15.3113	28.1663	48.2875	18300
10L9	6.7967	15.3090	28.1623	48.2810	11529
10L16	6.7978	15.3113	28.1663	48.2877	22692
20L9	6.7977	15.3109	28.1656	48.2869	19215
20L16	6.7981	15.3119	28.1671	48.2892	39711

Table 8.2: Multilayered fiber-reinforced 0°/90° laminated beam, uniform transverse pressure case: convergence analysis, transversal displacement component $-u_z$. Comparison between various cross-section LE models adopted, for different load conditions.

In terms of displacement distributions and equilibrium paths, all the adopted models provide consistent results. Convergence is already achieved when using pure LW discretization models, such as the 2L9 and 2L16 expansions. As discussed in the previous section, the convergent models for displacement distributions is not typically associated with the convergent model for a detailed three-dimensional stress analysis of the material. For this reason now, convergence in terms of stress distributions is discussed. Figure 8.29 depict the through-the-thickness distribution of the Cauchy stress components for an applied pressure of $p = 162$ kPa. The stress distributions are evaluated at the symmetry section, for $x = 0$ and $y = 40$ mm, close to the y-symmetry section. All three-dimensional stress components are consistently computed across the different cross-section kinematic models. Perfect agreement is observed for the normal σ_{yy} and transverse σ_{yz} components, while the remaining also show good agreement. Minor discrepancies arise due to the adoption of refined kinematics in the z-direction of the cross-section, instead of the transverse x-direction. In particular, for the transverse component σ_{yz} shown in Fig. 8.29(d) discontinuities and non-zero values at the beam edges are observed. Theoretical consistency is achieved when the P_{yz} stress component is analyzed, shown in Fig. 8.30, and higher-order models are employed. This behavior can be explained by the significant influence of large strains in hyperelastic soft structures, which strongly affect the distribution of the first Piola–Kirchhoff

stress tensor. Since this tensor is computed from the second Piola–Kirchhoff stress tensor **S** within the Total Lagrangian displacement-based finite element formulation (with conservative loading), the equilibrium with external loads is guaranteed on the Cauchy's stress components, linked by the deformation gradient.

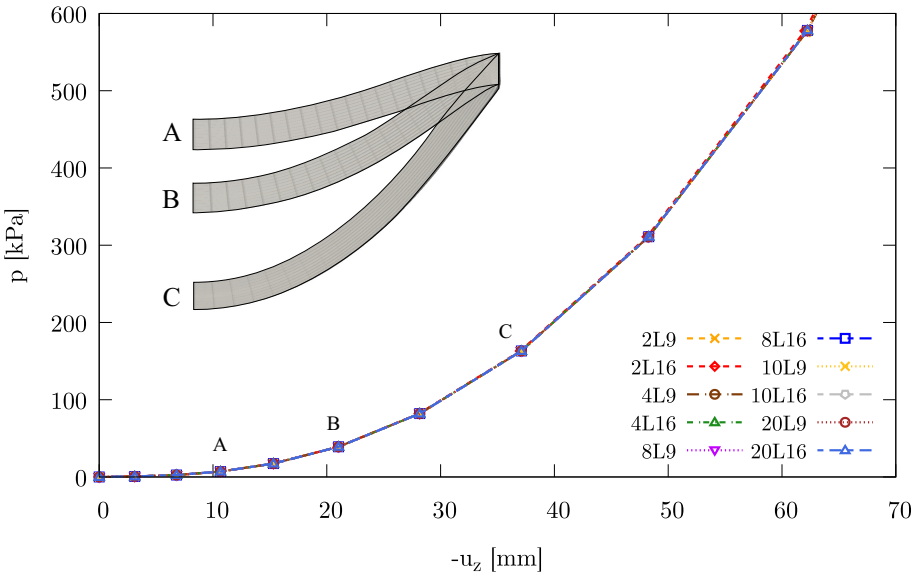

Figure 8.27: Multilayered fiber-reinforced 0°/90° laminated beam, uniform transverse pressure case: equilibrium path, transversal displacement $-u_z$ versus applies load p. Comparison between paths obtained adopting different cross-section kinematics.

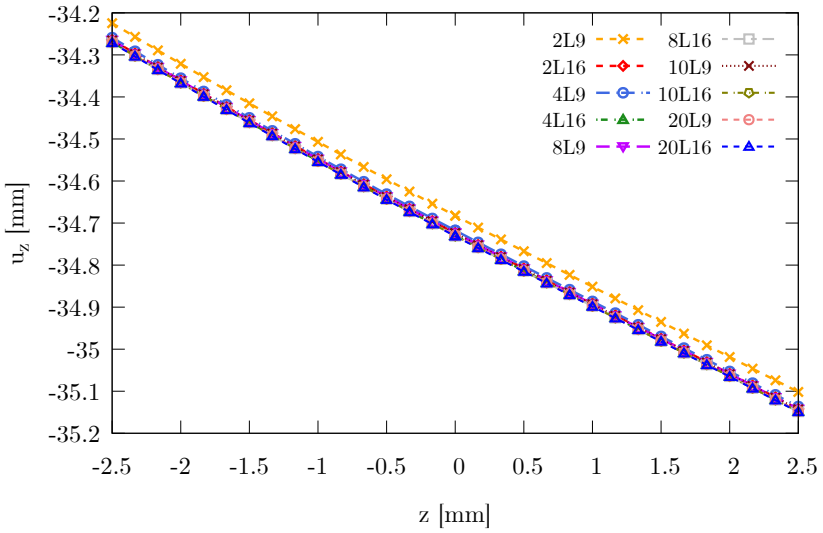

Figure 8.28: Multilayered fiber-reinforced 0°/90° laminated beam, uniform transverse pressure case: through-the-thickness transversal displacement u_z distribution, measured at $y = 40$ mm, for an applied transversal pressure of $p = 162$ kPa. Comparison betwwen various cross-section expansion models.

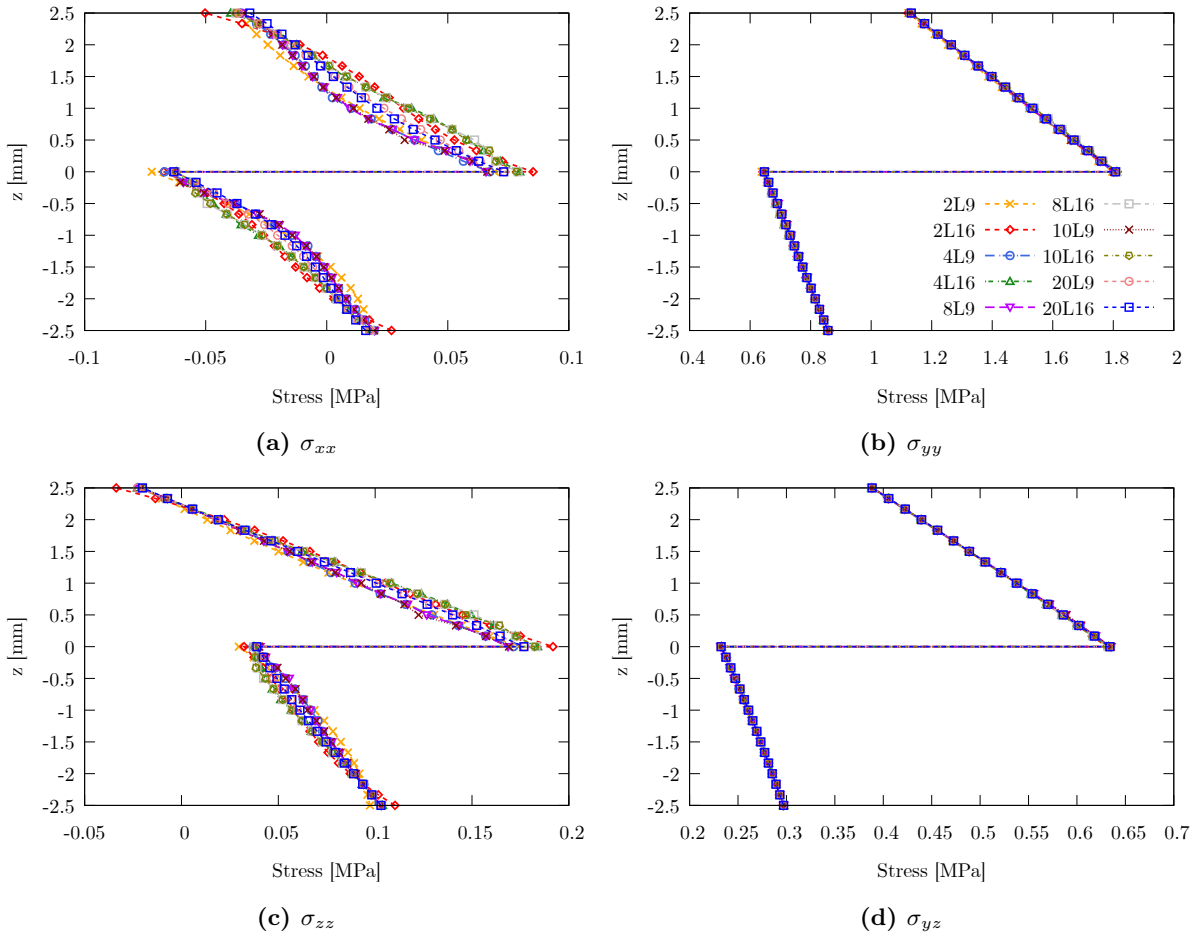

(a) σ_{xx} **(b)** σ_{yy}

(c) σ_{zz} **(d)** σ_{yz}

Figure 8.29: Multilayered fiber-reinforced 0°/90° laminated beam, uniform transverse pressure case: through-the-thickness stress components distribution, measured at $y = 40$ mm and $x = 0$ mm at the x-symmetry section, for an applied transverse pressure of $p = 162$ kPa.

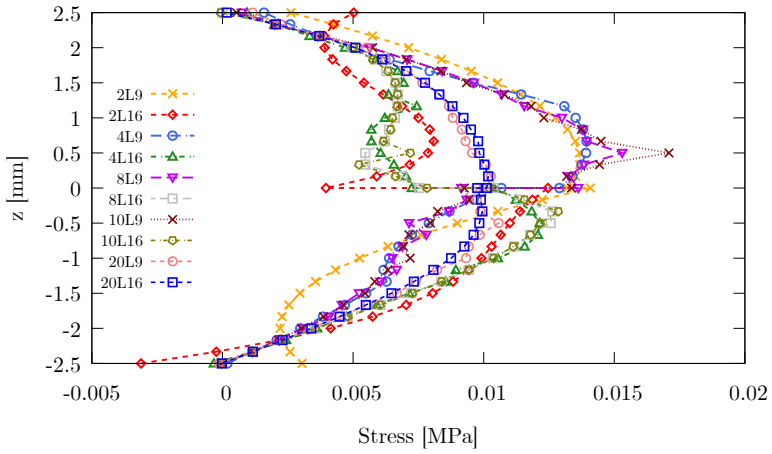

Figure 8.30: Multilayered fiber-reinforced 0°/90° laminated beam, uniform transverse pressure case: through-the-thickness distribution of P_{yz} component, measured at $y = 40$ mm and $x = 0$ mm at the x-symmetry section, for an applied transverse pressure of $p = 162$ kPa.

8.4.2 Uniform uniaxial tension

The numerical results reported in Table 8.3 present the horizontal displacement u_y at point "A" of the beam, shown in Fig. 8.26(b) specifically at the end section for $y = 10$ mm, computed for various values of the applied traction pressure. The discretization models adopt the same cross-section kinematics previously discussed. Results are provided for different values of the applied transversal pressure, comparing the solutions obtained with the various cross-section expansion models. Figure 8.31(a) illustrates the equilibrium path for the uniaxial tension test, obtained through static analysis with a load-control procedure. The maximum applied load is set to $p_{max} = 30$ MPa, distributed over 20 equal increments. From the small-strain regime up to moderate and large strains, the numerical solutions from different models exhibit excellent agreement. In the same figure, the deformed configurations of the structure in various specified load conditions are also reported. Figure 8.31(b) depicts the cross-sectional displacement at the symmetry section, highlighting the influence of the applied traction pressure on cross-section warping, stretching, and other local effects. Finally, Fig. 8.32 shows the through-the-thickness distribution of the vertical displacement u_z, measured at the symmetry section ($y = 0$ mm, $x = 0$ mm) for $p = 13.5$ MPa. The results obtained with different cross-section kinematics reveal a slightly parabolic profile of the transversal displacement component. As in the previous case, the

	u_y [mm]				
Model	$p = 4.5$ MPa	$p = 12$ MPa	$p = 18$ MPa	$p = 24$ MPa	**DOFs**
2L9	7.7553	14.6649	18.3484	21.2875	2745
2L16	7.7574	14.6690	18.3536	21.2935	5124
4L9	7.7563	14.6670	18.3507	21.2898	4941
4L16	7.7574	14.6686	18.3525	21.2916	9516
8L9	7.7571	14.6689	18.3533	21.2930	9333
8L16	7.7579	14.6699	18.3545	21.2930	18300
10L9	7.7571	14.6690	18.3534	21.2931	11529
10L16	7.7579	14.6699	18.3545	21.2943	22692
20L9	7.7578	14.6700	18.3548	21.2946	19215
20L16	7.7580	14.6703	18.3534	21.2943	39711

Table 8.3: Multilayered fiber-reinforced $0°/90°$ laminated beam, uniaxial tension test: convergence analysis, horizontal displacement component u_y measured at the point A. Comparison between various cross-section LE models adopted for different load conditions.

displacement distributions and equilibrium paths predicted by the different models are perfectly matching. Convergence is already achieved with pure LW discretization models, such as the 2L9 and 2L16 expansions. The discussion now focuses on stress distributions. Convergence is discussed again in terms of stress distributions. In the following, both Cauchy's stress and first Piola-Kirchhoff stress components are discussed. Figure 8.33 presents the through-the-thickness distribution of the Cauchy stress components when a uniform traction pressure of $p = 15.5$ MPa is applied. Again, stresses are evaluated at the symmetry section, for $x = 0$ and $y = 2.5$ mm, close to the y-symmetry plane. For all adopted cross-section kinematic models, the three-dimensional stress components are consistently computed. Perfect agreement is observed for the normal components σ_{yy} and P_{yy}, while σ_{xx} show good agreement across models but major discrepancies are observed between less and more refined cross-section discretizations, due to less refinement in the x-direction of the expansion model. Significant discrepancies appear also for the normal components σ_{zz} where discontinuities and variations in both global and local slopes are observed.

In this case, the presence of large strains requires refined structural theories and kinematic models to accurately compute the deformation gradient **F**, and consequently the second Piola–Kirchhoff stress tensor **S**. Coarser cross-section discretizations, instead, may lead to inconsistent results. A similar behavior is observed for the transverse shear components σ_{yz} shown in Fig. 8.33(d) and P_{yz}, depicted in Fig. 8.34. With coarser discretizations, discontinuities and non-zero values at the beam edges appear, in contradiction with equilibrium and compatibility requirements. In contrast, refined cross-section models satisfy the global equilibrium conditions, leading to non-symmetric global stress distributions induced by local shear effects. Specifically, for the P_{yz} component, equilibrium and compatibility are fully satisfied, while a non-symmetric distribution is observed as a direct consequence of local shear phenomena.

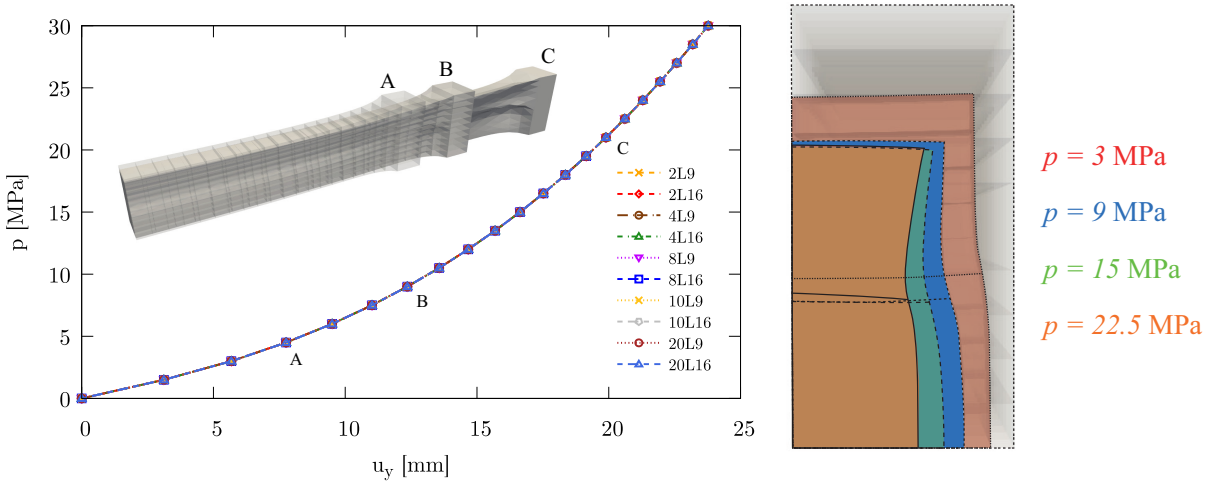

(a) Equilibrium path **(b)** Cross-section kinematics for 10L16

Figure 8.31: Multilayered fiber-reinforced 0°/90° laminated beam, uniaxial tension test: equilibrium path, transversal displacement u_y versus applies load p. Comparison between paths obtained adopting different cross-section kinematics.

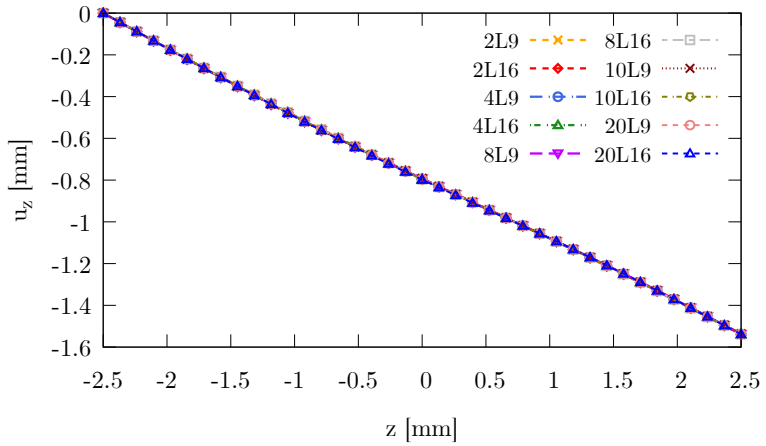

Figure 8.32: Multilayered fiber-reinforced 0°/90° laminated beam, uniaxial tension test: through-the-thickness transversal displacement u_z distribution, measured at the symmetry section for $x = 0$ mm, obtained with different cross-section kinematics.

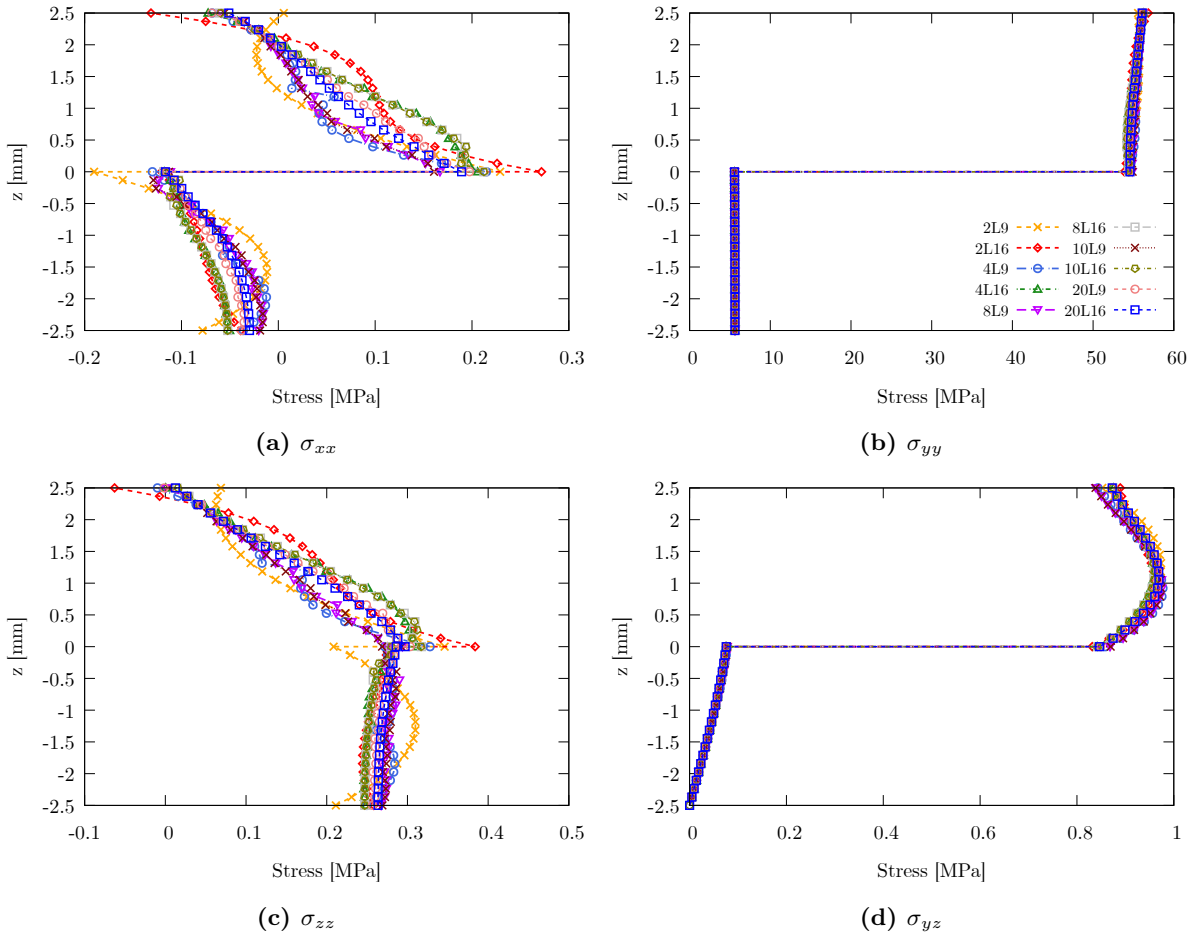

(a) σ_{xx} **(b)** σ_{yy}

(c) σ_{zz} **(d)** σ_{yz}

Figure 8.33: Multilayered fiber-reinforced 0°/90° laminated beam, uniaxial tension test: through-the-thickness stress components distribution, measured at $y = 2.5$ mm and $x = 0$ mm, for an applied traction pressure of $p = 13.5$ MPa.

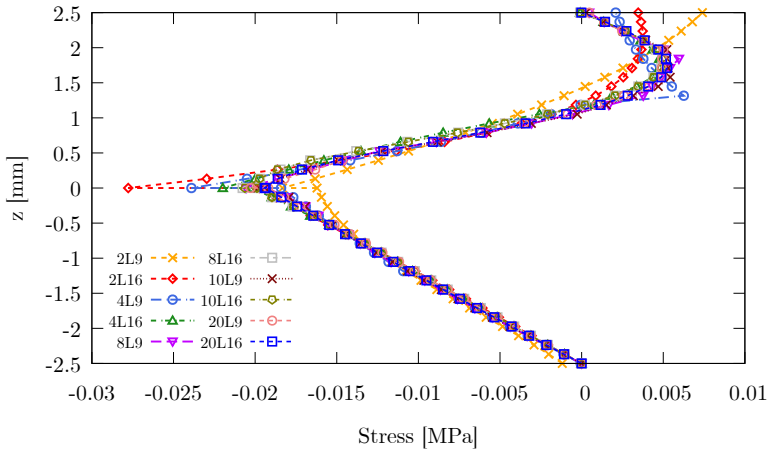

Figure 8.34: Multilayered fiber-reinforced 0°/90° laminated beam, uniaxial tension test: through-the-thickness distribution of P_{yz} component, measured at $y = 2.5$ mm and $x = 0$ mm, for an applied traction pressure of $p = 13.5$ MPa.

8.5 Multilayered laminated $0°/45°/-45°/0°$ reinforced beam

The final case study in the transversely isotropic hyperelastic modeling concerns the static analysis of a multilayered four-layer laminated beam. The following investigations once again focus on the influence of the adopted structural theory on the mechanical response of the structure. Two different configurations are again considered to analyze both the effects of large displacements and strains, in pure bending and stretching problems. In the first configuration, a cantilever beam with a square cross-section, with total length $L_b = 100$ mm and lateral side $a = 10$ mm, is subjected to a uniform transverse pressure applied on the top surface, as illustrated in Fig. 8.35(a). In the second configuration, a beam of length $L_s = 50$ mm and lateral side $a = 10$ mm is analyzed under a uniform uniaxial traction pressure, as shown in Fig. 8.35(b). The beam consists of four layers of equal thickness, $h_l = a/4$, each with different fiber orientations. Due to the symmetry of both the geometry and the applied loads, only one-fourth of the structure is modeled in the numerical analyses.

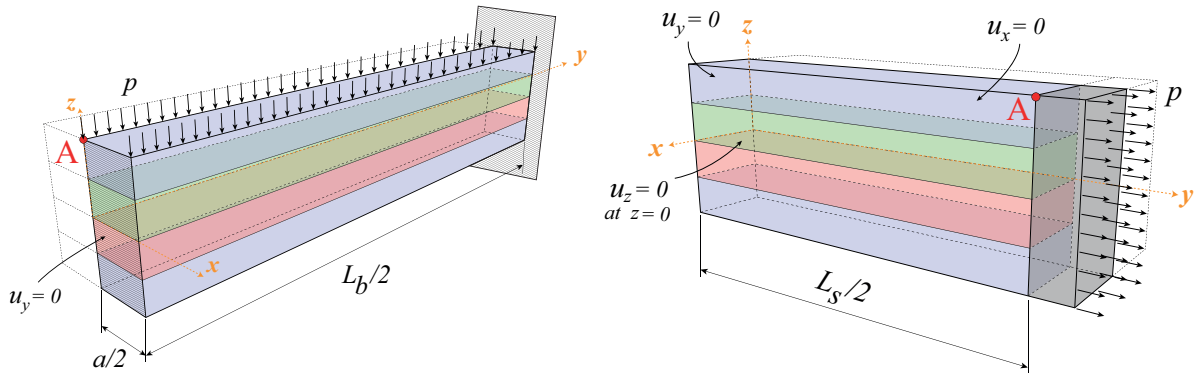

(a) Bending problem **(b)** Uniaxial test problem

Figure 8.35: Multilayered fiber-reinforced $0°/45°/-45°/0°$ laminated beam: geometrical features and boundary conditions.

The material behavior is described using the same strain energy function introduced in Sec. 8.4; hence, Eq. (8.11) is adopted once again. The material parameters are $\mu = 1$ MPa, $\lambda = 4$ MPa, and $\gamma = 0.375$ MPa, consistent with the previous studies. The structure consists of four fibrous soft-material layers, with fiber orientations varying within the x–y plane. The continuous fiber reinforcement, defined in the anisotropic hyperelastic constitutive model, is represented by the unit vector $\boldsymbol{a}_0 = (\sin\theta, \cos\theta, 0)$, where θ is measured from the y axis in the x–y plane. The global stacking sequence, from the bottom to the top layer, is $0°/45°/-45°/0°$. As performed in the previous analyses, for convergence reasons, again 20 B4 cubic finite elements are adopted for the discretization of the beam axis. The influence of different cross-section expansions is again analyzed, due to the presence of higher-order effects in the cross-sectional behavior at large strain, modeling the beam sub-domains adopting again parabolic L9 (nine-node) and cubic L16 (sixteen-node) polynomials. The computational cost is again quantified in terms of the total number of degrees of freedom of the adopted discretization.

8.5.1 Uniform transverse pressure

Table 8.4 shows the numerical results for the transversal displacement u_z, evaluated at point "A" of the beam shown in Fig. 8.35(a) in correspondence of the symmetry section, evaluated in

the reported load conditions. The results are provided for different values of the applied transversal pressure, comparing the solutions obtained with various cross-section expansion models. Figure 8.36 shows the equilibrium path computed using the previously introduced discretization models along the beam cross-section. The analysis is carried out through a static solver with an arc-length type constraint. From the small-displacement regime to the moderate/large-displacement regime, the numerical solutions exhibit an excellent agreement among all the considered discretization models. Figure 8.37 illustrates the through-the-thickness distribution of the transversal displacement u_z, measured at the x-symmetry section for $y = 5$ mm, near the y-symmetry section, for the considered discretization models. Again, in terms of displacement distribution, perfect agreements among solution is observed but convergence has to be discussed also in terms of stress distributions.

	$-u_z$ [mm]				
Model	$p = 6.01$ kPa	$p = 35.02$ kPa	$p = 156.84$ kPa	$p = 455.65$ kPa	**DOFs**
4L9	3.9373	13.2365	26.8623	42.2488	4941
4L16	3.9414	13.2501	26.8891	42.2975	9516
8L9	3.9398	13.2444	26.8772	42.2855	9333
8L16	3.9421	13.2523	26.8935	42.3096	18300
8L92	3.9414	13.2501	26.8891	42.2975	15555
8L162	3.9414	13.2501	26.8891	42.2975	32025
12L9	3.9403	13.2460	26.8801	42.2933	13725
12L16	3.9422	13.2528	26.8945	42.3107	27084
16L9	3.9405	13.2467	26.8813	42.2957	18117
16L16	3.9423	13.2529	26.8948	42.3113	35868

Table 8.4: Multilayered fiber-reinforced $0°/45°/-45°/0°$ laminated beam, uniform transverse pressure case: convergence analysis, transversal displacement component $-u_z$ measured at the symmetry plane. Comparison between various cross-section LE models adopted for different load conditions.

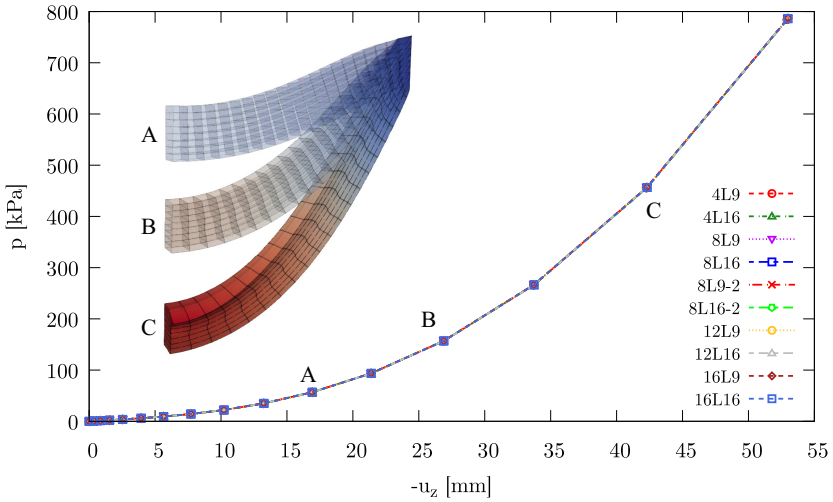

Figure 8.36: Multilayered fiber-reinforced $0°/45°/-45°/0°$ laminated beam, uniform transverse pressure case: equilibrium path, transversal displacement $-u_z$ versus applies load p. Comparison between paths obtained adopting different cross-section kinematics.

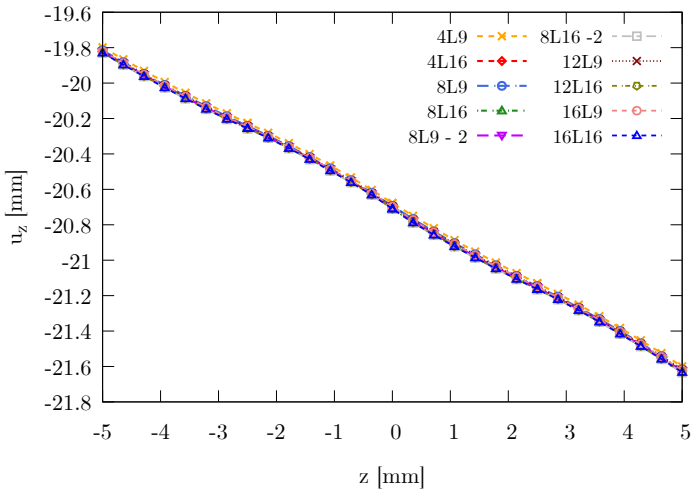

Figure 8.37: Multilayered fiber-reinforced $0°/45°/-45°/0°$ laminated beam, uniform transverse pressure case: through-the-thickness transversal displacement u_z distribution, measured at the symmetry section for $x = 0$ mm, at the section at $y = 20$ mm, obtained with different cross-section kinematics.

Figure 8.38 show the through-the-thickness distribution of the normal stress components under a uniform transverse pressure of $p = 156.85$ kPa. The stresses are again evaluated along the x-symmetry section at $y = 20$ mm. In particular, the proposed results in terms of the Cauchy stress components and the corresponding first Piola–Kirchhoff stress components are discussed in terms of compatibility and equilibrium requirements for further considerations. For the same loading condition of $p = 156.85$ kPa, Fig. 8.39 shows the through-the-thickness distribution of the transverse normal and shear first Piola-Kirchhoff stress components. Overall, the results are in a good agreement across the different cross-section kinematic models in the case of P_{yz} where minor discrepancies are found in correspondence of the z-symmetry section, with consistent predictions achieved for all proposed cross-section expansion models. However, major discrepancies in the case of P_{xz} appear when coarser cross-section kinematic models are adopted in the finite element definition. In particular, one can observe that some models are not able to handle correctly equilibrium conditions at beam edges, even if compatibility and stress continuity is guaranteed. The normal stress components σ_{yy} and σ_{zz} exhibit a perfect overlap of the computed distributions. As previously discussed, the transverse normal component P_{yz} shown in Fig. 8.39(b) satisfies both compatibility and equilibrium conditions. In contrast, the actual σ_{yz} component shows non-zero transverse shear stresses at the beam edges, which arise from the dead load assumption under conservative (non-follower) loading. Finally, it is reaffirmed that large strains strongly affect the distribution of the first Piola–Kirchhoff stress tensor, since it is computed from the PK2 stress tensor $\mathbf{S}$.

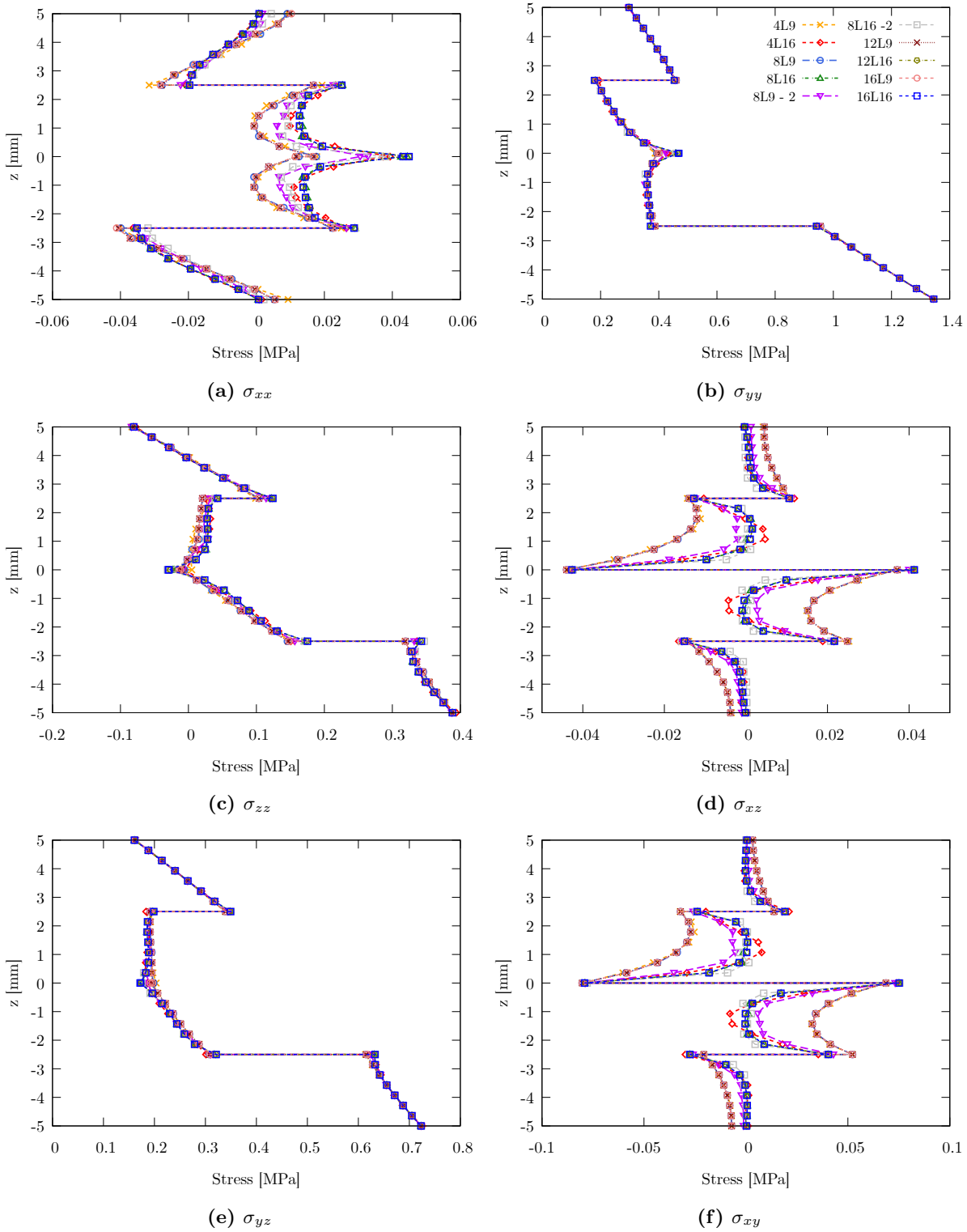

(a) σ_{xx} **(b)** σ_{yy}

(c) σ_{zz} **(d)** σ_{xz}

(e) σ_{yz} **(f)** σ_{xy}

Figure 8.38: Hyperelastic $0°/45°/-45°/0°$ laminate, uniform transversal pressure case: through-the-thickness distribution of normal stress components, measured at $y = 20$ mm and $x = 0$ mm, for an applied transverse pressure of $p = 156.85$ kPa. Comparison between stress components obtained from different cross-section expansion models.

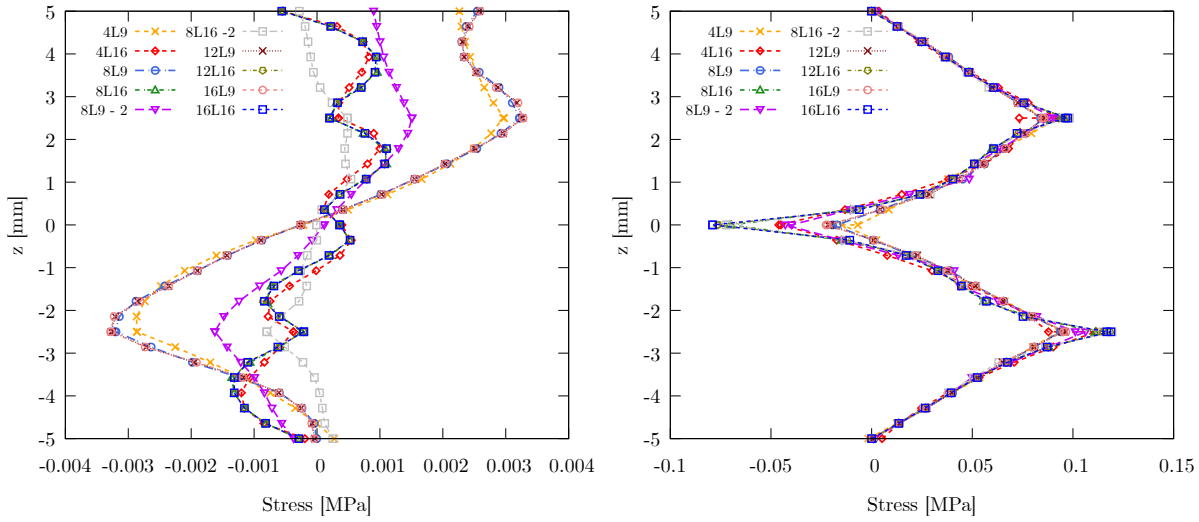

(a) P_{xz} **(b)** P_{yz}

Figure 8.39: Hyperelastic $0°/45°/-45°/0°$ laminate, uniform transversal pressure case: through-the-thickness distribution of transverse normal and shear stress components, measured at $y = 20$ mm and $x = 0$ mm, for an applied transverse pressure of $p = 156.85$ kPa. Comparison between stress components obtained from different cross-section expansion models.

8.5.2 Uniform uniaxial tension

The following discussion presents and comments on the results obtained for the uniaxial tension test. Table 8.5 reports the numerical values of the horizontal displacement u_y measured at point "A" of the beam shown in Fig. 8.35(b), specifically at the end section for $y = 25$ mm. In this investigation, the previously discussed cross-section models are adopted within the mathematical formulations. Results are provided for different applied traction pressure values. Figure 8.40(a) illustrates the equilibrium path for the uniaxial tension test, obtained through static analysis with a load-control procedure. The maximum traction pressure is set to $p_{max} = 20$ MPa and applied in 15 equal increments. From the small-strain regime to moderate and large strains, the numerical solutions obtained with the different cross-section models show excellent agreement. Figure 8.40(b) depicts the cross-sectional displacement at the symmetry section, highlighting the influence of the applied traction pressure on local effects such as warping and stretching. Figure 8.41 presents the through-the-thickness distribution of the vertical displacement u_z, measured at the symmetry section ($y = 0$ mm, $x = 0$ mm) under $p = 13.5$ MPa. The results reveal a parabolic profile of the transversal displacement component across the thickness. Figure 8.42 shows the through-the-thickness distribution of the normal stress components for a uniform traction pressure of $p = 8$ MPa. The stresses are evaluated along the x-symmetry section at $y = 5$ mm, comparing the actual Cauchy stress components with the corresponding first Piola–Kirchhoff stress components. Figure 8.43 reports the through-the-thickness distribution of the transverse normal and shear stress components for the same loading condition ($p = 8$ MPa), again evaluated along the x-symmetry section at $y = 5$ mm. The comparison between the Cauchy stress components and the corresponding Piola–Kirchhoff components is also addressed.

In large strain scenarios, the normal σ_{zz} and P_{zz} components present notable disparities, such as discontinuities and variations in global and local gradients when considering different cross-section kinematics. These discrepancies arise due to the influence of significant displacement

Model	u_y [mm]				DOFs
	$p = 4$ MPa	$p = 8$ MPa	$p = 12$ MPa	$p = 16$ MPa	
4L9	17.2623	27.6715	35.3166	41.4984	4941
4L16	17.2956	27.7278	35.3888	41.5829	9516
8L9	17.2678	27.6852	35.3383	41.5272	9333
8L16	17.3004	27.7387	35.4052	41.6044	18300
8L92	17.2949	27.7275	35.3890	41.5837	15555
8L162	17.3045	27.7461	35.4152	41.6164	32025
12L9	17.2689	27.6884	35.3437	41.5350	13725
12L16	17.3008	27.7397	35.4069	41.6066	27084
16L9	17.2692	27.6892	35.3452	41.5371	18117
16L16	17.3009	27.7399	35.4073	41.6072	35868

Table 8.5: Hyperelastic $0°/45°/-45°/0°$ laminate, uniaxial tension test: convergence analysis, horizontal displacement component u_y measured at the point A. Comparison between various cross-section LE models adopted for different load conditions.

derivatives, necessitating the adoption of refined structural theories to accurately compute the deformation gradient $\mathbf{F}$, for which the displacement derivatives are approximated using higher-order shape functions are refined polynomial expression of the displacement field. Consequently, employing coarser discretization schemes for cross-sections may yield inconsistent predictions. The transverse normal component P_{yz} shown in Fig. 8.43(b) is satisfying the compatibility and equilibrium conditions. The necessity of higher-order refined models in large strain hyperelasticity is generally attributed to volumetric locking prevention and computation of physical quantities, such as hydrostatic pressure, without any stabilization technique. A representation of the cross-section warping and deformation along the beam axis is given in Fig. 8.44. These local effects, such as warping and twisting, are captured accurately by refined kinematics. Typically, non-conventional stress distribution within the body arises from these highly deformed states.

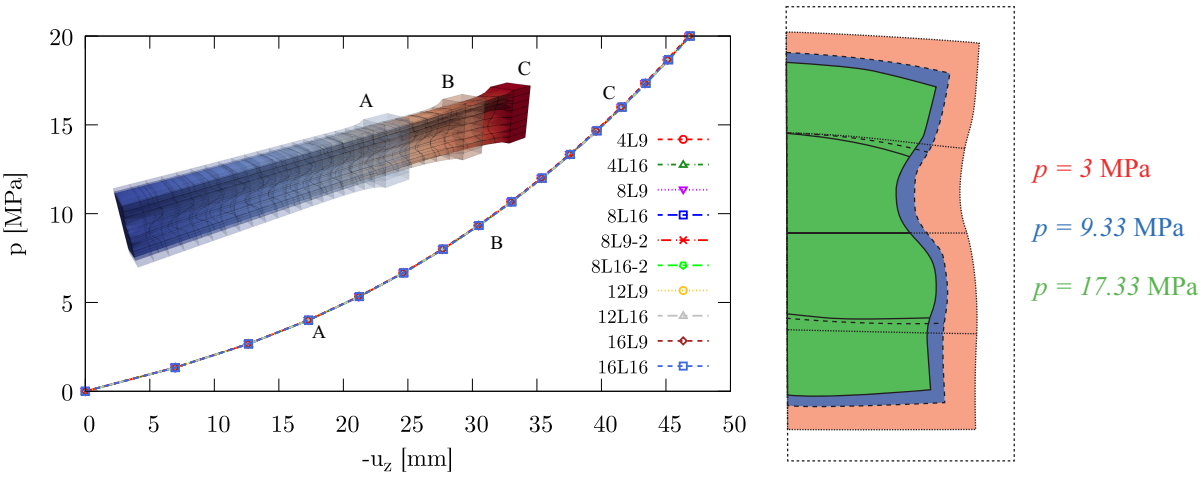

(a) Equilibrium path **(b)** Cross-section kinematics for 10L16

Figure 8.40: Hyperelastic $0°/45°/-45°/0°$ laminate, uniaxial tension test: equilibrium path, transversal displacement u_y versus applies load p. Comparison between paths obtained adopting different cross-section kinematics.

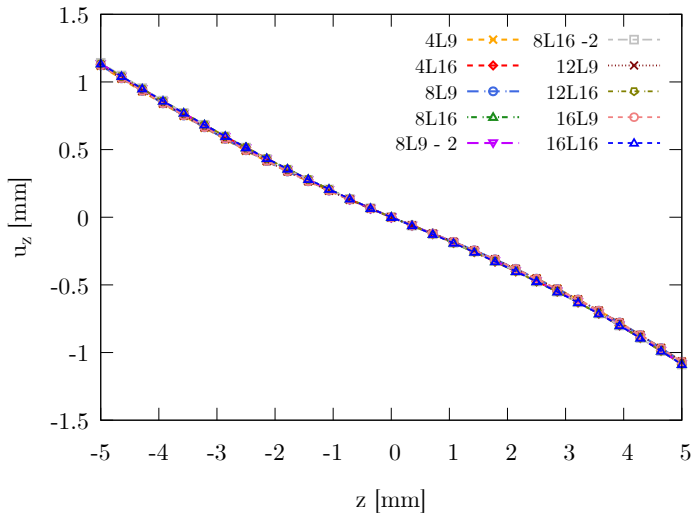

Figure 8.41: Hyperelastic $0°/45°/-45°/0°$ laminate, uniaxial tension test: through-the-thickness transversal displacement u_z distribution, measured at the symmetry section for $x = 0$ mm, obtained with different cross-section kinematics.

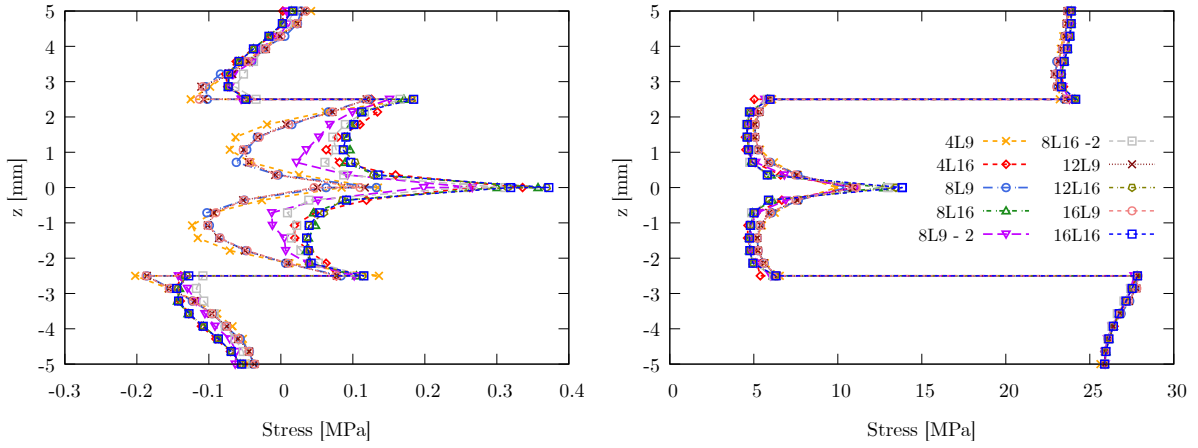

(a) σ_{xx} **(b)** σ_{yy}

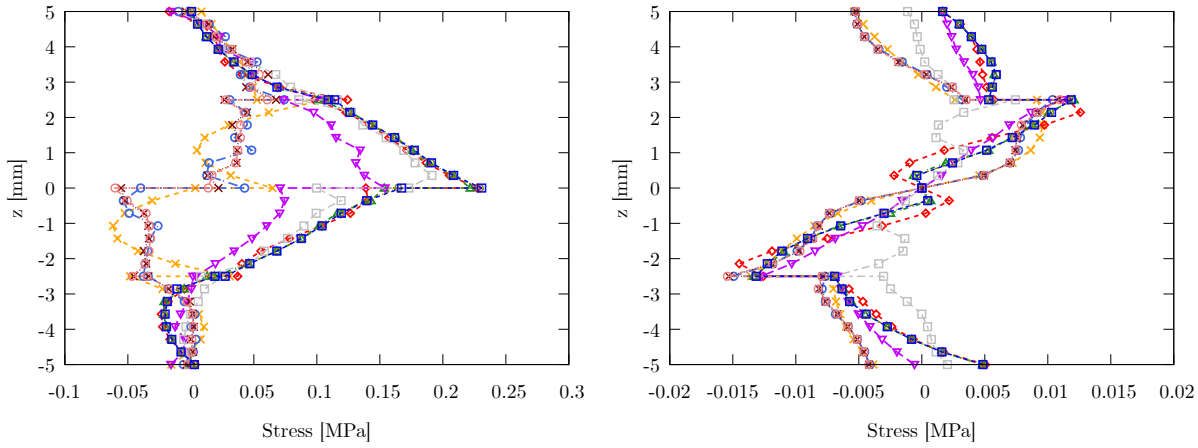

(c) σ_{zz} **(d)** σ_{xz}

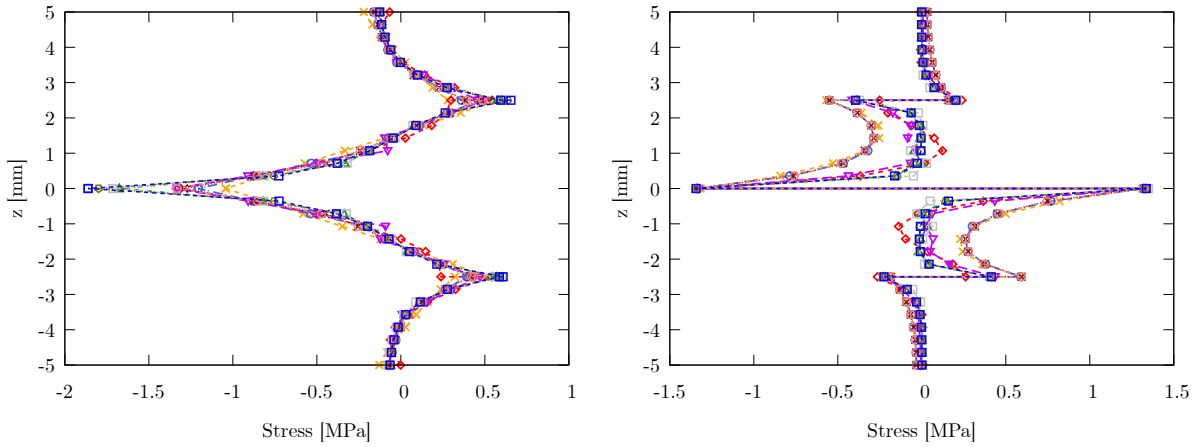

(e) σ_{yz} **(f)** σ_{xy}

Figure 8.42: Hyperelastic $0°/45°/-45°/0°$ laminate, uniaxial tension test: through-the-thickness distribution of normal stress components, measured at $y = 5$ mm and $x = 0$ mm, for an applied traction pressure of $p = 8$ MPa. Comparison between stress components obtained from different cross-section expansion models.

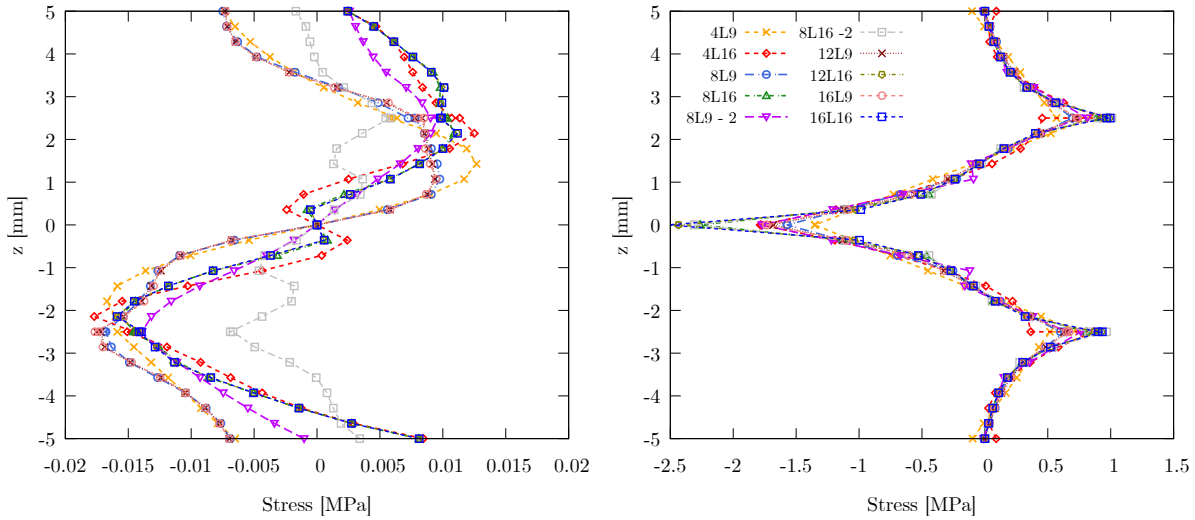

(a) P_{xz} **(b)** P_{yz}

Figure 8.43: Hyperelastic $0°/45°/-45°/0°$ laminate, uniaxial tension test: through-the-thickness distribution of transverse normal and shear stress components, measured at $y = 5$ mm and $x = 0$ mm, for an applied traction pressure of $p = 8$ MPa. Comparison between stress components obtained from different cross-section expansion models.

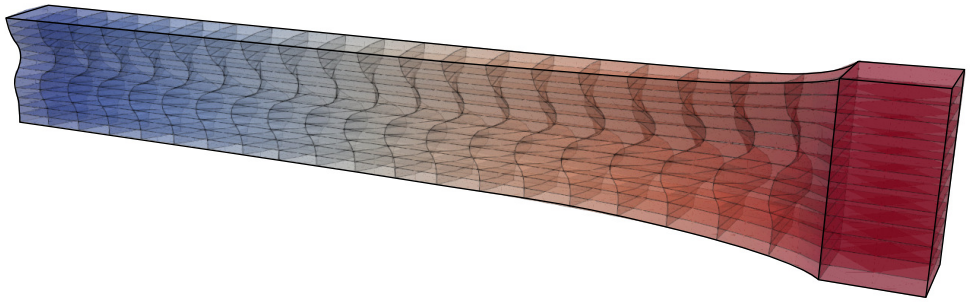

Figure 8.44: Hyperelastic $0°/45°/-45°/0°$ laminate, uniaxial tension test: cross-section kinematics representation for an applied traction pressure of $p = 18.6$ MPa, obtained adopting 12L16 cubic element in the cross-section discretization. Displacement magnitude contour.

8.6 Discussion

The proposed results suggest that:

- The transversely isotropic hyperelastic constitutive law has been successfully implemented in an invariant finite element formulation, including the fiber reinforcement direction via Cartesian unit vectors, and the straightforward implementation of any anisotropic model by means of the structural tensor representation. This approach has been directly integrated within the numerical quadrature procedure, ensuring an accurate representation of complex fiber distributions. Again, a validation against analytical reference solutions has been performed, considering the simple shear test with different fiber orientations. The results, showing perfect agreement between solutions, confirm the robustness of the present implementation.

- The accuracy and the efficiency of the present higher-order modeling of fiber-reinforced soft materials and structures have been further validated through benchmark problems involving multilayered structures under different fiber distributions. While both ESLm and LWm yield accurate displacement distributions and natural frequencies, some inconsistencies in the three-dimensional stress state have been observed when ESLm formulations are adopted in scenarios involving large strains or displacements, due to the limitations of TE–based kinematics. In contrast, the hierarchical enrichment of the displacement field in an LW context, where refined, higher-order approximations of different cross-section or thickness sub-components are defined independently, ensures the accurate computation of displacement gradients and strain invariants, allowing for the correct representation of the anisotropic response of fiber-reinforced hyperelastic structures.

- The fulfillment of the C_z^0 requirements has been extensively analyzed again in terms of both first Piola–Kirchhoff and Cauchy stress tensors. In the case of multilayered configurations, these equilibrium requirements have been satisfied by refined cross-section or thickness expansions, typically more advanced than those employed in the modeling of linear elastic multilayered structures, due to the presence of both geometric and material nonlinearities.

- The computational efficiency and accuracy of the proposed approach have been demonstrated with several case studies involving the large strain analysis of transversely isotropic fiber reinforced structures. Convergence analyses have proven that the adoption of higher-order kinematic models along the beam axis or reference plate mid-surface allows for the definition of computationally advantageous FE models with fewer DOF, while maintaining high levels of accuracy, both in the static and modal cases. In addition, the use of higher-order structural theories and LWm guarantees that the computation of accurate predictions will be less refined discretizations without affecting the solution quality;

- The linearized vibration analyses have highlighted the strong influence of fiber orientation on the modal response of reinforced structures. This effect manifests not only in stiffness variations but also in the modal interaction mechanisms observed in the frequency–pressure response, where crossing and veering of vibration modes occur under large strains. The influence of pre-stretch conditions has also been assessed, showing that the evolution of natural frequencies depends simultaneously on the applied pre-stress and the fiber configuration. These results demonstrate the complex coupling between reinforcement direction, pre-stretch state, and dynamic response, which must be carefully accounted for in predictive modeling.

Chapter 9

Orthotropic hyperelasticity and biological tissue modeling

This section presents several case studies and numerical results for the static and linearized modal analysis of fiber-reinforced hyperelastic materials, with applications to the large displacement and strain analysis of biological tissues. The analyses are performed using the current implementation of higher-order models, which enhances the capabilities of the proposed approach in terms of hyperelastic constitutive modeling and the inclusion of anisotropic effects in the model. The results are compared against reference solutions obtained from conventional 3D finite element models implemented in ABAQUS.

"*[...] A dragon one instant, a butterfly the next, and something indescribable in between.*"

- Leissa A.W. "On a curve veering aberration"
J. Appl. Math. Phys. ZAMP, 25 (1) (1974), pp. 99-111.

9.1 Validation procedure of the present methodology

The first case study analyzed is the simple shear test of an incompressible, fiber-reinforced cubic specimen. As discussed in Sec. 7.1, an analytical solution is available for this simple configuration. These analysis are carried out to validate the proposed methodology, comparing the results with the reference exact solution. This patch-test problem is analyzed with a single element discretization, to assess the consistency of the model implemented. For this reason, in the following, both 1D beam and 2D plate model will be discussed. The mathematical models adopted in this patch-test employ 1L4-1B2 linear models in the case of beam CUF element, and 1Q4-1LE2 linear models in the case of plate CUF element, as already described in Sec. 7.1 . A graphical representation of the two discretization model adopted is provided in Fig. 7.1, instead the geometry and boundary conditions are depicted in Fig. 9.1.

In the following, the material model is written in terms of isotropic matrix contribution, volumetric strain energy function component and an additional anisotropic part depending on both the fiber directions embedded in the material:

$$\Psi = \Psi_{vol}(J) + \Psi_{iso}(\bar{I}_1, \bar{I}_2) + \Psi_{ani}(\bar{I}_1, \bar{I}_2, \bar{I}_4, \bar{I}_5, \bar{I}_6, \bar{I}_7) \tag{9.1}$$

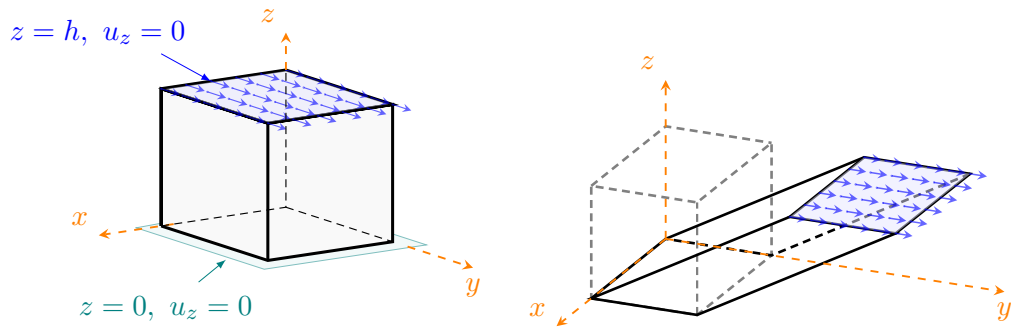

(a) Geometry and boundary conditions **(b)** Deformed configuration

Figure 9.1: Orthotropic hyperelasticity, validation test: geometrical features and boundary conditions considered in the shear test.

The analytical solution of the approached problem is here carried out. Considering the known expression of the deformation gradient, one can straightforwardly derive the expression of the right Cauchy-Green strain tensor and, consequently the analytic expression of the additional pseudo-invariant of the deformation, function of the two independent fiber reinforcement directions, to analytically evaluate the second Piola-Kirchhoff stress tensor by the constitutive law written in the material reference frame, and by the Piola transform compute the expression of the first Piola-Kirchhoff and Cauchy's stress tensors.

Let (x^0, y^0, z^0) the coordinates of the generic material point of the cube in the material configuration, denote also with (x, y, z) the coordinate of the deformed particle measured again the material configuration. For a shear test the deformation field components for the shear problem in the $y - z$ plane are:

$$f(x,y,z): \begin{cases} x = x^0 \\ y = y^0 + \gamma z^0 \\ z = z^0 \end{cases} \qquad \mathbf{F} = \begin{bmatrix} 1 & 0 & 0 \\ 0 & 1 & \gamma \\ 0 & 0 & 1 \end{bmatrix} \qquad \mathbf{C} = \mathbf{F}^T\mathbf{F} = \begin{bmatrix} 1 & 0 & 0 \\ 0 & 1 & \gamma \\ 0 & \gamma & 1+\gamma^2 \end{bmatrix}$$

where γ is a positive real number. Again, since incompressibility is imposed thus $J = \det \mathbf{F} = 1$, the volumetric component of $\mathbf{S}$ is identically null. Supposing again, in the Cartesian material reference frame, that the two fiber reinforcement vectors are $\boldsymbol{a}_0 = (a_x, a_y, a_z)^T$ and $\boldsymbol{g}_0 = (g_x, g_y, g_z)^T$, the invariants and pseudo-invariants required for the computation of physical quantities are:

$$\begin{cases} I_1 = 3 + \gamma^2 \\ I_2 = -3 - 2\gamma^2 \\ I_3 = 1 \end{cases} \qquad \begin{cases} I_4 = a_x^2 + a_y(a_y + a_z\gamma) + a_z(a_y\gamma + a_z(1+\gamma^2)) \\ I_5 = a_x^2 + a_y(a_y + a_z\gamma^2) + a_z(a_y\gamma^2 + a_z(1+\gamma^2)^2) \\ I_6 = g_x^2 + g_y(g_y + g_z\gamma) + g_z(g_y\gamma + g_z(1+\gamma^2)) \\ I_7 = g_x^2 + g_y(g_y + g_z\gamma^2) + g_z(g_y\gamma^2 + g_z(1+\gamma^2)^2) \end{cases}$$

Note that, since $J = 1$, $I_j = \bar{I}_j$, thus the strain energy function adopted is conveniently adopted for the derivative computation without any particular algebraic manipulation. Independently of the mathematical model adopted for the strain energy function model, the normal and transverse shear stress components can be straighforwrdly defined following the constitutive law in the decoupled approach, whose analytical expression are given by:

$$
\begin{aligned}
S_{xx} &= -\frac{2}{3}\Bigg[a_z^2\frac{\partial\bar{\Psi}}{\partial\bar{I}_4}+2a_z^2\frac{\partial\bar{\Psi}}{\partial\bar{I}_5}-2a_x^2\left(\frac{\partial\bar{\Psi}}{\partial\bar{I}_4}+2\frac{\partial\bar{\Psi}}{\partial\bar{I}_5}\right)+\frac{\partial\bar{\Psi}}{\partial\bar{I}_1}\gamma^2+a_z^2\frac{\partial\bar{\Psi}}{\partial\bar{I}_4}\gamma^2+6a_z^2\frac{\partial\bar{\Psi}}{\partial\bar{I}_5}\gamma^2+\\
&+ 2a_z^2\frac{\partial\bar{\Psi}}{\partial\bar{I}_5}\gamma^4+a_y^2\left(\frac{\partial\bar{\Psi}}{\partial\bar{I}_4}+2\frac{\partial\bar{\Psi}}{\partial\bar{I}_5}(1+\gamma^2)\right)+2a_ya_z\gamma\left(\frac{\partial\bar{\Psi}}{\partial\bar{I}_4}+2\frac{\partial\bar{\Psi}}{\partial\bar{I}_5}(2+\gamma^2)\right)+2\frac{\partial\bar{\Psi}}{\partial\bar{I}_7}\gamma^2g_y^2+\\
&- \left(\frac{\partial\bar{\Psi}}{\partial\bar{I}_6}+2\frac{\partial\bar{\Psi}}{\partial\bar{I}_7}\right)(2g_x^2-g_y^2)+2\gamma\left(\frac{\partial\bar{\Psi}}{\partial\bar{I}_6}+2\frac{\partial\bar{\Psi}}{\partial\bar{I}_7}(2+\gamma^2)\right)g_yg_z+\left(\frac{\partial\bar{\Psi}}{\partial\bar{I}_6}+2\frac{\partial\bar{\Psi}}{\partial\bar{I}_7}+\right.\\
&+ \left.\left(\frac{\partial\bar{\Psi}}{\partial\bar{I}_6}+6\frac{\partial\bar{\Psi}}{\partial\bar{I}_7}\right)\gamma^2+2\frac{\partial\bar{\Psi}}{\partial\bar{I}_7}\gamma^4\right)g_z^2\Bigg] \qquad (9.2)
\end{aligned}
$$

$$
\begin{aligned}
S_{yy} &= \frac{1}{3}\Bigg[-2(1+\gamma^2)\left(\frac{\partial\bar{\Psi}}{\partial\bar{I}_1}+a_x^2\left(\frac{\partial\bar{\Psi}}{\partial\bar{I}_4}+2\frac{\partial\bar{\Psi}}{\partial\bar{I}_5}\right)+\left(\frac{\partial\bar{\Psi}}{\partial\bar{I}_6}+2\frac{\partial\bar{\Psi}}{\partial\bar{I}_7}\right)g_x^2\right)-4\gamma(1+\gamma^2)\left(a_y^2\frac{\partial\bar{\Psi}}{\partial\bar{I}_5}\gamma+\right.\\
&+ a_z^2\frac{\partial\bar{\Psi}}{\partial\bar{I}_5}\gamma+a_ya_z\left(\frac{\partial\bar{\Psi}}{\partial\bar{I}_4}+\frac{\partial\bar{\Psi}}{\partial\bar{I}_5}(2+\gamma^2)\right)+\frac{\partial\bar{\Psi}}{\partial\bar{I}_7}\gamma g_y^2+\left(\frac{\partial\bar{\Psi}}{\partial\bar{I}_6}+\frac{\partial\bar{\Psi}}{\partial\bar{I}_7}(2+\gamma^2)\right)g_yg_z+\frac{\partial\bar{\Psi}}{\partial\bar{I}_7}\gamma g_z^2\Bigg)+\\
&- 2(-2+\gamma^2)\left(\frac{\partial\bar{\Psi}}{\partial\bar{I}_1}+a_y^2\left(\frac{\partial\bar{\Psi}}{\partial\bar{I}_4}+2\frac{\partial\bar{\Psi}}{\partial\bar{I}_5}\right)+2a_ya_z\frac{\partial\bar{\Psi}}{\partial\bar{I}_5}\gamma+g_y\left(\frac{\partial\bar{\Psi}}{\partial\bar{I}_6}g_y+2\frac{\partial\bar{\Psi}}{\partial\bar{I}_7}(g_y+\gamma g_z)\right)\right)+\\
&- 2(1+\gamma^2)^2\left(\frac{\partial\bar{\Psi}}{\partial\bar{I}_1}+a_z^2\frac{\partial\bar{\Psi}}{\partial\bar{I}_4}+2a_z\frac{\partial\bar{\Psi}}{\partial\bar{I}_5}(a_z+a_y\gamma+a_z\gamma^2)+\frac{\partial\bar{\Psi}}{\partial\bar{I}_6}g_z^2+\right.\\
&+ \left.2\frac{\partial\bar{\Psi}}{\partial\bar{I}_7}g_z(g_z+\gamma(g_y+\gamma g_z))\right)\Bigg] \qquad (9.3)
\end{aligned}
$$

$$
\begin{aligned}
S_{zz} &= \frac{1}{3}\Bigg[-2\left((a_x^2+a_y^2-2a_z^2)\left(\frac{\partial\bar{\Psi}}{\partial\bar{I}_4}+2\frac{\partial\bar{\Psi}}{\partial\bar{I}_5}\right)+2a_ya_z\left(\frac{\partial\bar{\Psi}}{\partial\bar{I}_4}+\frac{\partial\bar{\Psi}}{\partial\bar{I}_5}\right)\gamma+\right.\\
&+ \left(\frac{\partial\bar{\Psi}}{\partial\bar{I}_1}+a_z^2\frac{\partial\bar{\Psi}}{\partial\bar{I}_4}+2a_y^2\frac{\partial\bar{\Psi}}{\partial\bar{I}_5}\right)\gamma^2+4a_ya_z\frac{\partial\bar{\Psi}}{\partial\bar{I}_5}\gamma^3+2a_z^2\frac{\partial\bar{\Psi}}{\partial\bar{I}_5}\gamma^4+\left(\frac{\partial\bar{\Psi}}{\partial\bar{I}_6}+2\frac{\partial\bar{\Psi}}{\partial\bar{I}_7}\right)g_x^2\Bigg)+\\
&- 2\left(\frac{\partial\bar{\Psi}}{\partial\bar{I}_6}+2\frac{\partial\bar{\Psi}}{\partial\bar{I}_7}(1+\gamma^2)\right)g_y^2-4\gamma\left(\frac{\partial\bar{\Psi}}{\partial\bar{I}_6}+\frac{\partial\bar{\Psi}}{\partial\bar{I}_7}+2\frac{\partial\bar{\Psi}}{\partial\bar{I}_7}\gamma^2\right)g_yg_z+\\
&- \left.2\left(\frac{\partial\bar{\Psi}}{\partial\bar{I}_6}(-2+\gamma^2)+2\frac{\partial\bar{\Psi}}{\partial\bar{I}_7}(-2+\gamma^4)\right)g_z^2\right] \qquad (9.4)
\end{aligned}
$$

$$
S_{xy} = 2\left[a_xa_y\left(\frac{\partial\bar{\Psi}}{\partial\bar{I}_4}+2\frac{\partial\bar{\Psi}}{\partial\bar{I}_5}\right)+a_xa_z\frac{\partial\bar{\Psi}}{\partial\bar{I}_5}\gamma+\left(\frac{\partial\bar{\Psi}}{\partial\bar{I}_6}+2\frac{\partial\bar{\Psi}}{\partial\bar{I}_7}\right)g_xg_y+\frac{\partial\bar{\Psi}}{\partial\bar{I}_7}\gamma g_xg_z\right] \qquad (9.5)
$$

Due to the analytical complexity, the full expressions of the Cauchy's stress components are not reported here, as well as the expressions of the first Piola-Kirchhoff stress tensor, although they can be readily computed by the Piola transform. The consistency and capabilities of the present CUF-based methodology are assessed by analyzing the shear test in six different fiber orientations, considering different generic fiber reinforcement vectors. Three different fiber distributions are here analyzed: (i) two fiber directions laying on the (x, z) plane, considering an angle β_{12} between directions; (ii) two fiber reinforcements along the x and y axes; (iii) two fiber reinforcements along the x and z axes; A graphical representation of the proposed case studies is provided in Fig. 9.2. These proposed fiber distribution cases are then analyzed in different biological tissue models, analyzing different strain energy function models for the numerical simulation of biological tissues.

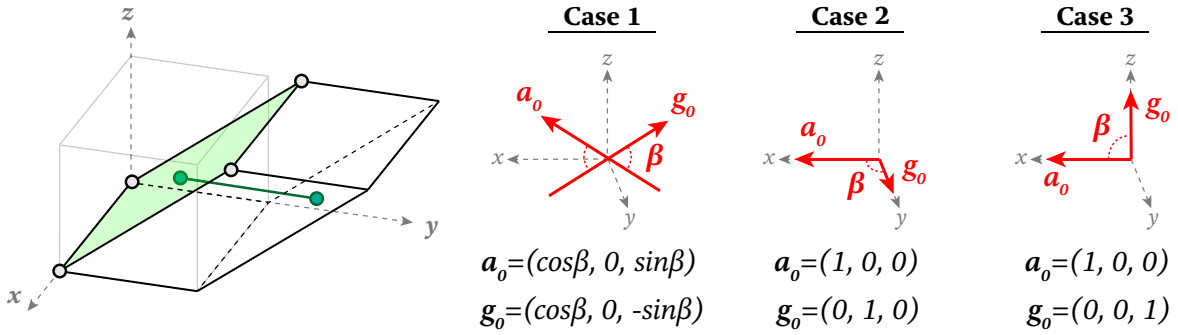

Figure 9.2: Orthotropic hyperelasticity, validation test: geometrical representation of the three fibers configurations analyzed and the representative 1D CUF discretization adopted.

9.1.1 Holzapfel-Gasser-Ogden (HGO) compressible model

The first material model considered is the Holzapfel-Gasser-Ogden (HGO) model for compressible fiber reinforced material, presented in [197], in its decoupled formulation. The three terms of the decoupled strain energy function Eq. (9.1) are then introduced:

$$\Psi_{vol}(I_3) = \frac{K}{2}(J-1)^2 \tag{9.6}$$

$$\Psi_{iso}(I_1, I_2, I_3) = \frac{\mu}{2}(\bar{I}_1 - 1) \tag{9.7}$$

$$\Psi_{aniso}(I_3, I_4, I_5, I_6, I_7) = \frac{k_1}{2k_2}\left(e^{k_2(\bar{I}_4-1)^2} - 1\right) + \frac{k_1}{2k_2}\left(e^{k_2(\bar{I}_6-1)^2} - 1\right) \tag{9.8}$$

In this model, K is the material bulk modulus, μ is the initial infinitesimal shear modulus of the Neo-Hookean isotropic ground-matrix, in which the two fiber reinforcements are continuously embedded. The fiber contributions, characterized by the material constants k_1 and k_2 instead are the load-bearing phase at higher strains [198]. The shear test is then performed, considering the material model proposed here and the material constants listed in Table 9.1, adapted from literature examples. For each case of fiber distribution considered, the nonlinear static analysis is performed to obtain the stretch-stress material response.

Figure 9.3 show the stretch-stress response of the HGO compressible material, in the case of $\mathbf{a}_0 = (\cos\beta, 0, \sin\beta)$ and $\mathbf{g}_0 = (\cos\beta, 0, -\sin\beta)$, where the comparison between the analytical solution and the numerical stress-strain response obtained by 1D beam (a) ad 2D plate (b) models. The same comparison is proposed in Fig. 9.4 for the second fiber distribution case, where $\mathbf{a}_0$ = (1,0,0) and $\mathbf{g}_0$ = (0,1,0). Figure 9.5, finally, depict the same comparison between analytical and numerical model in the third fiber distribution case, where $\mathbf{a}_0$ = (1,0,0) and $\mathbf{g}_0$ = (0,0,1). A perfect match is observed, both 1D beam and 2D plate numerical results perfectly predict the analytical reference solution, for each fiber distribution configuration considered.

K [kPa]	μ [kPa]	k_1 [kPa]	k_2 [-]
$1 \cdot 10^5$	0.33	0.562	0.7112

Table 9.1: Orthotropic hyperelasticity, validation test, compressible HGO model case: material properties adopted.

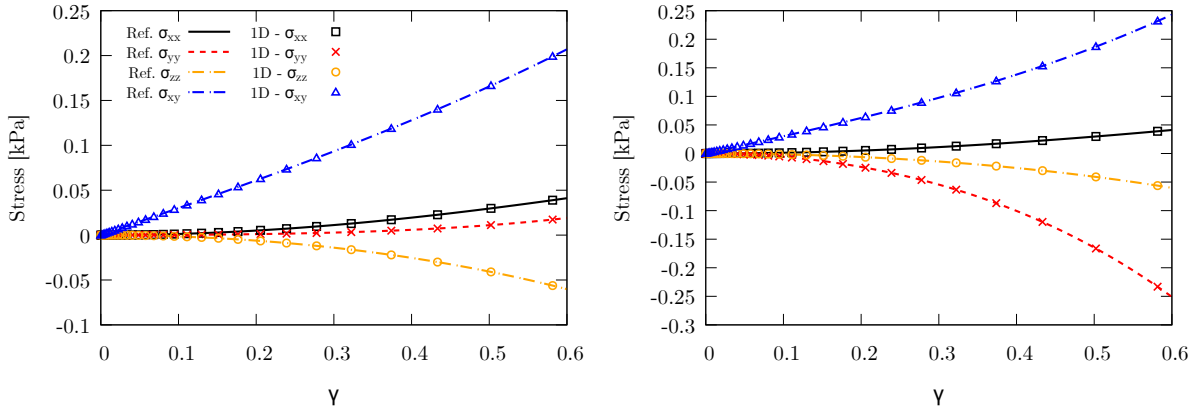

(a) Cauchy's stress $\boldsymbol{\sigma}_{ij}$ **(b)** 2nd Piola-Kirchhoff stress $\mathbf{S}_{ij}$

Figure 9.3: Orthotropic hyperelasticity, validation test, compressible HGO model case: comparison between analytic and 1D beam CUF numerical solution, fiber case (i).

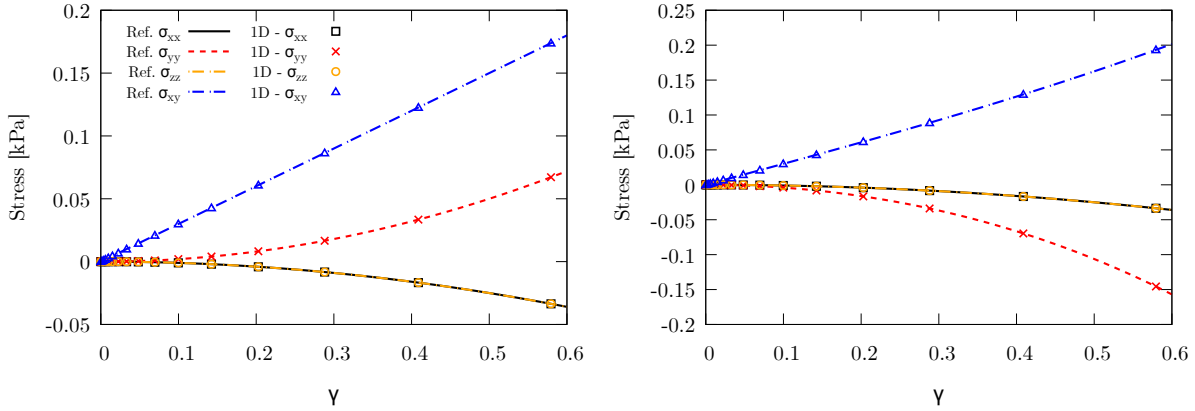

(a) Cauchy's stress $\boldsymbol{\sigma}_{ij}$ **(b)** 2nd Piola-Kirchhoff stress $\mathbf{S}_{ij}$

Figure 9.4: Orthotropic hyperelasticity, validation test, compressible HGO model case: comparison between analytic and 1D beam CUF numerical solution, fiber case (ii).

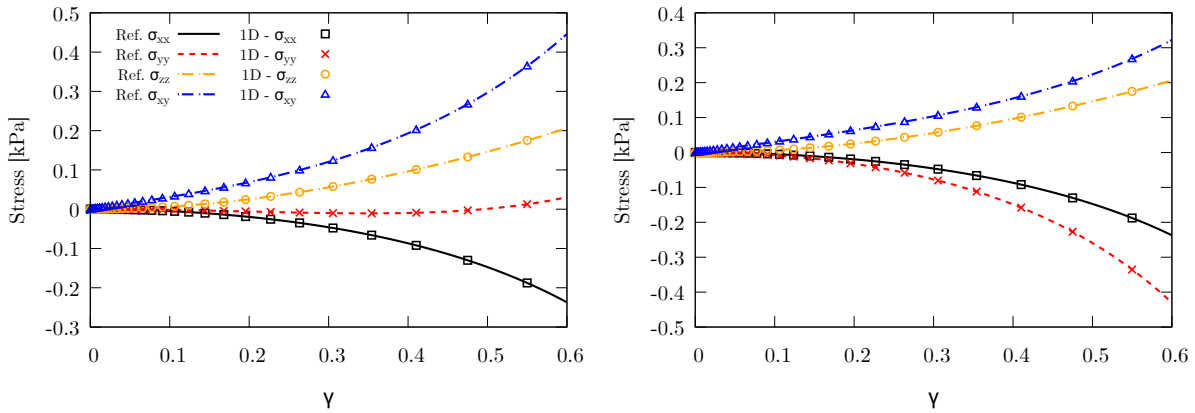

(a) Cauchy's stress $\boldsymbol{\sigma}_{ij}$ **(b)** 2nd Piola-Kirchhoff stress $\mathbf{S}_{ij}$

Figure 9.5: Orthotropic hyperelasticity, validation test, compressible HGO model case: comparison between analytic and 1D beam CUF numerical solution, fiber case (iii).

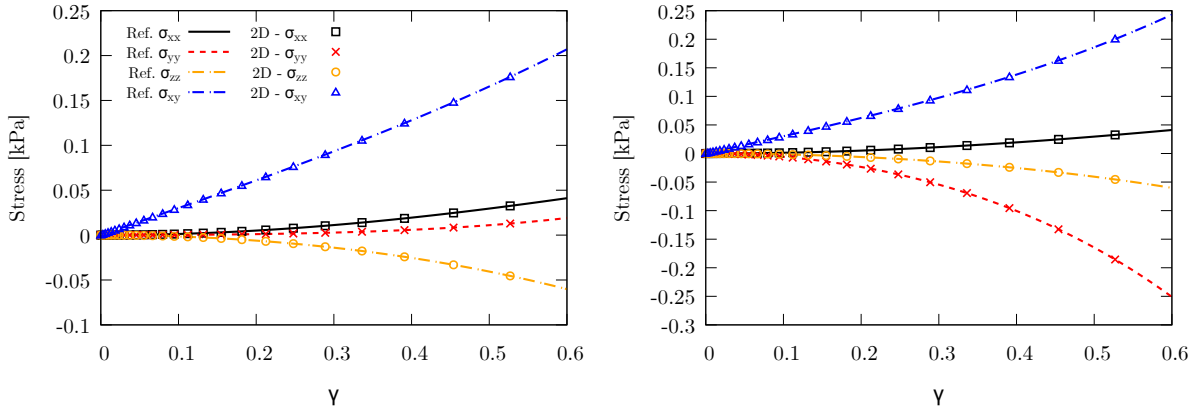

(a) Cauchy's stress $\boldsymbol{\sigma}_{ij}$ **(b)** 2nd Piola-Kirchhoff stress $\mathbf{S}_{ij}$

Figure 9.6: Orthotropic hyperelasticity, validation test, compressible HGO model case: comparison between analytic and 2D plate CUF numerical solution, fiber case (i).

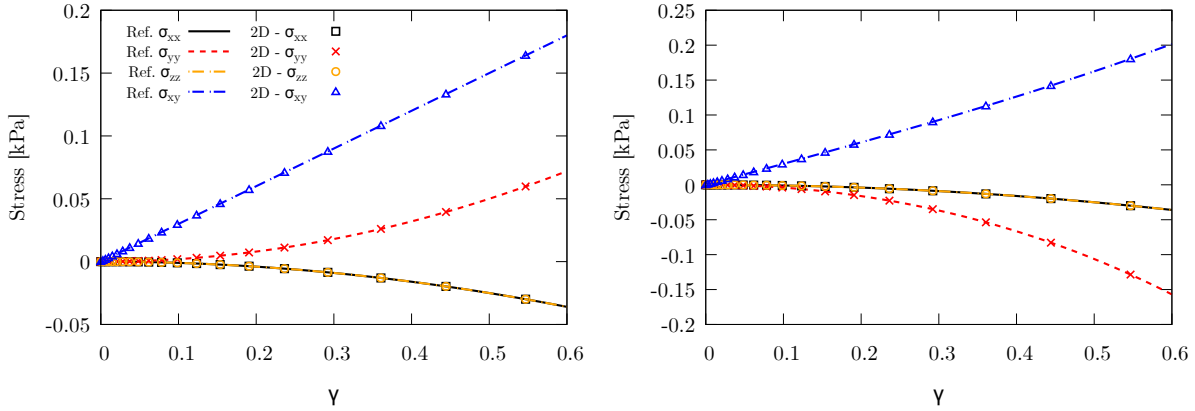

(a) Cauchy's stress $\boldsymbol{\sigma}_{ij}$ **(b)** 2nd Piola-Kirchhoff stress $\mathbf{S}_{ij}$

Figure 9.7: Orthotropic hyperelasticity, validation test, compressible HGO model case: comparison between analytic and 2D plate CUF numerical solution, fiber case (ii).

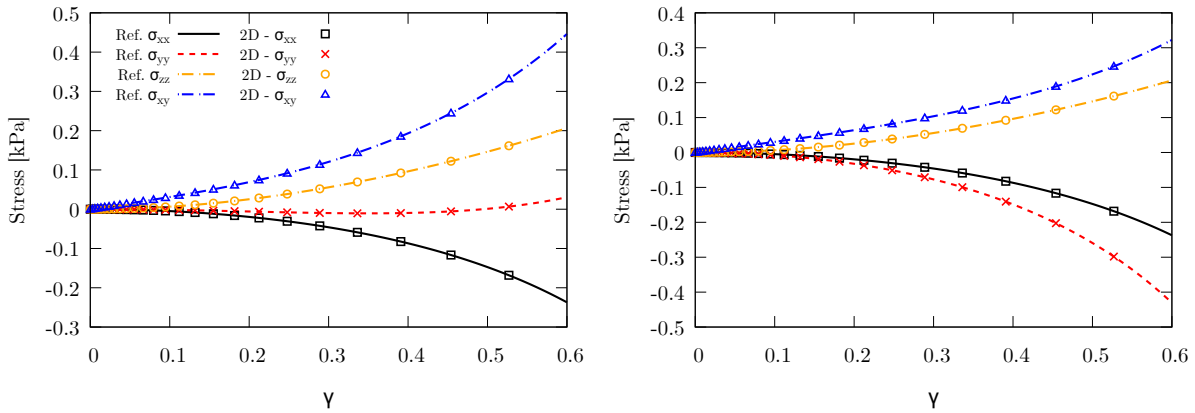

(a) Cauchy's stress $\boldsymbol{\sigma}_{ij}$ **(b)** 2nd Piola-Kirchhoff stress $\mathbf{S}_{ij}$

Figure 9.8: Orthotropic hyperelasticity, validation test, compressible HGO model case: comparison between analytic and 2D plate CUF numerical solution, fiber case (iii).

9.1.2 Holzapfel-Gasser-Ogden (HGO) model for distributed and dispersed fibers

The second material model considered is the Holzapfel-Gasser-Ogden (HGO) model for statistically distributed fibers, considering dispersion effects, presented in [26], in its decoupled formulation. In general, from experimental evidence, it is assumed that the isotropic ground-matrix is the load-carrying phase at small strain, instead the load carrying mechanisms at higher strain is characterized by the collagen fiber embedding [54]. In simple models, where this stiffening effects has been introduced by means of exponential strain energy potentials [197], the embedded collagen has been model with parallel aligned fibres distributions. This assumption can help in models for some particular soft tissue, but is not physically consistent with the micro-structural configurations of different biological tissues, like intima and adventitia layer of an artery, where dispersed fibers are instead observed [26]. The mechanical mechanism of fiber-reinforced with dispersed fibers is still a challenging research topic in the constitutive modeling of soft biological tissue. In the modified HGO model, the dispersion effect of the fibers along their reference direction, indicated by $\mathbf{a}_{0,i}$, is included in the anisotropic potential Eq. (9.8) by means of the structural tensor, following objectivity arguments:

$$\mathbf{H}_i = k\mathbf{I} + (1-3k)\mathbf{a}_{0,i} \otimes \mathbf{a}_{0,i} \quad \rightarrow \quad \bar{E}_i = \mathbf{H}_i : \bar{\mathbf{C}} - 1 = k\bar{I}_1 + (1-3k)\bar{I}_i - 1, \quad i = 4{,}6 \tag{9.9}$$

where k is the dispersion parameter, introduced as a scalar measure of statistically oriented fiber distribution in a global sense, representing the "degree of anisotropy". The isotropic mechanism is represented by considering $k = 1/3$, whereas perfectly aligned fibers along the direction $\mathbf{a}_{0,i}$ correspond to $k = 0$ [26]. In all the other cases, with $0 < k < 1/3$, the dispersion parameter, typically obtained from experimental data, models the effect of fiber dispersion on the mechanical response of the tissue, modeled using a specific orientation probability density functions and three-dimensional dispersion arguments [26], which characterizes the complex behavior through both isotropic and anisotropic invariants. A perfect match is observed, both 1D beam and 2D plate numerical results perfectly predict the analytical reference solution, for each fiber dispersion configuration considered.
The strain energy function model adopted, as proposed by the reference, is:

$$\begin{aligned}
\Psi &= \Psi_g(\bar{\mathbf{C}}) + \Psi_{f,i}(\bar{\mathbf{C}}, \mathbf{H}_i(\mathbf{a}_{0,i}, \bar{\mathbf{C}})) = \\
&= \frac{\mu}{2}(\bar{I}_1 - 3) + \frac{k_1}{2k_2}\left[e^{k_2 E_1^2} - 1\right] + \frac{k_1}{2k_2}\left[e^{k_2 E_2^2} - 1\right] = \\
&= \frac{\mu}{2}(\bar{I}_1 - 3) + \frac{k_1}{2k_2}\left[e^{k_2(k\bar{I}_1 + (1-3k)\bar{I}_4 - 1)^2} - 1\right] + \frac{k_1}{2k_2}\left[e^{k_2(k\bar{I}_1 + (1-3k)\bar{I}_6 - 1)^2} - 1\right]
\end{aligned} \tag{9.10}$$

where $\Psi_g(\bar{\mathbf{C}})$ is the isotropic ground-matrix model, and $\Psi_{f,i}(\bar{\mathbf{C}}, \mathbf{H}_i(\mathbf{a}_{0,i}, \bar{\mathbf{C}}))$ is the anisotropic potential characterized for each embedded fiber family. In the following, a cubic specimen of a representative iliac advential aortic layer is considered, and the associated material parameters, considered from Gasser *et al.* [197] are given by $K = 10^4$ kPa, $\mu = 2.7$ kPa, $k_1 = 5.1$ kPa and $k_2 = 15.4$. To analyze the effects of the fiber dispersion parameter, only the fiber distribution case (iii) has been considered in the following. Figure 9.9 show the stretch-stress response of the HGO model, in the case of $\mathbf{a}_0 = (1{,}0{,}0)$ and $\mathbf{g}_0 = (0{,}0{,}1)$, where the comparison between the analytical solution and the numerical stress-strain response, in terms of 2nd Piola-Kirchhoff stress components, obtained by 1D beam (a) ad 2D plate (b) models is proposed. The same comparison, regarding the Cauchy's stress components obtained for the same test case, is proposed in Fig. 9.10.

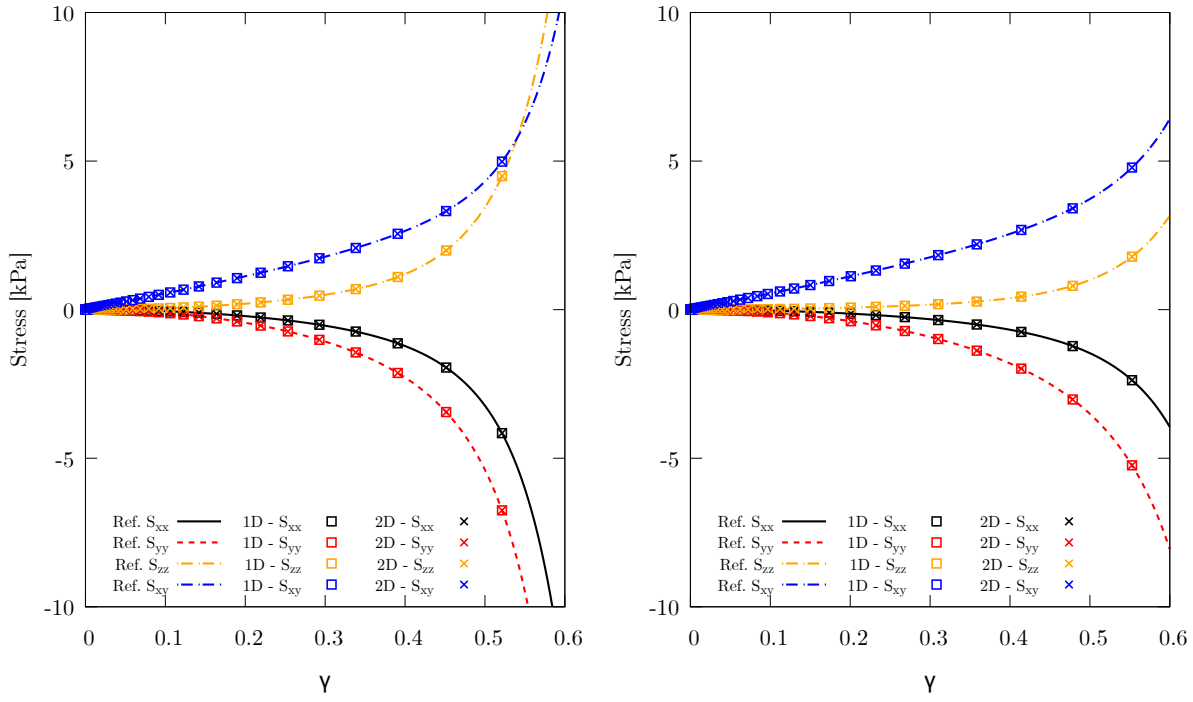

(a) $k = 0$, fibres perfectly aligned

(b) $k = 0.1$

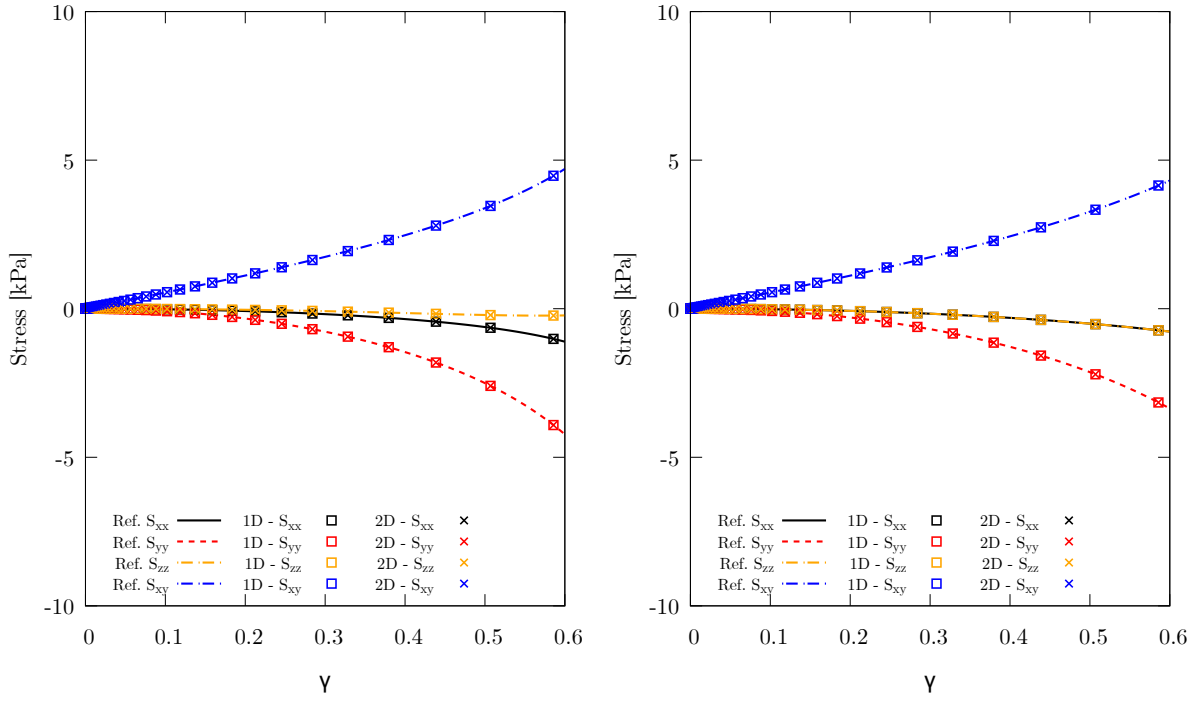

(c) $k = 0.226$

(d) $k = 0.\bar{3}$, fibers perfectly dispersed

Figure 9.9: Orthotropic hyperelasticity, validation test, HGO model for dispersed fibers: comparison between analytic and 1D/2D CUF numerical solutions, considering the two fiber directions along the x and z axis. 2nd Piola-Kirchhoff stress tensor components for different values of the fiber dispersion parameter.

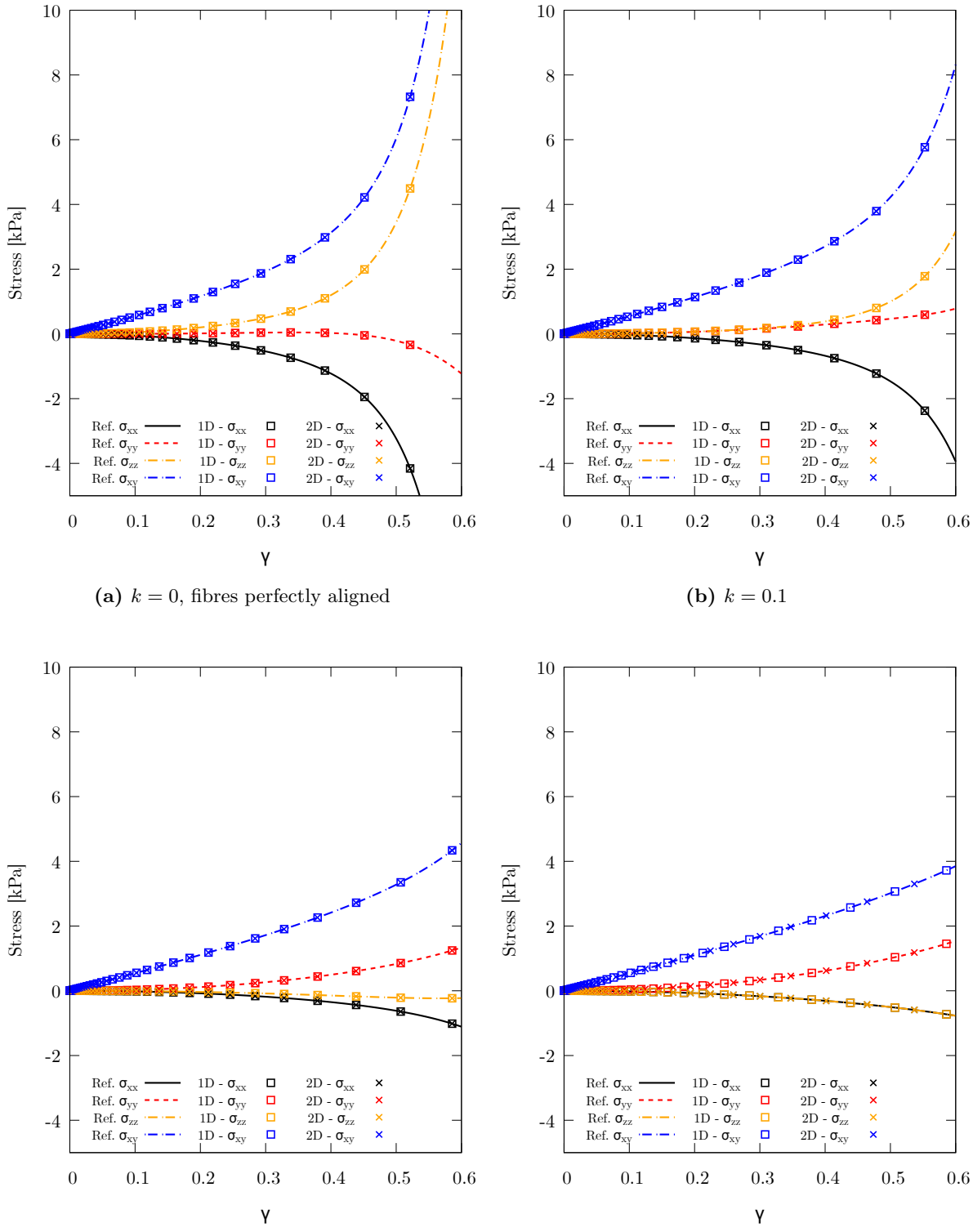

(a) $k = 0$, fibres perfectly aligned

(b) $k = 0.1$

(c) $k = 0.226$

(d) $k = 0.\bar{3}$, fibers perfectly dispersed

Figure 9.10: Orthotropic hyperelasticity, validation test, HGO model for dispersed fibers: comparison between analytic and 1D/2D CUF numerical solutions, considering the two fiber directions along the x and z axis. Cauchy's stress tensor components for different values of the fiber dispersion parameter.

9.2 Effects of large displacements on biological tissue multilayered specimen

In this proposed case study, a numerical model for the large strain analysis a multilayered plate composed of iliac adventitial strips, whose material models has been proposed by Gasser et al. [26], is presented in the CUF framework. The analysis focuses on a biological-like simply-supported plate, analyzing how fiber dispersion and orientation affect the static and linearized vibration responses of the structure. The strain energy function function model is the Holzapfel–Gasser–Ogden (HGO) potential for dispersed fiber proposed in Eq. (9.10), here adopted without any assumption on the tension/compression behavior of collagen fibers:

$$\Psi = \frac{K}{2}\left(\frac{J^2-1}{2} - \log J\right) + \frac{\mu}{2}(\bar{I}_1 - 3) + \sum_{j=4,6} \frac{k_1}{2k_2}\left[e^{k_2(k\bar{I}_1+(1-3k)\bar{I}_j-1)^2} - 1\right] \tag{9.11}$$

where k_1 and k_2 are model constants calibrated from experiments, k is the fiber dispersion parameter, K is the bulk modulus, and μ is the shear modulus of the Neo-Hookean ground-matrix. In the case study, a rectangular plate of two equal thickness layers is analyzed, considering $h_l = 1$ mm for each layer, with dimensions $a = 100$ mm and $b = 50$ mm, as depicted in Fig. 9.11(a). Material parameters are taken from [26], thus $\mu = 7.64$ kPa, $k_1 = 996.6$ kPa, $k_2 = 524.6$, and $K = 38.147$ MPa, with density fixed to a typical value of $\rho = 1300$ kg/m^3. The value of the bulk modulus has been computed and chosen to enforce a nearly incompressible behavior, in a resulting $\nu = 0.4999$. The fiber distribution considered is a two-families straight fibers arranged in the x–y plane, for each layer, as illustrated in Fig. 9.11(b), with different opening angles $\gamma_1 = 45°$ and $\gamma_2 = 30°$.

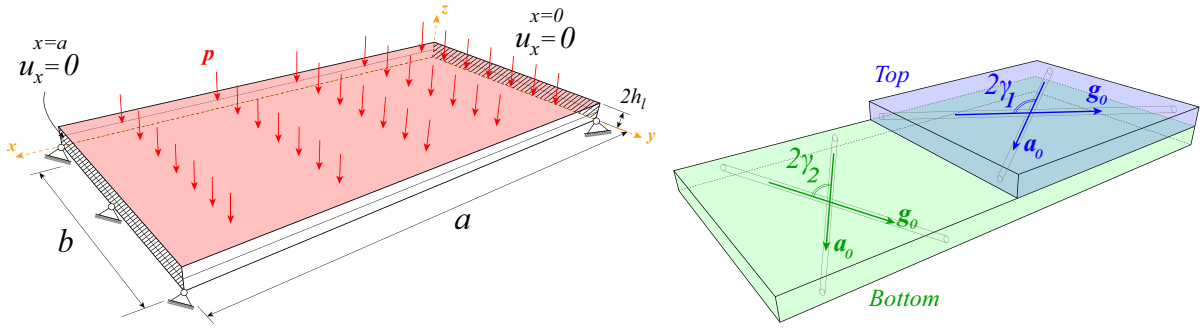

(a) Geometry and boundary conditions. **(b)** Fiber distributions.

Figure 9.11: Multilayered aortic iliac plate: geometry and material characteristics.

Through static, modal, and non-trivial linearized vibration analyses of the presented plate, the capabilities of the present modeling approach and incorporation of anisotropic effects within the FE definition are assessed. To address the mathematical inconsistencies of the built-in HGO implementation in ABAQUS under large deformations [82], a custom `UANISOHYPER_INV` subroutine was developed to implement a more general strain energy function framework within the reference 3D ABAQUS model. This subroutine implements Eq. (9.10) and its derivatives, as suggested in [199], enabling the simulation of fiber-reinforced material models, avoiding the inconsistencies observed regarding the ABAQUS HGO formulation. The results obtained adopting higher-order 2D CUF models and 3D hexahedral FEM solutions are extensively compared to

assess the accuracy and efficiency of the present modeling approach. In ABAQUS, the reference model uses 13924 C3D20 (20-node quadratic brick) elements. Modal analyses are performed around the undeformed equilibrium configuration, in two different material configurations: dispersed fibers case ($k = 0.226$) and perfectly aligned fibers case ($k = 0$). Tables 9.2 and 9.3 summarize the convergence analysis results for the two fiber cases, in which the influence of mid-surface discretization and theory of structure approximation on the first ten natural frequencies is extensively analyzed. In both material configuration considered, 2D CUF models achieve accurate results with up to 8% of the DOF required by the ABAQUS reference mesh (Model E). Afterwards, after an initial assessment of the capabilities of 2D plate model, the static nonlinear analyses of the plates in both material configurations are also conducted, investigating again the same discretization and kinematic assumptions of the modal analysis to assess the effect of midsurface modeling and through-thickness approximation. The accuracy is measured again computing the relative percentage difference against the 3D benchmark, while efficiency is terms of DOF required by the computation.
Figure 9.12(a) depict the equilibrium path for the dispersed fiber case ($k = 0.226$), while Fig. 9.12(b) shows the case of perfectly aligned fibers ($k = 0$). In both, the global load–displacement response is compared with the fully 3D reference solution.

	Parabolic expansion per layer (1 LE2)				**Cubic expansion per layer (1 LE3)**				**ABQ 3D**
Mode	Model A 10×10 Q9	Model C 10×15 Q9	Model E 15×20 Q9	Model G 20×20 Q9	Model B 10×10 Q9	Model D 10×15 Q9	Model F 15×20 Q9	Model H 20×20 Q9	**C3D20**
1	$1.667^{(1.66\%)}$	$1.651^{(0.68\%)}$	$1.645^{(0.35\%)}$	$1.645^{(0.33\%)}$	$1.662^{(1.35\%)}$	$1.646^{(0.36\%)}$	$1.640^{(0.01\%)}$	$1.640^{(0.00\%)}$	1.640
2	$4.612^{(2.69\%)}$	$4.531^{(0.87\%)}$	$4.510^{(0.40\%)}$	$4.509^{(0.38\%)}$	$4.596^{(2.32\%)}$	$4.514^{(0.50\%)}$	$4.493^{(0.02\%)}$	$4.492^{(0.01\%)}$	4.492
3	$4.920^{(0.91\%)}$	$4.899^{(0.49\%)}$	$4.890^{(0.31\%)}$	$4.890^{(0.30\%)}$	$4.899^{(0.48\%)}$	$4.877^{(0.03\%)}$	$4.868^{(0.16\%)}$	$4.867^{(0.17\%)}$	4.875
4	$9.223^{(4.17\%)}$	$8.954^{(1.12\%)}$	$8.895^{(0.46\%)}$	$8.893^{(0.44\%)}$	$9.183^{(3.72\%)}$	$8.913^{(0.66\%)}$	$8.855^{(0.01\%)}$	$8.853^{(0.01\%)}$	8.854
5	$10.025^{(1.20\%)}$	$9.962^{(0.57\%)}$	$9.939^{(0.33\%)}$	$9.938^{(0.32\%)}$	$9.974^{(0.69\%)}$	$9.909^{(0.03\%)}$	$9.886^{(0.21\%)}$	$9.884^{(0.22\%)}$	9.906
6	$15.071^{(2.47\%)}$	$14.933^{(1.53\%)}$	$14.795^{(0.59\%)}$	$14.790^{(0.56\%)}$	$14.994^{(1.95\%)}$	$14.845^{(0.93\%)}$	$14.708^{(0.00\%)}$	$14.704^{(0.03\%)}$	14.708
7	$15.522^{(3.34\%)}$	$15.053^{(0.22\%)}$	$15.041^{(0.14\%)}$	$15.040^{(0.13\%)}$	$15.555^{(3.56\%)}$	$14.973^{(0.31\%)}$	$14.959^{(0.41\%)}$	$14.958^{(0.42\%)}$	15.020
8	$15.641^{(2.67\%)}$	$15.344^{(0.72\%)}$	$15.293^{(0.38\%)}$	$15.291^{(0.37\%)}$	$15.430^{(1.28\%)}$	$15.248^{(0.08\%)}$	$15.196^{(0.26\%)}$	$15.194^{(0.27\%)}$	15.235
9	$19.683^{(1.00\%)}$	$19.604^{(0.60\%)}$	$19.570^{(0.42\%)}$	$19.568^{(0.41\%)}$	$19.528^{(0.21\%)}$	$19.439^{(0.25\%)}$	$19.400^{(0.45\%)}$	$19.398^{(0.46\%)}$	19.488
10	$21.727^{(3.42\%)}$	$21.228^{(1.05\%)}$	$21.111^{(0.49\%)}$	$21.106^{(0.47\%)}$	$21.576^{(2.70\%)}$	$21.072^{(0.30\%)}$	$20.954^{(0.26\%)}$	$20.949^{(0.28\%)}$	21.008
DOFs	6615	9765	19065	25215	9261	13671	26691	35301	234009

Table 9.2: Multilayered aortic iliac plate, dispersed fiber case $k = 0.226$, modal analysis: convergence analysis for the first ten natural frequencies [Hz]. Comparison between 2D CUF and 3D ABAQUS model results. In brackets, the percentage difference is given.

	Parabolic expansion per layer (1 LE2)				**Cubic expansion per layer (1 LE3)**				**ABQ 3D**
Mode	Model A 10×10 Q9	Model C 10×15 Q9	Model E 15×20 Q9	Model G 20×20 Q9	Model B 10×10 Q9	Model D 10×15 Q9	Model F 15×20 Q9	Model H 20×20 Q9	**C3D20**
1	$3.283^{(1.75\%)}$	$3.255^{(0.89\%)}$	$3.243^{(0.54\%)}$	$3.243^{(0.52\%)}$	$3.222^{(0.12\%)}$	$3.191^{(1.08\%)}$	$3.178^{(1.47\%)}$	$3.178^{(1.49\%)}$	3.226
2	$8.630^{(1.96\%)}$	$8.536^{(0.86\%)}$	$8.506^{(0.50\%)}$	$8.505^{(0.49\%)}$	$8.477^{(0.16\%)}$	$8.376^{(1.03\%)}$	$8.344^{(1.41\%)}$	$8.343^{(1.42\%)}$	8.464
3	$10.295^{(0.99\%)}$	$10.257^{(0.62\%)}$	$10.239^{(0.44\%)}$	$10.238^{(0.43\%)}$	$10.150^{(0.43\%)}$	$10.109^{(0.84\%)}$	$10.091^{(1.02\%)}$	$10.090^{(1.02\%)}$	10.194
4	$16.534^{(2.55\%)}$	$16.253^{(0.81\%)}$	$16.187^{(0.40\%)}$	$16.185^{(0.38\%)}$	$16.217^{(0.58\%)}$	$15.918^{(1.27\%)}$	$15.848^{(1.70\%)}$	$15.847^{(1.71\%)}$	16.123
5	$19.917^{(0.87\%)}$	$19.845^{(0.51\%)}$	$19.813^{(0.34\%)}$	$19.812^{(0.34\%)}$	$19.654^{(0.46\%)}$	$19.578^{(0.84\%)}$	$19.548^{(1.00\%)}$	$19.547^{(1.00\%)}$	19.745
6	$27.299^{(3.23\%)}$	$26.674^{(0.86\%)}$	$26.544^{(0.37\%)}$	$26.540^{(0.36\%)}$	$26.778^{(1.25\%)}$	$26.113^{(1.26\%)}$	$25.975^{(1.78\%)}$	$25.972^{(1.79\%)}$	26.446
7	$28.436^{(1.01\%)}$	$28.291^{(0.49\%)}$	$28.240^{(0.31\%)}$	$28.238^{(0.31\%)}$	$28.057^{(0.34\%)}$	$27.910^{(0.86\%)}$	$27.861^{(1.03\%)}$	$27.860^{(1.04\%)}$	28.152
8	$31.812^{(0.09\%)}$	$31.799^{(0.05\%)}$	$31.791^{(0.03\%)}$	$31.790^{(0.02\%)}$	$31.360^{(1.33\%)}$	$31.342^{(1.39\%)}$	$31.331^{(1.42\%)}$	$31.331^{(1.42\%)}$	31.783
9	$33.549^{(0.86\%)}$	$33.448^{(0.56\%)}$	$33.397^{(0.40\%)}$	$33.394^{(0.39\%)}$	$32.900^{(1.09\%)}$	$32.785^{(1.44\%)}$	$32.731^{(1.60\%)}$	$32.729^{(1.61\%)}$	33.263
10	$36.249^{(1.76\%)}$	$35.841^{(0.61\%)}$	$35.739^{(0.32\%)}$	$35.736^{(0.31\%)}$	$35.751^{(0.36\%)}$	$35.344^{(0.78\%)}$	$35.245^{(1.06\%)}$	$35.243^{(1.07\%)}$	35.624
DOFs	6615	9765	19065	25215	9261	13671	26691	35301	234009

Table 9.3: Multilayered aortic iliac plate, perfectly aligned fiber case $k = 0$, modal analysis: convergence analysis for the first ten natural frequencies [Hz]. Comparison between 2D CUF and 3D ABAQUS model results. In brackets, the percentage difference is given.

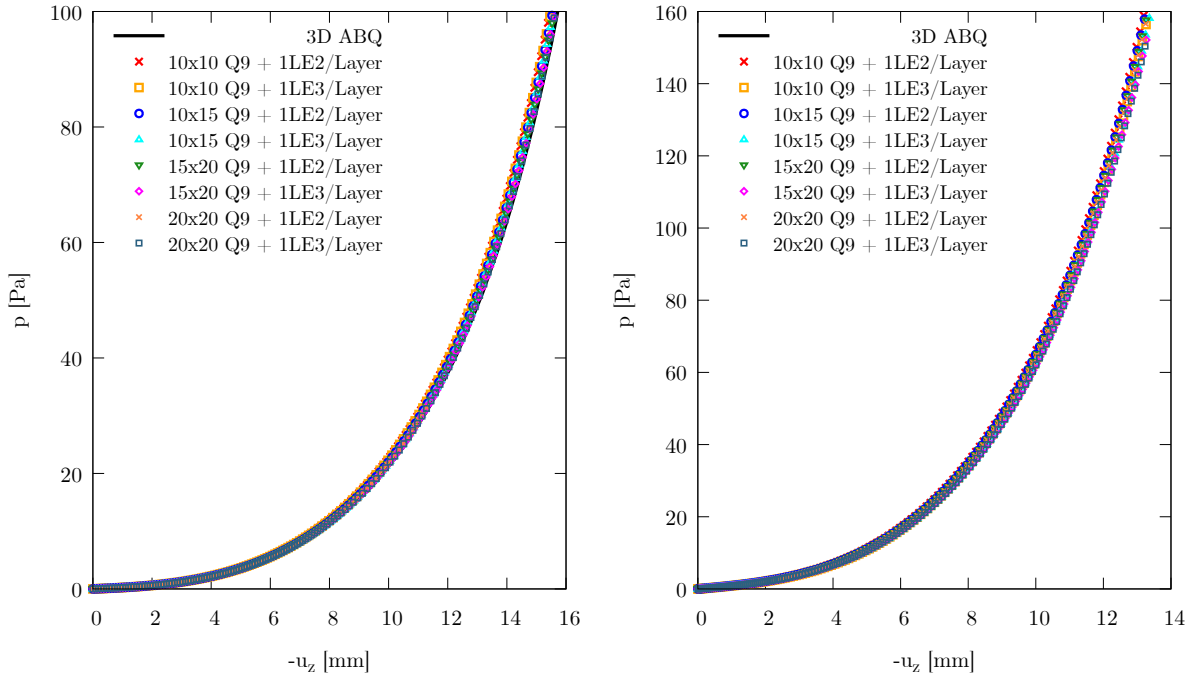

(a) $k = 0.226$ **(b)** $k = 0$

Figure 9.12: Multilayered aortic iliac plate: equilibrium paths obtained of the simply supported plate subjected to uniform traction pressure. Comparison between high-order 2D CUF models and 3D ABAQUS reference solution.

The results of the static nonlinear analysis, as previously discussed, is exploited as the basis for the subsequent non-trivial linearized vibration investigation. For each computed non-trivial equilibrium state, the linearized modal analysis is solved for each computed equilibrium state, in both material conditions scenarios, to assess the influence of fiber dispersion parameters on the modal behavior of the structure when pre-stressed conditions are considered. Figure 9.13 depicts the pressure–frequency curve for the dispersed fiber case ($k = 0.226$) within the small-displacement regime. In particular, Fig. 9.13(a) illustrates the evolution of the first four natural frequencies, while Fig. 9.13(b) reports the corresponding results for the next four modes (fifth to eighth). The same analysis is extended to the full equilibrium path in Fig. 9.14, highlighting modal interactions in the large-strain regime for the multilayered biological plate with dispersed fibers.

The same comparison is proposed in Fig. 9.15 for the converged $20 \times 20 + 1$LE2 model, where results are benchmarked against fully 3D ABAQUS simulations. Specifically, Fig. 9.15(a) compares the first ten natural frequencies across various non-trivial equilibrium states, while Fig. 9.15(b) depicts the overall evolution of the first ten vibration modes. These results reveal distinct modal interactions, which vary between the small- and large-strain regimes.

To further examine these phenomena, the Modal Assurance Criterion (MAC) is analyzed. Figure 9.16 shows MAC matrices comparing the vibration modes of the undeformed reference configuration with those obtained from linearized vibration analyses around selected deformed states (as specified in the figure). The results show that, for slightly deformed configurations in the small-strain regime, the normal modes remain independent, with clear evidence of mode swapping and crossing.

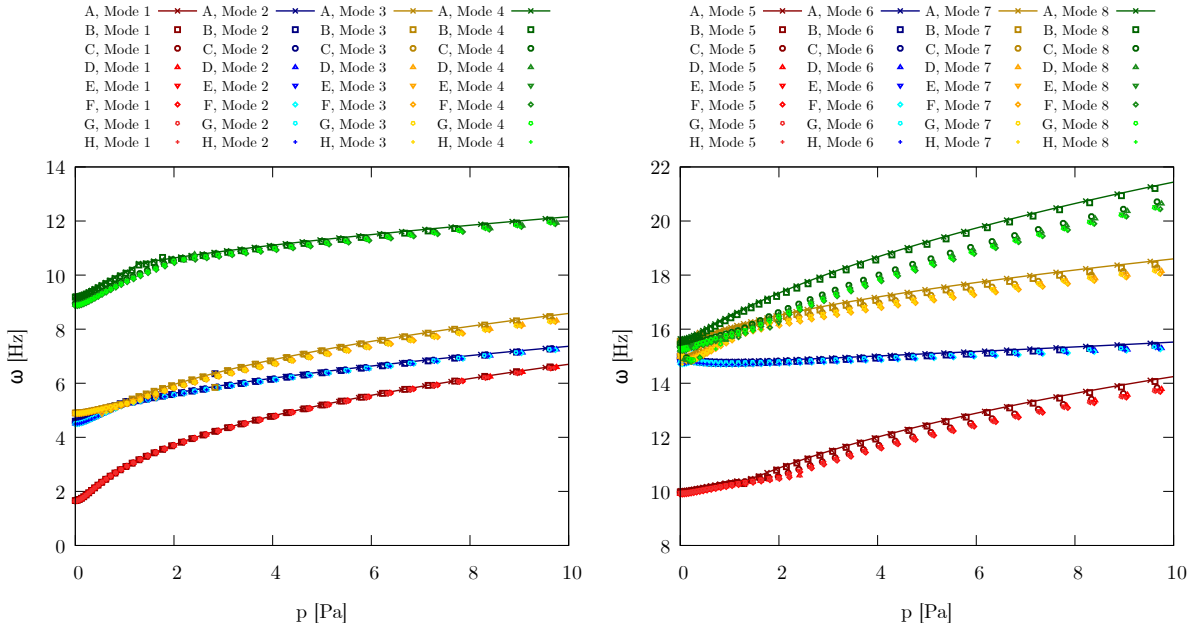

(a) Modes 1-4 **(b)** Modes 5-8

Figure 9.13: Multilayered aortic iliac plate, dispersed fibers case ($k = 0.226$): variation of the first eight natural frequencies along the equilibrium path, small strain regime. Influence of structural theory and reference mid-surface discretization.

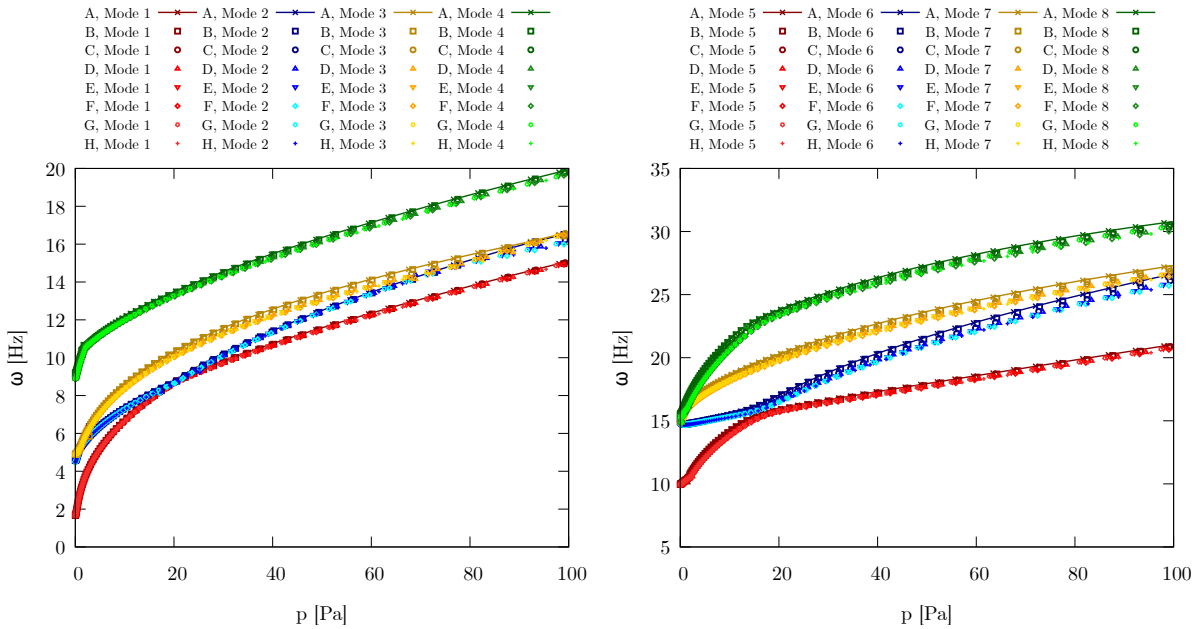

(a) Modes 1-4 **(b)** Modes 5-8

Figure 9.14: Multilayered aortic iliac plate, dispersed fibers case ($k = 0.226$): variation of the first eight natural frequencies along the equilibrium path, large strain regime. Influence of structural theory and reference mid-surface discretization

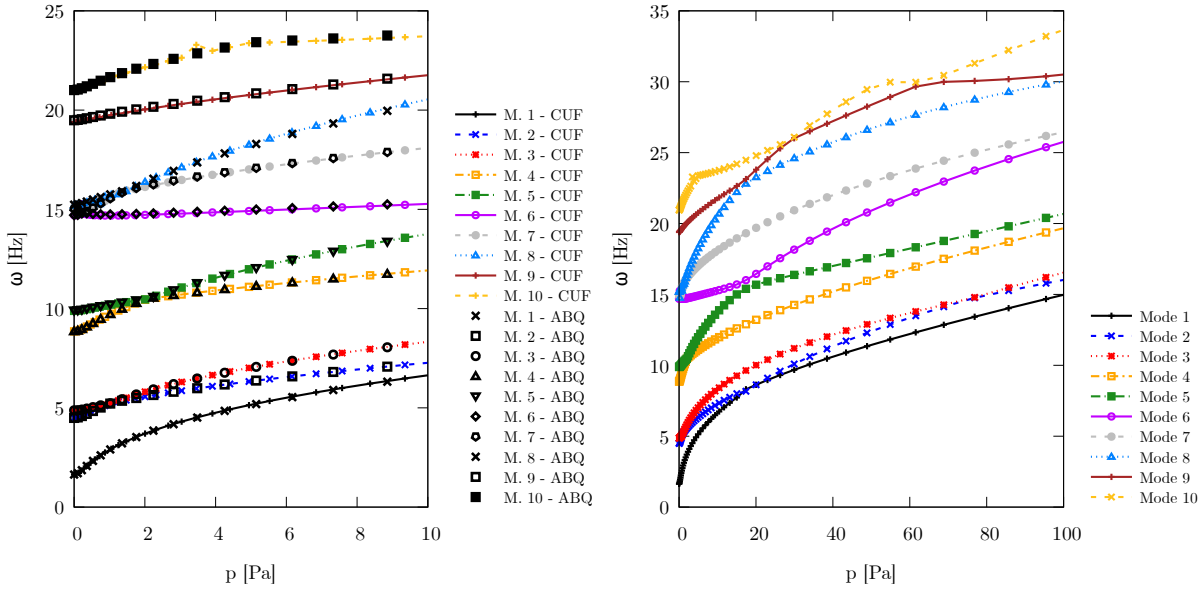

(a) Small strain regime **(b)** Global strain regime

Figure 9.15: Multilayered aortic iliac plate, dispersed fibers case ($k = 0.226$): variation of the first ten natural frequencies along the equilibrium path. Comparison between high-order 2D CUF models and 3D ABAQUS reference solution.

In the large-strain regime, more evident modal interactions are noted, such as the mode 4–5 interaction shown in Fig. 9.16(b). To further characterize this phenomenon, the corresponding vibration modes are illustrated in Fig. 9.17. The modal shapes clearly indicate a veering effect, where the interacting modes lose their original characteristics, giving rise to distinct modal shapes. The fifth and sixth modes, in particular, follow smooth solution paths until they approach each other near $p = 18$ Pa. At this point, instead of intersecting continuously, the two frequency–pressure curves undergo an avoided crossing, each deflecting to follow the trajectory that the other mode would have taken [200].

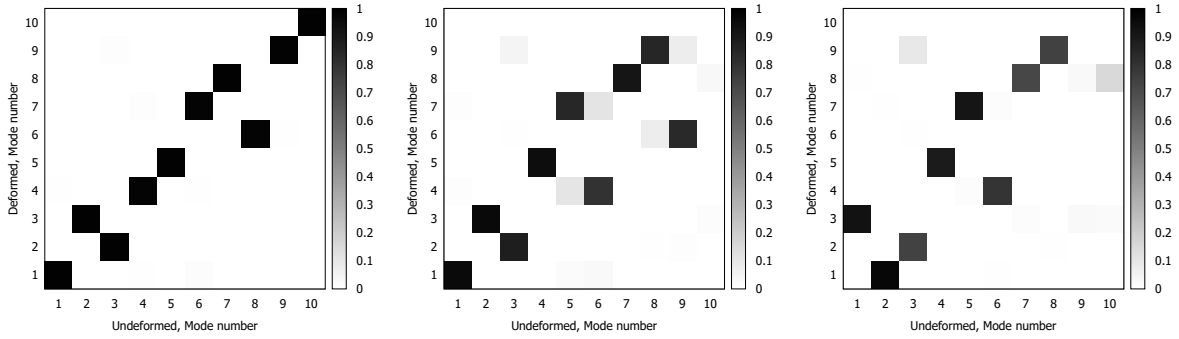

(a) $p = 1.38$ Pa **(b)** $p = 21.44$ Pa **(c)** $p = 73.18$ Pa

Figure 9.16: Multilayered aortic iliac plate, dispersed fibers case ($k = 0.226$): MAC matrix computed comparing the undeformed modal shapes with respect to different deformed configuration modal shapes. The deformed configuration state is indicated in the sub-caption.

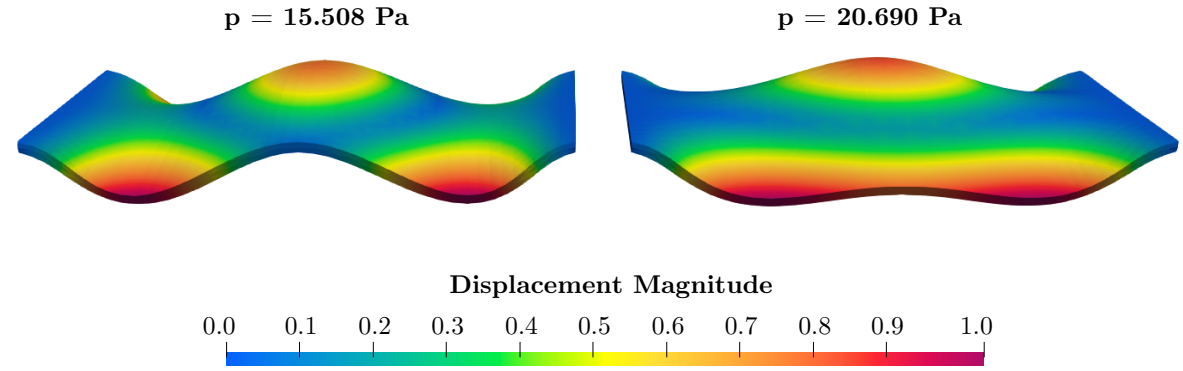

(a) Mode 5, for the two indicated deformed configurations

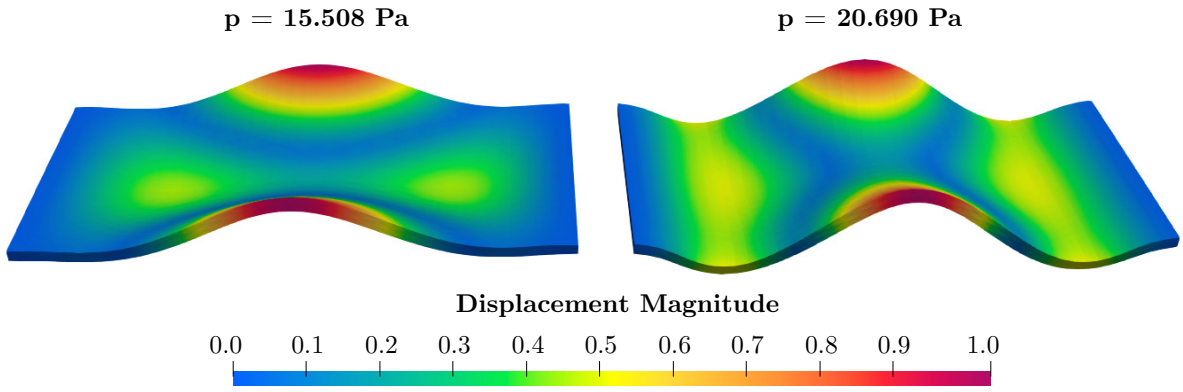

(b) Mode 6, for the two indicated deformed configurations

Figure 9.17: Multilayered aortic iliac plate, dispersed fibers case ($k = 0.226$): eigenvector representation on the undeformed structures, modes 5 and 6, veering observed.

The same linearized vibration analysis is next performed for the perfectly aligned fiber case ($k = 0$). For each non-trivial equilibrium state, the linearized vibration problem is again defined and solved. Figure 9.18 depicts the pressure–frequency curves in the small-displacement regime. The first four natural frequencies are reported in Fig. 9.18(a), while Fig. 9.18(b) illustrates modes five to eight. The full behavior in the analyzed load range of the equilibrium path is further investigated and reported in Fig. 9.19, where modal interactions in the large-strain regime are highlighted, in the case of the multilayered biological plate with perfectly aligned fibers. Figure 9.20 compares the results obtained with the converged $20 \times 20 + 1$ LE2 model against fully 3D ABAQUS simulations. Figure 9.20(a) reports the comparison for the first ten natural frequencies at selected equilibrium states, while Fig. 9.20(b) shows the global evolution of these modes. The results shows excellent agreement of the proposed 2D CUF model results with the reference ABAQUS, assessing the capability of the proposed high-order model to accurately capture the nonlinear effects, given by both geometrical and material nonlinearities, on the vibration behavior of anisotropic hyperelastic materials. In particular, the nonlinear anisotropic constitutive behavior of the plate has given different modal behavior and responses considering different values of the fiber dispersion parameters. Modal interactions are further

investigated again using the MAC criterion. Figure 9.21 shows MAC matrices comparing the undeformed reference configuration with linearized vibration solutions at different deformed states (as indicated in the captions). For small strains, the normal modes remain independent, with crossing phenomena being observed. At large strains, more evident interactions appear, such as the mode 4–5 interaction shown in Fig. 9.21(b). A consistent behavior already observed in the case of dispersed fiber plate is again noted, but for higher natural frequencies and modal interactions occurring at relatively higher loads. In particular, Fig. 9.20(b), compared with Fig. 9.15(b), highlights that the observed modal interactions shifts to larger pressures in the aligned case, due to the increased material stiffness. The interaction between the fifth and sixth modes is fully analyzed now around $p = 85$ Pa. Figure 9.22(a) compares the fifth mode shapes at $p = 83.64$ Pa and $p = 92.89$ Pa, while Fig. 9.22(b) reports the same comparison for the sixth mode. Differently with respect to the case of dispersed fibers, the aligned configuration exhibits a crossing phenomenon. The frequency–pressure curves intersect without significant alteration of the corresponding mode shapes. Thus, while the solution paths exchange trajectories, the modal patterns remain unaffected [200].

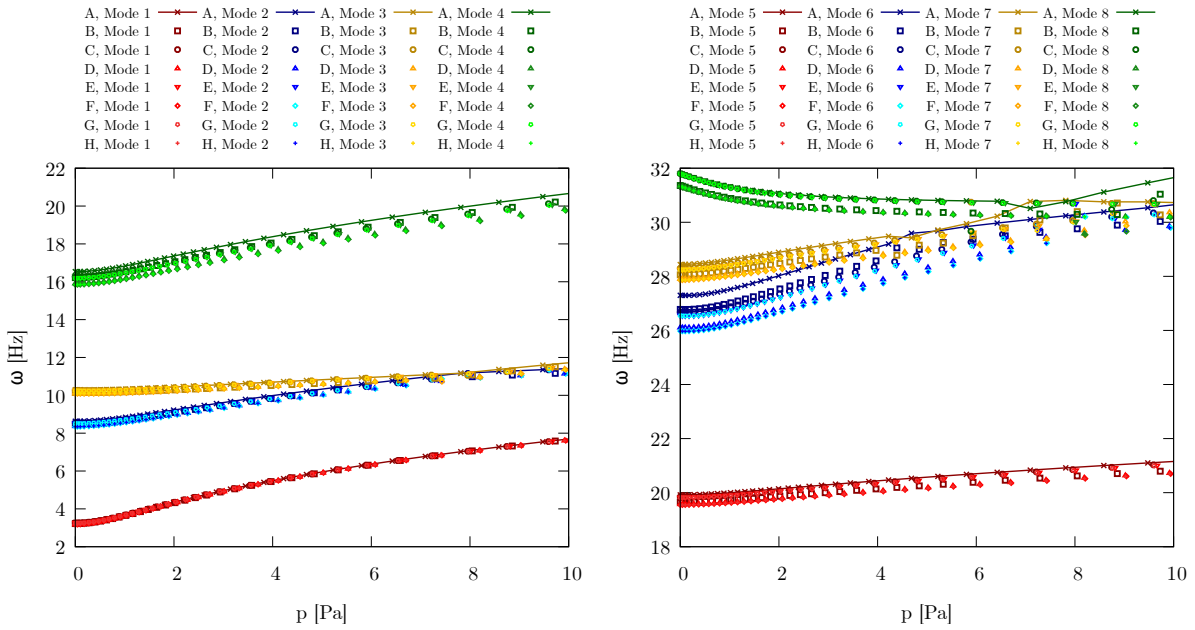

(a) Modes 1-4 **(b)** Modes 5-8

Figure 9.18: Multilayered aortic iliac plate, perfectly aligned fibers case ($k = 0$): Variation of the first eight natural frequencies along the equilibrium path, small strain regime. Influence of structural theory and reference mid-surface discretization.

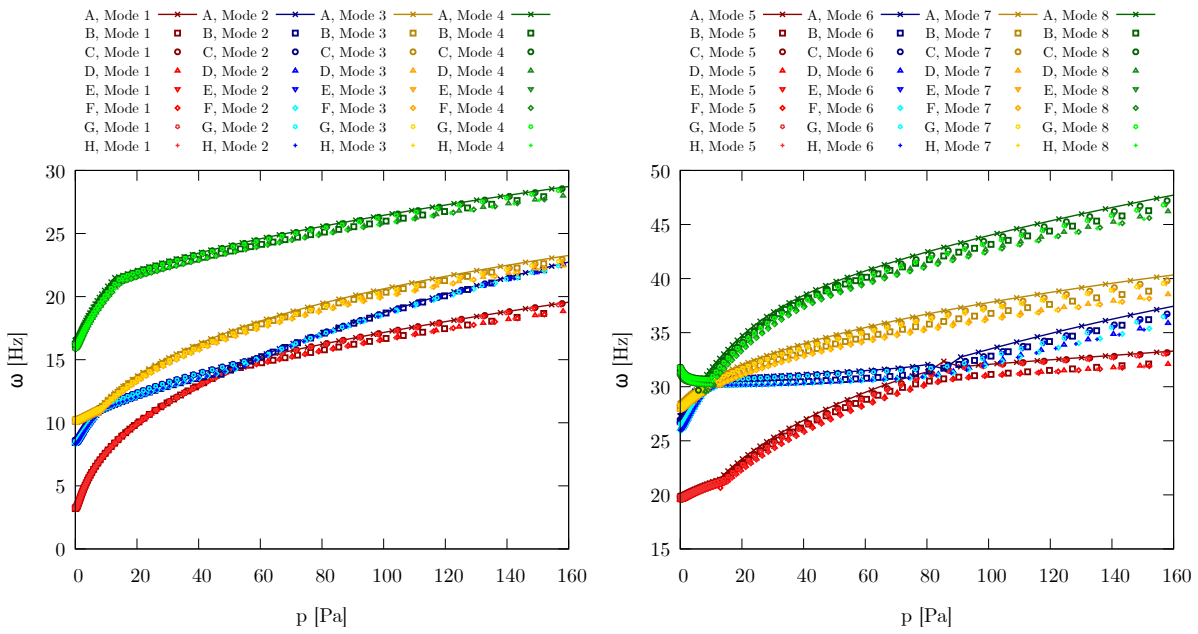

(a) Modes 1-4 **(b)** Modes 5-8

Figure 9.19: Multilayered aortic iliac plate, perfectly aligned fibers case ($k = 0$): variation of the first eight natural frequencies along the equilibrium path, large strain regime. Influence of structural theory and reference mid-surface discretization.

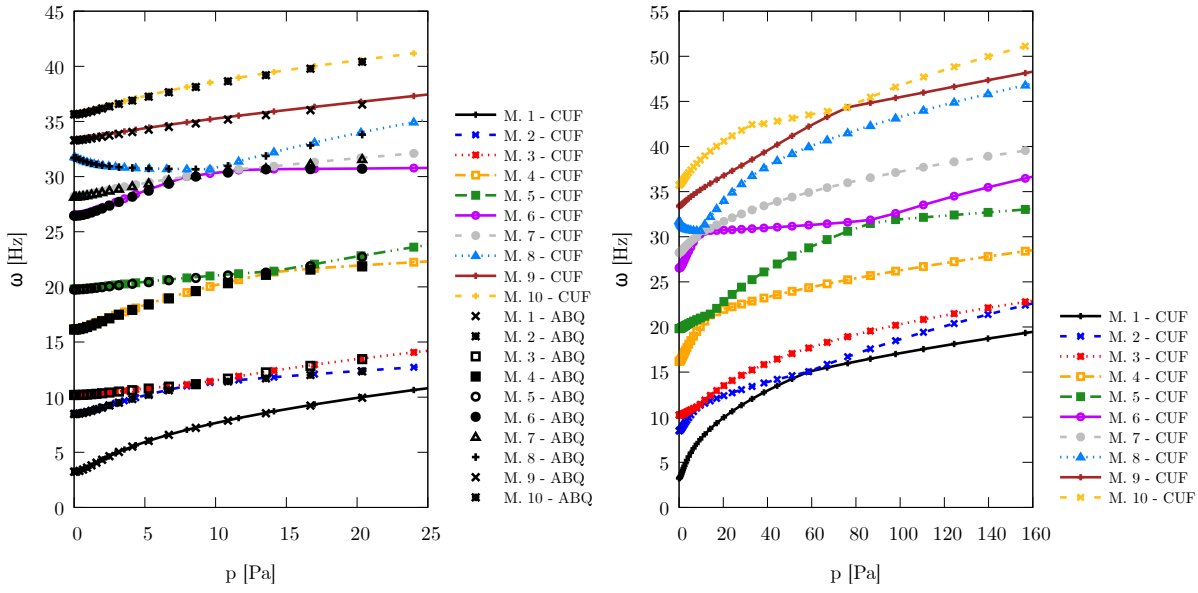

(a) Small strain regime **(b)** Global strain regime

Figure 9.20: Multilayered aortic iliac plate, perfectly aligned fibers case ($k = 0$): variation of the first ten natural frequencies along the equilibrium path. Comparison between high-order 2D CUF models and 3D ABAQUS reference solution.

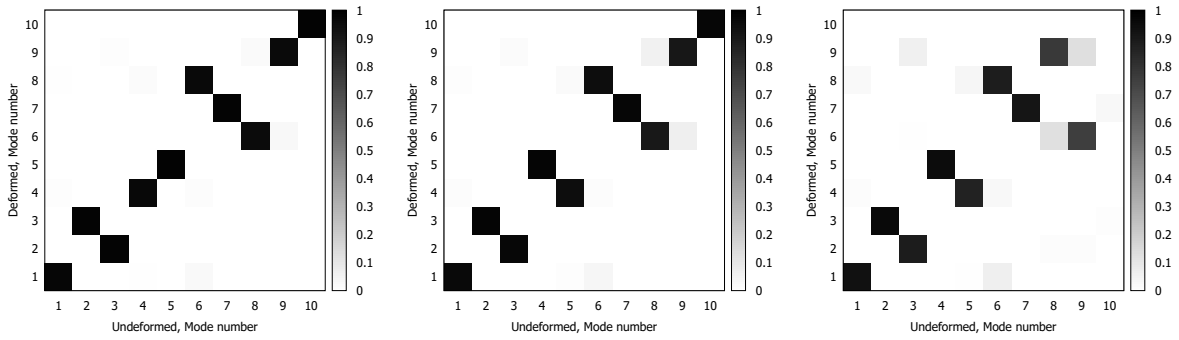

(a) $p = 8.60$ Pa **(b)** $p = 15.38$ Pa **(c)** $p = 53.52$ Pa

Figure 9.21: Multilayered aortic iliac plate, perfectly aligned fibers case ($k = 0$): MAC matrix computed comparing the undeformed modal shapes with respect to different deformed configuration modal shapes. The deformed configuration state is indicated in the sub-caption.

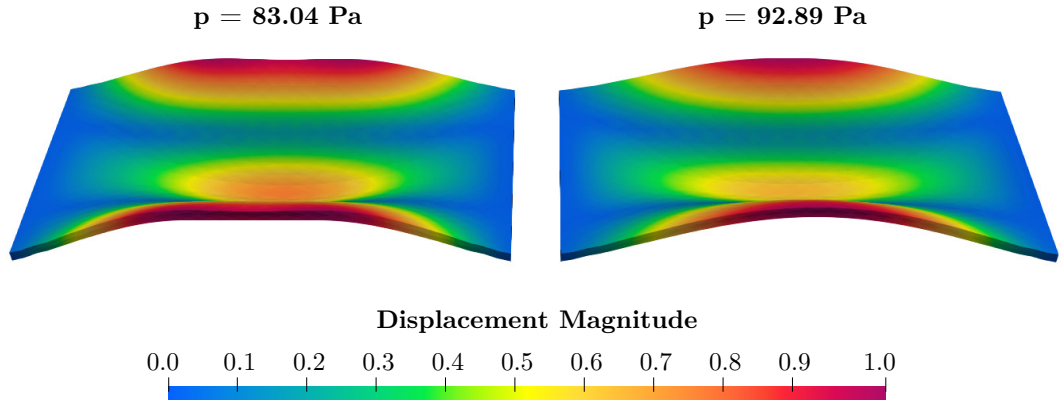

(a) Mode 5, for the two indicated deformed configurations

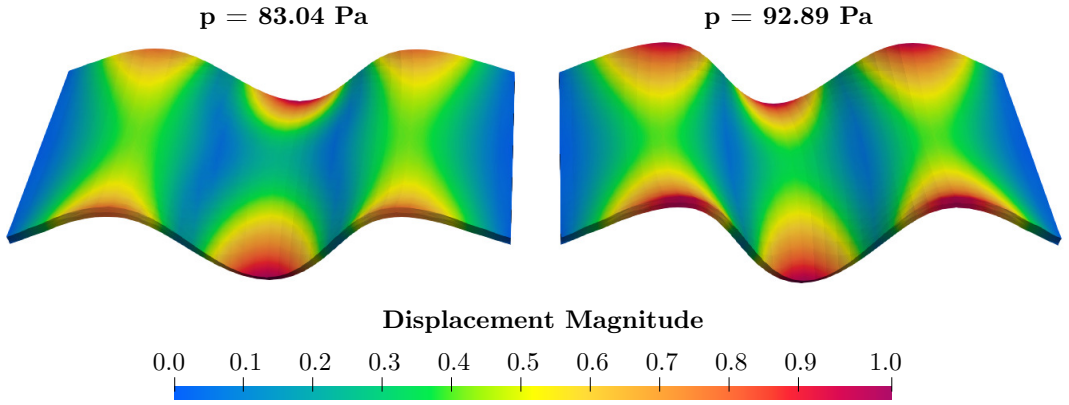

(b) Mode 6, for the two indicated deformed configurations

Figure 9.22: Multilayered aortic iliac plate, perfectly aligned fibers case ($k = 0$): eigenvector representation on the undeformed structures, modes 5 and 6, crossing observed.

9.2.1 Effects of large strain on biological tissue modal behavior

The final case study addresses the large strain analysis of a nearly incompressible arterial wall specimen subjected to uniform traction pressure. As proposed in Gasser et al. [26], the material considered is again simulating iliac adventitial strips, but in accounting now for fiber stiffening while excluding fibers in compression. The focus is on assessing the influence of fiber dispersion and large strains on both the static and dynamic responses of the structure. The numerical results obtained adopting now higher-order 1D CUF models are compared against reference numerical solutions obtained using fully 3D hexahedral elements for validation purposes, since they provide a direct discretization of the governing equations without relying on any superimposed kinematic assumptions. For this purpose, the strain energy function adopted corresponds to the Holzapfel–Gasser–Ogden (HGO) model as implemented in the ABAQUS commercial software [192], given in Eq. (9.12):

$$\Psi = \frac{K}{2}\left(\frac{J^2-1}{2} - \log J\right) + \frac{\mu}{2}(\bar{I}_1 - 3) + \sum_{j=4,6} \frac{k_1}{2k_2}\left[e^{k_2 < k\bar{I}_1 + (1-3k)\bar{I}_j - 1>^2} - 1\right] \tag{9.12}$$

Here, the parameters μ, k_1, k_2, K, and k are considered the same values as shown in the previous case study, while the operator $< x >= \frac{1}{2}(x + |x|)$ denotes the Macauley bracket. The specimen is modeled as a rectangular beam with dimensions $w = 2$ mm, $h = 1$ mm, and $L = 10$ mm, clamped at one end and subjected to a uniform traction pressure at the opposite free end. To replicate a practical uniaxial tension test, the load boundary condition is applied via a rigid block attached to the free-end section, rather than directly on its surface. The geometry and material properties are illustrated in Fig. 9.23. Given the material properties considered, the specimen is again modeled in the nearly incompressible regime. The fiber distribution is given by two symmetric unit vectors, $\boldsymbol{a}_0$ and $\boldsymbol{g}_0$, lying in the x–y plane and inclined at an angle $\gamma = 30°$ with respect to the y-axis, as depicted in Fig. 9.23.

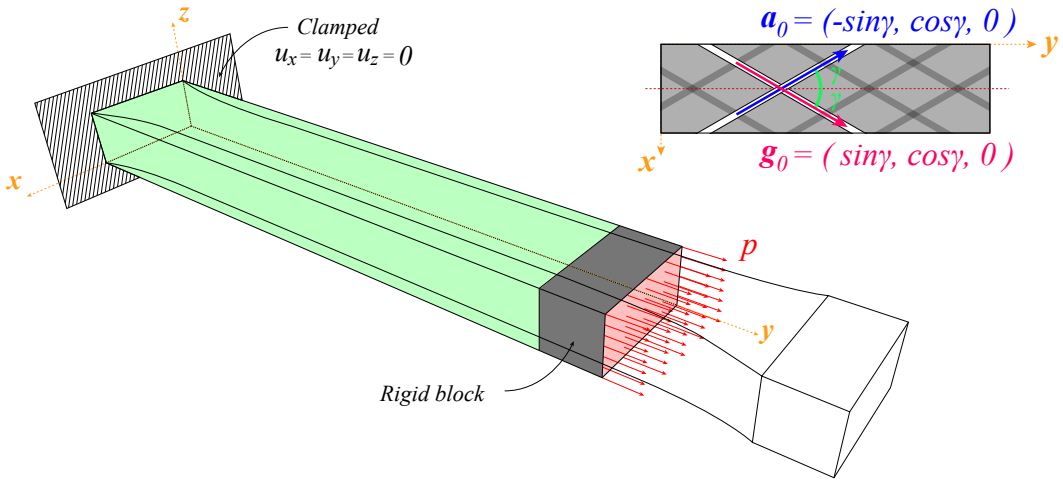

Figure 9.23: Finite strain analysis of an aortic iliac strip: geometrical and material features considered.

The numerical results obtained adopting higher-order 1D CUF models are again compared against reference numerical solutions obtained in ABAQUS, to assess the modeling capabilities and the performances of the proposed approach. In this case study, the tension–compression behavior is modeled using the built-in ABAQUS formulation. Many 1D CUF models will be employed to compute both the static equilibrium path and the modal response of the aortic

iliac strip at large strain, with 3D results adopted as benchmarks. The ABAQUS reference model consists of 6734 C3D20 elements, for a total of 95514 DOFs. A convergence analysis of the modal properties around the trivial equilibrium state is first conducted. Following previous findings, cubic B4 finite elements are adopted along the beam axis, while different cross-section discretizations with parabolic L9 subdomains are tested to mitigate volumetric locking [178]. The strip is initially modeled as clamped at both ends, imposing $u_x = u_y = u_z = 0$ at $x = 0$ and $x = L$. Table 9.4 reports the convergence results for the first three natural frequencies of the linearized vibration problem around the undeformed equilibrium state. Both dispersed ($k = 0.226$) and perfectly aligned ($k = 0$) fiber configurations are analyzed, investigating the influence of the theory of structure approximation (given by LE-models, as previously addressed from previous discretization convergence analyses) and FE refinement along the beam axis. The results show that all proposed discretizations provide accurate natural frequencies, with relative percentage differences below 3%. Larger errors are noted in the perfectly aligned case ($k = 0$), which also exhibits higher natural frequencies and a stiffer overall response, suggesting that more refined discretizations are required in this configuration. Convergence is reached with 20 B4 elements along the axis, for which relative percentage differences below 1% are observed for all refined cross-section expansions. Moreover, the CUF models achieve these accuracy levels with a reduction of 69–88% in DOF compared to the ABAQUS reference, confirming both the consistency and efficiency of the present modeling strategy. The use of higher-order models effectively alleviates numerical instabilities and locking phenomena [178]. Based on these discussed findings, further analyses in the case of static and linearized vibration analysis will be performed using the convergent beam axis discretization model, which exploits 20 B4 cubic elements, while investigating the influence of structural approximation through different L9 expansions, as reported in the convergence analysis results.

		Dispersed fibers k = 0.226			**Perfectly aligned fibers k = 0**			
Mesh	**Exp.**	**Mode 1**	**Mode 2**	**Mode 3**	**Mode 1**	**Mode 2**	**Mode 3**	**DOF**
10 B4	16 L9	$89.329^{(1.76\%)}$	$184.508^{(1.02\%)}$	$204.205^{(1.19\%)}$	$106.305^{(1.55\%)}$	$201.683^{(-0.33\%)}$	$276.915^{(2.99\%)}$	7533
	24 L9	$89.342^{(1.77\%)}$	$185.028^{(1.30\%)}$	$204.137^{(1.15\%)}$	$105.810^{(1.08\%)}$	$202.003^{(-0.17\%)}$	$272.986^{(1.53\%)}$	11067
	35 L9	$89.112^{(1.51\%)}$	$184.141^{(0.82\%)}$	$203.749^{(0.96\%)}$	$105.457^{(0.74\%)}$	$201.105^{(-0.62\%)}$	$272.247^{(1.25\%)}$	15345
15 B4	16 L9	$88.732^{(1.08\%)}$	$183.903^{(0.69\%)}$	$203.340^{(0.76\%)}$	$105.990^{(1.25\%)}$	$201.541^{(-0.40\%)}$	$275.452^{(2.44\%)}$	11178
	24 L9	$88.704^{(1.04\%)}$	$184.437^{(0.98\%)}$	$203.175^{(0.68\%)}$	$105.337^{(0.63\%)}$	$201.872^{(-0.24\%)}$	$270.658^{(0.66\%)}$	16422
	35 L9	$88.467^{(0.77\%)}$	$183.503^{(0.47\%)}$	$202.782^{(0.48\%)}$	$105.013^{(0.32\%)}$	$200.946^{(-0.70\%)}$	$270.106^{(0.46\%)}$	22270
20 B4	16 L9	$88.455^{(0.76\%)}$	$183.628^{(0.54\%)}$	$202.963^{(0.57\%)}$	$105.847^{(1.11\%)}$	$201.480^{(-0.43\%)}$	$274.776^{(2.19\%)}$	14823
	24 L9	$88.404^{(0.70\%)}$	$184.166^{(0.83\%)}$	$202.751^{(0.47\%)}$	$105.150^{(0.45\%)}$	$201.816^{(-0.27\%)}$	$269.800^{(0.34\%)}$	21777
	35 L9	$88.166^{(0.43\%)}$	$183.210^{(0.31\%)}$	$202.359^{(0.27\%)}$	$104.839^{(0.15\%)}$	$200.878^{(-0.73\%)}$	$269.322^{(0.16\%)}$	30195
ABQ	6734 C3D20	87.788	182.650	201.810	104.681	202.354	268.882	95514

Table 9.4: Finite strain analysis of an aortic iliac strip, cases $k = 0.226$ and $k = 0$: convergence analysis for the first three natural frequencies [Hz]. Comparison between high-order 1D model results and 3D ABAQUS solution. In brackets, the percentage difference with respect to ABAQUS is given.

Using the converged discretization models, the nonlinear static analysis of the aortic iliac specimen is carried out. The two fiber configurations addressed in the previous modal analysis are again considered, thus dispersed fibers ($k = 0.226$) and perfectly aligned fibers ($k = 0$) are analyzed, investigating the influence of the material conditions on the uniaxial response of the material. Figure 9.24 presents the global equilibrium path of the specimen, comparing the numerical results obtained via different 1D CUF models with the 3D ABAQUS reference solution, comparing also the results obtained for both fiber distributions. As anticipated from the modal

analysis, the perfectly aligned fiber case exhibits an evidently stiffer response than the dispersed configuration.

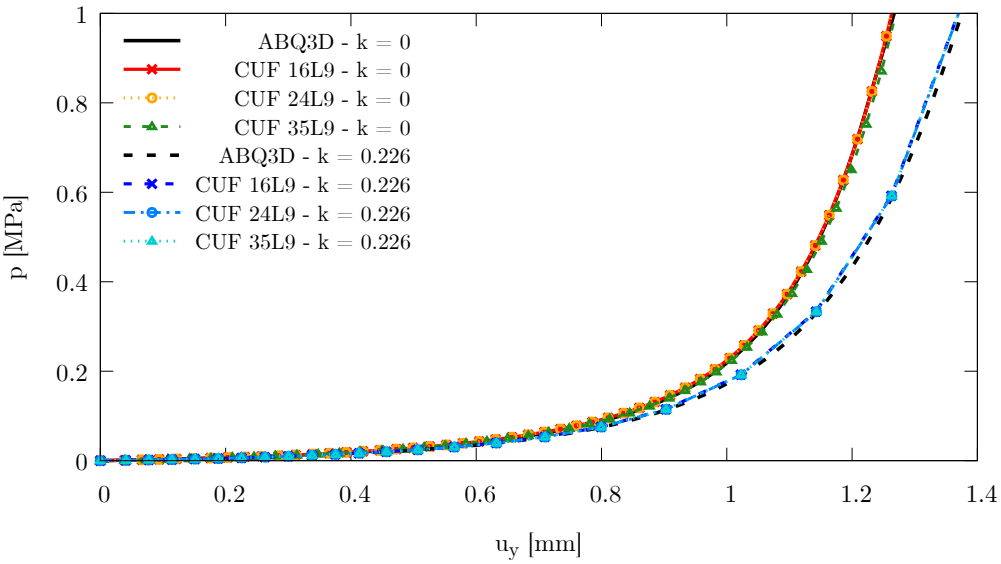

Figure 9.24: Finite strain analysis of an aortic iliac strip, cases $k = 0.226$ and $k = 0$: equilibrium path for different LE cross-section expansion models. Comparison between higher-order 1D CUF models and the reference 3D ABAQUS solutions.

The non-trivial equilibrium states computed in the nonlinear static analysis define the deformed configurations around which the linearized vibration problem is solved. For both fiber dispersion cases, the variation of natural frequencies and mode shapes, when different stretch configurations are examined, is investigated. Figure 9.25 depicts the pressure–frequency curves for the dispersed fiber case ($k = 0.226$) in the small-displacement regime. In particular, Fig. 9.25(a) shows the evolution of the first four natural frequencies obtained from the previously introduced cross-section models, while Fig. 9.25(b) presents the corresponding results for modes five through eight. The complete equilibrium path is shown in Fig. 9.26, highlighting modal interactions in the large-strain regime of the multilayered biological plate with dispersed fibers. Near the undeformed equilibrium state, at very small strains, evident variations are observed in the first eight natural frequencies, with modal interactions occurring between modes 2–3–4, 5–6, and 7–8. These effects, noted for axial stretch still close to unity and very small strains applied, of frequency increase and modal interactions can be attributed to a stiffening effect caused by the activation of fiber traction energy. At small strain, the applied energy via the traction load is primarily converted by the material for microstructural internal reorganization, leading to increased stiffness as fibers rotate and align [26]. The results also confirm that all cross-section discretization models provide accurate predictions, with solutions showing excellent agreement across all non-trivial equilibrium states.

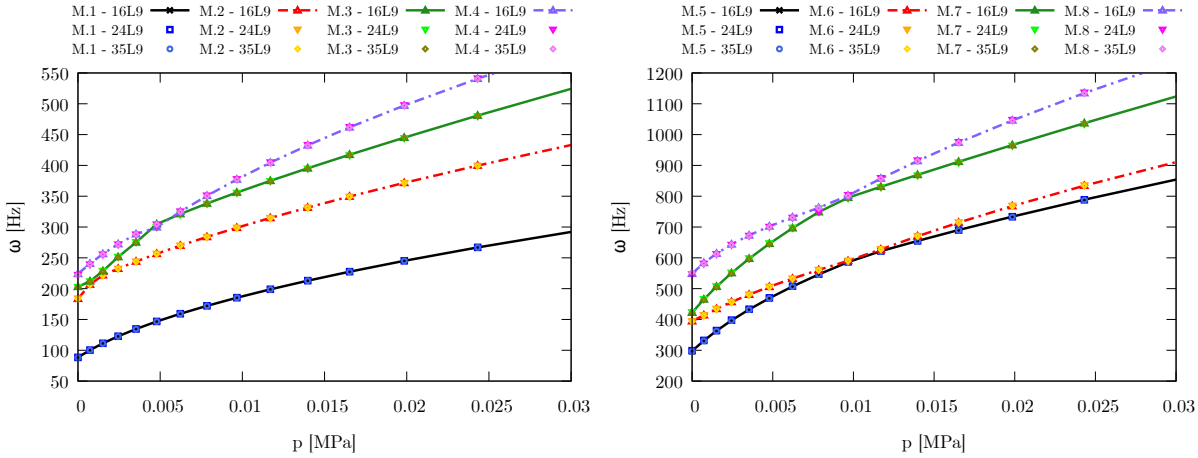

(a) Modes 1-4 **(b)** Modes 5-8

Figure 9.25: Finite strain analysis of an aortic iliac strip, dispersed fiber case $k = 0.226$: variation of the natural frequencies in the small strain regime. Comparison between different LE expansion models.

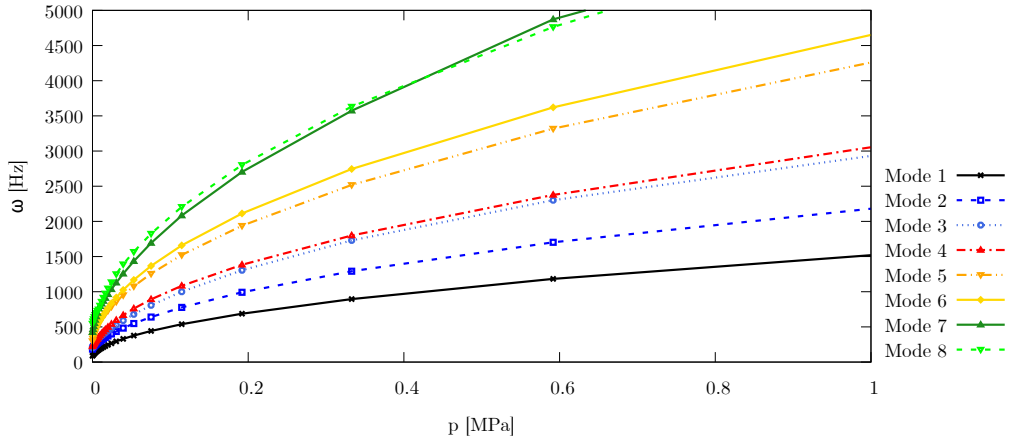

Figure 9.26: Finite strain analysis of an aortic iliac strip, dispersed fiber case $k = 0.226$: variation of the natural frequencies in the whole computed equilibrium strain regime. Representation of dispersion curves for the first eight normal modes of vibration.

As in the previous case studies, modal interactions are further examined using the MAC criterion. Figure 9.27 presents MAC matrices comparing the vibration modes of the undeformed reference configuration with those obtained from linearized vibration analyses around selected deformed states, as specified in the captions. The modal interactions identified at small strains in Fig. 9.25 are analyzed in greater detail by inspecting the mode shapes at the corresponding non-trivial equilibrium states. Figure 9.28 compares the second and third mode shapes across different configurations, while Fig. 9.29 reports the same comparison for the seventh and eighth modes. Unlike the cases discussed in the previous section, the observed interactions here correspond to crossings. This behavior is further confirmed by the correlations revealed in the MAC matrices.

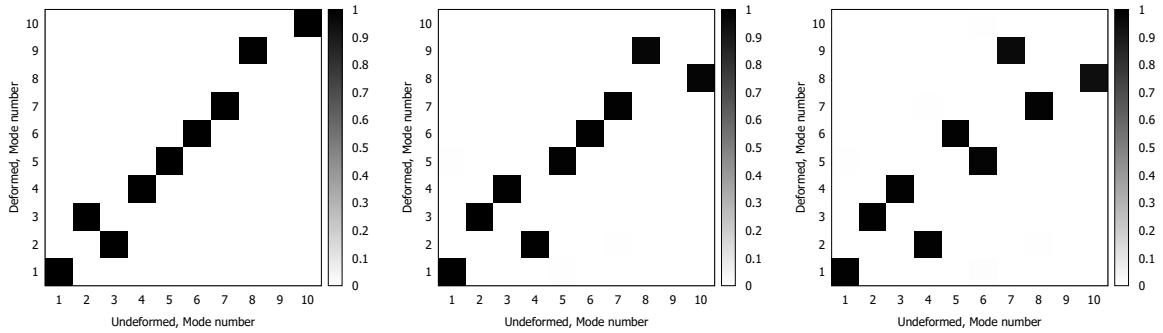

(a) $p = 1.51$ kPa **(b)** $p = 6.22$ kPa **(c)** $p = 13.97$ kPa

Figure 9.27: Finite strain analysis of an aortic iliac strip, dispersed fiber case $k = 0.226$: MAC matrices, comparing the normal modes of vibration around the deformed equilibrium states against the reference undeformed normal models of vibration. Deformed configurations reported in the caption.

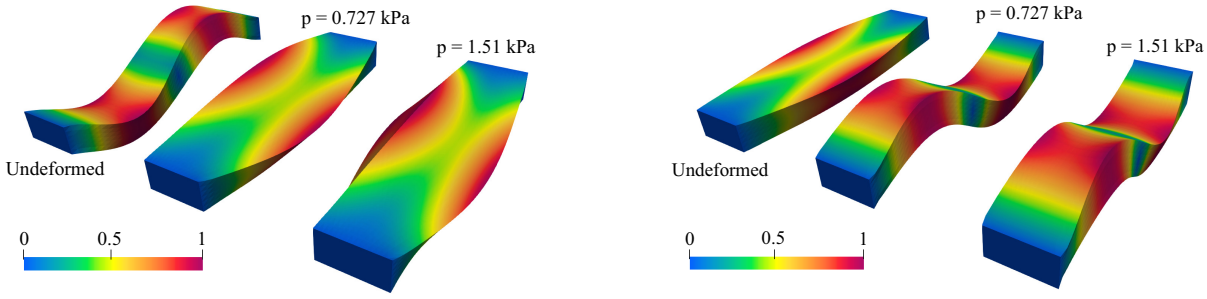

(a) Mode 2 **(b)** Mode 3

Figure 9.28: Finite strain analysis of an aortic iliac strip, dispersed fiber case $k = 0.226$: graphical representation of modes II and III for different deformed configurations. Comparison between different pre-stress applied.

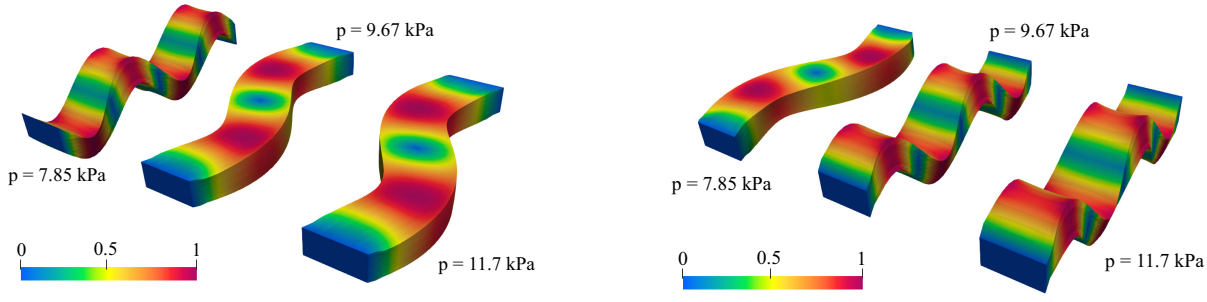

(a) Mode 7 **(b)** Mode 8

Figure 9.29: Finite strain analysis of an aortic iliac strip, dispersed fiber case $k = 0.226$: graphical representation of modes VII and VIII for different deformed configurations. Comparison between different pre-stress applied.

The same analysis is now carried out for the case of perfectly aligned fibers ($k = 0$). Figure 9.30 shows the pressure–frequency curves in the small-displacement regime: Fig. 9.30(a) reports the variation of the first four natural frequencies obtained with the previously introduced cross-section models, while Fig. 9.30(b) presents the corresponding results for modes five through eight. The complete equilibrium path is illustrated in Fig. 9.31, highlighting modal interactions in the large-strain regime for the multilayered biological plate with aligned fibers. Near the undeformed equilibrium state, modal interactions are observed for several partially loaded configurations characterized by very small stretch ratios. As in the dispersed fiber case, these interactions are driven by the activation of fiber traction energy and the associated microstructural reorganization at small strain, which contribute to the stiffening response of the strip. Once again, the results confirm an excellent agreement across all cross-section discretization models, with perfectly matching solutions at each non-trivial equilibrium state.

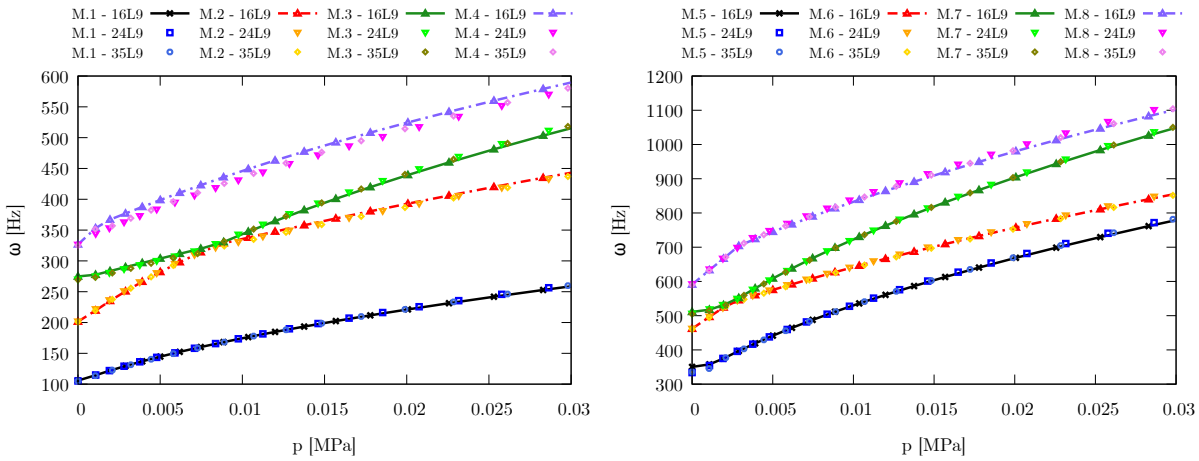

(a) Modes 1-4 **(b)** Modes 5-8

Figure 9.30: Finite strain analysis of an aortic iliac strip, perfectly aligned fiber case $k = 0$: variation of the natural frequencies in the small strain regime. Comparison between different LE expansion models.

The correlation between vibration modes across different deformed configurations is again analyzed using the MAC criterion, as shown in Fig. 9.27, where deformed states are compared against the undeformed reference configuration. The modal interactions identified at small strains in Fig. 9.30 are further examined by inspecting the corresponding mode shapes. Figure 9.33 compares the second and third mode shapes at selected deformed states, while Fig. 9.34 reports the same comparison for the sixth and seventh modes. In both cases, the results indicate crossings between the vibration modes, confirming the interaction mechanism suggested by the MAC analysis.

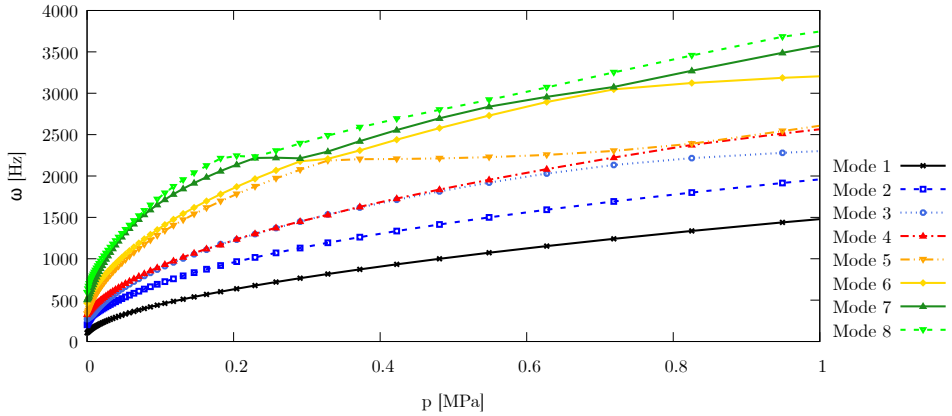

Figure 9.31: Finite strain analysis of an aortic iliac strip, perfectly aligned fiber case $k = 0$: variation of the natural frequencies in the whole computed equilibrium strain regime. Representation of dispersion curves for the first eight normal modes of vibration.

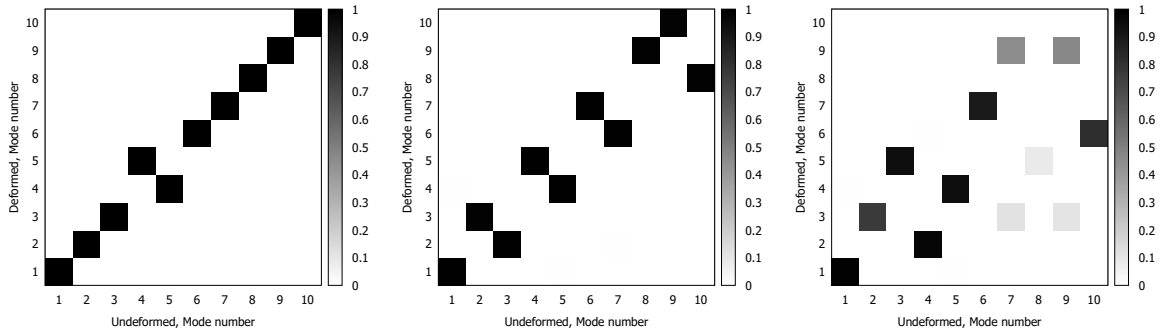

(a) $p = 1.92$ kPa **(b)** $p = 8.37$ kPa **(c)** $p = 95.75$ kPa

Figure 9.32: Finite strain analysis of an aortic iliac strip, perfectly aligned fiber case $k = 0$: MAC matrices, comparing the normal modes of vibration around the deformed equilibrium states against the reference undeformed normal models of vibration. Deformed configurations reported in the caption.

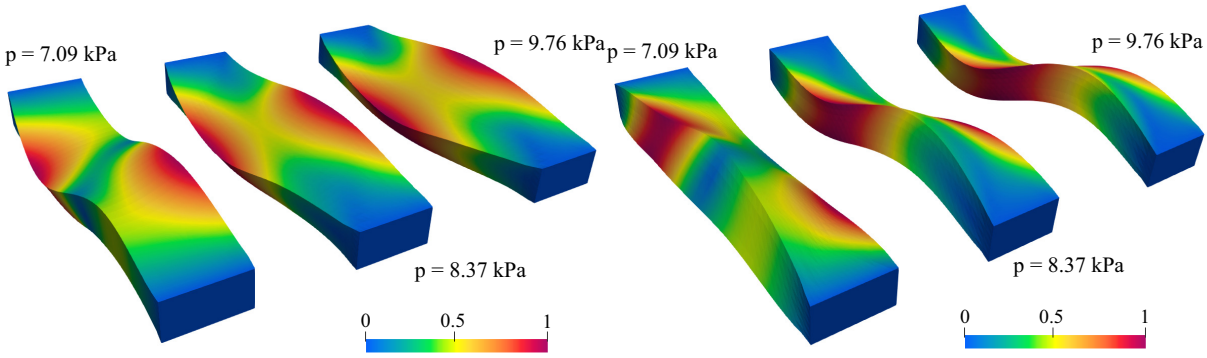

(a) Mode 2 **(b)** Mode 3

Figure 9.33: Finite strain analysis of an aortic iliac strip, perfectly aligned fiber case $k = 0$: graphical representation of modes II and III for different deformed configurations. Comparison between different pre-stress applied.

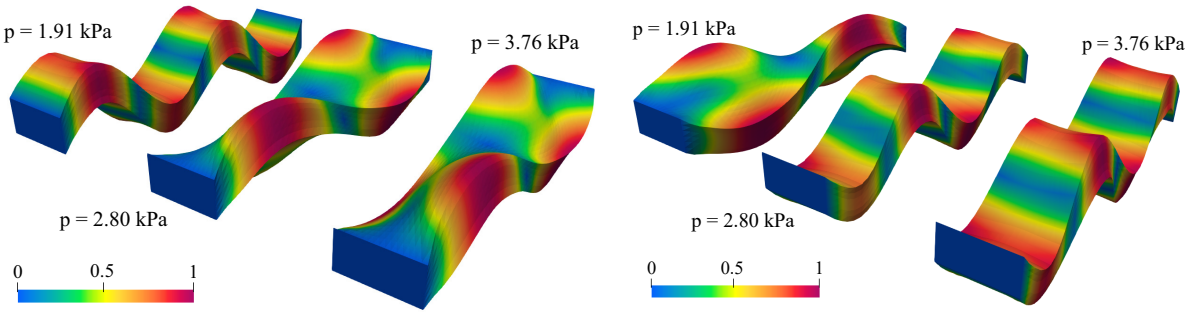

(a) Mode 6 **(b)** Mode 7

Figure 9.34: Finite strain analysis of an aortic iliac strip, perfectly aligned fiber case $k = 0$: graphical representation of modes VI and VII for different deformed configurations. Comparison between different pre-stress applied.

9.3 Discussion

The proposed results suggest that:

- The orthotropic hyperelastic constitutive law has been successfully implemented in an invariant finite element formulation, including the two fiber families, fiber reinforcement via Cartesian unit vectors, and the straightforward implementation of any anisotropic model by means of the structural tensor representation. This approach has been directly integrated within the numerical quadrature procedure, ensuring an accurate representation of complex fiber distributions. Again, a validation against analytical reference solutions has been performed, considering the simple shear test with different fiber orientations and constitutive hyperelastic models, including anisotropy effects and fiber dispersion. The results, showing perfect agreement between solutions, confirm the robustness of the present implementation.

- The accuracy and the efficiency of the present higher-order modeling of fiber-reinforced soft

materials and structures have been further validated through benchmark problems involving large displacement and finite strain analysis of multilayered fiber-reinforced biological-like structures. Based on the previously introduced concepts of convergence and accuracy of FE discretization models, LWm and LE-class models are primarily adopted to ensure the computation of accurate results. As shown by the results, accurate displacement distributions and natural frequencies have been observed. Again, computationally advantageous FE models with fewer DOF, while maintaining high levels of accuracy, have been developed. In addition, the adoption of LE-class models enables efficient modeling of structural behavior without compromising solution quality.

- A strong influence of the fiber dispersion parameter has been observed. Depending, in particular, on the type of load applied, the fiber dispersion leads to different mechanical response mechanisms in terms of nonlinear static behavior. In particular, it has been observed that a stiffer structural response occurs for perfectly aligned fibers, as expected, with respect to the case of dispersed fibers.

- In terms of linearized vibration analyses, the fiber dispersion parameter has a strong influence on the modal response of reinforced structures. In particular, modal interactions and aberrations have been observed at small strain when tension/compression behavior of the fiber reinforcement has been included in the constitutive model. Additionally, the effects of fiber dispersion have also been observed in the aberration effects, where mode shapes interact in a different manner depending on the value of k, leading to crossing phenomena rather than veering.

- The proposed results demonstrate a complex coupling between reinforcement direction, pre-stretch state, and dynamic response, which must be carefully accounted for in predictive modeling.

Chapter 10

Conclusions

The static and linearized vibration analyses of hyperelastic materials have been presented in this thesis work. The adoption of the Carrera Unified Formulation (CUF) allowed the implementation of lower- to higher-order theory of structure based finite element models, accounting for geometrical and material nonlinearities governed by the hyperelastic constitutive law. A numerical framework based on one-dimensional beam (1D) and two-dimensional plate (2D) models has been proposed for research analyses of isotropic and anisotropic soft materials and structures, with applications to biological tissue modeling.

10.1 Remarks

This thesis presents a novel numerical framework based on finite element procedures for the large-strain analysis of hyperelastic materials and structures. The nonlinear material response, governed by the hyperelastic constitutive law, has been investigated in the case of isotropic and fiber-reinforced soft materials. The analyses have been performed within the CUF framework, a well-established formalism exploited to define efficient and accurate one- and two-dimensional models. The implementation of finite element procedures based on the higher-order theory of structures has been achieved through the recursive and hierarchical formalism introduced by CUF. In this context, the accuracy of Equivalent-Single-Layer (ESL) models, Layer-Wise (LW), and Component-Wise (CW) models has been extensively investigated. First, the continuum mechanics approach employed in the present work is presented, focusing on the kinematic and energetic descriptors used in soft material modeling at large strains. The governing equations for such nonlinear materials have been written in both weak and strong forms, considering classical balance laws. In particular, energetic arguments are exploited to define the local and global forms of the equations with respect to the material and spatial reference frames. Second, the nonlinear hyperelastic framework has been extensively discussed, with particular emphasis on the invariant formalism typically adopted in the constitutive modeling of such materials and structures. The basic principles have been proposed within the context of isotropic hyperelasticity, extending naturally the proposed concept to the nonlinear anisotropic constitutive law for fiber-reinforced soft materials. In particular, the closed-form expressions for stress tensors and tangent elastic moduli have been provided, ensuring the exact analytic computation of involved physical quantities without relying on approximate methods. Subsequently, the adopted unified approach of beam and plate theories has been discussed. The implementation of lower- to higher-order finite element models is proposed within the rigorous framework of CUF. The CUF allowed for the straightforward definition of ESLm and CW/LWm without any loss of

generality. As shown in the theoretical derivation of the model, the key features of the present modeling approach is given by the independent nature of the final formal expression of the displacement field from the adopted polynomial expansion. In particular, the order of the theory of structure can be assigned as a formal input to the analysis, achieving a desired level of accuracy and obtaining refined 1D and 2D models with three-dimensional capabilities. The nonlinear governing equations have then been redefined in matrix form, following the imposed polynomial expansion of the displacement field, and introducing, by means of variational principles, the basic building block of the present methodology: the Fundamental Nuclei (FN). The FN represent the basic unit entries of FE matrices, specifically the internal and external force vectors, mass, and tangent stiffness matrix, formally defined without dependence on the kinematic assumptions used in the displacement field definition. In this sense, the final, resulting FE procedure is a pure, fully nonlinear, displacement-based model. The capabilities of the presented modeling approach, based on higher-order theory of structures with three-dimensional capabilities, have been initially assessed by analyzing isotropic soft structures. Attention has been paid to predicting accurate displacement and three-dimensional stress distributions, comparing the proposed results with analytical reference solutions and benchmark problems analyzed using a classical 3D FE formulation available in commercial software. In particular, the effects of the boundary conditions, the pre-stressed configurations, and the adopted theory of structure on the pure mechanical and vibration response of the materials have been investigated. Afterwards, the present FE formulation was validated in the framework of isotropic hyperelasticity. This approach has been extensively adopted in modeling continuously fiber-reinforced soft materials and structures, with a focus on applications to biological tissues. Specifically, the implementation of constitutive models for distributed and dispersed fiber-reinforced materials within a FE framework has been discussed, including anisotropic effects at micro-scale in the macroscopic material response. These peculiar behaviors have been investigated by means of pure mechanical analysis of aortic iliac materials and biological-like structures at large strains.

10.2 Main contributions

The main novelties and principal contributions proposed and carried out during this period of the doctoral research can be summarized as follows:

- The hyperelastic framework has been derived rigorously, following variational principles. In particular, the final resulting expression of the tangent elastic moduli has been proposed to straightforwardly implement any hyperelastic model without making any assumptions about the strain energy density function considered.
- The proposed modeling strategy based on the CUF has been extensively adopted to introduce a hierarchical FE derivation procedure, independent of the kinematic assumption made of the displacement field. In particular, the hyperelastic framework has been consistently introduced, following classical continuum mechanics arguments and linearization principles, to include the effects of material nonlinearities in the model, without making any assumptions about the hyperelastic model considered.
- The proposed higher-order 1D beam and 2D plate models can accurately predict complex three-dimensional displacement and stress states in isotropic and anisotropic soft materials.
- The adoption of higher-order theories allows for the definition of efficient models that guarantee a high level of accuracy with reduced DOF required by the numerical simulation with respect to classical FE formulation.

- The proposed CUF-based LW and CW models are introduced for the first time, presenting a hierarchical and general FE framework for the pure mechanical analysis of multilayered soft structures, whose analysis has been limited to simplified models in the literature.

- In the framework of nonlinear analysis, the adopted methodology allows for comparing various kinematic approximations of the structural behavior, which has not been investigated in the literature since available models are typically based on classical 3D FE formulations.

- Classical structural theories have been proven inadequate for the large strain analysis of soft structures, due to the superimposed kinematic assumption of these lower-order theories regarding the cross-section or through-the-thickness behavior. In this sense, high-order approximations can be considered a valid alternative when analyzing displacement distributions. However, inconsistencies and limitations have been observed when investigating stress distributions at large strains, as discussed in the case of isotropic circular plate stress distribution provided in Fig. 8.13, or displacement distribution as discussed in the case of large strain analysis of multilayered beams under concentrated loads as provided in Fig. 7.30 and Table 7.18 when thick structures are considered. Thus, a CW or LW modeling approach is preferred for accurate stress predictions.

- A detailed stress analysis in terms of the reference first Piola-Kirchhoff stress tensor and spatial Cauchy stress tensor has been conducted in different cases, assessing the fulfillment of the C_z^0 requirements. From theoretical considerations, a key aspect of the present approach is the fulfillment of compatibility conditions for the first Piola-Kirchhoff stress tensor. This is justified by the definition of the proposed methodology under a Total Lagrangian approach. Unlike the case of linear elastic materials, for which the Cauchy and the second Piola-Kirchhoff stress tensors are the reference stress measures, the equilibrium requirements are satisfied for the corresponding stress measure defined with respect to the material coordinates. Additionally, due to the presence of both geometrical and material nonlinearities, as well as numerical instability phenomena like volumetric locking due to incompressibility, the C_z^0 requirements have been satisfied by refined cross-section or thickness expansions. In the case of pure displacement-based models, without any assumption of separate interpolation of stress variables, like in mixed methods, the equilibrium conditions are satisfied axiomatically via refinement of the kinematic assumptions.

- Natural frequencies and mode shapes are strongly influenced by the pre-stressed non-trivial equilibrium state. From the proposed results, complex or non-monotonic variation of the natural frequencies with the applied loads has been observed. In particular, in the case of compressible materials, the internal stress is also compared at large strain to demonstrate the influence of geometrical and pure nonlinear stiffness terms on the variation of natural frequencies. It has been shown that, in the case of compressible materials, natural frequencies propose monotonic decreasing behavior even if the pre-stretch applied is increasing, due to the reduction of internal stress given by the constitutive nonlinear material response. For this reason, even at small strains, mode aberrations such as veering and crossing have been observed and extensively analyzed.

- Compressibility plays a crucial role when highly deformed structural configurations of materials and structures are investigated. In particular, refined models are required to obtain accurate mode shapes and natural frequencies, as well as deformed configurations, since a general stiffer response is observed for nearly incompressible materials. This has

been extensively analyzed by means of large strain analysis and modal analysis of nearly-incompressible beam and multilayered plate structures, where higher natural frequencies with respect to the compressible cases have been found.

- Additionally, compressibility has a strong influence on the stability and accuracy of the FE model. As discussed in the proposed case studies, as in the case of Sec. 7.2 and Sec. 7.3 regarding the static and vibration of thick and slender beams, when nearly incompressible material behavior is considered, higher-order theories of structures with refined discretization models are needed to deal with volumetric locking at large strains. In particular, the capabilities of classical displacement-based models, such as 3D FE or lower-order beam and plate theories, have been shown to be limited in the incompressible limit, and they rely on more complex and involved FE formulations, such as the hybrid formulation, to mitigate locking phenomena and achieve convergent results in the incompressible regime. Otherwise, computationally burden models have to be adopted in the case of pure displacement-based formulations. This has also been observed in biological tissue analysis, as in the case described in Sec. 9.2.1, where expensive 3D models have been adopted because no hybrid formulation is available in the reference commercial software when the Holzapfel-Gasser-Ogden model is considered. Due to the complexity of the mathematical formalism, convergent results can be obtained by adopting only refined discretization models. In the present work, the capabilities of the higher-order, pure displacement-based approach for nearly incompressible structures have been established. Within his formal strategy, locking phenomena have been mitigated by adopting enriched kinematics and refined structural theories, straightforwardly implemented through the hierarchical formalism of the governing equations.

- For dispersed and perfectly aligned fiber-reinforced biological tissues, stiffening behavior at small strains is strongly observed. Although this cannot be correctly observed by means of a pure static analysis, where the fiber stiffening effects and hardening behavior are evident at large strains, the linearized vibration analysis showed material stiffening at small strains. This is justified by the micro-structural reconfiguration induced by the application of traction load, which activates the collagen fiber reinforcement. As discussed, since the fiber families within the materials are contributing to the material response only when they are in traction, at small strain there are coupling and energy transmission effects that contribute to a global material stiffening.

- Different fiber-reinforcement models have been investigated in the case of biological tissues. In particular, a strong effect of the mathematical formulation adopted for the tension/compression behavior is observed. From the proposed literature review, in the proposed approach, different models have been adopted to investigate the capabilities of the present numerical approach, showing good agreement with the available solutions in each material modeling case.

10.3 Future activities

In this work, a versatile FE procedure for the numerical analysis of hyperelastic soft materials and structures is presented, enabling accurate and efficient modeling in a nonlinear continuum mechanics context. Although this approach has presented numerous significant opportunities, various perspectives and developments can be envisioned. In particular, starting from the proposed work, future research will include:

- The implementation of hybrid finite element procedures, also referred to as mixed finite element procedures, where a distinct and independent interpolation of the hydrostatic pressure is proposed. This solution is typically explored when incompressibility is considered.
- Introduction of multi-physics effects, such as thermo-, piezo-hyperelasticity, and the analysis of magneto-sensitive materials. Innovative manufacturing processes have enabled the development of novel materials whose deformation state is controlled by means of multi-physics loads, such as temperature or voltage variations within the material.
- Component-Wise modeling of biological tissues, analyzing the influence of fiber-matrix interactions at meso- and microscopic levels. Adoption of refined, higher-order, Node-Dependent kinematics model to develop advanced numerical model for the simulation of biological tissues, introducig physically-consistent representation of embedded fibers within the material matrix.

The last point of discussion proposes an alternative and efficient tool for investigating the more complex mechanical behavior of biological tissues, exploiting the key modeling capabilities of the proposed approach. The possibility to incorporate different material behavior in a structural-theory-based scenario allows to analyze complex three-dimensional stress and deformation states, incorporating the fiber effects within the model without relying on specific constitutive hyperelastic models. This is particularly effective when fiber-matrix interactions, calibration of constitutive parameters, homogenization, and other pure mechanical problems are considered, as it includes an accurate representation of the three-dimensional behavior of independent material phases within the model. This allows to include, within the same numerical model, different descriptions of different phases. Figure 10.1 proposes a preliminary numerical model developed for the large strain analysis of a multi-phase biological tissue, considering an isotropic matrix embedded with two families of fibers arranged in a symmetrical way, along shifted planes, to include three-dimensional effects.

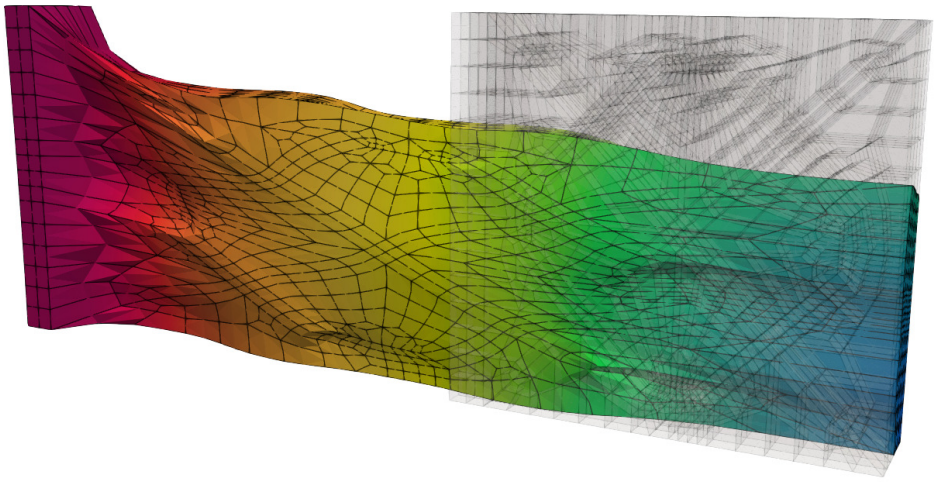

Figure 10.1: Component-Wise modeling of a biological tissue. Beam model with different fiber arrangements.

In the proposed approach, a unique beam model consisting of different expansions is proposed, including within the same representation of beam theory, different structural theories.

Moreover, by building on already-introduced advanced numerical models based on the implementation of Node-Dependent Kinematics and variable-kinematics approaches [201], different structural theories can be embedded within the same finite element model. In this way, refined yet distinct approaches can be considered for the numerical modeling of different phases, e.g., higher-order plate models for the matrix and beam models for the fibers, as shown in Fig. 10.2.

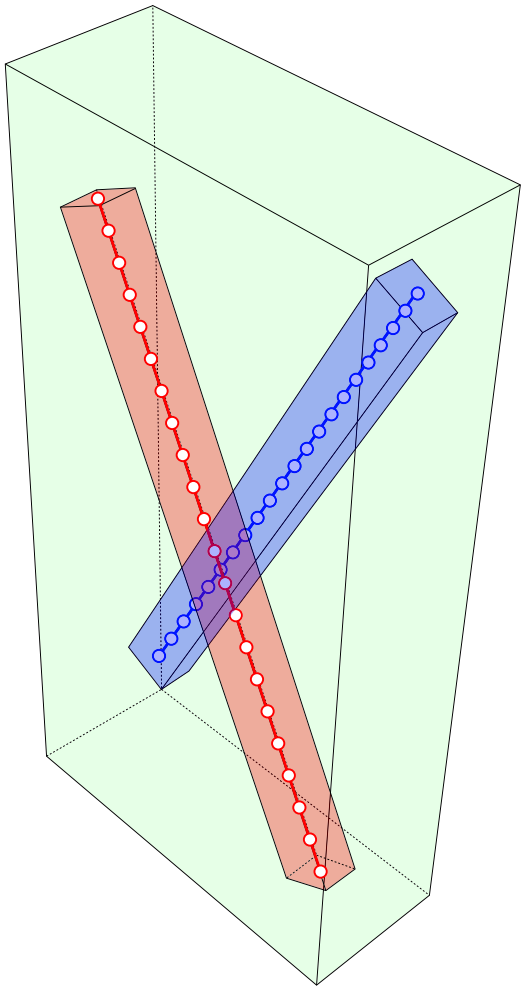

Figure 10.2: Component-Wise modeling of a biological tissue. Beam model with different fiber arrangements.

Appendix A

List of publications

A.1 Journal articles

1. Pagani A., **Chiaia P.**, Filippi M., Cinefra M. "Unified three-dimensional finite elements for large strain analysis of compressible and nearly incompressible solids". Mechanics of Advanced Materials and Structures, DOI: 10.1080/15376494.2023.2229832.

2. **Chiaia P.**, Pagani A., Cinefra M., Carrera E. "Analysis of transversely isotropic compressible and nearlyincompressible soft material structures by high order unified finite elements". Mechanics of Advanced Materials and Structures, DOI: 10.1080/15376494.2023.2273962

3. Pagani A., **Chiaia P.**, Carrera E. "Vibration of solid and thin-walled slender structures made of soft materials by high-order beam finite elements". International Journal of Non-Linear Mechanics, DOI: 10.1016/j.ijnonlinmec.2023.104634

4. Azzara R., Carrera E., **Chiaia P.**, Filippi M., Pagani A., Petrolo M., Zappino E. "Geometrically nonlinear static analysis of multi-component structures through variable kinematics finite elements". Acta Mechanica, DOI: 10.1007/s00707-024-04084-w

5. **Chiaia P.**, Pagani A., Carrera E. "Large strain and 3D stress analysis of laminated fibre-reinforced soft material structures with high order beam finite elements". Computers & Structures, DOI: 10.1016/j.compstruc.2025.107735

6. **Chiaia P.**, Cinefra M. and Carrera E. "Curvilinear 2|3D finite elements for the analysis of shells with arbitrary curvature and variable thickness". Computers & Structures, DOI: 10.1016/j.compstruc.2025.107911

7. **Chiaia P.**, Pagani A., Carrera E. "Higher-order finite element modeling of biological tissues under large strain conditions". Submitted to Journal of Sound and Vibration.

A.2 Conference proceedings

1. Pagani A., **Chiaia P.**, Filippi M., Cinefra M. "Unified hexahedral finite elements for large strains analysis of compressible and nearly incompressible materials", in Proceeding of the 1st International Conference on Advanced Topics in Mechanics of Materials, Structures and Constructions, AToMech1, Al Khobar, Saudi Arabia, 12-14th March 2023.

2. Pagani A., **Chiaia P.**, Carrera E. "Small amplitude free vibration of soft materials and structures by high order finite elements", in Proceeding of the 13th International Symposium on Vibrations of Continuous Systems, ISVCS13, Pomeroy, Canada, 30th July - 4th August 2023.

3. **Chiaia P.**, Pagani A., Cinefra M., Carrera E. "High order 1D and 2D CUF models for transversely isotropic compressible and nearly-incompressible soft materials and structures", in Proceeding of the 3rd International Conference on Computations for Science and Engineering, Napoli, Italy, 20-23th September 2023.

4. Augello R., Pagani A., **Chiaia P.**, Carrera E. "A higher-order beam finite element for the folding analysis of composite made booms with silicone matrix and carbon fibers", in Proceedings of the 74rd International Astronautical Congress (IAC), Baku, Azerbaijan, 2-6 October, 2023.

5. **Chiaia P.** "Modal analysis of hyperelastic structures in non-trivial equilibrium states via higher-order plate finite elements", in Proceedings of the 4th Aerospace PhD Days 2024, Scopello, Italia, 9-13 May, 2024. DOI: 10.21741/9781644903193-7.

6. Pagani A., **Chiaia P.**, Carrera E. "Stress and free vibration analysis of fibre-reinforced soft structures by 2D high order finite elements", in Proceedings of the 15th International Conference on Computational Structures Technology, Praga, Cezk Republic, 4-6 September, 2024. DOI: 10.4203/ccc.9.13.2

7. Sironi T., **Chiaia P.**, Cinefra M., Grande A.M., Pagani A. "Non Linear Thermo-Mechanical Numerical Model for Space Deployable Structures Actuated With Smart Materials", in Proceedings of the ASME 2025 Aerospace Structures, Structural Dynamics, and Materials Conference, SSDM2025, Houston, Texas, May 5-7, 2025, DOI: 10.1115/SSDM2025-152319.

8. Pagani A., **Chiaia P.**, Carrera E. "Linearized vibration analysis of fibre-reinforced multilayered soft materials by high order 2D finite elements", in Proceeding of the 14th International Symposium on Vibrations of Continuous Systems, ISVCS14, Grundlsee, Salzkammergut, Austria, July 27 - August 2, 2025.

9. Cinefra M., **Chiaia P.** and Carrera E. "Novel curvilinear 2|3D unified finite element formulations for the analysis of complex structures", accepted for publication in Proceeding of the 10th CEAS-28th AIDAA International Congress, AIDAACEAS2025, Turin, Italy, 1-4 December, 2025.

10. **Chiaia P.**, Filippi M., Pagani A. and Carrera E. "Effects of pre-stressed conditions on the dynamic and acoustic behavior of composite sandwich panels", accepted for publication in Proceeding of the 10th CEAS-28th AIDAA International Congress, AIDAACEAS2025, Turin, Italy, 1-4 December, 2025.

11. Fontanella A.P., Sironi T., **Chiaia P.**, Cinefra M. and Pagani A. "Nonlinear Buckling Analysis of Variable Cross Section Beams Using the Carrera Unified Formulation", accepted for publication in Proceeding of the 10th CEAS-28th AIDAA International Congress, AIDAACEAS2025, Turin, Italy, 1-4 December, 2025.

Appendix B

Tangent elasticity tensor for orthotropic materials

In the present appendix, the full, analytic closed form expression of the rescaled tangent elasticity tensor for the computation of the Lagrangian incremental elastic moduli, required by Eq. (3.35) is proposed. One can express the tangent elastic moduli without considering the general dependence of the strain energy function model, and deriving it in a more general framework as here proposed:

$$
\begin{aligned}
J^{4/3}\mathbb{C} &= 4\frac{\partial^2\Psi}{\partial\bar{\mathbf{C}}\partial\bar{\mathbf{C}}} = \\
&= \left(\frac{\partial^2\bar{\Psi}}{\partial\bar{I}_1\partial\bar{I}_1} + 2\frac{\partial^2\bar{\Psi}}{\partial\bar{I}_1\partial\bar{I}_2} + \frac{\partial\bar{\Psi}}{\partial\bar{I}_2} + \bar{I}_1^2\frac{\partial^2\bar{\Psi}}{\partial\bar{I}_2\partial\bar{I}_2}\right)\mathbf{I}\otimes\mathbf{I} + \\
&- \left(\frac{\partial^2\bar{\Psi}}{\partial\bar{I}_1\partial\bar{I}_2} + \bar{I}_1\frac{\partial^2\bar{\Psi}}{\partial\bar{I}_2\partial\bar{I}_2}\right)(\bar{\mathbf{C}}\otimes\mathbf{I} + \mathbf{I}\otimes\bar{\mathbf{C}}) + \\
&+ \frac{\partial^2\bar{\Psi}}{\partial\bar{I}_2\partial\bar{I}_2}\bar{\mathbf{C}}\otimes\bar{\mathbf{C}} - \frac{\partial\bar{\Psi}}{\partial\bar{I}_2}\mathbb{S} + \\
&+ \left(\frac{\partial^2\bar{\Psi}}{\partial\bar{I}_1\partial\bar{I}_4} + \bar{I}_1\frac{\partial^2\bar{\Psi}}{\partial\bar{I}_2\partial\bar{I}_4}\right)(\mathbf{I}\otimes\boldsymbol{a}_0\otimes\boldsymbol{a}_0 + \boldsymbol{a}_0\otimes\boldsymbol{a}_0\otimes\mathbf{I}) + \\
&- \left(\frac{\partial^2\bar{\Psi}}{\partial\bar{I}_2\partial\bar{I}_4}\right)(\bar{\mathbf{C}}\otimes\boldsymbol{a}_0\otimes\boldsymbol{g}_0 + \boldsymbol{a}_0\otimes\boldsymbol{a}_0\otimes\bar{\mathbf{C}}) \\
&+ \left(\frac{\partial^2\bar{\Psi}}{\partial\bar{I}_4\partial\bar{I}_4}\right)(\boldsymbol{a}_0\otimes\boldsymbol{a}_0\otimes\boldsymbol{a}_0\otimes\boldsymbol{a}_0) + \\
&+ \left(\frac{\partial^2\bar{\Psi}}{\partial\bar{I}_1\partial\bar{I}_5} + \bar{I}_1\frac{\partial^2\bar{\Psi}}{\partial\bar{I}_2\partial\bar{I}_5}\right)(\boldsymbol{a}_0\otimes\bar{\mathbf{C}}\boldsymbol{a}_0\otimes\mathbf{I} + \boldsymbol{a}_0\bar{\mathbf{C}}\otimes\boldsymbol{a}_0\otimes\mathbf{I} + \mathbf{I}\otimes\boldsymbol{a}_0\otimes\bar{\mathbf{C}}\boldsymbol{a}_0 + \mathbf{I}\otimes\boldsymbol{a}_0\bar{\mathbf{C}}\otimes\boldsymbol{a}_0) + \\
&- \left(\frac{\partial^2\bar{\Psi}}{\partial\bar{I}_2\partial\bar{I}_5}\right)(\boldsymbol{a}_0\otimes\bar{\mathbf{C}}\boldsymbol{a}_0\otimes\bar{\mathbf{C}} + \boldsymbol{a}_0\bar{\mathbf{C}}\otimes\boldsymbol{a}_0\otimes\bar{\mathbf{C}} + \bar{\mathbf{C}}\otimes\boldsymbol{a}_0\otimes\bar{\mathbf{C}}\boldsymbol{a}_0 + \bar{\mathbf{C}}\otimes\boldsymbol{a}_0\bar{\mathbf{C}}\otimes\boldsymbol{a}_0) \\
&+ \frac{\partial^2\bar{\Psi}}{\partial\bar{I}_5\partial\bar{I}_5}(\boldsymbol{a}_0\otimes\bar{\mathbf{C}}\boldsymbol{a}_0\otimes\boldsymbol{a}_0\otimes\bar{\mathbf{C}}\boldsymbol{a}_0 + \boldsymbol{a}_0\otimes\bar{\mathbf{C}}\boldsymbol{a}_0\otimes\boldsymbol{a}_0\bar{\mathbf{C}}\otimes\boldsymbol{a}_0 + \\
&\qquad + \boldsymbol{a}_0\bar{\mathbf{C}}\otimes\boldsymbol{a}_0\otimes\boldsymbol{a}_0\otimes\bar{\mathbf{C}}\boldsymbol{a}_0 + \boldsymbol{a}_0\bar{\mathbf{C}}\otimes\boldsymbol{a}_0\otimes\boldsymbol{a}_0\bar{\mathbf{C}}\otimes\boldsymbol{a}_0) +
\end{aligned}
\tag{B.1}
$$

$$
\begin{aligned}
&+ \left(\frac{\partial^2\bar{\Psi}}{\partial\bar{I}_4\partial\bar{I}_5}\right)(\boldsymbol{a}_0\otimes\bar{\mathbf{C}}\boldsymbol{a}_0\otimes\boldsymbol{a}_0\otimes\boldsymbol{a}_0+\boldsymbol{a}_0\bar{\mathbf{C}}\otimes\boldsymbol{a}_0\otimes\boldsymbol{a}_0\otimes\boldsymbol{a}_0+\\
&\qquad +\boldsymbol{a}_0\otimes\boldsymbol{a}_0\otimes\boldsymbol{a}_0\otimes\bar{\mathbf{C}}\boldsymbol{a}_0+\boldsymbol{a}_0\otimes\boldsymbol{a}_0\otimes\boldsymbol{a}_0\bar{\mathbf{C}}\otimes\boldsymbol{a}_0)+\\
&+ \frac{\partial\bar{\Psi}}{\partial\bar{I}_5}\frac{\partial\bar{I}_5}{\partial\bar{\mathbf{C}}^2}+ \qquad\qquad (B.2)\\
&+ \left(\frac{\partial^2\bar{\Psi}}{\partial\bar{I}_1\partial\bar{I}_6}+\bar{I}_1\frac{\partial^2\bar{\Psi}}{\partial\bar{I}_6\partial\bar{I}_2}\right)(\mathbf{I}\otimes\boldsymbol{g}_0\otimes\boldsymbol{g}_0+\boldsymbol{g}_0\otimes\boldsymbol{g}_0\otimes\mathbf{I})+\\
&+ \left(\frac{\partial^2\bar{\Psi}}{\partial\bar{I}_1\partial\bar{I}_7}+\bar{I}_1\frac{\partial^2\bar{\Psi}}{\partial\bar{I}_2\partial\bar{I}_7}\right)(\boldsymbol{g}_0\bar{\mathbf{C}}\otimes\boldsymbol{g}_0\otimes\mathbf{I}+\boldsymbol{g}_0\bar{\mathbf{C}}\otimes\boldsymbol{g}_0\otimes\mathbf{I}+\mathbf{I}\otimes\boldsymbol{g}_0\otimes\bar{\mathbf{C}}\boldsymbol{g}_0+\mathbf{I}\otimes\boldsymbol{g}_0\bar{\mathbf{C}}\otimes\boldsymbol{g}_0)+\\
&- \frac{\partial^2\bar{\Psi}}{\partial\bar{I}_2\partial\bar{I}_6}(\boldsymbol{g}_0\otimes\boldsymbol{g}_0\otimes\bar{\mathbf{C}}+\bar{\mathbf{C}}\otimes\boldsymbol{g}_0\otimes\boldsymbol{g}_0)+\\
&- \frac{\partial^2\bar{\Psi}}{\partial\bar{I}_2\partial\bar{I}_7}(\boldsymbol{g}_0\otimes\bar{\mathbf{C}}\boldsymbol{g}_0\otimes\bar{\mathbf{C}}+\boldsymbol{g}_0\bar{\mathbf{C}}\otimes\boldsymbol{g}_0\otimes\bar{\mathbf{C}}+\bar{\mathbf{C}}\otimes\boldsymbol{g}_0\otimes\bar{\mathbf{C}}\boldsymbol{g}_0+\bar{\mathbf{C}}\otimes\boldsymbol{g}_0\bar{\mathbf{C}}\otimes\boldsymbol{g}_0)+\\
&+ \frac{\partial^2\bar{\Psi}}{\partial\bar{I}_6\partial\bar{I}_4}(\boldsymbol{g}_0\otimes\boldsymbol{g}_0\otimes\boldsymbol{a}_0\otimes\boldsymbol{a}_0+\boldsymbol{a}_0\otimes\boldsymbol{a}_0\otimes\boldsymbol{g}_0\otimes\boldsymbol{g}_0)+\\
&+ \frac{\partial^2\bar{\Psi}}{\partial\bar{I}_6\partial\bar{I}_5}(\boldsymbol{g}_0\otimes\boldsymbol{g}_0\otimes\boldsymbol{a}_0\otimes\bar{\mathbf{C}}\boldsymbol{a}_0+\boldsymbol{g}_0\otimes\boldsymbol{g}_0\otimes\boldsymbol{a}_0\bar{\mathbf{C}}\otimes\boldsymbol{a}_0+\\
&\qquad \boldsymbol{a}_0\otimes\bar{\mathbf{C}}\boldsymbol{a}_0\otimes\boldsymbol{g}_0\otimes\boldsymbol{g}_0+\boldsymbol{a}_0\bar{\mathbf{C}}\otimes\boldsymbol{a}_0\otimes\boldsymbol{g}_0\otimes\boldsymbol{g}_0)+\\
&+ \frac{\partial^2\bar{\Psi}}{\partial\bar{I}_6\partial\bar{I}_6}(\boldsymbol{g}_0\otimes\boldsymbol{g}_0\otimes\boldsymbol{g}_0\otimes\boldsymbol{g}_0)+\\
&+ \frac{\partial^2\bar{\Psi}}{\partial\bar{I}_6\partial\bar{I}_7}(\boldsymbol{g}_0\otimes\bar{\mathbf{C}}\boldsymbol{g}_0\otimes\boldsymbol{g}_0\otimes\boldsymbol{g}_0+\boldsymbol{g}_0\bar{\mathbf{C}}\otimes\boldsymbol{g}_0\otimes\boldsymbol{g}_0\otimes\boldsymbol{g}_0+\\
&\qquad \boldsymbol{g}_0\otimes\boldsymbol{g}_0\otimes\boldsymbol{g}_0\otimes\bar{\mathbf{C}}\boldsymbol{g}_0+\boldsymbol{g}_0\otimes\boldsymbol{g}_0\otimes\boldsymbol{g}_0\bar{\mathbf{C}}\otimes\boldsymbol{g}_0)+\\
&+ \frac{\partial^2\bar{\Psi}}{\partial\bar{I}_7\partial\bar{I}_5}(\boldsymbol{g}_0\otimes\bar{\mathbf{C}}\boldsymbol{g}_0\otimes\boldsymbol{a}_0\otimes\bar{\mathbf{C}}\boldsymbol{a}_0+\boldsymbol{g}_0\otimes\bar{\mathbf{C}}\boldsymbol{g}_0\otimes\boldsymbol{a}_0\bar{\mathbf{C}}\otimes\boldsymbol{a}_0+\\
&\qquad \boldsymbol{g}_0\bar{\mathbf{C}}\otimes\boldsymbol{g}_0\otimes\boldsymbol{a}_0\otimes\bar{\mathbf{C}}\boldsymbol{a}_0+\boldsymbol{g}_0\bar{\mathbf{C}}\otimes\boldsymbol{g}_0\otimes\boldsymbol{a}_0\bar{\mathbf{C}}\otimes\boldsymbol{a}_0+\\
&\qquad \boldsymbol{a}_0\otimes\bar{\mathbf{C}}\boldsymbol{a}_0\otimes\boldsymbol{g}_0\otimes\bar{\mathbf{C}}\boldsymbol{g}_0+\boldsymbol{a}_0\otimes\bar{\mathbf{C}}\boldsymbol{a}_0\otimes\boldsymbol{g}_0\bar{\mathbf{C}}\otimes\boldsymbol{g}_0+\\
&\qquad \boldsymbol{a}_0\bar{\mathbf{C}}\otimes\boldsymbol{a}_0\otimes\boldsymbol{g}_0\otimes\bar{\mathbf{C}}\boldsymbol{g}_0+\boldsymbol{a}_0\bar{\mathbf{C}}\otimes\boldsymbol{a}_0\otimes\boldsymbol{g}_0\bar{\mathbf{C}}\otimes\boldsymbol{g}_0)+\\
&+ \frac{\partial^2\bar{\Psi}}{\partial\bar{I}_4\partial\bar{I}_7}(\boldsymbol{g}_0\otimes\bar{\mathbf{C}}\boldsymbol{g}_0\otimes\boldsymbol{a}_0\otimes\boldsymbol{a}_0+\boldsymbol{g}_0\bar{\mathbf{C}}\otimes\boldsymbol{g}_0\otimes\boldsymbol{a}_0\otimes\boldsymbol{a}_0+\\
&\qquad \boldsymbol{a}_0\otimes\boldsymbol{a}_0\otimes\boldsymbol{g}_0\otimes\bar{\mathbf{C}}\boldsymbol{g}_0+\boldsymbol{a}_0\otimes\boldsymbol{a}_0\otimes\boldsymbol{g}_0\bar{\mathbf{C}}\otimes\boldsymbol{g}_0)+\\
&+ \frac{\partial^2\bar{\Psi}}{\partial\bar{I}_7\partial\bar{I}_7}(\boldsymbol{g}_0\otimes\bar{\mathbf{C}}\boldsymbol{g}_0\otimes\boldsymbol{g}_0\otimes\bar{\mathbf{C}}\boldsymbol{g}_0+\boldsymbol{g}_0\bar{\mathbf{C}}\otimes\bar{\mathbf{C}}\boldsymbol{g}_0\otimes\boldsymbol{g}_0\bar{\mathbf{C}}\otimes\boldsymbol{g}_0+\\
&\qquad \boldsymbol{g}_0\bar{\mathbf{C}}\otimes\boldsymbol{g}_0\otimes\boldsymbol{g}_0\otimes\bar{\mathbf{C}}\boldsymbol{g}_0+\boldsymbol{g}_0\bar{\mathbf{C}}\otimes\boldsymbol{g}_0\otimes\boldsymbol{g}_0\bar{\mathbf{C}}\otimes\boldsymbol{g}_0)+\\
&+ \frac{\partial\bar{\Psi}}{\partial\bar{I}_7}\frac{\partial^2\bar{I}_7}{\partial\bar{\mathbf{C}}^2} \qquad\qquad (B.3)
\end{aligned}
$$

Appendix C

Modeling of complex structures

C.1 Geometrically nonlinear problem

Within the context of geometrically nonlinear analysis, namely the analysis of linear elastic materials in a large displacement contexts, the nonlinear governing equation in weak form are derived again by means of the the PVW, carried out in Eq. (2.59):

$$\delta\mathcal{L}_{int} + \delta\mathcal{L}_{ine} = \delta\mathcal{L}_{ext} \tag{C.1}$$

where $\mathcal{L}_{int}$ is the internal strain energy, $\mathcal{L}_{ext}$ is the work done by external loads, $\mathcal{L}_{ine}$ is the work done by inertia loads and δ denotes the virtual variation. Differently with respect to the case of hyperelastic materials, in the case of classical linear elasticity, the internal strain energy contribution can be straightforwardly defined using the Hooke's law:

$$\text{(a) } \delta\mathcal{L}_{int} = \int_\Omega \delta\mathbf{E}^T\boldsymbol{\sigma}dV \qquad \text{(b) } \delta\mathcal{L}_{ext} = \int_\Omega \delta\boldsymbol{u}^T dV \qquad \text{(c) } \delta\mathcal{L}_{ine} = \int_\Omega \delta\boldsymbol{u}^T\rho\ \ddot{\boldsymbol{u}}dV \tag{C.2}$$

where $\boldsymbol{\sigma}$ is the Cauchy's stress tensor, $\mathbf{E}$ is the Green-Lagrange strain tensor, $\boldsymbol{f}$ is the vector of external loads, $\ddot{\boldsymbol{u}}$ is the acceleration vector and all volume integrals are referred to the material configuration. Adopting again the same Total Lagrangian approach, all volume integrals are referred to the material reference frame. As done for the case of hyperelastic finite element formulation, the proposed approach is now derived in the case of geometrically nonlinear context.

Internal energy contribution

The internal strain energy defined in Eq.(C.2)(a) is rewritten as:

$$\begin{aligned}
\delta\mathcal{L}_{int} &= \int_\Omega \delta\boldsymbol{u}_{sj}^T(\mathbf{B}_l^{sj} + 2\mathbf{B}_{nl}^{sj})^T\boldsymbol{\sigma}dV = \delta\boldsymbol{u}_{sj}^T\left[\int_\Omega (\mathbf{B}_l^{sj} + 2\mathbf{B}_{nl}^{sj})^T\mathbb{C}(\mathbf{B}_l^{\tau i} + \mathbf{B}_{nl}^{\tau i})dV\right]\boldsymbol{u}_{\tau i} = \\
&= \delta\boldsymbol{u}_{sj}^T\mathbf{K}_{S,ll}^{\tau sij}\boldsymbol{u}_{\tau i} + \delta\boldsymbol{u}_{sj}^T\mathbf{K}_{S,lnl}^{\tau sij}\boldsymbol{u}_{\tau i} + \delta\boldsymbol{u}_{sj}^T\mathbf{K}_{S,nll}^{\tau sij}\boldsymbol{u}_{\tau i} + \delta\boldsymbol{u}_{sj}^T\mathbf{K}_{S,nlnl}^{\tau sij}\boldsymbol{u}_{\tau i} \quad = \qquad \text{(C.3)} \\
&= \delta\boldsymbol{u}_{sj}^T\mathbf{K}_{ll}^{\tau sij}\boldsymbol{u}_{\tau i} + \delta\boldsymbol{u}_{sj}^T\mathbf{K}_{S_1}^{\tau sij}\boldsymbol{u}_{\tau i} = \delta\boldsymbol{u}_{sj}^T\mathbf{K}_S^{\tau sij}\boldsymbol{u}_{\tau i} \qquad \text{(C.4)}
\end{aligned}$$

The quantity $\mathbf{K}_S^{\tau sij}$ is the 3x3 FN of the *secant stiffness matrix* [130], $\mathbf{K}_{ll}^{\tau sij}$ is the 3x3 FN of its linear contribution, and $\mathbf{K}_{S_1}^{\tau sij} = \mathbf{K}_{S,lnl}^{\tau sij} + \mathbf{K}_{S,nll}^{\tau sij} + \mathbf{K}_{S,nlnl}^{\tau sij}$ is 3x3 FN nonlinear contribution,

given again by the nonlinear strain components of the Green-Lagrange strain tensor. The terms defined in Eq. (C.4) are here explicitly reported:

$$\begin{cases} \mathbf{K}_{S,ll}^{\tau sij} = \int_\Omega \mathbf{B}_l^{sjT} \mathbb{C} \mathbf{B}_l^{\tau i} dV \\ \mathbf{K}_{S,lnl}^{\tau sij} = \int_\Omega \mathbf{B}_l^{sjT} \mathbb{C} \mathbf{B}_{nl}^{\tau i} dV \\ \mathbf{K}_{S,nll}^{\tau sij} = \int_\Omega 2\mathbf{B}_{nl}^{sjT} \mathbb{C} \mathbf{B}_l^{\tau i} dV \\ \mathbf{K}_{S,nlnl}^{\tau sij} = \int_\Omega 2\mathbf{B}_{nl}^{sjT} \mathbb{C} \mathbf{B}_{nl}^{\tau i} dV \end{cases} \tag{C.5}$$

External load contribution

Following the previous derivation procedure for the internal strain contribution, the matrix-form of the external load term in the variational principle is expressed starting from the definition in Eq. (C.2)(b):

$$\delta \mathcal{L}_{ext} = \int_\Omega \delta \boldsymbol{u}^T \boldsymbol{f} dV = \int_\Omega \delta \boldsymbol{u}_{sj}^T F_s N_j \boldsymbol{f} \; dV = \delta \boldsymbol{u}_{sj}^T \mathbf{F}_{ext}^{sj} \tag{C.6}$$

where $\mathbf{F}_{ext}^{sj}$ the 3x1 FN of the external forces vector:

$$\mathbf{F}_{ext}^{sj} = \int_\Omega F_s N_j \boldsymbol{f} \; dV \tag{C.7}$$

Inertia load contribution

Regarding the inertial contribution of the energetic balance principle, one can write, following the same derivation procedure, the matrix form of the inertial energy contribution starting from the definition in Eq. (C.2)(c):

$$\delta \mathcal{L}_{ine} = \int_\Omega \delta \boldsymbol{u}^T \rho \; \ddot{\boldsymbol{u}} dV = \int_\Omega \delta \boldsymbol{u}_{sj}^T F_s N_j \rho F_\tau N_i \ddot{\boldsymbol{u}}_{\tau i} dV = \delta \boldsymbol{u}_{sj}^T \mathbf{M}^{\tau sij} \ddot{\boldsymbol{u}}_{\tau i} \tag{C.8}$$

where $\mathbf{M}^{\tau sij}$ the 3x3 FN of the mass matrix:

$$\mathbf{M}^{\tau sij} = \int_\Omega F_s N_j \; \rho \; \mathbf{I} \; F_\tau N_i dV \tag{C.9}$$

Considering then the defined matrix-form of the energetic contributions to variational principle, the matrix form of the governing equation is:

$$\delta \boldsymbol{u}_{sj} : \quad \mathbf{K}_S^{\tau sij} \boldsymbol{u}_{\tau i} + \mathbf{M}^{\tau sij} \ddot{\boldsymbol{u}}_{\tau i} = \mathbf{F}_{ext}^{sj} \tag{C.10}$$

In the CUF framework, as observed for the previously introduced physical quantities, also the FN of the secant stiffness matrix is defined regardless of the polynomial approximation adopted in the displacement field definition, thus the final nonlinear matrix-form equation Eq. (C.10) is valid for any arbitrarily chosen polynomial expansion. Considering the specific kinematic models for the 1D beam axis or 2D mid-surface, namely assigning the set of N_i and N_j shape function, and the theory of structure approximation F_τ and F_s along the beam cross-section or plate mid-surface, one can derive hierarchically and automatically the final form of the nonlinear

governing equation by means of the summation over the FE and CUF indices expansion (thus over the indices i, j, τ and s). More details about the generic expansion of the FN can be found in [129].

The summation over indices τ, s, i and j gives the internal and external forces vectors and the mass matrix for the single element considered, obtained straightforwardly by following the CUF assembling procedure [129]. Assembling the FE matrices along the discretization considered, the final definition of PVW in matrix form states:

$$\mathbf{K}_s(\boldsymbol{u})\boldsymbol{u} + \mathbf{M}\ddot{\boldsymbol{u}} = \mathbf{F}_{ext}(\boldsymbol{f}) \tag{C.11}$$

The linearization procedure of the Eq. (C.11) follows the same steps already provided in Sec. 5.3, obtaining the final incremental system of equation Eq. (5.27). In this context, also the tangent stiffness matrix is defined following the same approach, with the main simplification given by the assumption of constant elasticity tensor given by the Hooke's law. For this reason, the framework provided in the context of linearized equations for hyperelasticity is still perfectly valid in the context of geometrically nonlinear analysis, by considering the constant elasticity tensor given by linear elasticity.

C.2 Variable-kinematics approach

Complex structures can be modeled following different approaches. Typically, complex geometries are analyzed by means of pure 3D FE discretization, given the generality of the element shape that can be adopted in various contexts. In the following, a modeling approach of complex structure to defined computationally efficient and accurate discretization for geometrically nonlinear analysis of structure is proposed. This methodology is established again by means of the CUF, and the capabilities given by the LE-class models, as discussed in Sec. 4.1 and Sec. 4.2. The proposed approach is based on the variable-kinematics modeling of 1D and 2D finite elements. The variable-kinematics models, originally introduced by Zappino and Carrera [201] and extended to geometrically nonlinear structural analysis [202], are purely displacement-based finite element formulations. Thanks to the adoption of LE-class models, within the 1D beam and 2D plate finite element definitions, the resulting DOF directly correspond to the Cartesian displacement components, defined in physical independent nodes. This feature enables the a straightforward coupling of different FE models, with different kinematic descriptions or structural approximations, regardless of the imposed mathematical definition by exploiting superposition principles. The final assembled model, where both pure 3D FE and higher-order 1D/2D models are present, is performed by enforcing the correspondence of displacement components at common shared nodes between distinct discretization models. When nodes from different finite element models are merged, the global FE matrices, such as the tangent stiffness matrix or the internal force vector, as assembled considering the superposition and nodal correspondence. Figure C.1 illustrates this variable-kinematics assembling procedure, showing the coupling procedure at assembly level between refined 1D beam models and 3D hexahedral models. The proposed approach reflects typical assembling strategies used in commercial software between classical FE formulation. In this sense, the proposed approach based on variable-kinematic modeling and LE-class expansion models, a straightforward, efficient and natural coupling between FE approaches is established, exploiting direct connections between higher-order 1D beam models with conventional 3D elements at the nodal level. This strategy makes it possible to locally refine complex geometries using advanced beam models, while overcoming the well-known limitations of classical beam theories—such as rigid cross-section assumptions, incompatibility of

transverse normal and shear stresses at beam edges, or uniform shear stress distributions across the section. Leveraging the CUF formalism, the method avoids the need for ad-hoc coupling techniques (e.g., Lagrange multipliers).

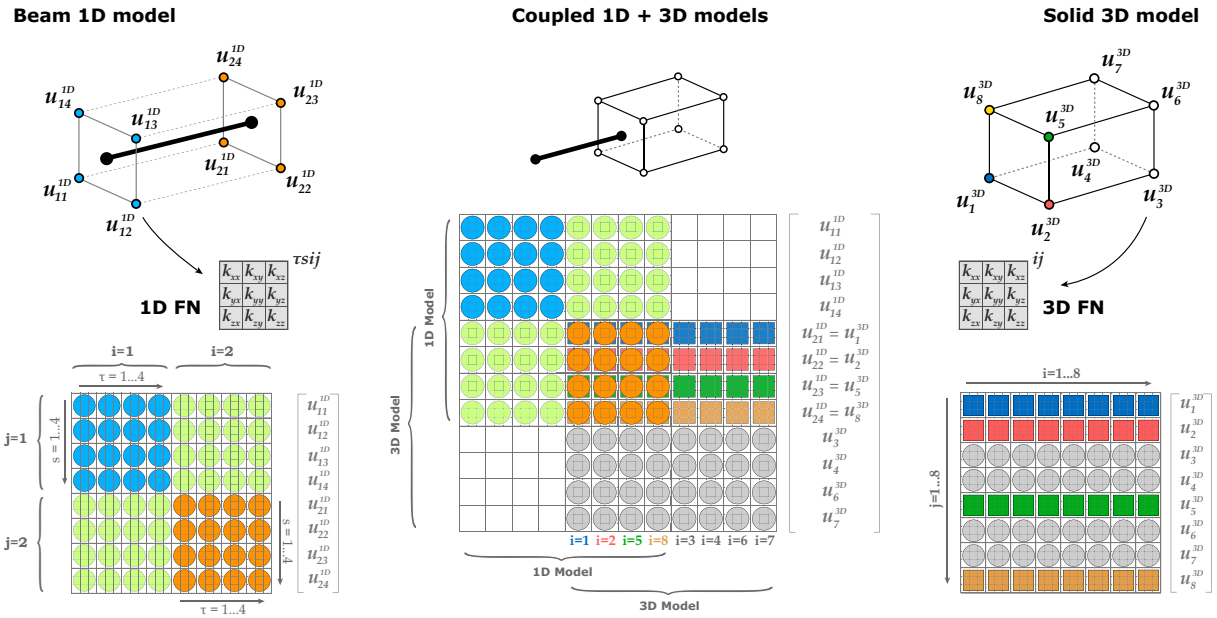

Figure C.1: Coupled 1D-3D models: assembling procedure.

According to the theoretical framework proposed, a 3D discretization model and a 1D cross-section expansion model have to be matched through the superposition of common nodes. This ensure continuity and smooth transitions between elements, without relying on numerical techniques for model coupling. When classical models or Rigid Body Elements (RBE) are used to connect variable-kinematics models, local effects may be observed at the element interfaces. In particular, due to the Poisson effect, the displacement field may become discontinuous across the interface. Refined beam models, however, can capture cross-section warping, thereby avoiding such inconsistencies at the transitions interfaces. However, the displacement continuity can generate stress concentrations and oscillations, that can still arise within the transition zone as a consequence of the direct coupling.

C.3 Numerical results

This section presents the numerical results obtained via variable-kinematics for the geometrically nonlinear analysis of structures with complex geometries. The proposed model results are compared against literature results available or against reference solutions obtained by classical FE implemented in commercial codes. Several case studies are examined to demonstrate the effectiveness of the proposed variable-kinematics models

C.3.1 Clamped angle frame

The first case study addresses the geometrically nonlinear static analysis of a clamped L-shaped frame. This benchmark problem has been analyzed by many authors, here the reference work of Zouari et al. [203] is reported for comparison purposes. This benchmark problem is

typically analyzed within the framework of plane-strain finite element models, here instead th three-dimensional extension of the reported case study is proposed, analying the large-deflection response of the L-shaped frame in a 3D set. The frame is clamped at the left end and subjected to a horizontal force applied at the top-right end, as illustrated in Figure C.2. The frame dimensions considered are $L = 0.1$ m, $h = 0.01$ m, and thickness $t = 0.01$ m. The material properties are defined by a Young's modulus $E = 3 \cdot 10^{11}$ Pa and a Poisson's ratio $\nu = 0.3$, and consistently introduced starting from the non-dimensional parameters reported in the reference study. The adopted discretization employs unified 1D beam finite element models for the two straight sides and a 3D hexahedral model for the corner. Each square-section beam is modeled with a single L9 cross-section expansion element and N_{B4} cubic elements along the axis, while the corner is discretized using a single H27 parabolic hexahedral element. The resulting mesh is shown in Figure C.2(b). A convergence study is first performed by increasing the number of finite elements along the straight beams, to assess the influence of the beam axis kinematics on the numerical results and displacement distributions. Tables C.1–C.2 compare the displacement components predicted by the 1D-3D variable-kinematics models for different values of the shear load considered against the reference solution, reporting the measured percentage difference between solutions in brackets. The computed equilibrium paths, obtained with each FE model introduced, is reported in Figure C.3, measuring the displacement components at the load application point.

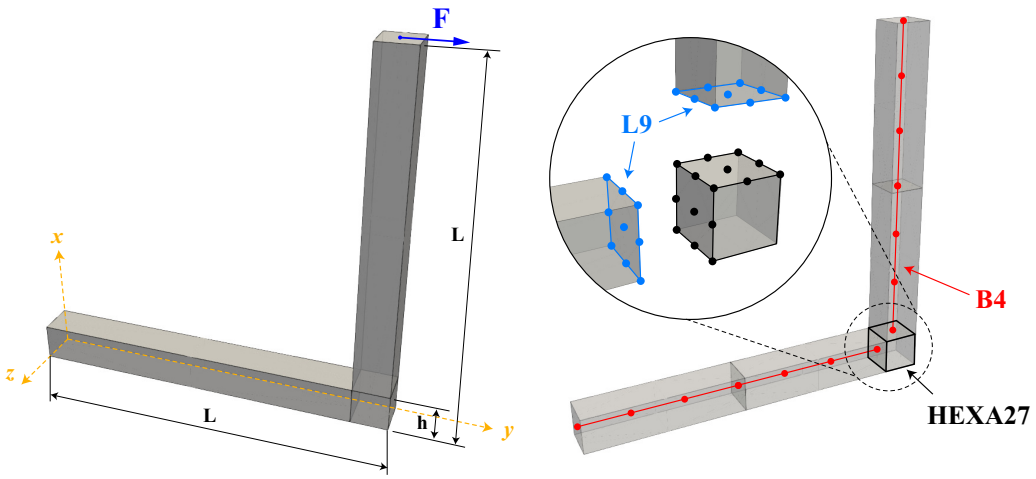

(a) Geometrical features **(b)** Merging nodes between models

Figure C.2: Clamped angle frame: geometry and multi-dimensional discretization adopted.

Figure C.4 shows the stress contours for σ_{xx} and σ_{yy} obtained with the 4B4–1L9 + 1H27 discretization model. The convergence study listed demonstrate that the 2B4+1L9 model already provides a convergent solution. Although minor differences are observed across the tested discretizations, all cases yield to accurate displacement predictions. The measured percentage differences between variable-kinematic models and the reference solution are observed to be lower than 1% for each model considered. In most load conditions, accuracy improves with the increasing number of finite elements along the beam axis. Overall, the proposed variable-kinematics models demonstrate high efficiency in terms of computational cost. An approximate 85% reduction in degrees of freedom is achieved when comparing the 1B4 model with the 10B4 model, without any significant loss of accuracy.

F [kN]	$\mathbf{u_{y_{ref}}}$ [203]	**1 B4**	**2 B4**	**4 B4**	**5 B4**	**10 B4**
4	1.6490	$1.6375^{(-0.695\%)}$	$1.6428^{(-0.374\%)}$	$1.6394^{(-0.584\%)}$	$1.6391^{(-0.602\%)}$	$1.6391^{(-0.598\%)}$
8	2.9820	$2.9600^{(-0.737\%)}$	$2.9664^{(-0.523\%)}$	$2.9615^{(-0.688\%)}$	$2.9611^{(-0.702\%)}$	$2.9612^{(-0.697\%)}$
12	3.9990	$3.9694^{(-0.741\%)}$	$3.9735^{(-0.639\%)}$	$3.9682^{(-0.769\%)}$	$3.9679^{(-0.779\%)}$	$3.9681^{(-0.773\%)}$
16	4.7610	$4.7273^{(-0.708\%)}$	$4.7279^{(-0.696\%)}$	$4.7228^{(-0.802\%)}$	$4.7225^{(-0.808\%)}$	$4.7228^{(-0.803\%)}$
20	5.3330	$5.3001^{(-0.618\%)}$	$5.2973^{(-0.670\%)}$	$5.2925^{(-0.759\%)}$	$5.2923^{(-0.763\%)}$	$5.2926^{(-0.758\%)}$
24	5.7750	$5.7389^{(-0.626\%)}$	$5.7333^{(-0.721\%)}$	$5.7288^{(-0.80\%)}$	$5.7287^{(-0.802\%)}$	$5.7290^{(-0.797\%)}$
28	6.1200	$6.0822^{(-0.617\%)}$	$6.0747^{(-0.741\%)}$	$6.0703^{(-0.812\%)}$	$6.0702^{(-0.813\%)}$	$6.0705^{(-0.808\%)}$
32	6.3950	$6.3561^{(-0.609\%)}$	$6.3471^{(-0.749\%)}$	$6.3429^{(-0.815\%)}$	$6.3429^{(-0.815\%)}$	$6.3432^{(-0.811\%)}$
36	6.6180	$6.5786^{(-0.595\%)}$	$6.5687^{(-0.744\%)}$	$6.5646^{(-0.807\%)}$	$6.5646^{(-0.807\%)}$	$6.5649^{(-0.803\%)}$
40	6.8030	$6.7625^{(-0.595\%)}$	$6.7522^{(-0.747\%)}$	$6.7480^{(-0.809\%)}$	$6.7480^{(-0.808\%)}$	$6.7483^{(-0.804\%)}$
DOF		243	405	729	891	1701

Table C.1: L-shaped clamped frame: tip horizontal displacement measured at the load point application [mm], convergence analysis and comparison between results obtained by 1D+3D CUF models and the reference.

F [kN]	$\mathbf{u_{x_{ref}}}$ [203]	**1 B4**	**2 B4**	**4 B4**	**5 B4**	**10 B4**
4	-0.7860	$-0.7789^{(-0.898\%)}$	$-0.7845^{(-0.185\%)}$	$-0.7827^{(-0.414\%)}$	$-0.7825^{(-0.442\%)}$	$-0.7826^{(-0.438\%)}$
8	-1.6710	$-1.6538^{(-1.028\%)}$	$-1.6639^{(-0.424\%)}$	$-1.6604^{(-0.635\%)}$	$-1.6600^{(-0.660\%)}$	$-1.6601^{(-0.654\%)}$
12	-2.5300	$-2.5043^{(-1.016\%)}$	$-2.5161^{(-0.550\%)}$	$-2.5115^{(-0.732\%)}$	$-2.5109^{(-0.754\%)}$	$-2.5111^{(-0.747\%)}$
16	-3.3040	$-3.2723^{(-0.960\%)}$	$-3.2836^{(-0.618\%)}$	$-3.2784^{(-0.773\%)}$	$-3.2778^{(-0.792\%)}$	$-3.2780^{(-0.786\%)}$
20	-3.9750	$-3.9430^{(-0.804\%)}$	$-3.9527^{(-0.560\%)}$	$-3.9474^{(-0.695\%)}$	$-3.9467^{(-0.711\%)}$	$-3.9470^{(-0.705\%)}$
24	-4.5570	$-4.5197^{(-0.819\%)}$	$-4.5275^{(-0.648\%)}$	$-4.5220^{(-0.768\%)}$	$-4.5214^{(-0.782\%)}$	$-4.5216^{(-0.776\%)}$
28	-5.0540	$-5.0150^{(-0.773\%)}$	$-5.0209^{(-0.655\%)}$	$-5.0154^{(-0.763\%)}$	$-5.0148^{(-0.776\%)}$	$-5.0151^{(-0.770\%)}$
32	-5.4820	$-5.4411^{(-0.746\%)}$	$-5.4454^{(-0.667\%)}$	$-5.4400^{(-0.766\%)}$	$-5.4394^{(-0.777\%)}$	$-5.4397^{(-0.772\%)}$
36	-5.8510	$-5.8094^{(-0.711\%)}$	$-5.8124^{(-0.660\%)}$	$-5.8070^{(-0.751\%)}$	$-5.8064^{(-0.762\%)}$	$-5.8067^{(-0.757\%)}$
40	-6.1720	$-6.1294^{(-0.690\%)}$	$-6.1314^{(-0.657\%)}$	$-6.1261^{(-0.744\%)}$	$-6.1255^{(-0.754\%)}$	$-6.1258^{(-0.749\%)}$
DOF		243	405	729	891	1701

Table C.2: L-shaped clamped frame: tip vertical displacement measured at the load point application [mm], convergence analysis and comparison between results obtained by 1D+3D CUF models and the reference.

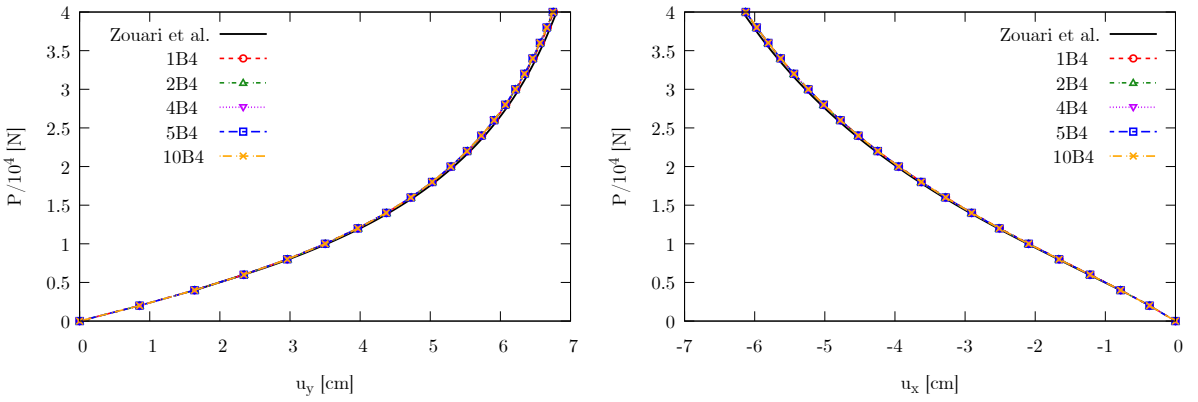

(a) Tip horizontal displacement u_y

(b) Tip vertical displacement u_x

Figure C.3: L-shaped clamped frame: equilibrium paths for different beam axis discretization models, comparison against reference literature results.

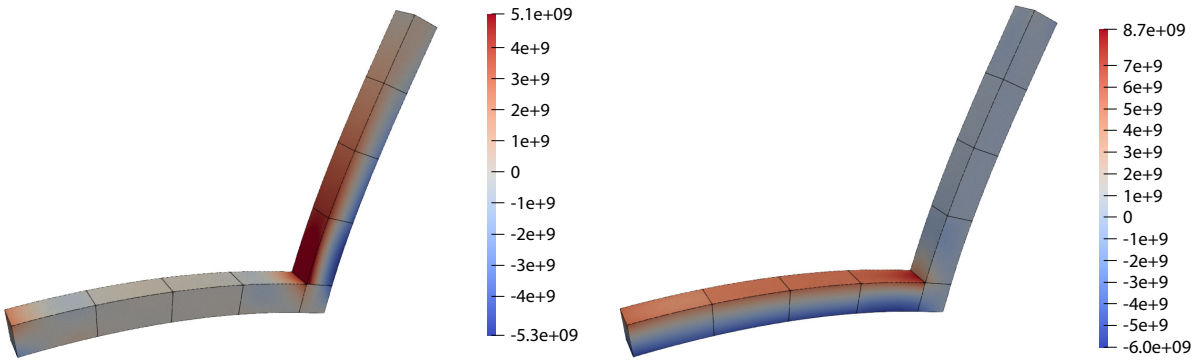

(a) σ_{xx} **(b)** σ_{yy}

Figure C.4: L-shaped clamped frame: contour of the stress component obtained for a value of the applied load $P = 8.474 \cdot 10^3$ N, stress reported in [Pa].

C.3.2 Clamped frame subjected to shear load

The first case study analyzes a clamped angle frame with a curved connecting zone. The geometry and boundary conditions are depicted in Figure C.5. The structure is made of two straight frame segments, each of length $L = 200$ mm with cross-section dimensions $t = 10$ mm and $h = 30$ mm, joined by a curved 90° corner with an internal radius of $R = 20$ mm. The frame is made of aluminum, whose material constants are expressed in terms of Young modulus $E = 70$ GPa and Poisson ratio $\nu = 0.3$. The straight segments are modeled using unified 1D beam finite elements, while the corner is modeled with 3D hexahedral elements. Different cross-section expansion models are considered, employing N_h L9 elements along the lateral side and N_{B4} elements along the beam axis. The curved corner is discretized with $N_h \times N_{tan}$ H27 hexahedral parabolic elements, where N_h denotes the number of elements along the radial direction and N_{tan} along the tangential curved direction. Figure C.6 illustrates the discretization adopted and the variable-kinematics coupling achieved through node correspondence between the 1D and 3D models. The frame is clamped at one end and subjected to a vertical out-of-plane concentrated load applied at the center of the free end.

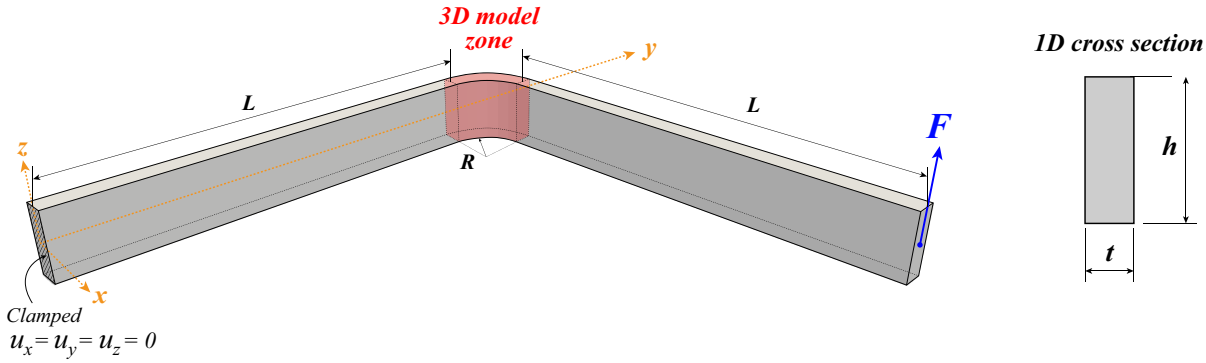

Figure C.5: Clamped angle frame: geometry and multi-dimensional discretization adopted.

The first numerical investigation focuses on the convergence analysis, investigating the effects of beam axis FE discretization, cross-section expansion models, and the 3D refinement adopted for the corner modeling. The results obtained via the present variable-kinematics models are compared with those obtained from a fully 3D numerical solution performed using the commercial software ABAQUS. In the study, both the accuracy and efficiency of the proposed approach are assessed by comparing the required computational cost by each model and the relative percentage difference between the solutions. For each test case, the mathematical model is characterized in terms of the total number of L9 expansion elements, the number of elements used in the circumferential direction for the corner, and the total number of cubic B4 models employed along each straight frame discretization. Tables C.3–C.4 report the displacement components obtained with variable-kinematics models under different shear load levels, alongside the reference solution, measuring the corresponding displacement components at the point load applications. Relative errors with respect to the reference are reported in brackets. Finally, Figure C.7 presents the equilibrium paths, showing the displacement components at the point of load application, obtained with 20 N_{B4} B4 elements, plotting the results obtained adopting each previously listed cross-section expansion models and 3D hexahedral discretizations.

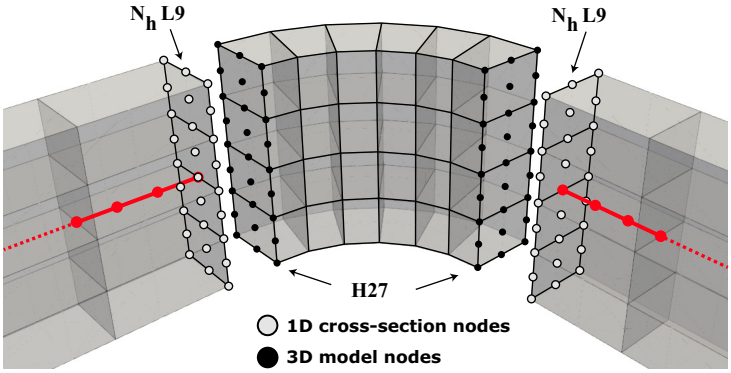

Figure C.6: Clamped angle frame with curved connector: multi-dimensional discretization adopted.

The convergence study for the out-of-plane load case demonstrates that each model provide accurate predictions of the displacement components u_z and u_x, across all the FE models considered. In particular, the out-of-plane component u_z is consistently captured across all displacement regimes, whereas the in-plane component u_x shows slight deviations when coarser discretizations are adopted, particularly in the low-displacement regime. This behavior is linked to the strong nonlinearity of the problem at small load levels, where discrepancies are found relatively small and below 5%. Similar observations arise from the convergence analysis under shear loading. In this case, the displacement component orthogonal to the load direction is consistently predicted with high accuracy across all models. In both analyses, the absolute percentage differences between the variable-kinematics results and the ABAQUS 3D solutions is found similar across all discretizations. Even coarser models with a reduced number of elements along the beam axis allow for accurate displacement predictions. Accuracy is observed to be strongly dependent of the cross-section kinematic description the curved corner 3D discretization. While coarse meshes improve computational efficiency, the configuration 4L9–10B4 + 4×6 H27 achieves reliable accuracy with a 94% reduction in computational cost compared to the reference solution, while maintaining acceptable percentage differences relative to refined models.

Model		$-u_x$ [mm]				
L9/H27	**B4**	$F = 2.25$ kN	$F = 5.25$ kN	$F = 8.25$ kN	$F = 12.75$ kN	**DOF**
2L9 + 2x6H27	10	$20.4665^{(4.20\%)}$	$62.3523^{(2.57\%)}$	$90.6258^{(1.71\%)}$	$114.5720^{(1.03\%)}$	3285
	15	$20.4777^{(4.15\%)}$	$62.3722^{(2.54\%)}$	$90.6437^{(1.69\%)}$	$114.5840^{(1.02\%)}$	4635
	20	$20.4823^{(4.13\%)}$	$62.3804^{(2.52\%)}$	$90.6510^{(1.68\%)}$	$114.5885^{(1.02\%)}$	5985
2L9 + 2x8H27	10	$20.4543^{(4.26\%)}$	$62.3288^{(2.61\%)}$	$90.6041^{(1.73\%)}$	$114.5586^{(1.04\%)}$	3465
	15	$20.4653^{(4.20\%)}$	$62.3485^{(2.57\%)}$	$90.6218^{(1.71\%)}$	$114.5704^{(1.03\%)}$	4815
	20	$20.4699^{(4.18\%)}$	$62.3567^{(2.56\%)}$	$90.6290^{(1.70\%)}$	$114.5749^{(1.03\%)}$	6165
4L9 + 4x6H27	10	$21.2387^{(0.58\%)}$	$63.8391^{(0.25\%)}$	$92.1500^{(0.05\%)}$	$115.9014^{(0.12\%)}$	5913
	15	$21.2508^{(0.53\%)}$	$63.8601^{(0.21\%)}$	$92.1687^{(0.03\%)}$	$115.9137^{(0.13\%)}$	8343
	20	$21.2560^{(0.50\%)}$	$63.8691^{(0.20\%)}$	$92.1765^{(0.02\%)}$	$115.9186^{(0.13\%)}$	10773
4L9 + 4x8H27	10	$21.2260^{(0.64\%)}$	$63.8152^{(0.28\%)}$	$92.1282^{(0.08\%)}$	$115.8881^{(0.10\%)}$	6237
	15	$21.2380^{(0.59\%)}$	$63.8361^{(0.25\%)}$	$92.1467^{(0.06\%)}$	$115.9003^{(0.12\%)}$	8667
	20	$21.2431^{(0.56\%)}$	$63.8450^{(0.24\%)}$	$92.1545^{(0.05\%)}$	$115.9051^{(0.12\%)}$	11097
3D ABQ	6000 C8D20R	21.3636	63.9962	92.1986	115.7670	92247

Table C.3: Clamped angle frame with curved connector: tip vertical displacement measured at the load point application [mm], convergence analysis and comparison between results obtained by 1D+3D CUF models and the reference.

Model		u_z [mm]				
L9/H27	**B4**	$F = 2.25$ kN	$F = 5.25$ kN	$F = 8.25$ kN	$F = 12.75$ kN	**DOF**
2L9 + 2x6H27	10	$105.7439^{(1.34\%)}$	$179.0502^{(1.13\%)}$	$213.6598^{(0.74\%)}$	$242.4510^{(0.52\%)}$	3285
	15	$105.7804^{(1.31\%)}$	$179.0947^{(1.10\%)}$	$213.7070^{(0.72\%)}$	$242.5055^{(0.50\%)}$	4635
	20	$105.7955^{(1.30\%)}$	$179.1128^{(1.09\%)}$	$213.7259^{(0.71\%)}$	$242.5273^{(0.49\%)}$	5985
2L9 + 2x8H27	10	$105.7218^{(1.37\%)}$	$179.0368^{(1.13\%)}$	$213.6566^{(0.74\%)}$	$242.4537^{(0.52\%)}$	3465
	15	$105.7581^{(1.33\%)}$	$179.0812^{(1.11\%)}$	$213.7036^{(0.72\%)}$	$242.5082^{(0.50\%)}$	4815
	20	$105.7732^{(1.32\%)}$	$179.0993^{(1.10\%)}$	$213.7226^{(0.71\%)}$	$242.5300^{(0.49\%)}$	6165
4L9 + 4x6H27	10	$107.4332^{(0.23\%)}$	$180.5947^{(0.27\%)}$	$214.7964^{(0.21\%)}$	$243.2478^{(0.20\%)}$	5913
	15	$107.4721^{(0.27\%)}$	$180.6419^{(0.25\%)}$	$214.8467^{(0.19\%)}$	$243.3065^{(0.17\%)}$	8343
	20	$107.4886^{(0.28\%)}$	$180.6616^{(0.24\%)}$	$214.8674^{(0.18\%)}$	$243.3306^{(0.16\%)}$	10773
4L9 + 4x8H27	10	$107.4108^{(0.21\%)}$	$180.5814^{(0.28\%)}$	$214.7933^{(0.22\%)}$	$243.2506^{(0.20\%)}$	6237
	15	$107.4495^{(0.25\%)}$	$180.6285^{(0.26\%)}$	$214.8435^{(0.19\%)}$	$243.3092^{(0.17\%)}$	8667
	20	$107.4660^{(0.26\%)}$	$180.6482^{(0.25\%)}$	$214.8642^{(0.18\%)}$	$243.3332^{(0.16\%)}$	11097
3D ABQ	6000 C8D20R	107.1850	181.0920	215.2570	243.7270	92247

Table C.4: Clamped angle frame with curved connector: tip vertical displacement measured at the load point application [mm], convergence analysis and comparison between results obtained by 1D+3D CUF models and the reference.

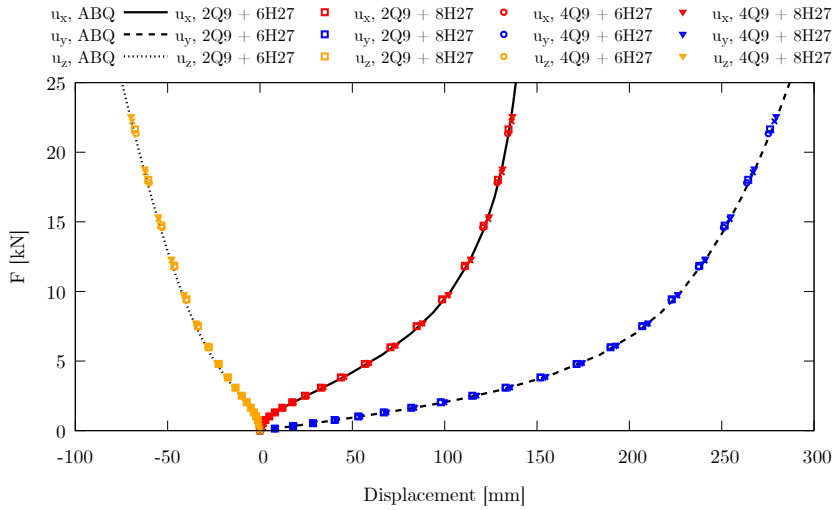

(a) Global computed equilibrium path

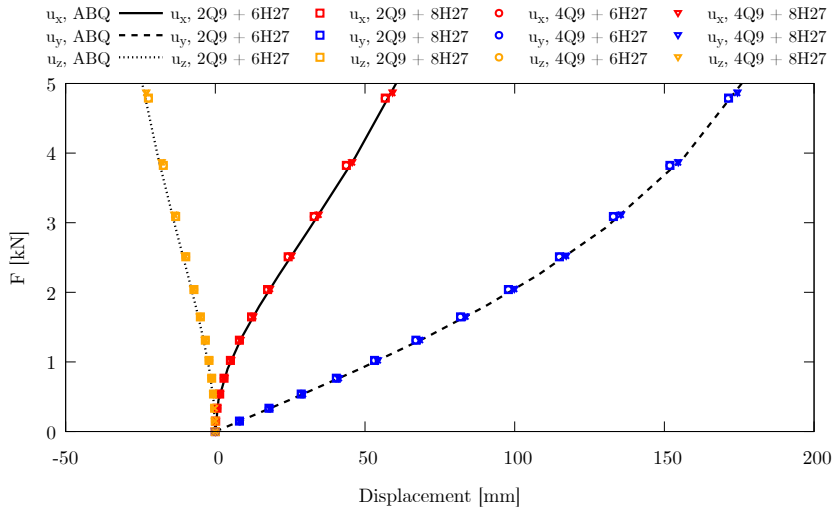

(b) Low- to moderate displacement regime

Figure C.7: Clamped angle frame with curved connector: computed equilibrium paths and comparison with the reference 3D elasticity solution obtained via ABAQUS software.

C.3.3 Doubly-curved beam subjected to uniform loads

The next case study addresses the static analysis of a clamped doubly-curved beam. The structural response is examined under two distinct loading conditions. First, a uniform tensile load is applied at the free tip along the y-direction. Subsequently, the nonlinear static response is investigated under a transverse shear pressure applied at the same free end. The beam geometry is defined by a length $L = 30$ mm, curvature radius $R = 2$ mm, section height $h = 6$ mm, thickness $t = 3$ mm, and a mid-span inclination of $\theta = 10°$. Figure C.8(a) depicts the geometrical features considered, while Fig. C.8(b) shows the applied boundary conditions and loading configurations investigated in the following.

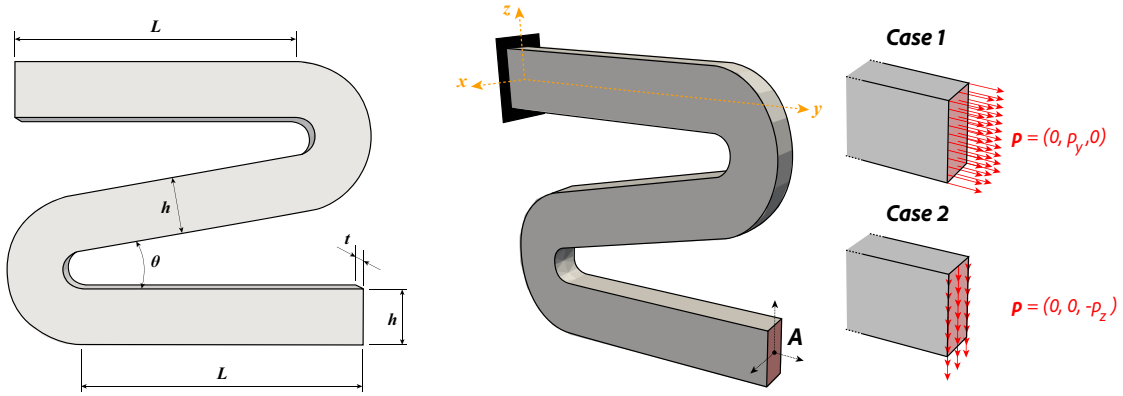

(a) Geometrical features **(b)** Boundary conditions, load cases

Figure C.8: Doubly-curved beam subjected to uniform loads: case study reference description.

The mechanical response is evaluated by evaluating the Cartesian displacement components at point "A," located at the free end of the beam, as indicated in Fig. C.8(b). The material considered is aluminum, for which the mechanical properties are defined in terms Young's modulus of $E = 70$ GPa and a Poisson's ratio of $\nu = 0.3$. The frame discretization is exploit either CUF 1D beam finite element models for each straight frame and 3D hexahedral models for the two curved connecting regions. The straight beam-like segments are modeled with 1D CUF elements, employing N_y cubic B4 elements coupled with N_E L9 elements across the beam cross-section. For the curved regions, consistently with respect to the cross-section partitions defined by the 1D expansion models, the FE model is performed with N_E parabolic H27 elements along the radial direction and N_t H27 elements along the span. Each model configuration is therefore denoted as N_y B4–N_E L9 + $N_E \times N_t$ H27. The adopted discretization scheme and the node-merging procedure for variable-kinematics models are illustrated in Fig. C.9. The numerical responses obtained with higher-order variable-kinematics models are compared against a reference solution obtained via 3D FE models implemented in ABAQUS.

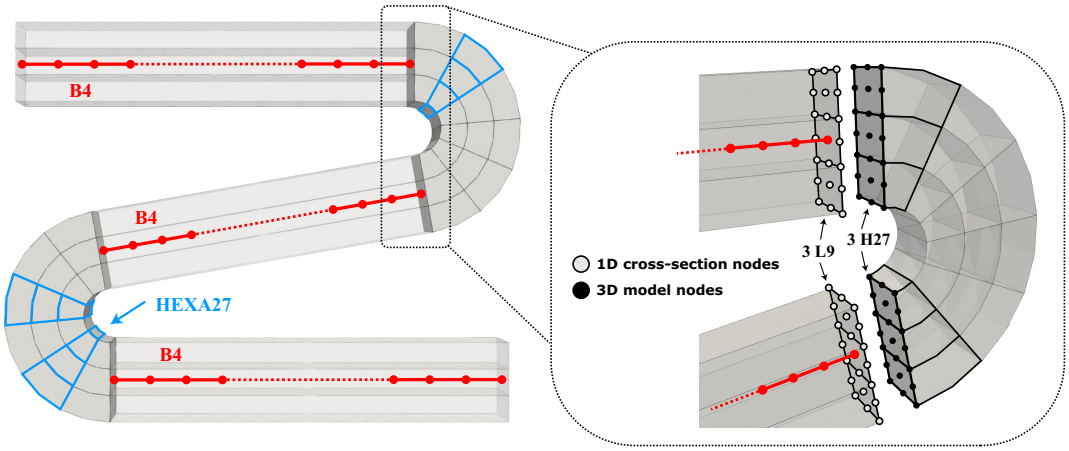

Figure C.9: Doubly-curved beam subjected to uniform loads: multi-dimensional discretization adopted. Example representation of nodes superposition along the radial direction of the curved frame.

A convergence study is performed by evaluating the displacement components at point "A" considering different discretization models, in particular considering progressively increasing number of beam and hexahedral elements. Table C.5 shows the comparison between the results obtained with variable-kinematics discretization models and the full 3D reference solutions computed with ABAQUS, in the case of application of a traction pressure load. For three deformed configurations and load value considered, reported in the table, the horizontal displacement u_y and vertical displacement u_z at point "A" are reported, highlighting the influence of the adopted mathematical model and the relative percentage differences between solutions. The same comparison, regarding the shear pressure load case, is proposed in Table C.6. Finally, the full equilibrium paths are computed, enabling a broader assessment of the structural response over the entire load range.

		$p = 900$ MPa		$p = 1650$ MPa		$p = 2400$ MPa		
B4	**Model**	u_y	u_z	u_y	u_z	u_y	u_z	**DOF**
2	2 L9 + 4x2 H27	$52.767^{(1.98\%)}$	$20.466^{(0.27\%)}$	$62.830^{(3.38\%)}$	$22.784^{(0.20\%)}$	$67.639^{(4.32\%)}$	$23.502^{(0.20\%)}$	1575
	2 L9 + 6x2 H27	$52.844^{(1.84\%)}$	$20.470^{(0.29\%)}$	$62.881^{(3.30\%)}$	$22.785^{(0.20\%)}$	$67.679^{(4.27\%)}$	$23.501^{(0.21\%)}$	1935
	3 L9 + 4x3 H27	$52.836^{(1.85\%)}$	$20.176^{(1.15\%)}$	$62.837^{(3.37\%)}$	$22.642^{(0.83\%)}$	$67.603^{(4.37\%)}$	$23.421^{(0.55\%)}$	2205
	3 L9 + 6x3 H27	$52.913^{(1.71\%)}$	$20.180^{(1.13\%)}$	$62.887^{(3.29\%)}$	$22.643^{(0.82\%)}$	$67.642^{(4.32\%)}$	$23.421^{(0.55\%)}$	2709
5	2 L9 + 4x2 H27	$52.755^{(2.00\%)}$	$20.451^{(0.20\%)}$	$62.823^{(3.39\%)}$	$22.766^{(0.28\%)}$	$67.635^{(4.33\%)}$	$23.486^{(0.27\%)}$	2790
	2 L9 + 6x2 H27	$52.833^{(1.86\%)}$	$20.455^{(0.22\%)}$	$62.875^{(3.31\%)}$	$22.768^{(0.27\%)}$	$67.675^{(4.27\%)}$	$23.487^{(0.26\%)}$	3150
	3 L9 + 4x3 H27	$52.822^{(1.88\%)}$	$20.179^{(1.13\%)}$	$62.827^{(3.38\%)}$	$22.642^{(0.82\%)}$	$67.598^{(4.38\%)}$	$23.420^{(0.55\%)}$	3609
	3 L9 + 6x3 H27	$52.901^{(1.73\%)}$	$20.184^{(1.11\%)}$	$62.879^{(3.30\%)}$	$22.644^{(0.81\%)}$	$67.638^{(4.33\%)}$	$23.421^{(0.55\%)}$	4410
10	2 L9 + 4x2 H27	$52.754^{(2.01\%)}$	$20.448^{(0.18\%)}$	$62.821^{(3.39\%)}$	$22.764^{(0.29\%)}$	$67.632^{(4.33\%)}$	$23.485^{(0.27\%)}$	4815
	2 L9 + 6x2 H27	$52.832^{(1.86\%)}$	$20.453^{(0.20\%)}$	$62.873^{(3.31\%)}$	$22.766^{(0.28\%)}$	$67.672^{(4.28\%)}$	$23.486^{(0.27\%)}$	5175
	3 L9 + 4x3 H27	$52.821^{(1.88\%)}$	$20.179^{(1.14\%)}$	$62.826^{(3.39\%)}$	$22.642^{(0.82\%)}$	$67.597^{(4.38\%)}$	$23.420^{(0.55\%)}$	6741
	3 L9 + 6x3 H27	$52.900^{(1.73\%)}$	$20.184^{(1.11\%)}$	$62.878^{(3.31\%)}$	$22.644^{(0.82\%)}$	$67.637^{(4.33\%)}$	$23.421^{(0.55\%)}$	7245
ABQ	1140 C3D20R	53.833	20.411	65.028	22.830	70.696	23.549	21249

Table C.5: Doubly-curved beam subjected to uniform loads, traction pressure case: horizontal u_z and vertical u_y displacements components [mm]. Comparison between variable-kinematics discretization model and ABAQUS 3D reference solutions for different load conditions.

		$p = 500$ MPa		$p = 1000$ MPa		$p = 1500$ MPa		
B4	**Model**	$-u_y$	$-u_z$	$-u_y$	$-u_z$	$-u_y$	$-u_z$	**DOF**
2	2 L9 + 4x2 H27	$18.666^{(1.28\%)}$	$40.510^{(1.81\%)}$	$21.208^{(0.48\%)}$	$56.567^{(2.94\%)}$	$23.146^{(0.15\%)}$	$65.563^{(3.82\%)}$	1575
	2 L9 + 6x2 H27	$18.659^{(1.32\%)}$	$40.600^{(1.59\%)}$	$21.205^{(0.49\%)}$	$56.643^{(2.81\%)}$	$23.146^{(0.15\%)}$	$65.623^{(3.73\%)}$	1935
	3 L9 + 4x3 H27	$18.664^{(1.29\%)}$	$40.582^{(1.64\%)}$	$21.211^{(0.46\%)}$	$56.631^{(2.83\%)}$	$23.153^{(0.18\%)}$	$65.613^{(3.75\%)}$	2205
	3 L9 + 6x3 H27	$18.657^{(1.33\%)}$	$40.672^{(1.42\%)}$	$21.208^{(0.48\%)}$	$56.707^{(2.70\%)}$	$23.153^{(0.18\%)}$	$65.672^{(3.66\%)}$	2709
5	2 L9 + 4x2 H27	$18.674^{(1.24\%)}$	$40.510^{(1.81\%)}$	$21.233^{(0.36\%)}$	$56.577^{(2.92\%)}$	$23.217^{(0.46\%)}$	$65.619^{(3.74\%)}$	2790
	2 L9 + 6x2 H27	$18.665^{(1.29\%)}$	$40.599^{(1.60\%)}$	$21.228^{(0.38\%)}$	$56.652^{(2.79\%)}$	$23.214^{(0.45\%)}$	$65.678^{(3.65\%)}$	3150
	3 L9 + 4x3 H27	$18.672^{(1.26\%)}$	$40.581^{(1.64\%)}$	$21.235^{(0.35\%)}$	$56.642^{(2.81\%)}$	$23.222^{(0.48\%)}$	$65.670^{(3.66\%)}$	3609
	3 L9 + 6x3 H27	$18.663^{(1.3\%)}$	$40.671^{(1.42\%)}$	$21.230^{(0.38\%)}$	$56.717^{(2.68\%)}$	$23.220^{(0.47\%)}$	$65.729^{(3.58\%)}$	4410
10	2 L9 + 4x2 H27	$18.674^{(1.24\%)}$	$40.509^{(1.81\%)}$	$21.235^{(0.35\%)}$	$56.579^{(2.92\%)}$	$23.230^{(0.52\%)}$	$65.634^{(3.72\%)}$	4815
	2 L9 + 6x2 H27	$18.665^{(1.29\%)}$	$40.599^{(1.60\%)}$	$21.230^{(0.38\%)}$	$56.654^{(2.79\%)}$	$23.227^{(0.51\%)}$	$65.693^{(3.63\%)}$	5175
	3 L9 + 4x3 H27	$18.672^{(1.25\%)}$	$40.581^{(1.64\%)}$	$21.237^{(0.34\%)}$	$56.643^{(2.81\%)}$	$23.235^{(0.54\%)}$	$65.684^{(3.64\%)}$	6741
	3 L9 + 6x3 H27	$18.663^{(1.3\%)}$	$40.670^{(1.42\%)}$	$21.231^{(0.37\%)}$	$56.718^{(2.68\%)}$	$23.233^{(0.53\%)}$	$65.743^{(3.56\%)}$	7245
ABQ	1140 C3D20R	18.909	41.257	21.310	58.278	23.111	68.167	21249

Table C.6: Doubly-curved beam subjected to uniform loads, shear pressure case: horizontal u_z and vertical u_y displacements components [mm]. Comparison between variable-kinematics discretization model and ABAQUS 3D reference solutions for different load conditions.

Figures C.10–C.11 illustrate the equilibrium curves of the frame under normal traction pressure, reporting separately the horizontal and vertical displacement components at point "A." The corresponding results for the shear traction pressure applied at the free end are shown in Figs. C.12–C.13. Stress distributions are reported in Figs. C.14–C.15, in which the contour plots of the normal and transverse stress components σ_{yy} and σ_{yz} under a normal pressure of $p = 900$ MPa are depicted Results are compared between the 10B4–3L9 + 6×3 H27 discretization and the ABAQUS 3D solution. A similar comparison is shown in Figs. C.16–C.17, where the normal σ_{yy} and σ_{zz} stress components are evaluated for the shear pressure case ($p = 500$ MPa), adopting the same discretization model. The convergence analysis for the traction pressure case shows that the vertical displacement component u_z is accurately predicted across all mathematical models. For the horizontal component u_y, moderate discrepancies (below 5%) appear and increase with the applied load. Comparable findings are observed in the shear pressure case: the displacement component orthogonal to the load direction is well predicted, while the transversal component exhibits reduced accuracy at higher pressures. In both load scenarios, the absolute percentage differences between the variable-kinematics results and the ABAQUS 3D solutions remain consistent across most discretizations. Even models with a limited number of beam-axis elements achieve good agreement, indicating that accuracy is not sensitive to the beam-axis discretization. Instead, the predictions depend strongly on the cross-section and corner discretizations (radial and tangential directions). Coarse discretizations provide a good balance between accuracy and efficiency: the 2B4–2L9 + 4×2 H27 model already yields reliable results with a 92% reduction in computational cost compared to the reference solution, while maintaining acceptable deviations from refined models. Stress contour plots confirm good agreement with the ABAQUS 3D reference, showing smooth distributions and consistent prediction of local stress concentrations at the curved corners. Minor discrepancies between the two approaches under traction and shear loading can be attributed to differences in the mathematical formulations and to local effects arising from the coupling of distinct structural theories in the corner regions. Finally, it is observed that the 3D solid model predicts a less stiff structural response than the variable-kinematics formulations, leading to larger displacements. This trend, also reported in previous works [204], can be linked to local stiffness variations at the interfaces, which represent critical zones of the structure, and to the different structural theories coupled within the corner regions.

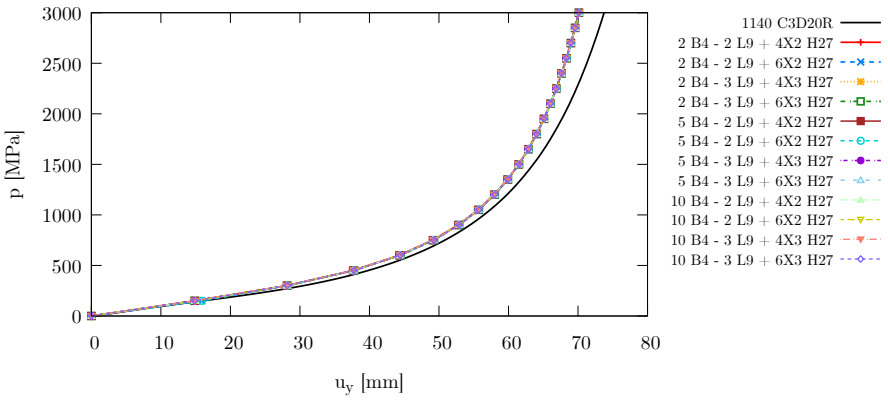

Figure C.10: Doubly-curved beam subjected to uniform loads, traction pressure case, $\mathbf{p} = (0, p_y, 0)$: equilibrium curve, horizontal displacement vs pressure applied.

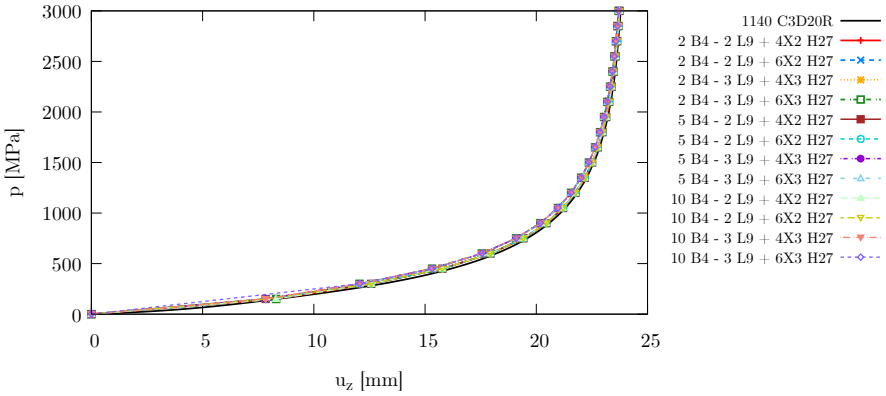

Figure C.11: Doubly-curved beam subjected to uniform loads, traction pressure case, $\mathbf{p} = (0, p_y, 0)$: equilibrium curves, vertical displacement vs pressure applied.

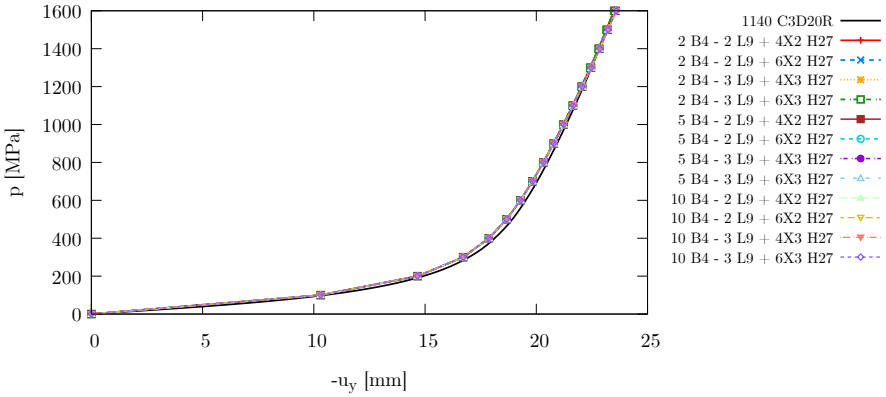

Figure C.12: Doubly-curved beam subjected to uniform loads, shear pressure case, $\mathbf{p} = (0, 0, -p_z)$: equilibrium curve, horizontal displacement vs pressure applied.

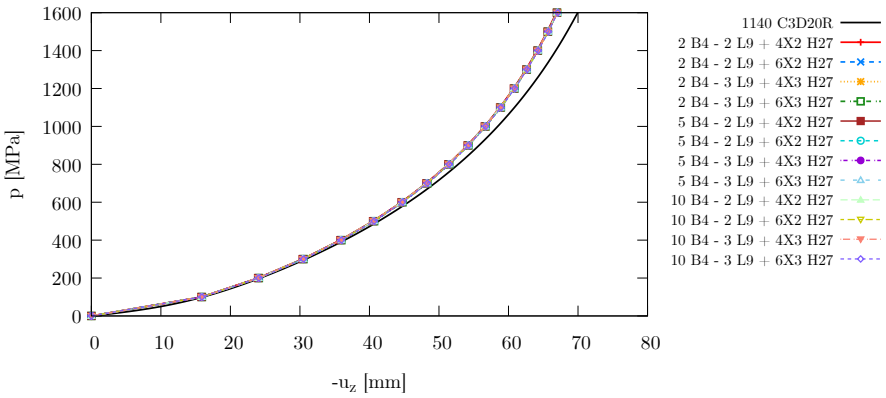

Figure C.13: Doubly-curved beam subjected to uniform loads, shear pressure case, $\mathbf{p} = (0, 0, -p_z)$: equilibrium curves, vertical displacement vs pressure applied.

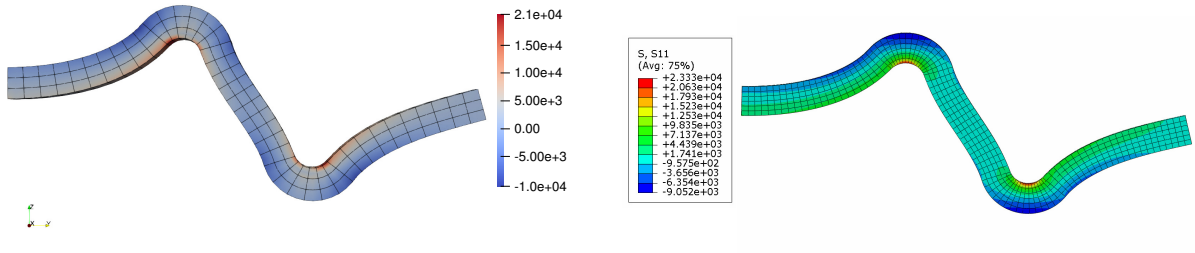

(a) Variable-kinematics **(b)** ABAQUS 3D

Figure C.14: Doubly-curved beam subjected to uniform loads, traction pressure case: contour plot of σ_{yy} stress component for $p = 900$ MPa, stress values in MPa. Comparison between variable-kinematic results and ABAQUS 3D solutions.

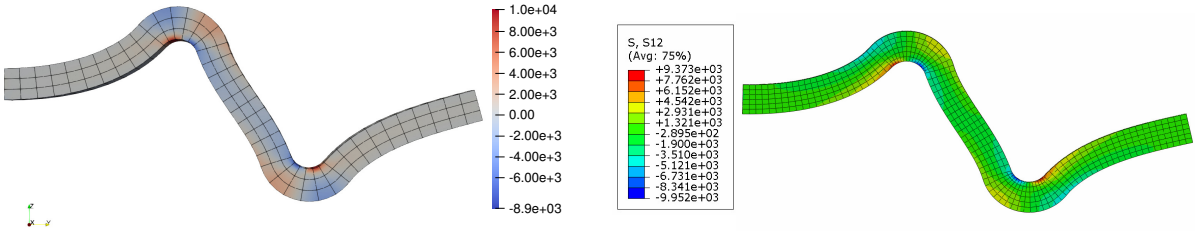

(a) Variable-kinematics **(b)** ABAQUS 3D

Figure C.15: Doubly-curved beam subjected to uniform loads, traction pressure case: contour plot of σ_{yz} stress component for $p = 900$ MPa, stress values in MPa. Comparison between variable-kinematic results and ABAQUS 3D solutions.

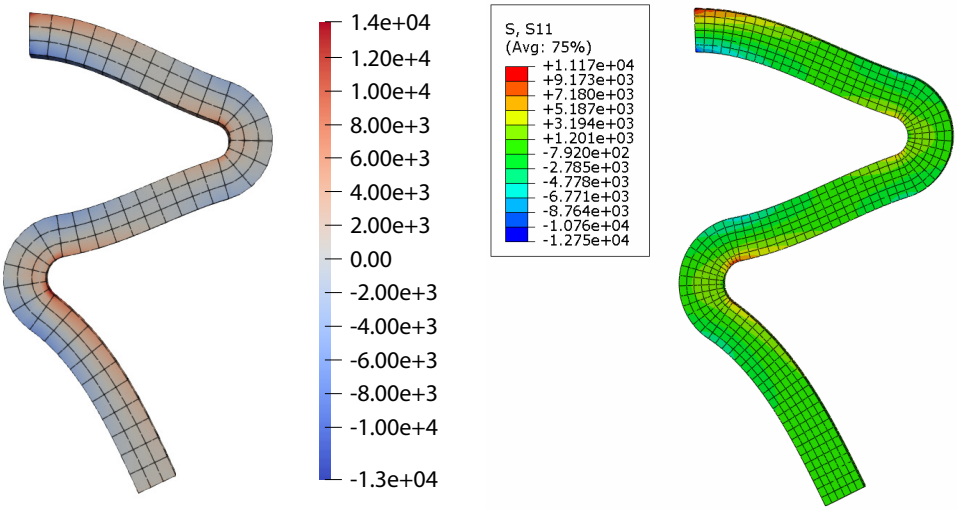

(a) Variable-kinematics **(b)** ABAQUS 3D

Figure C.16: Doubly-curved beam subjected to uniform loads, shear pressure case: contour plot of σ_{yy} stress component for $p = 500$ MPa, stress values in MPa. Comparison between variable-kinematic results and ABAQUS 3D solutions.

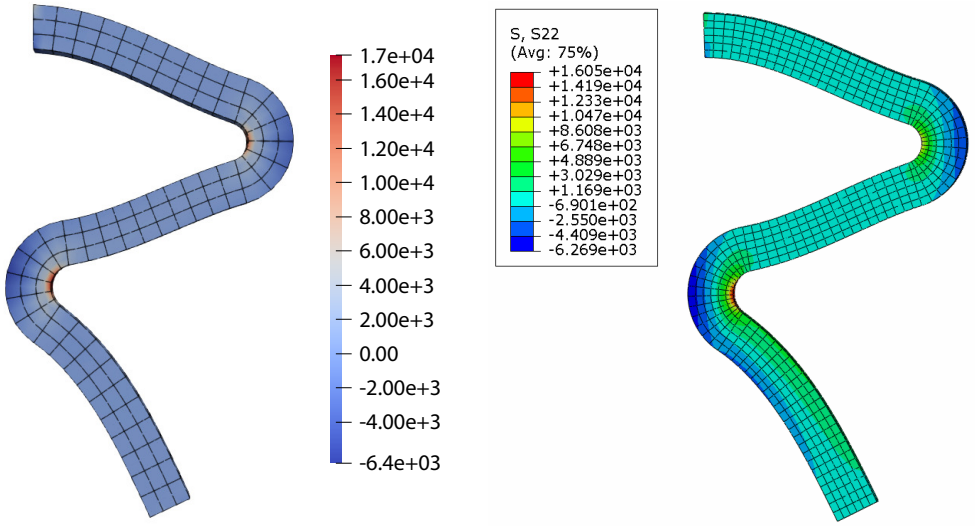

(a) Variable-kinematics **(b)** ABAQUS 3D

Figure C.17: Doubly-curved beam subjected to uniform loads, shear pressure case: contour plot of σ_{zz} stress component for $p = 500$ MPa, stress values in MPa. Comparison between variable-kinematic results and ABAQUS 3D solutions.

C.3.4 Pipe joint structure

The final case study in the geometrically nonlinear static analysis of complex structures, a representative and simplified pipe-like system connected through a central joint is analyzed under concentrated loads. This example highlights the capabilities of multi-dimensional finite element modeling, where classical hexahedral solid elements are used for the connecting regions and refined higher-order beam models are employed for the adjoining truss-like structures, exploring the capabilities of the present approach in thin-walled structural modeling. In the global symmetric frame, the joint connects two horizontal hollow beams with square cross-sections and two vertical hollow cylindrical beams with different internal and external radii. The geometry of the system and the boundary conditions adopted are illustrated in Fig. C.18, while the considered dimensions are reported in Table C.7. The frame is made of steel, with material properties defined by a Young modulus of $E = 210$ GPa and a Poisson's ratio of $\nu = 0.3$. For the 3D joint discretization, the red-colored region in Fig. C.18, only parabolic hexahedral H27 elements are employed. The horizontal square-section beams are modeled using refined beam elements, exploiting 20 parabolic L9 (nine-node) cross-section elements and five cubic B4 elements along the beam axis for each frame. The vertical cylindrical beams are modeled with 30 L9 elements across the circular cross-section and 10 cubic B4 elements along the axis. The discretization strategies

Sec. A		**Sec. B**		**Sec. C**		**Joint**	
l_{C1}	40 mm	l_{C2}	56 mm	l_Q	23 mm	h_J	24 mm
r_{ext}	13.2 mm	r_{ext}	8.2 mm	h_Q	12 mm	d	6 mm
r_{ext}	12 mm	r_{ext}	7 mm	t_Q	1.5 mm	w_J	17 mm

Table C.7: Pipe joint: dimensions of each sub-components.

adopted for the beams and the connecting region, enabled by LE models, are illustrated in Fig.

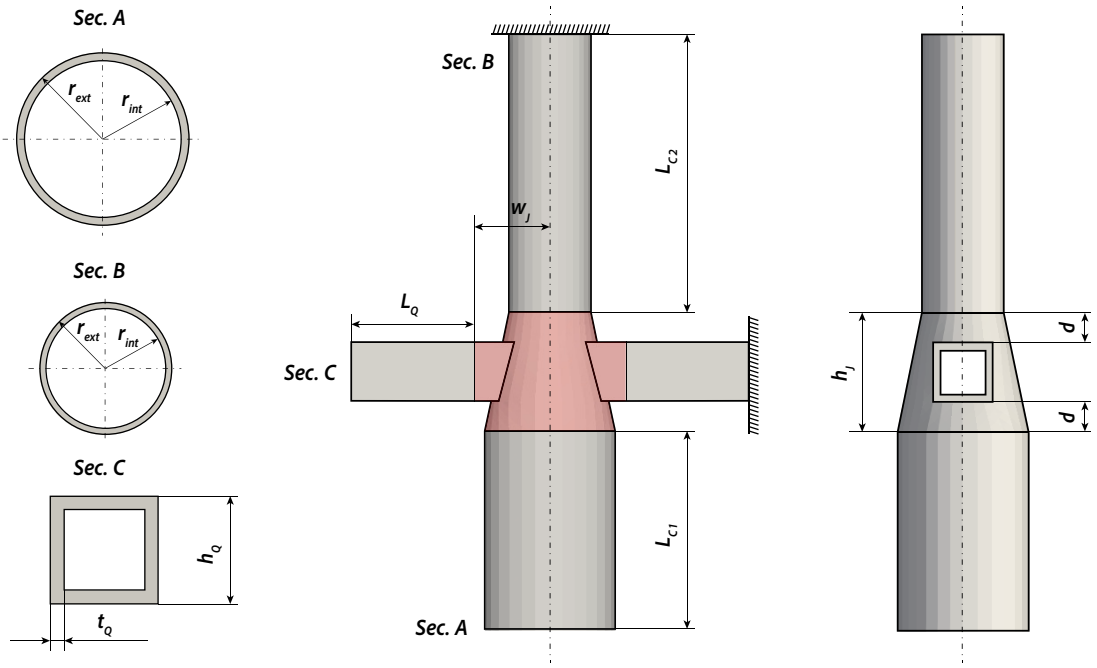

Figure C.18: Pipe joint: geometrical features and boundary conditions considered.

C.19. The applied loading conditions are shown in Fig. C.20: four concentrated forces F are applied at the free end of the cylindrical beam, while eight concentrated forces of magnitude $F/2$ are applied at the free end of the hollow square beam. The structural response is evaluated in terms of the displacement components of point "A," indicated in Fig. C.20, located at coordinates $(0, L_{C_1} + h_J + L_{C_2}, r_{ext_A})$. The equilibrium curves of the structure, describing the displacement of point "A" under incremental shear loads at the circular tip-free end, are reported in Fig. C.21. These curves highlight the differences between linear and nonlinear responses, with significant discrepancies emerging for shear loads greater than 6 kN. The corresponding displacement values at selected equilibrium points are provided in Table C.8, along with the computational cost expressed in terms of degrees of freedom (DOF). The structure exhibits an almost linear response in the moderate load range, while strongly nonlinear effects appear beyond this range. At higher loads, localized phenomena become evident, such as local buckling of the cylindrical clamped beam, occurring in the 9–10 kN range. Figure C.22(a) illustrates the deformed structure in two non-trivial equilibrium states, while Fig. C.23 shows the stress contour distribution in the joint region for the post-buckling configuration at $F = 10.14$ kN. The global equilibrium path indicates a highly nonlinear static response, with typical buckling behavior identified at the critical load of $F = 9.20$ kN, where small load variations lead to large displacement increments. In this regime, stress levels exceed the elastic limit, indicating that material nonlinearities should be accounted for. The proposed approach proves effective for capturing local effects such as stress concentrations and buckling, while maintaining computational efficiency. Compared with full 3D analyses, the computational cost is significantly reduced, requiring only about 60,000 DOF. The CUF-based FE formulation, being independent of kinematic assumptions and structural theory approximations, enables a seamless discretization of different beam cross-sections within a unified framework. By tailoring the cross-section expansion discretization to meet accuracy requirements and coupling constraints, the method provides an efficient and accurate tool for

advanced finite element modeling of complex structures.

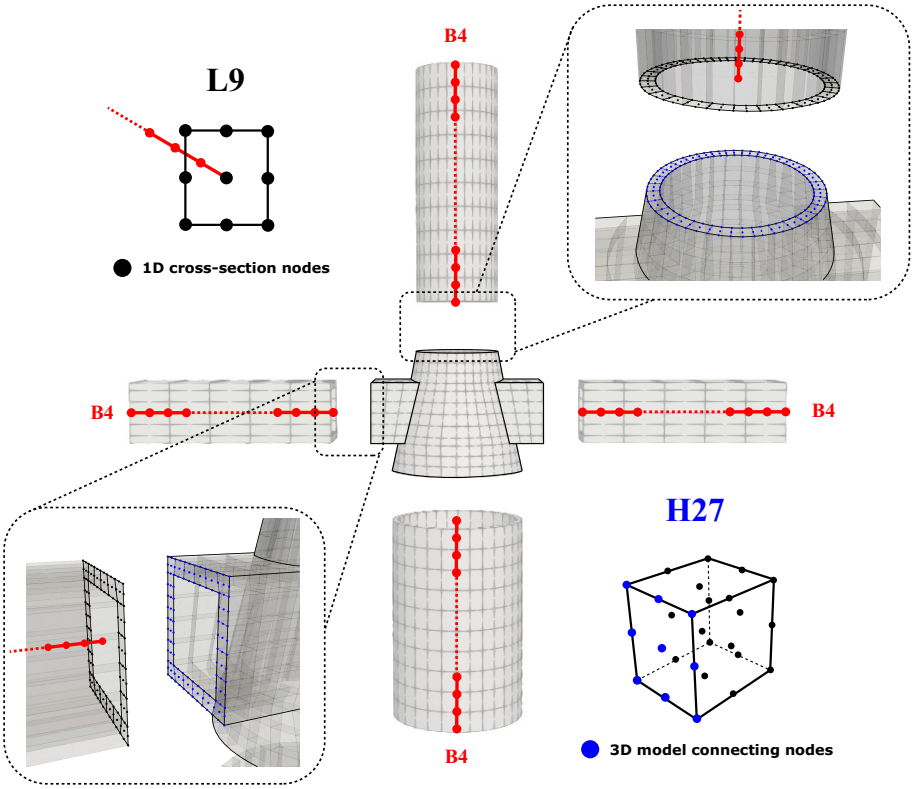

Figure C.19: Pipe joint: multi-dimensional discretization modeling adopted and variable-kinematics models assembling.

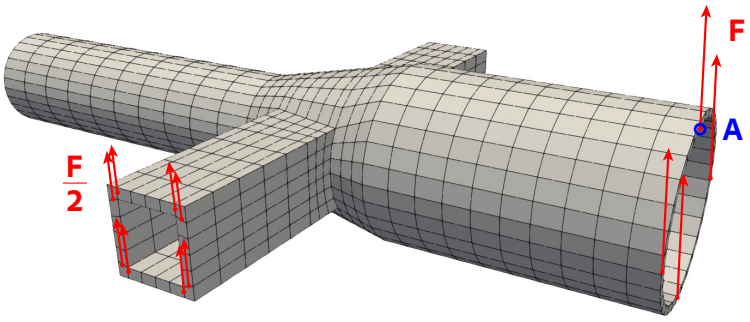

Figure C.20: Pipe joint: reference frame and load conditions.

Equilibrium conditions							
F [kN]	u_x [mm]	u_y [mm]	u_z [mm]	F [kN]	u_x [mm]	u_y [mm]	u_z [mm]
0.00	0.0000	0.0000	0.0000	5.61	-4.9101	3.1180	13.2871
0.05	-0.0312	0.0197	0.1351	9.20	-8.1083	5.6731	19.6508
0.16	-0.1002	0.0631	0.4284	10.14	-15.9897	10.6175	25.9269
0.40	-0.2558	0.1608	1.0631	10.58	-18.8694	12.6802	27.6567
0.91	-0.6191	0.3880	2.4284	10.16	-21.9841	14.9957	28.4426
1.76	-1.2831	0.8014	4.6121	10.46	-20.0800	13.5115	27.9940
3.17	-2.5373	1.5832	8.0492	10.53	-18.5592	12.4582	27.4918
DOF				60138			

Table C.8: Pipe joint: displacement components measured at the point "A" for different values conditions.

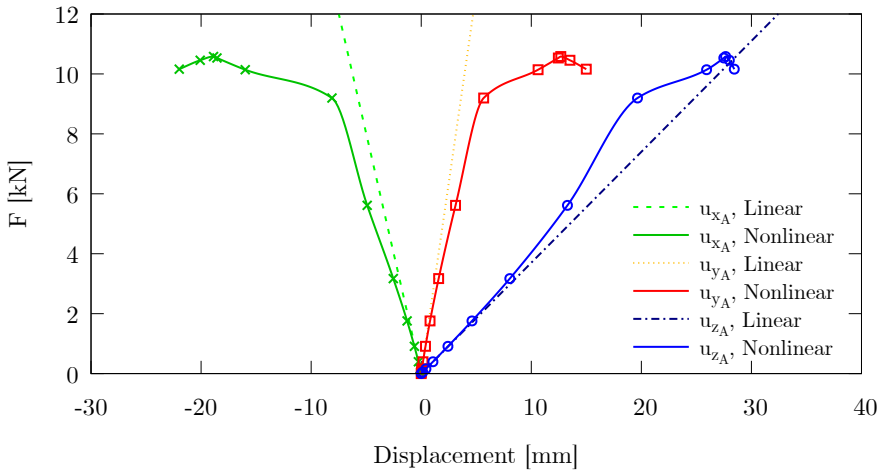

Figure C.21: Pipe joint: multi-dimensional discretization modelling adopted and variable-kinematics models assembling.

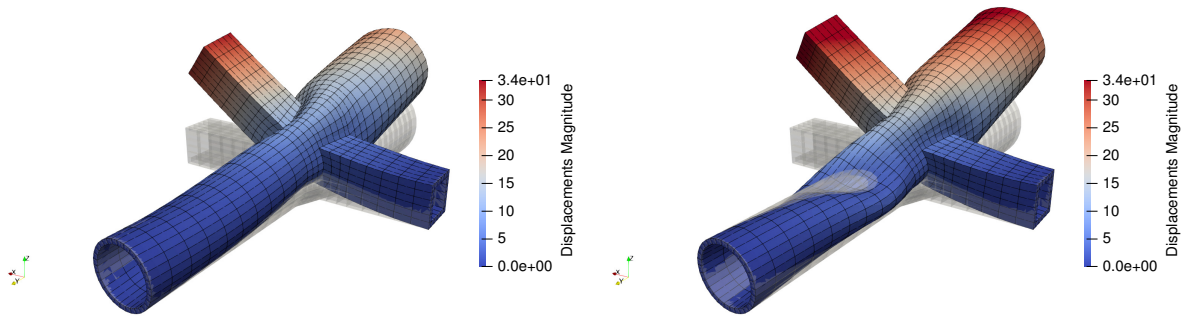

(a) $F = 9196.154$ N **(b)** $F = 10140.52$ N

Figure C.22: Pipe joint: deformed configurations for the local buckling representation, displacement in [mm].

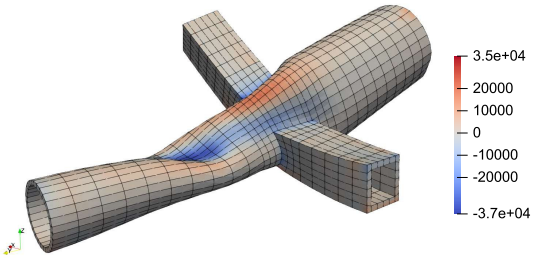

(a) σ_{xx}

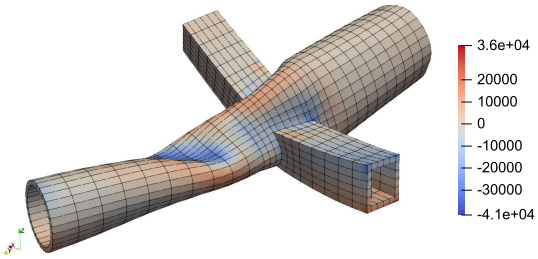

(b) σ_{yy}

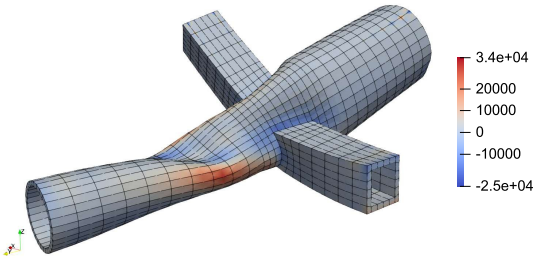

(c) σ_{zz}

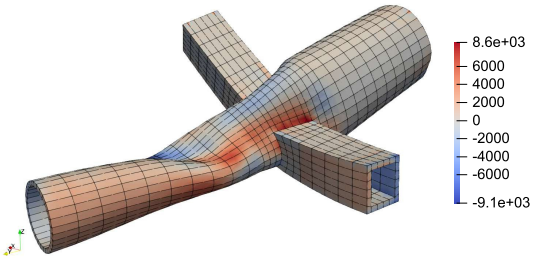

(d) σ_{yz}

Figure C.23: Pipe joint: plot contour of stress components for $F = 10.14$ kN, stress in [MPa].

Bibliography

[1] Ogden R. W. *Non-linear Elastic Deformations*. Chichester, E. Horwood, New York: Halsted Press, 1984, p. 532. ISBN: 0486696480.

[2] Sautter K.B., Meßmer M., Teschemacher T., and Bletzinger K.-U. "Limitations of the St. Venant–Kirchhoff material model in large strain regimes". In: *International Journal of Non-Linear Mechanics* 147 (Dec. 2022), p. 104207. ISSN: 0020-7462. DOI: 10.1016/j.ijnonlinmec.2022.104207.

[3] Treloar L.R.G. *The Physics of Rubber Elasticity*. Ed. by Oxford University Press. OUP Oxford, 2005.

[4] Gent A. N. "A New Constitutive Relation for Rubber". In: *Rubber Chemistry and Technology* 69.1 (Mar. 1996), pp. 59–61. ISSN: 0035-9475. DOI: 10.5254/1.3538357.

[5] Horgan C.O. and Saccomandi G. "Finite thermoelasticity with limiting chain extensibility". In: *Journal of the Mechanics and Physics of Solids* 51.6 (June 2003), pp. 1127–1146. ISSN: 0022-5096. DOI: 10.1016/s0022-5096(02)00144-8.

[6] Horgan C.O. and Saccomandi G. "Constitutive Models for Compressible Nonlinearly Elastic Materials with Limiting Chain Extensibility". In: *Journal of Elasticity* 77.2 (Nov. 2004), pp. 123–138. ISSN: 1573-2681. DOI: 10.1007/s10659-005-4408-x.

[7] Saccomandi G. "Nonlinear Elasticity for Soft Fibrous Materials". In: *Nonlinear Mechanics of Soft Fibrous Materials*. Springer Vienna, 2015, pp. 121–173. ISBN: 9783709118382. DOI: 10.1007/978-3-7091-1838-2_3.

[8] Horgan C.O. and Saccomandi G. "Simple Torsion of Isotropic, Hyperelastic, Incompressible Materials with Limiting Chain Extensibility". In: *Journal of Elasticity* 56.2 (Aug. 1999), pp. 159–170. ISSN: 1573-2681. DOI: 10.1023/a:1007606909163.

[9] Horgan C.O. and Saccomandi G. "Constitutive Modelling of Rubber-Like and Biological Materials with Limiting Chain Extensibility". In: *Mathematics and Mechanics of Solids* 7.4 (Aug. 2002), pp. 353–371. ISSN: 1741-3028. DOI: 10.1177/108128028477.

[10] Ghoreishy M.H.R., Naderkhamse M., Karrabi M., and Naderi G. "Finite element analysis of a rubber bearing base isolator under vertical and horizontal loads using a nonlinear hyper-viscoelastic material model". In: *Polymer Testing* 137 (Aug. 2024), p. 108522. ISSN: 0142-9418. DOI: 10.1016/j.polymertesting.2024.108522.

[11] Wang Y., Xue H., Chen H., and Qiang J. "A dynamic visco-hyperelastic model of dielectric elastomers and their energy dissipation characteristics". In: *Applied Physics A* 112.2 (May 2013), pp. 339–347. ISSN: 1432-0630. DOI: 10.1007/s00339-013-7740-1.

[12] Hariharaputhiran H. and Saravanan U. "A new set of biaxial and uniaxial experiments on vulcanized rubber and attempts at modeling it using classical hyperelastic models". In: *Mechanics of Materials* 92 (Jan. 2016), pp. 211–222. ISSN: 0167-6636. DOI: 10.1016/j.mechmat.2015.09.003.

[13] Cheon K.M., Akpudo U.E., Kareem A.B.and Nwabufo O.C., Jeon H.R., and Hur J.W. "An FEA-Assisted Decision-Making Framework for PEMFC Gasket Material Selection". In: *Energies* 15.7 (Apr. 2022), p. 2580. ISSN: 1996-1073. DOI: 10.3390/en15072580.

[14] Somanath S., Marimuthu R., and Krishnapillai Shankar. "Frequency domain analysis of pre-stressed elastomeric vibration isolators". In: *Defence Technology* 25 (July 2023), pp. 33–47. ISSN: 2214-9147. DOI: 10.1016/j.dt.2022.10.004.

[15] Silber G., Alizadeh M., and Salimi M. "Large Deformation Analysis for Soft Foams Based on Hyperelasticity". In: *Journal of Mechanics* 26.3 (Sept. 2010), pp. 327–334. ISSN: 1811-8216. DOI: 10.1017/s1727719100003889.

[16] Gariya N., Kumar P., and Prasad B. "Stress and bending analysis of a soft pneumatic actuator considering different hyperelastic materials". In: *Materials Today: Proceedings* 65 (2022), pp. 3126–3131. ISSN: 2214-7853. DOI: 10.1016/j.matpr.2022.05.352.

[17] Shintake J., Cacucciolo V., Floreano D., and Shea H. "Soft Robotic Grippers". In: *Advanced Materials* 30.29 (May 2018). ISSN: 1521-4095. DOI: 10.1002/adma.201707035.

[18] Cacucciolo V., Renda F., Poccia E., Laschi C., and Cianchetti M. "Modelling the nonlinear response of fibre-reinforced bending fluidic actuators". In: *Smart Materials and Structures* 25.10 (Sept. 2016), p. 105020. ISSN: 1361-665X. DOI: 10.1088/0964-1726/25/10/105020.

[19] Holzapfel G.A., Humphrey J.D., and Ogden R.W. "Biomechanics of soft biological tissues and organs, mechanobiology, homeostasis and modelling". In: *Journal of The Royal Society Interface* 22.222 (Jan. 2025). ISSN: 1742-5662. DOI: 10.1098/rsif.2024.0361.

[20] Arnold N., Scott J., and Bush T.R. "A review of the characterizations of soft tissues used in human body modeling: Scope, limitations, and the path forward". In: *Journal of Tissue Viability* 32.2 (May 2023), pp. 286–304. ISSN: 0965-206X. DOI: 10.1016/j.jtv.2023.02.003.

[21] Upadhyay K., Fuhg J.N., Bouklas N., and Ramesh K.T. "Physics-informed data-driven discovery of constitutive models with application to strain-rate-sensitive soft materials". In: *Computational Mechanics* (June 2024). ISSN: 1432-0924. DOI: 10.1007/s00466-024-02497-x.

[22] Holzapfel G.A. and Weizsäcker H.W. "Biomechanical behavior of the arterial wall and its numerical characterization". In: *Computers in Biology and Medicine* 28.4 (July 1998), pp. 377–392. ISSN: 0010-4825. DOI: 10.1016/s0010-4825(98)00022-5.

[23] Holzapfel G.A. and Ogden R.W. "Constitutive modelling of passive myocardium: a structurally based framework for material characterization". In: *Philosophical Transactions of the Royal Society A: Mathematical, Physical and Engineering Sciences* 367.1902 (Sept. 2009), pp. 3445–3475. ISSN: 1471-2962. DOI: 10.1098/rsta.2009.0091.

[24] Chen S., Ní A.A., and Roccabianca S. "A microstructurally inspired constitutive model for skin mechanics". In: *Biomechanics and Modeling in Mechanobiology* 19.1 (Aug. 2019), pp. 275–289. ISSN: 1617-7940. DOI: 10.1007/s10237-019-01210-9.

[25] Alberini R., Terzano M., Holzapfel G.A., and Spagnoli A. "A discrete fiber dispersion model with octahedral symmetry quadrature for mechanical analyses of skin corrective surgeries". In: *Computer Methods in Applied Mechanics and Engineering* 438 (Apr. 2025), p. 117809. ISSN: 0045-7825. DOI: 10.1016/j.cma.2025.117809.

[26] Gasser T.C., Ogden R.W., and Holzapfel G.A. "Hyperelastic modelling of arterial layers with distributed collagen fibre orientations". In: *Journal of The Royal Society Interface* 3.6 (Sept. 2005), pp. 15–35. ISSN: 1742-5662. DOI: 10.1098/rsif.2005.0073.

[27] Tornifoglio B., Hughes C., Digeronimo F., Guendouz Y., Johnston R.D., and Lally C. "Imaging the microstructure of the arterial wall – ex vivo to in vivo potential". In: *Acta Biomaterialia* 199 (June 2025), pp. 18–34. ISSN: 1742-7061. DOI: 10.1016/j.actbio.2025.05.022.

[28] Holzapfel G.A. and Ogden R.W. "Constitutive modelling of arteries". In: *Proceedings of the Royal Society A: Mathematical, Physical and Engineering Sciences* 466.2118 (Mar. 2010), pp. 1551–1597. ISSN: 1471-2946. DOI: 10.1098/rspa.2010.0058.

[29] David T. and Brown R.G. In: *Transport in Biological Media*. Elsevier, 2013. Chap. Models of Cerebrovascular Perfusion. ISBN: 9780124158245. DOI: 10.1016/b978-0-12-415824-5.00007-2.

[30] Gadala M.S. and Oravas G.AE. "Numerical solutions of nonlinear problems of continua—I". In: *Computers & Structures* 19.5–6 (Jan. 1984), pp. 865–877. ISSN: 0045-7949. DOI: 10.1016/0045-7949(84)90187-1.

[31] Gadala Mohamed S. "Numerical solutions of nonlinear problems of continua—II. Survey of incompressibility constraints and software aspects". In: *Computers & Structures* 22.5 (Jan. 1986), pp. 841–855. ISSN: 0045-7949. DOI: 10.1016/0045-7949(86)90273-7.

[32] Bacciocchi M. and Tarantino A.M. "Finite torsion of transversely isotropic compressible hyperelastic circular cylinders". In: *International Journal of Mechanical Sciences* 303 (Oct. 2025), p. 110582. ISSN: 0020-7403. DOI: 10.1016/j.ijmecsci.2025.110582.

[33] Mantegazza A., De Marinis D., and De Tullio M.D. "Red blood cell transport in bounded shear flow: On the effects of cell viscoelastic properties". In: *Computer Methods in Applied Mechanics and Engineering* 428 (Aug. 2024), p. 117088. ISSN: 0045-7825. DOI: 10.1016/j.cma.2024.117088.

[34] Mirjavadi S.S., Forsat M., and Badnava S. "Nonlinear modeling and dynamic analysis of bioengineering hyper-elastic tubes based on different material models". In: *Biomechanics and Modeling in Mechanobiology* 19.3 (Dec. 2019), pp. 971–983. ISSN: 1617-7940. DOI: 10.1007/s10237-019-01265-8.

[35] Russ J., Slesarenko V., Rudykh S., and Waisman H. "Rupture of 3D-printed hyperelastic composites: Experiments and phase field fracture modeling". In: *Journal of the Mechanics and Physics of Solids* 140 (July 2020), p. 103941. ISSN: 0022-5096. DOI: 10.1016/j.jmps.2020.103941.

[36] Damanpack A.R., Bodaghi M., and Liao W.H. "Experimentally validated multi-scale modeling of 3D printed hyper-elastic lattices". In: *International Journal of Non-Linear Mechanics* 108 (Jan. 2019), pp. 87–110. ISSN: 0020-7462. DOI: 10.1016/j.ijnonlinmec.2018.10.008.

[37] Hyre M. R. and Pulliam R. M. "Balloon/Stent Expansion Dynamics in Stenotic Arteries". In: *Volume 2: Biomedical and Biotechnology Engineering*. IMECE2008. ASMEDC, Jan. 2008, pp. 565–573. DOI: 10.1115/imece2008-68060.

[38] Alfano F., Navas P., Lamata P., García K.F., Ortuño J.E., Zamora O.B., Lizarraga S., Santos A., Pascau J., Goicolea J.M., and Ledesma-Carbayo M.J. "Patient-specific visco-hyperelastic mechanical model for breast tumor localization in surgical planning". In: *Bioengineering & Translational Medicine* (July 2025). ISSN: 2380-6761. DOI: 10.1002/btm2.70044.

[39] Bathe K.-J. *Finite Element Procedures*. Prentice Hall, 1996, p. 1037. ISBN: 0133014584.

[40] Crisfield M. A., Moita G. F., Lyons L. P. R., and Jelenić G. "Enhanced lower-order element formulations for large strains". In: *Computational Mechanics* 17.1–2 (Dec. 1995), pp. 62–73. ISSN: 1432-0924. DOI: 10.1007/bf00356479.

[41] Chamberland É., Fortin A., and Fortin M. "Comparison of the performance of some finite element discretizations for large deformation elasticity problems". In: *Computers & Structures* 88.11–12 (June 2010), pp. 664–673. ISSN: 0045-7949. DOI: 10.1016/j.compstruc.2010.02.007.

[42] Hadjicharalambous M., Lee J., Smith N.P., and Nordsletten D.A. "A displacement-based finite element formulation for incompressible and nearly-incompressible cardiac mechanics". In: *Computer Methods in Applied Mechanics and Engineering* 274 (June 2014), pp. 213–236. ISSN: 0045-7825. DOI: 10.1016/j.cma.2014.02.009.

[43] Key S.W. "A variational principle for incompressible and nearly-incompressible anisotropic elasticity". In: *International Journal of Solids and Structures* 5.9 (Sept. 1969), pp. 951–964. ISSN: 0020-7683. DOI: 10.1016/0020-7683(69)90081-x.

[44] Kevin M.M., Behrooz F., and J. Patrick M. "Novel hyperelastic models for large volumetric deformations". In: *International Journal of Solids and Structures* 193-194 (June 2020), pp. 474–491. DOI: 10.1016/j.ijsolstr.2020.01.019.

[45] Van Huyssteen D. and Reddy B.D. "A virtual element method for transversely isotropic hyperelasticity". In: *Computer Methods in Applied Mechanics and Engineering* 386 (Dec. 2021), p. 114108. ISSN: 0045-7825. DOI: 10.1016/j.cma.2021.114108.

[46] Bombarde D.S., Silla L.N., Gautam S.S., and Nandy A. "A Comprehensive Comparative Review of Various Advanced Finite Elements to Alleviate Shear, Membrane and Volumetric Locking". In: *Archives of Computational Methods in Engineering* 31.4 (Mar. 2024), pp. 1979–2013. ISSN: 1886-1784. DOI: 10.1007/s11831-023-10050-x.

[47] Herrmann L.R. "Elasticity equations for incompressible and nearly incompressible materials by a variational theorem." In: *AIAA Journal* 3.10 (Oct. 1965), pp. 1896–1900. ISSN: 1533-385X. DOI: 10.2514/3.3277.

[48] Sussman T. and K.J. Bathe. "A finite element formulation for nonlinear incompressible elastic and inelastic analysis". In: *Computers & Structures* 26.1–2 (Jan. 1987), pp. 357–409. ISSN: 0045-7949. DOI: 10.1016/0045-7949(87)90265-3.

[49] Brink U. and Stein E. "On some mixed finite element methods for incompressible and nearly incompressible finite elasticity". In: *Computational Mechanics* 19.1 (Nov. 1996), pp. 105–119. ISSN: 1432-0924. DOI: 10.1007/bf02824849.

[50] Xiang S., Du Z., Shi H., Yan Z., Sun Y., Wang J., and Liu Z. "A fiber-reinforced mesoscale constitutive model of tympanic membrane considering anisotropic deformation". In: *Acta Mechanica Sinica* 40.5 (Apr. 2024). ISSN: 1614-3116. DOI: 10.1007/s10409-024-23590-x.

[51] Winnicki K., Ochala-Klos A., Rutowicz B., Pekala P.A., and Tomaszewski K.A. "Functional anatomy, histology and biomechanics of the human Achilles tendon — A comprehensive review". In: *Annals of Anatomy - Anatomischer Anzeiger* 229 (May 2020), p. 151461. ISSN: 0940-9602. DOI: 10.1016/j.aanat.2020.151461.

[52] Stenfeldt K., Johansson C., and Hellström S. "The Collagen Structure of the Tympanic Membrane: Collagen Types I, II, and III in the Healthy Tympanic Membrane, During Healing of a Perforation, and During Infection". In: *Archives of Otolaryngology–Head & Neck Surgery* 132.3 (Mar. 2006), p. 293. ISSN: 0886-4470. DOI: 10.1001/archotol.132.3.293.

[53] Fung Y.C., Fronek K., and Patitucci P. "Pseudoelasticity of arteries and the choice of its mathematical expression". In: *American Journal of Physiology-Heart and Circulatory Physiology* 237.5 (Nov. 1979), H620–H631. ISSN: 1522-1539. DOI: 10.1152/ajpheart.1979.237.5.h620.

[54] Holzapfel G.A. and Gasser T.C. "A viscoelastic model for fiber-reinforced composites at finite strains: Continuum basis, computational aspects and applications". In: *Computer Methods in Applied Mechanics and Engineering* 190.34 (May 2001), pp. 4379–4403. ISSN: 0045-7825. DOI: 10.1016/s0045-7825(00)00323-6.

[55] Wang C., Garcia M., Lu X., Lanir Y., and Kassab G.S. "Three-dimensional mechanical properties of porcine coronary arteries: a validated two-layer model". In: *American Journal of Physiology-Heart and Circulatory Physiology* 291.3 (Sept. 2006), H1200–H1209. ISSN: 1522-1539. DOI: 10.1152/ajpheart.01323.2005.

[56] Weiss J.A. and Gardiner J.C. "Computational Modeling of Ligament Mechanics". In: *Critical Reviews in Biomedical Engineering* 29.3 (2001), pp. 303–371. ISSN: 0278-940X. DOI: 10.1615/critrevbiomedeng.v29.i3.20.

[57] Shearer T. "A new strain energy function for the hyperelastic modelling of ligaments and tendons based on fascicle microstructure". In: *Journal of Biomechanics* 48.2 (Jan. 2015), pp. 290–297. ISSN: 0021-9290. DOI: 10.1016/j.jbiomech.2014.11.031.

[58] Shearer T. "A new strain energy function for modelling ligaments and tendons whose fascicles have a helical arrangement of fibrils". In: *Journal of Biomechanics* 48.12 (Sept. 2015), pp. 3017–3025. ISSN: 0021-9290. DOI: 10.1016/j.jbiomech.2015.07.032.

[59] Kastelic J., Galeski A., and Baer E. "The Multicomposite Structure of Tendon". In: *Connective Tissue Research* 6.1 (Jan. 1978), pp. 11–23. ISSN: 1607-8438. DOI: 10.3109/03008207809152283.

[60] Grytz R. and Meschke G. "Constitutive modeling of crimped collagen fibrils in soft tissues". In: *Journal of the Mechanical Behavior of Biomedical Materials* 2.5 (Oct. 2009), pp. 522–533. ISSN: 1751-6161. DOI: 10.1016/j.jmbbm.2008.12.009.

[61] Stender C.J., Rust E., Martin P.T., Neumann E.E., R.J. Brown, and Lujan T.J. "Modeling the effect of collagen fibril alignment on ligament mechanical behavior". In: *Biomechanics and Modeling in Mechanobiology* 17.2 (Nov. 2017), pp. 543–557. ISSN: 1617-7940. DOI: 10.1007/s10237-017-0977-4.

[62] Chuong C. J. and Fung Y. C. "Three-Dimensional Stress Distribution in Arteries". In: *Journal of Biomechanical Engineering* 105.3 (Aug. 1983), pp. 268–274. ISSN: 1528-8951. DOI: 10.1115/1.3138417.

[63] Holzapfel G.A. *Nonlinear Solid Mechanics. A Continuum Approach for Engineering*. John Wiley & Sons, Chichester, West Sussex, UK, 2000, p. 455. ISBN: 9780471823193.

[64] Holzapfel G.A., Gasser T.C., and Ogden R.W. "Comparison of a Multi-Layer Structural Model for Arterial Walls With a Fung-Type Model, and Issues of Material Stability". In: *Journal of Biomechanical Engineering* 126.2 (Apr. 2004), pp. 264–275. ISSN: 1528-8951. DOI: 10.1115/1.1695572.

[65] Holzapfel G.A., Sommer G., Gasser T.C., and Regitnig P. "Determination of layer-specific mechanical properties of human coronary arteries with nonatherosclerotic intimal thickening and related constitutive modeling". In: *American Journal of Physiology-Heart and Circulatory Physiology* 289.5 (Nov. 2005), H2048–H2058. ISSN: 1522-1539. DOI: 10.1152/ajpheart.00934.2004.

[66] Holzapfel G.A., Gasser T.C., and Ogden R.W. "A New Constitutive Framework for Arterial Wall Mechanics and a Comparative Study of Material Models". In: *Journal of Elasticity* 61.1/3 (2000), pp. 1–48. DOI: 10.1023/a:1010835316564.

[67] Carpenter H.J., Gholipour A., Ghayesh M.H., Zander A.C., and Psaltis P.J. "A review on the biomechanics of coronary arteries". In: *International Journal of Engineering Science* 147 (Feb. 2020), p. 103201. ISSN: 0020-7225. DOI: 10.1016/j.ijengsci.2019.103201.

[68] Merodio J. and Ogden R.W. "Mechanical response of fiber-reinforced incompressible nonlinearly elastic solids". In: *International Journal of Non-Linear Mechanics* 40.2–3 (Mar. 2005), pp. 213–227. ISSN: 0020-7462. DOI: 10.1016/j.ijnonlinmec.2004.05.003.

[69] Peng X. Q., Guo Z. Y., and Moran B. "An Anisotropic Hyperelastic Constitutive Model With Fiber-Matrix Shear Interaction for the Human Annulus Fibrosus". In: *Journal of Applied Mechanics* 73.5 (May 2005), pp. 815–824. ISSN: 1528-9036. DOI: 10.1115/1.2069987.

[70] Pandolfi A. and Vasta M. "Fiber distributed hyperelastic modeling of biological tissues". In: *Mechanics of Materials* 44 (Jan. 2012), pp. 151–162. ISSN: 0167-6636. DOI: 10.1016/j.mechmat.2011.06.004.

[71] Freed A.D, Einstein D.R., and Vesely I. "Invariant formulation for dispersed transverse isotropy in aortic heart valves". In: *Biomechanics and Modeling in Mechanobiology* 4.2-3 (Aug. 2005), pp. 100–117. DOI: 10.1007/s10237-005-0069-8.

[72] Mansouri M.R., Beter J., Fuchs P.F., Schrittesser B., and Pinter G. "Quantifying matrix-fiber mechanical interactions in hyperelastic materials". In: *International Journal of Mechanical Sciences* 195 (Apr. 2021), p. 106268. ISSN: 0020-7403. DOI: 10.1016/j.ijmecsci.2021.106268.

[73] Nolan D.R., Gower A.L., Destrade M., Ogden R.W., and McGarry J.P. "A robust anisotropic hyperelastic formulation for the modelling of soft tissue". In: *Journal of the Mechanical Behavior of Biomedical Materials* 39 (Nov. 2014), pp. 48–60. ISSN: 1751-6161. DOI: 10.1016/j.jmbbm.2014.06.016.

[74] Wex C., Arndt S., Stoll A., Bruns C., and Kupriyanova Y. "Isotropic incompressible hyperelastic models for modelling the mechanical behaviour of biological tissues: a review". In: *Biomedical Engineering / Biomedizinische Technik* 60.6 (Jan. 2015). ISSN: 0013-5585. DOI: 10.1515/bmt-2014-0146.

[75] Humphrey J.D. *Cardiovascular Solid Mechanics: Cells, Tissues, and Organs*. Springer New York, 2002. ISBN: 9780387215761. DOI: 10.1007/978-0-387-21576-1.

[76] Federico S. and Gasser T.C. "Nonlinear elasticity of biological tissues with statistical fibre orientation". In: *Journal of The Royal Society Interface* 7.47 (Jan. 2010), pp. 955–966. ISSN: 1742-5662. DOI: 10.1098/rsif.2009.0502.

[77] Melnik A.V., Borja Da Rocha H., and Goriely A. "On the modeling of fiber dispersion in fiber-reinforced elastic materials". In: *International Journal of Non-Linear Mechanics* 75 (Oct. 2015), pp. 92–106. ISSN: 0020-7462. DOI: 10.1016/j.ijnonlinmec.2014.10.006.

[78] Li K., Ogden R.W., and Holzapfel G.A. "A discrete fibre dispersion method for excluding fibres under compression in the modelling of fibrous tissues". In: *Journal of The Royal Society Interface* 15.138 (Jan. 2018), p. 20170766. ISSN: 1742-5662. DOI: 10.1098/rsif.2017.0766.

[79] Fliege J. "The distribution of points on the sphere and corresponding cubature formulae". In: *IMA Journal of Numerical Analysis* 19.2 (Apr. 1999), pp. 317–334. ISSN: 1464-3642. DOI: 10.1093/imanum/19.2.317.

[80] Benítez J.M. and Montáns F.J. "The mechanical behavior of skin: Structures and models for the finite element analysis". In: *Computers & Structures* 190 (Oct. 2017), pp. 75–107. ISSN: 0045-7949. DOI: 10.1016/j.compstruc.2017.05.003.

[81] Li K., Ogden R.W., and Holzapfel G.A. "Computational method for excluding fibers under compression in modeling soft fibrous solids". In: *European Journal of Mechanics - A/Solids* 57 (May 2016), pp. 178–193. ISSN: 0997-7538. DOI: 10.1016/j.euromechsol.2015.11.003.

[82] Holzapfel G.A. and Ogden R.W. "On the tension–compression switch in soft fibrous solids". In: *European Journal of Mechanics - A/Solids* 49 (Jan. 2015), pp. 561–569. ISSN: 0997-7538. DOI: 10.1016/j.euromechsol.2014.09.005.

[83] Vergori L., Destrade M., McGarry P., and Ogden R.W. "On anisotropic elasticity and questions concerning its Finite Element implementation". In: *Computational Mechanics* 52.5 (May 2013), pp. 1185–1197. ISSN: 1432-0924. DOI: 10.1007/s00466-013-0871-6.

[84] Federico S., Grillo A., Imatani S., Giaquinta G., and Herzog W. "An energetic approach to the analysis of anisotropic hyperelastic materials". In: *International Journal of Engineering Science* 46.2 (Feb. 2008), pp. 164–181. ISSN: 0020-7225. DOI: 10.1016/j.ijengsci.2007.09.005.

[85] Euler L. "De curvis elasticis". In: (Geneva, 1774).

[86] Timoshenko S.P. "On the corrections for shear of the differential equation for transverse vibration of prismatic bars". In: *Philosophical Magazine* 41 (1922), pp. 744–746.

[87] Love A.E.H. "The small free vibrations and deformation of a thin elastic shell". In: *Philosophical Transactions of the Royal Society of London A* 179 (1888), pp. 491–546.

[88] Reissner E. "The effect of transverse shear deformation on the bending of elastic plates". In: *ASME Journal of Applied Mechanics* 12 (1945), pp. 68–77.

[89] Mindlin R.D. "Influence of rotatory inertia and shear on flexural motions of isotropic elastic plates". In: *ASME Journal of Applied Mechanics* 18 (1951), pp. 31–38.

[90] Zhen W., Jie M., Shengbo L., and Xiaohui. R. "Five-variable higher-order model for accurate analysis and design of laminated plates". In: *Acta Mechanica* 235.5 (Feb. 2024, DOI: 10.1007/s00707-024-03875-5), pp. 3073–3093. ISSN: 1619-6937. DOI: 10.1007/s00707-024-03875-5.

[91] Oden J.T. and Key J.E. "On the effect of the form of the strain energy function on the solution of a boundary-value problem in finite elasticity". In: *Computers & Structures* 2.4 (Sept. 1972), pp. 585–592. ISSN: 0045-7949. DOI: 10.1016/0045-7949(72)90010-7.

[92] Duffett G. and Reddy B.D. "The analysis of incompressible hyperelastic bodies by the finite element method". In: *Computer Methods in Applied Mechanics and Engineering* 41.1 (Nov. 1983), pp. 105–120. ISSN: 0045-7825. DOI: 10.1016/0045-7825(83)90055-5.

[93] Gruttmann F. and Taylor R. L. "Theory and finite element formulation of rubberlike membrane shells using principal stretches". In: *International Journal for Numerical Methods in Engineering* 35.5 (Sept. 1992), pp. 1111–1126. ISSN: 1097-0207. DOI: 10.1002/nme.1620350511.

[94] Ahmadi M., McBride A., Steinmann P., and Saxena P. "Plane stress finite element modelling of arbitrary compressible hyperelastic materials". In: *Acta Mechanica* 236.7 (May 2025), pp. 3975–3994. ISSN: 1619-6937. DOI: 10.1007/s00707-025-04310-z.

[95] Mansilla A.L.A., Ares G.D., Feijóo R.A., and Blanco P.J. "A mixed-order interpolation solid element for efficient arterial wall simulations". In: *Computational Mechanics* 73.1 (June 2023), pp. 67–87. ISSN: 1432-0924. DOI: 10.1007/s00466-023-02356-1.

[96] Ansari R., Hassani R., Faraji Oskouie M., and Rouhi H. "Large deformation analysis in the context of 3D compressible nonlinear elasticity using the VDQ method". In: *Engineering with Computers* 37.4 (Mar. 2020), pp. 3251–3263. ISSN: 1435-5663. DOI: 10.1007/s00366-020-00959-3.

[97] Hassani R., Ansari R., and Rouhi H. "Large deformation analysis of 2D hyperelastic bodies based on the compressible nonlinear elasticity: A numerical variational method". In: *International Journal of Non-Linear Mechanics* 116 (Nov. 2019), pp. 39–54. ISSN: 0020-7462. DOI: 10.1016/j.ijnonlinmec.2019.05.003.

[98] Velayati H.R. and Kordkheili S.A.H. "A particular manner to observe free-edge effects in hybrid elastomer/composites plates". In: *Composites Part C: Open Access* 11 (July 2023), p. 100369. ISSN: 2666-6820. DOI: 10.1016/j.jcomc.2023.100369.

[99] Balzani D., Gruttmann F., and Schröder J. "Analysis of thin shells using anisotropic polyconvex energy densities". In: *Computer Methods in Applied Mechanics and Engineering* 197.9–12 (Feb. 2008), pp. 1015–1032. ISSN: 0045-7825. DOI: 10.1016/j.cma.2007.10.005.

[100] Firouzi N. and Żur K.K. "On the generalized nonlinear mechanics of compressible, incompressible, isotropic, and anisotropic hyperelastic membranes". In: *International Journal of Solids and Structures* 264 (Mar. 2023), p. 112088. ISSN: 0020-7683. DOI: 10.1016/j.ijsolstr.2022.112088.

[101] Hong W. "Inverse Lagrangian formulation for the deformation of hyperelastic solids". In: *Extreme Mechanics Letters* 9 (Dec. 2016), pp. 30–39. ISSN: 2352-4316. DOI: 10.1016/j.eml.2016.04.009.

[102] L:B. Da Veiga, Brezzi F., Marini L.D., and Russo A. "The virtual element method". In: *Acta Numerica* 32 (May 2023), pp. 123–202. ISSN: 1474-0508. DOI: 10.1017/s0962492922000095.

[103] Van Huyssteen D. and Reddy B.D. "A virtual element method for isotropic hyperelasticity". In: *Computer Methods in Applied Mechanics and Engineering* 367 (Aug. 2020), p. 113134. ISSN: 0045-7825. DOI: 10.1016/j.cma.2020.113134.

[104] Karabelas E., Haase G., Plank G., and Augustin C.M. "Versatile stabilized finite element formulations for nearly and fully incompressible solid mechanics". In: *Computational Mechanics* 65.1 (Sept. 2019), pp. 193–215. ISSN: 1432-0924. DOI: 10.1007/s00466-019-01760-w.

[105] Lejeunes S., Boukamel A., and Cochelin B. "Analysis of Laminated Rubber Bearings with a Numerical Reduction Model Method". In: *Archive of Applied Mechanics* 76.5–6 (June 2006), pp. 311–326. ISSN: 1432-0681. DOI: 10.1007/s00419-006-0030-z.

[106] Leonetti L. and Verhelst H.M. "A hierarchic isogeometric hyperelastic solid-shell". In: *Computational Mechanics* 74.3 (Mar. 2024), pp. 723–742. ISSN: 1432-0924. DOI: 10.1007/s00466-024-02452-w.

[107] Kiendl J., Hsu M.C., Wu M.C.H., and Reali A. "Isogeometric Kirchhoff–Love shell formulations for general hyperelastic materials". In: *Computer Methods in Applied Mechanics and Engineering* 291 (July 2015), pp. 280–303. ISSN: 0045-7825. DOI: 10.1016/j.cma.2015.03.010.

[108] Nitti A., Kiendl J., Gizzi A., Reali A., and De Tullio M.D. "A curvilinear isogeometric framework for the electromechanical activation of thin muscular tissues". In: *Computer Methods in Applied Mechanics and Engineering* 382 (Aug. 2021), p. 113877. ISSN: 0045-7825. DOI: 10.1016/j.cma.2021.113877.

[109] Schulte J., Dittmann M., Eugster S.R., Hesch S., Reinicke T., dell'Isola F., and Hesch C. "Isogeometric analysis of fiber reinforced composites using Kirchhoff–Love shell elements". In: *Computer Methods in Applied Mechanics and Engineering* 362 (Apr. 2020), p. 112845. ISSN: 0045-7825. DOI: 10.1016/j.cma.2020.112845.

[110] Hansy-Staudigl E., Krommer M., and Humer A. "A complete direct approach to nonlinear modeling of dielectric elastomer plates". In: *Acta Mechanica* 230.11 (Oct. 2019), pp. 3923–3943. ISSN: 1619-6937. DOI: 10.1007/s00707-019-02529-1.

[111] Humer A., Pechstein A.S., Meindlhumer M., and Krommer M. "Nonlinear electromechanical coupling in ferroelectric materials: large deformation and hysteresis". In: *Acta Mechanica* 231.6 (Apr. 2020), pp. 2521–2544. ISSN: 1619-6937. DOI: 10.1007/s00707-020-02657-z.

[112] Liu Z., McBride A., Ghosh A., Heltai L., Huang W., Yu T., Steinmann P., and Saxena P. "Computational instability analysis of inflated hyperelastic thin shells using subdivision surfaces". In: *Computational Mechanics* 73.2 (July 2023), pp. 257–276. ISSN: 1432-0924. DOI: 10.1007/s00466-023-02366-z.

[113] Pascon J.P. "Finite element analysis of functionally graded hyperelastic beams under plane stress". In: *Engineering with Computers* 36.4 (May 2019), pp. 1265–1288. ISSN: 1435-5663. DOI: 10.1007/s00366-019-00761-w.

[114] Pascon J.P. "Large deformation analysis of plane-stress hyperelastic problems via triangular membrane finite elements". In: *International Journal of Advanced Structural Engineering* 11.3 (Aug. 2019), pp. 331–350. ISSN: 2008-6695. DOI: 10.1007/s40091-019-00234-w.

[115] Nayyar V., Ravi-Chandar K., and Huang R. "Stretch-induced stress patterns and wrinkles in hyperelastic thin sheets". In: *International Journal of Solids and Structures* 48.25–26 (Dec. 2011, DOI: 10.1016/j.ijsolstr.2011.09.004), pp. 3471–3483. ISSN: 0020-7683. DOI: 10.1016/j.ijsolstr.2011.09.004.

[116] Dadgar-Rad F. and Sahraee S. "Large deformation analysis of fully incompressible hyperelastic curved beams". In: *Applied Mathematical Modelling* 93 (May 2021), pp. 89–100. ISSN: 0307-904X. DOI: 10.1016/j.apm.2020.12.001.

[117] Hu W., Wu C.T., and Koishi M. "A displacement-based nonlinear finite element formulation using meshfree-enriched triangular elements for the two-dimensional large deformation analysis of elastomers". In: *Finite Elements in Analysis and Design* 50 (Mar. 2012), pp. 161–172. ISSN: 0168-874X. DOI: 10.1016/j.finel.2011.09.007.

[118] Dadgar-Rad F. and Firouzi N. "Large deformation analysis of two-dimensional visco-hyperelastic beams and frames". In: *Archive of Applied Mechanics* 91.10 (June 2021), pp. 4279–4301. ISSN: 1432-0681. DOI: 10.1007/s00419-021-02008-x.

[119] Salamatova V.Y., Vassilevski Y.V., and Wang L. "Finite Element Models of Hyperelastic Materials Based on a New Strain Measure". In: *Differential Equations* 54.7 (July 2018), pp. 971–978. ISSN: 1608-3083. DOI: 10.1134/s0012266118070145.

[120] Firouzi N. and Amabili M. "Two-dimensional growth of incompressible and compressible soft biological tissues". In: *European Journal of Mechanics - A/Solids* 103 (Jan. 2024), p. 105150. ISSN: 0997-7538. DOI: 10.1016/j.euromechsol.2023.105150.

[121] Reese S., Raible T., and Wriggers P. "Finite element modelling of orthotropic material behaviour in pneumatic membranes". In: *International Journal of Solids and Structures* 38.52 (Dec. 2001), pp. 9525–9544. DOI: 10.1016/s0020-7683(01)00137-8.

[122] Suchocki C. "Finite element implementation of slightly compressible and incompressible first invariant-based hyperelasticity: theory, coding, exemplary problems". In: *Journal of Theoretical and Applied Mechanics* (July 2017), p. 787. ISSN: 1429-2955. DOI: 10.15632/jtam-pl.55.3.787.

[123] Kulikov G.M. and Plotnikova S.V. "On the second Piola-Kirchhoff and Cauchy stress tensors in nonlinear shells subjected to displacement-dependent loads". In: *Mechanics of Advanced Materials and Structures* 31.16 (Feb. 2023), pp. 3564–3582. ISSN: 1537-6532. DOI: 10.1080/15376494.2023.2180121.

[124] Kulikov G.M., Plotnikova S.V., and Mamontov A.A. "Assessment of second Piola–Kirchhoff and Cauchy stress tensors in finite rotation sandwich and laminated shells under non-conservative pressure loads". In: *Acta Mechanica* 235.7 (May 2024), pp. 4489–4513. ISSN: 1619-6937. DOI: 10.1007/s00707-024-03925-y.

[125] Amabili M. *Nonlinear Mechanics of Shells and Plates in Composite, Soft and Biological Materials*. Cambridge University Press, p. 582. ISBN: 9781107129221.

[126] Carrera E. "Theories and Finite Elements for Multilayered Plates and Shells: A Unified compact formulation with numerical assessment and benchmarking". In: *Archives of Computational Methods in Engineering* 10.3 (Sept. 2003), pp. 215–296. ISSN: 1886-1784. DOI: 10.1007/bf02736224.

[127] Carrera E. and Ciuffreda A. "A unified formulation to assess theories of multilayered plates for various bending problems". In: *Composite Structures* 69.3 (July 2005), pp. 271–293. ISSN: 0263-8223. DOI: 10.1016/j.compstruct.2004.07.003.

[128] Carrera E. and Petrolo M. "Guidelines and Recommendations to Construct Theories for Metallic and Composite Plates". In: *AIAA Journal* 48.12 (Dec. 2010), pp. 2852–2866. ISSN: 1533-385X. DOI: 10.2514/1.j050316.

[129] Carrera E., Cinefra M., Zappino E., and Petrolo M. *Finite Element Analysis of Structures Through Unified Formulation*. Wiley, Chichester, West Sussex, UK, 2014, July 2014. DOI: 10.1002/9781118536643.

[130] Pagani A. and Carrera E. "Unified formulation of geometrically nonlinear refined beam theories". In: *Mechanics of Advanced Materials and Structures* 25.1 (Sept. 2016), pp. 15–31. DOI: 10.1080/15376494.2016.1232458.

[131] Carrera E., Pagani A., and Augello R. "Large deflection and post-buckling of thin-walled structures by finite elements with node-dependent kinematics". In: *Acta Mechanica* 232.2 (Nov. 2020), pp. 591–617. ISSN: 1619-6937. DOI: 10.1007/s00707-020-02857-7.

[132] Wu B., Pagani A., Chen W. Q., and Carrera E. "Geometrically nonlinear refined shell theories by Carrera Unified Formulation". In: *Mechanics of Advanced Materials and Structures* (Dec. 2019), pp. 1–21. ISSN: 1537-6532. DOI: 10.1080/15376494.2019.1702237.

[133] Carrera E., Pagani A., and Augello R. "Evaluation of geometrically nonlinear effects due to large cross-sectional deformations of compact and shell-like structures". In: *Mechanics of Advanced Materials and Structures* 27.14 (Sept. 2018), pp. 1269–1277. ISSN: 1537-6532. DOI: 10.1080/15376494.2018.1507063.

[134] Pagani A., Carrera E., and Augello R. "Evaluation of Various Geometrical Nonlinearities in the Response of Beams and Shells". In: *AIAA Journal* 57.8 (Aug. 2019), pp. 3524–3533. ISSN: 1533-385X. DOI: 10.2514/1.j057877.

[135] Carrera E., Pagani A., Augello R., and Wu B. "Popular benchmarks of nonlinear shell analysis solved by 1D and 2D CUF-based finite elements". In: *Mechanics of Advanced Materials and Structures* 27.13 (Feb. 2020), pp. 1098–1109. DOI: 10.1080/15376494.2020.1728450.

[136] Carrera E., Pagani A., Giusa D., and Augello R. "Nonlinear analysis of thin-walled beams with highly deformable sections". In: *International Journal of Non-Linear Mechanics* 128 (Jan. 2021), p. 103613. ISSN: 0020-7462. DOI: 10.1016/j.ijnonlinmec.2020.103613.

[137] M. Filippi, A. Pagani, and E. Carrera. "Accurate Nonlinear Dynamics and Mode Aberration of Rotating Blades". In: *Journal of Applied Mechanics* 85.11 (July 2018). ISSN: 1528-9036. DOI: 10.1115/1.4040693.

[138] Filippi M., Azzara R., and Carrera E. "Rotordynamic analyses with variable-kinematic beam and shell finite elements". In: *Mechanics of Advanced Materials and Structures* 31.1 (Aug. 2023), pp. 45–57. ISSN: 1537-6532. DOI: 10.1080/15376494.2023.2246221.

[139] Azzara R., Filippi M., and Carrera E. "Geometrically nonlinear transient analyses of rotating structures through high-fidelity models". In: *Composite Structures* 343 (Sept. 2024), p. 118265. ISSN: 0263-8223. DOI: 10.1016/j.compstruct.2024.118265.

[140] Shen J., Arruda M.R., Pagani A., Carrera E., Zappino E., Augello R., and Petrolo M. "Node-Dependent Kinematics Approach for Damage Analysis of Reinforced Concrete Structures". In: *Journal of Structural Engineering* 151.8 (Aug. 2025). ISSN: 1943-541X. DOI: 10.1061/jsendh.steng-13729.

[141] Nagaraj M.H., Reiner J., Vaziri R., Carrera E., and Petrolo M. "Progressive damage analysis of composite structures using higher-order layer-wise elements". In: *Composites Part B: Engineering* 190 (June 2020), p. 107921. ISSN: 1359-8368. DOI: 10.1016/j.compositesb.2020.107921.

[142] Filippi M., Entezari A., and Carrera E. "Unified finite element approach for generalized coupled thermoelastic analysis of 3D beam-type structures, part 2: Numerical evaluations". In: *Journal of Thermal Stresses* 40.11 (July 2017), pp. 1402–1416. ISSN: 1521-074X. DOI: 10.1080/01495739.2017.1336741.

[143] Sánchez-Majano A.R., Masia R., Pagani A., and Carrera E. "Microscale thermo-elastic analysis of composite materials by high-order geometrically accurate finite elements". In: *Composite Structures* 300 (Nov. 2022), p. 116105. ISSN: 0263-8223. DOI: 10.1016/j.compstruct.2022.116105.

[144] Carrera E., Cinefra M., and Fazzolari F.A. "Some Results on Thermal Stress of Layered Plates and Shells by Using Unified Formulation". In: *Journal of Thermal Stresses* 36.6 (June 2013), pp. 589–625. ISSN: 1521-074X. DOI: 10.1080/01495739.2013.784122.

[145] Cinefra M., Valvano S., and Carrera E. "A layer-wise MITC9 finite element for the free-vibration analysis of plates with piezo-patches". In: *International Journal of Smart and Nano Materials* 6.2 (Apr. 2015), pp. 85–104. ISSN: 1947-542X. DOI: 10.1080/19475411.2015.1037377.

[146] Marsden J.E. and Hughes J.R.T. *Mathematical Foundations of Elasticity*. Dover, Englewood Cliffs, N.J., Prentice-Hall, 1983, p. 556. ISBN: 0486678652.

[147] Bonet J. and Wood R.D. *Nonlinear Continuum Mechanics for Finite Element Analysis*. Cambridge University Press, 2010. ISBN: 9780511755446.

[148] Crisfield M. A. *Non-Linear Finite Element Analysis of Solids and Structures*. Wiley, 1996, p. 362. ISBN: 9780471970590.

[149] Lanczos C. *The Variational Principles of Mechanics*. Dover Publications, 1986, p. 418. ISBN: 0486650677.

[150] Reddy J.N. *Energy and Variational Methods in Applied Mechanics. with an introduction to the finite element method*. Wiley, 1984, p. 545. ISBN: 047189673X.

[151] Simo J.C. and Hugher T.J.R. *Computational Inelasticity*. Springer-Verlag, New York, 1998, p. 392. ISBN: 0387975209.

[152] Landau L.D. and Lifsits E.M. *Fisica teorica*. Editori Riuniti Univ. Press, 2010. ISBN: 9788864732022.

[153] Sahraee S. and Wriggers P. *Tensor Calculus and Differential Geometry for Engineers: With Solved Exercises*. Springer Nature Switzerland, 2023. ISBN: 9783031339530. DOI: 10.1007/978-3-031-33953-0.

[154] Suchocki C. and Jemioło S. "Polyconvex hyperelastic modeling of rubberlike materials". In: *Journal of the Brazilian Society of Mechanical Sciences and Engineering* 43.7 (June 2021). ISSN: 1806-3691. DOI: 10.1007/s40430-021-03062-w.

[155] Rivlin R.S. "Objectivity of the constitutive equation for a material with memory". In: *International Journal of Solids and Structures* 27.3 (1991), pp. 395–397. ISSN: 0020-7683. DOI: 10.1016/0020-7683(91)90090-3.

[156] Bonet J., Gil A.J., and Wood R. *Nonlinear Solid Mechanics for Finite Element Analysis: Statics. Statics*. Cambridge University Press, 2016, p. 350. ISBN: 9781107115798.

[157] Flory P.J. "Thermodynamic relations for high elastic materials". In: *Transactions of the Faraday Society* 57 (1961), p. 829. DOI: 10.1039/tf9615700829.

[158] Euler L. "Methodus inveniendi lineas curvas maximi minimive proprietategaudentes sive solutio problematis isoperimetrici latissimo sensu accepti". In: *Vol. 1.Berlin, Germany: Springer Science & Business Media* (1952).

[159] Timoshenko S.P. "On the transverse vibrations of bars of uniform cross-section". In: *Philosophical Magazine, Vol. 43, pp. 125–131* (1922).

[160] Carrera E., Giunta G., and Petrolo M. *Beam Structures: Classical and Advanced Theories. Classical and Advanced Theories*. Wiley, Chichester, West Sussex, UK, 2011, p. 208. ISBN: 9781119951049.

[161] Wang C.M., Reddy J.N., and Lee K.H. *Shear Deformable Beams and Plates*. Ed. by Elsevier. Elsevier Science, 2000, p. 312. ISBN: 9780080437842.

[162] Kapania R.K. and Raciti R. "Recent advances in analysis of laminated beams and plates. Part I - Sheareffects and buckling." In: *AIAA Journal* 27.7 (July 1989), pp. 923–935. ISSN: 1533-385X. DOI: 10.2514/3.10202.

[163] Kapania R.K. and Raciti S. "Recent Advances in Analysis of Laminated Beams and Plates, Part II: Vibrations and Wave Propagation". In: *AIAA Journal* 27.7 (July 1989), pp. 935–946. ISSN: 1533-385X. DOI: 10.2514/3.59909.

[164] Giunta G., Biscani F., Belouettar S., and Carrera E. "Analysis of thin-walled beams via a one-dimentional unified formulation thorugh a Navier-type solution". In: *International Journal of Applied Mechanics* 03.03 (Sept. 2011), pp. 407–434. ISSN: 1758-826X. DOI: 10.1142/s1758825111001056.

[165] Carrera E. and Petrolo M. "On the Effectiveness of Higher-Order Terms in Refined Beam Theories". In: *Journal of Applied Mechanics* 78.2 (Nov. 2010). ISSN: 1528-9036. DOI: 10.1115/1.4002207.

[166] Carrera E., Pagani A., and Petrolo M. "Classical, Refined, and Component-Wise Analysis of Reinforced-Shell Wing Structures". In: *AIAA Journal* 51.5 (May 2013), pp. 1255–1268. ISSN: 1533-385X. DOI: 10.2514/1.j052331.

[167] Kirchhoff G. "Uber das Gleichgewicht und die Bewegung einer elastischen Scheibe". In: *Journal für die reine und angewandte Mathematik, Vol. 40,pp. 51–88.* (1850).

[168] Reissner E. "The Effect of Transverse Shear Deformation on the Bending of Elastic Plates". In: *Journal of Applied Mechanics* 12.2 (June 1945), A69–A77. ISSN: 1528-9036. DOI: 10.1115/1.4009435.

[169] Reddy J.N. "A general non-linear third-order theory of plates with moderate thickness". In: *International Journal of Non-Linear Mechanics* 25.6 (Jan. 1990), pp. 677–686. ISSN: 0020-7462. DOI: 10.1016/0020-7462(90)90006-u.

[170] Reddy J.N. and Liu C.F. "A higher-order shear deformation theory of laminated elastic shells". In: *International Journal of Engineering Science* 23.3 (Jan. 1985), pp. 319–330. ISSN: 0020-7225. DOI: 10.1016/0020-7225(85)90051-5.

[171] Naghdi P.M. "A survey of recet progress in the theory of elastic shells". In: *Applied Mechanics Review, Vol. 9, pp. 365-368* (1956).

[172] Reddy J.N. *Mechanics of Laminated Composite Plates and Shells Theory and Analysis, Second Edition. Theory and Analysis, Second Edition*. Taylor & Francis Group, 2003, p. 858. ISBN: 9780203502808.

[173] Jemielita G. "On Kinematical Assumptions of Refined Theories of Plates: A Survey". In: *Journal of Applied Mechanics* 57.4 (Dec. 1990), pp. 1088–1091. ISSN: 1528-9036. DOI: 10.1115/1.2897635.

[174] Reissner E. "A Consistent Treatment of Transverse Shear Deformations in Laminated Anisotropic Plates". In: *AIAA Journal* 10.5 (May 1972), pp. 716–718. ISSN: 1533-385X. DOI: 10.2514/3.50194.

[175] Carrera E. "Historical review of Zig-Zag theories for multilayered plates and shells". In: *Applied Mechanics Reviews* 56.3 (May 2003), pp. 287–308. ISSN: 2379-0407. DOI: 10.1115/1.1557614.

[176] Carrera E. "On the use of the Murakami's zig-zag function in the modeling of layered plates and shells". In: *Computers & Structures* 82.7–8 (Mar. 2004), pp. 541–554. ISSN: 0045-7949. DOI: 10.1016/j.compstruc.2004.02.006.

[177] Carrera E. "C_z^0 requirements—models for the two dimensional analysis of multilayered structures". In: *Composite Structures* 37.3–4 (Mar. 1997), pp. 373–383. ISSN: 0263-8223. DOI: 10.1016/s0263-8223(98)80005-6.

[178] Chiaia P., Pagani A., and Carrera E. "Large strain and 3D stress analysis of laminated fiber-reinforced soft material structures with high order beam finite elements". In: *Computers & Structures* 313 (June 2025), p. 107735. ISSN: 0045-7949. DOI: 10.1016/j.compstruc.2025.107735.

[179] Carrera E. "C_z^0 Reissner-Mindlin multilayered plate elements including Zig-Zag and interlaminar stress continuity". In: *International Journal for Numerical Methods in Engineering* 39.11 (June 1996), pp. 1797–1820. ISSN: 1097-0207. DOI: 10.1002/(sici)1097-0207(19960615)39:11<1797::aid-nme928>3.0.co;2-w.

[180] Carrera E. "Theories and finite elements for multilayered, anisotropic, composite plates and shells". In: *Archives of Computational Methods in Engineering* 9.2 (June 2002), pp. 87–140. ISSN: 1886-1784. DOI: 10.1007/bf02736649.

[181] Reddy J.N. *Mechanics of Laminated Composite Plates and Shells*. CRC Press, Nov. 2003. ISBN: 9780429210693. DOI: 10.1201/b12409.

[182] Carrera E. and Petrolo M. "Refined beam elements with only displacement variables and plate/shell capabilities". In: *Meccanica* 47.3 (Aug. 2011), pp. 537–556. ISSN: 1572-9648. DOI: 10.1007/s11012-011-9466-5.

[183] Carrera E., Maiarú M., and Petrolo M. "Component-wise analysis of laminated anisotropic composites". In: *International Journal of Solids and Structures* 49.13 (June 2012), pp. 1839–1851. ISSN: 0020-7683. DOI: 10.1016/j.ijsolstr.2012.03.025.

[184] Wu B., Pagani A., Filippi M., Chen W.Q., and Carrera E. "Large-deflection and post-buckling analyses of isotropic rectangular plates by Carrera Unified Formulation". In: *International Journal of Non-Linear Mechanics* 116 (Nov. 2019), pp. 18–31. ISSN: 0020-7462. DOI: 10.1016/j.ijnonlinmec.2019.05.004.

[185] Reddy J.N. *Introduction to Nonlinear Finite Element Analysis*. Oxford University Press, 2014. ISBN: 019852529X.

[186] Crisfield M.A. "An arc-length method including line searches and accelerations". In: *International Journal for Numerical Methods in Engineering* 19.9 (Sept. 1983), pp. 1269–1289. DOI: 10.1002/nme.1620190902.

[187] Carrera E. "A study on arc-length-type methods and their operation failures illustrated by a simple model". In: *Computers & Structures* 50.2 (Jan. 1994), pp. 217–229. ISSN: 0045-7949. DOI: 10.1016/0045-7949(94)90297-6.

[188] Pagani A., Chiaia P., and Carrera E. "Vibration of solid and thin-walled slender structures made of soft materials by high-order beam finite elements". In: *International Journal of Non-Linear Mechanics* 160 (Apr. 2024), p. 104634. ISSN: 0020-7462. DOI: 10.1016/j.ijnonlinmec.2023.104634.

[189] Carrera E., Pagani A., Azzara R., and Augello R. "Vibration of metallic and composite shells in geometrical nonlinear equilibrium states". In: *Thin-Walled Structures* 157 (Dec. 2020), p. 107131. ISSN: 0263-8231. DOI: 10.1016/j.tws.2020.107131.

[190] Batoz J.N. and Dhatt G. "Incremental displacement algorithms for nonlinear problems". In: *International Journal for Numerical Methods in Engineering* 14.8 (Jan. 1979), pp. 1262–1267. ISSN: 1097-0207. DOI: 10.1002/nme.1620140811.

[191] Pagani A. and Carrera E. "Unified one-dimensional finite element for the analysis of hyperelastic soft materials and structures". In: *Mechanics of Advanced Materials and Structures* 30.2 (Dec. 2021), pp. 342–355. ISSN: 1537-6532. DOI: 10.1080/15376494.2021.2013585.

[192] Smith M. *ABAQUS/Standard User's Manual, Version 6.9*. English. United States: Dassault Systèmes Simulia Corp, 2009.

[193] Liu H.Y. and Qiu L.C. "Three dimensional large deformation and fracture simulation of soft materials using non-ordinary state-based peridynamics with Mooney–Rivlin model". In: *Construction and Building Materials* 490 (Sept. 2025), p. 142574. ISSN: 0950-0618. DOI: 10.1016/j.conbuildmat.2025.142574.

[194] Carlos C.M. and Armando O. "Role of anisotropic invariants in numerically modeling soft biological tissues as transversely isotropic hyperelastic materials: A comparative study". In: *International Journal of Non-Linear Mechanics* 138 (Jan. 2022), p. 103833. DOI: 10.1016/j.ijnonlinmec.2021.103833.

[195] Beheshti A and Ansari R. "Finite element analysis of compressible transversely isotropic hyperelastic shells". In: *Acta Mechanica* (Mar. 2023). DOI: 10.1007/s00707-023-03536-z.

[196] Chiaia P., Pagani A., Cinefra M., and Carrera E. "Analysis of transversely isotropic compressible and nearly-incompressible soft material structures by high order unified finite elements". In: *Mechanics of Advanced Materials and Structures* (Nov. 2023), pp. 1–17. ISSN: 1537-6532. DOI: 10.1080/15376494.2023.2273962.

[197] Gasser T.C., Schulze-Bauer C.A.J., and Holzapfel G.A. "A Three-dimensional Finite Element Model for Arterial Clamping". In: *Journal of Biomechanical Engineering* 124.4 (July 2002), pp. 355–363. ISSN: 1528-8951. DOI: 10.1115/1.1485284.

[198] Roach M.R. and Burton A.C. "The reason for the shape of the distensibility curves of arteries". In: *Canadian Journal of Biochemistry and Physiology* 35.1 (Jan. 1957), pp. 681–690. ISSN: 0576-5544. DOI: 10.1139/y57-080.

[199] Fehervary H., Maes L., Vastmans J., Kloosterman G., and Famaey N. "How to implement user-defined fiber-reinforced hyperelastic materials in finite element software". In: *Journal of the Mechanical Behavior of Biomedical Materials* 110 (Oct. 2020), p. 103737. ISSN: 1751-6161. DOI: 10.1016/j.jmbbm.2020.103737.

[200] Leissa A.W. "On a curve veering aberration". In: *Zeitschrift für angewandte Mathematik und Physik ZAMP* 25.1 (Jan. 1974), pp. 99–111. ISSN: 1420-9039. DOI: 10.1007/bf01602113.

[201] Zappino E. and Carrera E. "Multidimensional Model for the Stress Analysis of Reinforced Shell Structures". In: *AIAA Journal* 56.4 (Apr. 2018), pp. 1647–1661. DOI: 10.2514/1.j056384.

[202] Azzara R., Carrera E., Chiaia P., Filippi M., Pagani A., Petrolo M., and Zappino E. "Geometrically nonlinear static analysis of multi-component structures through variable-kinematics finite elements". In: *Acta Mechanica* (Sept. 2024). ISSN: 1619-6937. DOI: 10.1007/s00707-024-04084-w.

[203] Zouari W., Hammadi F., and Ayad R. "Quadrilateral membrane finite elements with rotational DOFs for the analysis of geometrically linear and nonlinear plane problems". In: *Computers & Structures* 173 (Sept. 2016), pp. 139–149. ISSN: 0045-7949. DOI: 10.1016/j.compstruc.2016.06.004.

[204] Pagani A., Chiaia P., Filippi M., and Cinefra M. "Unified three-dimensional finite elements for large strain analysis of compressible and nearly incompressible solids". In: *Mechanics of Advanced Materials and Structures* (July 2023), pp. 1–21. DOI: 10.1080/15376494.2023.2229832.